Nanomagnetism and Spintronics

Edited by
Teruya Shinjo

Elsevier
The Boulevard, Langford Lane, Kidlington, Oxford OX5 1GB, UK
Radarweg 29, PO Box 211, 1000 AE Amsterdam, The Netherlands

First edition **2009**

British Library Cataloguing in Publication Data
A catalogue record for this book is available from the British Library

Library of Congress Cataloging-in-Publication Data
A catalog record for this book is available from the Library of Congress

For information on all Butterworth-Heinemann publications visit our web site at books.elsevier.com

Printed and bound in Great Britain
09 10 10 9 8 7 6 5 4 3 2 1

ISBN: **978-0-444-53114-8**

PREFACE

Permanent magnets have been known to exist in nature since antiquity and their behaviour has always been a matter of great interest. By the 19th century, the origin of magnetism had been investigated and the fundamental physical concepts underlying the phenomenon of magnetism had been understood to a considerable extent. In the 20th century, magnetism became a central feature in condensed matter physics and was the subjects of various theoretical and experimental studies. At the same time, remarkable progress was achieved in developing industrial applications of magnetism, and many kinds of magnetic materials were utilized for practical purposes. A characteristic feature of the study of magnetism is that theoretical and experimental studies are performed in tight collaboration. Another characteristic is that the gap between basic studies and the development of actual technical applications is rather small. The rapid development of magnetic recording technology can be cited as an example of the great success of the industrial application of magnetism. The modern hard-disk-drive system built in each computer, which is a typical magnetic device designed on the nanoscale, has been critical to the recent enhancement in computational capacity. Then, one might suppose that magnetism is already a too mature field to expect any more novel discoveries in the 21st century. However, this speculation is apparently wrong. If we look back at the progress in magnetism research, we see that many fruitful breakthroughs have appeared in a rather continuous manner. Hence, it is very probable that we will often meet something new in future studies on magnetism. A rapidly growing area in the study of magnetism is spintronics, which is the main subject of this book. State-of-the-art spintronics devices require nanoscale designs and fabrication techniques, thus making nanomagnetism an essential aspect of modern magnetism.

In the last quarter of the 20th century, the most outstanding breakthrough in the field of magnetism was the discovery of giant magnetoresistance (GMR) effect. In 1988, GMR effect was reported in Fe/Cr multilayers by Baibich et al. [Ref. [9] in Chapter 1], which was the first experiment to reveal that the electric conductance is significantly influenced by the spin structure, parallel or anti-parallel, even at room temperature. The discovery of GMR attracted great attention to the interaction between magnetism and transport phenomena and inspired many investigations into the role of spin in transport phenomena not only from the viewpoint of understanding the basic magnetism but also from the viewpoint of developing technical applications. By utilizing the GMR principle, magnetic recording heads were successfully fabricated rather soon after the discovery. Owing to the great impact of the discovery of GMR effect, the 2007 Nobel prize in physics was awarded to the discoverers of GMR, Albert Fert (France) and Peter Grünberg

(Germany). Nowadays the term spintronics is used to generally refer to the studies on the interplay between spin and transport.

This book consists of an overview in Chapter 1, followed by six chapters by 12 co-authors covering the various aspects of spintronics. Each chapter begins with a short introduction and main content covers the latest developments until 2008. I hope that this book will be useful to graduate students and those engaged in industrial research on nanomagnetism and spintronics. Finally, I would like to express my sincere gratitude to all the co-authors for their laborious cooperations.

Teruya Shinjo
January 2009

CHAPTER 1

Overview

Teruya Shinjo

Contents

Abstract

This overview is a brief introduction to the subjects covered by this book, nanomagnetism and spintronics. The discovery of giant magnetoresistance (GMR) effect is described together with a brief survey of the studies prior to the discovery of GMR. Studies on various kinds of magnetoresistance (MR) effect that were inspired by the GMR effect are reviewed and recent topics are introduced. In many novel phenomena involving the interplay of electric conductance and magnetization, the role of the "spin current" has been revealed to be important and the possibility for exploiting these phenomena in spintronics devices has been suggested. Nanostructured samples are indispensable to fundamental studies on spintronics and also to various technical devices, and therefore gaining an understanding of nanomagnetism is a crucial current issue. At the end of this chapter, the scope of this book is described with summarizing the content of each chapter.

Key Words: GMR effect, Magnetoresistance, Non-coupled GMR multilayers, Spin-valve, Spintronics, Nanomagnetism.

1. INTRODUCTION

An electron has two attributes, "charge" and "spin". The main aim of condensed matter physics is to understand the behaviour of electrons and for the most part, the subject is the charge of the electron. In contrast, magnetism originates from the other attribute, spin. Uncompensated electron spins are the reason why individual

International Institute for Advanced Studies, Kizu 619-0225, Japan

Nanomagnetism and Spintronics
DOI: 10.1016/B978-0-444-53114-8.00001-7

atoms possess local magnetic moments. If there is an exchange coupling between the magnetic moments of neighbouring atoms, a magnetic order on a macroscopic scale may form at low temperatures. If the sign of the coupling is positive, the magnetic moments are aligned parallel to each other (i.e. ferromagnetism) and if negative, anti-parallel to each other (i.e. anti-ferromagnetism). The critical temperature at which this magnetic order is lost is higher, if the coupling is stronger. The critical temperature of a ferromagnetic material is called the Curie temperature (T_c) and that of an anti-ferromagnetic material, the Nĕel temperature (T_N). Before the discovery of giant magnetoresistance (GMR), the investigations on the charges and spins of electrons were usually considered to be independent of each other and little attention was paid to the correlation between these two attributes: charge and spin.

Magnetoresistance (MR) is a term widely used to mean the change in the electric conductivity due to the presence of a magnetic field. A variety of MR effects are known and their characteristics depend on the material. Namely, MR effects in metallic, semiconducting and insulating materials have different characteristics. Ferromagnetic materials with metallic conductance exhibit the anisotropic magnetoresistance (AMR) effect, that is, the dependence of conductance on the relative angle between the electric current and magnetization. Normally the resistance is smaller if the electric current flows in a direction perpendicular to the direction of magnetization than parallel. AMR is regarded to originate from spin–orbit interactions. The change of resistance (MR ratio) due to the AMR effect is fairly small, a few percent for $Ni_{80}Fe_{20}$ alloy (permalloy) at room temperature, but this phenomenon is very useful in technical applications, for instance in sensors. Before the discovery of GMR, the construction of read-out heads utilizing the AMR effect for magnetic storage devices had already been planned. The principle of magnetic recording is as follows: Data are stored by nanoscale magnets in a recording medium (disc or tape) and the direction of magnetization of individual regions on the medium corresponds to one bit. To read out the data, a sensor (i.e. read-out head) must detect very small magnetic fields straying on the surface of the recording medium. Compared with a conventional coil head, a head using the MR effect (i.e. MR head) can be much smaller and has the advantage of being able to convert magnetically stored data directly into electric signals. High-density recording can be realized by reducing the size of each memory region and by enhancing the sensitivity of the detecting head. For ultra-high-density recording, a much larger MR ratio than that possible with the AMR effect is necessary but a search for new materials having a large MR ratio at room temperature appeared to be futile. Some magnetic semiconductors have been found to exhibit very large MR ratios but their Curie temperatures are lower than room temperature and they require excessively large magnetic fields, making them unsuitable for technical applications.

There have been a number of resistance measurements on ferromagnetic thin films and small resistance change was generally observed in the vicinity of the magnetization reversal field. In the process of magnetization reversal, domain walls are formed and the spin directions in the domain wall are deviated from the easy direction. Then, a change in resistance is expected owing to the AMR effect. On the other hand, a non-collinear spin structure that forms in the reversal process

can serve as an electron scattering centre and eventually the resistance is increased. In practice, an increase in resistance at the magnetization reversal is often observed in the case of ferromagnetic amorphous alloy films with perpendicular magnetization. From such results, it was recognized that the spin structure has an influence on conductance, but still not much attention was paid to these phenomena since the observed MR anomalies were not satisfactorily large. Velu *et al.* [1] studied the behaviours of metallic sandwich systems with the structure, non-magnetic/magnetic/non-magnetic layers. The design of their sample was [Au 30 nm/Co 0.3 nm/Au 30 nm]. They observed an increase in resistance during magnetization reversal: 6% at 4 K and 1% at 300 K, respectively. The obtained MR ratio was not remarkably large. However if the Co layer thickness is taken into account, which is only a few atomic layers and is much smaller than the total thickness of the Au layers, the contribution of the magnetic structure change to the total conductance is considerably large.

During 1980s, multilayers with artificial superstructures were actively investigated [2, 3]. Because of the progress in thin film preparation techniques, it became possible to deposit two or more elements alternately in order to construct artificially designed periodic structures with nanoscale wavelengths. Such artificial superstructured multilayers are new materials that do not exist in nature and can therefore be expected to possess novel physical properties. Multilayers were fabricated by combining various metallic elements and their superconducting, magnetic and lattice dynamical properties have been investigated. Resistance measurements also were performed on magnetic multilayers, for example, Au/Co superlattices, but the observed MR effect was not significantly large [4]. This was because the role of interlayer coupling was not yet properly taken into consideration. It was suggested that noticeable enhancement in the MR effect was not induced by a superlattice effect or an interface effect of multilayers.

2. DISCOVERY OF GMR

Grünberg and his group [5] were investigating the magnetic properties of Fe/Cr/Fe sandwich systems. They measured the magnetic behaviour of the two Fe layers by changing the thickness of Cr spacer layers. Initially, the main aim of their experiment was to clarify the role of the Cr layer inserted in between Fe layers. If an ultra-thin Cr layer has an anti-ferromagnetic spin structure analogous to that of bulk Cr, the relative spin directions of the two outermost atom layers should change from parallel to anti-parallel, depending on the number of atomic layers in the Cr layer (odd or even). As the number of atomic Cr layers is increased, the interlayer coupling between Fe layers should alternate in a layer-by-layer fashion. In other words, the sign of the interlayer coupling should oscillate between plus and minus, with every additional atomic Cr layer. However, the observed result was somewhat different from the naïve speculation. The magneto-optic Kerr effect and spin-polarized electron diffraction measurements suggested that there exists a rather strong anti-ferromagnetic exchange interaction between Fe layers separated by a Cr spacer layer when the Cr layer thickness is around 1 nm [6, 7].

That is, the magnetizations in the two Fe layers are spontaneously oriented anti-parallel to each other and are aligned parallel if the external field is enough large. Binasch *et al.* [8] measured also the resistance of Fe/Cr/Fe sandwich films and found that the resistance in the anti-parallel alignment is larger than that in the parallel alignment. This clearly evidences that the conductance is influenced by the magnetic structure and thus the physical principle of the GMR effect was demonstrated in such sandwich structures. However, the observed MR ratio, about 1.5%, was not large enough to have a significant impact.

Really "giant" magnetoresistance was first observed in Fe/Cr multilayers by the group of Fert in 1988 [9]. They were interested in the curious behaviour of the interlayer coupling in the Fe/Cr/Fe structure found by Grünberg *et al.* [5] and intended to visualize the role of interlayer coupling in a multilayered structure. They have prepared epitaxial Fe(0 0 1)/Cr(0 0 1) multilayers with the typical structure [Fe(3 nm)/Cr(0.9 nm)] $\times$ 60 and systematically measured the magnetic properties including magnetoresistance. The magnetization curves indicated that the remanent magnetization is zero and ferromagnetic saturation occurs at magnetic fields higher than 2 T. These features correspond to the existence of rather strong anti-ferromagnetic interlayer coupling. Surprising results were obtained in the measurements of resistance under external fields. The resistance decreased with an increase in the applied field and was almost a half at the saturation field at 4 K (see Fig. 10 in Chapter 2). The MR ratio was nearly 20% even at room temperature, a strikingly large value at that time for a metallic substance. This fantastic discovery was first reported very briefly at the International Conference on Magnetism (ICM at Paris, 1988) as an additional part of a paper. The surprising MR data were quite new and therefore not yet mentioned in the rěsumě of the conference. A great discovery is often obtained as an unexpected observation.

The results of this GMR experiment confirmed the existence of a strong anti-ferromagnetic interlayer coupling between Fe layers separated by a Cr spacer layer. The mechanism of the GMR was phenomenologically explained rather soon after the discovery by considering the spin-dependent scattering of conduction electrons. The scattering probability for conduction electrons at the interface of the ferromagnetic layer should depend on the spin direction, up or down. For instance, an up-spin electron is considered to penetrate without scattering from a Cr layer into an Fe layer with magnetization in the up-spin direction, while a down-spin electron is scattered. If the Fe layers have anti-parallel magnetic structure, both up- and down-spin electrons soon meet an Fe layer having a magnetization in the opposite direction (within two Fe layers' distance) and accordingly the possibility of scattering is rather high for both types of electrons. In contrast, if all the Fe layers have parallel magnetizations, down-spin electrons are scattered at every Fe layer whereas up-spin electrons can move across long distance, without scattering. In other words, up-spin electrons will have a long mean-free path but down-spin electrons have a very short mean-free path. Total conductance of the system is the sum of that by up-spin electrons and by down-spin electrons. Because of the long mean-free path of up-spin electrons, the total resistance is much smaller in the state with parallel magnetizations than in the anti-parallel state. A comprehensive explanation of the GMR effect is presented by Inoue in Chapter 2.

The GMR experiment brought two key issues to the fore: interlayer coupling and spin-dependent scattering. Although interlayer coupling was reported in the Fe/Cr/Fe sandwich system and later in Co/Cu multilayers by Cebollada *et al.* [10], before the discovery of GMR, it was hard to image a multilayered structure with anti-parallel magnetizations, that is, "giant anti-ferromagnet". By applying an external field, the giant anti-ferromagnet can be converted into ferromagnetic. The GMR effect is the difference in conductance between these two states. In general, very large magnetic fields are necessary to change an intrinsic anti-ferromagnetic spin structure into ferromagnetic. In contrast, in the case of multilayers, the anti-parallel structure (giant anti-ferromagnet) generated by interlayer coupling can be turned into a parallel structure (ferromagnetically saturated structure) by a moderate magnetic field. This is the key behind the discovery of GMR, which seems to be the first successful experiment to utilize spin structure manipulation. The anti-parallel alignment of Fe layers' magnetizations at zero field and the reorientation into parallel alignment by an increase in the external field were confirmed by neutron diffraction technique for Fe/Cr multilayers [11]. A magnetic diffraction peak corresponding to the twice of the adjacent Fe layer distance was observed, which indicates that the direction of magnetization alternates at every adjacent Fe layer. This is clear evidence for the formation of a giant anti-ferromagnetic arrangement in an Fe/Cr multilayer. The mechanism behind GMR is thus attributed to the change in the internal magnetic structure. This is apparently different from that of AMR, which is induced by a directional change of the total magnetization.

The behaviour of Cr spacer layers sandwiched between ferromagnetic Fe layers has been extensively studied by Grünberg *et al.* and also many other groups, using sandwich films and multilayers. The dependence of the interlayer coupling on the Cr layer thickness has been examined in detail. For a systematic experiment on thickness dependence, a sample with a wedge-shaped spacer layer is very useful [12]. A wedge layer is prepared by slowly sliding the shutter during the film deposition to effect a variation in thickness from zero to some 10 nm over a macroscopic length. To study the interlayer coupling, sandwich samples with a wedge-shaped spacer layer are prepared. Then, by applying Kerr rotation technique, the magnetic hysteresis curves at confined regions are measured. This method became very fashionable and was utilized not only for Fe/Cr/Fe structure but also for many metallic elements. Bulk Cr metal is known to have peculiar anti-ferromagnetic properties and the spin structure of ultra-thin Cr layers is very complicated, being not satisfactorily understood even today. Although many studies have been performed on the interlayer coupling, the relation between the interlayer coupling and the intrinsic anti-ferromagnetism of Cr metal is not fully accounted for and the effect of this anti-ferromagnetism is usually neglected in discussions on the GMR properties of Fe/Cr systems.

The discovery of GMR effect in Fe/Cr multilayers inspired various experiments on interlayer coupling in many other metals aiming to explore the nature of the MR effect in other elements. The existence of interlayer coupling was confirmed in many non-magnetic metals, making it clear that the interlayer coupling does not originate from the intrinsic magnetic properties of the spacer layer.

If the interlayer coupling is anti-ferromagnetic, the GMR effect is almost always observed, that is, the resistance in anti-ferromagnetic state is larger than that in ferromagnetic state. In the study of Co/Cu multilayers, a striking result was obtained: the interlayer coupling across the Cu layer oscillates with variations in its thickness [13, 14]. Because the MR effect is caused by anti-ferromagnetic interlayer coupling, the MR measurement can be utilized as a tool to clarify that the sign of the interlayer coupling is negative. In the plot of the MR ratio as a function of Cu layer thickness, peaks of MR ratio were found to appear periodically with an interval of about 1 nm. Parkin *et al.* prepared multilayers combining Co and various non-magnetic metals, and found that the oscillation of interlayer coupling occurs rather generally with a wavelength of 1–1.5 nm [15, 16]. The oscillation of the interlayer coupling was an amazing result and was the subject of many subsequent investigations. In the case of simple normal metals, the oscillatory feature was accounted for by considering the band structure and a relation with the quantum well state has been argued. Thus, through the studies on the oscillatory interlayer coupling behaviour, our understanding of the electronic structure of thin metal film has been significantly advanced. About 10 years after the discovery of GMR witnessed a boom in studies on interlayer coupling but scientific progress in more recent years has not been remarkable. This book does not include a chapter on interlayer coupling. See other publications [17, 18] for review articles on interlayer coupling studies.

3. DEVELOPMENT OF GMR STUDIES

The GMR effect is the result of change in the magnetic structure, between anti-parallel and parallel alignments. In the cases of Fe/Cr and Co/C multilayers, the anti-parallel configuration that originates from the anti-ferromagnetic interlayer exchange coupling is converted into ferromagnetic configuration by an externally applied field. The magnitude of the external field necessary for this conversion is determined by the strength of the interlayer coupling. Because of the strong interlayer coupling, the magnetic field required to induce the MR effect in Fe/Cr multilayers is significantly large (about 2 T). In the case of Co/Cu system, the coupling is somewhat weaker and the necessary field smaller. Nevertheless, the saturation field value is too high for the MR effect to be exploited in technical applications such as magnetic recording sensors.

Another type of GMR was demonstrated in 1990, by using non-coupled multilayer samples [19]. Multilayers comprising two magnetic elements were prepared by successively stacking NiFe (3 nm), Cu (5 nm), Co (3 nm) and Cu (5 nm) layers. Since the Cu spacer layer is not very thin, the interlayer coupling between the NiFe and Co layers is negligibly small and their magnetizations are independent. NiFe is a typical soft magnetic material but Co is magnetically rather hard. Owing to the small coercive force of the NiFe layer compared with that of the Co layer, the magnetization of the NiFe layer changes direction much earlier than that of the Co layer. Thus, an anti-parallel alignment of magnetizations is realized when the external field is increasing (and also when it is decreasing). This is not due to

interlayer coupling but because of the difference in coercive forces. A remarkable enhancement in resistance (i.e. GMR) was observed in the field region for this induced anti-ferromagnetic configuration. The experimental results are presented in the next chapter (Fig. 12 in Chapter 2). This demonstration of non-coupled GMR confirms that the interlayer coupling has no direct influence on the MR properties. In other words, GMR and interlayer coupling are independent issues. For these non-coupled multilayers as well, the establishment of an anti-parallel magnetic structure was confirmed by using the neutron diffraction method [20]. Non-coupled GMR multilayers can serve as a model system for fundamental research, with several advantages, for instance, the fact that the spin structure is easily manipulated. A survey of the basic studies on non-coupled GMR multilayers is presented elsewhere [21]. A feature of non-coupled GMR, that is very important from a technical point of view, is the high sensitivity to external field. The resistance change occurs at weak fields if the soft magnetic component has a sufficiently small coercive force. Since NiFe is a typical soft magnetic material, the MR effect in a multilayer including NiFe component can show a high sensitivity under fields on the order of 10 Oe.

The potential for the use of the GMR effect in technical applications was revealed in the result of studies on non-coupled multilayers. A practical application of GMR effect for magnetic recording heads was achieved by using non-coupled type sandwich films with only two magnetic components. At nearly the same time as the studies on non-coupled type GMR multilayers, Dieny *et al.* [22] published a paper on a non-coupled GMR sandwich system that was named the "spin valve". The initial design of the spin-valve structure was NiFe(15 nm)/Cu(2.6 nm)/NiFe(15 nm)/FeMn(10 nm). There are two ferromagnetic NiFe layers and an anti-ferromagnetic FeMn layer is attached to one of the NiFe layers to increase the required coercive force via the exchange anisotropy. The other NiFe layer behaves freely as a soft magnet. Therefore, the two NiFe layers are called the "pinned" and "free" layers, respectively. Because of the ease in controlling the magnetic properties, the spin-valve system was adopted for commercial magnetic recording heads. Although the initial spin-valve structure was very simple, various kinds of improvements were attempted promptly soon after. To enhance the coercive force of the pinned layer, a simple anti-ferromagnetic layer (FeMn) used originally was replaced by a complicated structure combined with an anti-ferromagnet (MnPt) and a synthetic anti-ferromagnetic layer. An example of a synthetic anti-ferromagnet is FeCo/Ru/FeCo, which acts as a powerful magnetic anchor due to the strong interlayer coupling across the Ru layer. Because the large surface magnetic moments are essentially important for spin-dependent scattering, surfaces of both free and pinned layers were covered by ultra-thin FeCo layers with a few atom layers thick, which are supposed to have a large magnetic moment. Concerning the material for the spacer layer, Cu seems to be the best choice and has always been used. At the beginning, sandwich systems did not show such large MR values as multilayer systems. However, remarkable improvements were achieved within a short time and fairly large MR ratios were realized in refined spin-valve systems. Perhaps the improvement in quality from a crystallographic viewpoint was one of the keys to this success. There are

many ideas for further progress: the introduction of reflective layers (ultra-thin oxide layers) on each surface, which will reflect the conduction electrons without energy loss, and the insertion of a nano-oxide layer with many microscopic holes in the spacer layer, which may be useful to collimate the electron path. A number of industrial research groups joined in the competition for the GMR head business and consequently various trials were performed.

Eventually the MR ratio of the spin-valve system has been increased satisfactorily for commercial purposes. Within 10 years from the discovery, the GMR principle has been successfully exploited in commercial magnetic recording technology. The commercial products called spin-valve or GMR head have greatly contributed to the progress of magnetic recording technology as shown in Fig. 1. The progress of recording technology is typically expressed by the increase in recording density. The GMR head was integral to the recent increase from 10 Mbit to 1 Tbit/sqi. The industrial application of the new GMR phenomenon was realized in such a short interval because the application of AMR effect in a similar manner was just in progress. It is interesting to note that although interlayer

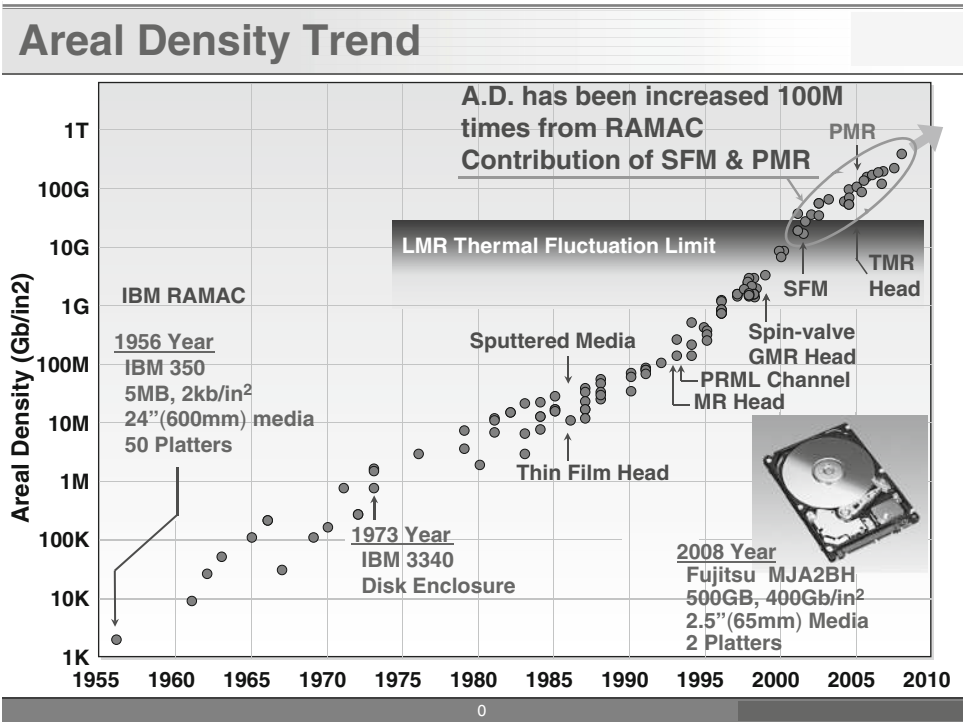

FIGURE 1 Progress of magnetic recording technology: density of recording (bit per square inch) versus year (by courtesy of Fujitsu Ltd). SFM and PMR mean synthetic anti-ferromagnetism and perpendicular magnetic recording, respectively. Thermal fluctuation limit indicates the highest attainable boundary for recording density, due to superparamagnetism, supposed before the appearance of GMR, TMR, SFM and PMR.

coupling and multilayer structure were key conditions for the discovery of the GMR effect, commercial spin-valve heads have neither a periodic multilayered structure nor anti-ferromagnetic interlayer coupling through a spacer layer. As a matter of fact, a strong anti-ferromagnetic interlayer coupling through Ru layer is utilized in the structure of the pinned layer but the magnetic coupling between pinned and free magnetic layers through a Cu spacer layer is negligibly small. On the other hand, initially the spin-valve structure started with only a few layers but today's improved spin valve is actually a multilayer consisting of more than 10 layers. A similar trend is seen in the case of recording media materials for magnetic data storage. Namely, the magnetic substance on a recent hard disk is a multilayer consisting of more than 10 different layers with nanoscale thicknesses. Spin-valve heads and hard disk media indicate that multilayers with artificial nanoscale designs are prototypical advanced functional materials.

4. FURTHER PROGRESS IN MR EXPERIMENTS

How to enhance the MR effect is an attractive challenge for scientists in fundamental physics and also for researchers in industries. The GMR effect has been observed in multilayers and sandwich samples in many combinations of magnetic and non-magnetic metallic elements but concerning the magnitude of MR ratio, eventually Fe/Cr and Co/Cu seem to be the optimum selections. There are many reports for the investigations to use compounds (e.g. oxides or semiconductors) as magnetic constituents in GMR systems. In some investigations, considerably large MR ratios were obtained at low temperatures but those at room temperature were fairly small.

There can be several strategies to search larger GMR effects as the following: (1) taking the CPP geometry, (2) using the tunnelling current, (3) using half-metal as the magnetic constituent and (4) using the ballistic current. Usually resistance measurements for thin metallic specimens are carried out in a conventional geometry to use an electric current flowing in the film plane. Such configuration is called the CIP (with current in the plane) geometry. In contrast, resistance measurements in the other geometry, the CPP (with current perpendicular to the plane), are very inconvenient for thin metallic films. An enhancement of MR ratio is, however, expected in the CPP geometry compared with the CIP geometry because the GMR effect is a phenomenon for the electrons passing through interfaces. Before the discovery of GMR, it was not expected that any remarkable effect may happen in the CIP geometry. Fortunately, this naïve speculation was not correct and significantly large MR effect has been obtained in the CIP geometry, even at room temperature. However if measurements in the CPP geometry are available, further enhancement of MR ratio is obtainable. The first measurement on extremely small resistance of GMR systems in the CPP geometry has been attempted by Pratt *et al.* [23], using superconducting electrodes, and an apparent increase of MR ratio at low temperatures was observed. To avoid the inconvenience in the measurements on a too small resistance in the CPP geometry, the application of nanofabrication technique is worthwhile for metallic GMR systems.

Gijs *et al*. [24] have prepared micro-column samples of GMR system for the first time and confirmed the enhancement of MR ratio in the CPP geometry at room temperature. Experiments in the CPP geometry are important not only for the purpose to enhance the MR ratio but also to investigate the mechanism of spin-dependent scattering. In the case of the CPP geometry, the electric current is regarded to be constant in the sample, while the current in the CIP geometry is not homogeneous and the estimation of current density distribution is a hard job. It is therefore difficult to argue quantitatively the spin-dependent scattering probability from CIP experimental results. The discovery of GMR has revealed that fortunately the MR effect in the CIP geometry is not too small at room temperature and subsequently commercial products for recording heads could be prepared using the principle of GMR in the CIP geometry. However, CPP-GMR has a definite potential for further enhancement of the MR ratio. The low resistivity of CPP systems may be a merit from a viewpoint of application. Therefore, further extension of CPP-MR studies is awaited. CPP experiments have evidenced that the application of nanoscale fabrication techniques is very crucial for the further progress of material sciences.

Recently, remarkable advance has been achieved in MR experiments using tunnelling current (tunnelling magnetoresistance, TMR). Basically, the sample structure for TMR measurements is very simple; two magnetic electrodes are separated by an insulating barrier and the difference of conductance in the states of parallel and anti-parallel magnetizations is measured. Since the TMR is a phenomenon for the electrons passing through the barrier, the geometry of measurement is equal to CPP-GMR. Trials to use a tunnelling current were already initiated in 1975 by Julliere [25] and in 1982 by Maekawa and Gäfvert [26], and were followed by several groups. But observation of perceivable MR effect was very difficult and the reproducibility was poor, because at that time it was difficult to prepare ultra-thin tunnelling barriers without pinhole. The preparation techniques for thin oxide films have progressed in the 1990s, in relation with the flourishing of high T_c superconducting oxide research. Inspired by the success of GMR measurements, attempts for TMR have revived and outstanding breakthrough was obtained in 1996 [27, 28]. Miyazaki and Tezuka prepared three-layer junctions, Fe/Al_2O_3/Fe, and observed MR ratio of 30% at 4 K and 18% at 300 K. Afterwards many groups joined in active research on TMR. Nowadays the size of TMR samples is very small, being prepared by nanoscale fabrication, and such samples with very limited area have an advantage that the possibility of pinhole is relatively less. Thus, it has become rather easy to obtain large MR ratio at room temperature reproducibly. More recently, a remarkable progress was achieved by using MgO as the tunnelling barrier instead of Al_2O_3 [29, 30]. Yuasa *et al*. prepared FeCo/MgO/FeCo junctions using epitaxially grown MgO layers as tunnelling barriers, and observed such enormous MR ratios as 200% at 300 K and 400% at 4 K. The application of TMR effect with such very large MR ratios into commercial recording heads has already started and TMR heads have become the successor of GMR heads. In the case of TMR also, the initial sample structure was a simple three-layer structure but the actual structure of recent TMR heads is a sophisticated multilayer, similar to that of spin-valve heads.

The theoretical background of TMR phenomena is given in Chapter 2 by Inoue. The geometry of TMR is analogous to CPP-GMR and the conductance is determined by the spin polarization at the interface of ferromagnet. If the spin polarizations of two ferromagnets are P_1 and P_2, the MR ratio is expected to be $2P_1P_2/(1 - P_1P_2)$. Therefore, to utilize a half-metal as the electrodes in a TMR system is an attractive approach because a ferromagnetic metal with a larger polarization can make a larger MR ratio. The definition of half-metal is that only one kind of spin exists at the Fermi level owing to a big spin splitting of the energy band, and only up spins participate in the tunnelling conduction. From band calculation, certain metallic compounds such as Heusler alloys are regarded as examples of half-metal. Some successful results of TMR experiments utilizing Heusler alloys are introduced also in Chapter 2. It is therefore confirmed that a half-metal is efficient to enhance the TMR effect and infinitively large MR ratio may be realized if rigorously 100% half-metal is available. For the further extension of spintronics, it is an urgent issue to establish the technique to create a current with a full spin polarization (i.e. an ideal spin current source).

5. THE SCOPE OF THIS BOOK

This book is organized by six chapters following this overview. The fundamental knowledge on up-to-date topics relating to nanomagnetism and spintronics is presented here. The authors for the seven chapters are Japanese and French who are actively involved in the current investigations. Chapter 2 described by Inoue is an introduction to spin-dependent transport in ferromagnetic metallic systems and the theoretical backgrounds for GMR, TMR and other magnetoresistance effects are explained. Recent development of spin Hall effect studies also is briefly mentioned. This chapter will be useful as a text for students who begin to study physics on magnetotransport phenomena in ferromagnetic metallic materials. The main subject of Chapter 3 by Suzuki, Tulapurkar and Chappert is the spin injection of which studies are recently progressing remarkably. Novel phenomena induced by the spin torque transferred by electric current, such as current-induced magnetization switching and spin-torque diode effect, in GMR and TMR junctions are described. Basic physical concepts and feasibility for application are argued. In Chapter 4, Ono and Shinjo explain experimental results on magnetic domain wall motion in ferromagnetic nanowires. Dynamical properties of magnetic vortex core in ferromagnetic nanodot systems are also introduced. Theoretical aspects of domain wall motion induced by electric current are discussed by Kohno and Tatara in Chapter 5. Studies on dynamical behaviour of magnetic domain wall with micro-magnetic simulation are presented in Chapter 6 by Thiaville and Nakatani. Finally in Chapter 7, Ohno and Matsukura survey recent developments on ferromagnetic III–V compound semiconductors, typically Mn-substituted GaAs. Their electric and magnetic properties are surveyed and novel phenomena relating to spintronics, such as current-induced domain wall motion and electric field control of ferromagnetic phase are introduced.

Although the title of this book is nanomagnetism, there is no section for the traditional issues on nanoscale magnetic clusters. From a long time ago, magnetic properties of clusters (with limited number of atoms) have been of great interests from theoretical and experimental points of view, but the progress in recent years is not remarkable. In industrial applications, on the other hand, such as magnetic recording technology, the size of magnetic elements becomes smaller and smaller, down to the scale of a few nm. Therefore, it is very crucial to understand the influence of interface atom layer and size reduction on local magnetic moment, anisotropy and dynamical characteristics. An example of computational simulation for nanoscale ferromagnetic clusters was recently reported by Entel *et al.* [31]. Comprehensive studies using large-scale computers will give us useful guidance for further development of spintronic studies. Here is no chapter describing spintronic properties of compounds such as perovskite oxides [32], carbon nanotubes and graphenes, and organic molecules, although they may become key players for future spintronic devices.

This book is not able to cover whole relevant areas of nanomagnetism and spintronics. However, the author hopes that this book will be useful for the readers to recognize the significance of this field. It is certain that the field, nanomagnetism and spintronics, will continue to grow.

In this chapter, the author introduced a part of his investigation carried out at Kyoto University where he has served for 36 years. He would like to express his gratitude for the collaborators.

REFERENCES

[1] Velu, E., Dupas, C., Renard, D., Renard, J. P., and Seiden, J. (1988). *Phys. Rev. B* **37**, 668.
[2] Shinjo, T., and Takada, T. (eds.) (1987). *In* "Metallic Superlattices". Elsevier, Amsterdam.
[3] Shinjo, T. (1991). *Surf. Sci. Rep.* **12**, 49.
[4] Takahata, T., Araki, S., and Shinjo, T. (1989). *J. Magn. Magn. Mater.* **82**, 287.
[5] Grünberg, P., Schreiber, R., Pang, Y., Brodsky, M. B., and Sowers, H. (1986). *Phys. Rev. Lett.* **57**, 2442.
[6] Saurenbach, F., Walz, U., Hinchey, L., Grünberg, P., and Zinn, W. (1988). *J. Appl. Phys.* **63**, 3473.
[7] Carbone, C., and Alvarado, S. F. (1987). *Phys. Rev. B* **39**, 2433.
[8] Binasch, G., Grünberg, P., Saurenbach, F., and Zinn, W. (1989). *Phys. Rev. B* **39**, 4828.
[9] Baibich, M. N., Broto, J. M., Fert, A., Nguyen Van Dau, F., Etienne, P., Creuzet, G., Friederich, A., and Chazelas, J. (1988). *Phys. Rev. Lett.* **61**, 2472.
[10] Cebollada, A., Martinez, J. L., Gallego, J. M., de Miguel, J. J., Miranda, R., Ferrer, S., Batallan, F., Fillion, G., and Rebouillat, J. P. (1989). *Phys. Rev. B* **39**, 9726.
[11] Hosoito, N., Araki, S., Mibu, K., and Shinjo, T. (1990). *J. Phys. Soc. Jpn.* **59**, 1925.
[12] Ungaris, J., Celotta, R. J., and Pierce, D. T. (1991). *Phys. Rev. Lett.* **67**, 140.
[13] Mosca, D. H., Petroff, F., Fert, A., Schroeder, P. A., Pratt, W. P. Jr., and Loloee, R. (1991). *J. Magn. Magn. Mater.* **94**, 1.
[14] Parkin, S. S. P., Bhadra, R., and Roche, K. P. (1991). *Phys. Rev. Lett.* **66**, 2152.
[15] Parkin, S. S. P., More, N., and Roche, K. P. (1990). *Phys. Rev. Lett.* **64**, 2304.
[16] Parkin, S. S. P. (1991). *Phys. Rev. Lett.* **67**, 3598.
[17] Hartmann, U. (ed.) (1999). *In* "Magnetic Multilayers and Giant Magnetoresistance". Springer, Berlin.
[18] Mills, D. L., and Bland, J. A. C. (eds.) (2006). *In* "Nanomagnetism, Ultrathin Films, Multilayers and Nanostructures". Elsevier, New York.

[19] Shinjo, T., and Yamamoto, H. (1990). *J. Phys. Soc. Jpn.* **59**, 3061.
[20] Hosoito, N., Ono, T., Yamamoto, H., Shinjo, T., and Endoh, Y. (1995). *J. Phys. Soc. Jpn.* **64**, 581.
[21] Maekawa, S., and Shinjo, T. (eds.) (2002). *In* "Spin Transport in Magnetic Nanostructures". Taylor & Francis, London.
[22] Dieny, B., Speriosu, V. S., Parkin, S. S. P., Gurney, B. A., Wilhoit, D. R., and Mauri, D. (1991). *Phys. Rev. B* **43**, 1297.
[23] Pratt, W. P. Jr., Lee, S. F., Slaughter, J. M., Loloee, R., Schroeder, P. A., and Bass, J. (1991). *Phys. Rev. Lett.* **66**, 3060.
[24] Gijs, M. A. M., Lenczowski, S. K. J., and Giesbers, J. B. (1993). *Phys. Rev. Lett.* **70**, 3343. A review article for CPP GMR studies is, Gijs, M. A. M., and Bauer, G. E. W., (1997) *Adv. Phys.* **46,** 235.
[25] Julliere, M. (1975). *Phys. Lett. A* **54**, 225.
[26] Maekawa, S., and Gäfvert, U. (1982). *IEEE Trans. Magn.* **18**, 707.
[27] Tezuka, N., and Miyazaki, T. (1996). *J. Appl. Phys.* **79**, 6262.
[28] Moodera, J. S., and Kinder, L. B. (1996). *J. Appl. Phys.* **79**, 4724.
[29] Yuasa, S., Nagahama, T., Fukushima, A., Suzuki, Y., and Ando, K. (2004). *Nat. Mater.* **3**, 868.
[30] Parkin, S. S. P., Kaiser, C., Panchula, A., Rice, P. M., Hughes, B., Samant, M., and Yang, S. H. (2004). *Nat. Mater.* **3**, 862.
[31] Entel, P., Grunner, M. E., Rollmann, G., Hucht, A., Sahoo, S., Zayak, A. T., Herper, H. C., and Dannenberg, A. (2008). *Philos. Mag.* **88**, 2725.
[32] A recent review article on perovskite manganites, for instance, is: Tokura, Y. (2006). *Rep. Prog. Phys.* **69**, 797.

CHAPTER 2

GMR, TMR and BMR

Jun-ichiro Inoue

Contents

Department of Applied Physics, Nagoya University, Nagoya 464-8603, Japan

Nanomagnetism and Spintronics
DOI: 10.1016/B978-0-444-53114-8.00002-9

Abstract

Novel magnetotransport phenomena appear when magnet sizes become nanoscale. Typical examples of such phenomena are giant magnetoresistance (GMR) in magnetic multilayers, tunnel magnetoresistance (TMR) in ferromagnetic tunnel junctions and ballistic magnetoresistance (BMR) in magnetic nanocontacts. In this chapter, we first briefly review the relationship between spin-dependent resistivity and electronic structures in metals and alloys, and describe microscopic methods for investigating electrical transport. We then review the essential aspects of GMR, TMR and BMR, emphasizing the role of the electronic structures of the constituent metals of these junctions and the effects of roughness on the electrical resistivity (or resistance). The important factors that control GMR are shown to be the spin-dependent random potential at interfaces and band matching/mismatching between magnetic and non-magnetic layers. For TMR, several factors are shown to be important in determining the MR ratio, including the shape of the Fermi surface of the electrodes, the symmetry of the wave functions, electron scattering at interfaces and spin-slip tunnelling. An interpretation of TMR in Fe/MgO/Fe and of an oscillation of TMR is presented. TMR in granular films and in the Coulomb-blockade regime is also described.

We further give brief explanation for other MR effects, normal MR, anisotropic MR (AMR) and colossal MR (CMR) to clarify the essential difference between these MRs: GMR, TMR and BMR. Interesting transport properties, anomalous and spin Hall effects originated from the spin–orbit interaction are also introduced briefly.

Key Words: GMR, TMR, BMR, Two-current model, Spin-dependent resistivity, α-Parameter, CIP-GMR, CPP-GMR, Granular TMR, MR ratio, Interface roughness, Multilayers, Ferromagnetic tunnel junctions, Fe/MgO/Fe, Ferromagnetic nanocontact, Spin polarization, Half-metals, Coulomb blockade, Normal MR, AMR, CMR, Spin–orbit interaction, AHE, SHE, Inverse SHE, Spin accumulation, Kubo formula, Recursive Green's function method, Conductance quantization.

1. INTRODUCTION

The magnetism of materials [1] is carried by electron spin, while electrical transport is caused by the motion of electron charge. While these two fundamental properties of solids have been well known for many centuries, the electron and

spin were not discovered until the beginning of the twentieth century [2, 3]. The fields of magnetism and electrical transport have developed almost independently. However, as the fabrication techniques of micro- and nanoscale samples have progressed rapidly, the field of spin electronics or spintronics has been developed, where the coupling of electron spin and charge plays an important role. In paramagnets, the number of up- and down-spin electrons is the same and no effect of spin appears in the electrical transport. However, the difference in the number of up- and down-spin electrons in ferromagnets causes complex properties in which magnetism effects electrical transport and vice versa. For example, the control of spins by an electric field and the control of electrical current by a magnetic field are fundamental issues in the field of spintronics.

The fundamental properties of spintronics are closely related to the length scale L characteristic of samples and to the motion of electrons in metals. There are several length scales that characterize the properties of electrons in metals.

The z-component of spin s_z takes one of two values $\pm 1/2$ and is not necessarily conserved, that is, it is time dependent due to such effects as the spin–orbit interaction (SOI) and interactions between electrons. Therefore, the length for which the spin of an electron is conserved is finite. This length is called the spin-flip mean free path and typically takes values in the range 10^2 nm–10^1 μm. Due to scattering of electrons, the length an electron travels with a fixed spin direction is much shorter than the spin-flip mean free path. This length is called the spin-diffusion length λ_{spin}. To find the spin-polarized current in non-magnetic metals it is necessary that the system length L be much shorter than λ_{spin}.

In ferromagnetic metals, due to the imbalance between the number of electrons with up and down spins, the current may be spin polarized. Because the electrical resistivity is governed by the mean free path ℓ, which characterizes the scattering process of electrons, it is necessary that $\ell \ll \lambda_{\mathrm{spin}}$ in order that the spin polarization of the current be meaningful. When this condition is satisfied, the spin polarization of the current is well defined and the up- and down-spin electrons may be treated independently. This is called Mott's two-current model [4]. When the condition is satisfied, the two-current model holds even in systems for which $L \gg \lambda_{\mathrm{spin}}$.

Another important length scale is the Fermi wave length λ_{F}, which characterizes the electronic states. In general, $\ell \gg \lambda_{\mathrm{F}}$. This length scale becomes important when interference occurs between wave functions of electrons. The velocity of electrons on the Fermi surface is given by the Fermi velocity v_{F} and hence the time scale for an electron with v_{F} travelling a distance ℓ is given by $\tau = \ell / v_{\mathrm{F}}$, the relaxation time.

As mentioned above, progress in nanofabrication techniques has made it possible to create artificial structures such as magnetic multilayers and nanocontacts, the characteristic scale length L of which can be shorter than λ_{spin} or ℓ and can even be close to λ_{F}. In these cases, novel transport phenomena occur; giant magnetoresistance (GMR), tunnel magnetoresistance (TMR) and ballistic magnetoresistance (BMR) are typical examples. GMR occurs when the layer thickness of magnetic multilayers is close to or shorter than ℓ. BMR occurs when the scale of the contact region of two ferromagnets is close to λ_{F}. TMR is a phenomenon in which the overlap of wave functions of electrons in two separated ferromagnetic metals becomes small.

In this chapter, we first review the spin dependence of electrical resistivity in metals and alloys and explain the phenomena of GMR, TMR and BMR. Theoretical methods to calculate the conductivity or conductance will be presented in Section 3, though the reader may skip pass this section and move directly to the section on magnetoresistive properties.

GMR, TMR and BMR appear in multilayers, tunnel junctions magnetic nanocontact, respectively. The magnetoresistive phenomena also appear in bulk systems. Typical examples are normal MR in normal metals and semiconductors, anisotropic MR (AMR) in transition metals and alloys and colossal MR (CMR) in manganites. To clarify the essential difference between these MRs, we will give a brief explanation of normal MR, AMR and CMR in Section 7.

SOI, which is responsible to AMR, gives rise to other interesting transport properties such as anomalous Hall effect (AHE) and spin Hall effect (SHE) which recently attract much interests in both technological aspect and fundamental physics. Since SOI is a coupling of spin and orbital motion of electrons, current control of spin and magnetic control of charge via SOI are possible. This is the reason that SOI attracts much interests in the technological aspect. Therefore, we introduce AHE and SHE in Section 7, in addition to a spin accumulation caused by SOI in the non-equilibrium state.

Other aspects on the spin-dependent transport and may be found in several textbooks and review articles [5–16]. Electronic and magnetic properties of solids may be found, for example, in Harrison's [17] and Chikazumi's textbook [18].

2. SPIN-DEPENDENT TRANSPORT IN FERROMAGNETIC METALS

One of the most important requirements for magnetoresistance (MR) in nanoscale ferromagnets is spin dependence of the electrical resistivity. In this section, we review spin-dependent resistivity (or conductivity) in ferromagnetic bulk metals and alloys, emphasizing the role of the electronic states on the resistivity at low temperatures.

2.1. Electronic states and magnetism in transition metals and alloys

Few ferromagnetic materials are composed of a single element. The exceptions are the transition metals (TMs), such as Fe, Co and Ni, and rare earth metals. This is in marked contrast to superconductivity, which appears in many pure metals. In rare earth metals, electrons responsible for transport and magnetism can be distinguished. However, this distinction is not clear in TMs, that is, both s- and d-electrons contribute to transport and magnetism. A high Curie temperature is another characteristic of TM ferromagnets.

The electronic structure of TMs consists of mainly s- and d-orbitals. The relative position of the Fermi level E_F to the s- and d-states depends on the material, that is, the number of s + d electrons per atom. Figure 1 shows the schematic density of states (DOS) of the typical TMs Cr, Fe and Co, and the DOS of Cu. The electronic states are composed of wide s-bands and narrow d-bands. The d-part of the DOS is high because the d-states are localized near atoms. The s- and d-states hybridize to form complicated electronic states.

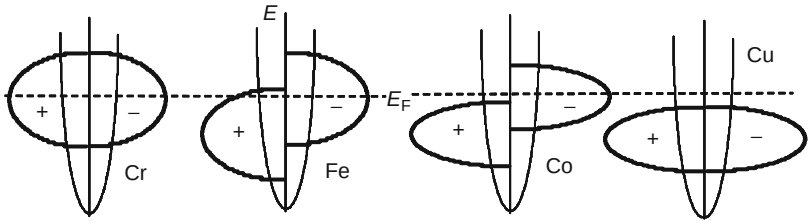

FIGURE 1 Schematic density of states (DOS) of Cr, Fe, Co and Cu. + and − indicate majority and minority spin states, respectively, identical to up (↑) and down (↓) spin, respectively, in uniformly magnetized materials.

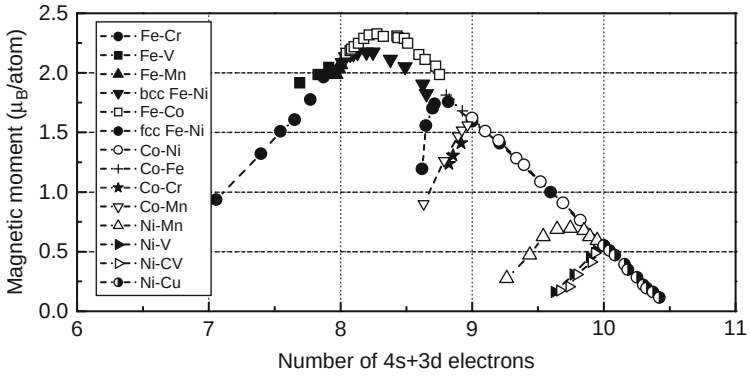

FIGURE 2 Slater–Pauling curve [19].

The electronic structures shown in Fig. 1 for TMs give rise to the characteristic features of both magnetism and electrical transport. A typical example of the former is the Slater–Pauling curve of the magnetization of TM alloys, as shown in Fig. 2 [19–22]. The linear part of the slope with 45° may be easily understood by changing the filling of the DOS with electrons. The branches deviating from the main curves can be explained only by introducing changes in the DOS due to random impurity potentials.

As mentioned above, the two-current model for electrical transport holds well in TMs and their alloys. Hence, the electrical resistivity depends on spin in ferromagnetic metals and alloys. The spin dependence of the resistivity is governed by the spin dependence of the electronic states near the Fermi level, and by spin-dependent impurity potentials in ferromagnetic alloys. We will review the spin-dependent resistivity in detail in the next section.

2.2. α-parameter

The simplest formula for the electrical conductivity σ is given by the Drude formula:

$$\sigma = \frac{e^2 n \tau}{m}, \tag{1}$$

where e, n, τ and m are the electrical charge, carrier density, lifetime and effective mass of carrier electrons, respectively. For ferromagnets, the spin dependence of these quantities must be taken into account in the Drude formula, since the electronic states of ferromagnets are spin polarized due to the number of up ($\uparrow$) and down ($\downarrow$) spin electrons not being compensated. Basically, n, m and τ are all spin dependent. Most important is the spin dependence of the lifetime, since it affects electron scattering most strongly.

The lifetime is related to the mean free path ℓ via the relation $\ell = v_F\tau$, where v_F is the Fermi velocity. For typical ferromagnetic metals, ℓ is much shorter that the spin-diffusion length λ_{spin}, and therefore the spins of the carrier electrons are well conserved in the time scale τ. In this case, $\uparrow$ and $\downarrow$ spin electrons can be treated independently in evaluating the electrical conductivity, that is, $\sigma = \sum_s \sigma_s$ with $s = \uparrow$ or $\downarrow$. This assumption is the Mott's two-current model.

Although Mott's two-current model explains the experimental results of electrical resistivity in ferromagnetic metals, it is rather difficult to confirm the model directly by experiment, since $\sigma_\uparrow$ and $\sigma_\downarrow$ cannot be separated independently from the σ data. However, Fert and Campbell [23, 24] have approached the problem by measuring the residual resistivity and temperature dependence for various binary and ternary alloys and succeeded in deducing the ratio $\rho_\downarrow/\rho_\uparrow$ ($=\sigma_\uparrow/\sigma_\downarrow$) for diluted alloys of Fe, Co and Ni metals.

The ratio is referred to as the α-parameter. α-parameters for TM impurities in Fe are presented in Fig. 3. We can see that α-parameter strongly depends on the species of the impurity atoms. In the next sections, we show how the material dependence of the α-parameter is related to the electronic states of ferromagnets.

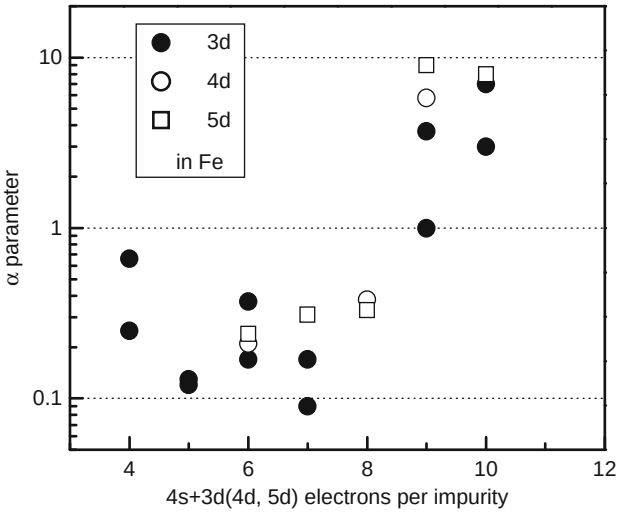

FIGURE 3 Experimental values of α-parameters for 3d, 4d and 5d TM impurities in Fe [23, 24].

2.3. Spin-dependent resistivity in TM alloys

The spin dependence of τ caused by impurity scattering of electrons in ferromagnetic metals may be evaluated by using the formula

$$\tau_s^{-1} = (2\pi/\hbar) N_i V_s^2 D_s(E_F), \tag{2}$$

which is given by the Born approximation, where N_i, V_s and D_s (E_F) are the impurity density, scattering potential and DOS at the Fermi energy E_F, respectively. Here, both V_s and $D_s(E)$ are spin ($s = \uparrow$ or $\downarrow$) dependent. Equation (2) indicates that the lifetime becomes short as the scattering potential becomes large and the number of final states of the scattering process increases.

Let us consider TM impurities in Fe. The impurities give rise to a spin-dependent potential V_s in Fe even when the impurity is non-magnetic, since the DOS $D_s(E)$ of Fe is spin dependent. Since $D_\uparrow(E_F) \sim D_\downarrow(E_F)$ for ferromagnetic Fe, the spin dependence of the lifetime is caused mainly by V_s.

The magnitude of V_s may be evaluated crudely by assuming that the DOS of TM impurities are unchanged from the bulk case and that the number of d-electrons and magnetic moment impurities are also unchanged from those of the bulk state. The latter assumption may be validated from the charge neutrality condition and from neutron diffraction measurements of local moments in ferromagnetic alloys. On the other hand, the former assumption is believed to be truly crude.

Under these assumptions, V_s is given by the relative shift of the d-level of impurities with respect to that of Fe, since the Fermi level (or the chemical potential) for TM impurities and Fe metal should coincide. The values of $\Delta V_{\xi s} = V_{\xi s} - V_{Fe0}$ thus determined are shown in Fig. 4 [25]. Here ξ indicates the atomic species of the impurities and V_{Fe0} is the d-level of paramagnetic Fe.

From this figure, we can see that $|V_{Fe\downarrow}| \simeq |V_{Cr}|$ and $|V_{Fe\uparrow}| \gg |V_{Cr}|$, where the spin suffix of V_{Cr} is omitted since Cr is assumed to be non-magnetic in Fe. The results indicate that the band matching between Fe and Cr is quite good for the $\downarrow$ spin state, while it is rather poor for the $\uparrow$ spin state. Schematic shapes of the DOS for Cr, Fe, Co and Cu with a common Fermi level are shown in Fig. 1. The results deduced above may be easily understood from the relative positions of the d-DOS.

Since $\Delta V_{\xi s}$ is simply V_s in the Drude formula, we find $\rho_\uparrow \gg \rho_\downarrow$ for Cr impurities in Fe metal. This is in good agreement with the α-parameters shown in Fig. 3. The present crude estimate of V_s may be validated by first-principles calculations, which give the same results for the spin-dependent resistivity for Cr impurities in Fe. A detailed study of the residual resistivity in the first-principles method has been presented by Mertig [26]. The study reproduces the experimental trends of the spin-dependent residual resistivity in Fe, Co and Ni.

2.4. Spin-dependent resistivity due to ferromagnetic impurities in novel metals

The residual resistivity due to TM impurities in metals is well described by the Anderson model [27]. The lifetime in this model is given as

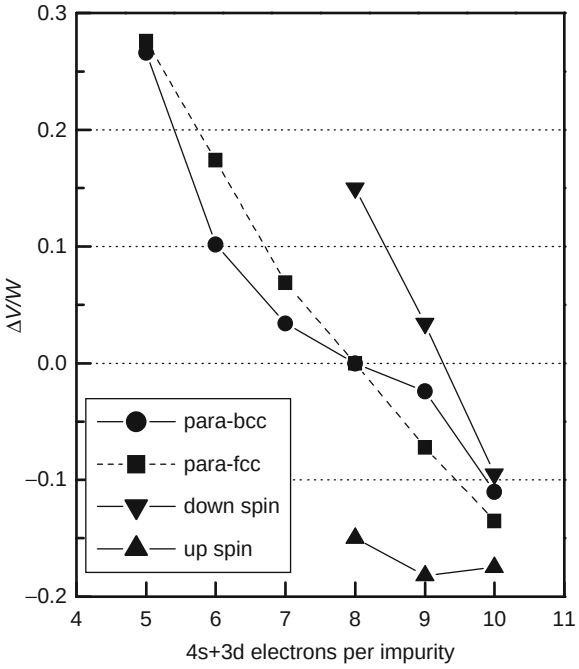

FIGURE 4 Calculated spin-dependent impurity potentials in Fe. The potentials are measured from the potential of paramagnetic Fe. *W* indicates the effective bandwidth of the 3d-bands [25].

$$\tau_s^{-1} = 5(2\pi/\hbar)N_i V_{sd}^2 D_{ds}(E_F), \tag{3}$$

where V_{sd} represents s–d mixing between the conduction state and localized d-states of impurities, and $D_{ds}(E_F)$ is the DOS of impurities at E_F with spin s. The factor 5 comes from the degeneracy of the d-states of TM impurities.

Equation (3) is similar to Eq. (2) with V_s and D_s replaced by V_{sd} and D_{ds}. This is to be expected since the conduction electrons (s-electrons) are scattered into d-states via s–d mixing. It should be noted, however, that $D_{ds}(E)$ is not a bare DOS of the impurity d-states, but rather is a renormalized DOS broadened due to s–d mixing. Figure 5 shows the schematic shape of the DOS of V, Cr, Fe and Ni impurities in a free-electron band. First-principles band calculations also show an electronic structure of TM impurities similar to those shown in the figure [28].

Despite its simplicity, the Anderson model satisfactorily explains the tendency of the residual resistivity caused by TM impurities, in Cu for example. Experimental and theoretical results are shown in Fig. 6 [29]. The horizontal axis of this figure is the number of 4s + 3d electrons n per atom. $n = 5$, 6, 8 and 10 correspond to V, Cr, Fe and Ni, respectively. Since the DOS of Ni impurities is almost occupied, $D_{ds}(E_F)$ is too low to be exchange split. Therefore, the residual resistivity is spin-independent and small for Ni impurities. Fe impurities, on the other hand, are magnetized and the DOS is exchange split, as shown in Fig. 5. Because E_F is located near the peak of $D_{d\downarrow}(E)$, the residual resistivity becomes large. For Cr

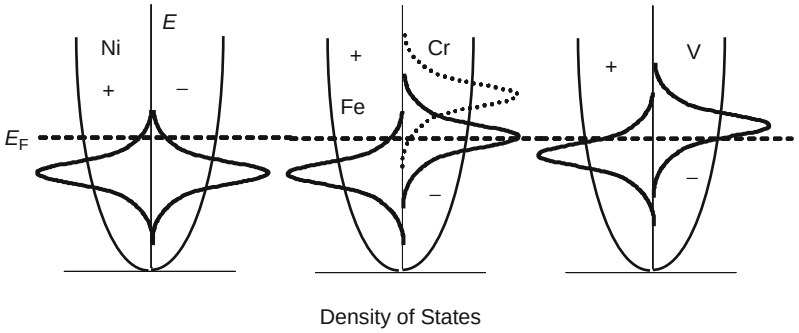

FIGURE 5 Density of states of Ni, Fe, Cr and V impurities in Cu. The + spin state of Cr impurities is the same as that of Fe impurities.

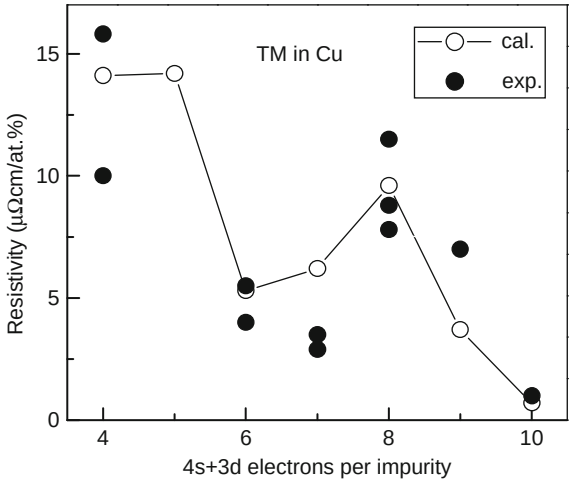

FIGURE 6 Calculated (open circles) and experimental (filled circles) values of residual resistively caused by TM impurities in Cu [29].

impurities, $D_{d\downarrow}(E)$ shifts to higher energy, while $D_{d\uparrow}(E)$ remains unshifted, E_F is located in a low $D_{d\downarrow}(E)$ region. As a result, the resistivity due to Cr impurities is smaller than that for Fe impurities. The resistivity becomes large again for V impurities, since $D_{d\downarrow}(E)$ also shifts to higher energy.

The interpretation of the residual resistivity for TM impurities in Cu gives $\rho_\downarrow/\rho_\uparrow \gg 1$ for Fe impurities and $\rho_\downarrow/\rho_\uparrow \ll 1$ for V impurities. The results are also consistent with the material dependence of the α-parameter.

2.5. Two-band model

The material dependence of the α-parameter $\rho_\downarrow/\rho_\uparrow$ given by experiments (Fig. 3) and that estimated theoretically for TM impurities in Fe and in Cu may be understood by adopting a two-band model [30]. The model consists

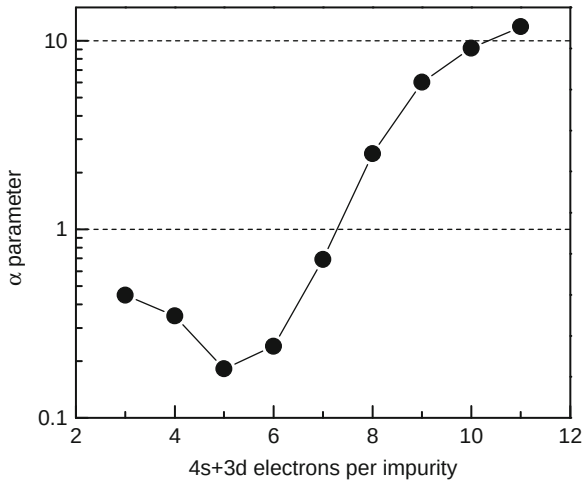

FIGURE 7 Calculated α-parameters for TM and noble metal impurities in Fe (as an example host metal) as a function of the number of 4s + 3d electrons of the impurities [30].

of a broad s-like band and narrow d-like bands with a mixing between the s- and d-bands.

Taking Fe as the host metal for example, the electronic state of TM–Fe alloys may be given by a random distribution of d-levels ϵ_{TM} and ϵ_{Fe} of the TM and Fe atoms, respectively. By applying the coherent potential approximation [31–34] to the random distribution of d-levels, one may calculate the DOS and electrical resistivity of TM–Fe alloys.

The spin dependence of the residual resistively $\rho_{\downarrow}/\rho_{\uparrow}$ thus calculated is shown in Fig. 7 as a function of the number of 4s + 3d electrons per atom. The results reproduce the experimental tendency rather well. The calculated results can be easily understood in terms of matching/mismatching of the d-electronic states between impurities and host atoms.

For Ag impurities ($n = 11$) in Fe, the matching of the $\uparrow$ spin state is good, resulting in $\rho_{\downarrow}/\rho_{\uparrow} \gg 1$, while for Cr impurities band matching is better for $\downarrow$ spin bands, and therefore $\rho_{\downarrow}/\rho_{\uparrow} \ll 1$, as shown in Fig. 7.

3. MICROSCOPIC THEORY OF ELECTRICAL CONDUCTIVITY: LINEAR RESPONSE THEORY

In this section, we describe linear response theory and its application to layered structures. In the theory, the conductivity is given as a current–current correlation function, since the conductivity is the response of a current to an external electric field which drives the motion of the electrons. The correlation function is calculated for electronic states in the equilibrium state. That is, the fluctuation–dissipation relation in the equilibrium state determines the response of the electrical charge to the external field. In the following, we give formulations for

conductivity with current parallel and perpendicular to layer planes. Readers not concerned with the details of the theoretical framework may skip this section and jump to the sections on GMR, TMR and BMR.

In this section, we assume that Mott's two-current model holds and omit the spin suffixes. The basic model used is the tight-binding model with isotropic δ-function-type impurity potentials. General formalism of the Green's function used below, and theory of the electrical transport may be found in several textbooks [35, 36].

3.1. Kubo formula

Applying the one-electron approximation to the general expression of the linear response theory [37], we obtain the so-called Kubo–Greenwood formula for electrical conductivity:

$$\sigma = \frac{\pi\hbar}{\Omega}\mathrm{Tr}[\mathcal{J}\delta(E_\mathrm{F} - \mathcal{H})\mathcal{J}\delta(E_\mathrm{F} - \mathcal{H})], \tag{4}$$

where $\mathcal{H}$ is the Hamiltonian and $\mathcal{J}$ is the corresponding current operator. The two δ-functions in the equation represent current conservation and the response of the electrons on the Fermi surface to the electric field. Using the Green's function $\mathcal{G}^{\mathrm{R(A)}}(E)$, defined as

$$\mathcal{G}^{\mathrm{R(A)}}(E) = [E + (-)\mathrm{i}\eta - \mathcal{H}]^{-1}, \tag{5}$$

$$\mathcal{G}^{\mathrm{R(A)}}(E) = P[E - \mathcal{H}]^{-1} - (+)\mathrm{i}\pi\delta(E - \mathcal{H}), \tag{6}$$

the δ-functions are expressed in terms of the imaginary part of the Green's function, where R and A indicates the retarded and advanced Green's functions, respectively. The conductivity is thus expressed as

$$\sigma = \frac{\hbar}{\pi\Omega}\mathrm{Tr}\left[\mathcal{J}\left\{\mathcal{G}^\mathrm{A} - \mathcal{G}^\mathrm{R}\right\}\mathcal{J}\left\{\mathcal{G}^\mathrm{A} - \mathcal{G}^\mathrm{R}\right\}\right], \tag{7}$$

where E_F in the Green's function is omitted.

There are two methods for practical calculations of the conductivity using the expression given above. One is to adopt suitable approximations in the calculation of the conductivity and the other is to simulate the conductivity numerically for finite size systems with leads. In the following, we demonstrate the methods of calculation of the conductivity or conductance of multilayers adopting a Hamiltonian with random potentials:

$$\mathcal{H} = \mathcal{H}_0 + V, \tag{8}$$

where V indicates the random potentials.

3.2. Current parallel to planes

When the current flows parallel to the planes of the multilayers, the electrical conductivity can be calculated semi-analytically. This is because the system exhibits translational invariance parallel to the planes and momentum conservation

holds along this direction. In the formulation, the Green's function should first be evaluated, averaged statistically over the impurity distribution. We denote the average of the quantity A as $\langle A \rangle$. As a result of averaging, the self-energy due to electron scattering by the impurity potential V is introduced. The averaged Green's functions are expressed as

$$\tilde{\mathcal{G}}^{\mathrm{R(A)}}(E) = \langle (E + (-)\mathrm{i}\eta - \mathcal{H})^{-1} \rangle, \tag{9}$$

$$= \left(E + (-)\mathrm{i}\eta - \mathcal{H}_0 - \Sigma^{\mathrm{R(A)}} \right)^{-1}. \tag{10}$$

The self-energy Σ depends on both energy and momentum, in general. The simplest method to evaluate the self-energy is the Born approximation. In this approximation, it is given as $\Sigma^{\mathrm{R(A)}} = \langle V \mathcal{G}_0^{\mathrm{R(A)}} V \rangle$, where $\mathcal{G}_0^{\mathrm{R(A)}} = (E + (-)\mathrm{i}\eta - \mathcal{H}_0)^{-1}$, with an infinitesimally small real number η. When the magnitude of the impurity potential is large, the coherent potential approximation (CPA) is useful.

The statistical average for the electrical conductivity should be taken such that

$$\sigma = \frac{\hbar}{\pi \Omega} \mathrm{Tr} \langle \mathcal{J} \{ \mathcal{G}^{\mathrm{A}} - \mathcal{G}^{\mathrm{R}} \} \mathcal{J} \{ \mathcal{G}^{\mathrm{A}} - \mathcal{G}^{\mathrm{R}} \} \rangle. \tag{11}$$

We note that $\langle \mathcal{J}\mathcal{G}\mathcal{J}\mathcal{G} \rangle = \mathcal{J} \langle \mathcal{G}\mathcal{J}\mathcal{G} \rangle \neq \mathcal{J}\tilde{\mathcal{G}}\mathcal{J}\tilde{\mathcal{G}}$. Since the current operator does not account for the randomness caused by impurity potentials, the first equality holds. However, the average of the product of two Green's functions is not a product of two averaged Green's functions. Therefore, we must evaluate $\mathcal{J} \langle \mathcal{G}\mathcal{J}\mathcal{G} \rangle - \mathcal{J}\tilde{\mathcal{G}}\mathcal{J}\tilde{\mathcal{G}}$ correctly. We call this correction the "vertex correction" to the conductivity. Current conservation is satisfied when the vertex correction is evaluated self-consistently in the determination of the self-energy Σ. Since the imaginary part of the self-energy corresponds to the lifetime, the conductivity may diverge when Green's functions are used without the self-energy.

In the following, we consider a simple cubic lattice with isotropic δ-function-type impurity potentials. In this case, the vertex correction vanishes since the correct operator is odd in the momentum space. The current operator is a product of the electrical charge e and electron velocity along the current direction, that is, $\mathcal{J}_x = ev_x$. Since the velocity vector is the momentum derivative of the energy, we obtain

$$\mathcal{J}_x = e \frac{1}{\hbar} \frac{\partial E(\boldsymbol{k}_\parallel)}{\partial k_x} = \frac{e}{\hbar} 2ta \sin k_x a \tag{12}$$

for the energy eigenvalues $E(\boldsymbol{k}) = 2t\left(\cos k_x a + \cos k_y a + \cos k_z a \right)$ of a single orbital tight-binding model on the simple cubic lattice, where a and t are the lattice constant and transfer integral between the nearest-neighbour sites, respectively.

For multilayers with a finite number of layers, which can be considered pseudo-two-dimensional systems, the electrical conductivity at zero temperature may be evaluated as follows. Since there is no translational invariance along the direction perpendicular to the layers, it is convenient to express the coordination of the sites as $(\ell, \boldsymbol{i})$, where ℓ is the layer index and $\boldsymbol{i}$ is the position of the site within

a layer. After recovering the translational invariance by taking the statistical average over the impurity distribution of a layer, the wave vector $k_\parallel$ along a layer plane can be defined. Therefore, a Fourier transformation can be performed and the representation $(\ell, \boldsymbol{k}_\parallel)$ can be used, where $\boldsymbol{k}_\parallel = (k_x, k_y)$ for stacking along the z-axis.

In this representation, the current operator along the x-direction is given as $\mathcal{J}_x(\boldsymbol{k}_\parallel) = ev_x(\boldsymbol{k}_\parallel)$ and the vertex correction vanishes, as described above. Therefore, the electrical conductivity is given as

$$\sigma_{xx} = \frac{e^2\hbar}{\Omega\pi} \sum_{s\ell m k_\parallel} v_x(\boldsymbol{k}_\parallel) v_x(\boldsymbol{k}_\parallel) \operatorname{Im} \tilde{\mathcal{G}}^{\mathrm{R}}_{\ell m s}(\boldsymbol{k}_\parallel) \operatorname{Im} \tilde{\mathcal{G}}^{\mathrm{R}}_{m\ell s}(\boldsymbol{k}_\parallel), \tag{13}$$

where s denotes spin and ℓ and m are the layer suffixes. The Green's function is expressed as a matrix with a size determined by the number of layers.

3.3. Current perpendicular to layer planes

We now consider multilayers with two leads attached to the top and bottom of the multilayers with current flowing perpendicular to the layer planes. Because there is no translational invariance along the direction of current flow, the multilayers become scatterers and produce electrical resistivity even if the multilayers are perfect with no defects, impurities, etc. Since the system size is finite, it is convenient to consider the conductance defined as $\Gamma = (\sigma/L)S$ instead of the conductivity σ. Here, S and L are the cross section and length of the sample, respectively. From Eq. (4), the conductance is given as

$$\Gamma = \frac{\pi\hbar}{L^2} \mathrm{Tr}[\mathcal{J}\delta(E_\mathrm{F} - \mathcal{H})\mathcal{J}\delta(E_\mathrm{F} - \mathcal{H})]. \tag{14}$$

As the width of the multilayers is much larger than the thickness, we may regard the width as being nearly infinite and can express the electronic states using a mixed representation of layer number and wave vector parallel to the layer planes, that is, $(\ell, \boldsymbol{k}_\parallel)$ when no defects, impurities, etc., are included. When the multilayers include impurities or when the shape of the sample is complex, we must adopt a real space representation using $(\ell, \boldsymbol{i})$. Here, we define "sample" as being the region that exhibits electrical resistivity. For multilayers with leads, the region of the multilayers is the sample. For complex structures, we may choose the sample arbitrarily, even including the leads. For point contacts, the sample region may include only a few atoms. In tunnel junctions, the sample may be the insulating barrier region since the resistivity is governed by the insulating materials.

We rewrite Eq. (14) in a form applicable to numerical calculations. When electron hopping between layers, given by t, is non-zero only between nearest-neighbour sites, the conductance is given by

$$\Gamma = \frac{e^2t^2}{2h} \mathrm{Tr}\left[\bar{G}_{\ell,\ell+1}\bar{G}_{\ell+1,\ell} + \bar{G}_{\ell+1,\ell}\bar{G}_{\ell+1,\ell} - \bar{G}_{\ell,\ell}\bar{G}_{\ell+1,\ell+1} - \bar{G}_{\ell+1,\ell+1}\bar{G}_{\ell,\ell}\right], \tag{15}$$

where $\bar{G} = \mathcal{G}^{\mathrm{A}} - \mathcal{G}^{\mathrm{R}}$ and the trace indicates a sum over spins and sites in the layer. We have used the fact that the electrical current is independent of the position of the layers. When the multilayers are clean and the wave vector $\boldsymbol{k}_{\parallel}$ is well defined, the Green's functions are functions of $\boldsymbol{k}_{\parallel}$. However, when the sample has a complex structure, we must adopt a real space representation, and the Green's functions are matrices with a size determined by the sample width. Expression (15) has been given by Lee–Fisher [38].

3.4. Recursive Green's function method

The Green's function may be calculated once the Hamiltonian of the whole system is given. We here present a simple example to treat the Green's function using a one-dimensional model, in which the hopping integral between the nearest-neighbour sites is given by t and the atomic potentials are v_i. The Green's function is given as

$$\mathcal{G}(z) = \begin{bmatrix} \cdot & t & 0 & 0 & 0 \\ t & z - v_{\ell-1} & t & 0 & 0 \\ 0 & t & z - v_{\ell} & t & 0 \\ 0 & 0 & t & z - v_{\ell+1} & t \\ 0 & 0 & 0 & t & \cdot \end{bmatrix}^{-1}, \tag{16}$$

where $z = E \pm \mathrm{i}\eta$. We divide the system into left and right semi-infinite parts. When the ℓth site is an edge atom of the left part, $\mathcal{G}_{\ell\ell}$ is given as

$$\mathcal{G}_{\ell\ell}(z) = \frac{1}{z - v_{\ell} - t^2 \mathcal{G}_{\ell-1\ell-1}(z)}, \tag{17}$$

which connects the Green's function of the $(\ell - 1)$th atom with the ℓth atom. When the ℓth atom is far from the edge, we set $\mathcal{G}_{\ell\ell}(z) = \mathcal{G}_{\ell-1\ell-1}(z)$, since these atoms are equivalent. Solving this equality gives $\mathcal{G}_{\ell\ell}(z)$. The Green's functions for the right part are calculated using the same procedure. The Green's functions of the left and right parts are connected by the relation

$$\mathcal{G}(z) = \begin{bmatrix} \mathcal{G}^{-1}_{\ell\ell}(z) & t \\ t & \mathcal{G}^{-1}_{\ell+1\ell+1}(z) \end{bmatrix}^{-1}, \tag{18}$$

from which we obtain $\mathcal{G}_{\ell\ell}(z)$ and $\mathcal{G}_{\ell\ell+1}(z)$. This procedure to determine the layer Green's function is called the recursive Green's function method.

This method may be applied to systems which are much smaller than real systems in order to evaluate the conductivity of a real system. In this case, we first calculate the conductance and evaluate the conductivity as follows. Since the conductivity in the linear response regime is characterized by Ohm's law, where the resistivity increases linearly with the sample length, and the conductivity and conductance for finite size samples with width S and length L is given as $1/\Gamma = 1/\Gamma_{\mathrm{c}} + (L/\sigma S)$, we calculate the conductance as a function of L and estimate the value of σ from the slope of the $1/\Gamma$ versus L curve. Here, $1/\Gamma_{\mathrm{c}}$ is the contact resistance of the contact between the sample and the leads. Furthermore, the

conductance is calculated for many samples with different distributions of impurities by taking a statistical average of the conductance. This procedure is necessary since we are dealing with conductivity in the diffusive regime, in which electrical scattering is important for the conductivity.

3.5. Conductance quantization and Landauer formula

The current of a one-dimensional chain subject to a voltage is given as

$$I = 2e \int_{E_F}^{E_F+eV} D(E)v(E)\mathrm{d}E, \tag{19}$$

using the DOS $D(E)$ and the velocity of electrons $v(E)$. Using the relations for free electrons,

$$D(E) = \frac{1}{2\pi\hbar}\sqrt{\frac{m}{2E}}, \tag{20}$$

and $v(E) = p/m = \sqrt{2E/m}$, we get

$$I = \frac{2e^2}{h}V. \tag{21}$$

Therefore, the conductance is given as

$$\Gamma = 2e^2/h \tag{22}$$

in terms of physical constants. The factor 2 indicates spin degeneracy. Because only two propagating states exist in a one-dimensional chain, that is, left-going and right-going waves, there is only one conducting path (called a channel) where electrons flow for each spin. The channel gives a conductance of $2e^2/h$, which is called the quantum conductance. This value is 3.4×10^7 cm/s and is equal to $(26\ \mathrm{k\Omega})^{-1}$. The conductance of multi-pass systems is given by integer multiples of $2e^2/h$.

Even if the conductance is ballistic, the conductance for systems which have no translational invariance along the current direction is given as

$$\Gamma = \frac{2e^2}{h}T(E_F) \tag{23}$$

using the transmission coefficient $T(E_F)$ at the Fermi energy. When there are many channels, as in three-dimensional systems, and the wave vector parallel to planes is well defined, the total conductance is written as

$$\Gamma = \frac{2e^2}{h}\sum_{k_\parallel} T\left(E_F, \mathrm{k}_\parallel\right). \tag{24}$$

For a finite voltage, the expression is generalized for the current as

$$I = \frac{2e}{h}\sum_{k_\parallel}\int \mathrm{d}E\{f(E) - f(E+eV)\}T\left(E_F, \boldsymbol{k}_\parallel\right), \tag{25}$$

which is called the Landauer formula [39]. The result is also obtained in the non-equilibrium Green's function method [40].

4. GIANT MAGNETORESISTANCE

Magnetic multilayers are composed of an alternating stack of thin magnetic and non-magnetic layers. The thickness of each layer is a few nm. Trilayers, where a non-magnetic layer is sandwiched by two magnetic layers, can also be considered to be multilayers. Some magnetic multilayers show large magnetoresistance. When the non-magnetic layers are metals, the MR is called giant MR (GMR) and when the non-magnetic layer in a trilayer is an insulator, the MR is called tunnel MR (TMR).

Magnetic multilayers have the following two important characteristics:

(1) The alignment of the magnetization of the magnetic layers is easily controlled by an external magnetic field, since the coupling between the magnetization of the magnetic layers is weakened by the presence of the non-magnetic layer between them.

(2) Each layer is thin enough for carrier electrons to feel a change in the magnetization direction of the magnetic layers.

GMR and TMR depend strongly on the type of magnetic and non-magnetic layers, and their combination. In this section, we first explain how the experimental GMR results may be understood in terms of spin-dependent resistivity described in Section 2, and that the material dependence of GMR is strongly related to the electronic structure of the constituent metals of the multilayers.

4.1. Magnetic multilayers

The basic structure of magnetic multilayers composed of a ferromagnetic A metal and a non-magnetic B metal is shown in Fig. 8. The thickness of each layer is 1–10 nm and the number of layers ranges from 3 (for trilayers) to about 100. Fe, Co, Ni and their alloys are frequently used for the ferromagnetic A layers, while

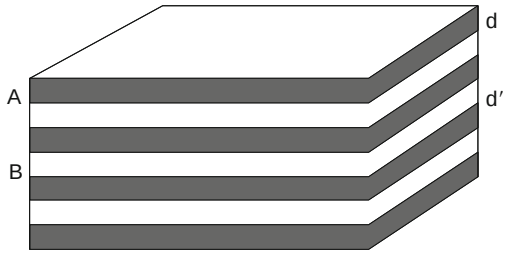

FIGURE 8 Schematic figure of magnetic multilayers with ferromagnetic A and non-magnetic B layers. *d* and *d*′ indicate the layer thickness.

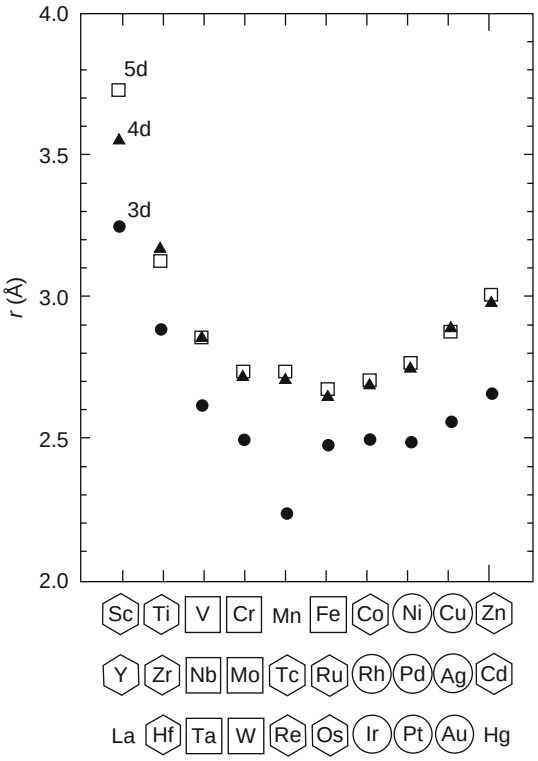

FIGURE 9 Atomic distance between nearest-neighbour sites and lattice structures in 3d, 4d and 5d transition metals. Circles, squares and hexagons under the figure show that the crystal structures of metals are fcc, bcc and hcp, respectively.

non-magnetic TMs such as Cr and Ru or noble metals Cu, Ag and Au are used for the non-magnetic B layers.

To fabricate high-quality magnetic multilayers, matching of the lattice constants of the constituent metals is important. Figure 9 shows the distance between nearest-neighbour atoms and the lattice structure of 3d, 4d and 5d TMs. We find that the matching of the atomic distance and lattice structure of Fe with Cr and Co with Cu are sufficiently good.

4.2. Experiments on GMR

4.2.1. GMR and exchange coupling

The first observation of antiparallel coupling between magnetic layers was reported by Grünberg *et al.* [41], for Fe/Cr trilayers. They also observed negative MR, that is, a resistivity reduction under an external magnetic field. The magnitude of the MR of Fe/Cr trilayers was observed to be a few percent. Two years later, Fert's group [42] reported MR as large as 40% for Fe/Cr multilayers. This MR was the largest so far observed for magnetic metal films and was called giant

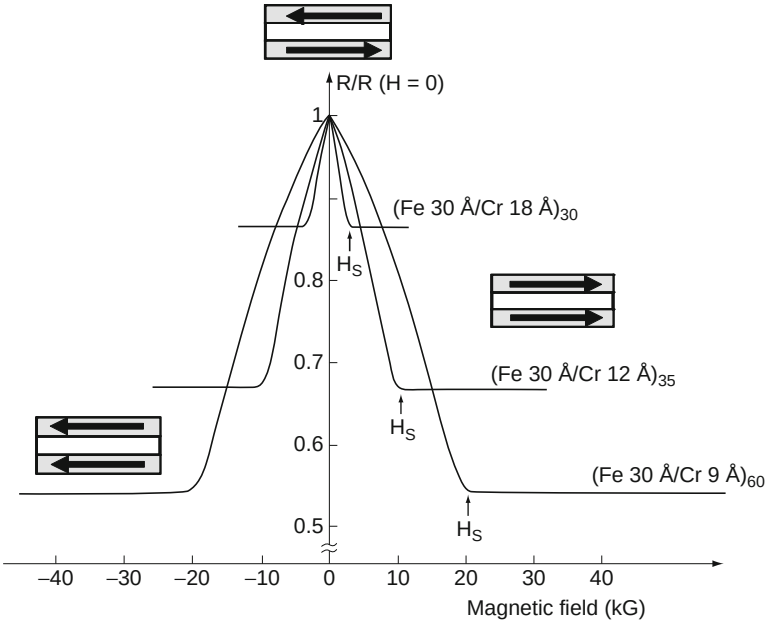

FIGURE 10 Resistivity change due to an external magnetic field for Fe/Cr multilayers [42].

MR (GMR). After the discovery of GMR, many experimental works have been performed [43–48].

Figure 10 shows the experimental results for Fe/Cr multilayers [42]. The resistivity decreases with increasing magnetic field due to a change in the alignment of the magnetization of the Fe layers. The resistivity is high when the alignment is antiparallel (AP) and is low when the alignment is parallel (P).

The magnitude of the MR is expressed by the so-called MR ratio, defined as

$$\mathrm{MR} = \frac{\rho_{\mathrm{AP}} - \rho_{\mathrm{P}}}{\rho_{\mathrm{AP}}}, \tag{26}$$

or

$$\mathrm{MR} = \frac{\rho_{\mathrm{AP}} - \rho_{\mathrm{P}}}{\rho_{\mathrm{P}}}, \tag{27}$$

where ρ_{AP} and ρ_{P} are the resistivity in AP and P alignment of the magnetization of the magnetic layers. Since usually $\rho_{\mathrm{P}} < \rho_{\mathrm{AP}}$, the definitions (26) and (27) are called as pessimistic and optimistic definition, respectively. In experiments, the optimistic definition Eq. (27) is usually used, while we use the definition Eq. (26) for the theoretical results in this chapter. Tables 1 and 2 show MR ratios observed for several combinations of magnetic and non-magnetic metals. We see that the MR ratio depends on the combination of metals. Fert' group pointed out in their first paper on GMR that the spin-dependent resistivity could be responsible for GMR; however, no detailed discussion on the material dependence was presented. (The many-body effect was ruled out since no anomalous dependence of ρ on

Table 1 MR ratios measured for various magnetic multilayers for current parallel to the layer planes

Multilayer	$\Delta\rho/\rho_P$ (%)	$\Delta\rho/\rho_{AP}$ (%)
Fe/Cr	108	52
Co/Cu	115	53
NiFe/Cu/Co	50	33
FeCo/Cu	80	44
NiFeCo/Cu	35	26
Ni/Ag	26	21
Co/Au	18	15
Fe/Mn	0.8	
Fe/Mo	2	
Co/Ru	7	
Co/Cr	2.6	
Fe/Cu	12	

Table 2 MR ratios measured for selected magnetic multilayers for current perpendicular to the planes

Multilayer	$\Delta\rho/\rho_P$ (%)	$\Delta\rho/\rho_{AP}$ (%)
Ag/Fe	42	30
Fe/Cr	108	52
Co/Cu	170	63

temperature has been observed [45]. The residual resistivity, however, was found to be very high.) Thus, an issue to be clarified is the material dependence of GMR and the relation between the MR ratio and the electronic structures of the constituent metals of the magnetic multilayers.

GMR appears when the AP alignment of the magnetization is changed to P alignment by an external magnetic field. Therefore, AP alignment of the magnetization is a prerequisite for GMR. A detailed study of the alignment of magnetization has found that the coupling of magnetization in magnetic layers changes as a function of the non-magnetic layer thickness [49]. The coupling between magnetic layers is called inter-layer exchange coupling [50–54]. Figure 11 shows an experimentally determined oscillation of coupling energy as a function of layer thickness [51]. The period of the oscillation is rather long and the magnitude decays as the thickness of the non-magnetic layer increases. The long period of oscillation has been confirmed in various experiments [55–57]. The features are very similar to those of the so-called RKKY interaction between magnetic impurities in metals [58]. The period of the oscillation of the inter-layer exchange coupling is determined by the Fermi wave vector $\boldsymbol{k}_F$, as in the RKKY interaction [59–64]. In the present case, however, the thickness of the non-magnetic layer changes discretely and therefore $(\pi/a - \boldsymbol{k}_F)$ can also be the period of oscillation,

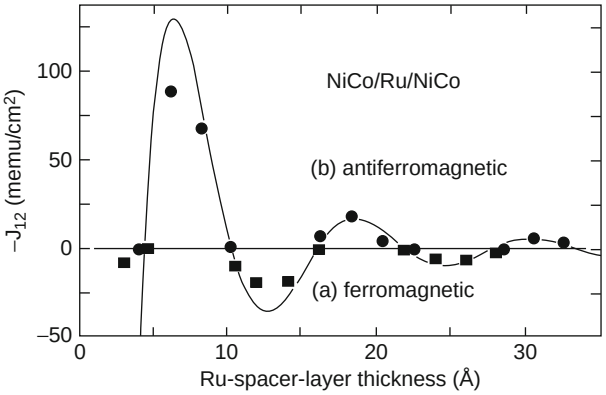

FIGURE 11 Oscillation of coupling energy as a function of non-magnetic layer thickness in NiCo/Ru/NiCo multilayers [51].

where a is the lattice distance. Since $\boldsymbol{k}_F$ in Cu, for example, is close to π/a, the period of oscillation of the exchange coupling becomes long. The decay of the magnitude for multilayers is proportional to L^2, where L is the non-magnetic layer thickness, in contrast to r^3 for the RKKY interaction.

4.2.2. Non-coupling type of GMR

Magnetic layers in multilayers are usually coupled magnetically (inter-layer exchange coupling). The inter-layer exchange coupling in Fe/Cr multilayers is rather strong to be controlled by the magnetic field. Multilayers with thicker non-magnetic layers have nearly zero exchange coupling; however, the magnetization direction of the magnetic layers may be controlled by using the difference in the coercive force between magnetic layers of different metals. An example is Co/Cu/NiFe multilayers shown in Fig. 12, in which NiFe is a soft magnet with a magnetization easily changed by a weak external magnetic field [65, 66].

4.2.3. Spin valve

Technological applications of GMR, for example, sensors, require a sharp response of the magnetization direction to the external magnetic field within a few Oe. To achieve such sensitivity, a trilayer structure with an attached antiferromagnetic has been designed. The magnetization of the magnetic layer adjacent to the antiferromagnetic layer is pinned by the antiferromagnetism and only the other magnetic layer responds to the external magnetic field. This kind of trilayer is called a spin valve [67–69]. PtMn or FeMn are typical antiferromagnets used in spin valves. An example of GMR in a spin-valve-type trilayer is shown in Fig. 13.

4.2.4. CPP-GMR

The experiments presented so far have used a geometry with the current flowing parallel to the layer planes. GMR with this geometry is called current-in-plane GMR (CIP-GMR). GMR with a geometry with current flowing perpendicular to the planes is called CPP-GMR.

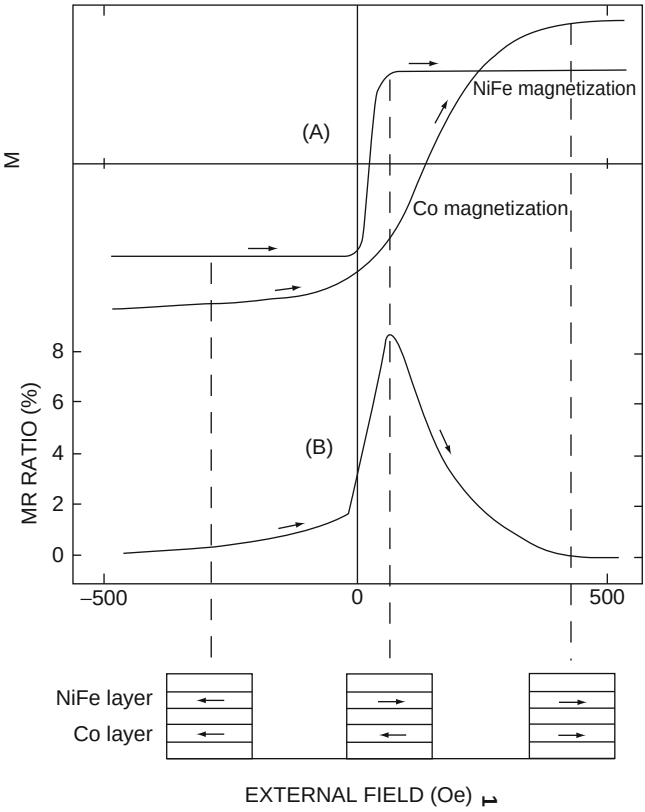

FIGURE 12 Experimental results of GMR for non-coupling Co/Cu/NiFe magnetic multilayers [65].

In CPP-GMR, the resistivity of a sample is too small to be detected, since the layer thickness is usually less than μm and the resistivity of the leads is overwhelming. To make a measurement of sample resistivity possible, several methods have been adopted. One is to utilize superconducting leads [70–72], the second one is to microfabricate the samples [73, 74], and to fabricate multilayered nanowire formed by electrodeposition into nanometre-sized pores of a template polymer membrane [75]. In the second case, the resistivity of the sample becomes as large as that of the leads because the resistivity of such systems is governed by the narrow region of the system.

The temperature dependence of CPP-GMR for a microfabricated sample of Fe/Cr multilayers is compared with that of CIP-GMR in Fig. 14. We see that CPP-GMR is much larger than CIP-GMR, which is a general trend for GMR. To interpret the results, the geometry of multilayers effects should be taken into account, in addition to the spin-dependent resistivity of ferromagnetic metals. Shinjo's group [76, 77] fabricated a zigzag structure of multilayers in which the current flows in angle to planes, and measured a rather high MR ratio.

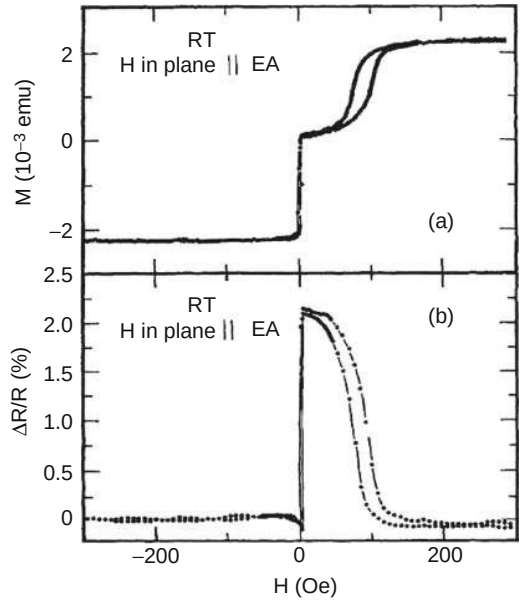

FIGURE 13 GMR in a spin-valve-type NiFe/Cu/NiFe/FeMn multilayer [67].

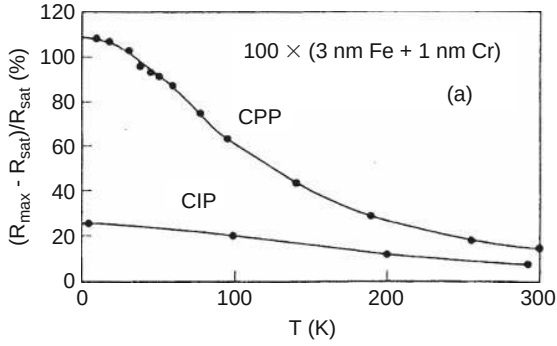

FIGURE 14 Temperature dependence of CPP- and CIP-GMR for Fe/Cr multilayers [73].

4.2.5. Granular GMR

GMR has been observed not only in magnetic multilayers, but also in granular films in which magnetized metallic grains of Co or Fe, for example, are distributed in non-magnetic metals, typically Cu or Ag [78–84]. The size of the grains is of nanoscale and the magnetic moments of the grains are nearly isolated from each other.

When an external magnetic field is applied, the random orientation of the magnetic moments of the grains is forced to be parallel, resulting in a decrease of the resistivity, as for magnetic multilayers. Example experimental results are shown in Fig. 15. The dependence of the resistivity on the magnetic field is

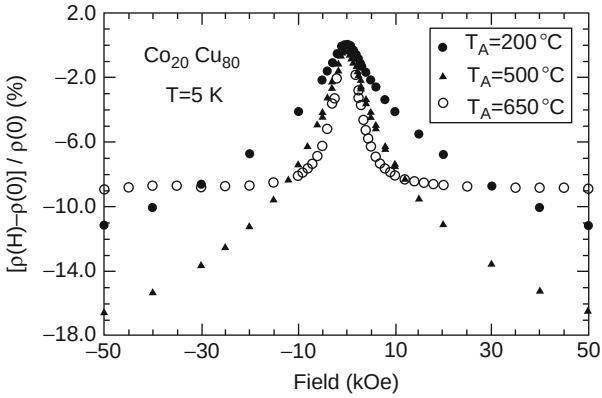

FIGURE 15 GMR in granular magnetic metals. Here, T_A is the annealing temperature of the samples [79].

strongly affected by the annealing temperature of the sample. When the annealing temperature is low, the MR does not saturate even at high magnetic field. This may be because isolated magnetic atoms and/or clusters still remain for low annealing temperature and they continue to respond to high magnetic fields.

4.3. Phenomenological theory of GMR

The typical length scale of a multilayer is the thickness L of each layer, which is of the order of 1 nm. Since the length scale is shorter than the mean free path and much shorter than the spin-diffusion length, Mott's two-current model is applicable to GMR in multilayers as a first approximation. The model is also applicable to granular GMR because the length scale of the sample is the diameter of the magnetic grains. Detailed experiments have shown that the spin-diffusion length in the multilayer, especially in CPP-GMR-type multilayers, may be different from that in metals and alloys [15, 85–89]. In the following, however, we adopt the simplest picture to explain the effect of GMR [25, 90].

In applying the two-current model to magnetic multilayers, the direction of the spin axis, up (↑) or down (↓), should be defined to deal with the resistivity. Because the magnetization of the magnetic layers is reversed by the magnetic field and the magnetization alignment can be either parallel or antiparallel, ↑ and ↓ spin states should be distinguished from the majority (+) and minority (−) spin states of each magnetic layer. We henceforth use the notation ↑ and ↓ spin states as the global spin axes and + and − spin states to express the electronic states of the magnetic metals. For P alignment, ↑ and ↓ spin states coincide with + and − spin states, respectively; however, they do not coincide for AP alignment. In the following, we adopt Eq. (26) for the MR ratio.

For simplicity, we consider a case where the current traverses a trilayer composed of a non-magnetic layer sandwiched by two ferromagnetic layers. Let ρ_+, ρ_- and ρ_0 be the majority and minority spin resistivities in the ferromagnetic

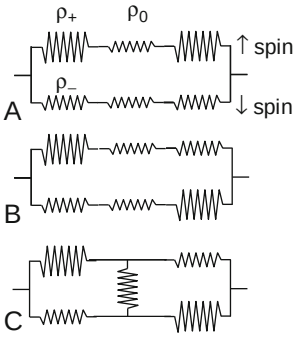

FIGURE 16 Equivalent circuit for the resistivity for (A) P alignment and (B) AP alignment of magnetization. (C) Equivalent circuit for the resistivity in multilayers which include spin-flip scattering.

layers and the resistivity in the non-magnetic layer, respectively. The total resistivity for P and AP alignment may be easily obtained by referring to the equivalent circuits shown in Fig. 16A and B, respectively. The resultant MR ratio is given as

$$\mathrm{MR} = \left(\frac{\rho_+ - \rho_-}{\rho_+ + \rho_- + 2\rho_0}\right)^2. \tag{28}$$

The MR ratio increases as the difference between the spin-dependent resistivities $\rho_+ - \rho_-$ increases.

When $\rho_+ + \rho_0$ and $\rho_- + \rho_0$ are rewritten as ρ_+ and ρ_-, the expression above is written as

$$\mathrm{MR} = \left(\frac{1-\alpha}{1+\alpha}\right)^2, \tag{29}$$

using the α-parameter $\alpha = \rho_-/\rho_+$. Thus, a combination of materials which gives a large value of the α-parameter gives rise to a large GMR. The combination of Fe and Cr gives a large GMR. In addition, the lattice matching between Fe and Cr layers is good.

4.4. Mechanism of GMR

4.4.1. Electronic states and spin-dependent resistivity in multilayers

The spin-dependent resistivity in ferromagnetic metals is closely related to the electronic structure of the metal and impurities introduced into the metal. The electronic structures of the constituent metals of the magnetic multilayers also govern the spin-dependent resistivity (or resistance) in multilayers. In this section, we describe possible sources of spin-dependent resistivity in multilayers from the viewpoint of electronic states:

- *Spin-dependent resistivity caused by interfacial roughness*. As described, the origin of the spin-dependent resistivity in metals and alloys is the spin dependence of

the scattering potentials caused by roughness. The roughness due to random arrangement of atoms also exists in multilayers. In molecular beam epitaxy (MBE) and sputtering fabrication methods, it is impossible to avoid intermixing of atoms at interfaces. The intermixing of magnetic A atoms and non-magnetic B atoms at an A/B interfaces gives rise to spin-dependent random potentials near the interface. The situation is similar to that in ferromagnetic alloys.

- *Band matching/mismatching at interfaces*. The essence of the origin of electrical resistivity is the absence of translational invariance along the current direction, because the momentum of electrons need not be conserved in this case. When the interfaces are clean, translational invariance parallel to the layer planes is satisfied and there is no electrical resistivity. Even in this case, however, there is electrical resistivity perpendicular to the layer planes, since there is no translational invariance along this direction for thin multilayers. In this case, the difference between the electronic structure of the constituent metals of the multilayers acts as a source of spin-dependent electrical resistivity and gives rise to CPP-GMR. In Co/Cu multilayers, for example, band matching between + spin states is much better than between − spin states, as schematically shown in Fig. 1. Therefore, $\rho_+ \ll \rho_-$ is realized. In Fe/Cr multilayers, the opposite relation, $\rho_- \ll \rho_+$, is realized. The spin dependence of the resistivity is the same as that obtained by spin-dependent random potentials.

Thus, both random potentials and matching/mismatching of the electronic structure cause the same spin dependence of the resistivity [25, 90–94]. For current flowing perpendicular to the planes, both are crucial for the spin dependence of the resistivity, while the spin-dependent random potential is likely to be more greatly responsible for GMR for current flowing parallel to the planes. The scattering at interfaces and layer-resolved GMR effect have also been studied for CIP-GMR [95, 96].

4.4.2. Estimate of GMR using spin-dependent potentials

We now estimate the MR ratio considering spin-dependent random potentials at interfaces. As mentioned, the material dependence of these random potentials is similar to that of the α-parameter. However, we can evaluate these random potentials more precisely by calculating the electronic states at interfaces for various multilayers and evaluate the spin-dependent resistivity and then calculate the MR ratio using Eq. (29). The calculated MR ratios are shown in Fig. 17 for Fe/TM and Co/TM multilayers [91].

This figure shows that the MR ratio has a peak for Fe/Cr multilayers and Co/Ru multilayers. In Fe/Cr multilayers, Cr atoms dissolved in the Fe layers and Fe atoms dissolved in the Cr layers give rise to spin-dependent random potentials. Because $V_{\mathrm{Fe}-} \sim V_{\mathrm{Cr}}$, while $V_{\mathrm{Fe}+} \ll V_{\mathrm{Cr}}$, both the dissolved Cr and Fe atoms result in $|V_+| \gg |V_-|$, which produces spin-dependent resistivity in such a way that $\rho_+ \gg \rho_-$. Therefore, the MR ratio of Fe/Cr multilayers becomes high. A similar situation may occur also in Fe/Pd multilayers, resulting in $\rho_+ \ll \rho_-$. In Fe/Pd multilayers, however, GMR has not been observed. This is because the Pd metal produces long range spin polarization when it is in contact with ferromagnetic

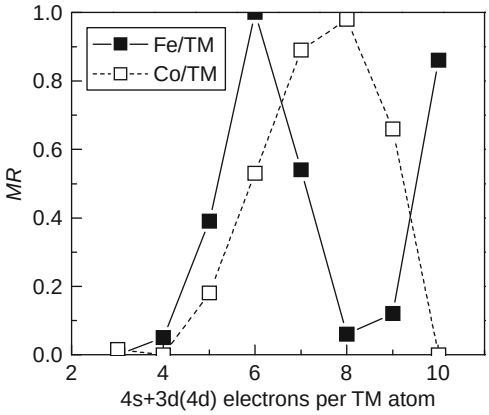

FIGURE 17 Theoretical estimate of MR ratio for Fe/TM and Co/TM multilayers for various TMs which are characterized by 4s + 3d(4d) electrons per atom [91].

metals, and as a result, the inter-layer exchange coupling between the Fe layers can be ferromagnetic irrespective to the thickness of the Pd layers. In Co/TM multilayers, the atomic potential of Co is lower than that of Fe (see Fig. 4) and the relations $V_{\mathrm{Co}-} \sim V_{\mathrm{TM}}$ and $V_{\mathrm{Co}+} \ll V_{\mathrm{TM}}$ occur for TM = Rh and Ru. Therefore, the MR ratios for Co/Rh and Co/Ru become high.

The results reproduce the trend of the material dependence of GMR. However, the calculated magnitude is much larger than the experimental results. This may be attributed to the simplified treatment of the random potential for the resistivity and to the fact that the spin-independent resistivity caused by phonons, lattice imperfections due to lattice mismatch, etc., is not accounted for. The high MR ratio of Fe/Cr multilayers may also be related to good lattice matching between the Fe and Cr layers, in addition to the fact that they possess the same bcc structure.

For Co/Cu multilayers, Co atoms dissolved in the Cu layers may govern the spin-dependent resistivity, since the conductivity of Cu is much higher than that of Co metal. As shown above, the α-parameter of Co impurities in Cu is larger than 1, because the Co + spin state is similar to that of Cu, while the Co − spin state is quite different from that of Cu. Therefore, we expect $\rho_+ \ll \rho_-$ for Co/Cu multilayers. The spin-dependent resistivity due to magnetic TM impurities in Cu may be estimated by applying the Anderson model. The MR ratio thus calculated is shown in Fig. 18 as a function of the number of d-electrons of the TM impurities [90]. The results are compared with the experimental values in the figure [97–102].

We see that the MR ratio becomes high for Co/Cu multilayers, consistent with experimental results. The calculated results indicate that Ni/Cu shows no MR, in contradiction to the experimental results. Since the DOS of the TM impurities is given by a Lorentzian shape in the present model and the Ni impurities carry no magnetic moments, no MR occurs. It has been confirmed, however, that a more realistic model does give MR for Ni/Cu multilayers [103, 104]. As for Fe/Cu multilayers, the theory gives a rather high MR ratio, whereas the MR ratios obtained in experiment are usually very small. The contradiction may be caused

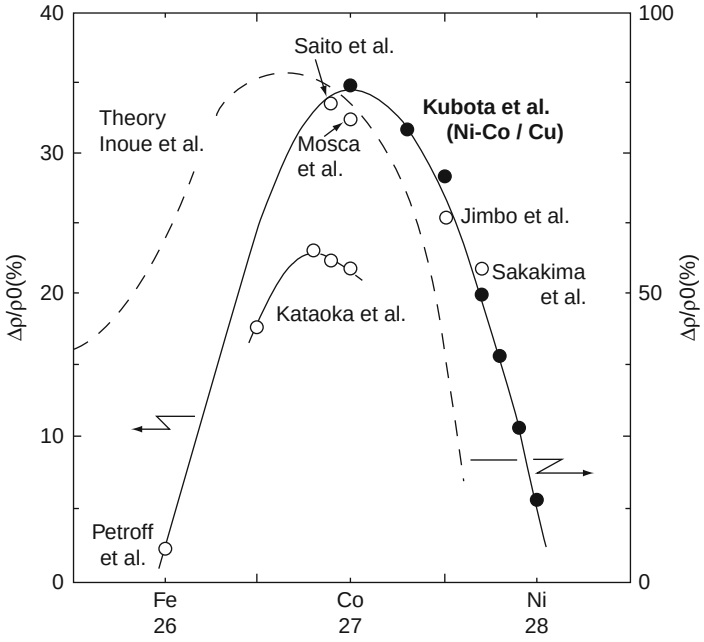

FIGURE 18 Theoretical estimate (broken curve) and experimental values (symbols) of MR ratio for TM/Cu multilayers as a function of the number of d-electrons [97].

by the fact that the lattice structure is not taken into account in the theory; because Fe is bcc and Cu is fcc, the lattice mismatch should reduce the MR ratio.

4.4.3. Microscopic theory of GMR

The discussion in the previous section does not take into account the geometry of the multilayers. Therefore, they are not able to distinguish between CIP- and CPP-GMR. To account for the effects of geometry, microscopic theory should be applied to the resistivity, which may be done by adopting the Kubo formula explained in the previous section.

Figure 19 shows the calculated MR ratios for CIP- and CPP-GMR in a simple tight-binding model for Fe/Cr multilayers with roughness at interfaces [105]. A supercell method is adopted in the calculations. The horizontal axis indicates the concentration of random atoms dissolved into the first layer of both the magnetic and non-magnetic layers. We find that CPP-GMR is much larger than CIP-GMR and that the former decreases with an increase in the degree of roughness, while the latter increases. Similar results have been obtained for the recursive Green's function method [106, 107].

The reason that CPP-GMR is much larger than CIP-GMR is that the current in CPP geometry always traverses the layer and both the spin-dependent potential and the effect of matching/mismatching of DOS contribute to the MR. On the other hand, in CIP geometry, the effect of matching/mismatching of the DOS is less effective and the MR becomes smaller. Furthermore, the spin-independent

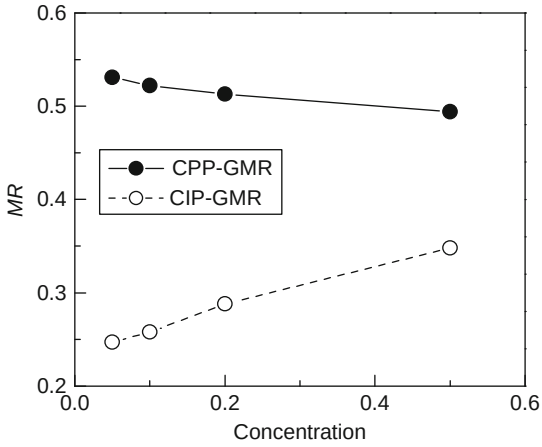

FIGURE 19 Calculated MR ratios for CIP- and CPP-GMR in a single band tight-binding model, where the MR ratio is defined in Eq. (26) [105].

contribution to the resistivity from the non-magnetic layers decreases the MR. The decrease of the MR ratio in CPP-GMR with increasing roughness may be understood as follows: without roughness (zero concentration), the matching and mismatching of ↓ spin and ↑ spin DOS give rise to strong spin dependence of the resistivity, resulting in a high MR ratio. In contrast, the spin dependence of the resistivity becomes weak with increasing roughness.

The MR ratio including a realistic electronic structure has been calculated for Fe/Cr multilayers and is shown in Fig. 20 as a function of non-magnetic layer

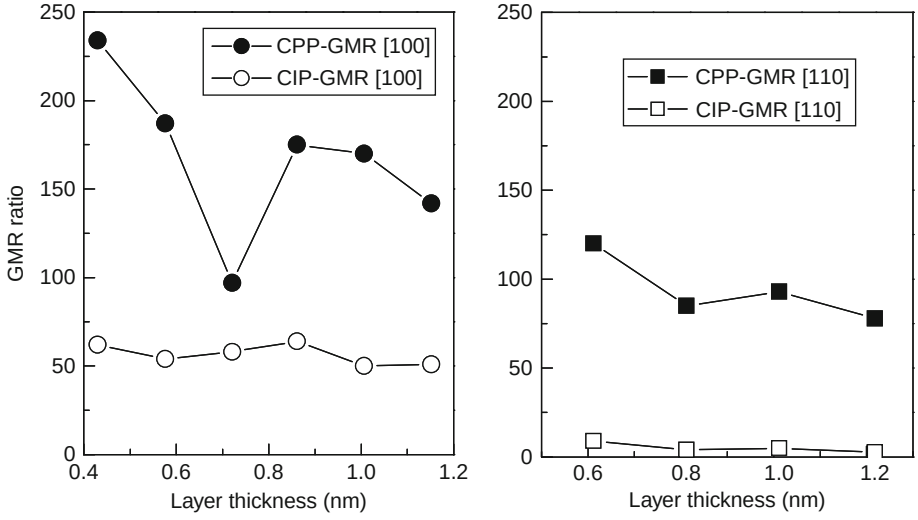

FIGURE 20 Calculated MR ratios for CIP- and CPP-GMR in first-principles band calculations for Fe/Cr multilayers [108].

thickness. The electronic structure was calculated using a supercell method and a Linear Muffin-Tin Orbital (LMTO) method without roughness [109, 110]. The symbols [1 0 0] and [1 1 0] in this figure indicate the stacking direction of the layer planes. Note that the definition of the MR ratio used is $\mathrm{MR} = (\Gamma_{\mathrm{P}} - \Gamma_{\mathrm{AP}})/\Gamma_{\mathrm{AP}} \times 100(\%)$, where Γ is the conductance calculated by the Landauer formula. We can see that the qualitative features are the same as those obtained in the simple model.

The present method has also been applied to granular GMR. The results are consistent with the experimental ones.

4.4.4. Simple picture of GMR

We have presented the mechanism of GMR in terms of spin-dependent resistivity and band matching/mismatching between magnetic and non-magnetic layers. These origins are closely related to each other and present a simple picture for the mechanism of GMR in magnetic multilayers, as shown in Fig. 21. In P alignment of the magnetization, one of the two spin channels has a low resistance (or resistivity) while the other has a high resistance. In AP alignment, both spin channels have high resistance (or resistivity), since both ↑ and ↓ spin electrons are scattered at some interfaces. As a result, the resistance in AP alignment is larger than that in P alignment.

4.5. Effects of spin-flip scattering

So far, we have not taken spin flip or spin diffusion into account. It is easy to do so in phenomenological theory. Adopting the equivalent circuit model shown in Fig. 16C, the resistivity in P and AP alignment may be given as

$$\rho_{\mathrm{P}} = \frac{2\rho_+\rho_-}{\rho_+ + \rho_-}, \tag{30}$$

$$\rho_{\mathrm{AP}} = \frac{2\rho_+\rho_- + \rho_{\mathrm{sf}}(\rho_+ + \rho_-)}{\rho_+ + \rho_- + 2\rho_{\mathrm{sf}}}, \tag{31}$$

where ρ_{sf} is the contribution to the resistivity by spin-flip scattering. ρ_{P} does not include ρ_{sf}, since the voltage drop at the middle of the circuit is the same for ↑ spin

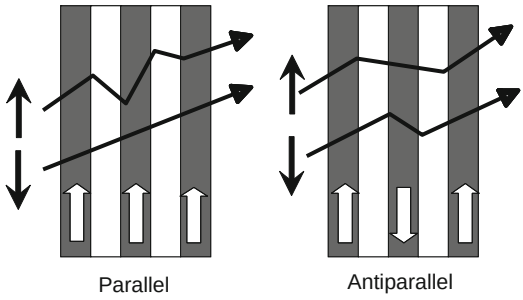

FIGURE 21 Schematic figure of spin-dependent resistivity in multilayers.

and ↓ spin channels. In AP alignment, taking $\rho_{sf} \to 0$ gives $\rho_{AP} = \rho_P$ and the MR disappears because the current is shorted. For an infinite ρ_{sf}, there is no spin-flip effect and the MR ratio decreases with decreasing ρ_{sf}. (Note that $2\rho_+ \equiv \rho_\uparrow$ and $2\rho_- \equiv \rho_\downarrow$ according to Fert *et al.* [24].)

Valet and Fert [111] have incorporated the effects of spin diffusion and layered structures by extending Boltzmann theory to include the spatial dependence of the distribution function in the non-equilibrium state. Under a finite voltage, they took into account spin accumulation and spin diffusion near the interfaces. They obtained general expressions for the spin-dependent resistivity, from which the following expressions are derived for simple cases:

$$J_s = \frac{\sigma_s}{e}\frac{\partial \bar{\mu}_s}{\partial x}, \tag{32}$$

$$\frac{e}{\sigma_s}\frac{\partial \bar{\mu}_s}{\partial x} = \frac{\bar{\mu}_s - \bar{\mu}_{-s}}{\lambda_{spin}^2}, \tag{33}$$

with

$$\bar{\mu}_s = \mu_s - eV(x), \tag{34}$$

where J_s, σ_s and μ_s are the current, conductivity and chemical potential of the spin s-state, respectively, and λ_{spin} is the spin-diffusion length.

Equation (32) is simply Ohm's law and Eq. (33) indicates a balance between the spin accumulation and spin-flip rate. Using the parameters given in Fig. 22, the MR ratio is calculated for an F/N/F trilayer as a function of L_F/L_N, where L_F and L_N are the thicknesses of the F and N layers, respectively. We can see that the MR ratio becomes small when the spin-diffusion length is short. Since we are

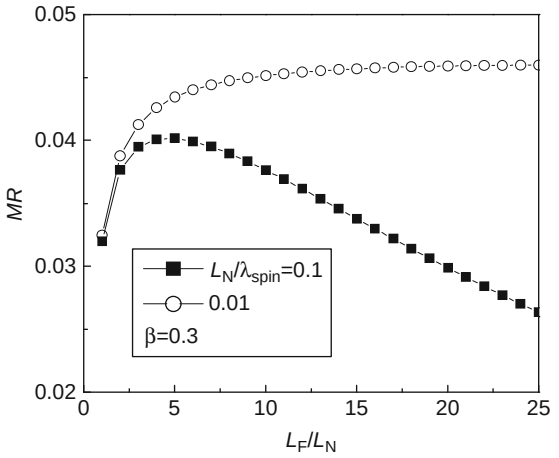

FIGURE 22 Calculated MR ratio in the Valet–Fert model. L_F and L_N are the thicknesses of the ferromagnetic and non-magnetic layers, respectively.

considering a trilayer, the MR ratio defined by Eq. (26) is very small. A non-zero value of $\bar{\mu}_s - \bar{\mu}_{-s}$ means that the chemical potential becomes spin dependent near the interface, due to the difference between the spin-dependent resistivity in the F and N layers, and indicates the existence of spin accumulation near the interface.

5. TUNNEL MAGNETORESISTANCE

TMR in ferromagnetic tunnel junctions (FTJs) was reported prior to the discovery of GMR [112, 113]. The observed MR ratios, however, were rather small at the time. A large TMR at room temperature was reported for Fe/Al–O/Fe in 1995 [114–116], and it has attracted considerable attention due to its wide potential application in sensors and memory storage devices in the near future. In the same year, tunnel-type MR was reported for metal-oxide ferromagnetic granular films [117, 118].

Many theoretical studies have so far investigated tunnel resistance and TMR [11, 119–123]. Since TMR is caused by tunnelling current through an insulating barrier, it is sensitive to physical factors such as temperature, voltage and the thickness and energy height of the barrier; it is also affected by scattering mechanisms. It is therefore vital to clarify the effects of each factor on TMR in order to develop technological applications of TMR.

In this section, we first overview the experimental results of TMR together with a phenomenological theory, and then describe the results obtained using microscopic theories. We also touch upon some recent experiments.

5.1. Ferromagnetic tunnel junctions

FTJs are made of a thin (about 1-nm-thick) non-magnetic insulator sandwiched between two ferromagnetic electrodes. A schematic figure of such a junction is shown in Fig. 23. The ferromagnetic metals used are predominantly Fe, Co and their alloys, while amorphous Al_2O_3 is one of the most stable materials for the insulating barrier. Recently, a single-crystal MgO layer has been used as the barrier to generate high TMR ratios.

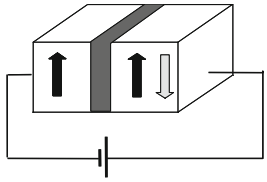

FIGURE 23 A schematic figure of the ferromagnetic tunnel junction.

The resistivity of the FTJ is reduced when the magnetization alignment of two ferromagnets is changed from AP to P alignment. This is similar to GMR, and the MR ratio is defined as

$$\mathrm{MR} = \frac{\rho_{\mathrm{AP}} - \rho_{\mathrm{P}}}{\rho_{\mathrm{AP}}}. \tag{35}$$

An alternative definition is often used in experimental studies; in this definition, ρ_{AP} in the denominator is replaced with ρ_{P}.

5.2. Experiments for TMR

Figure 24 shows the experimental results for the resistance in a Fe/Al–O/Fe tunnel junction as a function of the external magnetic field [114]. The resistance is high when the magnetization of the two ferromagnetic electrodes is antiparallel, and it is low when the magnetization is parallel. One of the characteristics of TMR is that the external magnetic field required to rotate the magnetization is sufficiently low. This is because there is almost no coupling between the magnetizations of the two electrodes as a result of the insulating barrier inserted between them. The AP and P alignments of the magnetization are realized by using a small difference in the coercive force between the two ferromagnets. The current flows perpendicular to the layer planes, which is similar to CPP-GMR. The resistance in the FTJs is much higher than that in CPP-GMR. This makes it possible to measure the junction resistance without microfabricating the samples. This could be considered to be another characteristic of TMR.

5.3. A phenomenological theory of TMR

5.3.1. MR ratio and spin polarization

The experimental results for TMR can be understood phenomenologically as follows. Let us denote the left and right electrodes as L and R, respectively. When the tunnelling process is independent of the wave vectors of tunnelling

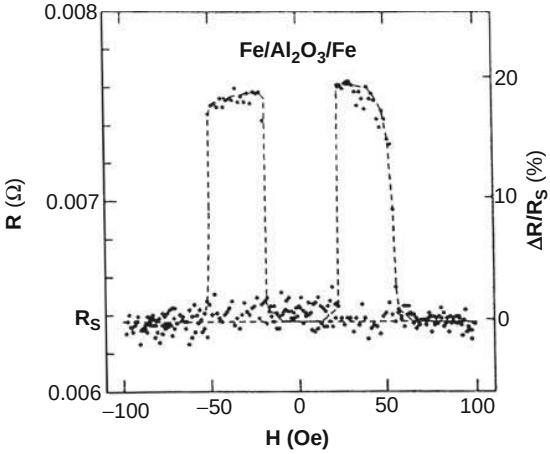

FIGURE 24 Experimental results for the resistance in an Fe/Al–O/Fe tunnel junction [114].

electrons, the tunnel conductance Γ is proportional to the product of the densities of states of the L and R electrodes, and is given by $\Gamma \propto \sum_s D_{\mathrm{L}s}(E_{\mathrm{F}})D_{\mathrm{R}s}(E_{\mathrm{F}})$, where s denotes the spin [112, 124]. The proportionality constant includes the transmission coefficient of electrons through the insulating barrier. Henceforth, the Fermi energy E_{F} is omitted for simplicity.

By using this expression, the conductance for P magnetization alignment is given by $\Gamma_{\mathrm{P}} \propto D_{\mathrm{L}+}D_{\mathrm{R}+} + D_{\mathrm{L}-}D_{\mathrm{R}-}$, and that for AP magnetization alignment is given by $\Gamma_{\mathrm{AP}} \propto D_{\mathrm{L}+}D_{\mathrm{R}-} + D_{\mathrm{L}+}D_{\mathrm{R}-}$. Since the resistivity $\rho_{\mathrm{P(AP)}}$ corresponds to $\Gamma^{-1}_{\mathrm{P(AP)}}$, the MR ratio is given by

$$\mathrm{MR} = \frac{\Gamma^{-1}_{\mathrm{AP}} - \Gamma^{-1}_{\mathrm{P}}}{\Gamma^{-1}_{\mathrm{AP}}} = \frac{2P_{\mathrm{L}}P_{\mathrm{R}}}{1 + P_{\mathrm{L}}P_{\mathrm{R}}}, \tag{36}$$

where $P_{\mathrm{L(R)}}$ is the spin polarization of L(R) electrodes and is defined by

$$P_{\mathrm{L(R)}} = \frac{D_{\mathrm{L(R)}+} - D_{\mathrm{L(R)}-}}{D_{\mathrm{L(R)}+} + D_{\mathrm{L(R)}-}}, \tag{37}$$

Although the transmission coefficient governs the magnitude of the tunnel conductance, it does not appear in the expression for the MR ratio.

An intuitive picture of the tunnelling process explained above is shown in Fig. 25. As shown in this figure, in P alignment, majority and minority spin electrons in the L electrode tunnel through the barrier into the majority and minority spin states in the R electrode, respectively. In AP alignment, however, the majority and minority spin electrons in L electrode tunnel into the minority and majority spin states in R electrode, respectively. The difference between the conductances of the P and AP alignments gives rise to TMR.

5.3.2. Spin polarization

Equation (36) indicates that the spin polarization of the electrodes governs the MR ratio. The spin polarization has been experimentally determined by using junctions of ferromagnet/Al/superconductor, or by analyzing the tunnelling spectrum obtained using point contacts [125–131]. Measured values of the spin polarization are shown in Table 3. Using these values, the experimentally measured MR ratios are explained rather well. For example, the MR ratio measured for Fe/Al–O/Fe junctions is about 0.3 and this value is close to the theoretical value

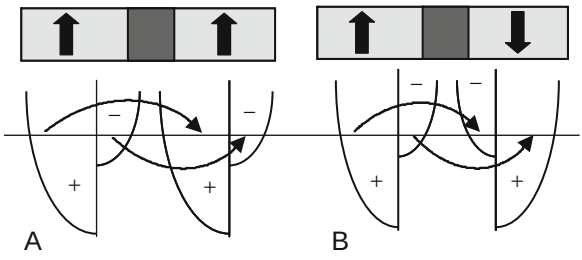

FIGURE 25 A schematic figure to show the tunnelling process in ferromagnetic tunnel junctions.

Table 3 Spin polarizations observed in tunnel junctions and point contacts for various metals [125–129]

Materials	Tunnel junctions	Point contacts
Fe	+0.40	0.42
Co	+0.35	0.37, 0.42
Ni	+0.23	0.32, 0.43
$Ni_{0.8}Fe_{0.2}$		0.37
Cu		0.0
NiMnSb		0.58
(LaSr)MnO_4	+0.70	0.78
CrO_2		0.90

calculated by using the experimental value of P for Fe. However, the MR ratio observed for a single-crystal Fe/MgO/Fe junction is 0.7–0.8, which cannot be explained in terms of the spin polarization of Fe.

It is also difficult to explain the spin polarization P by using a first-principles calculation. The ratios of P deduced from the height of the DOS at the Fermi energy are inconsistent with experimentally measured ones, for example, theoretical values for P are negative for Co and Ni, while experimental ones are positive. Bulk Fe has a positive value of P, while surface Fe has a negative value. To explain TMR, one should study the spin polarization of the tunnel conductance itself.

5.4. Free-electron model

To investigate the tunnelling process of electrons through a barrier, we first consider a one-dimensional free-electron model. Let us calculate the transmission probability for an electron injected from the left electrode with an energy E to tunnel through the barrier to the right electrode. Since the injection energy E is measured from the bottom of the energy band, it is spin dependent when the electrodes are ferromagnetic, and is expressed by E_s with $s = +$ (majority spin) or $-$ (minority spin).

Let Φ be the barrier potential determined from the Fermi energy and d be the barrier thickness, respectively, the decay rate of the wave function within the barrier is given by

$$\boldsymbol{k} = \sqrt{2m\Phi}/h, \tag{38}$$

in a free-electron model, where m is the effective mass of tunnelling electrons. The transmission coefficient may be given by

$$T_s \simeq \frac{16E_s\Phi}{(E_s+\Phi)^2}\mathrm{e}^{-2\kappa d}, \tag{39}$$

for $\kappa d \gg 1$. The spin dependence of the transmission coefficient appears in the prefactor of $\mathrm{e}^{-2\kappa d}$. Values of T_s are plotted as functions of Φ/E_+ for a given value

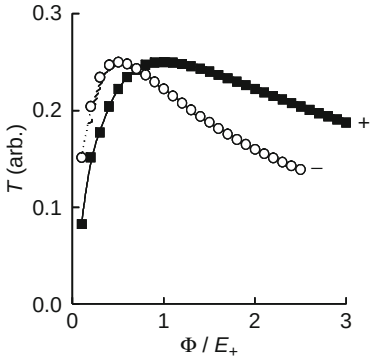

FIGURE 26 Calculated results for the spin-dependent transmission coefficient in the free-electron model for a ferromagnetic junction.

of E_+/E_- in Fig. 26. This figure shows that the sign of the spin polarization of the transmission coefficient depends on the value of Φ/E_+.

To evaluate the difference between the transmission coefficients for P and AP alignment of the magnetization, a generalized calculation should be performed [132, 133]. By performing such calculations, the conductances Γ_{P} and Γ_{AP} for P and AP alignments of the magnetization, respectively, can be obtained as [133]

$$\Gamma_{\mathrm{P(AP)}} \propto 1 + (-)P^2,$$
$$P = \left| \frac{k_{\mathrm{F}+} - k_{\mathrm{F}-}}{k_{\mathrm{F}+} - k_{\mathrm{F}-}} \frac{\kappa^2 - k_{\mathrm{F}+}k_{\mathrm{F}-}}{\kappa^2 + k_{\mathrm{F}+}k_{\mathrm{F}-}} \right|. \tag{40}$$

where k_{Fs} is the Fermi wave number for s-spin of the electrodes. Here, we have assumed that $\kappa d \gg 1$. The MR ratio defined as $\mathrm{MR} = (\Gamma_{\mathrm{P}} - \Gamma_{\mathrm{AP}})/\Gamma_{\mathrm{P}}$ gives $2P^2/(1 + P^2)$ for $P_{\mathrm{L}} = P_{\mathrm{R}} = P$.

It is possible to evaluate the value of P by calculating k_{Fs} in a first-principles calculation; however, the value of P is quite small (only a few percent) compared with experimentally measured values due to the factor $\left|k^2 - k_{\mathrm{F}+}k_{\mathrm{F}-}\right|$. To make a quantitative comparison between the experimental and theoretical values of P, a more realistic formulation or numerical calculation of P is desired, one which employs realistic electronic structures and that incorporates the effects of disorder at, for example, junction interfaces.

5.5. Ingredients for TMR

In the simple theories described above, the origin of TMR is either the spin dependence of the density of states or that of the transmission coefficient. However, as shown below, realistic electronic structures and disorder at interfaces exert a larger effect on determining the magnitude of TMR [134–139].

5.5.1. Role of the transmission coefficient

In the free-electron model, the spin dependence of the transmission coefficient resides in the prefactor of $\exp(-2\kappa d)$, which is generated by the matching conditions of the wave functions of tunnelling electrons at the interfaces. Although $\exp(-2\kappa d)$ is spin independent, it gives rise to a strong dependence on spin in the following way.

Equation (38) is the result obtained using a one-dimensional model, and it should be generalized to a three-dimensional case in such a way that

$$\kappa = \sqrt{2m(U - E(k_z))}/\hbar \tag{41}$$

with

$$E_F = E(k_\parallel) + E(k_z), \tag{42}$$

where U is the height of the barrier potential. We see that when $\kappa d \gg 1$, the electronic state which maximizes $E(k_z)$ (i.e. minimizes $E(k_\parallel)$ makes the largest contribution to the tunnelling conductance. Usually, such a state has $k_\parallel = (0,0)$, and the tunnelling conductance calculated by taking into account this state only agrees with the result obtained using the one-dimensional model. For junctions with thin tunnel barriers, however, the contribution from states with wave numbers besides $k_\parallel = (0,0)$ becomes large. Thus, we find that the electrons injected perpendicular to the barrier planes make the biggest contribution to tunnelling. This is merely the filter effect for the momentum of a tunnelling electron.

Since the electronic states of ferromagnets depend on spin, the tunnelling probability becomes spin dependent due to this momentum filter effect, and the decay rate may be written as $\kappa_s = \sqrt{2m(U - E_s(k_z))}/\hbar$. The spin-dependent κ_s can produce high TMR ratios.

5.5.2. Effects of Fermi surface

When a junction has no disorder and is translationally invariant along layer planes, the component of the wave vector $k_\parallel$ parallel to layer planes is conserved. This kind of tunnelling process is referred to as specular tunnelling. On the other hand, when $k_\parallel$ is not conserved, the tunnelling process is referred to as diffusive tunnelling. In this section, we consider specular tunnelling.

Tunnel junctions are usually composed of an insulating barrier sandwiched between two different ferromagnetic metals. Therefore, the Fermi surfaces of the L and R electrodes are generally different. Since $k_\parallel$ is conserved in specular tunnelling, only states on the Fermi surface with the same $k_\parallel$ may contribute to tunnelling.

In the free-electron model, the state with $k_\parallel = (0,0)$ is always included in the Fermi surface. However, this state may not be included in the complicated Fermi surfaces of, for example, transition metals. In particular, ferromagnets have spin-dependent Fermi surfaces, and thus the state with $k_\parallel = (0,0)$ may be included in one spin state, but not in the other spin state. In this case, the tunnelling conductance is strongly spin dependent. Furthermore, the tunnel conductance in AP alignment becomes very small because the $k_\parallel = (0,0)$ state may not contribute to tunnelling.

5.5.3. Symmetry of the wave function

In specular tunnelling, the difference between the symmetries of the wave functions of tunnelling electrons in L an R electrodes exerts a strong influence on TMR. The wave function of each state in metals has a specific symmetry, and electrons with a certain symmetry are not able to transfer into a state with different symmetry. Therefore, electrons on the L electrode can tunnel through the barrier into the R electrode only when the states specified by $k_{\parallel}$ in the L and R electrodes have the same symmetry; but this becomes impossible when the states are different. When the L and R electrodes are composed of different materials, the symmetry of the wave functions of tunnelling electrons plays an important role in tunnel conductance. In ferromagnets, the + and − electronic states are different in general. Therefore, when the magnetizations of the two electrodes are AP, the states on the Fermi surfaces of the L and R electrodes can have different symmetries. In this case, the electrons in these states are not able to tunnel through the barrier. The situation makes the tunnel conductance for AP alignment much smaller than that for P alignment, resulting in a large MR ratio.

Figure 27 shows the energy–momentum relation along the (0 0 1) direction for Fe and MgO [139, 140]. It can be seen from this figure that the symmetry of the + spin band is Δ_1 on E_F for Fe; however, the symmetry does not appear in the − spin band. This situation is realized in Fe/MgO/Fe junctions.

5.5.4. Effect of interfacial states

When a semiconductor (e.g. GaAs) is used as the barrier, interfacial states, called Shockley states, appear within the energy band gap. Since interfacial states are localized near the interface, they do not contribute to electron transport. For a thin semiconductor barrier, the states at one interface extend up to a few atomic layers inside the barrier and might overlap with those at the other interface. When the Fermi level is located within the energy region where the interfacial states exist, the tunnel conductance may be strongly enhanced by the interfacial states, thus effectively reducing the thickness of the barrier [141].

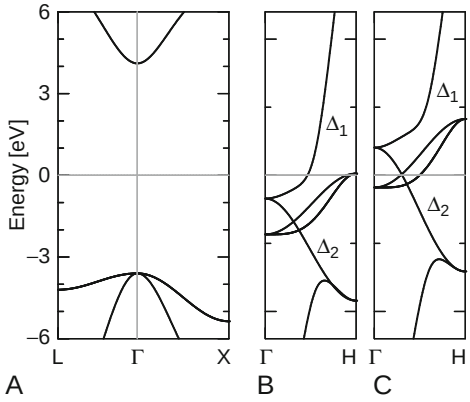

FIGURE 27 Electronic structure of Fe (majority and minority spin states) and MgO along the (0 0 1) direction [139].

5.5.5. Effect of electron scattering

Let us now consider diffusive tunnelling, which occurs when some disorder is present in junctions, and the wave vector $k_{\|}$ is not conserved. Interfacial roughness and amorphous-like insulators break translational invariance parallel to layer planes. Therefore, the parallel component of the wave vector no longer has to be conserved; that is, the wave vector $k_{\|}$ of incident electrons need not coincide with that $k'_{\|}$ of the transmitted electrons. In this section, we consider a situation in which the Fermi surfaces of the L electrode differs from that of the R electrode, as shown in Fig. 28. In the specular tunnelling case, states with Fermi wave vectors $k_{\|\mathrm{L}}>k_{\|}>k_{\|\mathrm{R}}$ cannot contribute to tunnelling. In the diffusive tunnelling case, on the other hand, this restriction is removed, and therefore those states having wave vectors $k_{\|}$ between $k_{\|\mathrm{L}}$ and $k_{\|\mathrm{R}}$ may contribute, which increases the tunnel conductance. Even when the Fermi surfaces of the L and R electrodes are the same and do not include the $k_{\|}=(0,0)$ state, tunnelling electrons take the $k_{\|}=(0,0)$ state virtually in the tunnelling process. The virtual process reduces the decay rate κ and consequentially increases tunnel conductance [137–139].

Let us consider some practical cases in which disorder exists between the electrodes and barrier layers. Here, we adopt a single-band tight-binding model (with a hopping integral t) and calculated the tunnel conductance by varying the magnitude of the disorder by the following procedure. The disorder is introduced in such a way that the atomic layer at each interface includes a random distribution of two types of atoms that constitute the electrodes and barrier. The tunnel conductance Γ is plotted as a function of the concentration c of the barrier atom in Fig. 29 for two different Fermi levels. The barrier is 10 atomic layers thick when $c=0$.

When the Fermi level is located at $E_{\mathrm{F}}=-4t$, Γ increases slightly at first and then decreases with increasing c. When $E_{\mathrm{F}}=0$, Γ increases considerably, forming a peak, and then becomes much smaller than the value at $c=0$. Note that Γ at $c=1$ is one order of magnitude smaller than that at $c=0$. The chained curve in Fig. 29A shows the contribution from diffusive tunnelling. When $E_{\mathrm{F}}=0$, the diffusive tunnelling is dominant and the chained curve is almost the same as the solid curve. These results show that the conductance increases with increasing roughness. This is in strong contrast with metallic transport in which electrical conductivity decreases with increasing roughness.

Once we have calculated the tunnel conductance, it is straightforward to evaluate the MR ratio. Figure 30 shows the calculated results of the MR ratio as

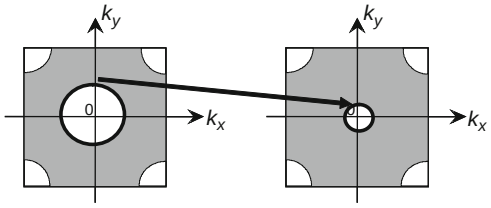

FIGURE 28 Projected Fermi surface on $\boldsymbol{k}_{\|}=(k_x, k_y)$ plane of left and right electrodes.

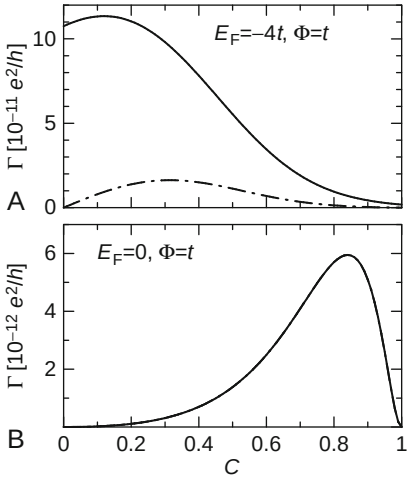

FIGURE 29 Calculated results of tunnel conductance as a function of roughness at interfaces of a tunnel junction for (A) $E_F = -4t$ and (B) $E_F = 0$, where c denotes the concentration of disordered atoms at the interface [139].

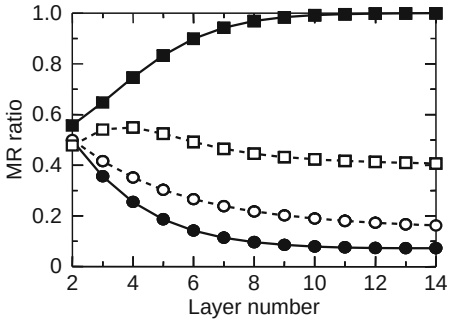

FIGURE 30 Calculated results of MR ratio as functions of barrier thickness (number of atomic layers) for $E_F = -5t$ (filled and open circles) and $E_F = 0$ (filled and open squares). Filled and open symbols denote the results without ($c = 0$) and with ($c = 0.5$) randomness, respectively. Results with randomness are plotted as functions of the average thickness of the barrier [138, 139].

functions of the number of atomic layers in the barrier for $E_F = 0$ (squares) and $-5t$ (circles). The position of the Fermi level of the former and the latter is close to the middle and bottom of the band, respectively. Filled symbols show the results without roughness, and open ones show those with roughness.

We see from the figure that the MR ratio depends strongly on the position of E_F. For $E_F = 0$, the state with $k_{\|} = (0, 0)$ is occupied by only minority ($-$) spin electrons. Therefore, the tunnel conductance for $-$ spin electrons becomes large, and the MR ratio is close to the maximum value of 1. With increasing roughness, majority ($+$) spin electrons in the state with $k_{\|} = (0, 0)$ begin to contribute to

tunnelling, and the MR ratio decreases considerably. For $E_F = -5t$, the state with $k_{\|} = (0, 0)$ is occupied by both + and − spin electrons, and the effect of roughness is smaller in this case.

5.5.6. Spin-flip tunnelling

The results presented thus far were obtained by assuming that the spin of tunnelling electrons is conserved. When there exist impurity spins within the barrier or near the interfaces, the tunnelling electrons may interact with these impurity spins and reverse their spins in the tunnelling process. This kind of spin-flip tunnelling may reduce the MR ratio. Interaction between conduction electrons and localized spins in electrodes may also produce similar effects.

In the case when tunnelling electrons interact with localized spins and flip their spins, the expression for TMR is easily obtained by using a simple model [142, 143]. When the magnetizations of the two electrodes are canted by an angle θ, the tunnel conductance is given by

$$\begin{aligned} \Gamma = \Gamma_0\{1 + \gamma\langle m^2\rangle\}(1 + P_L P_R \cos\theta) \\ +\gamma\langle \ell_+^2\rangle(1 - P_L P_R\, cos\theta)F(\beta\Delta), \end{aligned} \tag{43}$$

where

$$F(\beta\Delta) = \frac{\beta\Delta}{1 - e^{-\beta\Delta}}, \tag{44}$$

$$\langle m^2\rangle = S(S+1) + \langle m\rangle \coth(\beta\Delta/2), \tag{45}$$

$$\langle \ell_+^2\rangle = \{\coth(\beta\Delta/2) - 1\}\langle m\rangle, \tag{46}$$

$$\Delta = 2k_B T_C \langle m\rangle / S(S+1), \tag{47}$$

where $\beta = 1/k_B T$ and S is the spin of the localized electrons. T_C is an effective Curie temperature of the localized spins, and $\langle m\rangle = SB_S(\beta\Delta)$ with the Brillouin function B_S. γ denotes the degree of spin-flip tunnelling. When $\gamma = 0$, the expression above gives the usual expression for the MR ratio.

Numerical results for the temperature dependence of the MR ratio calculated by accounting for the spin-flip tunnelling are presented later.

5.5.7. Voltage dependence

The voltage drop in the tunnel junctions occurs at the insulating barrier since the resistance is highest at the barrier. When a voltage V is applied, the chemical potential shifts between the left and right electrodes in such a way that $|\mu_L - \mu_R| = eV$. Since electrons between μ_L and μ_R contribute to tunnelling in this case, a higher-order effect of V on the tunnelling conductance occurs, and the spin dependence of the electronic states of the ferromagnets is averaged. As a result, the MR ratio is usually reduced. When the left and right electrodes are made from different materials, the voltage dependence of the tunnel conductance becomes asymmetric.

When tunnelling electrons interact with elementary excitations such as phonons and magnons, they tunnel through the barrier being accompanied by these excitations. Because the tunnelling electrons lose their energy by interacting with these excitations, a characteristic feature appears in the current–voltage relation, which gives useful information on the excitation [144].

5.6. TMR in various systems

5.6.1. Fe/MgO/Fe

Calculations of MR ratios for disorder-free Fe/MgO/Fe FTJs have been performed by using a first-principles method and a realistic tight-binding model [135, 136]. The calculated results show that an extremely high MR ratio may be realized in clean samples. Being inspired by the results, single-crystal Fe/MgO/Fe samples were fabricated [145, 146] and high TMR ratios have been observed [147–149]. Figure 31 shows one of the experimental results for the MR ratio.

The experimentally observed MR ratio is much higher than that predicted by the phenomenological model. The large value may be elucidated using the principles mentioned in the previous section. First, the symmetry of the conduction bands of Fe plays an important role. The conduction band of + spin states of Fe has Δ_1 symmetry, which is composed of s-, p_z-, $d_{3z^2-r^2}$-orbitals, and contains the state with $k_{\|} = (0, 0)$. The Δ_1 band hybridizes with the s and p_z atomic orbitals of MgO. On the other hand, the conduction band of − spin states of Fe has Δ_2 symmetry composed of $d_{x^2-y^2}$ and does not contain the state with $k_{\|} = (0, 0)$, nor hybridize with the s and p_z atomic orbitals of MgO. Therefore, the decay rate of the wave function of the − spin electrons is much larger than that of + spin electrons, and as a result, the transmission coefficient of + spin electrons is much larger than that of − spin electrons. This gives rise to a large MR ratio.

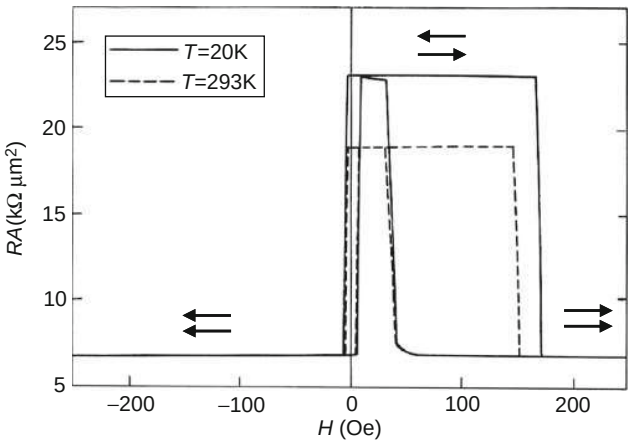

FIGURE 31 Experimental results for tunnel resistance as a function of external magnetic field [147].

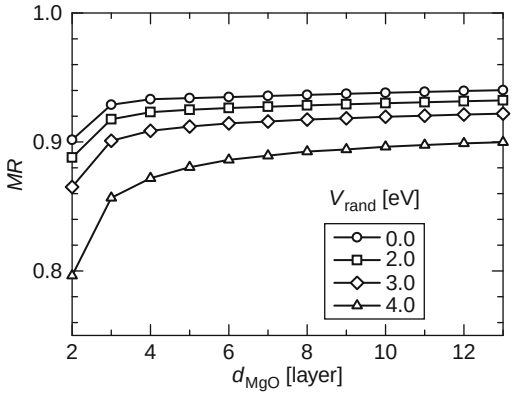

FIGURE 32 MR ratio calculated for Fe/MgO/Fe junctions with disorder as a function of MgO thickness [139].

The symmetry of the bands and the existence of $k_{\parallel} = (0, 0)$ state in the conduction bands exerts a strong influence on the MR ratio. When the MgO layer is thin, the state with $k_{\parallel} \neq (0, 0)$ also contributes to tunnelling, and the dependence of the MR ratio on MgO thickness is not simple in general.

When there is roughness in the junction, the momentum $k_{\parallel}$ need no longer be conserved. Then tunnelling via the $k_{\parallel} = (0, 0)$ state becomes possible for $-$ spin electrons, and the tunnel conductance of $-$ spin electrons increases resulting in a reduction in the spin asymmetry of the tunnel conductance, which causes the MR ratio to decrease. MR ratios calculated using the full tight-binding model that includes the effect of roughness are shown in Fig. 32. It can be seen that the MR ratio decreases with increasing roughness. The MR ratio $\sim$0.8 in the figure corresponds to a measured MR ratio that is about 400% in the optimistic definition of the MR ratio [139, 140]. Recently, similar high MR ratios have been reported.

Thus, we understand how a high MR ratio is realized in clean Fe/MgO/Fe junctions. However, high MR ratios also occur in disordered ferromagnetic electrodes such as FeCoB, which has an amorphous structure [150]. Possible reasons for this may be that B atoms may reside on regular sites in the fcc structure after annealing, and the electronic states of B atoms have energies that are distant from the Fermi energy.

5.6.2. Oscillation of TMR

When a non-magnetic layer is inserted between the barrier layer and one of the ferromagnetic electrodes, the TMR decreases rapidly with increasing the non-magnetic layer thickness [151–153]. The rapid decrease in the TMR ratio has been explained by taking into account the change in the electronic states near the interface [154]. However, an oscillation of TMR has been reported for samples in which a non-magnetic layer is inserted between the insulator and one of the two ferromagnets [155, 156]. The composition of the junction layers is NiFe/Al–O/Cu/Co, in which the Al–O layer is amorphous, but the Co and Cu layers are single

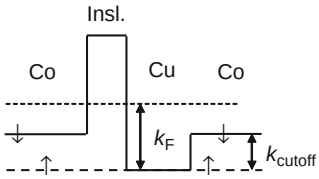

FIGURE 33 Schematic figure of the potential profile for a Co/insulator/Cu/Co junction in an antiparallel alignment of the magnetization.

crystals. Yuasa *et al.* observed an oscillation in the MR ratio as a function of the thickness of the Cu layer. The results showed that the oscillation period is given by the Fermi wavelength of Cu, and that the MR ratio oscillates around zero.

These observations seem to be reasonable, but they contradict theoretical predictions [157, 158]. Let us consider a Co/Al–O/Cu/Co junction for simplicity. A schematic figure of the potential profile is shown in Fig. 33. A quantum well is formed in the Cu $\downarrow$ spin state when the magnetization of the right Co layer is antiparallel to that of the left Co layer. In the figure, the left-hand-side level indicates the $+$ spin potential of Co, and the right-hand-side level indicates the $-$ spin potential of Co. Since the Cu potential matches the potential of the Co $+$ spin state, the situation shown in the figure is realized.

Now, the theoretical predictions for clean junctions in which $k_{\parallel}$ is conserved in the tunnelling process are as follows:

(1) $k_{\parallel}$ states on common Fermi surfaces of the L and R electrodes contribute to tunnelling.
(2) Since $k_{\parallel} = (0, 0)$ contributes to tunnelling in Co, its contribution is the largest.
(3) The filtering effect of $k_{\parallel} = (0, 0)$ state gives rise to an oscillation in the conductance with a period of k_F of Cu.
(4) An oscillation due to the cutoff wave vector k_{cutoff} shown in Fig. 33 appears in addition to the oscillation due to k_F.

Summing up these results, theory predicts that more than two periods appear in TMR oscillations and that the MR ratio oscillates about a finite value.

These theoretical results do not agree with experimental observations. These results, however, are modified when roughness is present, and become [159]:

- Since $k_{\parallel}$ need not be conserved, in principle all states of the Fermi surface projected on $k_{\parallel}$ plane contribute to tunnelling, and the conductance increases. In particular, tunnelling via quantum-well states becomes possible. Therefore, tunnel conductance in AP alignment of the magnetization Γ_{AP} increases, which makes the MR ratio small. The important point is not just the existence of a quantum-well state, but how the quantum-well state is formed. As shown in Fig. 33, the quantum-well state is formed by changing the magnetization alignment of the Co layers, and it is formed in the Cu layer inserted between the insulating barrier and the right Co layers.

- Due to the appearance of tunnelling paths via quantum-well states, the contribution to the oscillation period by k_{cutoff} decreases. This makes the oscillation period determined by k_{F} dominant.

With increasing roughness, the average value of the MR ratio gradually approaches zero, and its period tends to the value determined by k_{F}. Figure 34 shows results calculated using a simple model for MR ratios for the cases with and without roughness. We see that the multi-period oscillation becomes a single long period, and that the MR ratio oscillates about zero when disorder is introduced to the system. The calculated results show how specular tunnelling crosses over to diffusive tunnelling. In addition, the intensity of the MR ratio decays according to

$$\mathrm{MR} = \frac{1}{L_{\mathrm{NM}}} \exp\left(-\frac{\lambda_{\mathrm{NM}}}{L_{\mathrm{NM}}}\right), \tag{48}$$

where L_{NM} is the thickness of the non-magnetic layer (Cu) and λ_{NM} is the mean free path of electrons [159]. Figure 35 shows the new tunnelling paths appears via the quantum-well states. Spikes shown in Fig. 35B indicate the transmission coefficients appeared due to the disordered effects.

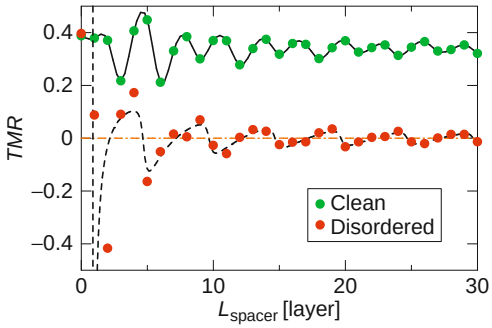

FIGURE 34 Calculated results of the MR ratio as functions of the spacer thickness obtained for clean (open circles) and disordered (filled circles) junctions. The solid curve is a visual guide, while the dashed curve is the result obtained using the stationary phase approximation [159].

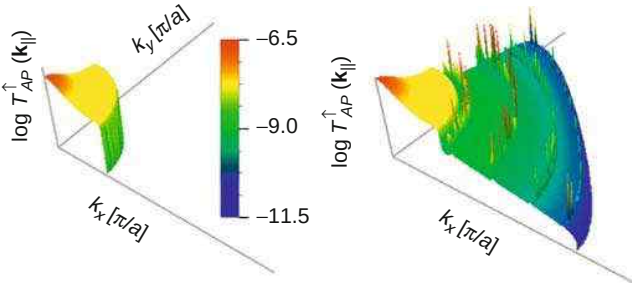

FIGURE 35 Momentum-resolved transmission probabilities in the antiparallel magnetization configuration for (A) clean and (B) disordered junctions [159].

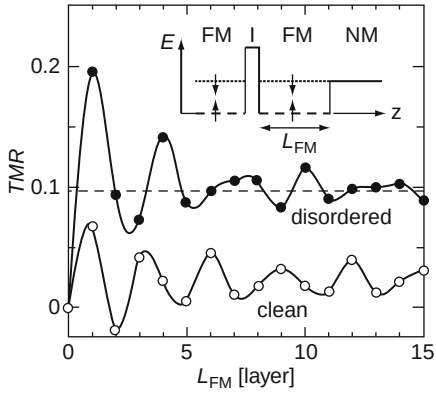

FIGURE 36 Calculated results for the TMR ratio for a tunnel junction of FM/I/FM/NM, the potential profile of which is shown in the inset. The MR ratio of the disordered junction is larger than that of the clean junction [160].

The theoretical result mentioned above shows that the toughness reduces the MR ratio due to additional tunnelling paths via quantum-well states in AP alignment. It should be noted that this reduction in the MR ratio is not a general result, since an increase in the MR ratio can be realized depending on the type of the quantum well [139].

Let us consider the quantum well shown in the inset of Fig. 36, where the quantum well is formed in the left ferromagnet between the insulator barrier and the non-magnetic electrodes. In P alignment of the magnetization, the quantum well is formed in the ↑ spin state, while it is formed in the ↓ spin state when the magnetization of the right ferromagnet is reversed. Since, in P alignment, there is poor matching of the ↑ spin Fermi surfaces between the left FM and right NM electrodes, roughness increases the ↑ spin conductance due to tunnelling channels via quantum-well states. In AP alignment, the matching of the ↓ spin Fermi surface of the left electrode and the right NM electrode is already good, and thus opening new channels via quantum-well states is ineffective. As a result, roughness increases the tunnel conductance in P alignment giving rise to an increase in the MR ratio. Figure 36 shows the calculated results for the MR ratio with and without roughness for the quantum-well state depicted in the inset. It shows that the MR ratio increases when roughness is present.

5.6.3. Tunnel junctions with half-metals

The DOS of metallic ferromagnets is usually spin dependent. When the DOS of either a ↑ or ↓ spin state is zero at the Fermi level, and one of two spin states is metallic and the other is insulating, the metals are referred to as half-metals. The spin polarization P of these half-metals is 100%, and therefore half-metals have potential applicability as magnetoresistive devices.

Many oxides, including CrO_2, Fe_3O_4 and perovskite $LaSrMnO_3$, have been shown to be half-metallic by using first-principles band calculations [161–163].

The first theoretical prediction for half-metallicity was done for Heusler alloys [161], which contain TM elements. Recently, it has been shown using the first-principles method that diluted magnetic semiconductors, such as (GaMn)As, may also be half-metallic. In experiments in which point contacts and tunnel junctions were used to measure spin polarization, lower values than 100% were obtained for P (e.g. 90% for CrO_2, 70–85% for $LaSrMnO_3$ and 60% for Heusler alloys) [164–166]. Recently, relatively high MR ratios have been observed in FTJs with Heusler alloys, suggesting that the value of P is about 86% [167, 168].

In the following, we briefly review the electronic states of half-metals, and give some experimental results for TMR in FTJs with half-metals.

5.6.3.1. Ferromagnetic tunnel junctions with manganites Perovskite manganites $(LaSr)MnO_3$ and $(LaCa)MnO_3$ show metallic ferromagnetism when La^{3+} ions in $LaMnO_3$, which is an antiferromagnet, are replaced with Sr^{2+} or Ca^{2+} ions [169, 170]. Let us first understand the origin of metallic ferromagnetism in the oxides [171, 172]. Since oxygen ions are always divalent, Mn ions are Mn^{3+} in $LaMnO_3$, and Mn^{4+} ions appear on replacing La ions with Sr or Ca. The Mn ions in the perovskite structure are surrounded by six oxygen ions which form a cubic octahedron, and therefore the degenerate d-levels are split into a doubly degenerate e_g-state and a triply degenerate t_{2g}-state (crystal field splitting) as shown in Fig. 37A.

Four electrons in a Mn^{3+} ion occupy the d-level, as shown in Fig. 37A to satisfy strong Hund's rule coupling. (The Hund's rule coupling energy is stronger than the energy splitting of the d-levels caused by the crystal field.) Since the orbitals in the t_{2g}-state are d_{xy}-, d_{yz}- and the d_{zx}-orbitals overlap weakly with oxygen p-orbitals, three electrons in the t_{2g}-state behave as localized spins with $S = 3/2$ (Fig. 36B). One electron in the e_g-state can be itinerant only when the Coulomb interaction is weak in $LaMnO_3$. That is, $LaMnO_3$ is a Mott insulator. When La ions are replaced with Sr or Ca ions and Mn^{4+} ions appear, the e_g-electrons on Mn^{3+} ions may hop onto vacant e_g-states in Mn^{4+}. In this case, the spin of the e_g-electron should be parallel to the t_{2g} localized spin on Mn^{4+} ion, because of the strong Hund's rule coupling. Since hopping of e_g-electrons lowers their kinetic energy, a parallel alignment of the localized spins of neighbouring Mn ions is favourable. This is a simple picture of the so-called double exchange interaction.

Because the ferromagnetism of perovskite manganites occurs due to strong Hund's rule coupling between e_g-electrons and t_{2g} localized spins, only up-spin

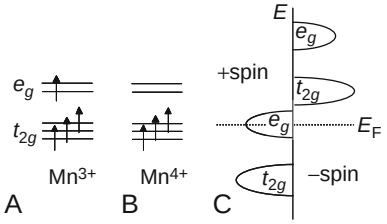

FIGURE 37 Electronic states of (A) Mn^{3+} and (B) Mn^{4+}, and schematic figure of the d-density of states of manganites.

electrons exist in the e_g-state, and down-spin states appear in the high-energy region. As a result, a half-metallic state is realized in the e_g-state as shown in Fig. 37C. The value of P measured for (LaSr)MnO_4 from the Andreev reflection is about 70%, the MR ratio of a tunnel junction made of (LaSr)MnO_4 is 1800% at low temperatures (using the optimistic definition), indicating that (LaSr)MnO_4 is almost half-metallic [173].

The TMR ratio of manganite tunnel junctions, however, decreases rapidly with increasing temperature and becomes almost zero near room temperature [173–178]. Some of the experimental results are shown in Fig. 38, in which the pessimistic definition of the MR ratio is used. Here, the barrier materials are either $SrTiO_3$ (STO) or $LaAlO_3$ (LAO). A dip of the MR ratio near $T/T_C \sim 0.2$ may be due to structural change in the barrier materials. The result that the MR ratio becomes zero at temperatures below T_C is another characteristic of manganite tunnel junctions.

Figure 39 shows the theoretical results for the temperature dependence of the MR ratio calculated using a simple model which takes into account the double exchange interaction [179]. Hund's rule coupling has been expressed as a ferromagnetic exchange interaction $K\boldsymbol{s}_i \cdot \boldsymbol{S}_i$ on site i with an interaction constant K. The spin of the tunnelling electron may flip because of the exchange interaction, resulting in effective spin-flip tunnelling. This reduces the MR ratio with increasing temperature, that is, increasing spin fluctuations of the localized spins. This decrement, however, is not so strong as that observed at low temperatures. The rapid decrease in the MR ratio observed at low temperature may be due to a change in the electronic and magnetic states of manganites at the interfaces.

Hybrid tunnel junctions have been made using Co and manganite as ferromagnetic electrodes. In this case, the sign of the MR ratio depends on the barrier materials. Junctions with Al_2O_3 exhibit a negative MR, which is usual; however, those with $SrTiO_3$ have positive MR [180, 181]. This may be attributed to the difference between the symmetry of the wave functions in Al_2O_3 and $SrTiO_3$, which changes the spin-dependent decay rate.

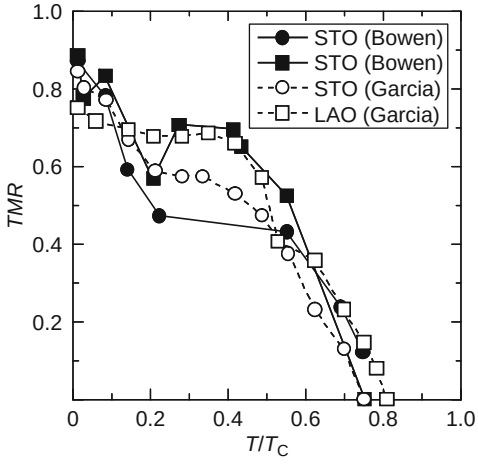

FIGURE 38 Temperature dependence of the MR ratio for manganite tunnel junctions [173–175].

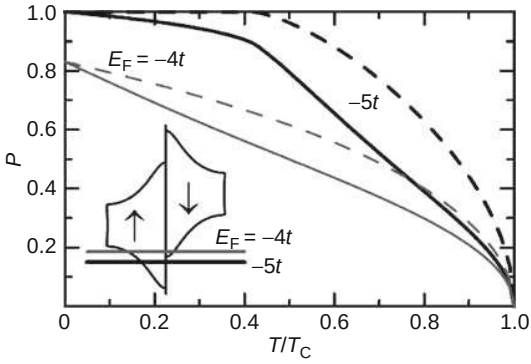

FIGURE 39 Theoretical results of the temperature dependence of the MR ratio [179].

5.6.3.2. Tunnel junctions with Heusler alloys The half-metallic characteristic of the electronic states in metallic ferromagnets was first predicted for NiMnSb in a first-principles band calculation. Later, it was shown in a first-principles band calculation that many Heusler alloys have half-metallic DOS. There are two types of structures in Heusler alloys, namely half-Heusler with an XYZ lattice and full-Heusler with an X_2YZ lattice, where X = Ni, Co, Pt; Y = Cr, Mn, Fe and Z = Sb, Ge, Al, etc. The basic lattice structure is composed of two nested bcc lattices. The half-Heusler lattice has vacant sites, which are occupied by X atoms in full-Heusler alloys.

Let us look at the global features of the DOS of a full-Heusler alloy, for example, Co_2MnAl. The up- and down-spin states of Mn atoms are strongly exchange split, and the majority spin state is below the Fermi level. Although the minority spin band is located above the Fermi level, bonding bands appear in the low-energy region due to strong pd hybridization. This strong pd hybridization produces a hybridization gap at the Fermi energy. Since the d-electron number of Co atoms exceeds that of Mn atoms, the majority spin state has unoccupied states. The strong pd hybridization also makes a gap in the local DOS of Co. A schematic figure of the half-metallic DOS is shown in Fig. 40.

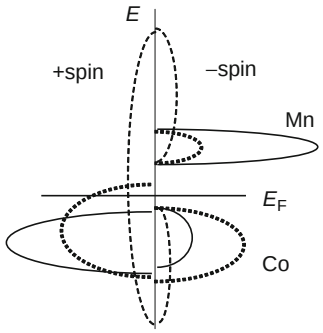

FIGURE 40 A schematic DOS of a full-Heusler alloy.

Thus, the origin of the half-metallicity of the Heusler alloys is the strong exchange splitting and pd hybridization. In experiments, however, the order of degree of ordered alloys is usually less than 1, and the value of P measured so far is much less than 100%. Recently, a tunnel junction made of full-Heusler alloys was produced and it exhibits a relatively high MR ratio at low temperature, indicating a substantial improvement in the quality of the sample. Figure 41 shows one of the experimental results [167, 168, 182]. Nevertheless, the temperature dependence of the MR ratios is rather strong, similar to that in manganite tunnel junctions.

There may be several reasons for the strong temperature dependence of the MR ratio. First, the electronic and magnetic states of Heusler alloys at the interface can differ from those in the bulk state [183]. Secondly, spin-flip tunnelling might occur as in manganite tunnel junctions [143, 184]. Figure 42 shows calculated results for the temperature dependence of the MR ratio in a phenomenological model that takes spin-flip tunnelling into account. These results are rather similar to those shown in Fig. 39; however, they are not sufficient to explain the strong temperature dependence at low temperatures observed in experiments.

Recently, quite high MR ratios have been observed in tunnel junctions using CoFeB ferromagnetic alloys and Heusler alloys [185–190]. These MR ratios at room temperature (RT) and helium temperature (LT) have been summarized in Table 4.

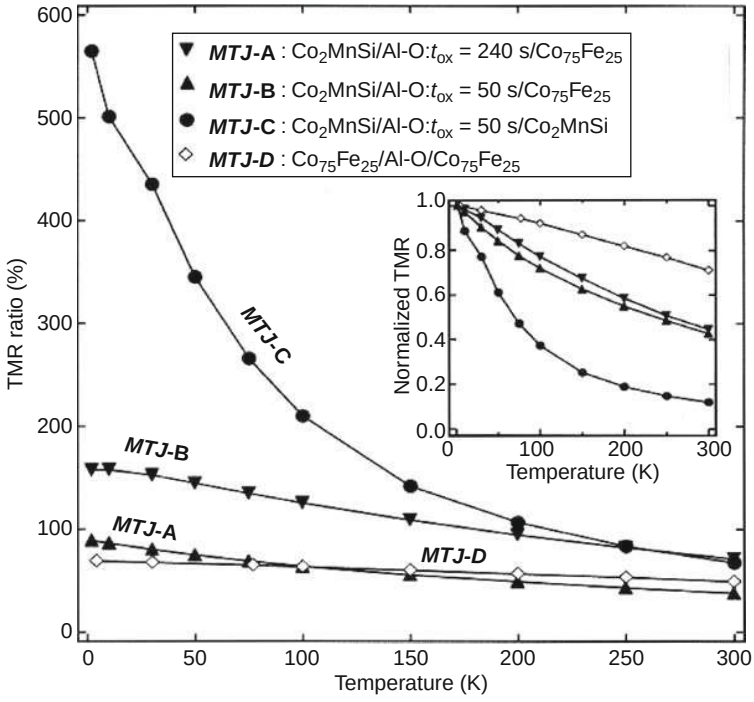

FIGURE 41 Experimental results for the temperature dependence of tunnel junctions made of Heusler alloys [168].

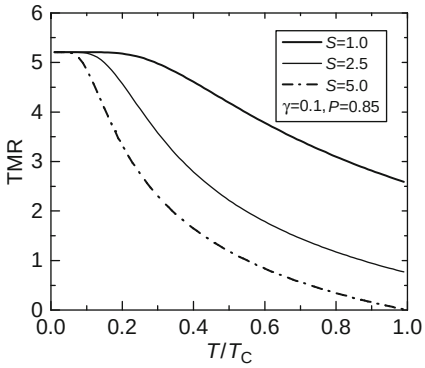

FIGURE 42 Calculated results for the temperature dependence of the MR ratio in a model that takes spin-flip tunnelling into account.

Table 4 TMR ratios observed using MgO barrier with CoFeB and/or Heusler alloys

	MR ratios (%)		
Junctions	LT	RT	References
CoFeB/MgO/CoFeB	1010	500	[186, 187]
$Co_2Cr_{0.6}Fe_{0.4}$/MgO/$Co_{50}Fe_{50}$	317	109	[188]
$Co_2FeAl_{0.5}Si_{0.5}$/MgO/$Co_2FeAl_{0.5}Si_{0.5}$	390	220	[189]
Co_2MnGe/MgO/$Co_{50}Fe_{50}$	376	160	[190]

In addition, it should be noted that an oscillation of the TMR ratio observed in Ref. [149] has been confirmed by Matsumoto *et al.* [191] and Ishikawa *et al.* [190].

5.6.3.3. Tunnel junctions with diluted magnetic semiconductors Semiconductors are the essential materials for silicon-based technologies. Recently, the field of semiconductor spintronics has been developed; it is concerned with ways to control the spin degree of freedom of electrons in semiconductors [192]. One of the most direct methods to introduce spin degrees of freedom in semiconductors is to introduce magnetic ions into semiconductors. Such semiconductors are referred to as magnetic semiconductors or as diluted magnetic semiconductors (DMSCs) when the magnetic ions are diluted.

Basic research into DMSCs of II–VI compounds has been performed for decades [193]. However, their Curie temperatures are not sufficiently high for technological applications and they are not metallic. In the late 1990s, DMSCs of III–V-based compounds were successfully fabricated by introducing Mn ions and by using a low-temperature MBE technique [194–196]; using this technique, it is possible to grow crystals in a non-equilibrium state, preventing Mn ions from precipitation. The highest T_C achieved at that time was 110 K for 5.5% Mn-doped (GaMn)As [197]. Recent fabrication techniques have succeed in producing DMSCs of III–V compounds that have T_Cs as high as approximately 200 K [198, 199].

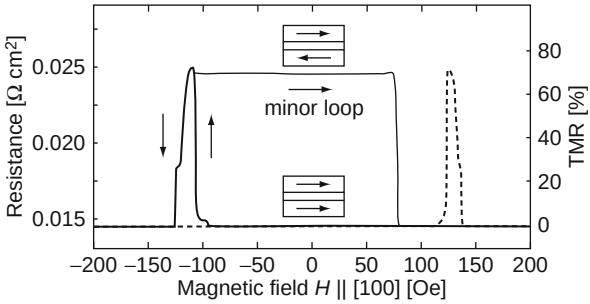

FIGURE 43 Experimental results for the TMR effect in tunnel junctions made of (GaMn)As [200].

First-principles band calculations have shown that the electronic structure of (GaMn)As is half-metallic. Thus, a high MR ratio might be expected for tunnel junctions having electrodes made from (GaMn)As and a barrier of AlAs. The experimental results for the resistivity as function of the external magnetic field strength are shown in Fig. 43 [200]. Recently, MR ratios as high as 290% have been reported [201].

A different mechanism of the TMR, however, has recently been proposed. Gould *et al.* [202] have observed a spin-valve-like TMR in (GaMn)As/Al–O/Au junctions in which only one magnetic layer exists. The result has been attributed to a change in the density of states at the top of the valence band due to the magnetic anisotropy of (GaMn)As, and the phenomenon is called tunnelling anisotropic magnetoresistance (TAMR). TAMR has been confirmed also for (GaMn)As/GaAs/(GaMn)As junctions [203, 204]. Therefore, the previous results observed in DMSC junctions might be caused by a change in the relative direction between magnetization and crystal orientation. However, Saito *et al.* [205] have reported that the intrinsic TMR exists in (GaMn)As/ZnSe/(GaMn)As junctions and the contribution by TAMR can be one tenth of the total magnetoresistance.

5.7. Coulomb blockade and TMR

5.7.1. TMR in granular magnets

A fairly large MR was observed in thin films in which magnetic grains of Co are imbedded in oxides such as Si–O [117, 118]; this observation was made at almost the same time as when a large TMR was discovered in Fe/Al–O/Fe tunnel junctions. To distinguish these two tunnel MRs, we hereafter denote the TMR in junctions as junction TMR and that observed in granular systems as granular TMR.

5.7.1.1. Tunnel conductance in granular systems Paramagnetic granular systems exhibit a peculiar temperature dependence of the resistivity. Abeles *et al.* [206, 207] have explained it in terms of a charging effect and structural characteristics. When an electron hops from one grain to a neighbouring grain (see Fig. 44),

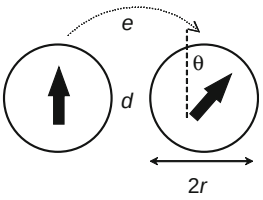

FIGURE 44 Tunnelling of an electron between two grains, the magnetizations of which are canted by an angle θ.

the distribution of charge changes, breaking the charge neutrality in the grains. The internal energy of these grains increases because of the Coulomb repulsion between electrons in the grains. This increase in the energy is the charging energy, which is written as E_C hereafter. A pair of grains may correspond to a condenser, and E_C depends on the size of the grains and on the distance between them. Therefore, E_C increases with decreasing size of the grains.

When the thermal energy k_BT is smaller than E_C, an electron is prevented from hopping to neighbouring grains due to an increase in the energy E_C; this is the so-called Coulomb blockade. At high temperatures, an electron is thermally activated to overcome the charging energy and is able to hop to neighbouring grains. Therefore, the conductance of an electron between two grains is proportional to $\exp(-E_C/k_BT)$. The transmission probability for an electron to tunnel through the barrier with a width d between two grains is proportional to $\exp(-2\kappa d)$, where $\kappa = \sqrt{2m^*(U - E_F)}/\hbar$, and where m^* is the effective mass of the electron, U is the barrier height and E_F is the Fermi energy. The tunnel conductance between two grains is thus given by

$$\Gamma \propto \exp(-2\kappa d - E_C/k_BT). \tag{49}$$

In granular films, the grain size (r) distributes, and therefore both d and r distribute. Nevertheless, Abeles *et al.* have explained the relationship between r and d in the following manner. Let us consider a relatively large region, say several 10^3 nm^3. Over such a large region, the ratio of the volumes of metallic grains and oxides will be equal to that of the entire sample with a fixed composition. In this case, large size grains should be surrounded by thicker oxide regions, that is, $r \propto d$. Since the charging energy is produced by the Coulomb interaction, it may be assumed that $E_C \approx e^2/r \propto 1/d$. This relation also holds when we consider the grain as a condenser. In this case, $E_C = e^2/2C \approx e^2 d/2r^2 \propto 1/d$. In any case, one may write $E_C = C_0/d$, where C_0 is a constant. The conductance is then given by

$$\Gamma \propto \exp(-2\kappa d - C_0/k_BTd). \tag{50}$$

We further assume that the distribution of d is sufficiently small compared with the d dependence of Γ. Under this assumption, the total conductance of the sample may be given by the conductance of a parallel circuit of these small regions. In this case, the current flows through regions that have the smallest

resistance. That is, the total conductance is given by the conductance that maximizes $\exp(-2\kappa d - C_0/k_B T d)$ for a given temperature. The resultant conductance is given by

$$\Gamma \propto \exp\left[-2\sqrt{2\kappa C_0/k_B T}\right]. \tag{51}$$

This result shows that the resistance $R = 1/\Gamma$ increases as $\exp\left(1/\sqrt{T}\right)$ with decreasing temperature, in good agreement with the experimental observations.

The temperature dependence shown above may be interpreted intuitively as follows. The Boltzmann factor $\exp(-E_C/k_B T)$ indicates competition between the charging energy and the thermal energy. At high temperatures, electrons may hop to smaller grains even when E_C is large. Therefore, electrons prefer to hop to smaller grains, since they have smaller tunnelling rates $\exp(-2\kappa d)$. At low temperatures, on the other hand, electrons tend to hop to larger grains, which have smaller charging energies E_C. A schematic figure depicting this situation is shown in Fig. 45.

5.7.1.2. Granular TMR The MR ratio of the granular TMR is given by [208]

$$\mathrm{MR} = \frac{\Gamma^{-1}(0) - \Gamma^{-1}(H)}{\Gamma^{-1}(0)} = \frac{P^2}{1 + P^2}, \tag{52}$$

which is just half the MR ratio of junction TMR. This is due to the random distribution of the magnetization direction of the grains when no external magnetic field is applied.

The above result is obtained as follows. Consider the two ferromagnetic grains L and R shown in Fig. 44. The magnetizations of the R grain is canted by an angle θ with respect to that of the L grain. In this case, the transition probability for an electron on the L grain to hop to the same spin state on the R grain is given by $\cos^2(\theta/2)$, and that to the opposite spin state on the R grain is $\sin^2(\theta/2)$. Thus, the probability of an electron tunnelling between L and R grains is given by

$$T_{\uparrow\uparrow} = D_{R+} D_{R+} \cos^2(\theta/2) + D_{L+} D_{R-} \sin^2(\theta/2), \tag{53}$$

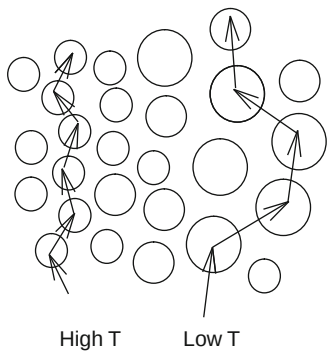

FIGURE 45 A schematic figure showing the hopping of electrons at high and low temperatures.

$$T_{\uparrow\uparrow} = D_{\mathrm{L}-} D_{\mathrm{R}-} \cos^2(\theta/2) + D_{\mathrm{L}-} D_{\mathrm{R}+} \sin^2(\theta/2), \tag{54}$$

where $D_{\mathrm{L}+(-)}$ and $D_{\mathrm{R}+(-)}$ are majority (minority) spin DOS of the L and R grains, respectively. The total tunnelling probability is given by

$$T = T_{\uparrow\uparrow} + T_{\uparrow\uparrow} \propto 1 + P^2 \cos\theta, \tag{55}$$

where

$$P^2 = \frac{(D_{\mathrm{L}+} - D_{\mathrm{L}-})(D_{\mathrm{R}+} - D_{\mathrm{R}-})}{(D_{\mathrm{L}+} + D_{\mathrm{L}-})(D_{\mathrm{R}+} + D_{\mathrm{R}-})}. \tag{56}$$

The spin of the tunnelling electron is assumed to be conserved in the tunnelling process.

The tunnel conductance in the absence of a magnetic field is given by

$$\Gamma(0) \propto \langle 1 + P^2 \cos\theta \rangle_{\mathrm{av}} = 1; \tag{57}$$

when an external magnetic field H is applied it is

$$\Gamma(H) = 1 + P^2. \tag{58}$$

We then obtain Eq. (52).

Figure 46 shows the experimental results for granular TMR [118]. They are consistent with theoretical results at high temperatures. In the figure, the MR ratio increases at low temperatures, which may be explained in terms of a higher-order effect of the Coulomb blockade.

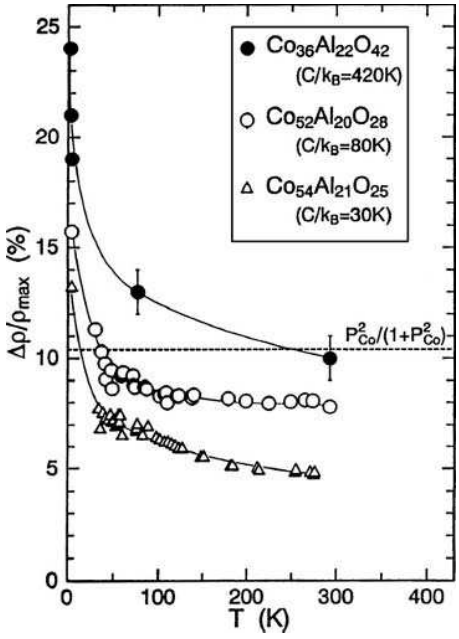

FIGURE 46 Experimental results for granular TMR [118].

5.7.2. Coulomb-blockade TMR

Let us consider a well-controlled structure such as the one shown in Fig. 47, in which a nanoscale grain is separated from two ferromagnetic electrodes by two insulating barriers. The grain can be either ferromagnetic or paramagnetic. When the grain is sufficiently small, the effect of charging energy, that is, the Coulomb blockade becomes important [209, 210]. The terms "charging energy" and "Coulomb blockade" refer to essentially the same concept; here, we adopt the latter terminology.

We assume that the grain has a charge of Ne. In this case, the electrostatic energy of the grain is given by

$$U(N) = \frac{(\mathrm{Ne})^2}{2C} - \mathrm{Ne}\varphi = \frac{1}{\sqrt{2C}}(\mathrm{Ne} - C\varphi)^2 - \frac{C\varphi^2}{2}, \tag{59}$$

where C is the effective capacitance of the grain and φ is the electrostatic potential. When no current flows, charge neutrality is satisfied, giving $\mathrm{Ne} = C\varphi$. As a current begins to flow, and the number of electrons on the grain increases by one, the energy increases by $e^2/2C$. When the temperature is sufficiently low and the bias voltage is lower than the charging energy $e^2/2C$, no electron can hop onto the grain. This is the Coulomb blockade. With increasing bias voltage, the number of electron hopping onto the grain increases discretely. As a result, the current increases stepwise and the conductance changes oscillatory with increasing bias voltage. The oscillation of the conductance is referred to as the Coulomb oscillation. The current can be controlled by the gate voltage, and it is therefore possible to allow one electron to tunnel through the grain; such a device is called a single-electron transistor.

When the electrodes are ferromagnetic, TMR also appears and the MR ratio oscillates according to the Coulomb oscillation [211, 212]. It is noteworthy that TMR occurs even when the grain is paramagnetic. This is because the tunnelling rates of the two insulating barriers depend on the magnetization alignment of the electrodes. An example of the theoretical results of the oscillation of the TMR is shown in Fig. 48, in which the grain is assumed to be paramagnetic.

Now, it may be questioned that a current never flows when the Coulomb blockade is effective. In reality, there exists a leakage current, which is caused by the following process. Since energy conservation need not apply over short time periods due to the uncertainty principle, a process appears to occur in which an electron moves from the grain to the R electrode almost simultaneously as another electron hops onto the grain from the L electrode. This tunnelling process is called cotunnelling, since two tunnelling process occur almost simultaneously.

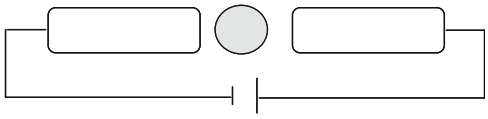

FIGURE 47 A schematic figure of a double tunnel junction for which the Coulomb blockade appears.

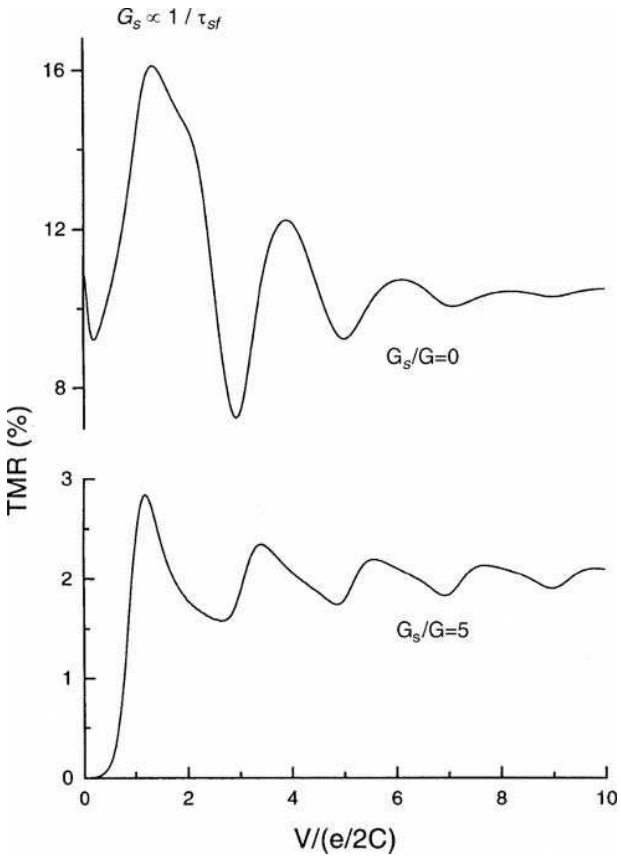

FIGURE 48 Theoretical results for the oscillation of TMR ratios in the Coulomb-blockade regime. Here the grain is assumed to be paramagnetic [212].

The tunnel rate of cotunnelling is proportional to a product of the runnel rates for R and L tunnel barriers. In this case, the MR ratio is twice as large as that for the usual TMR, since the spin dependence of the tunnel rates of both barriers contribute. The increase in the TMR ratio at low temperatures shown in Fig. 46 may be explainable in terms of cotunnelling [213].

6. BALLISTIC MAGNETORESISTANCE

When a current flows in a region that has a length scale shorter than the mean free path, the conductance becomes quantized. The quantization of the conductance was discovered by van Wees *et al.* [214] in a two-dimensional electron gas (2DEG). They controlled the width of a channel in which electrons flowed by applying a gate voltage to 2DEG, and observed that the conductance changed in a stepwise manner, in steps of $2e^2/h$.

This phenomenon of quantized conductance may be understood as follows. Constricted regions, in which a current flows, may be considered to be pseudo-one-dimensional. The electronic state of such constricted regions is continuous along the direction of current flow, but it is quantized perpendicular to the current flow. The quantization of the electronic state is characterized by the Fermi wavelength λ_F. When the width of the constricted region is close to λ_F, only one state is available for electrons, and therefore two electrons (having up and down spins) may contribute to a current, giving rise to a conductance of $\Gamma_0 = 2e^2/h$. If the width of the sample is increased, the conductance increases stepwise in steps of $\Gamma = 2e^2/h \times n$. A simple derivation of quantized conductance has been given in Section 3. The length scale of the constricted region is usually smaller than the mean free path, and the effect of scattering may be neglected. Such transport is referred to as ballistic transport.

Conductance quantization was first observed in semiconductors. Conductance quantization can be easily observed in semiconductors since λ_F is several 10 nm. By contrast, λ_F in metals is 1 nm, which makes the observation of conductance quantization difficult in conventional metals. In this section, we will briefly review (1) conductance quantization in paramagnetic metals, (2) conductance quantization in ferromagnetic metals and (3) MR effects in ballistic transport, called BMR.

6.1. Conductance quantization in metals

6.1.1. Paramagnetic metals

To realize ballistic transport in metals, the constricted region should be less than 1 nm. Potential methods for achieving this include the break-junction method in which a narrow wire is slowly bent to produce a small link just before breakdown of the wire, and the point-contact method in which the sharp tip of metallic wire is contacted onto the metal's surface. Fabrication of such a state in a controllable manner is quite difficult usually, making it necessary to make many repeated observations and then to take a statistical average in order to deduce meaningful conclusions.

In pseudo-one-dimensional systems such as 2DEG with gate control, the electronic state that is responsible for electrical conduction is well defined (it is called a channel). The quantized conductance $\Gamma_0 = 2e^2/h$ is specific to each channel. On the other hand, in the break-junction or point-contact methods in metals, each electronic state does not necessarily produce $\Gamma_0 = 2e^2/h$. This is because the constricted region in metals is too small to well define the wave vector in the current direction, that is, conservation of momentum is broken and scattering of electrons may occur in the constricted region. In other words, the constricted region itself is a scatterer, making the transmission coefficient for electrons passing through the region less than 1. Therefore, the conductance may be given by

$$\Gamma = \sum_i \Gamma_0 \tau_i, \tag{60}$$

where τ_i is the transmission coefficient of the ith channel.

When $\tau_i = 0$ or 1, the conductance Γ is an integer multiple of Γ_0. In metallic constrictions, since $0 < \tau_i < 1$, it is rather difficult to conclude that Γ is an integer multiple of Γ_0 from measurements. Scheer *et al.* [215] have performed realistic calculations of the conductance for point contacts and many experiments with break junctions and point contacts. They found that the characteristics of the channel in a single-atom contact are determined by the number and type of orbitals in the valence band. For example, s- and p-orbitals are responsible for conduction in Al, but d-orbitals are important in Nb. In every channel $0 < \tau_i < 1$, but the total conductance is approximately an integer multiple of Γ_0 after summing the contributions from many channels. Figure 49 shows the calculated results of the transmission coefficient for a single-atom contact. It shows that the transmission coefficient varies continuously with a change in the position of the Fermi energy.

6.1.2. Ferromagnetic metals

The factor of 2 that appears in the quantized conductance Γ_0 indicates spin degeneracy. Since spin degeneracy is lifted in ferromagnets, conductance quantization might be expected to be given by $\Gamma_0/2 = e^2/h$. To confirm this expectation, many experiments have performed with break junctions and point contacts made of ferromagnets. Figure 50 shows the average conductance observed for many

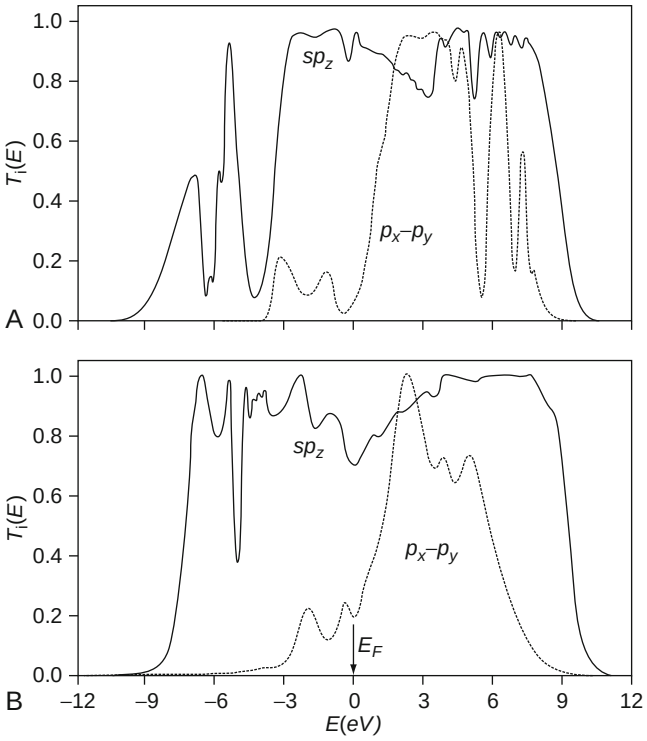

FIGURE 49 Calculated results for the transmission coefficient for Al one-atom contact in the two extreme cases of (A) short and (B) long necks [216].

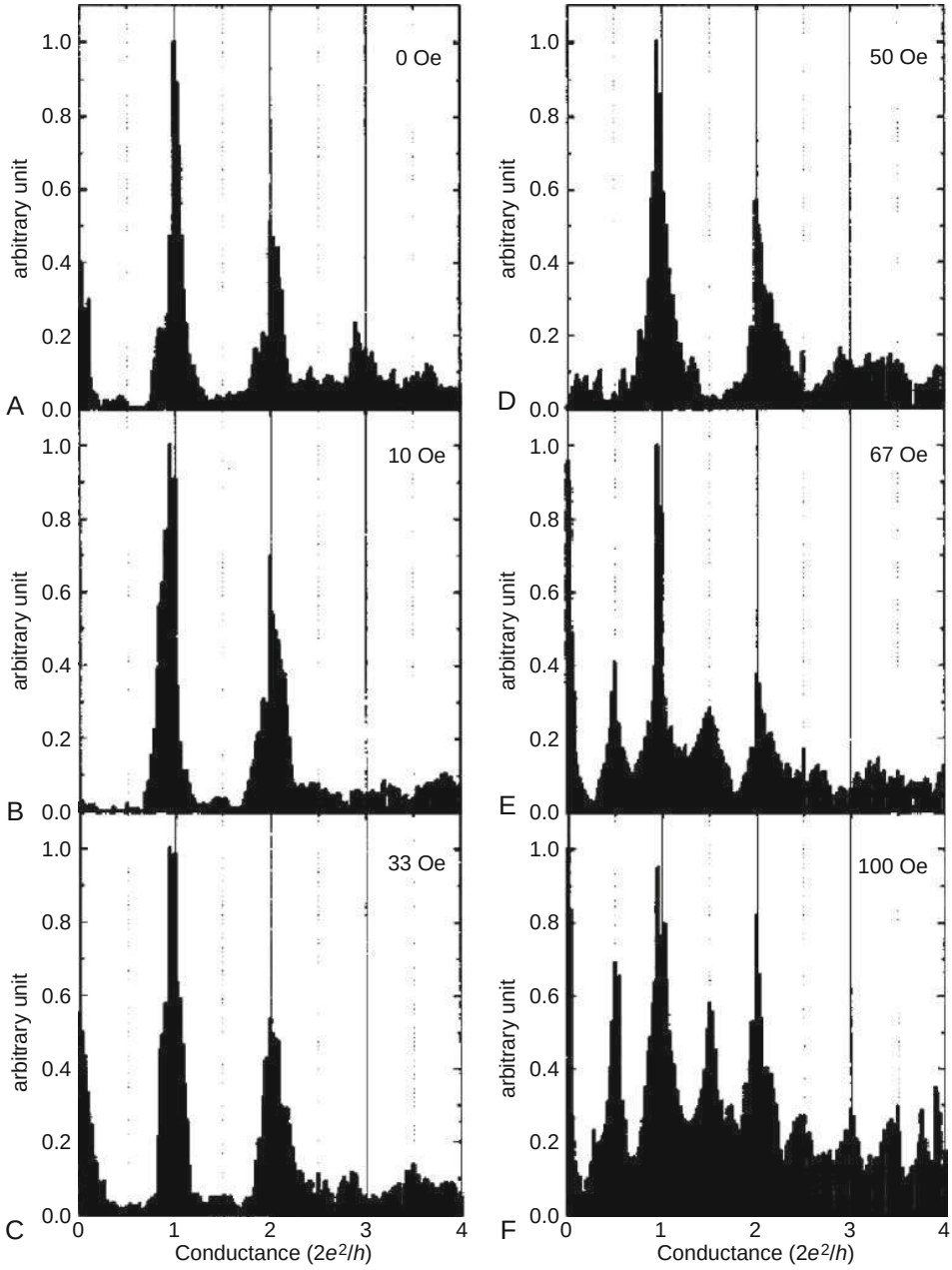

FIGURE 50 Experimental results of conductance quantization performed for many break junctions of Ni wires with and without an external magnetic field [217].

break junctions made from Ni wires [217]. The results show that the quantized conductance is Γ_0 when an external magnetic field H of less than 50 Oe is applied, but it is $\Gamma_0/2$ when $H > 50$ Oe. The results are closely related to BMR described in the next section, and they are analyzed in detail there. Finally, it has been reported that a conductance quantization of $\Gamma_0/2$ was also observed in non-constricted Au by using chemical potential control.

6.2. Experiment and theory of BMR

6.2.1. Experiments

García *et al.* [218] have measured the MR effect for Ni point contacts, and reported that the MR ratio becomes large when the conductance approaches Γ_0. The maximum MR ratio was 280% (for the pessimistic definition). There results are shown in Fig. 51. The MR effect thus observed was termed BMR.

Later Chopra and Hua [219, 220] have reported that the MR ratio is 3000–10,000% for usual point contacts of Ni or those produced by electrodeposition. However, the resistance in their measurements is 10–100 Ω, which is much smaller than the inverse of the quantization conductance $\Gamma_0^{-1} = 12.9\text{k}\Omega$. Thus, the conductive properties of their samples may differ from those observed by García *et al.* Furthermore, the MR ratio observed by electrodeposition can be either positive or negative.

6.2.2. Interpretation of BMR

So far there have been several mechanisms proposed for BMR; however, complete understanding of this phenomenon has yet to be achieved. One of the theoretical interpretations of BMR is to attribute the large MR to the vanishing of the domain

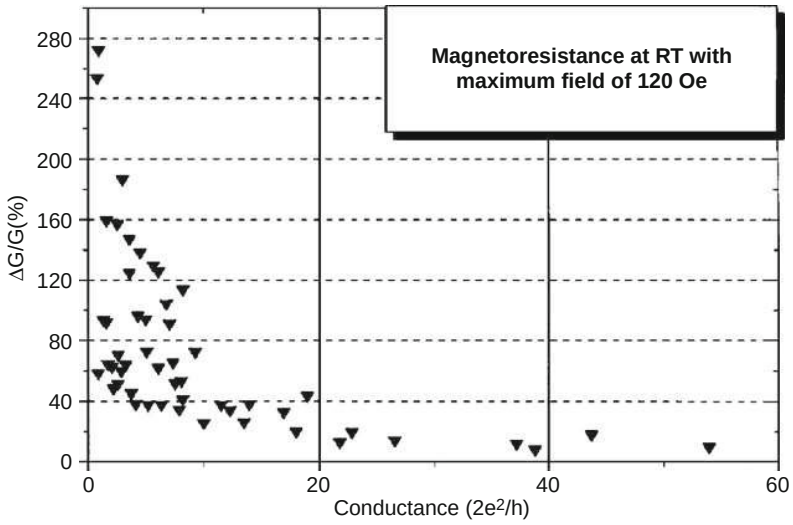

FIGURE 51 Experimental results of conductance change as a function of quantized conductance in point contacts [218].

walls (DWs) at the ferromagnetic constriction [221]. An AP alignment between the magnetizations of the ferromagnetic wire and the surface of a ferromagnetic film may produce a DW in the region of the contact. Bruno [222] has pointed out the width of a DW can be sufficiently narrow to produce a large MR effect. Tatara *et al.* have calculated the BMR ratio for narrow DWs and showed that the MR ratio increases with decreasing DW width. Both conductance quantization and shrinkage of the DW region are responsible for the large BMR. On the other hand, it should be noted that a realistic calculation of BMR gives 70% at most for a planar DW; that is for a DW in which the magnetization changes direction within a single atomic layer [223].

Imamura *et al.* [224] have studied the conductance quantization for nanocontacts of two ferromagnets, and showed that the parameter region at which a conductance quantization of $\Gamma_0/2 = e^2/h$ appears depends on the alignment of the magnetization of the two ferromagnets. A difference in the conductance quantization between the P and AP alignments of the magnetization may give rise to a large MR ratio.

These theories, however, have neglected realistic electronic states, such as multi-orbitals. We have already mentioned that the quantization of conduction is strongly influenced by the number and type of orbitals. First-principles band calculations are useful to confirm this point. Such calculations have been done by the Mertig group for an atomic contact composed of transition atoms. Their results indicate that the electronic states responsible for conduction are s-like and that the spin dependence of the conduction is caused by a d-like density of states. The transmission coefficient for these states is less than 1 and changes continuously with a change in the Fermi level. In addition, they confirmed that the MR ratio was not large and was at most 50% [225, 226].

Other proposed mechanisms include a magnetoelastic mechanism and diazotization of the nanoconstricted region. While the former mechanism is easy to understand, it does not explain the experimental observations that the MR effect is independent of the direction of magnetization. The role of diazotization on the MR effect has been studied only for a uniform surface; no investigation of nanoconstriction has been performed yet [227].

7. OTHER MR EFFECTS: NORMAL MR, AMR AND CMR

The MR so far described occurs in nanoscale magnets. There are other interesting MRs in bulk systems; these include the well-known phenomena of normal MR, anisotropic MR and colossal MR, which was reinvestigated recently in perovskite manganites. In this section, we briefly describe these MR phenomena.

7.1. Normal MR

When both a magnetic field $\boldsymbol{H}$ and an electric field $\boldsymbol{E}$ are applied to electron systems, the electrons drift in the direction of $\boldsymbol{H} \times \boldsymbol{E}$. However, the external magnetic field does not produce any additional current; instead, it produces

only a Hall voltage perpendicular to the electric field, which is called the normal Hall effect. When there are two or more types of carrier, the MR that is produced is called normal MR [24].

In the case when two types of carrier exist say $i = 1, 2$, the total conductivity when both $\boldsymbol{H}$ and $\boldsymbol{E}$ are applied is given by

$$\sigma = \sigma_1 + \sigma_2 - (\bar{\boldsymbol{J}}_1 + \bar{\boldsymbol{J}}_2) \cdot \frac{E \times H}{E^2}, \tag{61}$$

where σ_i is the conductivity for the ith carrier and $\bar{\mathrm{J}}_i$ is determined by

$$\sigma_i \boldsymbol{E} = \bar{\boldsymbol{J}}_i / n_i e c + \boldsymbol{H} \times \bar{\boldsymbol{J}}_i \tag{62}$$

where n_i is the carrier density, e is the charge of an electron and c is the velocity of light. The second term in the expression for σ indicates the MR effect.

7.2. Anisotropic magnetoresistance

Anisotropic MR is a phenomenon that occurs in ferromagnets in which the resistivity depends on the angle between the current and magnetization directions. Figure 52 shows the experimental results obtained for the change in resistivity of Ni when a magnetic field is applied parallel and perpendicular to the current direction. The rapid change in the resistivity at low magnetic fields is due to magnetization rotation, and the linear change at high magnetic fields is due to the so-called forced effect. The magnitude of AMR is obtained by extrapolating the resistivity change to $H = 0$.

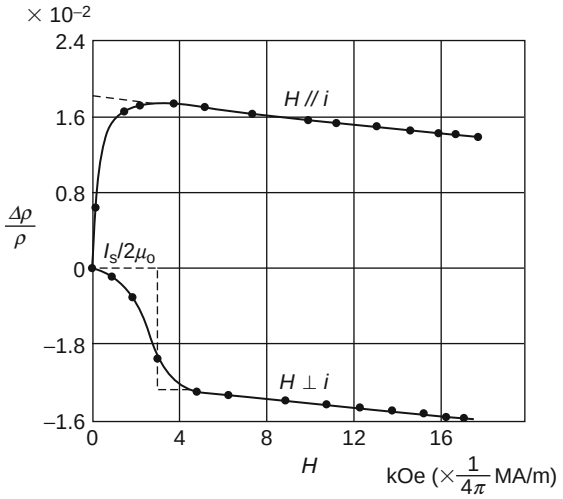

FIGURE 52 Experimental results for AMR in Ni [18].

A phenomenological theory of AMR follows. Let the magnetization $\boldsymbol{M}$ be parallel to the z-direction, and the relative angle between $\boldsymbol{M}$ and $\boldsymbol{J}$ be θ. The relationship between the electric field $\mathbf{E}$ and the current $\mathbf{J}$ is given by

$$\begin{pmatrix} E_x \\ E_y \\ E_z \end{pmatrix} = \begin{pmatrix} \rho_\perp & -\rho_{\mathrm{H}} & 0 \\ \rho_{\mathrm{H}} & \rho_\perp & 0 \\ 0 & 0 & \rho_\parallel \end{pmatrix} \begin{pmatrix} J_x \\ J_y \\ J_z \end{pmatrix}, \tag{63}$$

in general, where ρ_{H} is the Hall resistivity. Substituting the relation between the electric field and the current into the expression for the total resistivity, $\rho = \mathrm{E}\cdot\mathrm{J}/E^2$, we obtain

$$\rho = \rho_\perp + \left(\rho_\parallel - \rho_\perp\right)\cos^2\theta. \tag{64}$$

When the samples are polycrystalline, it should be averaged over the angle to give

$$\rho = \rho_\perp + \left(\rho_\parallel - \rho_\perp\right)/3 \equiv \bar{\rho}. \tag{65}$$

When $\boldsymbol{H}\|\boldsymbol{M}$, $\rho = \rho_\parallel$ and when $\boldsymbol{H}\perp\boldsymbol{M}$, $\rho = \rho_\perp$, one may define the MR ratio as

$$\frac{\Delta\rho}{\bar{\rho}} = \frac{\rho_\parallel - \rho_\perp}{\bar{\rho}}. \tag{66}$$

Since the current direction in AMR depends on the magnetization (i.e. the spins of electrons), the SOI is a possible origin of AMR. The role of SOI is twofold; one is mixing the up- and down-spin states of the d-states, and the other is the generation of a scattering probability from the up- (down-) to down- (up-) spin states. In transition metal alloys, such as Co alloys, the conductivity is dominated by free electrons, such as up-spin electrons. When mixing between the up- and down-spin states occurs, scattering from the up-spin state to the down-spin states increases $\rho_\uparrow$. On the other hand, d-states at the Fermi level are reduced by the mixing, and therefore $\rho_\downarrow$ decreases. Thus we may write the effect of SOI as

$$\rho_{\uparrow(\downarrow)} = \rho_{0\uparrow(\downarrow)} + (-)\gamma\rho_{0\uparrow(\downarrow)}, \tag{67}$$

where γ is a constant. The magnitude of γ depends on the angle between the current and magnetization, resulting in a MR called AMR. This expression can be approximated by

$$\begin{aligned} \rho_{\parallel\uparrow(\downarrow)} &= \rho_{0\uparrow(\downarrow)} + (-)\gamma_\perp\rho_{0\uparrow(\downarrow)} + (-)\left(\gamma_\parallel - \gamma_\perp\right)\rho_{0\uparrow(\downarrow)} \\ &\sim \rho_{\perp\uparrow(\downarrow)} + (-)\gamma\rho_{\perp\uparrow(\downarrow)}, \end{aligned} \tag{68}$$

and by redefining $\gamma_\parallel - \gamma_\perp$ as γ we obtain

$$\frac{\Delta\rho}{\bar{\rho}} \sim \frac{\rho_\parallel - \rho_\perp}{\rho_\parallel + \rho_\perp} \sim \gamma(\alpha - 1), \tag{69}$$

where the parameter α is given by $\left(\alpha = \rho_{\perp\downarrow}/\rho_{\perp\uparrow}\right)$. Thus, the AMR ratio is related to the spin-dependent resistivity via the parameter α. The results agree well with experimental ones.

To estimate the value of γ, the transition probability should be calculated using, for example, the golden rule. A detailed description has been presented in a paper by Smit [228].

7.3. Colossal magnetoresistance

Mn ions in $LaMnO_3$ (LMO) are trivalent and each Mn ion has one electron in the e_g-state, and three electrons in the t_{2g}-state. The electronic states of LMO are related with the important factors given below that govern the physical properties of manganites:

- Since each Mn ion has one electron in an e_g-orbital, LMO must be metallic unless there is a strong Coulomb interaction between electrons. Since LMO is an antiferromagnetic insulator, the Coulomb interaction should play an important role in the magnetic and transport properties.
- The e_g-state consists of degenerate $d_{x^2-y^2}$- and $d_{3z^2-r^2}$-orbitals. Therefore the e_g-electron can be in either the $d_{x^2-y^2}$- or $d_{3z^2-r^2}$-orbital, that is, the electron is free to choose either of these orbitals; that is, it has an orbital degree of freedom, in addition to charge and spin degrees of freedom.
- The orbital degeneracy also gives rise to lattice distortion, for example, Jahn–Teller distortion lifts the orbital degeneracy. Therefore, the electron-lattice interaction is expected to be strong in manganites, especially for those in the insulating phase.
- Because of the octahedron configuration of the oxygen ions, t_{2g}-orbitals hybridize less with oxygen p-orbitals than e_g-orbitals, and electrons in the t_{2g}-state behave as if they had a localized spin with $S = 3/2$. The spin of e_g-electron couples ferromagnetically with t_{2g}-spins due to strong Hund's rule coupling.

When La ions are replaced with Sr or Ca ions, Mn^{4+} ions are introduced, and the e_g-electrons can become mobile under strong Hund's rule coupling, electron-lattice interaction, and Coulomb interaction, with the addition of an orbital degree of freedom. They produce a rich variety of phenomena, in both magnetism and transport. As for magnetism, manganites exhibit various magnetic orderings that depend on the dopant. LMO is a layered antiferromagnet (AF), which can be converted to a metallic (M) ferromagnet (F) by replacing La with Sr or Ca at approximately 30% doping. At approximately 50% doping of Sr or Ca, manganites exhibit a complicated AF (CE-type AF). Upon further doping, they show chain-type AF (C-type AF) and finally they show usual AF (G-type AF). The AF state is usually insulating; however, A-type AF often shows metallicity near 50% doping. Charge-ordered (CO) states also appears depending on the magnetic state.

The so-called colossal magnetoresistance (CMR) is also related to magnetism and charge ordering [229–234]. This phenomenon may be classified into three types:

(1) The high-temperature phase is a paramagnetic insulator (PI), and the low-temperature phase is a metallic ferromagnet (MF). In this case, the resistivity shows a peak at the Curie temperature, which decreases dramatically with applied magnetic field, and the peak shifts towards higher temperatures.

The higher the resistivity in PI phase, the sharper the peak becomes, and the larger the MR effect becomes. When the high-temperature phase is MF, the peak structure in the resistivity diminishes.

(2) The high-temperature phase is a PI, which changes to MF phase on reducing the temperature. Upon a further decrease in temperature, the phase makes a first-order transition into a CO-AF phase. When an external magnetic field is applied, the first-order transition temperature shifts to lower temperatures, resulting in a spread of the metallic region. Therefore, applying a magnetic field produces a huge change in the resistivity. This may be an insulator to metal transition. In this case, however, no peak appears near the Curie temperature in the high-temperature region.

(3) The high-temperature PI phase changes into a CO phase with decreasing temperature, and its resistivity becomes high. With a further decrease in the temperature, a CO-AF phase appears, and the resistivity becomes higher. When the magnetic field is applied, a first-order transition from a low-temperature CO-AF to a MF occurs. This is also an insulator–metal transition produced by the magnetic field.

Thus, CMR is related to insulator–metal transitions. Although several mechanisms of CMR of the first type have been proposed, few theories have been proposed for the second and third ones. Typical models for explaining CMR include the so-called double exchange model, the critical scattering mechanism, double exchange with Jahn–Teller distortion, the percolation model and the localization model. We will not describe these models in detail, rather detail descriptions can be found in various review articles [235–238].

8. SPIN–ORBIT INTERACTION AND HALL EFFECTS

We have shown that the SOI gives rise to the magnetoresistance known as AMR. Since SOI is a coupling of spin and orbital motion of electrons, it also gives rise to other interesting transport properties called as anomalous Hall effect (AHE) and spin Hall effect (SHE) as well as electric field-induced spin accumulation in 2DEG. Although the theoretical studies are performed for bulk systems, the experimental measurements are usually done for mesoscopic or nanosize systems. We therefore give a brief explanation on these properties.

8.1. Spin–orbit interaction

SOI is a relativistic effect and the corresponding Hamiltonian is given by

$$H_{\mathrm{SO}} = -\frac{e\hbar}{4m^2c^2}(\boldsymbol{\sigma}\cdot[\boldsymbol{E}\times\boldsymbol{p}]), \tag{70}$$

$$\simeq \frac{e}{2m^2c^2}\left(\frac{\mathrm{d}V}{r\mathrm{d}r}\right)(\boldsymbol{s}\cdot\boldsymbol{l}), \tag{71}$$

where c is the light velocity, E is an electric field induced by a potential gradient $\mathrm{d}V/\mathrm{d}r$ and $\boldsymbol{l}$ is the orbital angular momentum. There are several origins of the internal electric field:

- Inversion asymmetry of the lattice such as the zincblende structure. The SOI is called Dresselhaus-type SOI [239].
- Inversion asymmetry of the structure such as the 2DEG. The SOI is called Rashba-type SOI [240, 241].
- $\ell - s$ coupling on atoms.
- Potential gradient caused by impurity potential and $\ell - s$ coupling of atoms.

Since the first three types of SOI are called intrinsic SOI since they reside uniformly in the system, the last one is called an extrinsic SOI as it is caused by impurity potentials. The SOI in semiconductors is usually caused by the Dresselhaus- and/or the Rashba-type SOI, while that in metal and alloys may be related to the $\ell - s$ coupling.

The SOI shown above may be recasted in different ways to clarify the role on the transport properties. Since Eq. (70) may be written as $H_{\mathrm{SO}} \propto \boldsymbol{\sigma}\cdot\boldsymbol{h}_{\mathrm{eff}}$, one may consider that the SOI subsists a momentum-dependent effective magnetic field. It is also rewritten as $H_{\mathrm{SO}} \propto [\boldsymbol{\sigma} \times \boldsymbol{E}]\cdot\boldsymbol{p}$, from which one can derive a velocity $v = \mathrm{d}H_{\mathrm{SO}}/\mathrm{d}\boldsymbol{p} \propto [\boldsymbol{\sigma} \times \boldsymbol{E}]$, for conduction electrons. The velocity is called anomalous velocity. It is also noted that the SOI results in complex wave functions of electrons, from which a phase called Berry phase appears. As shown below, Berry phase may be interpreted to be an effective magnetic field in the momentum space.

8.2. Anomalous Hall effect

The Hall effect was discovered in 1879 by Edwin Hall [242] when he was studying the force acting on the charged particles under an external electric field $\boldsymbol{E}_{\mathrm{ext}}$ and a magnetic field $\boldsymbol{H}_{\mathrm{ext}}$. This is the so-called "ordinary" Hall effect in which the electrons are deflected into the direction of $\boldsymbol{E}_{\mathrm{ext}} \times \boldsymbol{H}_{\mathrm{ext}}$ due to the Lorentz force. In ferromagnets, the Hall effect consists of two contributions, the ordinary Hall effect and the "anomalous" Hall effect [243, 244] being proportional not to $\boldsymbol{H}_{\mathrm{ext}}$ but to the magnetization $\boldsymbol{M}$ of the ferromagnet. The Hall resistivity ρ_{H} is thus given as

$$\rho_{\mathrm{H}} = R_0 H + 4\pi R_{\mathrm{s}} M. \tag{72}$$

The first and second terms are the ordinary and anomalous Hall effect, respectively. Coefficients R_0 and R_{s} are called as ordinary and anomalous Hall coefficient, respectively.

In experiments, with increasing H_{ext}, ρ_{H} changes rapidly at first, and then tends to increase in proportion to H. The initial rapid change in ρ_{H} is caused by the alignment of the domain magnetization. After the alignment of the domain magnetization, ρ_{H} changes in proportional to H_{ext}. The constant increment gives the value of R_0, and the extrapolated value of ρ_{H} to $H_{\mathrm{ext}} = 0$ gives the value of $4\pi R_{\mathrm{s}} M$.

Historically, an intrinsic mechanism, which results from the Berry phase, was first proposed for AHE [245]. The essential point in the theory is that there is a contribution to the velocity from the Berry phase $\Omega(\mathbf{k})$ as shown by

$$\dot{\boldsymbol{x}} = \frac{1}{\hbar}\frac{\partial \varepsilon(\boldsymbol{k})}{\partial \boldsymbol{k}} - \dot{\boldsymbol{k}} \times \Omega(\boldsymbol{k}), \tag{73}$$

$$\hbar\dot{\boldsymbol{k}} = -e\boldsymbol{E}_{\text{ext}} - e\dot{\boldsymbol{x}} \times \boldsymbol{B}_{\text{ext}}. \tag{74}$$

We see that the velocity $\dot{x}$ has a component perpendicular to $\boldsymbol{E}_{\text{ext}}$ even when $\boldsymbol{B}_{\text{ext}} = 0$. A term $e\boldsymbol{E}_{\text{ext}} \times \Omega(\boldsymbol{k})$ reminds us that $\Omega(\boldsymbol{k})$ plays a role of an effective magnetic field. Because $\Omega(\boldsymbol{k})$ is a quantity in the momentum space and is dependent on the wave vector, the effective field may be interpreted as a magnetic field in the momentum space. The AHE caused by intrinsic mechanisms is called "intrinsic" AHE.

Most of the experiments, however, have been interpreted by extrinsic mechanisms, skew-scattering (SS) [246] and side-jump (SJ) [247]. In SS mechanism, the up- and down-spin electrons are scattered into opposite directions as shown in Fig. 53A; on the other hand, in SJ mechanism, there occurs a displacement of the electron path as shown in Fig. 53B. In ferromagnets, the intrinsic spin imbalance makes the spin-up and spin-down charge Hall currents asymmetric and produces a Hall voltage proportional to the spin polarization, that is, magnetization. The AHE caused by extrinsic mechanisms is called "extrinsic" AHE.

The SS mechanism is originated from electron scattering by impurity potentials and SOI. On the other hand, the SJ is caused by the anomalous velocity due to SOI. Therefore, the Hall conductivity due to SS depends on the lifetime τ, while that due to SJ is independent of τ. As for explicit expressions of SS and SJ, readers may refer to a work by Crepieux and Bruno [248] for example. Since

$$R_{\text{s}} = \rho_{xy} = \left(\sigma^{-1}\right)_{xy} = -\frac{\sigma_{xy}}{\sigma_{xx}^2 + \sigma_{xy}^2} \sim -\frac{\sigma_{xy}}{\sigma_{xx}^2},$$

and $\sigma_{xx} \propto \tau$, SS mechanism gives $\rho_{xy} \propto \rho$, while SJ gives $\rho_{xy} \propto \rho^2$. Therefore, a relation

$$\rho_{xy} = a\rho + b\rho^2 \tag{75}$$

where a and b are constants, is generally hold and has been used for experimental analysis. It is noted that the intrinsic spin Hall conductivity may also be brought about in the SJ mechanism, since the SJ mechanism is caused by the anomalous velocity.

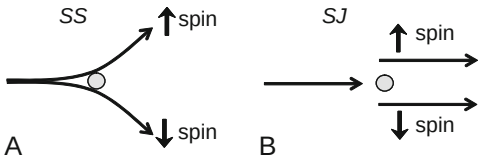

FIGURE 53 Schematic figures for (A) skew-scattering (SS) and (B) side-jump mechanisms.

Most of the experiments have so far been analyzed by using the expression above, but the intrinsic AHE has recently been revisited to give quantitative explanations of AHE in ferromagnetic semiconductors as well as Fe [249–251].

8.3. Spin Hall effect

As mentioned, the extrinsic AHE appears due to spin-dependent scattering. The up- and down-spin electrons are scattered into opposite directions, resulting in spin-up and spin-down charge Hall currents along the perpendicular direction of $\mathbf{E}_{\mathrm{ext}}$. The intrinsic spin imbalance makes the two charge Hall currents asymmetric and produces a Hall voltage. For non-magnets, although the two charge Hall currents cancel and no Hall voltage develops, spin-dependent scattering still produces the up- and down-"spin" currents (flow of spins) that flow in the opposite directions, as long as the SOI is non-vanishing. We thus expect a Hall effect solely with spin, which is called spin Hall effect (SHE). A schematic view of SHE is shown in Fig. 54. When the spin Hall current is originated from scattering of electrons by impurity potentials with SO interaction, the effect may be called "extrinsic" SHE [252, 253].

As in the case of AHE, one can conceive of an intrinsic SHE in non-magnets on which no external magnetic field is applied. Murakami *et al.* [254] have predicted for p-type semiconductors that the effective magnetic field originated from the Berry phase makes up- and down-spin electrons drift towards opposite directions and leads to SHE. SOI that exists universally in any materials may also produce the intrinsic SHE even for n-type semiconductors. Sinova *et al.* [255] have predicted a constant spin Hall conductivity $e/8\pi$ for 2DEG with a Rashba-type SOI produced by the asymmetry of the potential. The intrinsic SHE is a result of the inherent property, that is, a uniform SOI, of the material, as opposed to the extrinsic SHE caused by scattering.

Although the SHE does not accompany the Hall voltage, one may expect that a spin polarization of opposite signs appears at the edges even in the absence of applied magnetic fields, irrespective to extrinsic or intrinsic SHE. In the non-equilibrium state, the flows of up- and down-spin electrons into opposite directions are compensated by spin-flip scattering caused by the SO interaction itself or by another spin-dependent scattering, and give rise to a spin accumulation at the edges of the sample.

Elucidating the nature of the pure SHE is now an emergent issue for experimentalists. In spite of the difficulties associated with the absence of the Hall

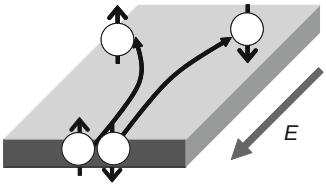

FIGURE 54 Schematic view of the spin Hall effect.

voltage in the pure SHE, two groups have succeeded in measuring the spin accumulation in non-magnetic semiconductors by optically detecting the spin accumulation at the sample edge. Kato *et al.* [256, 257] spatially resolved the Kerr rotation of the reflected light from n-type bulk GaAs and InGaAs samples and found accumulation of opposite sign at the two edges of the sample. Subsequently, Wunderlich *et al.* [258] measured the polarization of light emitted from a p–n junction placed at the edge of a structure. Kato *et al.* suggested that the observed effect may be the extrinsic SHE, as the spin Hall conductivity is low and independent of the crystal orientation, whereas Wunderlich *et al.* concluded that the effect is consistent with the intrinsic SHE, since the magnitude of the polarization is consistent with the theoretical prediction. The interpretation of the experimental results appears not straightforward, because the current theories predict that the intrinsic SHE can strongly be suppressed by disorder effects [259], orbital Hall current [260]. Furthermore, the effect of the disorder on SHE depends on the type of SOI [261], for example, small Dresselhaus-type SOI, which is intrinsic but orientation dependent, is calculated to be sufficient to explain the observed Kerr rotation in strained InGaAs samples used by Kato *et al.* [256] On the other hand, a recent theory on the extrinsic effect predicts the observed SHE within experimental error with no adjustable parameters [262].

The SHE has a practical relevance to the field of the spintronics, where spin polarization, manipulation and detection are essential. Theoretical studies to link SHE with measurable quantities such as spin accumulation and optical signature are highly desired, because even if spin Hall current itself is intrinsic, the stationary spin accumulation is a result of a balance between spin Hall current and intrinsic/extrinsic effects of the spin relaxation at the edges of the sample [263]. Another interesting aspect of the SHE is the quantized SHE. Recently, quantized SHE is suggested theoretically for undoped graphene in the absence of the external magnetic field because of a gap produced by SOI [264, 265].

The SHE is observed not only in semiconductors but also in normal metals and transition metals so far as the SOI exists. Valenzuela and Tinkham [266] and Kimura *et al.* [267] have reported the measurement of inverse SHE in Al and Pt, respectively. They injected spin-polarized current into a narrow non-magnetic metal in a device shown schematically in Fig. 55. The injected current gives rise to a spin-dependent shift of the chemical potential. Since the shift of the chemical potential decays with increasing the distance from the point of the spin injection, a Hall current is induced. The spatial dependence of the spin-up and spin-down chemical potentials have opposite signs, and up-spin and down-spin Hall

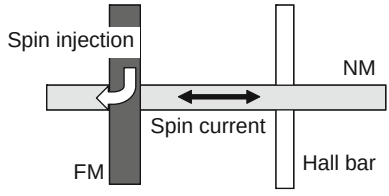

FIGURE 55 Experimental setup to measure the inverse SHE.

currents flow into opposite directions. This means a spin Hall current is induced by the spin injection into non-magnetic metals.

The spin Hall current observed for Pt by using a local Hall bar [267] is rather large as compared with the SHE observed in semiconductors. A large value of the spin Hall conductivity has also been predicted for Pt and transition metals theoretically by using a realistic tight-binding model [268].

8.4. Rashba 2DEG and spin accumulation

The Rashba Hamiltonian for 2DEG is given as

$$H_0 = \begin{pmatrix} \frac{\hbar^2}{2m}k^2 & \mathrm{i}\lambda\hbar k_- \\ -\mathrm{i}\lambda\hbar k_+ & \frac{\hbar^2}{2m}k^2 \end{pmatrix}, \tag{76}$$

where $k_\pm = k_x \pm \mathrm{i}k_y$ with $\mathbf{k} = (k_x, k_y)$ the electron momentum in the 2DEG plane, λ is the spin–orbit coupling. The eigenvalues are given as

$$E_{k\pm} = \frac{\hbar^2 k^2}{2m} \pm \lambda\hbar\mathrm{k}. \tag{77}$$

Thus, the free-electron states are split into two branches and the Fermi lines are two concentric circles as shown in Fig. 56. It should be noted that the direction of spin is dependent on momentum. The feature is a strong contrast to the Zeeman spin splitting. The momentum-dependent spin state is responsible to the SHE and spin accumulation shown below.

Former Russian scientists have predicted the spin accumulation in the Rashba split 2DEG systems with diffusive transport regime [269–271]. Inoue *et al.* [272] have confirmed the result in the Green's function method. The spin accumulation is in-plane and given as

$$\langle s_y \rangle = 4\pi e D_0 \lambda \tau E, \tag{78}$$

where D_0 is the density of states at the Fermi level and τ is the lifetime. The physical reason of the spin accumulation is simple. As mentioned earlier, in the equilibrium state, the spins with $k_x > 0$ point towards $+y$ direction in average, and

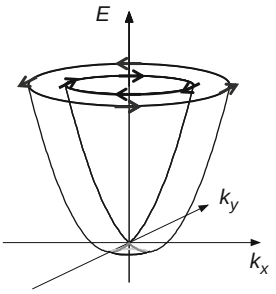

FIGURE 56 Energy dispersion relation for 2DEG with Rashba-type spin–orbit interaction.

those with $k_x < 0$ point towards $-y$ direction, and they cancel out in the equilibrium state. However, in the non-equilibrium state under external electric field along x-direction, number of spins with $k_x > 0$ is more than those with $k_x < 0$, and $\langle s_y \rangle$ becomes non-zero.

Several attempts to observe the in-plane spin accumulation have been done and successful results have been reported by several groups [273–275] using optical detection.

9. PERSPECTIVE

In this chapter, we briefly reviewed the relationship between spin-dependent resistivity and electronic structures in metals and alloys, and described microscopic methods for investigating electrical transport. We then reviewed the essential aspects of GMR, TMR and BMR, emphasizing the role of the electronic structures of constituent metals of these junctions and the effects of roughness on the electrical resistivity (or resistance). It was shown that the important factors that govern GMR are the spin-dependent random potential at interfaces and band matching/mismatching between magnetic and non-magnetic layers. For TMR, several factors were shown to be important in determining the MR ratio, including the shape of Fermi surface of the electrodes, the symmetry of the wave functions, electron scattering at interfaces and spin-slip tunnelling. An interpretation of TMR in Fe/MgO/Fe and of an oscillation of TMR were presented. TMR in granular films and in the Coulomb-blockade regime was also described. A brief review of normal MR, AMR and CMR was given. Anomalous and spin Hall effects originated from the SOI are also briefly explained.

The effects of GMR and TMR have now been applied to several devices, such as sensors and memories. Despite a simple structure of the FTJs, they give rise to large effect, and therefore are quite suitable for the technological applications. It is interesting that huge room-temperature TMR appears in junctions with the familiar ferromagnet Fe. Recently, observed oscillation of TMR in Fe/MgO/Fe junctions is another interesting phenomenon [149]. Although the MR effect is a simple phenomenon, it appears in various materials and junctions. It is expected that novel aspects of the MR may be found in near future.

The spin Hall effect predicted first theoretically and observed recently is a novel transport property which is related to a pure spin current. Since the spin current is usually non-conserving, the spin angular momentum can be transferred, for example, to magnetization, resulting in a current-induced magnetization reversal, which also attracts much interests recently.

ACKNOWLEDGEMENTS

The author thanks many peoples, especially H. Itoh, S. Maekawa, G.E.W. Bauer and Y. Asano for valuable discussions and collaborations. This work was supported by Next Generation Super Computing Project, Nanoscience Program, MEXT, Japan, and Grant-in-Aid for the 21st Century COE “Frontiers of Computational Science”.

REFERENCES

[1] Mattis, D. C. (1981). "The Theory of Magnetism I." Springer-Verlag, Berlin.
[2] Thomson, J. J. (1897). *Philos. Mag.* **44**, 293.
[3] Gerlach, W., and Stern, O. (1922). *Z. Phys.* **9**, 349.
[4] Mott, N. F. (1936). *Proc. R. Soc. Lond. Ser. A* **153**, 699; **156**, 368.
[5] Shinjo, T., and Takada, T. (1987). "Metallic Superlattices." Elsevier, Amsterdam.
[6] Levy, P. M. (1994). *In* "Solid State Physics" (H. Ehrenreich, and D. Turnbull, eds.), vol. 47, p. 367. Academic Press, Boston, MA.
[7] Miyazaki, T. (1996). "Electrochemical Technology", p. 279. Kodasha, Tokyo.
[8] Gijs, M. A. M., and Bauer, G. E. W. (1997). *Adv. Phys.* **46**, 285.
[9] Hartmann, U. (ed.) (1999). *In* "Magnetic Multilayers and Giant Magnetoresistance." Springer-Verlag, Berlin.
[10] Ziese, M., and Thornton, M. J. (eds.) (2001). *In* "Spin Electronics." Spinger-Verlag, Berlin.
[11] Tsymbal, E. Y., and Pettifor, D. G. (2001). *Solid State Phys.* **56**, 113.
[12] Maekawa, S., and Shinjo, T. (eds.) (2002). *In* "Spin Dependent Transport in Magnetic Nanostructures." Taylor and Francis, New York.
[13] Mills, D. L., and Bland, J. A. C. (eds.) (2006). *In* "Nanomagnetism." Elsevier, Amsterdam.
[14] Xu, Y. B., and Thompson, S. M. (eds.) (2006). *In* "Spintronic Materials and Technology." Taylor and Francis, New York.
[15] Bass, J., and Pratt, W. P. Jr. (2007). *J. Phys.: Condens. Matter* **19**, 183201.
[16] Tokura, Y. (2006). *Rep. Prog. Phys.* **69**, 797.
[17] Harrison, W. A. (1980). "Electronic Structure and the Properties of Solids." W. H. Freeman and Company, San Francisco, CA.
[18] Chikazumi, S. (1997). "Physics of Ferromagnetism", 2nd edn. Clarendon Press, Oxford.
[19] Crangle, J., and Hallam, G. C. (1963). *Proc. R. Soc. Lond. Ser. A* **272**, 119.
[20] Slater, J. C. (1937). *J. Appl. Phys.* **8**, 385.
[21] Pauling, L. (1938). *Phys. Rev.* **54**, 899.
[22] Bozorth, R. M. (1951). "Ferromagnetism." van Nostrand, New York.
[23] Fert, A., and Cambell, I. A. (1976). *J. Phys. F: Metal Phys.* **6**, 849.
[24] Campbell, I. A., and Fert, A. (1982). *In* "Ferromagnetic Materials" (E. P. Wohlfarth, ed.), vol. 3, p. 747. North-Holland, Amsterdam.
[25] Inoue, J., Oguri, A., and Maekawa, S. (1991). *J. Phys. Soc. Jpn.* **60**, 376.
[26] Mertig, I. (1999). *Rep. Prog. Phys.* **62**, 1.
[27] Anderson, P. W. (1961). *Phys. Rev.* **124**, 41.
[28] Podloucky, R., Zeller, R., and Dederichs, P. H. (1980). *Phys. Rev. B* **22**, 5777.
[29] Kittel, C. (1968). *Solid State Phys.* **22**, 1.
[30] Inoue, J., and Maekawa, S. (1993). *J. Magn. Magn. Mater.* **127**, L249.
[31] Soven, P. (1967). *Phys. Rev.* **156**, 809.
[32] Taylor, D. W. (1967). *Phys. Rev.* **156**, 1017.
[33] Velicky, B., Kirkpatrick, S., and Ehrenreich, H. (1968). *Phys. Rev.* **175**, 747.
[34] Brouers, F., and Vedyayev, A. V. (1972). *Phys. Rev. B* **5**, 346.
[35] Economou, E. N. (1983). "Green's Functions in Quantum Physics." Springer-Verlag, Berlin.
[36] Datta, S. (1995). "Electronic Transport in Mesoscopic Systems." Cambridge University Press, Cambridge.
[37] Kubo, R. (1957). *J. Phys. Soc. Jpn.* **17**, 975.
[38] Lee, P. A., and Fisher, D. S. (1981). *Phys. Rev. Lett.* **47**, 882.
[39] Landauer, R. (1957). *IBM J. Res. Dev.* **1**, 223.
[40] Caroli, C., Combescot, R., Nozières, J. P., and Saint-James, D. (1971). *J. Phys. C: Solid State Phys.* **4**, 916.
[41] Grünberg, P., Schreiber, R., Pang, Y., Brodsky, M. B., and Sowers, H. (1986). *Phys. Rev. Lett.* **57**, 2442.
[42] Baibich, M. N., Broto, J. M., Fert, A., Nguyen Van Dau, F., Petroff, F., Etienne, P., Creuzet, G., Friederich, A., and Chazelas, J. (1988). *Phys. Rev. Lett.* **61**, 2472.
[43] Binasch, G., Grünberg, P., Saurenbach, F., and Zinn, W. (1989). *Phys. Rev. B* **39**, 4828.

[44] Barnas, J., Fuss, A., Camley, R. E., Grünberg, P., and Zinn, W. (1990). *Phys. Rev. B* **42**, 8110.
[45] Barthelemhy, A., Fert, A., Baibich, M. N., Hadjoudj, S., and Petroff, F. (1990). *J. Appl. Phys.* **67**, 5908.
[46] Mosca, D. H., Petroff, F., Fert, A., Schroeder, P. A., Pratt, W. P. Jr., and Laloee, R. (1991). *J. Magn. Magn. Mater.* **94**, L1.
[47] Petroff, F., Barthelemhy, A., Hamzić, A., Fert, A., Etienne, P., Lequien, S., and Creuzet, G. (1991). *J. Magn. Magn. Mater.* **93**, 95.
[48] Schad, R., Potter, C. D., Beliën, P., Verbanck, G., Moshchalkov, V. V., and Bruynseraede, Y. (1994). *Appl. Phys. Lett.* **64**, 3500.
[49] Parkin, S. S. P., More, N., and Roche, K. P. (1990). *Phys. Rev. Lett.* **64**, 2304.
[50] Parkin, S. S. P. (1991). *Phys. Rev. Lett.* **67**, 3598.
[51] Parkin, S. S. P., and Mauri, D. (1991). *Phys. Rev. B* **44**, 7131.
[52] Petroff, F., Barthelemhy, A., Mosca, D. H., Lottis, D. K., Fert, A., Schroeder, P. A., Pratt, W. P. Jr., Loloee, R., and Lequien, S. (1991). *Phys. Rev. B* **44**, 5355.
[53] Purcell, S. T., Folkerts, W., Jonson, M. T., Mcgee, N. W. E., Jager, K., aan de Stegge, J., Zeper, W. B., Hoving, W., and Grünberg, P. (1991). *Phys. Rev. Lett.* **67**, 903.
[54] Qiu, Z. Q., Pearson, J., Berger, A., and Bader, S. D. (1992). *Phys. Rev. Lett.* **68**, 1398.
[55] Fullerton, E. E., Bader, S. D., and Robertson, J. L. (1996). *Phys. Rev. Lett.* **77**, 1382.
[56] Unguris, J., Celotta, R. J., and Pierce, D. T. (1991). *Phys. Rev. Lett.* **67**, 140.
[57] Unguris, J., Celotta, R. J., and Pierce, D. T. (1992). *Phys. Rev. Lett.* **69**, 1125.
[58] Wang, Y., Levy, P. M., and Fry, J. L. (1990). *Phys. Rev. Lett.* **65**, 2732.
[59] Bruno, P., and Chappert, C. (1991). *Phys. Rev. Lett.* **67**, 1602.
[60] Edwards, D. M., Mathon, J., Muniz, R. B., and Phan, M. S. (1991). *Phys. Rev. Lett.* **67**, 493.
[61] van Schilfgaarde, M., and Harrison, W. A. (1993). *Phys. Rev. Lett.* **71**, 3870.
[62] Mathon, J., Villeret, M., Muniz, R. B., d'Albuquerque e Castro, J., and Edwards, D. M. (1995). *Phys. Rev. Lett.* **74**, 3696.
[63] Bruno, P. (1995). *Phys. Rev. B* **52**, 411.
[64] Bruno, P., Kudrnovský, J., Drchal, V., and Turek, I. (1996). *Phys. Rev. Lett.* **76**, 4254.
[65] Shinjo, T., and Yamamoto, H. (1990). *J. Phys. Soc. Jpn.* **59**, 3061.
[66] Yamamoto, H., Okuyama, T., Dohnomae, H., and Shinjo, T. (1991). *J. Magn. Magn. Mater.* **99**, 243–252.
[67] Dieny, B., Speriosu, V. S., Parkin, S. S. P., Gurney, B. A., Wilhoit, D. R., and Mauri, D. (1991). *Phys. Rev. B* **43**, 1297.
[68] Dieny, B., Speriosu, V. S., Metin, S., Parkin, S. S. P., Gurney, B. A., Baumgart, P., and Wilhoit, D. R. (1991). *J. Appl. Phys.* **69**, 4774.
[69] Dieny, B. (1992). *Europhys. Lett.* **17**, 261.
[70] Pratt, W. P. Jr., Lee, S. F., Slaughter, J. M., Loloee, R., Schroeder, P. A., and Bass, J. (1991). *Phys. Rev. Lett.* **66**, 3060.
[71] Yang, Q., Holody, P., Lee, S. F., Henry, L. L., Loloee, R., Schroeder, P. A., Pratt, W. P. Jr., and Bass, J. (1994). *Phys. Rev. Lett.* **72**, 3274.
[72] Bass, J., and Pratt, W. P. Jr. (1999). *J. Magn. Magn. Mater.* **200**, 274.
[73] Gijs, M. A. M., Lenczowski, S. K. J., and Giesbers, J. B. (1993). *Phys. Rev. Lett.* **70**, 3343.
[74] Gijs, M. A. M., Lenczowski, S. K. J., van de Veerdonk, R. J. M., Giesbers, J. B., Johnson, M. T., and Faan de Stegge, J. B. (1994). *Phys. Rev. B* **50**, 16733.
[75] Piraux, L., George, J. M., Despres, J. F., Leroy, C., Ferain, E., Legras, R., Ounadjela, K., and Fert, A. (1994). *Appl. Phys. Lett.* **65**, 2484.
[76] Levy, P. M., Zhang, S., Ono, T., and Shinjo, T. (1995). *Phys. Rev. B* **52**, 16049.
[77] Ono, T., and Shinjo, T. (1995). *J. Phys. Soc. Jpn.* **64**, 363–366.
[78] Berkowitz, A. E., Mitchell, J. R., Carey, M. J., Yong, A. P., Zhang, S., Spada, F. E., Parker, F. T., Hutten, A., and Thomas, G. (1992). *Phys. Rev. Lett.* **68**, 3745.
[79] Xiao, J. Q., Jiang, J. S., and Chien, C. L. (1992). *Phys. Rev. Lett.* **68**, 3749.
[80] Xiao, J. Q., Jiang, J. S., and Chien, C. L. (1992). *Phys. Rev. B* **46**, 9266.
[81] Barnard, J. A., Waknis, A., Tan, M., Haftek, E., Parker, M. R., and Watson, M. L. (1992). *J. Magn. Magn. Mater.* **114**, L230.
[82] Rubinstein, M. (1994). *Phys. Rev. B* **50**, 3830.
[83] Wang, J. Q., and Xiao, G. (1994). *Phys. Rev. B* **50**, 3423.

[84] Hickey, B. J., Howson, M. A., Musa, S. O., and Wiser, N. (1995). *Phys. Rev. B* **51**, 667.
[85] Fullerton, E. E., Kelly, D. M., Guimpel, J., and Schuller, I. K. (1992). *Phys. Rev. Lett.* **68**, 859.
[86] Parkin, S. S. P. (1993). *Phys. Rev. Lett.* **71**, 1641.
[87] Gurney, B. A., Speriosu, V. S., Nozières, J. P., Lefakis, H., Wilhoit, D. R., and Need, O. U. (1993). *Phys. Rev. Lett.* **71**, 4023.
[88] Speriosu, V. S., Nozières, J. P., Gurney, B. A., Dieny, B., Huang, T. C., and Lefakis, H. (1993). *Phys. Rev. B* **47**, 11579.
[89] George, J. M., Pereira, L. G., Barthelemhy, A., Petroff, F., Steren, L., Duvail, J. L., and Fert, A. (1994). *Phys. Rev. Lett.* **72**, 408.
[90] Inoue, J., Itoh, H., and Maekawa, S. (1992). *J. Phys. Soc. Jpn.* **61**, 1149.
[91] Itoh, H., Inoue, J., and Maekawa, S. (1993). *Phys. Rev. B* **47**, 5809.
[92] Bauer, G. E. W. (1992). *Phys. Rev. Lett.* **69**, 1676.
[93] Bauer, G. E. W., Brataas, A., Schep, K. M., and Kelly, P. J. (1994). *J. Appl. Phys.* **75**, 6704.
[94] Schep, K. M., Kelly, P. J., and Bauer, G. E. W. (1995). *Phys. Rev. Lett.* **74**, 586.
[95] Camley, R. E., and Barnaś, J. (1989). *Phys. Rev. Lett.* **63**, 664.
[96] Zahn, P., Mertig, I., Richter, M., and Eschring, H. (1995). *Phys. Rev. Lett.* **75**, 2996.
[97] Kubota, H., and Miyazaki, T. (1994). *J. Magn. Soc. Jpn.* **18**, 335 (in Japanese).
[98] Saito, Y., and Inomata, K. (1991). *Jpn. J. Appl. Phys.* **30**, L1733.
[99] Kataoka, N., Saito, K., and Fujimori, H. (1992). *Mater. Trans. JIM* **33**, 151.
[100] Kataoka, N., Saito, K., and Fujimori, H. (1993). *J. Magn. Magn. Mater.* **121**, 383.
[101] Sakakima, H., Satomi, M., and Magn, J. (1993). *Magn. Mater.* **121**, 374.
[102] Kubota, H., Sato, M., and Miyazaki, T. (1995). *Phys. Rev. B* **52**, 343.
[103] Itoh, H., Hori, T., Inoue, J., and Maekawa, S. (1993). *J. Magn. Magn. Mater.* **121**, 344.
[104] Miyazaki, T., Kondo, J., Kubota, H., and Inoue, J. (1997). *J. Appl. Phys.* **81**, 5187.
[105] Itoh, H., Inoue, J., and Maekawa, S. (1995). *Phys. Rev. B* **51**, 342.
[106] Asano, Y., Oguri, A., and Maekawa, S. (1993). *Phys. Rev. B* **48**, 6192.
[107] Asano, Y., Oguri, A., Inoue, J., and Maekawa, S. (1994). *Phys. Rev. B* **49**, 12831.
[108] Schep, K. M. Ph.D. (1997), Thesis, Technical University of Delft, The Netherlands.
[109] Schep, K. M., Kelly, P. J., Bauer, G. E. W., and Magn, J. (1996). *Magn. Mater.* **156**, 385.
[110] Schep, K. M., van Hoof, J. B. A. N., Kelly, P. J., Bauer, G. E. W., and Inglesfield, J. E. (1997). *Phys. Rev. B* **56**, 10805.
[111] Valet, T., and Fert, A. (1993). *Phys. Rev. B* **48**, 7099.
[112] Julliere, M. (1975). *Phys. Lett. A* **54**, 225.
[113] Maekawa, S., and Gäfvert, U. (1982). *IEEE Trans. Magn.* **18**, 707.
[114] Miyazaki, T., and Tezuka, N. (1995). *J. Magn. Magn. Mater.* **151**, 403–410.
[115] Moodera, J. S., Kinder, L. R., Wong, T. M., and Meservey, R. (1995). *Phys. Rev. Lett.* **74**, 3273.
[116] Miyazaki, T., and Tezuka, N. (1995). *J. Magn. Magn. Mater.* **151**, 403–410.
[117] Fujimori, H., Mitani, S., and Ohnuma, S. (1995). *Mater. Sci. Eng. B* **31**, 219.
[118] Mitani, S., *et al.* (1998). *Phys. Rev. Lett.* **81**, 2799.
[119] Bratkovsky, A. M. (1997). *Phys. Rev. B* **56**, 2344.
[120] Guinea, F. (1998). *Phys. Rev. B* **58**, 9212.
[121] Tsymbal, E. Yu., and Pettifor, D. G. (1998). *Phys. Rev. B* **58**, 432.
[122] Mazin, I. I. (1999). *Phys. Rev. Lett.* **83**, 1427.
[123] Moodera, J. S., and Mathon, G. (1999). *J. Magn. Magn. Mater.* **200**, 248.
[124] Bardeen, J. (1961). *Phys. Rev. Lett.* **6**, 57.
[125] Tedrow, P. M., and Meservey, R. (1971). *Phys. Rev. Lett.* **26**, 192.
[126] Soulen, R. J. Jr., Byers, J. M., Osofsky, M. S., Nadgorny, B., Ambrose, T. F., Cheng, S. F., Broussard, P. R., Tanaka, C. T., Nowak, J., Moodera, J. S., Barry, A., and Coey, J. M. D. (1998). *Science* **282**, 85.
[127] Upadhyay, S. K., Palanisami, A., Louie, R. N., and Buhrman, R. A. (1998). *Phys. Rev. Lett.* **81**, 3247.
[128] Upadhyay, S. K., Louie, R. N., and Buhrman, R. A. (1999). *Appl. Phys. Lett.* **74**, 3881.
[129] Worledge, D. C., and Geballe, T. H. (2000). *Phys. Rev. Lett.* **85**, 5182.
[130] Kaiser, C., van Dijken, S., Yang, S. H., Yang, H., and Parkin, S. S. P. (2005). *Phys. Rev. Lett.* **94**, 247203.
[131] Kaiser, C., Panchula, A. F., and Parkin, S. S. P. (2005). *Phys. Rev. Lett.* **95**, 047202.
[132] Stearns, M. B. (1977). *J. Magn. Magn. Mater.* **5**, 167.

[133] Slonczewski, J. C. (1989). *Phys. Rev. B* **39**, 6995.
[134] MacLaren, J. M., Zhang, X. G., Butler, W. H., and Wang, X. (1999). *Phys. Rev. B* **59**, 5470.
[135] Mathon, J., and Umerski, A. (2001). *Phys. Rev. B* **63**, 220403.
[136] Butler, W. H., Zhang, X. G., Schulthess, T. C., and MacLaren, J. M. (2001). *Phys. Rev. B* **63**, 54416.
[137] Itoh, H., Kumazaki, T., Inoue, J., and Maekawa, S. (1998). *Jpn. J. Appl. Phys.* **37**, 5554.
[138] Itoh, H., Shibata, A., Kumazaki, T., Inoue, J., and Maekawa, S. (1999). *J. Phys. Soc. Jpn.* **69**, 1632.
[139] Itoh, H., and Inoue, J. (2006). *Trans. Magn. Soc. Jpn.* **30**, 1.
[140] Itoh, H. (2006). *J. Phys. D: Appl. Phys.* **40**, 1228.
[141] Honda, S., Itoh, H., and Inoue, J. (2006). *Phys. Rev. B* **74**, 155329.
[142] Inoue, J., and Maekawa, S. (1999). *J. Magn. Magn. Mater.* **198–199**, 167.
[143] Takada, I., Inoue, J., and Itoh, H. (2008). *J. Magn. Soc. Jpn.* **32**, 338.
[144] Zhang, S., Levy, P. M., Marley, A. C., and Parkin, S. S. P. (1997). *Phys. Rev. Lett.* **79**, 3744.
[145] Yuasa, S., Sato, T., Tamura, E., Suzuki, Y., Yamamori, H., Ando, K., and Katayama, T. (2000). *Europhys. Lett.* **52**, 344.
[146] Nagahama, T., Yuasa, S., Suzuki, Y., and Tamura, E. (2001). *Appl. Phys. Lett.* **79**, 4381.
[147] Yuasa, S., Fukushima, A., Nagahama, T., Ando, K., and Suzuki, Y. (2004). *Jpn. J. Appl. Phys.* **43**, L588.
[148] Parkin, S. S. P., Kaiser, C., Panchula, A. F., Rice, P. M., Hughes, B., Samant, M., and Yang, S. H. (2004). *Nat. Mater.* **3**, 862.
[149] Yuasa, S., Nagahama, T., Fukushima, A., Suzuki, Y., and Ando, K. (2004). *Nat. Mater.* **3**, 868.
[150] Djayaprawira, D. D., Tsunekawa, K., Nagai, M., Maehara, H., Yamagata, S., Watanabe, N., Yuasa, S., Suzuki, Y., and Ando, K. (2005). *Appl. Phys. Lett.* **86**, 092502.
[151] LeClair, P., Swagten, H. J. M., Kohlhepp, J. T., van de Veerdonk, R. J. M., and de Jonge, W. J. M. (2000). *Phys. Rev. Lett.* **84**, 2933.
[152] LeClair, P., Kohlhepp, J. T., Swagten, H. J. M., and de Jonge, W. J. M. (2001). *Phys. Rev. Lett.* **86**, 1066.
[153] LeClair, P., Kohlhepp, J. T., van de Vin, C. H., Wieldraaijer, H., Swagten, H. J. M., de Jonge, W. J. M., Davis, A. H., MacLaren, J. M., Moodera, J. S., and Jansen, R. (2002). *Phys. Rev. Lett.* **88**, 107201.
[154] Inoue, J., and Itoh, H. (2002). *J. Phys. D: Appl. Phys.* **35**, 1.
[155] Yuasa, S., Katayama, T., and Suzuki, Y. (2002). *Science* **297**, 234.
[156] Nagahama, T., Yuasa, S., Tamura, E., and Suzuki, Y. (2005). *Phys. Rev. Lett.* **95**, 086602.
[157] Mathon, J., Villeret, M., and Itoh, H. (1995). *Phys. Rev. B* **52**, R6983.
[158] Mathon, J., and Umerski, A. (1999). *Phys. Rev. B* **60**, 1117.
[159] Itoh, H., Inoue, J., Umerski, A., and Mathon, J. (2003). *Phys. Rev. B* **68**, 174421.
[160] Itoh, H., and Inoue, J. (2003). *J. Magn. Soc. Jpn.* **27**, 1013 (in Japanese).
[161] de Groot, R. A., Mueller, F. M., van Engen, P. G., and Buschow, K. H. J. (1983). *Phys. Rev. Lett.* **50**, 2024.
[162] Schwarz, K. (1986). *J. Phys. F: Metal Phys.* **16**, L211.
[163] Pickett, W. E., and Singh, D. J. (1996). *Phys. Rev. B* **53**, 1146.
[164] Wei, J. Y. T., Yeh, N. C., and Vasques, R. P. (1997). *Phys. Rev. Lett.* **79**, 5150.
[165] Hu, G., and Suzuki, Y. (2002). *Phys. Rev. Lett.* **89**, 276601.
[166] Dowben, P. A., and Skomski, R. (2004). *J. Appl. Phys.* **95**, 7453.
[167] Sakuraba, Y., Nakata, J., Oogane, M., Kubota, H., Ando, Y., Sakuma, A., and Miyazaki, T. (2005). *Jpn. J. Appl. Phys.* **44**, L1100.
[168] Sakuraba, Y., Hattori, M., Oogane, M., Kubota, H., Ando, Y., Sakuma, A., and Miyazaki, T. (2006). *J. Phys. D: Appl. Phys.* **40**, 1221.
[169] Wollan, E. O., and Koehler, W. C. (1955). *Phys. Rev.* **100**, 545.
[170] Urushibara, A., Moritomo, Y., Arima, T., Asamitsu, A., Kido, G., and Tokura, Y. (1995). *Phys. Rev. B* **51**, 14103.
[171] Inoue, J., and Maekawa, S. (1995). *Phys. Rev. Lett.* **74**, 3407.
[172] de Gennes, P. G. (1960). *Phys. Rev.* **118**, 141.
[173] Bowen, M., Bibes, M., Bathélémy, A., Contour, J. P., Anane, A., Lemaitre, Y., and Fert, A. (2003). *Appl. Phys. Lett.* **82**, 233.

[174] Bowen, M., Barthelemhy, A., Bibes, M., Jacquet, E., Contour, J. P., Fert, A., Ciccacci, E., Duò, L., and Bertacco, R. (2005). *Phys. Rev. Lett.* **95**, 137203.
[175] Garcia, V., Bibes, M., Barthelemhy, A., Bowen, M., Jacquet, E., Contour, J. P., and Fert, A. (2004). *Phys. Rev. B* **69**, 52403.
[176] Lu, Y., Li, X. W., Gong, G. Q., Xiao, G., Gupta, A., Lecoeur, P., Sun, J. Z., Wang, Y. Y., and Dravid, V. P. (1996). *Phys. Rev. B* **54**, R8357.
[177] Kwon, C., Kim, K. C. Robson, M. C., Gu, J. Y., Rajeswari, M., Venkatesan, T., and Ramesh, R. (1997). *J. Appl. Phys.* **81**, 4950.
[178] Obata, T., Mnako, T., Shimakawa, Y., and Kubo, Y. (1999). *Appl. Phys. Lett.* **74**, 290.
[179] Itoh, H., Ohsawa, T., and Inoue, J. (2000). *Phys. Rev. Lett.* **84**, 2501.
[180] De Teresa, J. M., Barthelemhy, A., Fert, A., Contour, J. P., Lyonnet, R., Montaigne, F., Seneor, P., and Vaurès, A. (1999). *Phys. Rev. Lett.* **82**, 4288.
[181] Velev, J. P., Belashchenko, K. D., Stewart, D. A., van Schilfgaarde, M., Jaswal, S. S., and Tsymbal, E. Y. (2005). *Phys. Rev. Lett.* **95**, 216601.
[182] Sakuraba, Y., Hattori, M., Oogane, M., Ando, Y., Kato, H., Sakuma, A., Miyazaki, T., and Kubota, H. (2006). *Appl. Phys. Lett.* **88**, 192508.
[183] Galanakis, I. (2002). *J. Phys.: Condens. Matter* **14**, 6329.
[184] Lezaic, M., Movropoulos, Ph., Enkovaara, J., Bihlmayer, G., and Brugel, S. (2006). *Phys. Rev. Lett.* **97**, 26404.
[185] Hayakawa, J., Ikeda, S., Lee, Y. M., Matsukura, F., and Ohno, H. (2006). *Appl. Phys. Lett.* **89**, 232510.
[186] Lee, Y. M., Hayakawa, J., Ikeda, S., Matsukura, F., and Ohno, H. (2006). *Appl. Phys. Lett.* **89**, 042506.
[187] Lee, Y. M., Hayakawa, J., Ikeda, S., Matsukura, F., and Ohno, H. (2007). *Appl. Phys. Lett.* **90**, 212507.
[188] Marukame, T., Ishikawa, T., Hatamata, S., Matsuda, K., Uemura, T., and Yamamoto, M. (2007). *Appl. Phys. Lett.* **90**, 012508.
[189] Tezuka, N., Ikeda, N., Sugimoto, S., and Inomata, K. (2007). *Jpn. J. Appl. Phys.* **46**, L454.
[190] Ishikawa, T., Hakamata, S., Matsuda, K., Uemura, T., and Yamamoto, M. (2008). *J. Appl. Phys.* **103**, 07A919.
[191] Matsumoto, R., Fukushima, A., Nagahama, T., Suzuki, Y., Ando, K., and Yuasa, S. (2007). *Appl. Phys. Lett.* **90**, 252506.
[192] Wolf, S. A., Awschalom, D. D., Buhrman, R. A., Daughton, J. M., von Molnar, S., Roukes, M. L., Chtchelkanova, A. Y., and Treger, D. M. (2001). *Science* **294**, 1488.
[193] Kossut, J., and Dobrowolski, W. (1993). *In* "Handbook of Magnetic Materials" (K. H. Buschow, ed.), vol. 7, p. 231. North-Holland, Amsterdam.
[194] Munekata, H., Ohno, H., von Molnar, S., Segmuller, A., Chang, L. L., and Esaki, L. (1989). *Phys. Rev. Lett.* **63**, 1849.
[195] Ohno, H., Munekata, H., von Molnar, S., and Chang, L. L. (1991). *J. Appl. Phys.* **69**, 6103.
[196] Ohno, H. (1998). *Science* **281**, 951.
[197] Matsukura, F., Ohno, H., Shen, A., and Sugawara, Y. (1998). *Phys. Rev. B* **57**, R2037.
[198] Nazmul, A. M., Amemiya, T., Shuto, Y., Sugawara, S., and Tanaka, M. (2005). *Phys. Rev. Lett.* **95**, 17201.
[199] Shuto, Y., Tanaka, M., and Sugawara, S. (2006). *J. Appl. Phys.* **99**, 08D516.
[200] Tanaka, M., and Higo, Y. (2001). *Phys. Rev. Lett.* **87**, 026602.
[201] Chiba, D., Matsukura, F., and Ohno, H. (2004). *Physica E* **21**, 966.
[202] Gould, C., Rüster, C., Jungwirth, T., Girgis, E., Schott, G. M., Giraud, R., Brunner, K., Schmidt, G., and Molenkamp, L. W. (2004). *Phys. Rev. Lett.* **93**, 117203.
[203] Rüster, C., Gould, C., Jungwirth, T., Sinova, J., Schott, G. M., Giraud, R., Brunner, K., Schmidt, G., and Molenkamp, L. W. (2005). *Phys. Rev. Lett.* **94**, 27203.
[204] Giddings, A. D., Khalid, M. N., Jungwirth, T., Wunderlich, J., Yasin, S. Campion, R. P., Edmonds, K. W., Sinova, J., Ito, K., Wang, K. Y., Williams, D., Gallagher, B. L., and Foxon, C. T. (2005). *Phys. Rev. Lett.* **94**, 127202.
[205] Saito, H., Yuasa, S., and Ando, K. (2005). *Phys. Rev. Lett.* **95**, 86604.
[206] Sheng, P., Abeles, B., and Arie, Y. (1973). *Phys. Rev. Lett.* **31**, 44.

[207] Herman, J. S., and Abeles, B. (1976). *Phys. Rev. Lett.* **37**, 1429.
[208] Inoue, J., and Maekawa, S. (1996). *Phys. Rev. B* **53**, R11927.
[209] Beenakker, C. W. (1991). *Phys. Rev. B* **44**, 1646.
[210] Ono, K., Shimada, H., and Ootuka, Y. (1997). *J. Phys. Soc. Jpn.* **66**, 1261.
[211] Barnas, J., and Fert, A. (1998). *Phys. Rev. Lett.* **80**, 1058.
[212] Brataas, A., Nazarov, Yu. V., Inoue, J., and Bauer, G. E. W. (1999). *Phys. Rev. B* **59**, 93.
[213] Takahashi, S., and Maekawa, S. (1998). *Phys. Rev. Lett.* **80**, 1758.
[214] van Wees, B. J., van Houten, H., Beenakker, C. W., van der Marel, D., and Foxton, C. T. (1988). *Phys. Rev. Lett.* **60**, 848.
[215] Scheer, E., Agraït, N., Cuevas, J. C., Yeyati, A. L., Ludoph, B., M-Rodero, A., Bollinger, G. R., van Ruetenbeek, J. M., and Urbina, C. (1998). *Nature* **394**, 154.
[216] Cuevas, J. C., Yeyati, A. L., and Rodero, A. M. (1998). *Phys. Rev. Lett.* **80**, 1066.
[217] Ono, T., Ooka, Y., Miyajima, H., and Otani, Y. (1999). *Appl. Phys. Lett.* **75**, 1622.
[218] García, N., Muñoz, M., and Zhao, Y. W. (1999). *Phys. Rev. Lett.* **82**, 2923.
[219] Chopra, H. D., and Hua, S. Z. (2002). *Phys. Rev. B* **66**, 020403(R).
[220] Hua, S. Z., and Chopra, H. D. (2003). *Phys. Rev. B* **67**, 060401(R).
[221] Tatara, G., Zhao, Y. W., Muñoz, M., and García, N. (1999). *Phys. Rev. Lett.* **83**, 2030.
[222] Bruno, P. (1999). *Phys. Rev. Lett.* **83**, 2425.
[223] van Hoof, J. B. A. N., Schep, K. M., Brataas, A., Bauer, G. E. W., and Kelly, P. J. (1999). *Phys. Rev. B* **59**, 138.
[224] Imamura, H., Kobayashi, N., Takahashi, S., and Maekawa, S. (2000). *Phys. Rev. Lett.* **84**, 1003.
[225] Bagrets, A., Papanikolaou, N., and Mertig, I. (2004). *Phys. Rev. B* **70**, 064410.
[226] Stepanyuk, V. S., Klavsyuk, A. L., Hergert, W., Saletsky, A. M., Bruno, P., and Mertig, I. (2004). *Phys. Rev. Lett.* **70**, 195420.
[227] Papanikolaou, N. (2003). *J. Phys.: Condens. Matter* **15**, 5049.
[228] Smit, J. (1951). *Physica* **16**, 612.
[229] Millis, A. J., Shraiman, B. I., and Mueller, R. (1996). *Phys. Rev. Lett.* **77**, 175.
[230] Varma, C. M. (1996). *Phys. Rev. B* **54**, 7328.
[231] Sheng, L., Xing, D. Y., Sheng, D. N., and Ting, C. S. (1997). *Phys. Rev. Lett.* **79**, 1710.
[232] Moreo, A., yunoki, S., and Dagotto, E. (1999). *Science* **283**, 2034.
[233] Vergés, J. A., Mayor, V., and Brey, L. (2002). *Phys. Rev. Lett.* **88**, 136401.
[234] Ramakrisman, T. V., Krishnamurthy, H. R., Hassan, S. R., and Venketeswara Pai, G. (2004). *Phys. Rev. Lett.* **92**, 157203.
[235] Tokura, Y. (ed.) (2000). *In* "Colossal Magnetoresistive Oxides." Gordon and Breach, London.
[236] Dagotto, E. (2002). "Nanoscale Phase Separation and Colossal Magnetoresistance." Springer-Verlag, New York.
[237] Chatterji, T. (ed.) (2002). *In* "Colossal Magnetoresistive Manganites." Kluwer Academic Publishers, London.
[238] Nagaev, E. L. (2002). "Colossal Magnetoresistance and Phase Separation in Magnetic Semiconductors." Imperial College Press, London.
[239] Dresselhaus, G. (1955). *Phys. Rev.* **100**, 580.
[240] Rashba, E. I. (1960). *Sov. Phys. Solid State* **2**, 1109.
[241] Bychkov, Y. A., and Rashba, E. I. (1984). *J. Phys. C* **17**, 6039.
[242] Hall, E. H. (1879). *Am. J. Math.* **2**, 287.
[243] Hall, E. H. (1880). *Philos. Mag.* **19**, 301.
[244] Kundt, A. (1893). *Ann. Phys. Chem.* **49**, 257.
[245] Karplus, R., and Luttinger, J. M. (1954). *Phys. Rev.* **95**, 1154.
[246] Smit, J. (1958). *Physica* **24**, 39.
[247] Berger, L. (1970). *Phys. Rev. B* **2**, 4559.
[248] Crepieux, A., and Bruno, P. (2001). *Phys. Rev. B* **64**, 14416.
[249] Jungwirth, T., Niu, Q., and MacDonald, A. H. (2002). *Phys. Rev. Lett.* **88**, 207208.
[250] Ohno, H. (1999). *J. Magn. Magn. Mater.* **200**, 110.
[251] Yao, Y., *et al.* (2004). *Phys. Rev. Lett.* **92**, 37204.
[252] D'yakonov, M. I., and Perel, V. I. (1971). *ZhETF Pis. Red.* **13**, 657.
[253] Hirsh, J. E. (1999). *Phys. Rev. Lett.* **83**, 1834.

[254] Murakami, S., Nagaosa, N., and Zhang, S. C. (2003). *Science* **301**, 1348.
[255] Sinova, J., Culcer, D., Niu, Q., Sinitsyn, N. A., Jungwirth, T., and MacDonald, A. H. (2004). *Phys. Rev. Lett.* **92**, 126603.
[256] Kato, Y. K., Myers, R. C., Gossard, A. C., and Awschalom, D. D. (2004). *Science* **306**, 1910.
[257] Sih, V., Myers, R. C., Kato, Y. K., Lau, W. H., Gossard, A. C., and Awschalom, D. D. (2005). *Nat. Phys.* **1**, 31.
[258] Wunderlich, J., Kaestner, B., Sinova, J., and Jungwirth, T. (2005). *Phys. Rev. Lett.* **94**, 047204.
[259] Inoue, J., Bauer, G. E. W., and Molenkamp, L. W. (2004). *Phys. Rev. B* **70**, 041303.
[260] Zhang, S., and Yang, Z. (2005). *Phys. Rev. Lett.* **94**, 066602.
[261] Bernevig, B. A., and Zhang, S. C. (2005). *Phys. Rev. Lett.* **95**, 16801.
[262] Engel, H. A., Halperin, B. I., and Rashba, E. I. (2005). *Phys. Rev. Lett.* **95**, 166605.
[263] Shchelushkin, R. V., and Brataas, A. (2005). *Phys. Rev. B* **71**, 045123.
[264] Kane, C. L., and Mele, E. J. (2005). *Phys. Rev. Lett.* **95**, 146802.
[265] Kane, C. L., and Mele, E. J. (2006). *Phys. Rev. Lett.* **95**, 226801.
[266] Valenzuela, S. O., and Tinkham, M. (2006). *Nature* **442**, 176.
[267] Kimura, T., Ohtani, Y., Sato, T., Takahashi, S., and Maekawa, S. (2007). *Phys. Rev. Lett.* **98**, 156601.
[268] Kontani, H., Naito, M., Hirashima, D. S., Yamada, K., and Inoue, J. J. Phys. Soc. Jpn. (2007). *J. Phys. Soc. Jpn.* **76,** 103702, see also Kontani, H., Tanaka, T., Hirashima, D. S., Yamada, K., and Inoue, J. (2008). *Phys. Rev. Lett.* **100,** 096601, and *Phys. Rev. Lett.* **102,** 016601 (2009).
[269] Vas'ko, F. T., and Prime, N. A. (1979). *Sov. Phys. Solid State* **21**, 994.
[270] Levitov, L. S., *et al.* (1985). *Zh. Eksp. Teor. Fiz.* **88**, 229.
[271] Edelstein, V. M. E. (1990). *Solid State Commun.* **73**, 233.
[272] Inoue, J., Bauer, G. E. W., and Molenkamp, L. W. (2003). *Phys. Rev. B* **67**, 33104.
[273] Kato, Y. K., Myers, R. C., Gossard, A. C., and Awschalom, D. D. (2004). *Phys. Rev. Lett.* **93**, 176601.
[274] Ganichev, S. D., Danilov, S. N., Schneider, P., Bel'kov, V. V., Golub, L. E., Wegscheider, W., Weiss, D., and Prettl, W. cond-mat/0403641.
[275] Yang, C. L., He, H. T., Lu, D., Cui, L. J., Zeng, Y. P., Wang, J. N., and Ge, W. K. (2006). *Phys. Rev. Lett.* **96**, 186605.

CHAPTER 3

Spin-Injection Phenomena and Applications

Yoshishige Suzuki,[†] **Ashwin A. Tulapurkar,**[†] and **Claude Chappert**[‡]

Contents

Abstract

The injection of direct current into a magnetic multilayer induces torque on the magnetic moments in the layer and results in the amplification of precessional motion and successive magnetization switching of the magnetic moments. These phenomena provide new techniques to write information into tiny magnetic cells and to construct oscillators and rectifiers that are several tens of nanometres in size. In this chapter, spin injections and spin

[†]Department of Materials Engineering Science, Graduate School of Engineering Science, Toyonaka, Osaka 560-8531, Japan
[‡]Institut d'Electronique Fondamentale, Bât. 220, Université Paris-Sud, F91405 Orsay cedex, France

Nanomagnetism and Spintronics
DOI: 10.1016/B978-0-444-53114-8.00003-0

torques in magnetic multilayers, which show giant magnetoresistance effect in current-perpendicular-to-the-plane (CPP-GMR) geometry, and magnetic tunnelling junctions (MTJs) are described. Further, mechanisms of spin-injection magnetization switching (SIMS) and its high-speed observations are explained. Then, phenomena related to spin injection, namely, spin-transfer oscillation (STO) and the spin-torque diode effect, are described. Finally, applications related to the spin-injection technology are reviewed.

1. SPIN INJECTION AND TORQUE

1.1. Spin injection

Electrons possess both charge $(-e)$ and spin angular momentum $(\hbar/2)$. Therefore, when an electron moves in a material, it carries not only a charge but also an angular momentum. In Fig. 1A, a schematic of electron transfer from a ferromagnetic material (FM) to a non-magnetic material (NM) [1] through an interface is

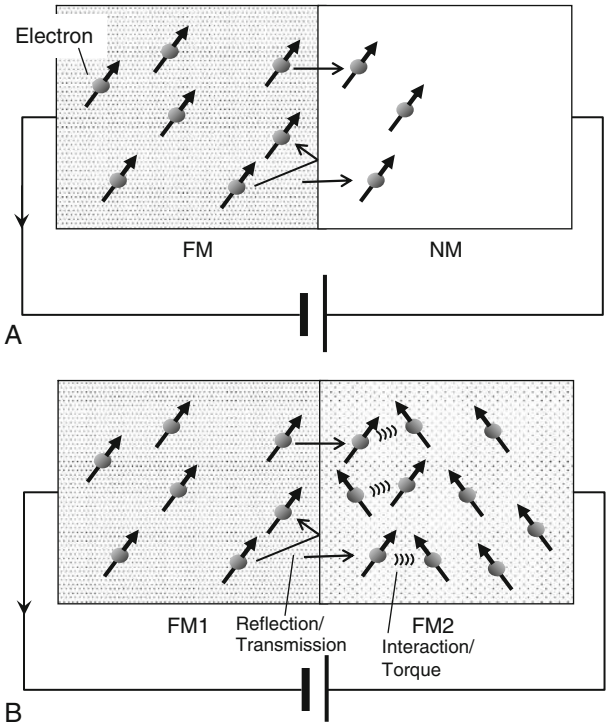

FIGURE 1 Spin injection across an interface. (A) Spin injection from a ferromagnetic material (FM) to a non-magnetic material (NM). Application of an electric charge current through the interface results in injection of a spin-polarized current into NM. (B) Spin injection from a ferromagnetic material (FM1) to another ferromagnetic material with different magnetization direction (FM2). Spin-dependent reflection and transmission at the interface give rise to the magnetoresistance effect. Injected spins interact with spins of the host material and exert torque on it.

shown. In the ferromagnetic material, since electron spins are polarized, an electric current accompanies the net flow of spins, that is, "spin current". The spins travelling as the spin current in the ferromagnet are then injected ("spin injection") into the non-magnetic material through the interface. The injected spins are subjected to spin relaxation because of spin–orbit interaction, and they lose their spin orientations as they move away from the interface. Spin-injection phenomena have been observed by detecting the emission of circularly polarized light from injected electrons in semiconductors such as GaAs [2–5], and by observing the spin-dependent electrochemical potentials in so-called non-local magnetoresistance geometries [6–11] or using the magnetoresistive/filtering effect [12].

What happens if we pass a current through two ferromagnetic materials with different magnetization orientations as shown in Fig. 1B? It is well known that the magnetoresistance effect occurs because of spin-dependent scattering (reflection) at the interface, as described in the previous chapter. In addition, the electron spins injected from the ferromagnetic material on the left-hand side (FM1) into the ferromagnetic material on the right-hand side (FM2) interact with the electron spins in FM2 through exchange interaction. As a result, a precession can be excited [13–15] and the magnetization can be switched [16–24] in FM2.

Before providing a detailed explanation of these interesting effects, let us discuss the concepts of "spin injection" and "spin current".

In a system in which many electrons are interacting, if the interaction between the electron spins is only exchange interaction, the total angular momentum of the electron system is conserved. Therefore, similar to the charge current density, which is derived from the conserved quantity, charge, one can define a flow of the spin angular momentum density, that is, spin current density:

$$\hat{j}^{\mathrm{S}}(\vec{x},t) = \sum_i \vec{v}_i(t)\vec{s}_i(\vec{x},t) + \left(\text{exchange mediated term}\right). \tag{1}$$

Here, $\vec{s}_i(\vec{x},t)$ and $\vec{v}_i(t)$ are the electron spin density and velocity of the ith electron, respectively, and $\sum$ is the sum over all the electrons concerned. The first term in Eq. (1) indicates that the flow of a spin-polarized electrons carries spin current, that is, angular momentum. The second term indicates that the spin angular momentum can be transferred by the exchange interaction even if the positions of the electrons are fixed. The latter term corresponds to a spin angular momentum transfer through spin waves. This term can be expressed locally and is roughly proportional to $\sum_{i,j}\vec{s}_i(\vec{x},t)\times\vec{\nabla}\vec{s}_j(\vec{x},t)$ if spins rotate continuously in space. Here, it should be noted that the spin current density, $\hat{j}^{\mathrm{S}}$, is a direct product of two vectors expressing the direction of the current flow and the direction of spin at the same time. The rule for conserving the spin angular momentum and the charge is expressed as follows:

$$\begin{cases} \dfrac{\partial \vec{s}}{\partial t} + \operatorname{div} \hat{j}^{\mathrm{S}} = 0, \\ \dfrac{\partial \rho}{\partial t} + \operatorname{div} \vec{j}^{\mathrm{Q}} = 0, \end{cases} \tag{2}$$

where ρ is the charge density, $\vec{j}^{\,\mathrm{Q}}$ is the electric current density and $\mathrm{div}\,\vec{A} = \left(\frac{\partial A_x}{\partial x} + \frac{\partial A_y}{\partial y} + \frac{\partial A_z}{\partial z}\right)$ expresses the divergence of flow $\vec{A}$.

Now, we consider a case where an electric field is applied to a large ferromagnetic material that is magnetized along $-\vec{e}_{\mathrm{spin}}(|\vec{e}_{\mathrm{spin}}| = 1)$. In the ferromagnetic materials, the spin angular momentum density, $\vec{s}$, is non-zero since the density of the majority spin electrons, n_+, is larger than that of the minority spin electrons, n_-:

$$\begin{cases} \vec{s} = \vec{s}_+ + \vec{s}_- = \dfrac{\hbar}{2}\vec{e}_{\mathrm{spin}}(n_+ - n_-), \\ \rho = \rho_+ + \rho_- = (-e)(n_+ + n_-). \end{cases} \tag{3}$$

Here, $\vec{s}_+$ ($\vec{s}_-$) and ρ_+ (ρ_-) are the spin density and charge density of the majority (minority) spin electrons. The direction of angular momentum is opposite to that of magnetization for the electrons. Hereafter, the treatment follows a derivation given by Valet and Fert [25], and suffixes $+$ and $-$ correspond to the majority and the minority spins, respectively.

As the system is large enough compared to the electron mean free path, the electrons flow diffusively by repeated scattering and acceleration. The scattering events, however, seldom change the spin orientation. Therefore, a physical picture can be constructed in which the majority and minority spin electrons flow diffusively independent of each other in each spin sub-channel (see Fig. 2). Since the

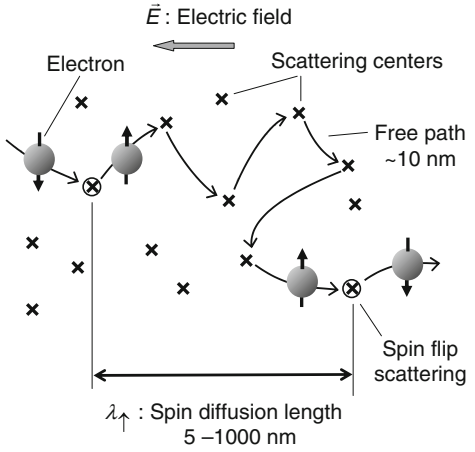

FIGURE 2 Drift flow of a free electron in a conductive material. An electron with negative charge ($-e$) is subject to an electric field $\vec{E}$ and accelerated towards the right. After a short travel, the electron is scattered by a scattering centre and its velocity changes. The electron is accelerated again until its next collision. Through the repetition of this process, the electron moves opposite to $\vec{E}$ on average. Then average distance between two scattering events is the mean free path. For metals at room temperature, the typical values of the mean free path are about 10 nm. During this drift motion, the electron seldom changes its spin direction. The average distance between two spin-flip events under zero electric field corresponds to the spin diffusion length, $\lambda_{\pm}$.

charge densities and drift velocities $(\vec{v}_+, \vec{v}_-)$ are different in different spin sub-channels, the electric conductivities (σ_+, σ_-), which are equal to (charge density) $\times$ (mobility), are also different in different spin sub-channels. As a result, the application of an electric field results not only in a drift charge current density, $\vec{j}^{\,\mathrm{Q,Drift}}$, but also in a drift spin current density, $\hat{j}^{\,\mathrm{S,Drift}}$:

$$\begin{cases} \hat{j}^{\,\mathrm{S,Drift}} = \vec{v}_+\vec{s}_+ + \vec{v}_-\vec{s}_- = \dfrac{\hbar}{2}\vec{e}_{\mathrm{spin}}\dfrac{1}{-e}(\sigma_+ - \sigma_-)\vec{E}, \\ \vec{j}^{\,\mathrm{Q,Drift}} = \vec{v}_+\rho_+ + \vec{v}_-\rho_- = (\sigma_+ + \sigma_-)\vec{E}. \end{cases} \tag{4}$$

Here, the second term in Eq. (1) is neglected for simplicity.

Next, let us consider the effect of current passing through the interface between a FM and a NM as shown in Fig. 3A. In the junction, we take two sections P and Q in the ferromagnetic material layer and the non-magnetic material layer, respectively. We assume that both P and Q are far enough from the interface to be affected by it. The spin current should be finite at P in the ferromagnetic material but zero at Q in the non-magnetic material as consequences of Eq. (4). Then, from the conservation law of spin momentum (Eq. (2)), it is expected that the spins will accumulate around the interface as time goes by. In reality, spin accumulation does not grow indefinitely but the accumulated spins are lost through spin–orbit coupling. To take this effect into account, we added spin relaxation terms to Eq. (2):

$$\begin{cases} \dfrac{\partial \vec{s}}{\partial t} + \mathrm{div}\ \hat{j}^{\,\mathrm{S}} = -\dfrac{\vec{s}_+ - \vec{s}_+^{\,\mathrm{eq}}}{\tau_+^{\mathrm{sf}}} - \dfrac{\vec{s}_- - \vec{s}_-^{\,\mathrm{eq}}}{\tau_-^{\mathrm{sf}}}, \\ \dfrac{\partial \rho}{\partial t} + \mathrm{div}\ \vec{j}^{\,\mathrm{Q}} = 0, \end{cases} \tag{2'}$$

where $\tau_\pm^{\mathrm{sf}}$ and $\vec{s}_\pm^{\,\mathrm{eq}}$ are the spin relaxation time and spin density in the thermal equilibrium condition in each spin sub-channel. $\tau_\pm^{\mathrm{sf}}$ defined in this chapter is half that defined in Ref. [25]. Since the density of states at the Fermi energy in metals, $N_\pm$, and the carrier density in semiconductors, $n_\pm$, are different for different spin sub-bands, the spin relaxation times are also different and are related as follows:

$$\begin{aligned} &\tau_+^{\mathrm{sf}}N_- = \tau_-^{\mathrm{sf}}N_+ : \text{Metals}, \\ &\tau_+^{\mathrm{sf}}n_- = \tau_-^{\mathrm{sf}}n_+ : \text{Non-degenerate semiconductors}. \end{aligned} \tag{5}$$

The accumulated spins also flow from the interface to the bulk by diffusion resulting in a diffusion spin current (Fig. 3B):

$$\begin{cases} \hat{j}^{\,\mathrm{S,Diffusion}} = -D_+\vec{\nabla}\vec{s}_+ - D_-\vec{\nabla}\vec{s}_-, \\ \vec{j}^{\,\mathrm{Q,Diffusion}} = -D_+\vec{\nabla}\rho_+ - D_-\vec{\nabla}\rho_-, \end{cases} \tag{6}$$

where $D_\pm$ is the diffusion constant of the electron in each spin sub-channel. The Einstein relation holds between the diffusion constants and the conductivities:

$$\begin{aligned} &\sigma_\pm = N_\pm e^2 D_\pm : \text{Metals}, \\ &\sigma_\pm = n_\pm e^2 D_\pm / kT : \text{Non-degenerate semiconductors}. \end{aligned} \tag{7}$$

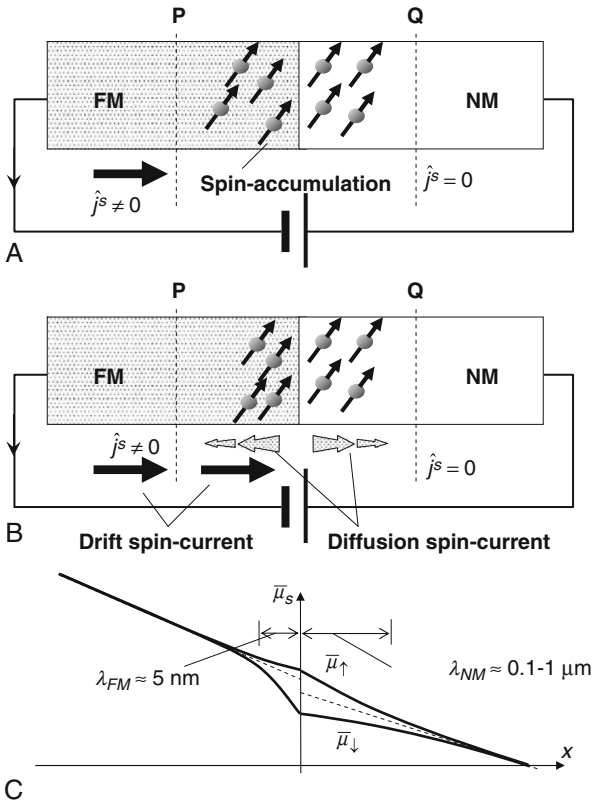

FIGURE 3 Spin accumulation, relaxation and diffusion during spin injection from a ferromagnetic material (FM) to a non-magnetic material (NM). (A) The spin current at section P is finite whereas that at Q is zero, that is, spins are injected into the interface region between P and Q but never leave it. As a result, the spins accumulate in the interface region. (B) The number of accumulated spins is decreased because of spin-flip scattering inside the interface region. Spin accumulation produces a gradient of the spin density and causes the spin diffusion current that moves spins away from the interface. (C) Associated electrochemical potential distribution. λ_{FM} and λ_{NM} are the average spin diffusion length of FM and NM. Detailed explanation is provided in text.

The gradient of the electron density in each spin sub-channels can be expressed by using spin-dependent chemical potentials, $\mu_\pm$, as follows:

$$\begin{aligned} &\vec{\nabla} n_\pm = N_\pm \vec{\nabla} \mu_\pm : \text{Metals}, \\ &\vec{\nabla} n_\pm \approx \pm n_\pm \vec{\nabla} \mu_\pm / kT : \text{Non-degenerate semiconductors}. \end{aligned} \tag{8}$$

A positive (negative) sign in the second line in Eq. (8) corresponds to electrons (holes) in the semiconductor. The above equations are valid only for a small change in $\mu_\pm$. In addition, we introduce an electrochemical potential, $\bar{\mu}_\pm = \mu_\pm - e\varphi$, to treat drift and diffusion at the same time. Here, φ is the electric scalar potential. By using $\bar{\mu}_\pm$, the charge current density in each spin sub-channel can be expressed simply as follows:

$$\vec{j}_{\pm}^{\mathrm{Q}} = \vec{j}_{\pm}^{\mathrm{Q,Drift}} + \vec{j}_{\pm}^{\mathrm{Q,Diffusion}} = \sigma_{\pm}\vec{\nabla}\bar{\mu}_{\pm}/e. \tag{9}$$

The total spin and charge current densities can be expressed in terms of the current densities appearing in Eq. (9) as

$$\begin{cases} \vec{j}^{\mathrm{S}} = \dfrac{\hbar}{2}\vec{e}_{\mathrm{spin}}\dfrac{\vec{j}_{+}^{\mathrm{Q}} - \vec{j}_{-}^{\mathrm{Q}}}{-e}, \\ \vec{j}^{\mathrm{Q}} = \vec{j}_{+}^{\mathrm{Q}} + \vec{j}_{-}^{\mathrm{Q}}. \end{cases} \tag{10}$$

The first equation in Eq. (10) is identical to Eq. (32) in Chapter 2.

For a given constant current, the growth of the spin accumulation continues until it balanced by spin diffusion and relaxation, and, then the system falls into a steady state. In the steady state, we obtain the following set of equations from Eqs (2′), (5), (9) and (10):

$$\begin{cases} \Delta\left(\bar{\mu}_{+} - \bar{\mu}_{-}\right) = \dfrac{\bar{\mu}_{+} - \bar{\mu}_{-}}{\lambda_{\mathrm{spin}}^{2}}, \\ \Delta\left(\sigma_{+}\bar{\mu}_{+} + \sigma_{-}\bar{\mu}_{-}\right) = 0, \end{cases} \tag{11}$$

where

$$\lambda_{\mathrm{spin}}^{-2} = \frac{\lambda_{+}^{-2} + \lambda_{-}^{-2}}{2},$$

$$\lambda_{\pm} = \sqrt{D_{\pm}\tau_{\pm}^{\mathrm{sf}}}.$$

Here, $\Delta = \frac{\partial^2}{\partial x^2} + \frac{\partial^2}{\partial y^2} + \frac{\partial^2}{\partial z^2}$ is the Laplacian. $\lambda_{\pm}$ is the spin diffusion length in each spin sub-channel. λ_{spin} is the average spin diffusion length. For non-degenerate semiconductors, it is often required to solve the Poisson equation in parallel with Eq. (11) to take the band bending and charge redistributions into account [26]. For semiconductors, if charge recombination and creation take place, the sources of the charges and spins must be taken into account by adding appropriate terms to Eq. (11) or to Eq. (2′) [26].

Equation (11) can be solved easily and are widely used to evaluate spin-dependent transport in the diffusive regime. For these calculations, the boundary conditions at the interfaces must be considered. In the simplest model, we assume the continuity of the electric current density, spin current density and electrochemical potential at the interface. If there is a particular spin relaxation at the interface, the discontinuity of the spin current density must be considered. On the other hand, for tunnelling junctions, the discontinuity of the electrochemical potential caused by spin-dependent interface resistances must be taken into account.

In Fig. 3C, the behaviour of the electrochemical potential is shown for the simplest case in which the electrical current, spin current and electrochemical potential are continuous at the interface. It is clear that the slopes of the electrochemical potentials are discontinuous at the interface to make the spin current

density in each spin sub-channel continuous. Under this condition, spin polarization of the injected current is calculated as follows:

$$\left(\text{spin polarization of the injected current}\right) = \frac{j_{\uparrow}^{\mathrm{Q}}(+0) - j_{\downarrow}^{\mathrm{Q}}(+0)}{j_{\uparrow}^{\mathrm{Q}}(+0) + j_{\downarrow}^{\mathrm{Q}}(+0)} = \frac{r^{\mathrm{FM}}}{r^{\mathrm{FM}} + r^{\mathrm{NM}}}\beta^{\mathrm{FM}}, \tag{12}$$

where

$$\beta^{\mathrm{FM}} \equiv \frac{\sigma_{+}^{\mathrm{FM}} - \sigma_{-}^{\mathrm{FM}}}{\sigma_{+}^{\mathrm{FM}} + \sigma_{-}^{\mathrm{FM}}},\ r^{\mathrm{FM}} \equiv \left(\frac{1}{\sigma_{+}^{\mathrm{FM}}} + \frac{1}{\sigma_{-}^{\mathrm{FM}}}\right)\lambda_{\mathrm{spin}}^{\mathrm{FM}},\ r^{\mathrm{NM}} \equiv \left(\frac{1}{\sigma^{\mathrm{NM}}/2} + \frac{1}{\sigma^{\mathrm{NM}}/2}\right)\lambda_{\mathrm{spin}}^{\mathrm{NM}}.$$

Here, $+0$ indicates the position at the right-hand side of the interface. $\uparrow$ and $\downarrow$ are the up and down spins in the NM, respectively. The up (down) spin in the NM is parallel to the majority (minority) spin in the FM. $\sigma_{+}^{\mathrm{FM}}\left(\sigma_{-}^{\mathrm{FM}}\right)$ is the electric conductivity at the majority(minority) spin sub-channel in the FM. σ^{NM} is the total electric conductivity of the NM. β^{FM} is the spin asymmetry of the electric conductivity in the FM. A large β^{FM} results in large spin polarization of the injected current. $\lambda_{\mathrm{spin}}^{\mathrm{FM}}\left(\lambda_{\mathrm{spin}}^{\mathrm{NM}}\right)$ is the spin diffusion length in the FM (NM). $r^{\mathrm{FM}}\left(r^{\mathrm{NM}}\right)$ expresses the difficulty in spin injection into the FM (NM) and is often regarded as the "spin (interface) resistance". As is clear from Eq. (12), spin injection from a FM to a NM is difficult if $r^{\mathrm{NM}} \gg r^{\mathrm{FM}}$. For example, if NM is a semiconductor and FM is a ferromagnetic metal, larger resistivity and spin diffusion length in the semiconductor provides a much larger spin resistance than that in the ferromagnetic metal. Therefore, spin injection from the FM to the NM will be difficult. This problem is known as "the conductance mismatch problem" [27].

Spin accumulation at the interface is obtained as follows:

$$\left(\text{spin accumulation}\right) = \frac{\hbar}{2}\frac{N^{\mathrm{NM}}}{2}\left(\mu_{\uparrow}(+0) - \mu_{\downarrow}(+0)\right) = -\frac{\hbar}{2}\frac{N^{\mathrm{NM}}}{2}\frac{r^{\mathrm{FM}}r^{\mathrm{NM}}}{r^{\mathrm{FM}} + r^{\mathrm{NM}}}\beta^{\mathrm{FM}}\frac{ej^{\mathrm{Q}}}{2}. \tag{13}$$

Here, N^{NM} is the total density of states at Fermi energy in the NM. If NM is a semiconductor, N^{NM} should be replaced by $\pm n/kT$. Here, n is the total carrier density and $+$ $(-)$ is for electrons (holes). Spin accumulation can be large if N^{NM} and β^{FM} are large, and both r^{FM} and r^{NM} are of the same order of magnitude. Therefore, a large accumulation is expected if both layers are the same kind of materials.

A way to overcome the conductance mismatch problem of spin injection into a semiconductor is to use a ferromagnetic semiconductor as a spin source [2, 3]. Ohno *el al*. used ferromagnetic GaMnAs as a spin source to inject spin-polarized holes into an InGaAs layer through a GaAs layer. In ZnS type direct gap semiconductors like InGaAs, light emitted by the recombination of the spin-polarized carriers, is up to 50% circularly polarized because of the selection rule at the Γ point ($S_{1/2}$ to $P_{3/2}$ transition). Therefore, by observing the degree of circular polarization one can estimate the spin polarization of the injected carriers.

Ohno *et al*. observed up about 10% circular polarization of the emitted light [2] at 6 K and could conclude a significant spin polarization (more than about 20%) of the injected carriers. Since GaMaAs has a relatively large spin resistance, they could achieve a reasonable conductance matching to a semiconductor.

Another way to inject spins into semiconductors is to insert a spin-dependent interface resistance [28]. A tunnel barrier at the interface, for example, may work as such a spin-dependent interface resistance. If the inserted interface resistance is sufficiently larger than the spin resistances, the polarization of the injected current will be determined by the spin asymmetry of the interface resistance, γ^{I}:

$$\left(\text{spin polarization of the injected current}\right) = -\gamma^{\mathrm{I}}, \tag{14}$$

where $\gamma^{\mathrm{I}} \equiv \frac{r_+^{\mathrm{I}} - r_-^{\mathrm{I}}}{r_+^{\mathrm{I}} + r_-^{\mathrm{I}}}$. In addition, spin accumulation is governed by the interface resistance as follows:

$$\left(\text{spin accumulation}\right) = \frac{\hbar}{2}\frac{N^{\mathrm{NM}}}{2} r^{\mathrm{NM}} \gamma^{\mathrm{I}} \frac{ej^{\mathrm{Q}}}{2}. \tag{15}$$

Using a tunnel barrier, large spin accumulation in the semiconductors can be expected. Motsnyi *et al*. [29] successfully injected spin-polarized current from the CoFe to the GaAs layer through an AlO_x barrier layer. In addition, they proved it undoubtedly by showing precession of the injected spins under an applied magnetic field with an oblique angle by again observing the polarization of the emitted light.

As shown above, the spins injected into III–V semiconductors have been detected by polarization analysis of the emitted light [2–5]. On the other hand, to detect the spins injected into non-magnetic metals, the detection of the spin-dependent chemical potential using a second ferromagnetic electrode has been often used. This method is called "non-local magnetoresistance (MR) measurement", and it offers an explicit proof of spin injection.

In Fig. 4A and B, submicron-scale wire junctions made by Jedema *et al*. [7] are shown. To measure the non-local MR effect, current was applied between Co1 and Al electrodes and the voltage generated between the Co2 and Al electrodes was measured. In this structure, there is no charge current between the Co1 and Co2 electrodes. By current injection, however, spin accumulation takes place at the interface between Co1 and Al electrodes and generates a spin diffusion current towards the Co2 electrode. In Fig. 4C, the electrochemical potentials associated with the above spin accumulation and spin current are shown together with the detection part (Co2). $\bar{\mu}_\uparrow$ and $\bar{\mu}_\downarrow$ split symmetrically at the interface between Co1 and Al electrodes (left-hand side in Fig. 4C) because of the spin accumulation. Here, the up spin is parallel to the majority spin in Co1. The gradients of the electrochemical potentials in the Al wire produce diffusion charge currents in both spin sub-channels. While these charge currents have the same magnitude, they are opposite in sign. Therefore, while there is no net charge current between the Co1 and Co2 electrodes, a spin current flows.

In the Co2 electrode, where the injected pure spin current is completely absorbed, different diffusion constants for different spins and the continuity of

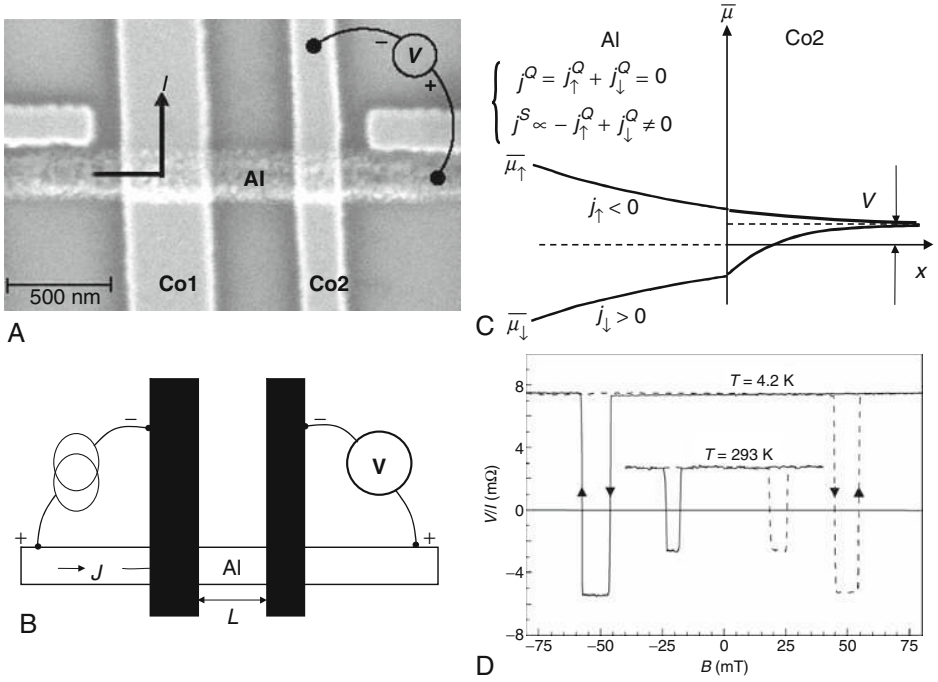

FIGURE 4 Non-local magnetoresistance measurement (after Ref. [7]). (A) SEM image of the sample. The sample consists of two parallel Co wires (Co1 and Co2) and an Al wire perpendicular to the Co wires. (B) Current, I, was applied between Co1 and the left side of the Al wire and voltage, V, that appeared between Co2 and the right side edge of the Al wire was measured. Non-local resistance, R, was defined as $R = V/I$. (C) Electrochemical potential distribution from the Al wire to the Co2 interface. On the Al side, the electrochemical potential splits symmetrically. The slope of the electrochemical potential drives the diffusion spin current. The spin current is absorbed by the Co2 electrode. Asymmetric splitting in the chemical potential in Co2 causes a voltage shift of the electrode. (D) Non-local resistance as a function of the applied magnetic field. Non-local resistance is always positive except in a particular range of the applied field where magnetizations in Co1 and Co2 are antiparallel. The results are well explained by employing, $D_{Al} = 0.43 \times 10^{-2}$ m^2/s (4.2 K), 0.27×10^{-2} m^2/s (293 K), $\lambda_{sf} = 0.65$ μm (4.2 K), 0.35 μm (293 K).

the current in each spin sub-channel require different slopes of the electrochemical potentials (right-hand side in Fig. 4C). As a consequence, a finite electromotive force, V, appears between the Co2 wire and the Al wire. This "non-local voltage" is expressed as follows the assuming a large contact resistance between Co2 and Al contact:

$$V = \pm\frac{1}{2}ej^{Q}\beta_{Co}^{2}\frac{r^{Co}r^{Al}}{r^{Co}+r^{Al}}\exp\left(-\frac{L}{\lambda_{spin}^{Al}}\right). \tag{16}$$

Here, a positive (negative) sign corresponds to the parallel (antiparallel) alignment of magnetization. In Fig. 4D, the signal detected by Jedema *et al.* is shown.

Antiparallel alignment is achieved in a particular range of the applied field and it shows a negative voltage output, as predicted by Eq. (16). The observed voltage was less than 1 μV for a 100 μA input current.

If we apply an external field perpendicular to the sample plane, a precession of the injected spins occurs. If the precession angle for travel from Co1 to Co2 equals 90°, the non-local signal disappears. Moreover, if the angle is greater than 90 °, the signal changes in sign. As a result, the non-local signal shows damped oscillation as a function of the external field strength. By using this Hanle effect [30], the spin diffusion length can be estimated correctly. The effect has been observed not only in metals [6, 7] and semiconductors [8, 29], but also in new materials like carbon nanotubes [9] and graphene [10, 31], thus providing clear evidence of spin injection. In Fig. 5, the MR effect and the Hanle effect observed for a multilayer graphene are illustrated [31].

Kimura *et al*. developed a structure similar to that shown in Fig. 4A but they replaced the Co2 electrode with a small permalloy (FeNi alloy) pad and injected a pure spin current into the pad. In this way, they were able to transfer sufficient angular momentum to the pad to reverse its magnetization [32]. This is the first demonstration of magnetization reversal using a pure spin current.

By using spin accumulation or spin pumping [33], we can inject a pure spin current that does not accompany a charge current, into non-magnetic materials. If there is spin–orbit interaction in the non-magnetic material into which a pure

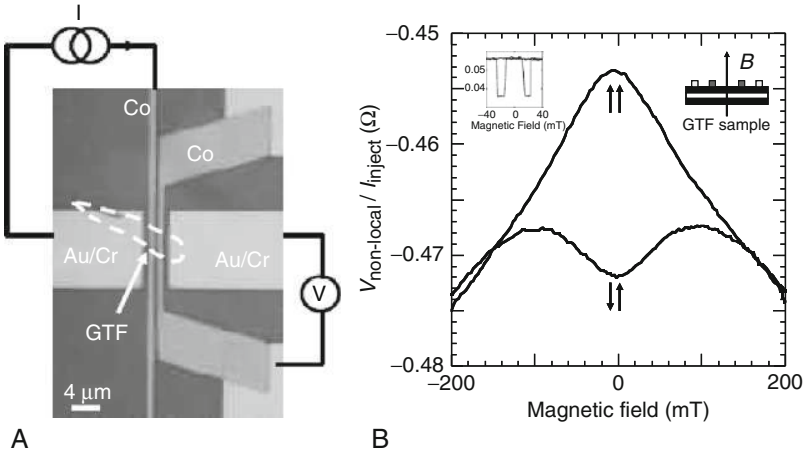

FIGURE 5 Spin-dependent transport in a multilayer graphene (after Refs [11, 29]). (A) Sample structure. The multilayer of graphene (a stack of several graphene sheets) is under four electrodes, two of which are ferromagnetic electrodes (Co1 and Co2). (B) Non-local resistance signal as a function of the external field that is applied perpendicular to the film plane. At zero applied field, the magnetizations of Co1 and Co2 electrodes are either parallel (upper curve) or antiparallel (lower curve). Precession of the injected spins results in damped oscillation of the non-local resistance signals as a function of the external field (Hanle effect). Solid curves are fitted using the diffusive transport model with $D_{graphene} = 2.1 \times 10^{-2}$ m^2/s (RT), $\lambda_{sf} = 1.6$ μm (RT). Insets show the non-local signal as a function of the in-plane external field and the sample structure.

spin current is injected, the flow of the spin is scattered asymmetrically by impurities and it produces a voltage along a direction that is perpendicular to both the current flow direction and the spin direction [34–37] (Fig. 6A and B). This phenomenon is called the "inverse spin Hall effect". In addition, a charge current inside a non-magnetic material may produce a spin current and spin accumulation along a direction perpendicular to the current direction. This "spin Hall effect" has been observed in semiconductors [38, 39] and metals [36] (Fig. 6C and D).

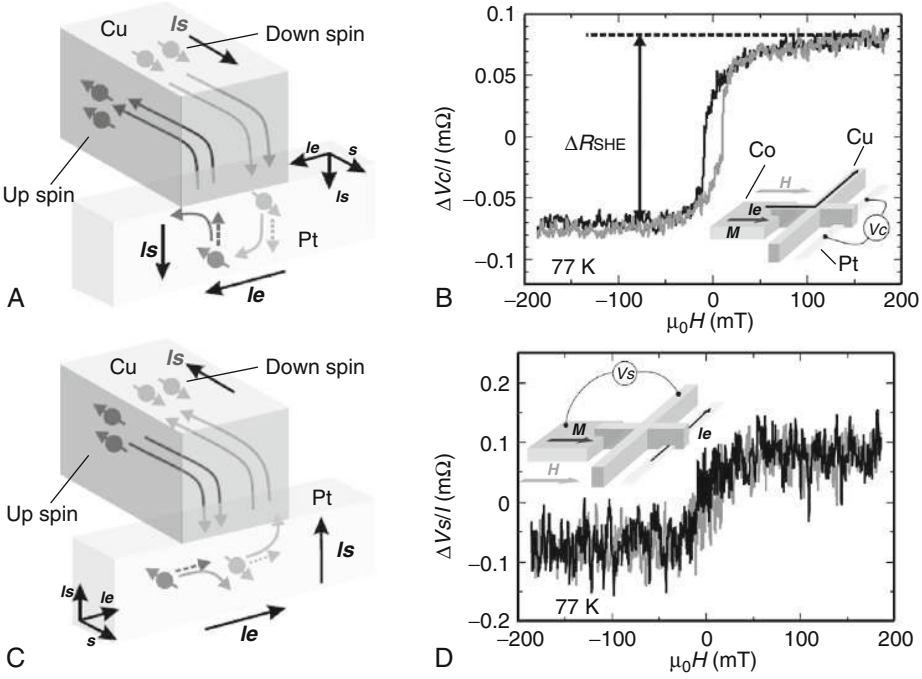

FIGURE 6 Inverse spin Hall effect and spin Hall effect in Pt wires (after Ref. [36]). (A) Graphical illustration of the inverse spin Hall effect. Pure spin current (I_s) is injected from a Cu electrode into a Pt wire. The spin current consists of up spin and down spin electrons moving in opposite directions. These electrons are scattered around the same side (left-hand side) of the Pt wire because of large spin–orbit coupling in the Pt, and produces voltage V_C. (B) The change in Hall resistance (V_C/I_e) due to the inverse spin Hall effect at 77 K. The inset shows the sample structure and the measurement configuration. Spin-polarized charge current (I_s) is injected from the Co electrode to the Cu electrode and it produces spin accumulation in the latter. The accumulated spins produce diffusion spin current and are injected into the Pt wire. The voltage along to the Pt wire (V_C) was measured. (C) Graphical illustration of the spin Hall effect. In the Pt wire, because of a charge current (I_e) the up spin and down spin electrons move along the same direction. These electrons, however, are subjected to the scattering towards the opposite direction and they produce a spin current (I_s). (D) The spin current injected into the Cu electrode produces a potential change in the Co electrode (V_s). The graph shows the spin accumulation signal (V_S/I_e) generated by the spin Hall effect at 77 K. The intensity of the signal is similar to that in (B) as a consequence of Onsager's reciprocal theorem.

Moreover, Murakami *et al*. predicted the existence of an "intrinsic" spin Hall effect, in which an electric field produces a dissipation-less spin current [40]. Wunderlich *et al*. claim that their observations agree with latter idea [39].

1.2. Spin-transfer torque

Next, we discuss what happens when spins are injected from one ferromagnetic layer (FM1) into another ferromagnetic layer (FM2). This spin injection gives rise to a torque on the FM layers, and as a result, one of the FM layers may switch its direction (called as spin-injection magnetization switching, SIMS) or undergo continuous oscillations (called as spin-torque oscillation, STO). SIMS and STO are usually performed by employing magnetic nano-pillars made of magnetic multilayers, as shown in Fig. 7. A typical device consists of two ferromagnetic layers (FM1 and FM2: Co, for example) and a non-magnetic layer (NM1: Cu or MgO, for example) inserted between them. When current is passed through this device, the electrons are first polarized by the FM1 and then injected into the FM2 through the NM1. The spins of the injected electrons interact with the spins in the host material by exchange interaction and exert torque. If the exerted torque is large enough, magnetization in FM2 is reversed or continuous precession is excited.

To simplify the problem, let us imagine an electron system in which the conduction electrons (s-electrons) and the electrons that hold local magnetic

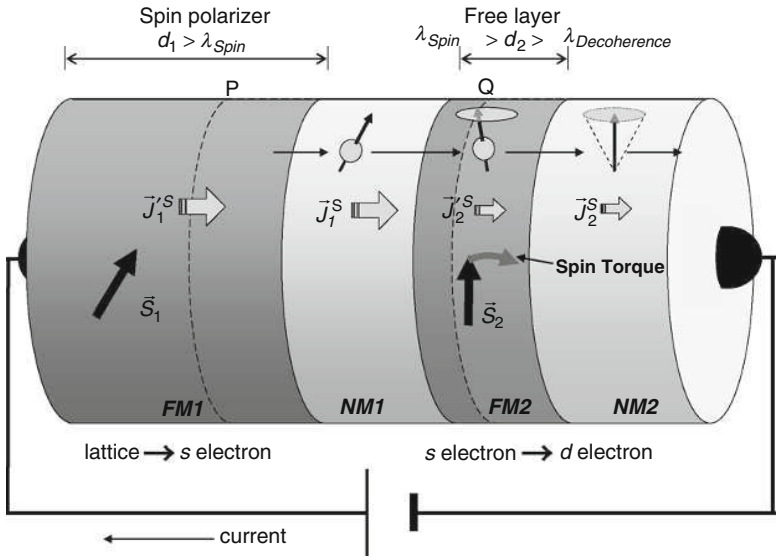

FIGURE 7 Schematic illustration of a magnetic nano-pillar consisting of two ferromagnetic layers and two non-magnetic layers. The electrons are spin polarized by the thick ferromagnetic layer (FM1: spin polarizer) and then injected into the thin ferromagnetic layer (FM2: free layer) through the non-magnetic layer (NM1). The injected spins undergo precession in FM2 and lose their transverse components. The lost spin components are transferred to the local spin moment in FM2, $\vec{S}_2$. Details are provided in the text.

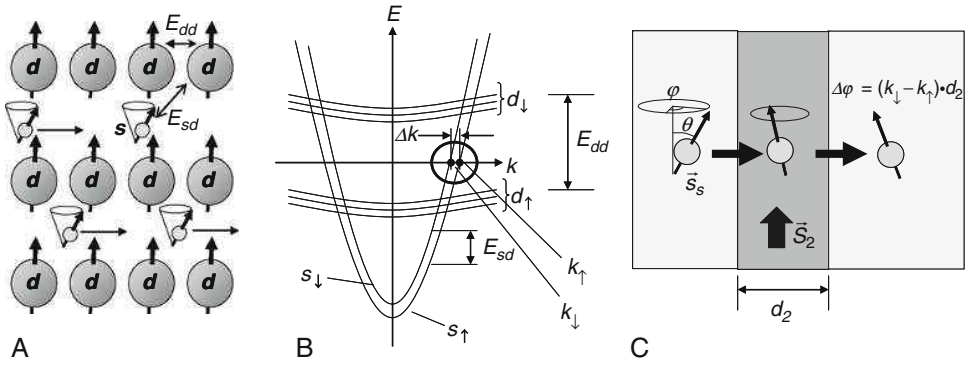

FIGURE 8 (A) A simple s–d model to describe the spin-transfer effect. s-Electrons flow among the localized d-electrons and contribute to a charge and spin current, while d-electrons create a single large local magnetic moment because of strong d–d exchange interaction. s–d exchange interaction causes a precession of s- and d-electrons. Since d-electrons create a single large spin moment, the precession angle of the d-electron system is considerably smaller than that of s-electrons. (B) Schematic band structure of a ferromagnetic 3D transition metal. s-Electrons are in the free electron like s-bands with small spin splitting whereas d-electrons are in the relatively narrow d-bands with large spin splitting. Because of the spin splitting, Fermi *k*-vectors for the majority and minority spin bands are different. (C) The injected spin shows a precession in a ferromagnetic layer as a consequence of different *k*-vectors for the majority and minority spin bands.

moments (d-electrons) interact with each other through exchange interactions (Fig. 8A). The exchange interaction (s–d exchange interaction) conserves the total spin angular momentum. Therefore, a decrease in the sub-total angular momentum of the conduction electrons equals the increase in the sub-total angular momentum of the d-electron system. In the magnetic pillar, if the spin angular momentum of a conduction electron changes because of the s–d interaction during transport through the FM2 layer, this amount of angular momentum should be transferred to the d-electrons in the FM2 layer. From Eq. (2),

$$\frac{\mathrm{d}\vec{S}_2}{\mathrm{d}t} = \vec{J}_1^{\mathrm{S}} - \vec{J}_2^{\mathrm{S}}, \tag{17}$$

where $\vec{S}_2$ is the total angular momentum in the FM2. The spin currents $\vec{J}_1^{\mathrm{S}}$ and $\vec{J}_2^{\mathrm{S}}$ are obtained by integrating the spin current density flowing in NM1 and NM2, respectively, over the cross-sectional area of the pillar. Since FM2 is very thin, we neglected the spin–orbit interaction in FM2. Equation (17) indicates that a torque can be exerted on the local angular momentum as a result of spin transfer from the conduction electrons. This type of the torque, which appears in Eq. (17), is called the "spin-transfer torque".

Next, we consider how $\vec{J}_1^{\mathrm{S}}$ and $\vec{J}_2^{\mathrm{S}}$ are determined for metallic junctions [16]. We assume that the FM1 layer is thicker than its spin diffusion length. Therefore, the conduction electrons after passing through the FM1 layer becomes spin-polarized along the angular momentum direction of the FM1, $\vec{S}_1$. They are then injected into

the NM1 layer. If $\vec{S}_1$ is oriented along (θ, ϕ) in a polar coordinate system, the spin function of the injected spin can be expressed as follows:

$$|(\theta,\phi)\rangle = \cos\frac{\theta}{2}\left|\uparrow\right\rangle + \mathrm{e}^{\mathrm{i}\phi}\sin\frac{\theta}{2}\left|\downarrow\right\rangle \quad \text{or} \quad \begin{pmatrix} \cos\dfrac{\theta}{2} \\ \mathrm{e}^{\mathrm{i}\phi}\sin\dfrac{\theta}{2} \end{pmatrix}. \tag{18}$$

Here, $|\uparrow\rangle$ and $|\downarrow\rangle$ are the spin eigenstates along the $+z$ and $-z$ directions, respectively. It is easy to understand that Eq. (18) expresses the spin state pointing in (θ, ϕ) direction if one examines that the expectation values of the Pauli matrices, $(\sigma_x, \sigma_y, \sigma_z)$, for the state are $(\cos\phi\sin\theta, \sin\phi\sin\theta, \cos\theta)$. Since FM2 is magnetized along the $-z$ direction, the s-electron bands are split into $s_\uparrow$ and $s_\downarrow$ bands (Fig. 8B). Therefore, the wave function of the injected s-electron is split into $s_\uparrow$ and $s_\downarrow$ partial waves (Bloch states) that belong to different wave vectors, that is, $k_\uparrow$ and $k_\downarrow$. As a result, the phase acquired during the travel in the FM2 layer with thickness d_2 will be $k_\uparrow d_2$ and $k_\downarrow d_2$ for each partial wave. Therefore, after a ballistic travel through a very thin FM2 layer the spin functions of the electron will be as follows:

$$\begin{pmatrix} \mathrm{e}^{\mathrm{i}k_\uparrow d_2} & 0 \\ 0 & \mathrm{e}^{\mathrm{i}k_\downarrow d_2} \end{pmatrix} \begin{pmatrix} \cos\dfrac{\theta}{2} \\ \mathrm{e}^{\mathrm{i}\phi}\sin\dfrac{\theta}{2} \end{pmatrix} = \mathrm{e}^{\mathrm{i}k_\uparrow d_2} \begin{pmatrix} \cos\dfrac{\theta}{2} \\ \mathrm{e}^{\mathrm{i}(\phi+(k_\downarrow - k_\uparrow)d_2)}\sin\dfrac{\theta}{2} \end{pmatrix}.$$

In the above expression, we can see that ϕ is altered by $\phi + (k_\downarrow - k_\uparrow)d_2$. This means that the spins of the conduction electrons were subject to a precession around $\vec{S}_2$ by $(k_\downarrow - k_\uparrow)d_2$ (rad) (Fig. 8C). For realistic cases, since most films are polycrystalline and each conduction electron travels along different crystal orientations, the phases and therefore the precession angles should be different for different electrons. As a result, the transverse components (x- and y-components) of the injected spins cancel each other and disappear on average. For this case, the change in the spin current that produces the spin-transfer torque will be as follows:

$$\frac{\mathrm{d}\vec{S}_2}{\mathrm{d}t} = g(\theta)\frac{J^{\mathrm{Q}}}{-e}\left(\frac{\hbar}{2}\begin{pmatrix}\cos\phi\sin\theta\\ \sin\phi\sin\theta\\ \cos\theta\end{pmatrix} - \frac{\hbar}{2}\begin{pmatrix}0\\0\\\cos\theta\end{pmatrix}\right) = g(\theta)\frac{J^{\mathrm{Q}}}{-e}\frac{\hbar}{2}\vec{\mathbf{e}}_2 \times (\vec{\mathbf{e}}_1 \times \vec{\mathbf{e}}_2), \tag{19}$$

where $\vec{\mathbf{e}}_1 = (\cos\phi\sin\theta, \sin\phi\sin\theta, \cos\theta)$ and $\vec{\mathbf{e}}_2 = (0, 0, 1)$ are unit vectors along the angular momenta in FM1 and FM2, respectively. $J^{\mathrm{Q}}/(-e)$ is the number of electrons flowing per unit time (J^{Q} is a charge current). $g(\theta)$ expresses the efficiency of spin transfer and is dependent on the spin polarization, P, of the conduction electron in the ferromagnetic layers and the relative angle between $\vec{S}_1$ and $\vec{S}_2$, that is, θ. Slonczewski [16] proposed a formula for the spin-transfer efficiency, $g(\theta)$, that is suitable for the CPP-GMR junctions by considering a free electron model:

$$g(\theta) = \left[-4 + \left(P^{-1/2} + P^{1/2}\right)^3 (3 + \cos\theta)/4\right]^{-1}. \tag{20}$$

In the above formula, the effects of electron reflection at the NM1/FM2 interface, which have not been discussed in this text, are also taken into account.

Next, we consider the spin-transfer torque exerted magnetic tunnel junctions (MTJs) according to the derivation given by Slonczewski [41, 42]. In this case, NM1 is a barrier layer made up of MgO or AlO. Again, we assume that FM1 is thick enough; therefore, at point P in FM1 (see Fig. 7), the conduction spins are relaxed and aligned parallel to $\vec{S}_1$. In addition, we assume that at point Q inside FM2, the spins of the conduction electrons have already lost their transverse spin component because of the above-mentioned decoherence mechanism and that the spins have aligned parallel to $\vec{S}_2$. Since the spins of the conduction electrons at P and Q are either the majority or minority spin of the host materials, the total charge current in the MTJ can be expressed as a sum of the following four components (Fig. 9):

$$J^{\mathrm{Q}} = J^{\mathrm{Q}}_{++} + J^{\mathrm{Q}}_{+-} + J^{\mathrm{Q}}_{-+} + J^{\mathrm{Q}}_{--}. \tag{21}$$

Here, suffixes + and − indicate the majority and minority spin channels, respectively. For example, J^{Q}_{+-} represents a charge current flow from the FM2 minority spin band into the FM1 majority spin band. These charge currents are expressed using the conductance for each spin sub-channel, $G_{\pm\pm}$.

$$\begin{cases} J^{\mathrm{Q}}_{\pm\pm} = VG_{\pm\pm}\cos^2\dfrac{\theta}{2}, \\ J^{\mathrm{Q}}_{\mp\pm} = VG_{\mp\pm}\sin^2\dfrac{\theta}{2}. \end{cases} \tag{22}$$

Here, V is the applied voltage. The angle dependence of the conductions can be derived from the fact that the spin functions in the FM1 are $|\mathrm{maj.}\rangle = \cos(\theta/2)|\uparrow\rangle + \sin(\theta/2)|\downarrow\rangle$ for the majority spins and $|\mathrm{min.}\rangle = \sin(\theta/2)|\uparrow\rangle - \cos(\theta/2)|\downarrow\rangle$ for the minority spins, and those in the FM2 are $|\uparrow\rangle$ and $|\downarrow\rangle$, respectively. Since the spin

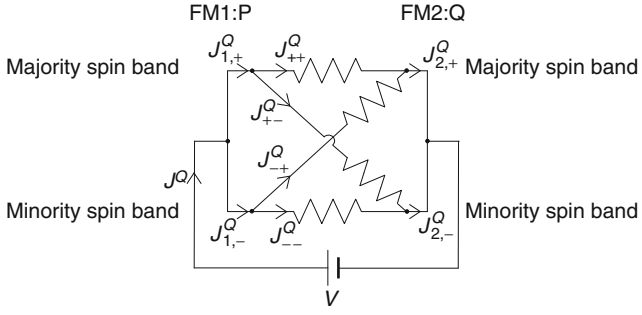

FIGURE 9 Circuit model of a magnetic tunnel junction (after Ref. [42]).

quantization axes at P and Q are parallel to $\vec{S}_1$ and $\vec{S}_2$, respectively, the spin currents at P and Q are obtained easily as follows:

$$\begin{cases} \vec{J}_1^{'S} = \dfrac{\hbar}{2}\dfrac{1}{-e}(J_{++}^{Q} + J_{+-}^{Q} - J_{-+}^{Q} - J_{--}^{Q})\vec{\mathbf{e}}_1, \\ \vec{J}_2^{'S} = \dfrac{\hbar}{2}\dfrac{1}{-e}(J_{++}^{Q} - J_{+-}^{Q} + J_{-+}^{Q} - J_{--}^{Q})\vec{\mathbf{e}}_2. \end{cases} \tag{23}$$

Therefore, after a straightforward calculation, the total current and spin-transfer torque are obtained as follows:

$$\begin{cases} J^{Q} = \dfrac{1}{2}V[(G_{++} + G_{--} + G_{+-} + G_{-+}) + (G_{++} + G_{--} - G_{+-} - G_{-+})\vec{\mathbf{e}}_2\cdot\vec{\mathbf{e}}_1] \\ \quad = \dfrac{1}{2}V[(G_{\mathrm{P}} + G_{\mathrm{AP}}) + (G_{\mathrm{P}} - G_{\mathrm{AP}})\cos\theta], \\ \dfrac{\mathrm{d}\vec{S}_2}{\mathrm{d}t} = \dfrac{\hbar}{2}\dfrac{1}{-e}\dfrac{1}{2}V[(G_{++} - G_{--}) + (G_{+-} - G_{-+})](\vec{\mathbf{e}}_2 \times (\vec{\mathbf{e}}_1 \times \vec{\mathbf{e}}_2)), \end{cases} \tag{24}$$

where G_{P} and G_{AP} are the conductance in the parallel and antiparallel configurations, respectively. In the first equation in Eq. (24), $\cos\theta$ dependence of the tunnel conductance can be seen. In the second equation, $\sin\theta$ dependence of the spin torque appears, similar to the case in Eq. (19). The important difference, however, is that in Eq. (19), the efficiency of spin transfer, $g(\theta)$, also has an angular dependence, while in the MTJs, the $\sin\theta$ dependence is exact since $G_{\pm\pm}$ does not have angular dependence. From this property, Slonczewski termed the coefficient in the second line of Eq. (24) as a "torquance", which is an analogue of the "conductance". This simple expression was obtained because the torque was expressed as a function of voltage in Eq. (24). If we rewrite the second line of Eq. (24) as function of the current, the spin-transfer efficiency is obtained as follows from comparison with Eq. (19):

$$g(\theta) = \frac{(G_{++} - G_{--} + G_{+-} - G_{-+})}{(G_{++} + G_{--} + G_{+-} + G_{-+}) + (G_{++} + G_{--} - G_{+-} - G_{-+})\vec{\mathbf{e}}_2\cdot\vec{\mathbf{e}}_1}. \tag{25}$$

As shown above, $g(\theta)$ for the MTJs also depends on the angle between $\vec{S}_1$ and $\vec{S}_2$.

Another important feature in the MTJs is that the torque has a bias voltage dependence because $G_{\pm\pm}$ has bias voltage dependence. In Fig. 10A, the theoretically predicted spin-transfer torque is plotted as a function of the bias voltage by fine lines [44]. As shown in the figure, the bias dependence of the spin-transfer torque is neither monotonic nor symmetric. The torque will be much higher at a large negative bias even if the magnetoresistance is smaller at such a high bias. This slightly complicated behaviour can be explained as follows from the second line in Eq. (24). Assume that the FM1 and FM2 are made of the same material. Now if we apply voltage, due to the symmetric conditions for tunnelling, the conductances G_{++} and G_{--} do not depend on the sign of the voltage. Thus the contribution to the torque from $(G_{++} - G_{--}) \times V$ term is odd with respect to the voltage.

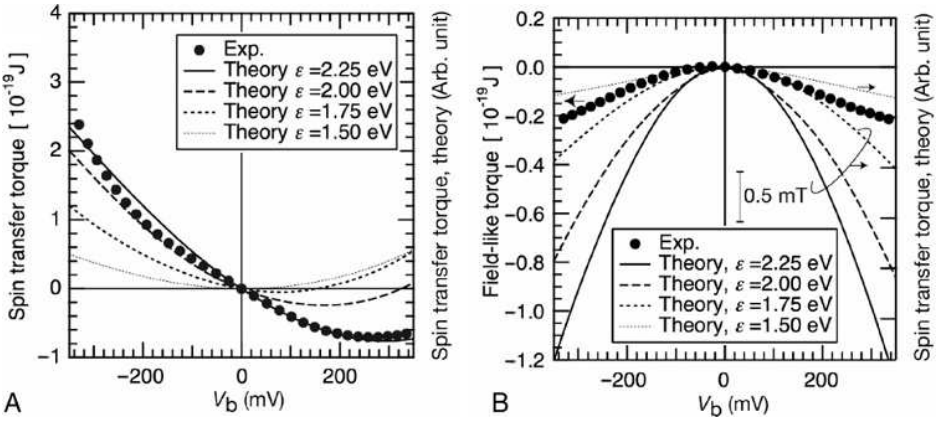

FIGURE 10 Bias dependence of the spin torques. (A) Bias dependence of the spin-transfer torque. (B) Bias dependence of field-like torque. Fine curves were obtained by theoretical model calculations (after Ref. [42]) with different spin splitting, ε. Points show the experimental result obtained for a CoFeB/MgO/CoFeB magnetic tunnel junction using the spin-torque diode effect (after Ref. [43]).

The conductances G_{+-} and G_{-+} are equal at 0 bias. For positive voltage, G_{+-} decreases, where as G_{-+} increases, thus giving a positive contribution to the spin torque. For negative voltage, due to the symmetry, we have opposite situation and $(G_{+-} - G_{-+})$ changes sign. But as the voltage is also negative, the net contribution is again positive. Therefore, $(G_{+-} - G_{+-}) \times V$ term is an even function of the voltage. This combination of odd and even terms gives an asymmetry in the spin torque as a function of voltage.

Sankey *et al*. [45] and Kubota *et al*. [43] experimentally observed the bias dependence of the torques. In Fig. 10A, the experimentally obtained bias voltage dependence of the spin-transfer torque in a CoFeB/MgO/CoFeB magnetic tunnel junction is plotted by large circles [43]. The torque was measured by using the "spin-torque diode effect", which will be explained later in this book (see Section 3.2). The experimental observations [43, 45] essentially agree with the model calculation.

1.3. Field-like torque

Even if it is assumed that $\vec{S}_2$ does not change in size, it may change in direction in two different ways. One is along the direction parallel to the spin-transfer torque, $(\vec{\mathbf{e}}_2 \times (\vec{\mathbf{e}}_1 \times \vec{\mathbf{e}}_2))$. Another is the direction parallel to $(\vec{\mathbf{e}}_1 \times \vec{\mathbf{e}}_2)$. If the torque is parallel to $(\vec{\mathbf{e}}_1 \times \vec{\mathbf{e}}_2)$, it has the same symmetry as a torque exerted by an external field. Therefore, the latter torque is called "field-like torque". It can also be called "accumulation torque" based on its origin, or "perpendicular torque" based on its direction in the multilayer system with in-plane magnetizations.

It has been pointed that one of the important origins of the field-like torque in the MTJs is the change in the interlayer exchange coupling through the barrier layer at a finite biasing voltage [44, 46]. In Fig. 10B, the theoretically obtained strength of the field-like torque is plotted as a function of the bias voltage [44]. As theoretically predicted for the symmetrical MTJs, the field-like torque is an even function of the bias voltage. Its strength itself is less than 1/5 that of the spin-transfer torque. The experimental results obtained so far [43, 45] seems to agree with this prediction.

The field-like torque could have originated from other mechanisms that are similar to those responsible for the "β-term" in magnetic nano-wires (see Chapters 5 and 6). Several mechanisms, such as a spin relaxation [47, 48], Gilbert damping itself [49], momentum transfer [50] and current-induced Ampere field have been proposed for the origin of the "β-term".

2. SPIN-INJECTION MAGNETIZATION REVERSAL

2.1. Amplification of the precession

In this and subsequent sections, we mainly focus on the two types of magnetic nano-pillars shown in Fig. 11: (a) pillars with magnetization perpendicular to the film plane (perpendicularly magnetized pillars) and (b) pillars with magnetization parallel to the film plane (in-plane magnetized pillars). These structures provide all the essential features necessary to understand the physics of spin-transfer effects and they are also important for practical applications. In addition, we assume that the perpendicularly magnetized and in-plane magnetized nano-pillars have a round and elliptical cross sections, respectively. The in-plane magnetized pillars have their magnetization parallel to the long axis of the ellipse.

As discussed in the previous section, an electric current passing through a magnetic nano-pillar composed of magnetic multilayers (Fig. 7) transfers spin angular momentum to the magnetic free layer and changes the direction of the local spins in the layer (Eqs (19) and (24)). The dynamic properties of the local spins can be expressed by the following Landau–Lifshitz–Gilbert (LLG) equation, which includes a spin-transfer torque term [16]:

$$\frac{\mathrm{d}\vec{S}_2}{\mathrm{d}t} = \gamma\vec{S}_2 \times \vec{H}_{\mathrm{eff}} - \alpha\vec{\mathbf{e}}_2 \times \frac{\mathrm{d}\vec{S}_2}{\mathrm{d}t} + g(\theta)\frac{J^{\mathrm{Q}}}{-e}\frac{\hbar}{2}\vec{\mathbf{e}}_2 \times (\vec{\mathbf{e}}_1 \times \vec{\mathbf{e}}_2). \tag{26}$$

The first term is the effective field torque; the second, Gilbert damping; and the third, the spin-transfer torque. $\vec{S}_2 = S_2\vec{\mathbf{e}}_2$ is the total spin angular momentum of the free layer and is opposite to its magnetic moment, $\vec{M}_2$.$\vec{\mathbf{e}}_2(\vec{\mathbf{e}}_1)$ is a unit vector that expresses the direction of the spin angular momentum of the free layer (fixed layer). For simplicity, we neglect the distribution of the local spin angular momentum inside the free layer and assume that the local spins within each magnetic cell are aligned in parallel and form a coherent "macrospin" [51, 52]. This assumption is not strictly valid since the demagnetization field and current-induced Oersted field inside the cells are not uniform. Such non-uniformities introduce incoherent

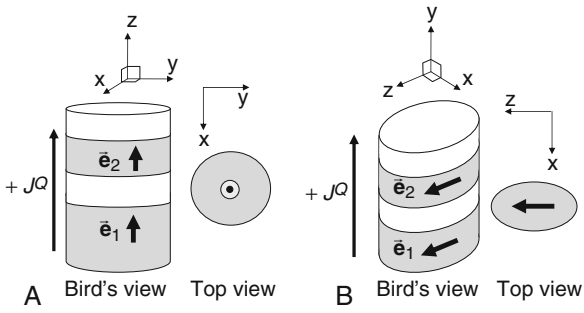

FIGURE 11 Typical structures of magnetic nano-pillars designed for spin-injection magnetization switching (SIMS) experiments. In the bird's-eye-view pictures, the upper magnetic layer acts as a magnetically free layer, whereas lower magnetic layers are thicker than the free layer and act as a spin polarizer. The spins in the lower layers are usually pinned by an exchange interaction at the bottom interface to an anti-ferromagnetic material. Therefore, the spin polarizer layer is often called the "pinned layer", "fixed layer" or "reference layer". In GMR nano-pillars, the layer between two ferromagnetic layers is made of a non-magnetic metal such as Cu. In MTJ nano-pillars, this interlayer is made of insulators such as MgO. The diameter of the pillar is around 100 nm, presently. The free layer is typically a few nanometres thick. (A) A magnetic nano-pillar with perpendicular magnetization. Because of the crystalline uniaxial anisotropy, the film has remnant magnetization and spin momentum perpendicular to the film plane. The pillar has a circular cross section. (B) A magnetic nano-pillar with in-plane magnetization. The pillar has an elliptical cross section with the long axis along parallel to the *z*-axis. Because of its shape anisotropy, the film has in-plane magnetization and spin momentum parallel to the *z*-axis.

precessions of the local spins and causes domain and/or vortex formation in the cell [52–54]. Despite the predicted limitations, the macrospin model is still useful, because of both its transparency and its validity for small excitations. The orbital moment, which is very small for 3D transition metals, is neglected in this treatment. γ is the gyromagnetic ratio, where $\gamma < 0$ for electrons ($\gamma = -2.21 \times 10^5 \mathrm{m/As}$ for free electrons). The effective field, $\vec{H}_{\mathrm{eff}}$, is a sum of the external field, demagnetization field and anisotropy field. It should be noted that the demagnetization field and the anisotropy field depend on $\vec{\mathbf{e}}_2$. $\vec{H}_{\mathrm{eff}}$ is derived from the magnetic energy, E_{mag}, and the total magnetic moment, M_2, of the free layer:

$$\vec{H}_{\mathrm{eff}} = \frac{1}{\mu_0 M_2} \frac{\partial E_{\mathrm{mag}}}{\partial \vec{\mathbf{e}}_2}, \tag{27}$$

where $\mu_0 = 4\pi \times 10^{-7} \mathrm{H/m}$ is the magnetic susceptibility of vacuum.

The first term determines the precessional motion of $\vec{S}_2$. In the second term, α is the Gilbert damping factor ($\alpha > 0$). $g(\theta)$ is a coefficient that expresses the efficiency of the spin-transfer process as a function of the relative angle, θ, between $\vec{S}_1$ and $\vec{S}_2$. Explicit expressions for $g(\theta)$ was introduced in the previous section for giant magnetoresistance (GMR) junctions (Eq. (20)) and magnetic tunnel junctions (MTJs) (Eq. (25)).

To understand the effects of the different torques, we first discuss the spin dynamics in a perpendicularly magnetized pillar with a cylindrical symmetry under an external magnetic field parallel to the axis of symmetry (Fig. 11A). The magnetic energy in this system comprises uniaxial magnetic anisotropy energy and Zeeman energy,

2.1.1. Cylindrical pillar with uniaxial anisotropy

$$E_{\mathrm{mag}} = -\frac{1}{2}\mu_0 M_2 H_{\mathrm{u}} \cos^2\theta + \mu_0 M_2 H_{\mathrm{ext}} \cos\theta + (\mathrm{const.}), \tag{28}$$

where H_{u} and H_{ext} are the effective uniaxial anisotropy field and external field, respectively. The magnetic uniaxial anisotropy energy is a sum of the crystalline anisotropy energy and the demagnetization energy:

$$\frac{1}{2}\mu_0 M_2 H_{\mathrm{u}} = K_{\mathrm{u}} v + \frac{1}{2}\mu_0 M_2 \frac{N_{\mathrm{demag}} M_2}{v}, \tag{29}$$

where K_{u} is a (crystalline) uniaxial anisotropy constant; v, the volume of the free layer; and N_{demag}, the demagnetizing factor. From Eq. (27), the effective field is $\vec{H}_{\mathrm{eff}} = -H_{\mathrm{u}} \cos\theta \vec{\mathbf{e}}_1 + H_{\mathrm{ext}} \vec{\mathbf{e}}_1$. Substituting this in Eq. (26), we get

$$\begin{cases} \dfrac{\mathrm{d}\vec{\mathbf{e}}_2}{\mathrm{d}t} \cong \gamma(-H_{\mathrm{u}} \cos\theta + H_{\mathrm{ext}})(\vec{\mathbf{e}}_2 \times \vec{\mathbf{e}}_1) - \alpha_{\mathrm{eff}}(\theta)\gamma H_{\mathrm{u}} \cos\theta \vec{\mathbf{e}}_2 \times (\vec{\mathbf{e}}_1 \times \vec{\mathbf{e}}_2), \\ \alpha_{\mathrm{eff}}(\theta) \equiv \alpha + \dfrac{1}{(-\gamma)H_{\mathrm{u}} \cos\theta} g(\theta) \dfrac{J^{\mathrm{Q}}}{-e} \dfrac{\hbar}{2S_2}. \end{cases} \tag{30}$$

Since α is small for 3D transition metals ($\alpha_{\mathrm{FeNi}} = 0.007$, e.g. [55]), small terms on the order of $O(\alpha^2)$ are neglected in the above equation. $\alpha_{\mathrm{eff}}(\theta)$ expresses the effective Gilbert damping coefficient of the free layer under spin-transfer torque. The directions of the torques are illustrated in Fig. 12. The effective field torque promotes a precession motion of $\vec{S}_2$ around $-\vec{H}_{\mathrm{eff}}$, while the damping torque tends to reduce the opening angle of the precession smaller. By the effective field and damping torques, $\vec{S}_2$ exhibits a spiral trajectory and finally aligns antiparallel to the effective field if a junction current, J^{Q}, is absent (Fig. 12A). It must be noted that the direction of $\vec{S}_2$ is opposite to that of its magnetic moment. Direction of the spin-transfer torque is also illustrated in Fig. 12B for the case where both $g(\theta)$ and J^{Q} are positive. If the current, J^{Q}, is sufficiently large, the spin-transfer torque overcomes the damping torque, resulting in negative effective damping. This negative damping results in an increase in the opening angle of the precession motion, that is, an amplification of the precession takes place. Depending on the angular dependence of the effective damping, the amplification of the precession motion leads to a limit cycle (spin-transfer oscillation, STO) or to a total magnetization reversal (spin-injection magnetization switching, SIMS) [56].

In Fig. 13, a trajectory for SIMS (a) is compared with trajectory for a magnetic field-induced magnetization switching (b) in a nano-pillar with in-plane magnetization. The figure also illustrates the magnetic potential shapes during switchings.

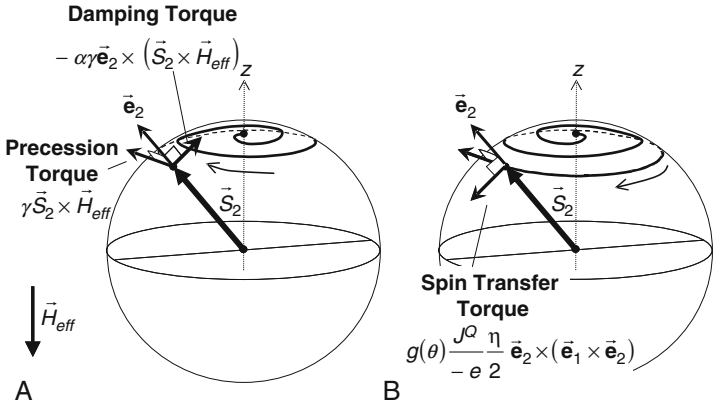

FIGURE 12 Illustration of the direction of each torque and trajectory of the free layer spin momentum for a nano-pillar with perpendicular remnant magnetization. (A) In the absence of an electric current, the precession of the free layer spin is damped. (B) Under an electric current, if the spin-transfer torque overcomes the damping torque, the precession of the free layer spin is amplified.

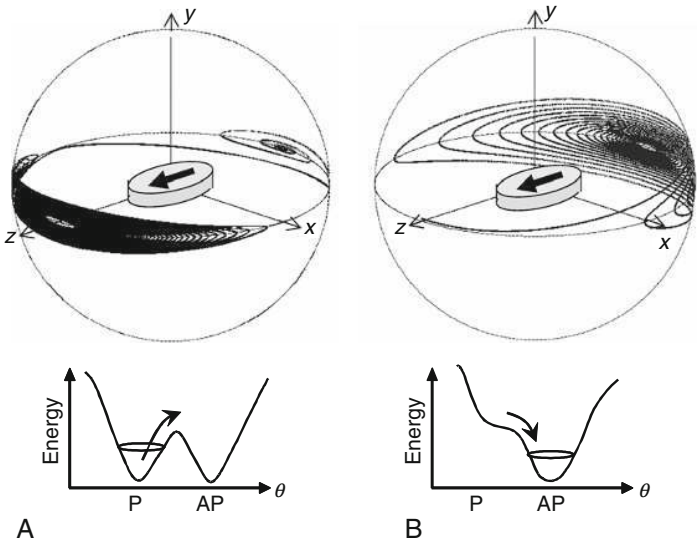

FIGURE 13 Comparison of the magnetization processes driven by (A) spin-transfer torque and (B) external magnetic field for in-plane magnetized nano-pillars.

In the absence of a current and an external magnetic field, the potential shows a double minimum for parallel (P) and antiparallel (AP) configurations of the local spin. For a particular case of SIMS, the spin-transfer torque does not affect the shape of the magnetic potential but amplifies the precession thereby providing energy to the local spin system. Once the orbital crosses the equator,

it converges rapidly to opposite direction since the spin-transfer torque extracts energy from the local spin system. In other words, the spin-transfer torque amplifies the precession in the front hemisphere, while enhancing the damping in the back hemisphere. In contrast to this process, the external magnetic field deforms the magnetic potential and the minimum on the P side disappears. Therefore, the local spin turns towards AP side. The local spin system, however, keeps excess energy in the back hemisphere. As a result, it cannot stop at once and shows precessional motion (ringing) in the back hemisphere.

The critical current at which the system becomes unstable to small deviations from equilibrium position is given by $\alpha_{\text{eff}}(\theta) = 0$. This "instability current" is obtained from Eq. (30) as follows.

2.1.2. Cylindrical pillar with uniaxial anisotropy

$$J_{\text{c0}}^{\text{Q}} = e\alpha \frac{-\gamma(H_{\text{u}}\cos\theta - H_{\text{ext}})}{g(\theta)} \frac{S_2}{\hbar/2} (\theta = 0 \text{ or } \pi). \tag{31}$$

If there is no stable limit cycle in between the parallel (P) and antiparallel (AP) states, the above equation gives the threshold current of SIMS, with $\theta = 0$ for P to AP switching and $\theta = \pi$ for AP to P switching.

2.2. Linearized LLG equation and instability current

To determine the instability current in a general system without cylindrical symmetry, we discuss the stability of $\vec{S}_2$ by linearizing the LLG equation to a small deviation from the static equilibrium point, $\vec{S}_2 = \vec{S}_2^{(0)} = S_2\vec{\mathbf{e}}_2^{(0)}$. In the equilibrium, with a static external field, $\vec{H}_{\text{eff}} = \vec{H}_{\text{eff}}^{(0)}$, and a constant current, $J^{\text{Q}} = J_0^{\text{Q}}$, the total static torque must be zero:

$$\gamma\vec{S}_2^{(0)} \times \vec{H}_{\text{eff}}^{(0)} + g(\theta_0)\frac{J_0^{\text{Q}}}{-e}\frac{\hbar}{2}\vec{\mathbf{e}}_2^{(0)} \times \left(\vec{\mathbf{e}}_1 \times \vec{\mathbf{e}}_2^{(0)}\right) = 0. \tag{32}$$

Around the equilibrium point, we apply a small deviation, $\delta\vec{\mathbf{e}}_2$, and observe its time evolution using the following linearized LLG equation [52]:

$$\frac{\mathrm{d}}{\mathrm{d}t}\delta\vec{\mathbf{e}}_2 \cong -\vec{\mathbf{e}}_2^{(0)} \times \left(\hat{\Omega} + \hat{\Omega}_{\text{ST}}\right)\delta\vec{\mathbf{e}}_2 + \alpha\vec{\mathbf{e}}_2^{(0)} \times \left(\vec{\mathbf{e}}_2^{(0)} \times \left(\hat{\Omega} + \hat{\Omega}_{\text{ST}}\right)\delta\vec{\mathbf{e}}_2\right), \tag{33}$$

where

$$\begin{cases} \hat{\Omega} \equiv \gamma\left(\vec{H}_{\text{eff}}^{(0)} \cdot \vec{\mathbf{e}}_2^{(0)}\right) - \gamma\dfrac{\partial\vec{H}_{\text{eff}}}{\partial\vec{\mathbf{e}}_2}, \\ \hat{\Omega}_{\text{ST}}\delta\vec{\mathbf{e}}_2 \equiv \dfrac{1}{e}\dfrac{\hbar}{2S_2}\left(g(\theta)J_0^{\text{Q}}(\vec{\mathbf{e}}_1 \times \delta\vec{\mathbf{e}}_2) + \left(\dfrac{\partial(gJ^{\text{Q}})}{\partial\vec{\mathbf{e}}_2}\cdot\delta\vec{\mathbf{e}}_2\right)\left(\vec{\mathbf{e}}_1 \times \vec{\mathbf{e}}_2^{(0)}\right)\right). \end{cases} \tag{34}$$

θ_0 is the angle between $\vec{\mathbf{e}}_1$ and $\vec{\mathbf{e}}_2^{(0)}$. Since $\delta\vec{\mathbf{e}}_2$ is orthogonal to $\vec{\mathbf{e}}_2^{(0)}$, we can express it as follows (see Fig. 14):

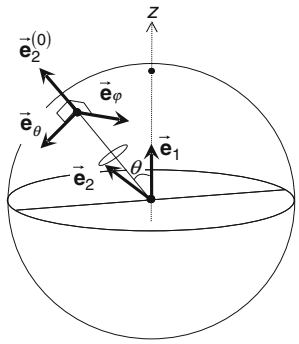

FIGURE 14 Coordinate system for linearization of LLG equation.

$$\delta\vec{\mathbf{e}}_2 \equiv a_\theta \vec{\mathbf{e}}_\theta + a_\phi \vec{\mathbf{e}}_\phi \equiv \begin{pmatrix} a_\theta \\ a_\phi \end{pmatrix}, \tag{35}$$

where

$$\begin{cases} \vec{\mathbf{e}}_\theta \equiv -\dfrac{\vec{\mathbf{e}}_2^{(0)} \times (\vec{\mathbf{e}}_1 \times \vec{\mathbf{e}}_2^{(0)})}{|\sin\theta_0|}, \\ \vec{\mathbf{e}}_\phi \equiv \dfrac{\vec{\mathbf{e}}_1 \times \vec{\mathbf{e}}_2^{(0)}}{|\sin\theta_0|}. \end{cases} \tag{36}$$

Using this coordinate system, Eq. (33) is rewritten as follows:

$$\frac{\mathrm{d}}{\mathrm{d}t}\begin{pmatrix} a_\theta \\ a_\phi \end{pmatrix} = \left(-\alpha + \mathrm{i}\hat{\sigma}_y\right)\left(\hat{\Omega} - \mathrm{i}\omega_{\mathrm{ST}}\hat{\sigma}_y\right)\begin{pmatrix} a_\theta \\ a_\phi \end{pmatrix}, \tag{37}$$

where $\omega_{\mathrm{ST}} = \frac{1}{e}\frac{\hbar}{2S_2}g(\theta)J_0^{\mathrm{Q}}\cos\theta_0.\sigma_y = \begin{pmatrix} 0 & -\mathrm{i} \\ \mathrm{i} & 0 \end{pmatrix}$ is the y-component of the Pauli's matrix. Here, the second term in $\hat{\Omega}_{\mathrm{ST}}$, which is zero for MTJs driven by constant voltage, is neglected. The time evolution of the solution to this equation is expressed by $\mathrm{e}^{\lambda t}$. In general, λ is a complex number. The imaginary part of the λ corresponds to the precession frequency of the free layer, whereas its real part represents the time evolution of the precession angle. If $\mathrm{Re}[\lambda] > 0$, the precession is amplified by the spin-transfer torque, and the equilibrium point is unstable to the perturbations. λ is an eigenvalue of the matrix $\left(-\alpha + \mathrm{i}\sigma_y\right)\left(\hat{\Omega} - \mathrm{i}\omega_{\mathrm{ST}}\sigma_y\right)$, and is obtained as follows:

$$\lambda \cong -\frac{1}{2}\mathrm{Tr}\left[\alpha\hat{\Omega} - \omega_{\mathrm{ST}}\right] \pm \mathrm{i}\sqrt{\det[\hat{\Omega}]} = -\frac{\Delta\omega}{2} \pm \mathrm{i}\omega_0, \tag{38}$$

where ω_0 and $\Delta\omega$ are the precession frequency and the full width at half maximum (FWHM) of the resonance, respectively. Finally, the instability current in the general system is estimated from $\mathrm{Re}[\lambda] = 0$ as follows.

2.2.1. General case

$$J_{c0}^{Q} = e\alpha \frac{\mathrm{Tr}[\hat{\Omega}]/2}{\cos\theta_0 g(\theta_0)} \frac{S_2}{\hbar/2}. \tag{39}$$

For a cylindrical pillar with uniaxial anisotropy, $\mathrm{Tr}[\hat{\Omega}]/2 = \sqrt{\det[\hat{\Omega}]} = \omega_0 = -\gamma(H_u - H_{ext}\cos\theta_0)$ both at $\theta_0 = 0$ and π. Substituting these values into the above equation, we regain Eq. (31). For an elliptical cell with in-plane magnetization, the magnetic energy is expressed as follows.

2.2.2. Elliptical pillar with in-plane magnetization

$$E_{mag} = \mu_0 M_2 H_{ext}\cos\theta + \frac{1}{2}\mu_0 M_2 \left(H_{\parallel}\cos^2\phi + H_{\perp}\sin^2\phi\right)\sin^2\theta + (\text{const.}), \tag{40}$$

where $H_{\parallel}$ and $H_{\perp}$ are the in-plane and out-of-plane effective anisotropy fields, respectively. The external field is assumed to be parallel to the z-axis in Fig. 11B. From Eqs (27) and (34), $\mathrm{Tr}[\Omega] = -\gamma\left(H_{\parallel} + H_{\perp} - 2H_{ext}\cos\theta_0\right)$ at $\theta_0 = 0$ and $\theta_0 = \pi$. Substituting these values, we get:

2.2.3. Elliptical pillar with in-plane magnetization

$$J_{c0}^{Q} = e\alpha \frac{-\gamma\left[\left(H_{\parallel} + H_{\perp}\right)/2 - H_{ext}\cos\theta_0\right]}{\cos\theta_0 g(\theta_0)} \frac{S_2}{\hbar/2} (\theta_0 = 0 \text{ or } \pi). \tag{41}$$

Here again, we should take $\theta_0 = 0$ for P to AP switching and $\theta_0 = \pi$ for AP to P switching. The instability current for the pillars with in-plane magnetization is large because of the large out-of-plane anisotropy field, which mainly consists of the demagnetization field. Explicit expressions for Ω are presented at the end of this chapter.

2.3. Spin-injection magnetization switching

SIMS was first predicted theoretically [16, 17] and was then experimentally demonstrated for a Co/Cu/Co nano-pillar with in-plane magnetization [18]. Subsequently, SIMS was also observed in the case of MTJs with AlO barriers [21] and MgO barriers [22, 23]. All those magnetic pillars had in-plane magnetization. And their cross sections were ellipses or rectangles. In 2006, SIMS was also observed in magnetic nano-pillars with perpendicular magnetization [24]. They employed Co/Ni multilayers to give a perpendicular crystalline anisotropy to the film.

In Fig. 15, a typical fabrication process for nano-pillars from a magnetic tunnel junction (for research purposes) is shown. First, (a) a magnetic multilayer including a magnetic tunnel junction is sputter deposited. The multilayer consists of a bottom electrode layer, an anti-ferromagnetic exchange bias layer (e.g. MnPt), a synthetic anti-ferromagnetic pinned layer (e.g. CoFeB/Ru/CoFe), an MgO barrier layer, a magnetic free layer (e.g. CoFeB) and a capping layer. The multilayer is then covered by a resist layer using a spin coater and transferred to an electron beam lithography machine. (b) After exposure and development, the sample with

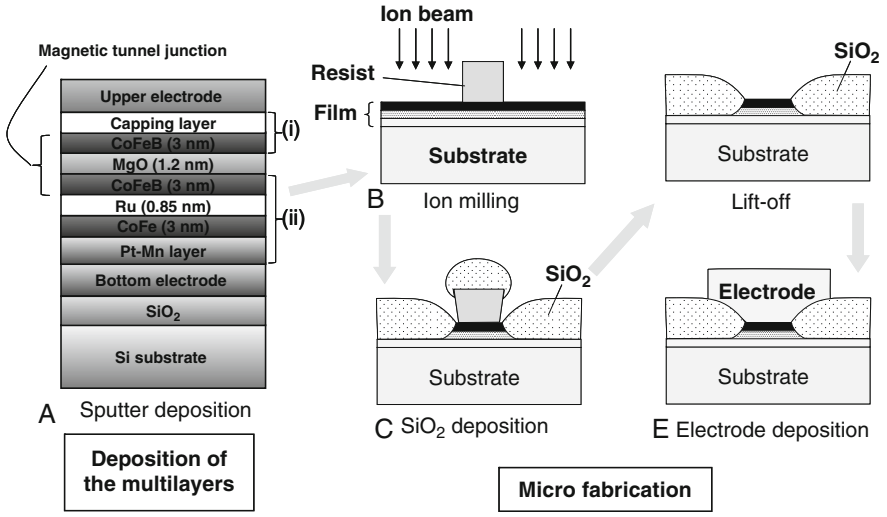

FIGURE 15 An example of the sample fabrication process for a spin-injection magnetization switching (SIMS) experiment. (A) A magnetic multilayer including the tunnelling barrier is first deposited under vacuum by a sputtering method. For memory applications, the film is deposited onto a CMOS and wiring complex after a chemical–mechanical planarization process. (B) After resist coating is applied using a spin coater, the resist is patterned by the electron beam lithography. Using the patterned resist, a part of the film is etched by ion beam bombardment. (C) Interlayer insulator (SiO_2) deposition using a self-alignment technique. (D) A lift-off process to open a contact hole. (E) Deposition of the upper electrode.

micro-patterned resist is transferred to an ion beam milling machine to remove parts of the multilayers and form magnetic pillars. (c) The outer side of the pillar is filled by a SiO_2 insulating layer. (d) The SiO_2 layer on the junction is lifted off with the resist by using a chemical solvent and ultrasonic scrubbing. Finally, (e) the top electrodes are deposited onto the junction under the vacuum.

A hysteresis loop obtained for a magnetic nano-pillar comprising a CoFeB/MgO/CoFeB tunnelling junction is shown in Fig. 16 [22]. The pillar has in-plane magnetization and elliptical cross section with the dimensions 100×200 nm^2. A current was applied as a series of 100 ms wide pulses. In between the pulses, the sample resistance was measured to check the magnetization configuration while the pulse height was swept between -1.5 and $+1.5$ mA. By this method, the effect of temperature increase during the application of the current on the resistance measurement could be eliminated. For the data shown in Fig. 16, the hysteresis measurement started at a zero pulse height for the P state (285 Ω). An increase in the pulse height caused a jump from the P state to the AP state (560 Ω) at $+0.6$ mA. Further increase in the pulse height followed by a reduction to zero current did not affect to the state. Subsequently, negative pulses were applied to the sample. At -0.35 mA, the sample switched its magnetization from the AP state to the P state. The average switching current density was about 6×10^6 A/cm^2. An intermediate resistance states between the P and the AP states were not observed

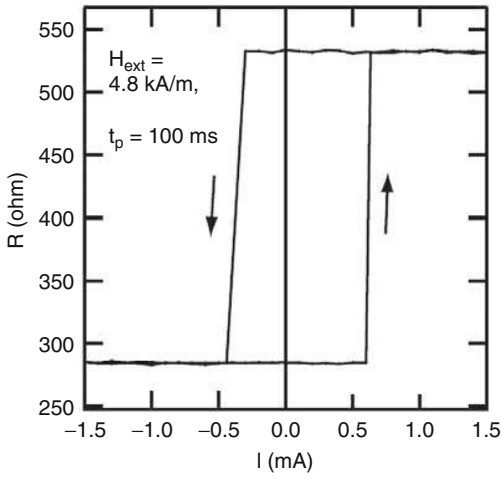

FIGURE 16 A typical spin-injection magnetization switching (SIMS) hysteresis loop obtained for a CoFeB/MgO/CoFeB MTJ (magnetic tunnel junction) (after Ref. [22]). The junction area, free layer thickness, resistance area product and MR ratio are 100 × 200 nm^2, 3 nm, 3 Ω μm^2 and about 100%, respectively. Measurements were performed at room temperature using electric current pulses of 100 ms duration. The resistance of the junction was measured after each pulse to avoid the effect of the heating on the sample resistance.

during either of the two switching events: the switching events were always abrupt and complete. The slope of the hysteresis loop at the switching point is only due to discrete measurement points that were not regularly placed because of the large change in the resistance. P to AP and AP to P switching events occurred at different current levels because of the dipole and the so-called orange peel coupling field from the pinned layer. In the experiment, an external field of −4.8 kA/m was applied to cancel these coupling fields. After the cancellation of the coupling fields, the hysteresis still exhibited a certain shift because of the following intrinsic mechanisms. For the MTJ nano-pillars, the asymmetrical voltage dependence of the torque, which was discussed in the previous section, causes a horizontal shift in the hysteresis curve. For the GMR nano-pillars, in contrast, the angle dependence of the spin-transfer efficiency results in a significant shift in the hysteresis loop.

Many efforts have been done to reduce threshold current of the switching. The first attempt is to reduce total spin angular momentum, S_2, in the free layer. SIMS requires effective injection of spin angular momentum that is equal to that in the free layer. Therefore, reduction in S_2 results a reduction in J_{c0}. Albert [57] showed that threshold current of the SIMS is proportional to the free layer thickness. Reduction in the free layer thickness reduces S_2 and J_{c0}. S_2 can also be reduced by reducing the magnetization of the ferromagnetic material. Especially in the nano-pillar with in-plane magnetization, since magnetization also affects to the size of the anisotropy field, J_{c0} is a quadratic function of the magnetization. Yagami *et al*. [58] reduced J_{c0} considerably by changing a material of the free layer from

CoFe (1.9×10^6 A/m) to CoFeB (0.75×10^6 A/m) and obtained 1.7×10^7 A/cm^2. Second attempt is to use double spin filter structure. This method was originally proposed by Berger [59]. By using this structure, Huai *et al*. [60] observed substantial reduction of the threshold current to 2.2×10^6 A/cm^2. Third attempt is to use perpendicular magnetic anisotropy, which can reduce the size of the anisotropy field. By this method, Nagase *el al*. [61] obtained a significant reduction of the threshold current under the required thermal stability factor for the MTJ nano-pillars with the CoFeB/[Pd/Co]x2/Pd free layer and FePt/CoFeB pined layer.

2.4. Switching time and thermal effects

Switching time of the SIMS has been investigated to test its applicability as an information writing technique and to clarify the dynamics of the SIMS itself. Observations of changes in the magnetic configuration in magnetic nano-pillars after an application of short pulses revealed the pulse width dependence of the threshold current and the probabilistic nature of the switching [62–64]. Very high-speed switching down to 200 ps [63] and precessional nature of the switchings [64, 65] have also been clarified.

An example of the pulse width dependence of the switching current for a CoFeB/MgO/CoFeB magnetic nano-pillar is shown in Fig. 17 [66]. The switching current increases for pulses with shorter pulses. This is because the switching requires a certain period of time for the amplification of the precession, and the

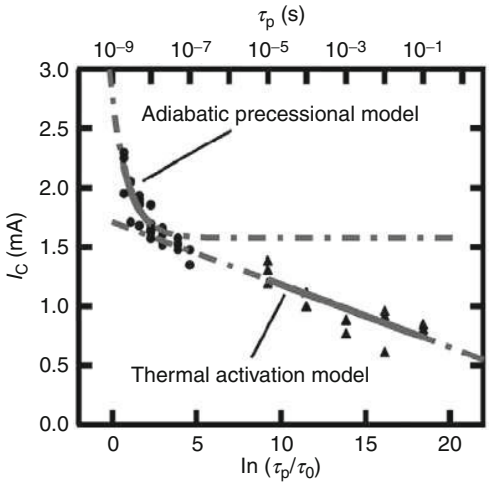

FIGURE 17 Pulse width dependence of the spin-injection magnetization switching (SIMS) in a CoFeB/MgO/CoFeB MTJ (magnetic tunnel junction) (after Ref. [66]). The junction area, free layer thickness, resistance area product and MR ratio are 110×330 nm^2, 2 nm, 17 Ω μm^2 and about 115%, respectively. Measurements were performed at room temperature using electric current pulses with duration from 2 ns to 100 ms.

required time is shorter for a larger current. This switching time, in principle, can be obtained by integrating the LLG equation with spin-transfer torque (Eq. (26)) [51]. For a cylindrical pillar with uniaxial magnetic anisotropy, the equation of motion for the opening angle of precession, θ, is derived from Eq. (30) as follows:

$$\frac{1}{\sin\theta}\frac{\mathrm{d}\theta}{\mathrm{d}t} \cong -\alpha(-\gamma)(H_{\mathrm{u}}\cos\theta - H_{\mathrm{ext}}) - g(\theta)\frac{J^{\mathrm{Q}}}{-e}\frac{\hbar}{2S_2} - \frac{\gamma H_{\mathrm{stochastic}}(t)}{\sin\theta}, \tag{42}$$

where $H_{\mathrm{stochastic}}$ is a stochastic field that expresses thermal agitation. In the treatment by now, we neglect $H_{\mathrm{stochastic}}$. To obtain the switching time, τ_{sw}, this equation can be integrated analytically by neglecting the θ-dependence of the efficiency:

2.4.1. Cylindrical pillar with a uniaxial anisotropy

$$\tau_{\mathrm{sw}} \cong \frac{J^{\mathrm{Q}}_{\mathrm{c0}}}{J^{\mathrm{Q}} - J^{\mathrm{Q}}_{\mathrm{c0}}}\frac{1}{\alpha(-\gamma)H_{\mathrm{u}}}\log\left(\frac{2}{\delta\theta_0}\right), \tag{43}$$

where J^{Q} and $J^{\mathrm{Q}}_{\mathrm{c0}}$ are the applied charge current and the critical current (Eq. (31)), respectively. $\delta\theta_0$ is the angle between the direction of magnetization and the easy axis at the beginning of amplification. For the thermal equilibrium, the average value of $\delta\theta_0$ is estimated as

$$\delta\theta_0 = \sqrt{\frac{k_{\mathrm{B}}T}{\mu_0 M_2 H_{\mathrm{u}}}} = \sqrt{\frac{1}{2\Delta}}, \tag{44}$$

where k_{B} is the Boltzmann constant and T is the absolute temperature. Δ is the thermal stabilization factor. For the nano-pillars with in-plane magnetization, an approximate expression for switching time is obtained replacing H_{u} and $J^{\mathrm{Q}}_{\mathrm{c0}}$ with $(H_{\perp} + H_{\parallel})/2$ and $J^{\mathrm{Q}}_{\mathrm{c0}}$ for the in-plane pillar (Eq. (41)), respectively, in Eq. (43).

2.4.2. Elliptical pillar with an in-plane magnetization

$$\tau_{\mathrm{sw}} \cong \frac{J^{\mathrm{Q}}_{\mathrm{c0}}}{J^{\mathrm{Q}} - J^{\mathrm{Q}}_{\mathrm{c0}}}\frac{2}{\alpha(-\gamma)(H_{\perp} + H_{\parallel})}\log\left(\frac{2}{\delta\theta_0}\right), \tag{45}$$

In Fig. 17, the theoretically expected switching time is shown by a dotted curve. The steep increase in the switching current for short switching times is well fitted by the theoretical curve, whereas the gradual decrease in the switching current for longer switching times is not explained by the theory. In addition, the switching current seems to be much smaller than that expected from Eq. (45) in the long switching time region.

Koch *et al*. [67] and Li and Zhang [68] explained the reduction in the switching current for long pulse durations by considering the thermal excitation of the macrospin fluctuation [67] induced by the stochastic field, $H_{\mathrm{stochastic}}(t)$. Because of the stochastic field, direction of the free layer spin angular momentum, $\vec{\mathbf{e}}_2$, is now also a stochastic variable. Therefore, we can only discuss its probability distribution, $p(\vec{\mathbf{e}}_2, t)$, taking into account the statistical nature of $H_{\mathrm{stochastic}}(t)$. By Langevin's method [69], $H_{\mathrm{stochastic}}(t)$ is related with the Gilbert damping constant:

$$\alpha \cong \frac{(-\gamma)\mu_0 M_2}{kT}\frac{1}{2}\int_{-\infty}^{\infty} \mathrm{d}\tau \langle H_{\mathrm{stochastic}}(t) H_{\mathrm{stochastic}}(t+\tau)\rangle, \tag{46}$$

where $\langle\rangle$ expresses an thermodynamical ensemble average. Using this fluctuation–dissipation theorem, the time evolution of $p(\vec{\mathbf{e}}_2, t)$ is expressed as follows:

$$\begin{cases} \dfrac{\partial p(\vec{\mathbf{e}}_2,t)}{\partial t} + \vec{\nabla}_{\vec{\mathbf{e}}_2}\cdot\vec{\boldsymbol{\jmath}}(\vec{\mathbf{e}}_2,t) = 0, \\ \vec{\boldsymbol{\jmath}}(\vec{\mathbf{e}}_2,t) = (1-\alpha\vec{\mathbf{e}}_2)\times\left(\vec{\mathbf{e}}_2\times\gamma\vec{\mathbf{H}}_{\mathrm{eff}} + g(\theta)\dfrac{J^{\mathrm{Q}}}{-e}\dfrac{\hbar/2}{S_2}\vec{\mathbf{e}}_2\times(\vec{\mathbf{e}}_1\times\vec{\mathbf{e}}_2)\right)p(\vec{\mathbf{e}}_2,t) \\ \qquad\qquad + \alpha\dfrac{kT}{S_2}\left(\vec{\mathbf{e}}_2\times\left(\vec{\mathbf{e}}_2\times\vec{\nabla}_{\vec{\mathbf{e}}_2}p(\vec{\mathbf{e}}_2,t)\right)\right), \end{cases} \tag{47}$$

where $\vec{\boldsymbol{\jmath}}(\vec{\mathbf{e}}_2, t)$ is the probability density current and $\vec{\nabla}_{\vec{\mathbf{e}}_2}(\vec{\nabla}_{\vec{\mathbf{e}}_2}\cdot)$ is gradient (divergence) along tangent of the sphere derivative with respect to the spin angular momentum direction. The first line in the expression of the probability density current is a drift current and is proportional to a sum of the three torques, that is, the precession torque, the damping torque and the spin-transfer torque. The second line expresses a thermal diffusion current of the probability density and is proportional to the gradient of the probability density. This is the Fokker–Planck equation [69] adapted for the LLG equation including spin-transfer torque [70–72].

For a cylindrical pillar with perpendicular uniaxial anisotropy, Eq. (47) can be reduced as follows:

$$\begin{cases} \dfrac{\partial}{\partial t}p(z,t) + \dfrac{\partial}{\partial z}\left\{-\dfrac{\alpha}{S_2}(1-z^2)\left[\dfrac{\mathrm{d}E_{\mathrm{eff}}(z)}{\mathrm{d}z} + k_{\mathrm{B}}T\dfrac{\partial}{\partial z}\right]p(z,t)\right\} = 0, \\ E_{\mathrm{eff}}(z) = \mu_0 M_2 H_{\mathrm{ext}} z - \dfrac{1}{2}\mu_0 M_2 H_{\mathrm{u}} z^2 + \dfrac{1}{\alpha}\dfrac{\hbar}{2}\dfrac{J^{\mathrm{Q}}}{e}\displaystyle\int g(z)\mathrm{d}z, \end{cases} \tag{47′}$$

where $E_{\mathrm{eff}}(z)$ is the effective magnetic energy and $z = \cos\theta$ is a z-component of $\vec{\mathbf{e}}_2$. Without charge current, both the equations have the Boltzmann distribution, $p(\vec{\mathbf{e}}_2) \propto \exp\left\{-\frac{E_{\mathrm{mag}}(\vec{\mathbf{e}}_2)}{k_{\mathrm{B}}T}\right\}$, as a solution for the thermal equilibrium. Under a current, the system is no more in equilibrium and the probability distribution deviates from the Boltzmann distribution in general. For cylindrical symmetry case, however, the system under a constant current may show Boltzmann-type distribution, $p(z) \propto \exp\left\{-\frac{E_{\mathrm{eff}}(z)}{k_{\mathrm{B}}T}\right\}$, taking the effective magnetic energy defined in Eq. (47′) as for a steady state. If the system is in out of equilibrium because of a charge current application, for example, the probability density currents start to flow to approach to the steady state.

The probabilistic distribution of the switching time, $p_{\mathrm{sw}}(t)$, and its integration, $P_{\mathrm{sw}}(t) = \int_0^t p_{\mathrm{sw}}(t_1)\mathrm{d}t_1$, in the thermal activation regime can be obtained by applying the Kramers' method [70] to Eq. (47) or (47′), for a case of the high thermal

barrier, that correspond to large thermal stability factor, small current and small external field, as follows:

$$\begin{cases} p_{\mathrm{sw}}(t) = \tau_{\mathrm{sw}}^{-1} \exp\left\{-\dfrac{t}{\tau_{\mathrm{sw}}}\right\}, \\ P_{\mathrm{sw}}(t) = 1 - \exp\left\{-\dfrac{t}{\tau_{\mathrm{sw}}}\right\}, \\ \tau_{\mathrm{sw}}^{-1}\left(J^{\mathrm{Q}}, H_{\mathrm{ext}}\right) \cong \tau_0^{-1} \exp\left\{-\Delta\left(1 - \dfrac{J^{\mathrm{Q}}}{J_{\mathrm{c0}}^{\mathrm{Q}}} - \dfrac{H_{\mathrm{ext}}}{H_{\mathrm{c}}}\right)^2\right\}, \end{cases} \tag{48}$$

where t is the elapsed time and τ_{sw} is the average switching time, $\tau_0^{-1} = \alpha(-\gamma)H_{\mathrm{u}}\sqrt{\frac{\Delta}{\pi}}$ attempt frequency. Δ is a thermal stability factor calculated for zero current and zero external field. Reader can find that the Néel–Brown's exponential law is valid under a current injection. An approximate expression for the pillars with in-plane magnetization is obtained by replacing H_{u} and $J_{\mathrm{c0}}^{\mathrm{Q}}$ with $\left(H_{\perp} + H_{\parallel}\right)/2$ and $J_{\mathrm{c0}}^{\mathrm{Q}}$ for the in-plane pillar (Eq. (41)), respectively, into Eq. (48). Equation (48) is accurate only when both the current and external field are sufficiently small. Li *et al*. solved Fokker–Plank equation for in-plane magnetization with small current and proposed a slightly different formula to also include a parameter, β [68]. In their paper, the term $\left(1 - \frac{J^{\mathrm{Q}}}{J_{\mathrm{c0}}^{\mathrm{Q}}} - \frac{H_{\mathrm{ext}}}{H_{\mathrm{c}}}\right)^2$ in Eq. (48) is replaced with $\left(1 - \frac{H_{\mathrm{ext}}}{H_{\mathrm{c}}}\right)^{\beta}\left(1 - \frac{J^{\mathrm{Q}}}{J_{\mathrm{c0}}^{\mathrm{Q}}}\right)$. The theoretical curve derived on the basis of the above-mentioned theory fits the experimental data well when reasonable parameter values are used (Fig. 17).

In the thermal activation regime, SIMS can occur at currents smaller than the critical current at 0 K because of thermal activations. And the switching time is distributed widely following an exponential law for a given applied current. In another way, if we apply current pulses with constant widths but different in heights (current), we will see the following switching current distribution:

$$p_{\mathrm{sw}}\left(J^{\mathrm{Q}}\right) = \frac{2\Delta}{J_{\mathrm{c0}}^{\mathrm{Q}}} \frac{\tau_{\mathrm{pulse}}}{\tau_{\mathrm{sw}}\left(J^{\mathrm{Q}}\right)} \exp\left\{-\frac{\tau_{\mathrm{pulse}}}{\tau_{\mathrm{sw}}\left(J^{\mathrm{Q}}\right)}\right\}, \tag{49}$$

where τ_{pulse} is the width of the applied pulse current and τ_{sw} is a function of the applied current (Eq. (48)). Experimentally, $J_{\mathrm{c0}}^{\mathrm{Q}}$ and Δ can be determined either from the pulse width dependence of the average switching current or from the switching current distribution measured using pulses with constant width.

In contrast to the thermal activation regime, switching occurs adiabatically for short and high pulses. Even for such adiabatic switching, the switching time is scattered because of the thermal distribution of the initial angle between the

directions of the free layer magnetization and pinned layer magnetization. One may avoid this problem by applying a small external field perpendicular to the easy axis of the system to force a definite initial angle [64].

For memory applications, a small switching current, small distribution of the switching current and switching time, and high thermal stability are required. From Eq. (31), the critical current is related to the thermal stability factor, Δ, as follows [51] for a pillar with perpendicular magnetization at room temperature:

2.4.3. Cylindrical pillar with a uniaxial anisotropy

$$|J_{c0}^{Q}| = \left| e\alpha \frac{\gamma H_u}{g(\theta_0)} \frac{S_2}{\hbar/2} \right| \cong \frac{\alpha\Delta}{|g(\theta_0)|} \frac{8\pi e k_B T}{h} \cong \frac{\alpha\Delta}{|g(\theta_0)|} \times 24(\mu A), \tag{50}$$

where h is the Planck's constant. To reduce the critical current while keeping Δ large, a material with a small damping constant and/or high spin-transfer efficiency should be developed. It should be noted, however, that a small damping constant will result a long switching time. Domain formation, that is, a smaller activation volume than the magnetic cell volume, reduces thermal stability factor and may make critical current to thermal stability factor ratio large. To avoid this problem, the cell volume should be smaller than the single domain limit. To obtain the expression for the elliptical pillar with in-plane magnetization, in which $H_\perp \gg H_\parallel$, we should multiply $H_\perp/(2H_\parallel)$ to the right-hand side of Eq. (50). Therefore, the critical current to the thermal stabilization factor ratios for the in-plane magnetized pillars are normally larger than that of the pillar with perpendicular magnetization.

2.5. High-speed measurements

The interesting aspects of the SIMS phenomenon are the small energy consumption and very high precession speed. To investigate the high-speed properties of the SIMS, time domain high-speed electrical observations have been performed [65, 66, 73–75]. The first observation was performed by Krivorotov *et al*. [73] for a $Ni_{80}Fe_{20}$ 4 nm/Cu 8 nm/$Ni_{80}Fe_{20}$ 4 nm GMR nano-pillar at 40 K. A free layer was micro-fabricated in an elliptical shape with dimensions of 130 × 60 nm^2. To obtain reproducible trajectories for adiabatic switching, they maintained the initial angle between the fixed layer spin and the free layer spin at about 30° by using an antiferromagnetic under layer to pin the spins in the fixed layer. Since the GMR nanopillars provide a very small output voltage, the authors averaged more than 10,000 of traces using a sampling oscilloscope with a 12-GHz bandwidth. After a background subtraction process, they obtained a transient signal that corresponds to the adiabatic switching of the free layer spin, as shown in Fig. 18 [73]. The precession of the free layer spin was clearly observed. The amplitude of the precession was amplified in the early stage of the switching and was then damped before the transition from the P state to the AP state at around 2 ns. The observed behaviour was slightly different from that predicted by the simple macrospin theory according to which continuous amplification of the precession should be observed until the transition (see Fig. 19A [54]). Krivorotov *et al*. explained this

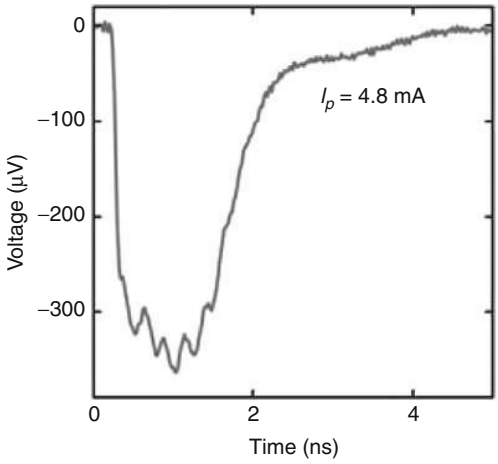

FIGURE 18 Time-resolved measurement of the spin-injection magnetization switching (SIMS) at 40 K. The observation was performed using a sampling oscilloscope. More than 10,000 traces were averaged for a NiFe/Cu/NiFe nano-pillar with elliptical cross-sectional dimensions of 130 × 60 nm^2. The initial angle between the free layer spin and the fixed layer spin was about 30° (after Ref. [73]).

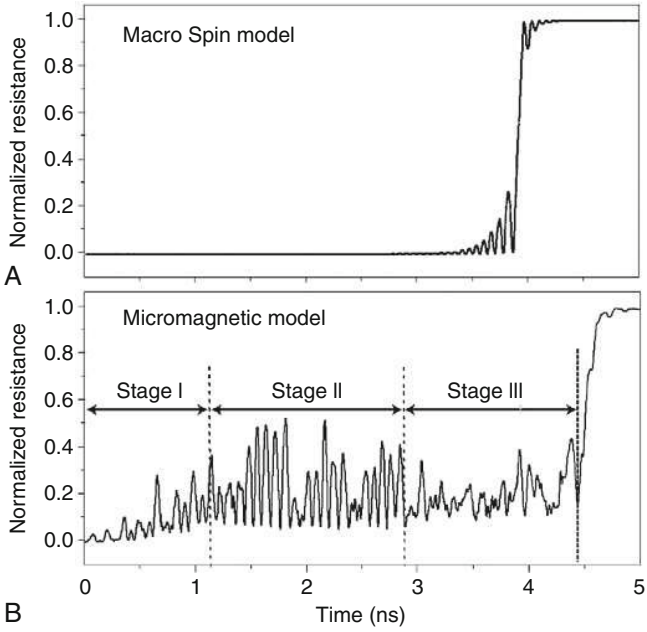

FIGURE 19 (A) Macromagnetic and (B) micromagnetic simulation of spin-injection magnetization switching (SIMS) at 0 K. A magnetic pillar with elliptical cross-sectional dimensions of 130 × 60 nm^2 was considered (after Ref. [54]).

deviation by a dephasings among the traces. If the precession contains phase noise, the averaging process carried out by the sampling oscilloscope decreases the observed precession amplitude. The authors stated that the spectrum line width of about 10 MHz obtained from the dephasing rate agreed with that obtained from precession noise spectrum measurement. This fact implies that in their sample, the phase noise dominated the spectrum line width of the precession. Krivorotov *et al*. [65] also clearly showed that, for large applied current, the switching time becomes multiples of the precession period (e.g. 200 ps) as that was already pointed by Devolder *et al*. [64] from their high-speed pulse measurements. This also means that only one extreme point out of two in the orbital (see Fig. 13A) was responsible for the switching. They explained this fact from their asymmetrical configuration of the magnetization.

The real-time single-shot observation of the SIMS has been performed by employing GMR pillars [65] and MTJs with a large electrical signal output [66, 74, 75]. In Fig. 20, (A) a circuit to observe real-time switching signal and (B) an example of a switching signal obtained by Tomita *el al*. [75] are shown. For the measurement, a CoFeB/MgO/CoFeB nano-pillar was placed at an end of an rf wave guide. A 10-ns pulse from a pulse generator was supplied to the MTJ through a power divider. The pulse was partially reflected by the MTJ depending on its resistance states and was provided to a high-speed storage oscilloscope with a 16-GHz bandwidth after being made to pass through the power divider again. In Fig. 20B, both the direct pulse signal and the reflected pulse signal are shown. Since the pulse reflectivity is dependent on the sample resistance, a magnetization switching event can be observed as a step in the reflected signal, as shown in the inset of Fig. 20B. To cancel parasitic signals generated by pulse reflections from the pulse generator and the cable connections, the obtained signal was numerically

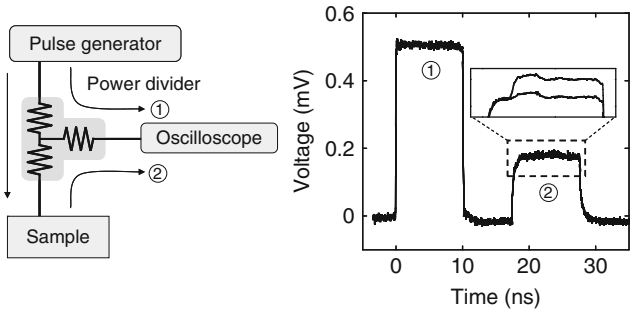

FIGURE 20 (A) Electric circuit and (B) an example of an obtained signal for a real-time single-shot observation of the SIMS process. Since an MTJ terminates an rf wave guide with certain mismatch in impedance, the supplied voltage pulse is partially reflected by the MTJ and observed by a high-speed single-shot oscilloscope with a 16-GHz bandwidth. The amplitude reflectivity of the MTJ is $(R_T - Z_0)/(R_T + Z_0)$, where R_T is the MTJ resistance and Z_0 is the characteristic impedance of the wave guide (50 Ω). Transition during a pulse causes a jump in the reflectivity and observed as a jump in the reflected voltage wave as shown in the inset in (B) (after Ref. [75]).

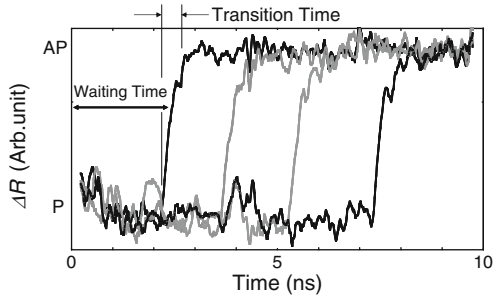

FIGURE 21 Real-time single-shot observation of the spin-injection magnetization switching (SIMS) process in a CoFeB/MgO/CoFeB nano-pillar. All the traces are obtained for the same value of current but show differences due to the probabilistic nature of switching. The employed current magnitude is 2.7 mA (2.4×10^7 A/cm^2), which is slightly smaller than J_{c0}^{Q}. The signals are normalized by the signal obtained without switching (after Ref. [75]).

divided by the signal obtained in the absence of switching; the resulting signals are shown in Fig. 21 for a current slightly below J_{c0}^{Q}. The signal shows a long waiting time followed by a short transition time (about 500 ps) as expected for a thermally assisted SIMS. The waiting time seems to vary considerably. Tomita *et al*. [75] also analysed 1000 single-shot data and obtained the distribution of the non-switched probability, $1 - P_{sw}(t)$, which should be a simple exponential function of the elapsed time according to Néel–Brown's law. The obtained distribution was not explained by simple Néel–Brown's law, but well fitted by considering a certain initial period in which the switching probability was negligibly small as shown in Fig. 22. Tomita *et al*. [75] named this initial period as a non-reactive time and explained that this was the time needed to complete a transition from the initial thermal equilibrium without current to a quasi-thermal equilibrium state

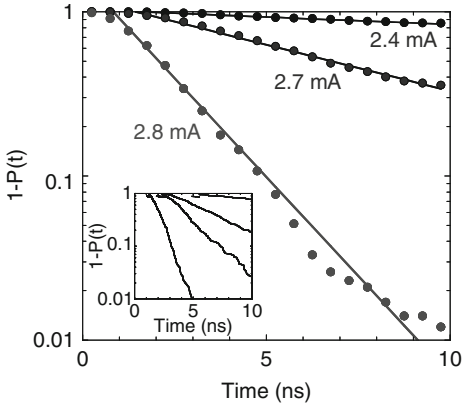

FIGURE 22 Non-switched probability, $1 - P_{sw}(t)$, as a function of elapsed time. The data deviates from Néel–Brown's law in the initial stage and are well fitted by the function $1 - P_{sw}(t) = e^{-(t-\tau_0)}$, where τ_0 is the non-reactive time (after Ref. [75]).

for a finite current. This behaviour was well reproduced by a micromagnetic simulation (inset in Fig. 22). Lee *et al*. also showed such a transition in his micromagnetic simulation [54] at 0 K. It is shown as "stage I" in Fig. 19B. This means that even at 0 K, the system makes a transition from the quiet initial state to an excited state, where the system shows the spatial distribution of the local spins in the cell, mainly because of the non-uniform demagnetization field.

The micromagnetic characteristics of the SIMS have been directly observed by Acremann *et al*. [76] and Strachan *et al*. [77] using transmission X-ray microscopy (STXM) with high spatial (30 nm) and temporal (70 ps) resolutions. Using bunches of X-ray from the synchrotron light source that was matched to the L_3 edge of Co atom, they could image the spin distribution of a GMR nano-pillar with in-plane magnetized $Co_{0.86}Fe_{0.14}$ free layer. They found that the magnetization reversal takes place via motion of a magnetic vortex. The position of the vortex core changes from inside the sample to outside, with decreasing sample size. Images of spin distribution during magnetization reversal of 180×110 nm^2 sample are shown in Fig. 23. In this case, the vortex core lies inside the sample during both AP to P and P to AP switching. Such a non-uniform reversal was attributed to non-uniformities initiated by the Oersted field generated by current. A dynamic process involving vortex formation and annihilation was predicted by Lee *et al*. [54]. In Fig. 19B "stage III" corresponds to a random domain state where a vortex can be generated and annihilated if the current is sufficiently large to produce a rotational magnetic field. The vortex formation should be avoidable in the case of a nano-pillar with a small J_{c0}^{Q} and small dimensions. Inhomogeneous precession

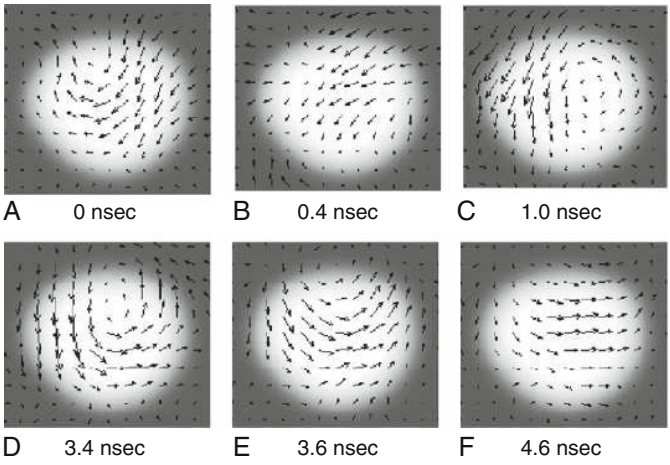

FIGURE 23 Spatial spin distribution in a GMR nano-pillar with $Co_{0.86}Fe_{0.14}$ free layer ($100 \times 150 \times 2$ nm^3) during magnetization switching observed by scanning transmission X-ray microscope (STXM) in a pump-probe manner. The top part shows the current pulses applied to the sample, and the various time points at which the images were taken by X-ray bunches. The sample switches from AP to P state during the positive pulse, and P to AP state during the negative pulse. The switching proceeds via a vortex motion during both the reversals. The current intensity was 1×10^8 A/cm^2 (after Ref. [77]).

caused by inhomogeneous demagnetization fields is serious in the nano-pillars with in-plane magnetization. However, it is expected to be less important in the nano-pillars with perpendicular magnetization.

3. HIGH-FREQUENCY PHENOMENA

3.1. Spin-transfer oscillation

From the beginning of spin-injection research using magnetic multilayers, it was thought that the electric current inside a ferromagnetic material may interact with the collective modes of spins and excite spin waves [13, 16, 17]. Actually, before the confirmation of the SIMS [18–20], spin dynamics in magnetic nano-pillars resulting from spin injection were observed as anomalies in derivative conductance spectra [14, 18, 78]. The first and complete observation of microwave emission from magnetic nano-pillars with in-plane magnetization was performed by Kiselev *et al*. in 2003 [15]. They employed Co/Cu/Co GMR nano-pillar with a $130 \times 70 \times 2$ nm^3 free layer and applied a direct current (more than J_{c0}^{Q}) and an external magnetic field (more than H_c) at the same time. The external field preferred parallel (P) configuration of the spins, while the direct current preferred antiparallel (AP) configuration. Under such a situation, the P state is unstable and the switching from P to AP state is prevented by the external field. As a result, the free layer spin is driven into a cyclic trajectory (limit cycle) with frequency typically in GHz range. Because of the GMR effect, the resistance of the pillar also oscillates with the continuous precession of the free layer spins. The oscillation of the resistance under a direct current bias results an rf (radio frequency) voltage that can be detected by a spectrum analyser or rf diode. In Fig. 24 the observed rf spectra taken under an external field of -2 kOe are shown. For current up to 2.4 mA, the spectrum intensity normalized by the square of the current is almost unchanged. The peak frequency matches with the FMR (ferromagnetic resonance) frequency of

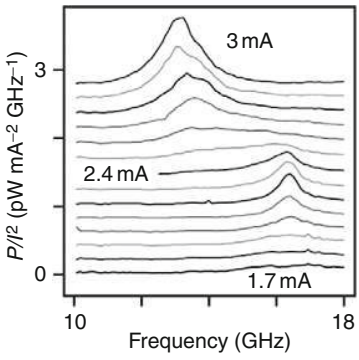

FIGURE 24 Rf power density spectra normalized by square of the injected current. The emission was observed for a GMR nano-pillar with in-plane magnetization under -2 kOe of the external field (after Ref. [15]).

the free layer and does not shift significantly under this magnitude of the current. A further increase in the applied current, however, results in a strong increase in the peak height and significant lowering of the peak frequency (red shift). Such behaviour was understood as the spontaneous excitation of the precessional motion of the macrospin. The maximum rf power obtained was about several tens of pW. This is the spin-transfer oscillation.

Condition to have a limit cycle can be understood using the LLG equation involving the spin-transfer torque (Eq. (26)) and magnetic energy of the macrospin (Eq. (27)). Change in the magnetic energy during one cycle of iso-energy trajectory of the free layer spin is estimated as follows [52]:

$$\Delta E_{\mathrm{mag}}(E) = \mu_0 M_2 \oint_{E_{\mathrm{mag}}=E} \left\{ -\alpha(-\gamma)|\vec{H}_{\mathrm{eff}} \times \vec{\mathbf{e}}_2|^2 + g(\theta)\frac{J^{\mathrm{Q}}}{-eS_2}\frac{\hbar}{2}(\vec{\mathbf{e}}_1 \times \vec{\mathbf{e}}_2)\cdot(\vec{H}_{\mathrm{eff}} \times \vec{\mathbf{e}}_2) \right\} \mathrm{d}t, \tag{51}$$

where integral should be done for one cycle of an iso-energy trajectory with energy E by taking time as a parameter. The first term in the integral is always negative and expresses energy consumption through the Gilbert damping. The second term in the integral can be positive depending on the sign of the current and expresses energy supply from the current source through the spin-transfer torque. The condition to have a stable limit cycle at energy E is as follows:

$$\begin{cases} \Delta E_{\mathrm{mag}}(E) = 0, \\ \dfrac{\mathrm{d}\Delta E_{\mathrm{mag}}(E)}{\mathrm{d}E} < 0. \end{cases} \tag{52}$$

As it can be seen in above equations, the condition is sensitive to the angle θ dependence of E_{mag} and $g(\theta)J^{\mathrm{Q}}$. Especially, in the nano-pillar with perpendicular magnetization, a higher-order crystalline anisotropy can also play a role. These conditions describing threshold currents of the SIMS (Eqs (31), (39), and (41)) and the STO (Eq. (52)) separate possible dynamic phases appearing in magnetic nano-pillars.

The phase diagram of a nano-pillar with in-plane magnetization under external field and a current injection obtained by Kiselev *et al.* [15] is illustrated in Fig. 25. For a zero external field and zero current the system is in the bistable state (P/AP in the figure). The application of a positive (negative) current causes the SIMS to undergo a transition from P (AP) to AP (P) state and stabilizes AP (P) state (dotted line (i)). The system shows hysteresis along the line (i). For zero current, if we apply a negative (positive, not shown) external field, the system switches to P (AP) state (dotted line (ii)). The system again shows a hysteresis along the line (ii). Now, we apply large negative external field, for example, −2 kOe. At zero applied current, the system is in P state with small precession of the spin caused by a thermal excitation. Under such large field, even if we supply a positive current larger than the threshold current of the SIMS, switching does not occur. Alternatively, the precession starts to be enhanced significantly and spontaneous oscillation starts. Further increase in current changes the orbital form from small angle oscillation to large angle oscillation and then out-of-plane oscillation (dotted line (iii)).

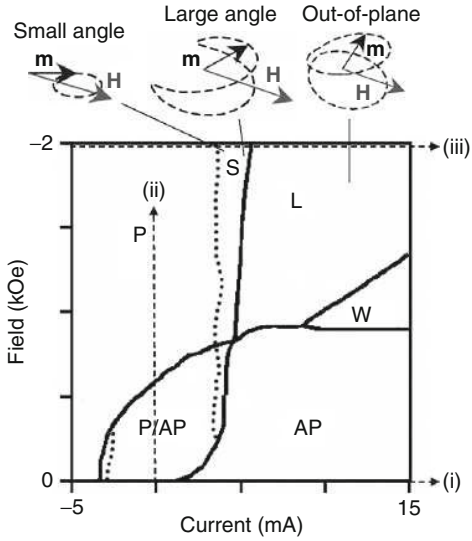

FIGURE 25 Phase diagram observed for the GMR nano-pillar with in-plane magnetization (after Ref. [15]).

Corresponding to the change in the orbital form, the oscillation frequency first shows a significant red shift (see Fig. 24 also) and then a blue shift. Along the line (iii), the system does not show hysteresis. When an intermediate negative field and a large positive current were applied, a new phase "W" shown in Fig. 25 appeared. The very wide spectra observed in region W were attributed to a chaotic motion of the spins [15]. The overall phase diagram was well explained by the micromagnetic simulation including the region "W" [54]. It was shown that vortex generations and annihilations were the main origin of the chaotic behaviour in "W" [54]. Deac [79] extended the phase diagram to positive field case using a nano-pillar with pinned layer and showed that a combination of a positive field and a negative current also produces STO. Phase diagram of a nano-pillar with perpendicular magnetization was obtained by Mangin *et al*. [24] and was quit different from the in-plane case. The obtained phase diagram was quit different from that in in-plane case. STO from a nano-pillar consisting of a free layer with in-plane magnetization, a perpendicularly magnetized polarizer and a reference layer with in-plane magnetization was observed by Houssameddine *et al*. [80]. The phase diagram of this system is in Ref. [80].

Apart from magnetic nano-pillars, the STO have also been observed in the case of magnetic nano-contacts. A schematic structure of the magnetic nano-contact is shown in Fig. 26A. In 2004, Rippard *et al*. [82] demonstrated that the line width of the rf emission spectrum emitted by a magnetic nano-contact can be as narrow as 1.89 MHz by applying a perpendicular magnetic field. The obtained line width corresponds to a very large Q-factor of about 18,000. Here Q is defined as Q = (peak frequency)/(line width). After this report the line width of the STO was investigated both experimentally [83–88] and theoretically [89–92]. Kim *et al*.

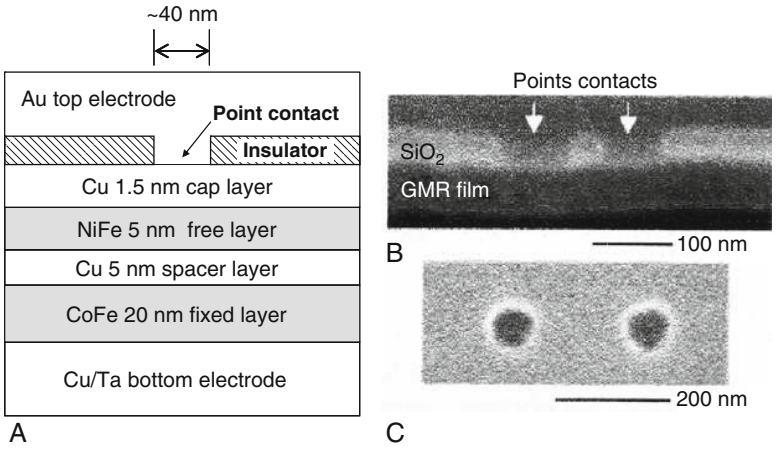

FIGURE 26 (A) Schematic cross section of the magnetic point contact. (B) Cross-sectional SEM image of the coupled point contacts that was used to observe mutual coupling of the STO. (C) SEM top image of the coupled point contacts (after Ref. [81]).

employed a general model of non-linear oscillator and showed that the special point in STO compared to the other oscillators is a strong amplitude dependence of the oscillation frequency. This non-linear coupling and thermal fluctuations produce a significant phase noise and dominate the line width. Therefore, the line width is proportional to the absolute temperature and depends on the size of the non-linear coupling between amplitude and frequency. By finding a configuration with small amplitude-frequency coupling, one may achieve in principle very small line width.

Output power of the STO in the nano-pillar with in-plane magnetization is expressed as follows [15, 88]:

$$\begin{cases} \text{Output power at fundamental frequency} \cong \eta\left(\mathrm{MR}'\right)^2\left(\dfrac{\Delta\theta}{2}\right)^2 \sin^2\theta_0 \dfrac{R(\theta_0)J^{Q^2}}{8}, \\ \text{Output power at the first harmonic} \cong \eta\left(\mathrm{MR}'\right)^2\left(\dfrac{\Delta\theta}{2\sqrt{2}}\right)^4 \cos^2\theta_0 \dfrac{R(\theta_0)J^{Q^2}}{8}, \\ \mathrm{MR}' = \dfrac{R(\pi)-R(0)}{R(\theta_0)}, \\ \eta = \dfrac{4R(\theta_0)Z_0}{\left(R(\theta_0)+Z_0\right)^2}. \end{cases} \tag{53}$$

Here, θ_0 and $\Delta\theta$ are the average and maximum angle between $\vec{\mathbf{e}}_2$ and $\vec{\mathbf{e}}_1$ during a limit cycle, respectively. $R(\theta)$ is the resistance of the nano-pillar when relative angle between $\vec{\mathbf{e}}_2$ and $\vec{\mathbf{e}}_1$ is equal to θ. η expresses the impedance mismatch

between wave guide and the nano-pillar. $\eta = 1$ corresponds to the case where impedance matching is established ($R(\theta) = Z_0$). In Eq. (53), $\Delta\theta$ is assumed to be small. If $\Delta\theta$ is large, $\Delta\theta/2$ in the first line and $(\Delta\theta)^2/8$ in the second line should be replaced by $J_1(\Delta\theta)$ and $J_2(\theta)$, respectively. Here, $J_n()$ is the Bessel's function of the first kind. As it is seen in Eq. (53), output at the fundamental frequency and odd number harmonics appears only when average angle between $\vec{\mathbf{e}}_2$ and $\vec{\mathbf{e}}_1$ is not zero. And power of the harmonics increases very rapidly with increase of the precession angle. Current and temperature dependence of $\Delta\theta$ are discussed in Refs [93, 94].

To obtain larger output power, it is important to use pillars with large MR ratio and with resistance that matches to the impedance of the wave guide (usually 50 Ω). Replacing a GMR pillar by the MTJ, we can expect significant increase in the output power [88, 95]. Deac *et al.* [88] showed large output power of 0.14 μW from a single CoFeB/MgO/CoFeB nano-pillar with 70×160 nm^2 cross section. The junction was specially designed to have the high MR ratio of about 100% (MR′ = 67% at zero bias) and the very low-resistance area product (RA = 4 Ω μm^2) [96]. In Fig. 27, the output power spectra obtained from CoFeB/MgO/CoFeB nano-pillar is shown. With increase of the current, the steep increase in power of the first harmonic peak at around 6 GHz can be seen. Figure 28 is a colour mapping of the output power as a

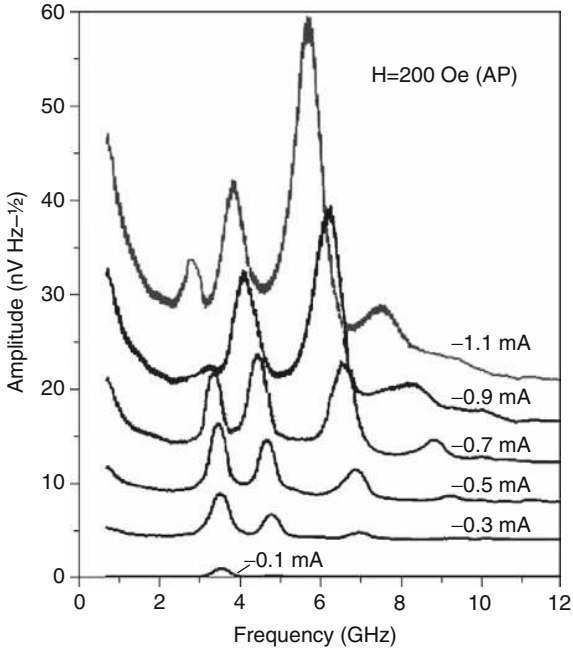

FIGURE 27 Rf power spectrum observed for a nano-pillar made from a low-resistance CoFeB/MgO/CoFeB MTJ with in-plane magnetization. Large rf power emission and steep increase of the first harmonics (around 6 GHz) intensity with increase of the injected current was observed (after Ref. [88]).

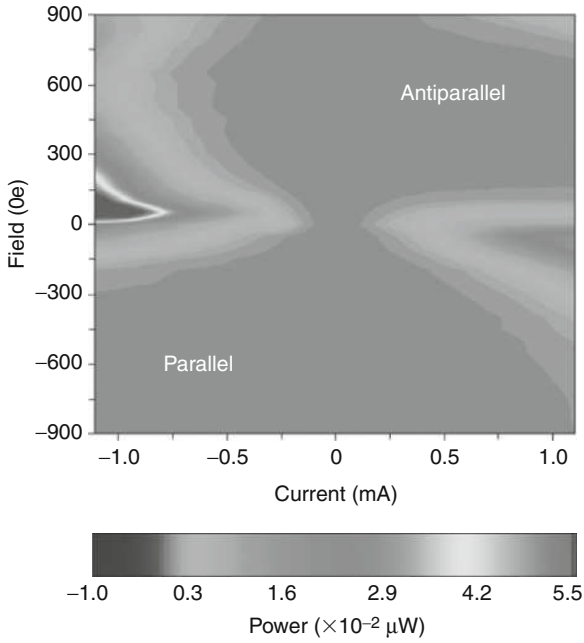

FIGURE 28 Rf power mapping observed for a nano-pillar made from CoFeB/MgO/CoFeB MTJ with in-plane magnetization. Large rf power emission was observed for positive applied field (AP) and negative current (after Ref. [88]).

function of the current and the external field. Large output was observed for two cases in which the external field and the current preferred opposite configurations of the spins. Among them, the combination of the positive field (AP) and the negative current gave larger power. This phenomenon was understood from the asymmetrical behaviour of the spin-transfer torque to the bias voltage. Because of the bias dependence of the spin current in MTJ, the spin-transfer torque is larger for the negative bias voltage in the CoFeB/MgO/CoFeB MTJs [43, 45] (see Fig. 10).

Another method to obtain higher output power was demonstrated by Kaka *et al*. [97] and Mancoff *et al*. [81]. They made two magnetic point contacts in very small distance (about 100 nm) (see Fig. 26B and C) and observed mutual coupling between them. By changing current passing through one of the oscillators, the oscillation frequencies of these two oscillators were approached. When the difference of two frequencies became enough small, the frequency were suddenly unified and two oscillators started to oscillate coherently at the same frequency. In addition, the total output power of these two oscillators was doubled by this coupling. By this way, if we can achieve coherent coupling of n oscillators, we may get n^2 time larger output power. Mutual coupling was mediated by spin waves in their oscillators; therefore, it was difficult to connect many oscillators. The electrical mutual coupling, however, is more realistic and also possible if the electric output of each oscillator is large enough [98].

3.2. Spin-torque diode effect

Recent advances have made it possible to fabricate MTJs with up to 500% magnetoresistance at room temperature [99–103]. Thus even a small change in the spin direction of MTJs can be easily detected by measuring the change in resistance. In this section, we introduce a new concept that MTJs may possess a rectification function [104], if we combine their large TMR with spin-torque effect. We will show below that this "spin-torque diode effect" provides a direct measure of the spin torque and contributes to an elucidation of the physics of the spin-torque phenomena [43, 45, 104, 105].

To observe the spin-torque diode effect, we may prepare a special nano-pillar in which both free layer and fixed layer magnetizations are lying in-plane but perpendicular to each other as shown in Fig. 29B. We then apply a negative current that induces a preferential parallel configuration of the spins. Thus resistance of the junction becomes smaller and we observe only a small negative voltage across the junction for a given current (Fig. 29A). Next we apply a positive current of the same amplitude. This current induces preferential antiparallel configuration and the resistance becomes higher. We observe a larger positive voltage appearing across the junction for a given current (Fig. 29C). This is the "spin-torque diode effect". The effect can be large if the frequency of the applied current matches with FMR frequency of the free layer. In other words, this effect provides sensitive FMR measurement technique of the nano-pillar moment excited by the spin torque. Therefore, the effect is useful to investigate the high-frequency dynamics of the nano-pillar and the physical mechanism of the spin torque itself.

To treat the bias voltage dependence of the response, here, we rewrite LLG equation including spin-transfer torque, field-like torque and stochastic filed as follows [106]:

$$\frac{d\vec{S}_2}{dt} = \gamma\vec{S}_2 \times \left(\vec{H}_{\text{eff}} + \vec{H}_{\text{stochastic}}\right) - \alpha\vec{\mathbf{e}}_2 \times \frac{d\vec{S}_2}{dt} + T_{\text{ST}}(V)V\vec{\mathbf{e}}_2 \times (\vec{\mathbf{e}}_1 \times \vec{\mathbf{e}}_2) + T_{\text{FT}}(V)V(\vec{\mathbf{e}}_2 \times \vec{\mathbf{e}}_1). \tag{26'}$$

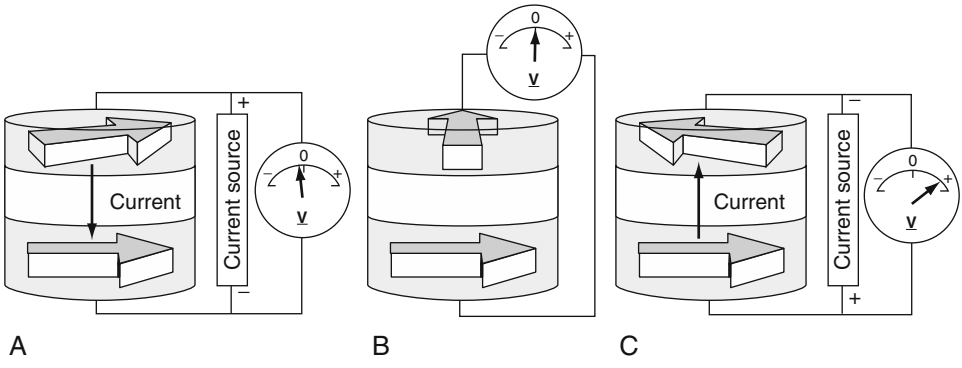

FIGURE 29 Schematic explanation of the spin-torque diode effect. (A) Negative current. (B) Null current. (C) Positive current [106].

Here, V is the applied voltage, $T_{\mathrm{ST}}(V) = \dfrac{\hbar}{2}\dfrac{1}{-e}\dfrac{1}{2}(G_{++} - G_{--} + G_{+-} - G_{-+})$ is the "torquance" that was defined in the second line in Eq. (24), while $T_{\mathrm{FT}}(V)$ is a unknown coefficient that expresses the size of the "field-like term". We linearize Eq. (26′) for a small deviation, $\delta\vec{\mathbf{e}}_2 \mathrm{e}^{-\mathrm{i}\omega t}$, around $\vec{\mathbf{e}}_2^{(0)}$ including a small oscillation component of the applied voltage, that is, $V(t) = V_0 + \delta V \mathrm{e}^{-\mathrm{i}\omega t}$, and small stochastic field, that is, $\vec{H}_{\mathrm{stochastic}}(\omega)\mathrm{e}^{-\mathrm{i}\omega t}$:

$$
\begin{aligned}
-\mathrm{i}\omega \begin{pmatrix} a_\theta \\ a_\phi \end{pmatrix} &= \left(-\alpha + \mathrm{i}\hat{\sigma}_y\right)\left(\hat{\Omega} + \omega_{\mathrm{FT}} - \mathrm{i}\omega_{\mathrm{ST}}\hat{\sigma}_y\right)\begin{pmatrix} a_\theta \\ a_\phi \end{pmatrix} \\
&\quad - \frac{\sin\theta_0}{S_2}\begin{pmatrix} T'_{\mathrm{ST}}(V_0) \\ T'_{\mathrm{FT}}(V_0) \end{pmatrix}\delta V - \mathrm{i}\hat{\sigma}_y\gamma\begin{pmatrix} H_{\mathrm{stochastic},\theta} \\ H_{\mathrm{stochastic},\phi} \end{pmatrix},
\end{aligned}
\tag{37′}
$$

where

$$
\begin{cases}
\hat{\Omega} \equiv (\omega_{i,j}) \equiv \gamma\left(\vec{H}_{\mathrm{eff}}^{(0)} \cdot \vec{\mathbf{e}}_2^{(0)}\right)\delta_{ij} - \dfrac{\gamma}{\mu_0 M_2}\dfrac{\partial^2 E_{\mathrm{mag}}}{\partial\vec{\mathbf{e}}_i \partial\vec{\mathbf{e}}_j} \quad (i,j = \theta \text{ or } \varphi), \\
\omega_{\mathrm{ST}} \equiv -\dfrac{T_{\mathrm{ST}}(V_0)V_0}{S_2}\cos\theta_0, \quad \omega_{\mathrm{FT}} \equiv \dfrac{T_{\mathrm{FT}}(V_0)V_0}{S_2}\cos\theta_0, \\
T'_{\mathrm{ST}}(V_0) \equiv \dfrac{\partial}{\partial V}(T_{\mathrm{ST}}(V_0)V_0), \quad T'_{\mathrm{FT}}(V_0) \equiv \dfrac{\partial}{\partial V}(T_{\mathrm{FT}}(V_0)V_0).
\end{cases}
\tag{54}
$$

In Eqs (37′) and (54), $\hat{\Omega}$ is unchanged from that defined in Eq. (34). Equation (38) is also modified as follows to include field-like torque:

$$
\lambda = -\mathrm{i}\omega \cong -\frac{1}{2}\mathrm{Tr}\left[\alpha\hat{\Omega} - \omega_{\mathrm{ST}}\right] \pm \mathrm{i}\sqrt{\det[\hat{\Omega} + \omega_{\mathrm{FT}}]} = -\frac{\Delta\omega}{2} \pm \mathrm{i}\omega_0. \tag{38′}
$$

Using above defined parameters, the solution of Eq. (37′) is a forced oscillatory motion around equilibrium, associated with the small driving rf voltage with frequency ω, and can be expressed as follows:

$$
\begin{aligned}
\begin{pmatrix} a_\theta \\ a_\phi \end{pmatrix} \cong \frac{1}{\omega^2 - \omega_0^2 + \mathrm{i}\omega\Delta\omega}&\begin{pmatrix} (\omega_{\phi\phi} + \omega_{\mathrm{FT}}) & -(\omega_{\theta\phi} - \omega_{\mathrm{ST}} - \mathrm{i}\omega) \\ -(\omega_{\phi\theta} + \omega_{\mathrm{ST}} + \mathrm{i}\omega) & (\omega_{\theta\theta} + \omega_{\mathrm{FT}}) \end{pmatrix} \\
&\left(\mathrm{i}\sigma_y \frac{\sin\theta_0}{S_2}\begin{pmatrix} T'_{\mathrm{ST}}(V_0) \\ T'_{\mathrm{FT}}(V_0) \end{pmatrix}\delta V - \gamma\begin{pmatrix} H_{\mathrm{stochastic},\theta} \\ H_{\mathrm{stochastic},\phi} \end{pmatrix}\right).
\end{aligned}
\tag{55}
$$

The explicit expression of $\hat{\Omega} = (\omega_{i,j})$ is given in Appendix.

From Eq. (55), we see that both the spin-transfer torque and the field-like torque can excite a uniform mode (FRM mode) in the free layer. The field-like torque excites FMR in the way the external magnetic field does, since it has the same symmetry as an external field, whereas FMR excited by a spin-transfer torque shows a 90° difference in the phase. This difference in the precessional phase is a consequence of the different directions of the respective torques (Fig. 12). In addition, the width of the resonance, $\Delta\omega$, is affected only by the

spin-transfer torque exerted by the direct voltage, V_0. This is the (anti)damping effect of the spin-transfer torque that was already discussed in the previous section. The filed-like torque exerted by a direct voltage V_0, changes the resonance frequency, ω_0, in a similar manner to an external field.

When the rf voltage across the MTJ is $\delta V \cos \omega t$, from Eqs (24) and (55) the precession motion and the oscillating part of the junction resistance, $\delta R \cos(\omega t + \varphi)$, which is linear in δV, are determined. Rf current through the junction can be approximated as $\delta V \cos \omega t / R(\theta_0)$. Thus from Ohm's law, the following additional voltages appear across the junction.

$$\delta R \cos(\omega t + \varphi) \times \frac{\delta V}{R(\theta_0)} \cos \omega t = \frac{\delta R}{R(\theta_0)} \frac{\delta V}{2} (\cos \varphi + \cos(2\omega t + \varphi)).$$

Here, we see that the frequencies of the additional voltages are zero (dc) and 2ω. It means that, under spin-torque FMR excitation, the MTJs may possess a rectification function and a mixing function. Because of these new functions, Tulapurkar *et al*. [104] referred to these MTJs as spin-torque diodes and these effects as "spin-torque diode effects". This is a non-linear effect that results from two linear responses, that is, the spin-torque FMR and Ohm's law.

For the case when the MTJ is placed at the end of an emission line, the explicit expression of the rectified dc voltage under a small bias voltage is as follows:

$$V_{\mathrm{dc}} \cong \frac{\eta}{4} \sin^2\theta_0 \frac{R(\theta_0)(G_{\mathrm{P}} - G_{\mathrm{AP}})}{S_2} \mathrm{Re}\left[\frac{(\omega_{\theta\phi} - \omega_{\mathrm{ST}} - \mathrm{i}\omega) T'_{\mathrm{ST}} + (\omega_{\phi\phi} + \omega_{\mathrm{FT}}) T'_{\mathrm{FT}}}{\omega^2 - \omega_0^2 + \mathrm{i}\omega\Delta\omega} \right] V_\omega^2, \tag{56}$$

where V_ω is the rf voltage amplitude applied to the emission line. η is the coefficient used to correct impedance matching between the emission line and a characteristic impedance of Z_0:

$$\eta = \left(\frac{2R(\theta_0)}{R(\theta_0) + Z_0} \right)^2. \tag{57}$$

If the emission line and the MTJ include some parasitic impedances (capacitance for most of the cases), we should employ an appropriate value of η to correct the effect [43, 45].

This is a type of homodyne detection and is, thus, phase-sensitive. The motion of the spin, illustrated in Fig. 29, corresponds to that excited by the spin-transfer torque at the resonance frequency. However, the motion of the spin excited by the field-like torque shows a 90° difference in phase. As a consequence, only the resonance excited by the spin-transfer torque can rectify the rf current at the resonance frequency. In Fig. 30, the dc voltage spectra predicted for the spin-transfer torque excitation and for the field-like torque are both shown. The spectrum excited by the spin-transfer torque exhibits a single, bell-shaped peak (dashed line) but that excited by the field-like torque is of a dispersion type (dotted line). This very clear difference provides us with an elegant method to distinguish spin-transfer torque from field-like torque [43, 45, 104, 105].

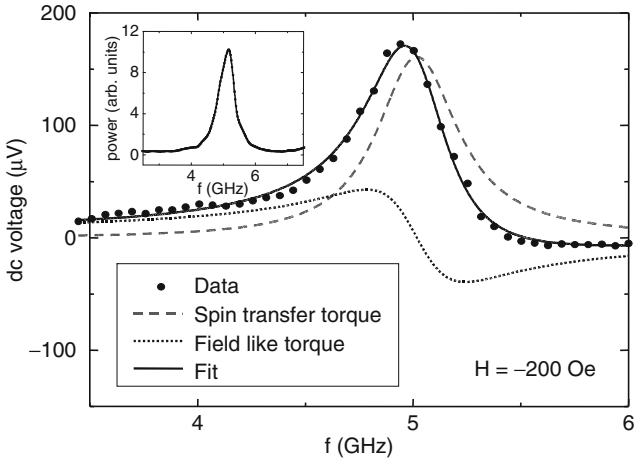

FIGURE 30 Spin-torque diode spectra for a CoFeB/MgO/CoFeB MTJ. Data (closed dots) are well fitted by a theoretical curve considering contributions from both the spin-transfer torque and the field-like torque. The inset shows the rf voltage dependence of the dc output voltage [106].

Figure 31 shows a schematic illustration of the measurement setup for spin-torque diode effect measurements with a cross-sectional view of the MTJ employed in Ref. [104]. The rf voltage was applied through a bias-T from a high-frequency oscillator and the dc voltages across the MTJ was detected using a dc nanovoltmeter.

In Fig. 30, an example of the diode spectrum (closed dots) is shown together with a fitting curve based on the theoretical expression (Eq. (56)) [106]. The data

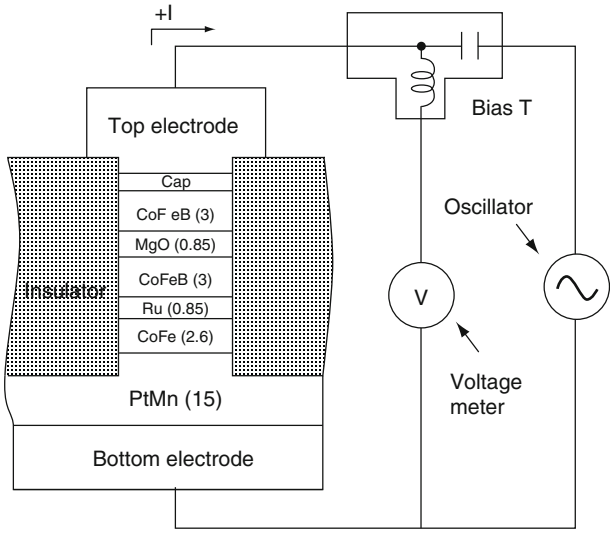

FIGURE 31 Measurement setup for the spin-torque diode effect measurements [106].

were taken at room temperature (RT) without applying dc bias voltage. The observed spectrum has an asymmetrical shape and was well fitted by Eq. (56). By this fitting, the spectrum was decomposed to a contribution from the spin-transfer term and from the field-like term. The intensity and even the sign of the field-like term contribution varied from sample to sample, while those of the spin-transfer term were reproducible. Therefore, it is thought that the contribution from the field-like term at zero bias voltage is very sensitive to small defects in the magnetic cell. By taking a sample that does not show a contribution from the field-like term, Kubota *et al*. [43] have investigated the dc bias voltage dependence of the spectra. The results that were already shown in Section 1 (Fig. 10) were well explained by band theory, in which bias-dependent spin sub-channel conductivities and bias-dependent interlayer magnetic coupling were taken into account [44]. According to Eq. (56), V_{dc} is proportional to V_{ω}^2. It has been confirmed and shown in the inset of Fig. 30.

An expression for the rectified dc voltage at the peak of the spectrum for $\theta_0 = \pi/2$ is shown below together with that for p–n junction semiconductor diodes:

$$(V_{\mathrm{dc}}(\theta_0))_{\mathrm{peak}} = \begin{cases} \dfrac{1}{4}\dfrac{G_{\mathrm{P}} - G_{\mathrm{AP}}}{G_{\mathrm{P}} + G_{\mathrm{AP}}}\dfrac{V_{\omega}^2}{V_{\mathrm{c}}} \ \text{(spin-torque diode)}, \\ \dfrac{1}{4}\dfrac{V_{\omega}^2}{k_{\mathrm{B}}T/e} \ \left(\text{p}-\text{n junction semiconductor diode}\right), \end{cases} \tag{58}$$

where $k_{\mathrm{B}}T/e$ is the thermal voltage (25 mV at RT). For both cases, the rectified voltage is a quadratic function of the applied rf voltage. Therefore, these detectors are referred to as quadratic detectors. Output voltage is scaled by the critical switching voltage, V_{c}, for the spin-torque diode and by $k_{\mathrm{B}}T/e$ for the p–n junction semiconductor diode. A typical critical switching voltage for MTJs was about 300 mV and was about 10 times larger than $k_{\mathrm{B}}T/e$ for the experiments in Refs [43, 104]. Therefore, the output of the spin-torque diode was smaller than that of the semiconductor diode. Increase in the MR ratio and reduction of the critical switching voltage will enhance the performance of the spin-torque diode.

4. FROM SPIN-TRANSFER TORQUE RAM TO MAGNETIC LOGIC

The last decades have seen a continuous race for miniaturization and cost reduction of electronic components, usually described by the "Moore's law". But this race is now approaching serious hurdles such as:

- The explosion of fabrication costs (for instance, a set of lithography masks in today's CMOS logic circuits costs about 1M$)
- The increasing variability of device properties (such as the threshold voltage of MOS transistor) on a single chip that threatens reliability
- Enhanced leakage currents in smaller transistors: starting from the 45 nm CMOS node, more energy is dissipated in standby mode than needed for actually operating (switching) the logic gates [107]

In parallel, the development of spin transfer in high magnetoresistance MgO tunnel junctions opens a new paradigm for fabricating very compact, non-volatile magnetoresistive cells, written by bipolar voltage pulses and compatible with the electrical characteristics of the smallest CMOS transistors. Moreover, the integration of such cells is done "above CMOS", that is, on planarized SiO_2 layers well above the Si wafer, which in practice can save wafer area, and make the integration easier.

The first application proposed was of course solid state magnetic storage in the magnetic random access memory (MRAM). Whether the spin-transfer version of MRAM, also called Spin-RAM or STT-MRAM, is able to compete with NAND Flash for mass storage of data is still debated, but this is by no way the only possible application of the Spin-RAM.

Microelectronic circuits are based on a few components: the microprocessor or CPU (central processing unit), a primary memory storing the information immediately needed by the processor, a series of input/output controllers, and peripheral units such as non-volatile memories to store data and codes. For optimum operation, the different elements must be adapted to each other, and so different levels of memory are used as "cache" between the processor and the main memory, ranging from small capacity but high speed near the processor (typically a SRAM), to higher capacity but lower speed for the main memory (typically a DRAM). Beyond, several kinds of non-volatile memories are used to store code (typically, Flash NOR) or data (Flash NAND or hard disk). In a microcontroller, all these elements are integrated on the same chip, including eventually the non-volatile memory. One speaks of "embedded memory". By associating the speed of SRAM with the much higher density of DRAM, Spin-RAM has the potential to become a "universal" embedded memory, able to take on nearly all memory functions in a microcontroller. Note that, because MRAM is non-volatile, such circuits could be powered off and on very rapidly, without loss of information, a key issue to get rid of standby power.

Finally, the spin-transfer magnetoresistive cell can also be used in programmable logic circuits, at different levels of dissemination in the circuit, to bring for instance instant on/off capability for reduced energy cost and zero standby power. At longer term the objective could even be to replace logic gates (up to a few tens of transistors) by purely magnetic devices, reducing the effective number of transistors per gate and thus contributing to extend Moore's law.

In the text below, we will review the MRAM development and discuss the main evolutions brought by the Spin-RAM cell for potential applications to MRAM and logic circuits.

4.1. The magnetic random access memory

Even before the discovery of the MTJ at room temperature, MRAM had been developed using AMR and then GMR effects [108]. The development of TMR promised much higher speed and density, and very rapidly the MRAM was considered as a major candidate for realizing a "universal memory technology", that is, a single technology that could finally replace all others in microcontrollers

and "Systems on Chip" (SoC) [109]. One of the first working MRAMs, using magnetic field for writing, was developed at IBM in 2000 [110].

A schematic diagram of MRAM is shown in Fig. 32A. As shown in the figure, MRAM consists of an array of magnetic tunnel junctions [112]. Each MTJ is situated between two perpendicular wires labelled as word line and bit line. The magnetization direction of the free layer of each MTJ can be changed by the magnetic fields created by passing currents through the word line and bit line. In principle, the vector sum of the magnetic fields is sufficient to change the magnetization of only the selected MTJ (shown by darker grey in Fig. 32A). The switching behaviour of the MTJ can be described by an astroid curve, which shows how the easy axis magnetic field required for switching changes with the hard axis magnetic field. For the astroid curve shown in Fig. 32B, the easy axis of the free

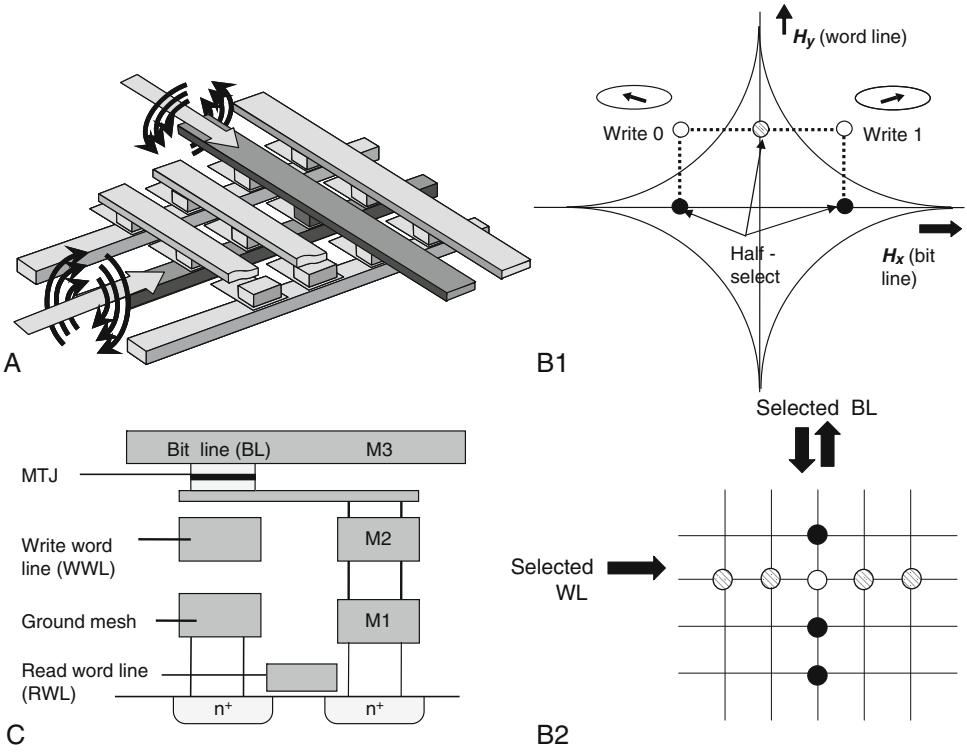

FIGURE 32 (A) Schematic diagram of MRAM. The MTJ marked by darker grey colour can be switched by combination of magnetic fields produced by passing currents through the top and bottom lines. (B) The astroid switching curve of the MTJ in response to magnetic fields along easy and hard axes. The curve is obtained assuming single domain particle with uniaxial anisotropy. The MTJ denoted by white colour is switched by the magnetic field, as it crosses the astroid boundary. The magnetic field on the half-select MTJs, marked by full and hatched colours, remain within the astroid and no switching takes place. (C) The reading scheme in one-transistor one-MTJ (1T1MTJ) architecture (after Ref. [111]).

layer is assumed to be along x-axis. The magnetic field generated by the current in the bit line is along x-axis, and by word line is along y-axis. Thus starting from zero field, if the applied field is increased beyond the astroid boundary and then returns to zero while remaining in the x-positive half-space, the free layer will be oriented along the positive x-axis. Whereas, if the applied field is increased beyond the astroid boundary, and returns to zero while remaining in the x-negative half-space, the free layer will be oriented along the negative x-axis. The MTJs marked by full and hatched dots are called half-selected, and their magnetization should not change during writing the selected MTJ, as the magnetic field remains within the astroid.

The reading of MTJs is done by measuring their resistance. A diode or a transistor must be inserted in series with the MTJs to select the bit to read and suppress non-direct conduction paths. A "one-transistor one-MTJ" (1T1MTJ) cell architecture is shown in Fig. 32C. The MTJ is connected to a FET whose drain contact is grounded. The gate of the FET is connected to the read word line (different from the write word line). The write bit line can be used as the top electrode of the MTJ to pass the measuring current.

It has been demonstrated that the write/read cycles of such MRAM circuits can be as low as 5 ns [113], while in laboratory experiments switching of single cells was achieved down to within about 100 ps [114–116]. However, this MRAM design suffers from several limitations. The most obvious ones are:

- Creating high enough magnetic field requires very high currents, for a large cost in wafer area and writing power.
- Moreover, with miniaturization one must increase the anisotropy field of the layers while reducing the field line cross section: a very sharp limit exists due to electromigration around 65 nm node. The magnetic field generated by the word and bit lines can be enhanced by "cladding", which concentrates the flux [117], but this gains only a small factor just able to slightly displace the limit.
- When including all distributions of switching fields, and the crosstalk between adjacent writing lines, the write reliability windows reduces to nothing.

The limitation mentioned in the last point can be overcome by using the toggle switching method [118]. In this method the free layer of the MTJ consists of two thin magnetic layers coupled anti-ferromagnetically through the exchange coupling, and the easy axis of the free layer is oriented at 45° of the word and bit lines. The free layer magnetization can be reversed by applying a sequence of currents to the word and bit lines as shown in Fig. 33A. The write phase diagram for toggle switching is shown in Fig. 33B. One can see from its square shape that the magnetic field on the half-select bits remains quite away from the switching boundary.

This clever improvement brought reliability to MRAM [120, 121], and made possible the first standalone MRAM product by Everspin [119], mainly targeted for replacing battery backed SRAM. But such MRAM can hardly be miniaturized beyond the 65 nm node of CMOS electronics, and is very limited in density (minimum cell size $\sim$20–40F^2, where F is the usual characteristic dimension of a CMOS node).

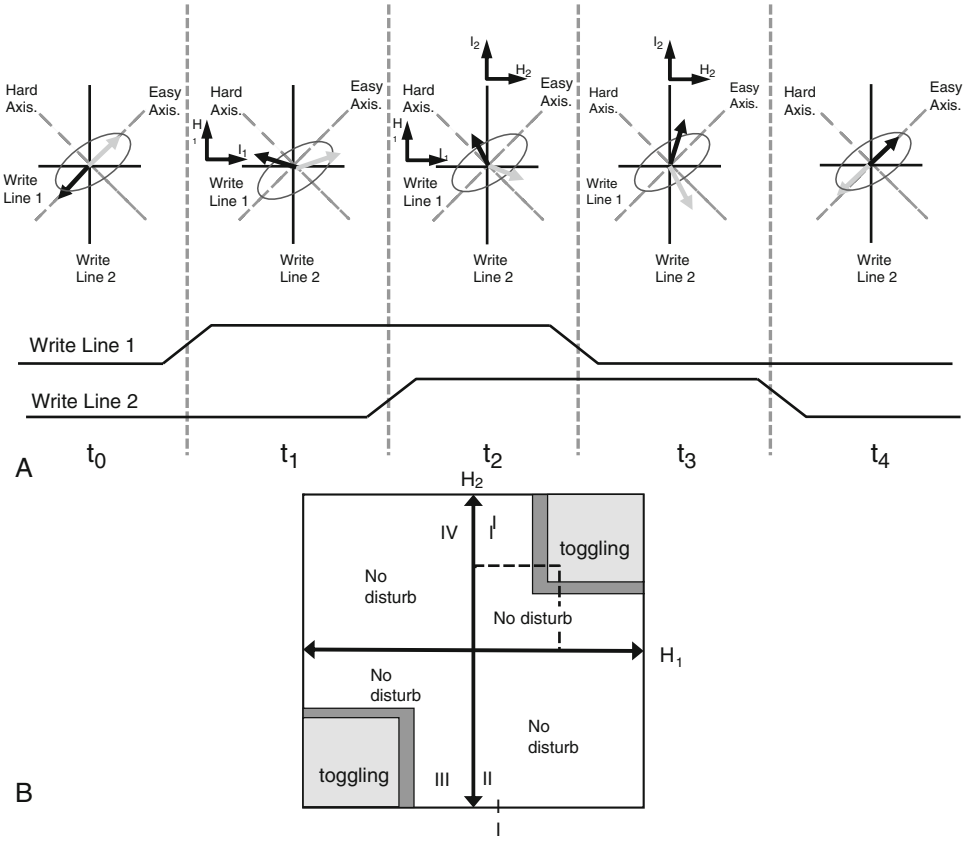

FIGURE 33 (A) The switching sequence of toggle-mode MRAM. The free layer is synthetic anti-ferromagnet, shown by dark and light arrows. The switching takes place upon application of two magnetic field pulses along *x*- and *y*-axes. The required timings of the pulses are shown. (B) The astroid curve for the synthetic anti-ferromagnetic free layer. The shape of the curve becomes square type (compare to Fig. 32B) (after Ref. [119]).

The TAS (thermally assisted switching)-MRAM was introduced to overcome all limits [122–126]: The schematic diagram of the MTJ used in the TAS-MRAM is shown in Fig. 34A. The energy barrier for reversal of the free layer is provided by exchange biasing it to an anti-ferromagnetic layer with moderate blocking temperature T_{B2}. A short current pulse through the tunnel junction raises the temperature of the stack above T_{B2}, thus suppressing the energy barrier, and the final direction of the free layer magnetization is then determined by cooling in a moderate magnetic field. The value of this writing field is determined at values around 50–100 Oe only by reliability issues (sensitivity to stray fields from external sources, distribution of anisotropy field in nominally isotropic cells, distribution of blocking temperature or fluctuations in the maximum temperature reached during a writing cycle), and so it is in principle only weakly dependent

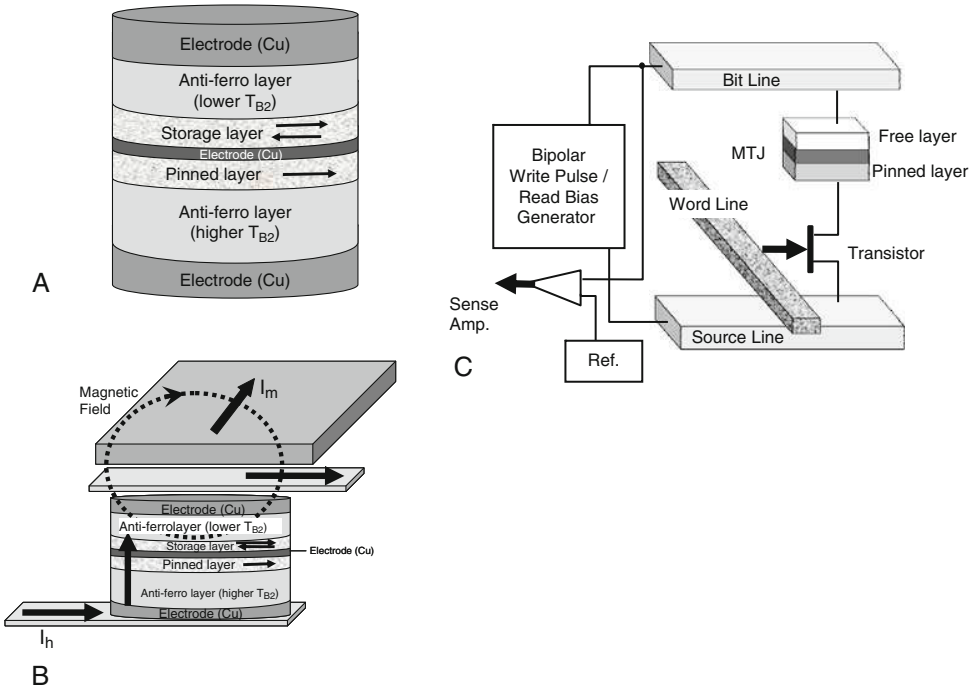

FIGURE 34 (A) Schematic diagram of the MTJ used in TAS-MRAM. The free layer/storage layer is pinned by an anti-ferromagnet with low blocking temperature T_{B2}. (Ref. [127]) (B) Switching process of TAS-MRAM. A current pulse is passed through the MTJ to increase its temperature above T_{B2}. The MTJ is then allowed to cool in a small magnetic field which determines the orientation of the free layer. (Ref. [127]) (C) Schematic diagram of STT-MRAM (after Ref. [130]).

on the cell size. Besides, the heating process requires a threshold current density, hence it is scalable. It is also possible to store 2 bits of information on one MTJ by using the large TMR ratio of MgO-based junctions and two writing lines, as shown in Ref. [126].

However, several limitations remain:

- The ultimate speed is high (approximately a few 10 ns) but limited by necessary compromise between fast heating at low current density (obtained by high thermal insulation of cell) and fast cooling (requires good thermal contact between MTJ core and the rest of the circuit).
- Because a non-negligible magnetic field has to be created by a current line of reducing cross section, the electromigration limit still exists, although it is less sharp and is postponed down to the 30–20 nm nodes.
- The variability and cyclability of exchange bias properties at very small cell dimensions remain a mostly unknown area [128].

4.2. The spin-transfer torque MRAM (or STT-RAM, or Spin-RAM)

The development of spin-transfer switching represented a huge step forward for MRAM perspective. A schematic diagram of 1T1MTJ STT-RAM is shown in Fig. 34C. The word line is connected to the gate of a transistor which is used to select the MTJ which is to be written or read. The writing is done through spin-transfer switching by applying either a positive or a negative voltage pulse between the source line and the bit line. The reading is done by applying a weaker voltage to the bit line to sense the resistance of the MTJ. Thus, the reading operation is the same as in field driven MRAM, but the writing is done differently. The cell architecture no longer requires to create magnetic fields, so the electromigration limit is no more critical, and much higher cell densities should be achievable (with minimum cell size down to $6–10F^2$).

STT-MRAM has been fully demonstrated in Refs [129, 130], following a previous version of field assisted STT-RAM [131]. Recently, a 32 Mbit embedded Spin-RAM demonstrator for SoCs was announced by NEC, with a read/write cycle time of 9 ns (Nikkei Electronics, 16 February 2009). Many studies on the down-scaling prospects of STT-RAM [111, 132–134] and on failure analysis [135] have been carried out. In short, minimizing the spin-transfer writing threshold of the MTJ is still required by a factor of about 4 or 5 to warrant high density, high speed and ultimate scalability, together with reducing the resistance area product to better match the CMOS transistor properties, but this maybe come in competition with fast reading as reading voltages near the threshold are likely to induce unwanted program events.

Further improvements in the STT-MRAM can be achieved by combining thermal assistance with spin torque in a TAS-MRAM stack such as the one of Fig. 34A and B. Indeed, a standard STT-RAM cell already undergoes non-negligible temperature rise during a write pulse [136].

4.3. Towards magnetic logic

Logic circuits are now everywhere, from computers to cell phones or cars. A MRAM memory bank can indeed be embedded in a programmable CMOS logic circuit, replacing other non-volatile memory technologies (such as Flash, Ferroelectric RAM, Phase Change RAM) to store the logic functions. We will rather consider here more innovative ways to add magnetism to logic. Performing binary logic operation requires a non-linear behaviour at a threshold, represented in CMOS electronic by the switch of the MOS transistor from conducting to insulator, controlled by a gate voltage. Switching of the magnetization of a magnetic nanostructure is indeed providing such a non-linear behaviour, and through a MTJ this switch can be transformed into an electric signal.

However, today's practical tunnel magnetoresistance amplitude is still far from reaching the several orders of magnitude observed in transistors, and the standard MTJ is only a two terminal device. Moreover, CMOS logic is based on a "static" operation mode: assuming no current leakage, energy consumption occurs only during the switch of the transistors at the rising or falling edge of

the clock, while the signal is kept available for the other logic gates at zero energy cost as long as the circuit is powered (similar to a SRAM ("Static" RAM) memory for instance). On the contrary, with a standard MTJ a non-zero current is necessary to get a voltage, hence power dissipation through Joule effect.

Last but not least, while in magnetic storage applications a non-negligible error rate can be compensated by limited redundancy and error correction codes, logic chips require undetectable error rates in their operation.

Here also, the recent breakthroughs in spin electronics, and specially spin-transfer torque effects, should help to bring "magnetic logic" to life. Different propositions can be distributed into three broad classes.

The most mature one is "mixed CMOS/MTJ logic". It consists in finely distributing MTJs above a CMOS logic circuit: the logic functions are still provided by CMOS transistors, but the MTJs provide enhanced functionalities such as instant on/off (allows to turn down power to bring energy cost to zero in standby mode, while recovering full functionalities), or enhanced radiation hardness. In principle, the number of transistors and the wafer area should be only moderately increased (MTJs are integrated above CMOS). In pioneer works, writing of the MRAM cells was made using magnetic field pulses [137, 138], but TAS-RAM or spin-transfer technology are rapidly becoming dominant. Typical example is the flip-flop, one of the most present logic function in today's logic circuits, proposed in magnetic non-volatile mode by Zhao *et al*. in 2006 [139, 140] and recently realized by NEC [141] (although with a simplified field induced writing, as shown in Fig. 35A). More demonstrations of magnetic logic circuits include TMR-based logic blocks [143], a full non-volatile adder [144], run-time reconfigurable circuits

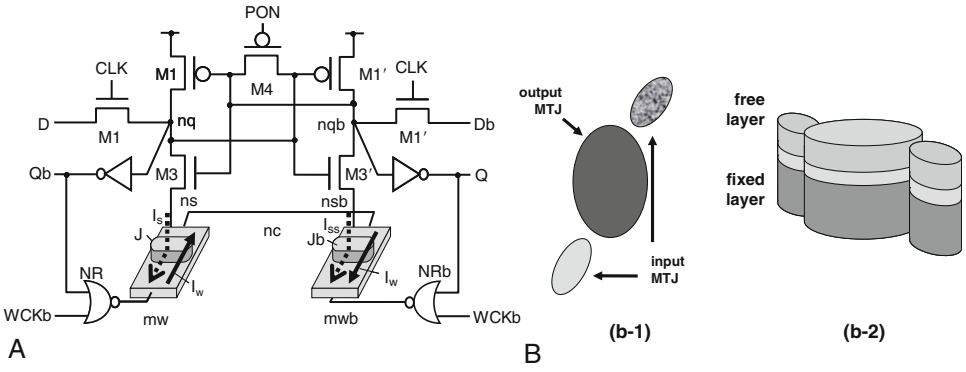

FIGURE 35 (A) Schematic diagram of non-volatile magnetic flip-flop. A bit of the data and its complement held in the latch circuit can be backed up into the pair of MTJs. Similarly, the data stored in the MTJ pair can also be recalled into the latch (after Ref. [141]). (B) Schematic diagram of spin-torque-based logic device. The energy barrier for magnetization reversal of the middle (output) MTJ can be controlled by the orientation of the free layers of the two side MTJs (inputs) (after Ref. [142]).

[145] for eventually a 3D stacked reconfigurable spin processor [146], and non-volatile FPGA [127, 147, 148]. Reviews can be found in Refs [149, 150].

A more advanced approach is based on using magnetic interactions between magnetic nanostructures, either isolated, or inserted into magnetoresistive elements, or more generally constituted by non-uniformities of magnetization such a domain wall or a vortex. A first example is the magnetic quantum cellular automata proposed by Cowburn *et al*. [151], in which lines and patterns of interacting quasi-circular dots would propagate information or perform basic logic operations (NOT, AND, etc.) through competing dipolar interactions, the energy being provided by an oscillating global magnetic field. This first proposition suffered from a too high error rate due to distribution in geometry of nominally identical dots. Imre *et al*. [152] later proposed a way of overcoming this issue by applying a saturating field, supposed to reliably take the dots magnetization to their stable minimum of energy when going back to zero field. However, none of these approaches can really lead to fast, CMOS integrable logic functions, first because magnetic fields are required. A real breakthrough in this class of magnetic logic circuits was recently proposed by Leem *et al*. [142]. As shown in Fig. 35B, interacting magnetic particles are free layers of closely spaced MTJ nano-pillars. Three adjacent pillars (two inputs and one central output) can for instance become a NAND or a NOR gate, depending on a choice of current threshold for the spin-transfer switching of the central pillar. At each clock steps, current pulses are sent to write the input dots and then update the configuration of the output dot. The authors also propose a way of chaining several such magnetic logic gates, applying the idea to the simulation of a ring oscillator [153]. Other recently proposed method are based on spin waves to transfer and process informations either through inductive coupling between unpatterned ferromagnetic layers [154, 155], or in patterned magnetic tracks with control of spin wave phase and spin wave interferences [156, 157].

Finally, a new class of logic gates might have been opened by the recently achieved reversible non-local switching of the magnetization by Yang *et al*. [158], towards the realization of logic operation through combination of spin accumulation of spin currents [159]. A logic gate based on spin accumulation effects in ferromagnetic semiconductors was also proposed in Ref. [160], together with means of chaining such gates.

ACKNOWLEDGEMENTS

Y. S. and A. T. would like to acknowledge all members in spintronics group in the AIST Japan, and Canon ANELVA for experiments and discussions. A. T. would also like to acknowledge magnetism group members of SLAC, USA for discussions. The authors express their gratitude to Ms. Rie Hasegawa for her continuous help to finish the chapter.

APPENDIX

I. Elliptical nano-pillar with an in-plane magnetization

For the in-plane magnetization case, we assume that $\hat{s}_1$ is fixed parallel to the easy axis of the free layer ($\hat{s}_1 = (0,0,1)$) and that an external field is applied in-plane ($\vec{H}_{\rm ext} = H_{\rm ext}(-\sin\theta_{\rm ext}, 0, -\cos\theta_{\rm ext})$). Here, the coordinate system in Fig. 11 is used. Then, $\hat{s}_2^{(0)}$ is aligned almost opposite to the external-field direction, $\hat{s}_2^{(0)} = (\sin\theta_0, 0, \cos\theta_0)$. We neglect the small deviation of $\hat{s}_2^{(0)}$ caused by dc voltage application. In this case, the magnetic energy and the effective field are

$$E_{\rm mag} = \mu_0 M\left(\vec{H}_{\rm ext}\cdot\hat{s}_2^{(0)} + \frac{1}{2}H_{\parallel,\rm H}\left(\hat{e}_x\cdot\hat{s}_2^{(0)}\right)^2 + \frac{1}{2}H_{\perp}^{'}\left(\hat{e}_y\cdot\hat{s}_2^{(0)}\right)^2 + \frac{1}{2}H_{\parallel,\rm E}\left(\hat{e}_z\cdot\hat{s}_2^{(0)}\right)^2\right),$$
$$\vec{H}_{\rm eff}^{(0)} = \frac{1}{\mu_0 M}\frac{\partial E_{\rm dipole\ and\ anisotropy}}{\partial\hat{s}_2^{(0)}} = \vec{H}_{\rm ext} + \begin{pmatrix} H_{\parallel,\rm H} & 0 & 0 \\ 0 & H_{\perp}^{'} & 0 \\ 0 & 0 & H_{\parallel,\rm E}\end{pmatrix}\hat{s}_2^{(0)}, \tag{A1}$$

where $H_{\parallel,\rm H}$, $H_{\perp}^{'}$ and $H_{\parallel,\rm E}$ are the demagnetization field for the *x*-, *y*-, and *z*-directions, respectively.

From Eq. (34), the $\hat{\Omega}$ matrix elements in $(\vec{\mathbf{e}}_\theta, \vec{\mathbf{e}}_\phi)$ coordinate system are calculated as follows:

$$\hat{\Omega} = \gamma H_{\rm ext}\cos(\theta_{\rm ext}-\theta_0) - \gamma\begin{pmatrix} H_\parallel\cos 2\theta_0 & 0 \\ 0 & H_\perp - H_\parallel\sin^2\theta_0\end{pmatrix}, \tag{A2}$$

where $H_\parallel \equiv H_{\parallel,\rm H} - H_{\parallel,\rm E}$ and $H_\perp \equiv H_{\perp}^{'} - H_{\parallel,\rm E}$ are in-plane and out-of-plane effective anisotropy fields, respectively.

II. Out-of-plane magnetization case

For the out-of-plane magnetization case, we assume that $\hat{s}_1$ is fixed perpendicular to the film plane ($\hat{s}_1 = (0,0,1)$) and that an external field is applied with angle ($\vec{H}_{\rm ext} = H_{\rm ext}(-\sin\theta_{\rm ext}, 0, -\cos\theta_{\rm ext})$). Here, the coordinate system in Fig. 1 is used. The free layer magnetization is assumed to have a perpendicular easy axis and to be tilted because of the in-plane external field, $\hat{s}_2^{(0)} = (\sin\theta_0, 0, \cos\theta_0)$. We again neglect the small deviation of $\hat{s}_2^{(0)}$ caused by the dc voltage application. In this case, the magnetic energy and the effective field are

$$E_{\rm mag} = \mu_0 M\left(\vec{H}_{\rm ext}\cdot\hat{s}_2^{(0)} + \frac{1}{2}H_{\parallel}^{''}\left[\left(\hat{e}_x\cdot\hat{s}_2^{(0)}\right)^2 + \left(\hat{e}_y\cdot\hat{s}_2^{(0)}\right)^2\right] + \frac{1}{2}\left(H_{\perp}^{''} - H_{\rm u}^{''}\right)\left(\hat{e}_z\cdot\hat{s}_2^{(0)}\right)^2\right),$$
$$\vec{H}_{\rm eff}^{(0)} = \frac{1}{\mu_0 M}\frac{\partial E_{\rm dipole\ and\ anisotropy}}{\partial\hat{s}_2^{(0)}} = \vec{H}_{\rm ext} + \begin{pmatrix} H_{\parallel}^{''} & 0 & 0 \\ 0 & H_{\parallel}^{''} & 0 \\ 0 & 0 & H_{\perp}^{''} - H_{\rm u}^{''}\end{pmatrix}\hat{s}_2^{(0)}, \tag{A3}$$

where $H_{\parallel}^{''}, H_{\perp}^{''}$ and $H_{u}^{'}$ are in-plane demagnetization field, out-plane demagnetization field and uniaxial anisotropy fields, respectively.

From Eq. (34), the $\hat{\Omega}$ matrix elements in $(\vec{\mathbf{e}}_{\theta}, \vec{\mathbf{e}}_{\phi})$ coordinate system are calculated as follows:

$$\hat{\Omega} = \gamma H_{\text{ext}} \cos(\theta_{\text{ext}} - \theta_0) - \gamma \begin{pmatrix} H_{\text{u}} \cos 2\theta_0 & 0 \\ 0 & H_{\text{u}} \cos^2 \theta_0 \end{pmatrix}, \qquad (A4)$$

where $H_{\text{u}} = H_{\text{u}}^{''} + H_{\parallel}^{''} - H_{\perp}^{''}$ is the effective uniaxial anisotropy field.

REFERENCES

[1] In this chapter, we call both paramagnetic and diamagnetic materials as a non-magnetic material.
[2] Ohno, Y., Young, D. K., Beschoten, B., Matsukura, F., Ohno, H., and Awschalom, D. D. (1999). *Nature* **402**, 790.
[3] Fiederling, R., Keim, M., Reuscher, G., Ossau, W., Schmidt, G., Waag, A., and Molenkamp, L. W. (1999). *Nature* **402**, 787.
[4] Jonker, B. T., Park, Y. D., Bennett, B. R., Cheong, H. D., Kioseoglou, G., and Petrou, A. (2000). *Phys. Rev. B* **62**, 8180; (2000). *Appl. Phys. Lett.* **77,** 3989.
[5] Jonker, B. T., Kioseoglou, G., Hanbicki, A. T., Li, C. H., and Thompson, P. E. (2007). *Nat. Phys.* **3**, 542–546.
[6] Johnson, M. (1993). *Phys. Rev. Lett.* **70**, 2142–2145.
[7] Jedema, F. J., Heersche, H. B., Filip, A. T., Baselmans, J. J. A., and van Wees, B. J. (2001). *Nature* **410**, 345; (2002). **416,** 713.
[8] Lou, X., Adelmann, C., Crooker, S. A., Garlid, E. S., Zhang, J., Reddy, K. S. M., Flexner, S. D., Palmstrom, C. J., and Crowell, P. A. (2007). *Nat. Phys.* **3**, 197–202.
[9] Tombros, N., van der Molen, S. J., and van Wees, B. J. (2006). *Phys. Rev. B* **73**, 233403.
[10] Tombros, N., Jozsa, C., Popinciuc, M., Jonkman, H. T., and van Wees, B. J. (2007). *Nature* **448**, 571–574.
[11] Ohishi, M., Shiraishi, M., Nouchi, R., Nozaki, T., Shinjo, T., and Suzuki, Y. (2007). *Jpn. J. Appl. Phys.* **46**, L605–L607.
[12] Appelbaum, I., Huang, B., and Monsma, D. J. (2007). *Nature* **447**, 295–298.
[13] Slonczewski, J. C. (1999). *J. Magn. Magn. Mater.* **195**, L261–L267.
[14] Tsoi, M., Jansen, A. G. M., Bass, J., Chiang, W. C., Seck, M., Tsoi, V., and Wyder, P. (1998). *Phys. Rev. Lett.* **80**, 4281; Erratum: (1998). **81,** 492.
[15] Kiselev, S. I., Sankey, J. C., Krivorotov, I. N., Emley, N. C., Schoelkopf, R. J., Buhrman, R. A., and Ralph, D. C. (2003). *Nature* **425**, 380–383.
[16] Slonczewski, J. C. (1996). *J. Magn. Magn. Mater.* **159**, L1–L7.
[17] Berger, L. (1996). *Phys. Rev. B* **54**, 9353–9358.
[18] Myers, E. B., Ralph, D. C., Katine, J. A., Louie, R. N., and Buhrman, R. A. (1999). *Science* **285**, 867–870.
[19] Sun, J. Z. (1999). *J. Magn. Magn. Mater.* **202**, 157–162.
[20] Katine, J. A., Albert, F. J., Buhrman, R. A., Myers, E. B., and Ralph, D. C. (2000). *Phys. Rev. Lett.* **84**, 3149–3152.
[21] Huai, Y., Albert, F., Nguyen, P., Pakala, M., and Valet, T. (2004). *Appl. Phys. Lett.* **84**, 3118–3120.
[22] Kubota, H., Fukushima, A., Ootani, Y., Yuasa, S., Ando, K., Maehara, H., Tsunekawa, K., Djayaprawira, D. D., Watanabe, N., and Suzuki, Y. (2005). *Jpn. J. Appl. Phys.* **44**, L1237–L1240.
[23] Diao, Z., Apalkov, D., Pakala, M., Ding, Y., Panchula, A., and Huai, Y. (2005). *Appl. Phys. Lett.* **87**, 232502.
[24] Mangin, S., Ravelosona, D., Katine, J. A., Carey, M. J., Terris, B. D., and Fullerton, E. E. (2006). *Nat. Mater.* **5**, 210.
[25] Valet, T., and Fert, A. (1993). *Phys. Rev. B* **48**, 7099.
[26] Zŭtić, I., Fabian, J., and Das Sarma, S. (2004). *Rev. Mod. Phys.* **76**, 1–88.
[27] Schmidt, G., Ferrand, D., Molenkamp, L. W., Filip, A. T., and van Wees, B. (2000). *Phys. Rev. B* **62**, R4790–R4793.

[28] Rashba, E. I. (2000). *Phys. Rev. B* **62**, R16267.
[29] Motsnyi, V. F., De Boeck, J., Das, J., Van Roy, W., Borghs, G., Goovaerts, E., and Safarov, V. I. (2002). *Appl. Phys. Lett.* **81**, 265.
[30] Johnson, M., and Silsbee, R. H. (1988). *Phys. Rev. B* **37**, 5326–5335.
[31] Shiraishi, M. Private communication.
[32] Kimura, T., Otani, Y., and Hamrle, J. (2006). *Phys. Rev. Lett.* 96, 037201.
[33] Mizukami, S., Ando, Y., and Miyazaki, T. (2002). *Phys. Rev. B* **66**, 104413.
[34] Saitoh, E., Ueda, M., Miyajima, H., and Tatara, G. (2006). *Appl. Phys. Lett.* **88**, 182509.
[35] Valenzuela, S. O., and Tinkham, M. (2006). *Nature* **442**, 176.
[36] Kimura, T., Otani, Y., Sato, T., Takahashi, S., and Maekawa, S. (2007). *Phys. Rev. Lett.* **98**, 156601; Erratum: (2007). *Phys. Rev. Lett.* **98,** 249901.
[37] Seki, T., Hasegawa, Y., Mitani, S., Takahashi, S., Imamura, H., Maekawa, S., Nitta, J., and Takanashi, K. (2008). *Nat. Mater.* **7**, 125–129.
[38] Kato, K., Myers, R. C., Gossard, A. C., and Awschalom, D. D. (2004). *Science* **306**, 1910–1913.
[39] Wunderlich, J., Kaestner, B., Sinova, J., and Jungwirth, T. (2005). *Phys. Rev. Lett.* **94**, 047204(1–4).
[40] Murakami, S., Nagaosa, N., and Zhang, S. C. (2003). *Science* **301**, 1348.
[41] Slonczewski, J. C. (1989). *Phys. Rev. B* **39**, 6995–7002.
[42] Slonczewski, J. C. (2005). *Phys. Rev. B* **71**, 024411(1–10).
[43] Kubota, H., Fukushima, A., Yakushiji, K., Nagahama, T., Yuasa, S., Ando, K., Maehara, H., Nagamine, Y., Tsunekawa, K., Djayaprawira, D. D., Watanabe, N., and Suzuki, Y. (2008). *Nat. Phys.* **4**, 37–41.
[44] Theodonis, I., Kioussis, N., Kalitsov, A., Chshiev, M., and Butler, W. H. (2006). *Phys. Rev. Lett.* **97**, 237205.
[45] Sankey, J. C., Cui, Y. T., Sun, J. Z., Slonczewski, J. C., Buhrman, R. A., and Ralph, D. C. (2008). *Nat. Phys.* **4**, 67–71.
[46] Edwards, D. M., Federici, F., Mathon, J., and Umerski, A. (2005). *Phys. Rev. B* **71**, 054407.
[47] Zhang, S., and Li, Z. (2004). *Phys. Rev. Lett.* **93**, 127204.
[48] Thiaville, A., Nakatani, Y., Miltat, J., and Suzuki, Y. (2005). *Europhys. Lett.* **69**, 990.
[49] Barnes, S. E., and Maekawa, S. (2005). *Phys. Rev. Lett.* **95**, 107204.
[50] Tatara, G., and Kohno, H. (2004). *Phys. Rev. Lett.* **92**, 086601.
[51] Sun, J. Z. (2000). *Phys. Rev. B* **62**, 570.
[52] Stiles, M. D., and Miltat, J. (2006). Spin dynamics in confined magnetic structures III. *In* "Topics in Applied Physics" (B. Hillebrands, and A. Thiaville, eds.), vol. 101, pp. 225–308. Springer, Berlin.
[53] Miltat, J., Albuquerque, G., Thiaville, A., and Vouille, C. (2001). *J. Appl. Phys.* **89**, 6982–6984.
[54] Lee, K. J., Deac, A., Redon, O., Nozières, J. P., and Dieny, B. (2004). *Nat. Mater.* **3**, 877.
[55] Mizukami, S., Ando, Y., and Miyazaki, T. (2001). *Jpn. J. Appl. Phys.* **40**, 580.
[56] Devolder, T., Crozat, P., Chappert, C., Miltat, J., Tulapurkar, A., Suzuki, Y., and Yagami, K. (2005). *Phys. Rev. B* **71**, 184401.
[57] Albert, F. J., Emley, N. C., Myers, E. B., Ralph, D. C., and Buhrman, R. A. (2002). *Phys. Rev. Lett.* **89**, 226802.
[58] Yagami, K., Tulapurkar, A., Fukushima, A., and Suzuki, Y. (2004). *Appl. Phys. Lett.* **85**, 5634–5636.
[59] Berger, L. (2003). *J. Appl. Phys.* **93**, 7693.
[60] Huai, Y., Pakala, M., Diao, Z., and Ding, Y. (2005). *Appl. Phys. Lett.* **87**, 222510.
[61] Nagase, T., Nishiyama, K., Nakayama, M., Shimomura, N., Amano, M., Kishi, T., and Yoda, H. (2008). Abstract: C1.00331, American Physics Society. March Meeting, New Orleans.
[62] Sun, J. Z., Myers, E. B., Albert, F. J., Sankey, J. C., Bonet, E., Buhrman, R. A., and Ralph, D. C. (2002). *Phys. Rev. Lett.* **89**, 196801.
[63] Tulapurkar, A. A., Devolder, T., Yagami, K., Crozat, P., Chappert, C., Fukushima, A., and Suzuki, Y. (2004). *Appl. Phys. Lett.* **85**, 53–58.
[64] Devolder, T., Chappert, C., Katine, J. A., Carey, M. J., and Ito, K. (2007). *Phys. Rev. B* **75**, 064402.
[65] Krivorotov, I. N., Emley, N. C., Buhrman, R. A., and Ralph, D. C. (2008). *Phys. Rev. B* **77**, 054440.
[66] Aoki, T., Ando, Y., Watanabe, D., Oogane, M., and Miyazaki, T. (2008). *J. Appl. Phys.* **103**, 103911.
[67] Koch, R. H., Katine, J. A., and Sun, J. Z. (2004). *Phys. Rev. Lett.* **92**, 088302.
[68] Li, Z., and Zhang, S. (2004). *Phys. Rev. B* **69**, 134416.

[69] Coffey, W., Kalmykov, Yu. P., and Waldron, J. T. (2004). "The Langevin Equation: With Applications to Stochastic Problems in Physics. Chemistry and Electrical Engineering", 2nd edn., vol. 14. World Scientific Series in Contemporary Chemical Physics. World Scientific, Singapore.
[70] Brown, W. F. Jr. (1963). *Phys. Rev.* **130**, 1677.
[71] Apalkov, D. M., and Visscher, P. B. (2005). *Phys. Rev. B* **72**, 180405(R)274–275.
[72] Apalkov, D. M., and Visscher, P. B. (2005). *J. Magn. Magn. Mater.* **286**, 370.
[73] Krivorotov, I. N., Emley, N. C., Sankey, J. C., Kiselev, S. I., Ralph, D. C., and Buhrman, R. A. (2005). *Science* **307**, 228.
[74] Devolder, T., Hayakawa, J., Ito, K., Takahashi, H., Ikeda, S., Crozat, P., Zerounian, N., Kim, J. V., Chappert, C., and Ohno, H. (2008). *Phys. Rev. Lett.* **100**, 057206.
[75] Tomita, H., Konishi, K., Nozaki, T., Kubota, H., Fukushima, A., Yakushiji, K., Yuasa, S., Nakatani, Y., Shinjo, T., Shiraishi, M., and Suzuki, Y. (2008). *Appl. Phys. Express* **1**, 061303.
[76] Acremann, Y., Strachan, J. P., Chembrolu, V., Andrews, S. D., Tyliszczak, T., Katine, J. A., Carey, M. J., Clemens, B. M., Siegmann, H. C., and Stohr, J. (2006). *Phys. Rev. Lett.* **96**, 217202.
[77] Strachan, J. P., Chembrolu, V., Acremann, Y., Yu, X. W., Tulapurkar, A. A., Tyliszczak, T., Katine, J. A., Carey, M. J., Scheinfein, M. R., Siegmann, H. C., and Stöhr, J. (2008). *Phys. Rev. Lett.* **100**, 247201.
[78] Tsoi, M., Jansen, A. G. M., Bass, J., Chiang, W. C., Tsoi, V., and Wyder, P. (2000). *Nature* **406**, 46.
[79] Deac, A., Liu, Y., Redon, O., Petit, S., Li, M., Wang, P., Nozières, J. P., and Dieny, B. (2007). *J. Phys.: Condens. Matter* **19**, 165208.
[80] Houssameddine, D., Ebels, U., Delaët, B., Rodmacq, B., Firastrau, I., Ponthenier, F., Brunet, M., Thirion, C., Michel, J. P., Prejbeanu-Buda, L., Cyrille, M. C., Redon, O., and Dieny, B. (2007). *Nat. Mater.* **6**, 447.
[81] Mancoff, F. B., Rizzo, N. D., Engel, B. N., and Tehrani, S. (2005). *Nature* **437**, 393.
[82] Rippard, W. H., Pufall, M. R., Kaka, S., Silva, T. J., and Russek, S. E. (2004). *Phys. Rev. B* **70**, 100406R.
[83] Sankey, J. C., Krivorotov, I. N., Kiselev, S. I., Braganca, P. M., Emley, N. C., Buhrman, R. A., and Ralph, D. C. (2005). *Phys. Rev. B* **72**, 224427.
[84] Mistral, Q., Kim, J. V., Devolder, T., Crozat, P., Chappert, C., Katine, J. A., Carey, M. J., and Ito, K. (2006). *Appl. Phys. Lett.* **88**, 192507.
[85] Petit, S., Baraduc, C., Thirion, C., Ebels, U., Liu, Y., Li, M., Wang, P., and Dieny, B. (2007). *Phys. Rev. Lett.* **98**, 077203.
[86] Thadani, K. V., Finocchio, G., Li, Z. P., Ozatay, O., Sankey, J. C., Krivorotov, I. N., Cui, Y. T., Buhrman, R. A., and Ralph, D. C. (2008). *Phys. Rev. B* **78**, 024409.
[87] Houssameddine, D., Florez, S. H., Katine, J. A., Michel, J. P., Ebels, U., Mauri, D., Ozatay, O., Delaet, B., Viala, B., Folks, L., Terris, B. D., and Cyrille, M. C. (2008). *Appl. Phys. Lett.* **93**, 022505.
[88] Deac, A. M., Fukushima, A., Kubota, H., Maehara, H., Suzuki, Y., Yuasa, S., Nagamine, Y., Tsunekawa, K., Djayaprawira, D. D., and Watanabe, N. (2008). *Nat. Phys.* **4**, 803.
[89] Kim, J. V. (2006). *Phys. Rev. B* **73**, 174412.
[90] Kim, J. V., Tiberkevich, V., and Slavin, A. N. (2008). *Phys. Rev. Lett.* **100**, 017207.
[91] Tiberkevich, V. S., Slavin, A. N., and Kim, J. V. (2008). *Phys. Rev. B* **78**, 092401.
[92] Kim, J. V., Mistral, Q., Chappert, C., Tiberkevich, V. S., and Slavin, A. N. (2008). *Phys. Rev. Lett.* **100**, 167201.
[93] Slavin, A. N., and Kabos, P. (2005). *IEEE Trans. Magn.* **41**, 1264.
[94] Tiberkevich, V., Slavin, A., and Kim, J. V. (2007). *Appl. Phys. Lett.* **91**, 192506.
[95] Houssameddine, D., Florez, S. H., Katine, J. A., Michel, J. P., Ebels, U., Mauri, D., Ozatay, O., Delaet, B., Viala, B., Folks, L., Terris, B. D., and Cyrille, M. C. (2008). *Appl. Phys. Lett.* **93**, 022505.
[96] Nagamine, Y., Maehara, H., Tsunekawa, K., Djayaprawira, D. D., Watanabe, N., Yuasa, S., and Ando, K. (2006). *Appl. Phys. Lett.* **89**, 162507.
[97] Kaka, S., Pufall, M. R., Rippard, W. H., Silva, T. J., Russek, S. E., and Katine, J. A. (2005). *Nature* **437**, 389.
[98] Georges, B., Grollier, J., Cros, V., and Fert, A. (2008). *Appl. Phys. Lett.* **92**, 232504.
[99] Yuasa, S., Fukushima, A., Nagahama, T., Ando, K., and Suzuki, Y. (2004). *Jpn. J. Appl. Phys.* **43**, L588.
[100] Yuasa, S., Nagahama, T., Fukushima, A., Suzuki, Y., and Ando, K. (2004). *Nat. Mater.* **3**, 868.

[101] Parkin, S. S. P., Kaiser, C., Panchula, A., Rice, P. M., Hughes, B., Samant, M., and Yang, S. H. (2004). *Nat. Mater.* **3**, 862.
[102] Hayakawa, J., Ikeda, S., Lee, Y. M., Matsukura, F., and Ohno, H. (2006). *Appl. Phys. Lett.* **89**, 232510.
[103] Yuasa, S., Fukushima, A., Kubota, H., Suzuki, Y., and Ando, K. (2006). *Appl. Phys. Lett.* **89**, 042505.
[104] Tulapurkar, A. A., Suzuki, Y., Fukushima, A., Kubota, H., Maehara, H., Tsunekawa, K., Djayaprawira, D. D., Watanabe, N., and Yuasa, S. (2005). *Nature* **438**, 339.
[105] Sankey, J. C., Braganca, P. M., Garcia, A. G. F., Krivorotov, I. N., Buhrman, R. A., and Ralph, D. C. (2006). *Phys. Rev. Lett.* **96**, 227601.
[106] Suzuki, Y., and Kubota, H. (2008). *J. Phys. Soc. Jpn.* **77**, 031002.
[107] Kim, N. S., Austin, T., Blaauw, D., Mudge, T., Flautner, K., Hu, J. S., Irwin, M. J., Kandemir, M., and Narayanan, V. (2003). *Computer* **36**, 68.
[108] Pohm, A. V., Beech, R. S., Bade, P. A., Chen, E. Y., and Daughton, J. M. (1994). *IEEE Trans. Magn.* **30**, 4650.
[109] Tehrani, S., Slaughter, J. M., Chen, E., Durlam, M., Shi, J., and DeHerren, M. (1999). *IEEE Trans. Magn.* **35**, 2814.
[110] Scheuerlein, R., Gallagher, W., Parkin, S., Lee, A., Ray, S., Robertazzi, R., and Reohr, W. (2000). "IEEE International Solid-State Circuits Conference, 2000. Digest of Technical Papers. ISSCC'2000", pp. 128–129.
[111] Maffitt, T. M., DeBrosse, J. K., Gabric, J. A., Gow, E. T., Lamorey, M. C., Parenteau, J. S., Willmott, D. R., Wood, M. A., and Gallagher, W. J. (2006). *IBM J. Res. Dev.* **50**, 25.
[112] Gallagher, W. J., and Parkin, S. S. P. (2006). *IBM J. Res. Dev.* **50**, 5.
[113] DeBrosse, J., Gogl, D., Bette, A., Hoenigschmid, H., Robertazzi, R., Arndt, C., Braun, D., Casarotto, D., Havreluk, R., Lammers, S., Obermaier, W., Reohr, W. R., Viehmann, H., Gallagher, W. J., and Muller, G. (2004). *IEEE J. Solid-State Circuits* **39**, 678.
[114] Kaka, S., and Russek, S. E. (2002). *Appl. Phys. Lett.* **80**, 2958.
[115] Gerrits, T., van den Berg, H. A. M., Hohlfeld, J., Bar, L., and Rasing, T. (2002). *Nature* **418**, 509.
[116] Schumacher, H. W., Chappert, C., Sousa, R. C., Freitas, P. P., and Miltat, J. (2003). *Phys. Rev. Lett.* **90**, 017204.
[117] Durlam, M., Naji, P., Omair, A., DeHerrera, M., Calder, J., Slaughter, J. M., Engel, B., Rizzo, N., Grynkewich, G., Butcher, B., Tracy, C., Smith, K., Kyler, K., Ren, J., Molla, J., Feil, B., Williams, R., and Tehrani, S. (2002). "Symposium on VLSI Circuits Digest of Technical Papers, 2002", pp. 158–161.
[118] Durlam, M., Addie, D., Akerman, J., Butcher, B., Brown, P., Chan, J., DeHerrera, M., Engel, B. N., Feil, B., Grynkewich, G., Janesky, J., Johnson, M., Kyler, K., Molla, J., Martin, J., Nagel, K., Ren, J., Rizzo, N. D., Rodriguez, T., Savtchenko, L., Salter, J., Slaughter, J. M., Smith, K., Sun, J. J., Lien, M., Papworth, K., Shah, P., Qin, W., Williams, R., Wise, L., and Tehrani, S. (2003). "IEEE International Electron Devices Meeting, 2003, IEDM'03 Technical Digest", pp. 34.6.1–34.6.3.
[119] Engel, B. N., Akerman, J., Butcher, B., Dave, R. W., DeHerrera, M., Durlam, M., Grynkewich, G., Janesky, J., Pietambaram, S. V., Rizzo, N. D., Slaughter, J. M., Smith, K., Sun, J. J., and Tehrani, S. (2005). *IEEE Trans. Magn.* **41**, 132.
[120] Yamamoto, T., Kano, H., Higo, Y., Ohba, K., Mizuguchi, T., Hosomi, M., Bessho, K., Hashimoto, M., Ohmori, H., Sone, T., Endo, K., Kubo, S., Narisawa, H., Otsuka, W., Okazaki, N., Motoyoshi, M., Nagao, H., and Sagara, T. (2005). *J. Appl. Phys.* **97**, 10P503.
[121] Aakerman, J., Brown, P., Gajewski, D., Griswold, M., Janesky, J., Martin, M., Mekonnen, H., Nahas, J. J., Pietambaram, S., Slaughter, J. M., and Tehrani, S. (2005). "43rd Annual International Reliability Physics Symposium", p. 163.
[122] Prejbeanu, I. L., Kula, W., Ounadjela, K., Sousa, R. C., Redon, O., Dieny, B., and Nozieres, J. P. (2004). *IEEE Trans. Magn.* **40**, 2625.
[123] Kerekes, M., Sousa, R. C., Prejbeanu, I. L., Redon, O., Ebels, U., Baraduc, C., Dieny, B., Nozieres, J. P., Freitas, P. P., and Xavier, P. (2005). "49th Annual Conference on Magnetism and Magnetic Materials", Jacksonville, FL, pp. 10P501–3.
[124] Sousa, R. C., Kerekes, M., Prejbeanu, I. L., Redon, O., Dieny, B., Nozieres, J. P., and Freitas, P. P. (2006). *J. Appl. Phys.* **99**, 08N904.
[125] Deak, J. G., Daughton, J. M., and Pohm, A. V. (2006). *IEEE Trans. Magn.* **42**, 2721.
[126] Leuschner, R., Klostermann, U. K., Park, H., Dahmani, F., Dittrich, R., Grigis, C., Hernan, K., Mege, S., Park, C., Clech, M. C., Lee, G. Y., Bournat, S., Altimime, L., and Mueller, G. (2006). "International Electron Devices Meeting, 2006, IEDM'06", pp. 1–4.

[127] Zhao, W., Belhaire, E., Dieny, B., Prenat, G., and Chappert, C. (2007). "International Conference on Field-Programmable Technology, 2007, ICFPT'2007", pp. 153–160.
[128] Baltz, V., Sort, J., Rodmacq, B., Dieny, B., and Landis, S. (2004). *Appl. Phys. Lett.* **84**, 4923.
[129] Kawahara, T., Takemura, R., Miura, K., Hayakawa, J., Ikeda, S., Lee, Y., Sasaki, R., Goto, Y., Ito, K., Meguro, T., Matsukura, F., Takahashi, H., Matsuoka, H., and Ohno, H. (2007). "International Solid-State Circuits Conference (ISSCC), Technical Digest", p. 480.
[130] Hosomi, M., Yamagishi, H., Yamamoto, T., Bessho, K., Higo, Y., Yamane, K., Yamada, H., Shoji, M., Hachino, H., Fukumoto, C., Nagao, H., and Kano, H. (2005). "IEEE International Electron Devices Meeting, 2005, IEDM Technical Digest", pp. 459–462.
[131] Jeong, W. C., Park, J. H., Oh, J. H., Jeong, G. T., Jeong, H. S., and Kinam, K. (2005). "Symposium on VLSI Circuits", p. 184.
[132] Zhu, J. G. (2008). *Proc. IEEE* **96**, 1786.
[133] Wang, X., Chen, Y., Li, H., Dimitrov, D., and Liu, H. (2008). *IEEE Trans. Magn.* **44**, 2479.
[134] Zhu, X., and Zhu, J. G. (2006). *IEEE Trans. Magn.* **42**, 2739.
[135] Li, J., Augustine, C., Salahuddin, S., and Roy, K. (2008). "45th ACM/IEEE Design Automation Conference, 2008, DAC'2008", pp. 278–283.
[136] Lee, D. H., and Lim, S. H. (2008). *Appl. Phys. Lett.* **92**, 233502.
[137] Black, W. C. Jr., and Das, B. (2000). *J. Appl. Phys.* **87**, 6674.
[138] Richter, R., Bar, L., Wecker, J., and Reiss, G. (2002). *Appl. Phys. Lett.* **80**, 1291.
[139] Zhao, W., Belhaire, E., and Chappert, C. (2007). "7th IEEE Conference on Nanotechnology, 2007, IEEE-NANO'2007", pp. 399–402.
[140] Zhao, W., Belhaire, E., Chappert, C., Javerliac, V., and Mazoyer, P. (2008). "9th International Conference on Solid-State and Integrated-Circuit Technology, 2008, ICSICT'2008", pp. 2136–2139.
[141] Sakimura, N. S., Sugibayashi, T., Nebashi, R., and Kasai, N. (2008). "IEEE Custom Integrated Circuits Conference, 2008, CICC'2008", pp. 355–358.
[142] Leem, L., and Harris, J. S. (2009). *J. Appl. Phys.* **105**, 07D102.
[143] Mochizuki, A., Kimura, H., Ibuki, M., and Hanyu, T. (2005). *IEICE Trans. Fundam. Electron. Commun. Comput. Sci.* **E88-A**, 1408–1415.
[144] Matsunaga, S., Hayakawa, J., Ikeda, S., Miura, K., Hasegawa, H., Endoh, T., Ohno, H., and Hanyu, T. (2008). *Appl. Phys. Express* **1**, 091301.
[145] Zhao, W., Belhaire, E., Chappert, C., and Mazoyer, P. (2009). *IEEE Trans. Magn.* **45**, 776.
[146] Sekikawa, M., Kiyoyama, K., Hasegawa, H., Miura, K., Fukushima, T., Ikeda, S., Tanaka, T., Ohno, H., and Koyanagi, M. (2008). "IEEE International Electron Devices Meeting, 2008, IEDM'2008", pp. 1–3.
[147] Paul, S., Mukhopadhyay, S., and Bhunia, S. (2008). "IEEE/ACM International Conference on Computer-Aided Design, 2008, ICCAD'2008", pp. 589–592.
[148] Guillemenet, Y., Torres, L., Sassatelli, G., and Bruchon, N. (2008). *Int. J. Reconfigurable Comput.* **2008**, ID723950.
[149] Wang, J. P., and Yao, X. (2008). *J. Nanoelectron. Optoelectron.* **3**, 12.
[150] Ikeda, S., Hayakawa, J., Lee, Y. M., Matsukura, F., Ohno, Y., Hanyu, T., and Ohno, H. (2007). *IEEE Trans. Electron Devices* **54**, 991.
[151] Cowburn, R. P., and Welland, M. E. (2000). *Science* **287**, 1466.
[152] Imre, A., Csaba, G., Ji, L., Orlov, A., Bernstein, G. H., and Porod, W. (2006). *Science* **311**, 205.
[153] Leem, L., and Harris, J. S. (2008). "IEEE International Electron Devices Meeting, 2008, IEDM Technical Digest", pp. 1.
[154] Khitun, A., Bao, M., Lee, J. Y., Wang, K. L., Lee, D. W., Wang, S., and Roshchin, I. V. (2008). *J. Nanoelectron. Optoelectron.* **3**, 24.
[155] Khitun, A., Mingqiang, B., and Wang, K. L. (2008). *IEEE Trans. Magn.* **44**, 2141.
[156] Kostylev, M. P., Serga, A. A., Schneider, T., Leven, B., and Hillebrands, B. (2005). *Appl. Phys. Lett.* **87**, 153501.
[157] Lee, K. S., and Kim, S. K. (2008). *J. Appl. Phys.* **104**, 053909.
[158] Yang, T., Kimura, T., and Otani, Y. (2008). *Nat. Phys.* **4**, 851.
[159] Brataas, A., Bauer, G. E. W., and Kelly, P. J. (2006). *Phys. Rep.* **427**, 157.
[160] Dery, H., Dalal, P., Cywinski, L., and Sham, L. J. (2007). *Nature* **447**, 573.

CHAPTER 4

Dynamics of Magnetic Domain Walls in Nanomagnetic Systems

Teruo Ohno* and **Teruya Shinjo†**

Contents

Abstract

Dynamical behaviour of magnetic domain wall (DW) is one of the main issues in the field of spintronics. In this chapter, several experimental studies in DW dynamics in nanomagnetic systems are described. For the study of DW motion in nanoscale wires, samples with a trilayer structure, ferromagnetic/non-magnetic/ferromagnetic, were prepared and the position of DW was estimated from electrical resistance measurements using GMR principle. The velocity of DW driven by an external field has been evaluated from the resistance change. On the other hand, current-driven DW motion in a single wire of ferromagnetic layer was studied by magnetic force microscopy (MFM).

Magnetic vortex structures are realized in nanoscale ferromagnetic dot systems. The behaviour of vortex core magnetization was observed by MFM.

*Institute for Chemical Research, Kyoto University, Uji 611-0011, Japan
†International Institute for Advanced Studies, Kizu 619-0225, Japan

Nanomagnetism and Spintronics
DOI: 10.1016/B978-0-444-53114-8.00004-2

Recent topics such as the motion of vortex core driven by a high-frequency AC current are introduced.

Key Words: Magnetic domain wall (DW), Field-driven DW motion, GMR method, Nucleation and propagation of DW, Ratchet effect, DW velocity, Mobility of DW, Current-driven DW motion, Magnetic vortex, Switching of vortex core magnetization, Current-driven resonant excitation.

1. INTRODUCTION

Weiss [1] pointed out in his famous paper on spontaneous magnetization in 1907 that ferromagnetic materials are not necessarily magnetized to saturation in the absence of an external magnetic field. Instead, they have magnetic domains, within each of which magnetic moments align. The formation of the magnetic domains is energetically favourable because this structure can lower the magnetostatic energy originating from the dipole–dipole interaction. The directions of magnetization of neighbouring domains are not parallel. As a result, between two neighbouring domains, there is a region in which the direction of magnetic moments gradually changes. This transition region is called a magnetic domain wall (DW).

Recent developments in nanolithography techniques make it possible to prepare nanoscale magnets with simple magnetic domain structure which is suitable for basic studies on the magnetization reversal. For example, in a magnetic wire with submicron width, two important processes in the magnetization reversal, nucleation and propagation of a magnetic DW, can be clearly seen. As shown in Fig. 1A, in a very narrow ferromagnetic wire, the magnetization is restricted to be directed parallel to the wire axis due to the magnetic shape anisotropy. When an external magnetic field is applied against the magnetization, a magnetic DW nucleates at the end of the wire and the magnetization reversal proceeds by the propagation of this DW through the wire (Fig. 1B and C).

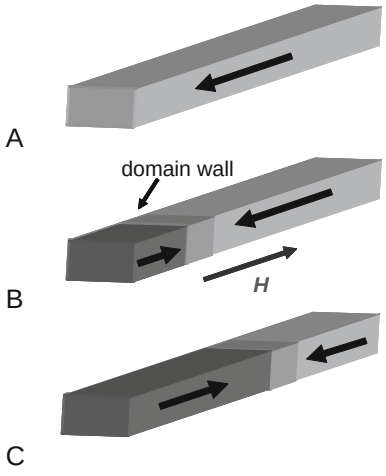

FIGURE 1 Schematic illustration of the magnetization reversal process in a magnetic wire.

2. FIELD-DRIVEN DW MOTIONS

2.1. Detection of domain-wall propagation by using GMR effect

As described above, a magnetic nanowire is a good candidate for the investigation of nucleation and propagation of a magnetic DW. However, it is very difficult to detect the propagation of the DW, because the change in magnetic moments in this process is very small due to the small volume of the magnetic wire. Here, the principle how to detect the DW propagation in magnetic wires by using the giant magnetoresistance (GMR) effect is described. The GMR effect is the change in electrical resistance caused by the change of the magnetic structure in magnetic multilayers [2]. This means that the magnetic structure of the system can be detected by resistance measurements. Consider the GMR system shown in Fig. 2, which is composed of magnetic, non-magnetic and magnetic layers. The resistance is the largest for the antiparallel magnetization configuration (Fig. 2A), and it is the smallest for the parallel configuration (Fig. 2D). During the magnetization reversal of one of the two magnetizations (Fig. 2B and C), the total resistance of the system is given by the sum of the resistances of the parallel magnetization part and the antiparallel magnetization part. Thus, the resistance of this system, R, is given by

$$R = \frac{x}{L} R_{\uparrow\uparrow} + \frac{L - x}{L} R_{\uparrow\downarrow}, \tag{1}$$

where x is the position of the DW, L is the length of the wire, $R_{\uparrow\uparrow}$ is the resistance for parallel configuration and $R_{\uparrow\downarrow}$ is the resistance for antiparallel configuration. This equation means that we can determine the position of DW by simple resistance measurements.

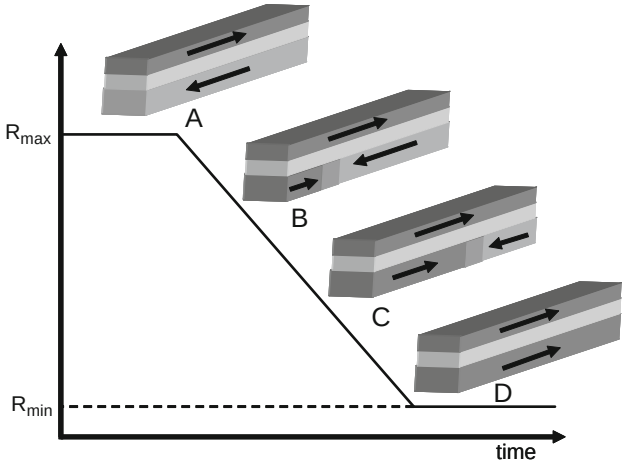

FIGURE 2 Schematic explanation for the detection of DW propagation in magnetic wires by using the magnetoresistance effect.

The above idea has been demonstrated experimentally [3]. The sample is a 500-nm-wide wire composed of $Ni_{81}Fe_{19}$(20 nm)/Cu(10 nm)/$Ni_{81}Fe_{19}$(5 nm) trilayer structure. Due to the large Cu layer thickness, the interlayer exchange coupling between the thin and thick NiFe layers is negligible. The magnetoresistance measurements are performed at 300 K under an external magnetic field along the wire axis. As seen in Fig. 3, the sample has four current–voltage terminals where the voltage is probed over a distance of 20 μm. Furthermore, the sample has an artificial neck (0.35-μm width) introduced at 1/3 distance from one voltage probe.

Figure 4 shows the resistance of the trilayer system as a function of an external magnetic field. Prior to the measurement, a magnetic field of 100 Oe was applied to achieve magnetization alignment in one direction. Then, the resistance was measured as the field was swept towards the counter direction. The result of the magnetoresistance measurement displays essentially four very sharp leaps. First and second leaps correspond to the magnetization reversal of the thin NiFe layer, whereas third and fourth leaps correspond to the magnetization reversal of the thick NiFe layer.

How the magnetization reversal takes place in the sample is the following. As long as the counter field is smaller than a critical field, the magnetizations of both thin and thick NiFe layers align parallel, and the resistance shows the lowest value. As the applied magnetic field exceeds 5 Oe, the resistance abruptly jumps and maintains constant value up to 10 Oe. Then, exceeding 10 Oe, the resistance abruptly jumps again and maintains the largest value up to 22 Oe. The result indicates that the antiparallel magnetization alignment is realized at an external field between 11 and 22 Oe, where the resistance shows the largest value. The ratio

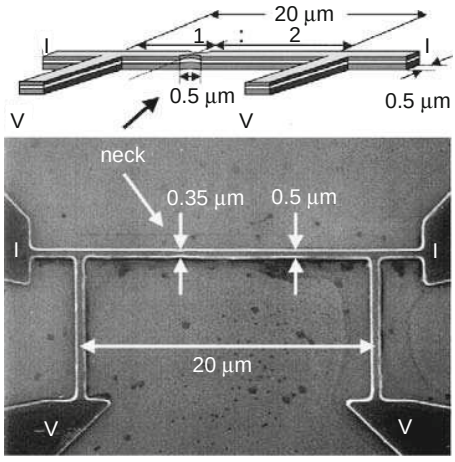

FIGURE 3 SEM image and schematic illustration of the sample. The sample consists of $Ni_{81}Fe_{19}$(20 nm)/Cu(10 nm)/$Ni_{81}Fe_{19}$(5 nm) [3].

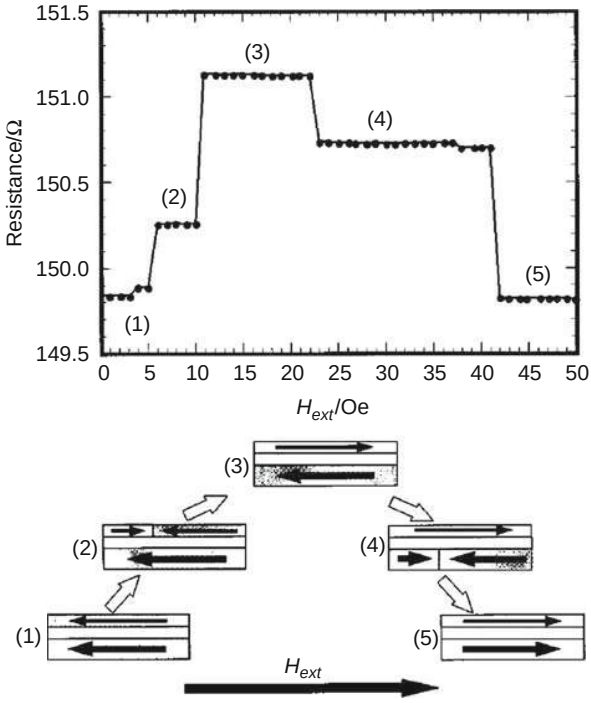

FIGURE 4 Resistance as a function of the external magnetic field at 300 K. The magnetic domain structures inferred from the resistance measurement and the direction of the external field are schematically shown [3].

of the resistance changes at first and second leap is 1:2. This means that one third of the total magnetization of the thin NiFe layer changes its direction at first leap in Fig. 4, since the GMR change is directly proportional to the switching layer magnetization. The ratio, one third, corresponds to the ratio of length between one voltage probe and the neck to the overall length of the wire between the voltage probes. Therefore, in this case, a magnetic DW nucleates in the shorter part of the wire (left side of the SEM image in Fig. 3) and propagates to the neck, where it is pinned up to 10 Oe. The second leap, upon exceeding 10 Oe, corresponds either to depinning of the magnetic DW from the neck, or to nucleation and propagation of another magnetic DW on the other side of the neck (right side of the SEM image in Fig. 3). These two possibilities cannot be distinguished from the result shown in Fig. 4. Though the nucleation position of a DW could not be determined in this experiment, one can inject a DW from one end of a wire by breaking its symmetry [4] or by applying a local magnetic field at the end of a wire [5]. Since the ratio of the resistance changes at third and fourth leap is also 1:2, the magnetization reversal of the thick NiFe layer takes place in the same manner as in the thin NiFe layer described above.

The above experiment shows that a magnetic DW can be trapped by the artificial neck structure introduced into the wire. This is an example of the control of magnetization reversal process by utilizing the designed structure of mesoscopic magnets. The strength of the trap potential of the artificial neck can be estimated by measuring the temperature dependence of the depinning field of a DW from the neck [6]. It was shown that the trap potential increases with a decrease of the neck width and it reaches 4.3×10^{-19} J (30,000 K) for the 250-nm-wide neck of in the 20-nm-thick and 500-nm-wide $Ni_{81}Fe_{19}$ wire. Thus, a DW pinned by the neck is stable against the thermal agitation of room temperature, and this kind of trap potential can be used to define a DW position in the spintronic devices.

It should be noted that the GMR method described here corresponds to a very high-sensitive magnetization measurement. For the sample investigated above, the sensitivity is as high as 10^{-13} emu (10^7 spins). The method, in principle, can be applied to smaller samples as far as the resistance of the samples can be measured and the relative sensitivity increases with decreasing sample volume. The GMR method for the detection of the DW position is also applicable to the study of the current-driven DW motion [7].

2.2. Ratchet effect in DW motions

A ratchet is a mechanism that can limit a motion to one direction, and it is realized on a macroscopic scale by use of a pawl and a wheel with asymmetric-shaped teeth, in which the pawl restricts the wheel to rotate in one direction. Feynman discussed the thermodynamic theory about the ratchet system in his famous lecture. Recently, it has been paid much attention as a model such as molecular motor in living bodies, muscle and the power of micro-machines [8–12].

As described in the previous section, an artificial neck in a magnetic wire works as a pinning potential for a DW motion. Because the energy of a DW is proportional to its area, a DW at wider position in a wire has a larger energy. This energy change of a DW along the wire axis produces the pinning potential for the DW, and this is the reason why we can trap a DW in the artificial neck. The force necessary to move the DW against the potential is given by the derivative of the DW energy with respect to the DW position, which is proportional to the slope of the artificial neck. Thus, we expect different depinning fields depending on the propagation direction of a DW, if we make the artificial structure asymmetric [13–15]. This difference in depinning field between rightward and leftward propagations leads to the unidirectional motion of a DW, that is, a ratchet effect. The experimental results on the ratchet effect in DW motions are presented in the following [15].

The samples were fabricated onto thermally oxidized Si substrates by means of e-beam lithography and lift-off method. Figure 5 shows a schematic illustration of a top view of the whole sample. A magnetic wire has a trilayered structure consisting of $Ni_{81}Fe_{19}$(5 nm)/Cu(20 nm)/$Ni_{81}Fe_{19}$(20 nm). The main body of the magnetic wire has four notches with asymmetric shape. The sample has four current–voltage probes made of non-magnetic material, Cu. Further, it has two narrow Cu wires crossing the ends of the magnetic wire and a wide Cu wire

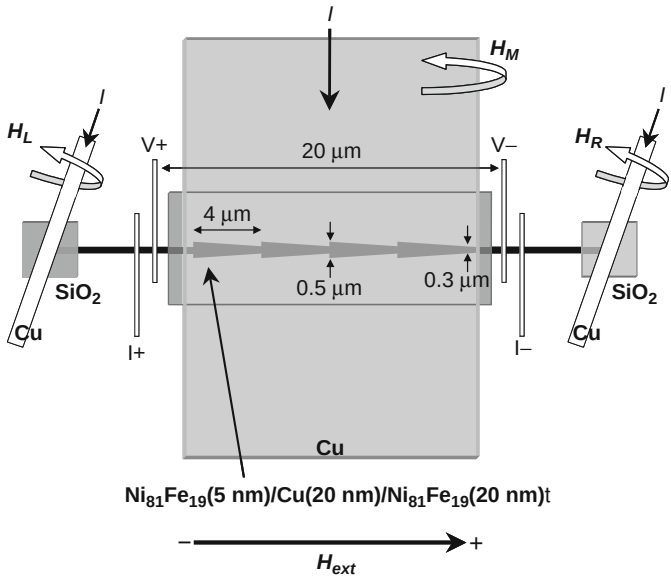

FIGURE 5 Schematic illustration of a top view of the whole sample. The black part is a trilayered magnetic wire consisting of NiFe(5 nm)/Cu(20 nm)/NiFe(20 nm). The main body of the magnetic wire has four asymmetric notches. A flow of electric current in the Cu wire crossing the magnetic wire generates a local magnetic field, which is used to nucleate a magnetic DW.

covering the notched part of the magnetic wire. These Cu wires are electrically insulated from the magnetic wire by SiO_2 layers of 50 nm in thickness. A flow of an electric current in each Cu wire can generate local magnetic fields, H_L, H_M or H_R, which acts on the left end, the main part with notches or the right end of the magnetic wire, respectively. H_L (H_R) can trigger the nucleation of a DW at the left (right) end of the magnetic wire. Thus, the propagation direction of a DW can be controlled by H_L (H_R).

Figure 6A shows a typical resistance change of the trilayered magnetic wire with asymmetric notches as a function of H_{ext} applied along the wire axis. The resistance increase at 10 Oe corresponds to the magnetization reversal of the NiFe (5 nm) layer, while the decrease in resistance at 160 Oe is due to the magnetization reversal of the NiFe(20 nm) layer. The magnetic DW was not pinned by asymmetric notches during the magnetization reversals of NiFe(20 nm) layer because of its large nucleation field.

To nucleate a DW in the NiFe(20 nm) layer at smaller H_{ext} and to pin the DW at the notch, we utilized the method generating a pulsed local magnetic field at the end of the magnetic wire. Figure 6B shows the result of the DW injection into the NiFe(20 nm) layer of the magnetic wire by H_L. The measurement procedure is the same as that shown in Fig. 6A, except applying H_L when $H_{ext} = 60$ Oe. The magnitude and the duration of the pulsed H_L were 200 Oe and 100 ns, respectively. The resistance abruptly decreased after the application of H_L and stayed at a value between the largest and the smallest values. The value of the resistance indicates

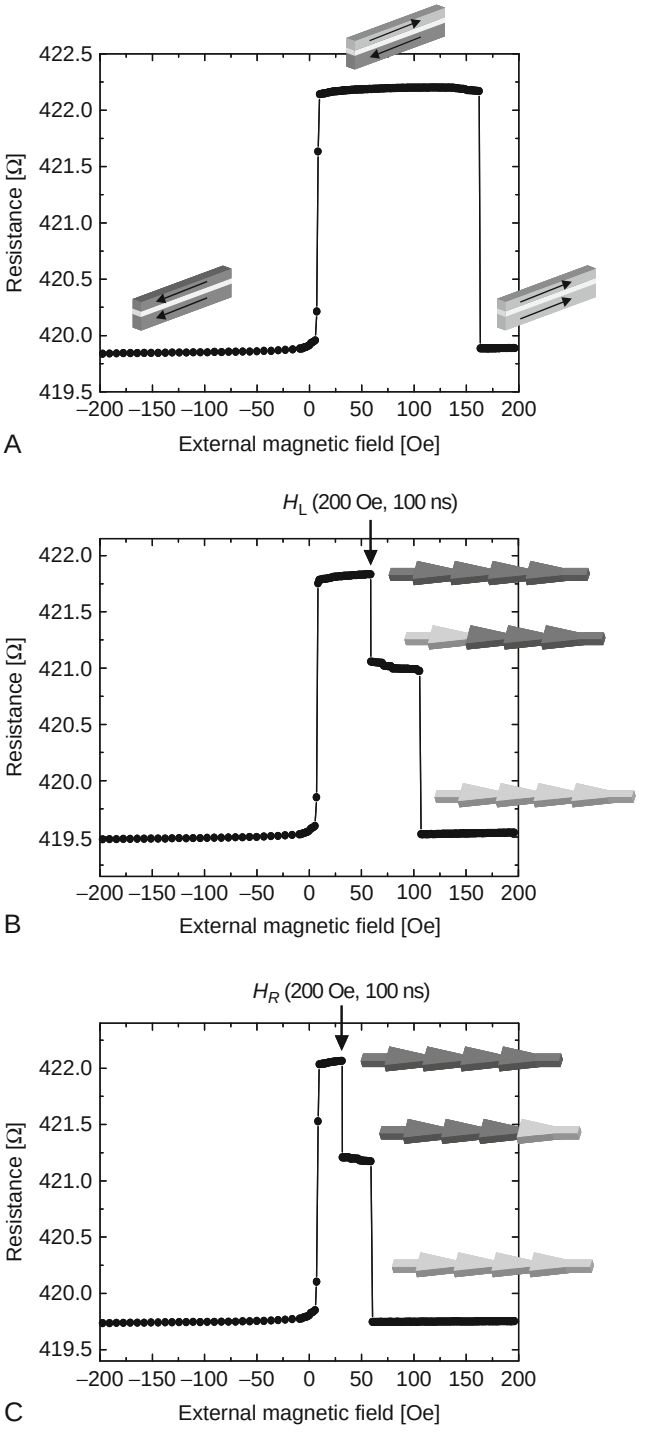

FIGURE 6 Resistance change of the trilayered magnetic wire with asymmetric notches as a function of the external magnetic field. The magnetic domain structures inferred from the resistance measurement are schematically shown. (A) Typical MR curve of the trilayered system. (B) A magnetic DW was injected into the NiFe(20 nm) layer from the left end of the magnetic wire by the pulsed H_L. (C) A DW was injected into the NiFe(20 nm) layer from the right end of the magnetic wire by pulsed H_R [15].

that a DW injected from the left by H_L was pinned at the first notch. By increasing H_{ext} after the injection of the DW, the resistance abruptly decreased to the smallest value at 98 Oe, which indicates that the DW propagated to the right end of the wire through the asymmetric notches. Thus, the depinning field for the rightward propagation of the DW can be determined to be 98 Oe. On the other hand, the depinning field for the leftward propagation of the DW can be determined from the result shown in Fig. 6C, which shows the MR measurement when the DW was injected from the right end of the wire by H_R. In this case, the depinning field was 54 Oe. Thus, the depinning field for the rightward propagation is much larger than that for the leftward propagation. If an AC magnetic field between the depinning fields for both directions is applied, a unidirectional DW motion will be induced, which should be called a "magnetic ratchet effect". The different DW propagation fields for rightward and leftward motions were also found in the experiment on submicron magnetic wires with a triangular structure [16].

The magnetic ratchet effect was also demonstrated in the current-driven DW motion; the critical current density necessary for the current-driven DW motion depends on the propagation direction of the DW. The DW moves more easily in the direction along which the slope of the asymmetric notch is smaller [17].

2.3. DW velocity measurements

Sixtus and Tonks [18] first measured the DW velocity in bulk magnetic wires in 1931. Figure 7 shows a schematic diagram of the circuit for the velocity measurements. Under a homogeneous magnetic field, a magnetic DW is nucleated by adding a local magnetic field, which is produced by an adding coil. The DW travelling along the wire from left to right produces successive voltage surges in two search coils, which are placed around the wire at a known separation.

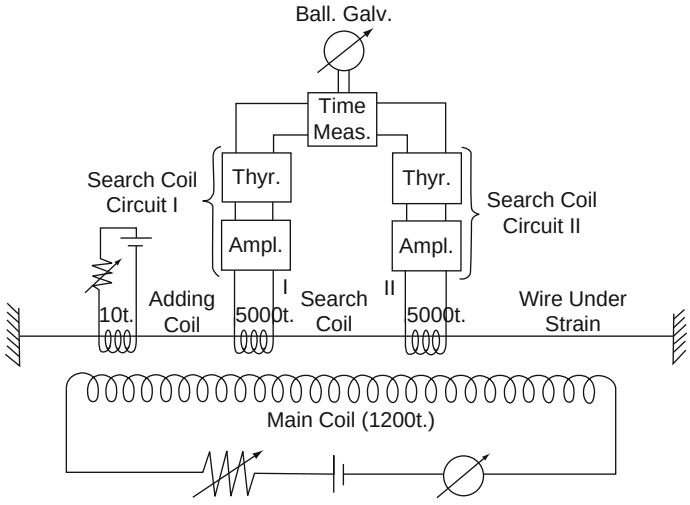

FIGURE 7 Schematic diagram of the circuit for velocity measurements by Sixtus and Tonks [18].

The velocity of the DW can be calculated from their time interval of the voltage surges and the separation of the coils. The DW velocity, obtained experimentally, was discussed in terms of the dissipation of the magnetic energy by eddy currents.

The GMR detection method described in Section 2.1 has an advantage in dynamical measurements because of its simplicity. Here, velocity measurements of a single DW propagating in a magnetic nanowire are presented [19]. Because the GMR detection method provides the information of a DW position, as shown in Eq. (1), the DW velocity, $v = \mathrm{d}x/\mathrm{d}t$, can be determined by the time-domain measurements, and v is given by

$$v = \frac{\mathrm{d}x}{\mathrm{d}t} = \frac{L}{R_{\uparrow\downarrow} - R_{\uparrow\uparrow}} \frac{\mathrm{d}R}{\mathrm{d}t}. \tag{2}$$

Thus, the GMR method can offer the time variation of the DW velocity. This is an advantage over conventional experimental methods, such as experiments by Sixtus and Tonks [18] and the DW velocity measurements by using the Kerr microscopy with a combination of a pulsed magnetic field, where only the average velocity of a DW can be obtained.

The samples for the DW velocity measurements have trilayer structures of $Ni_{81}Fe_{19}$(40 nm)/Cu(20 nm)/$Ni_{81}Fe_{19}$(5 nm). The width of the wire is 0.5 μm and the sample has four current–voltage terminals where the voltage is probed over a distance of 2 mm. The magnetic field was applied along the wire axis. The voltage across two voltage probes was monitored by a differential pre-amplifier and a digital oscilloscope. The current passing through the electromagnet was also monitored by the digital oscilloscope so as to obtain both resistance and applied magnetic field during the magnetization reversal simultaneously.

Figure 8 shows the resistance change of the trilayer system at 77 K as a function of an external magnetic field. Prior to the measurement, a magnetic field of 500 Oe was applied to align the magnetization in one direction. Then, the resistance was measured at 10-ms intervals with the sweeping field towards the counter direction at the sweeping rate of 20 Oe/s. The result indicates that the antiparallel magnetization alignment is realized in the field range between 80 and 120 Oe, where the resistance shows the largest value. The change in resistance at 80 and 120 Oe is attributed to the magnetization reversals of the 5-nm-thick NiFe and 40-nm-thick NiFe layers, respectively. Since there is no measured point during the magnetization reversal of the 40-nm-thick NiFe in Fig. 8, it is concluded that the magnetization reversal of the 40-nm-thick NiFe is completed within 10 ms. On the other hand, the magnetization reversal of the 5-nm-thick NiFe proceeds gradually with increasing an external magnetic field. This indicates that the magnetization reversal of the 5-nm-thick NiFe takes place by the successive pinning and depinning of a magnetic DW. Hereafter, we focus on the magnetization reversal of the 40-nm-thick NiFe.

Figure 9 shows an experimental result on the time variation of the resistance during the magnetization reversal of the 40-nm-thick NiFe layer. The data were collected at 40-ns intervals. The linear variation of resistance with time in Fig. 9 indicates that the propagation velocity of the magnetic DW is constant during the magnetization reversal of the 40-nm-thick NiFe layer. The propagation velocity of

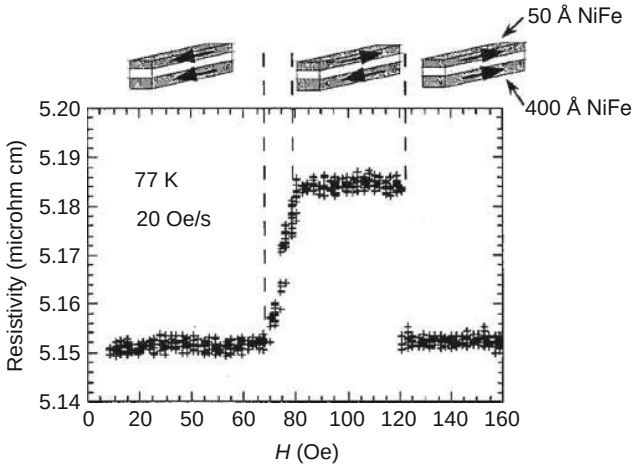

FIGURE 8 Resistance as a function of the external magnetic field at 77 K. The resistance was measured at 10-ms intervals with sweeping the field towards the counter direction at the sweeping rate of 20 Oe/s. The magnetic domain structures inferred from the resistance measurement are schematically shown [19].

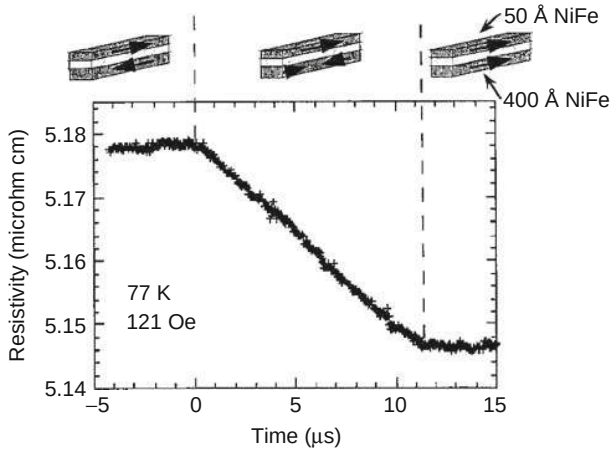

FIGURE 9 Time variation of the resistance during the magnetization reversal of the 40-nm-thick NiFe layer at 77 K, which was collected at 40-ns intervals. The applied magnetic field simultaneously monitored by digital oscilloscope was 121 Oe. As the sweeping rate of the applied magnetic field was 20 Oe/s, the variation of the applied magnetic field during magnetization reversal is less than 2×10^{-5} Oe, that is, the applied magnetic field is practically constant during the measurements [19].

the magnetic DW at the external magnetic field of 121 Oe is estimated to be 182 m/s, which is calculated from the separation (2 mm) of the two voltage probes and the time (11 μs) the wall travelled across it. Since the sweeping rate of the magnetic field was 20 Oe/s, the variation of the magnetic field during the magnetization reversal is less than 2×10^{-5} Oe, that is, the external magnetic field is regarded as constant during the measurements.

Since the reversal field of the 40-nm-thick NiFe varied in every measurement, ranging from 90 to 140 Oe, the wall velocities at various magnetic fields were obtained by repeating the measurements. The result at 100 K is shown in Fig. 10. The wall velocity depends linearly on the applied magnetic field, and it is described as $v = \mu(H - H_0)$, where v is the wall velocity, H the applied magnetic field, μ so-called wall mobility, and it is obtained that $\mu = 2.6$ (m/s Oe) and $H_0 = 38$ (Oe). Here, we utilized the statistical nature of the magnetization reversal field to obtain the external magnetic field dependence of the DW velocity. A similar but more sophisticated experiment was performed by Himeno *et al.* [20]. They set two Cu wires crossing the magnetic wire at the ends of the wire, which can produce a pulsed local magnetic field by a flow of a pulsed electric current. This pulsed local magnetic field can nucleate a DW at the end of the magnetic wire under a given external magnetic field. This enables us to determine the DW velocity as a function of the external magnetic field in a controlled manner.

Magneto-optic Kerr effect magnetometer in micron-scale spatial resolution, together with the pulsed magnetic field, offers another approach to measure a DW velocity. It has been reported that the very high DW velocity over 1000 m/s with high mobility of 30 m/s Oe was realized for a single-layer 5-nm-thick $Ni_{80}Fe_{20}$ wire with 200 nm in width [21]. Thus, the mobility in Ref. [21] is 10 times larger than that in Ref. [9]. This mystery has been resolved recently by the measurements of the DW velocity in the wide range of an external magnetic field [22]. Figure 11 shows the DW velocity as a function of an external magnetic field for the 20-nm-

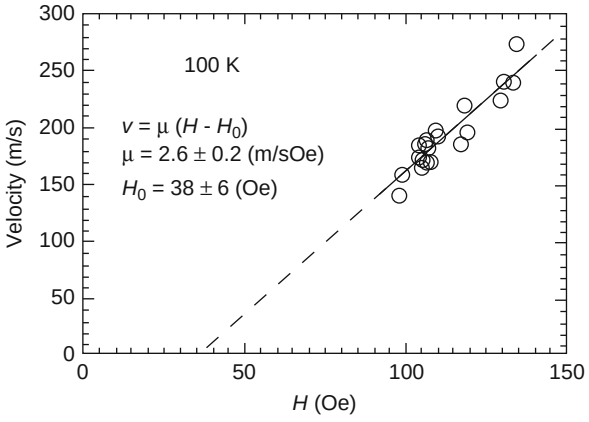

FIGURE 10 Dependence of DW velocity v on the amplitude H of the applied magnetic field at 100 K. The wall velocity depends linearly on the applied magnetic field and is described as $v = \mu(H - H_0)$, where $\mu = 2.6$ (m/s Oe) and $H_0 = 38$ (Oe) [19].

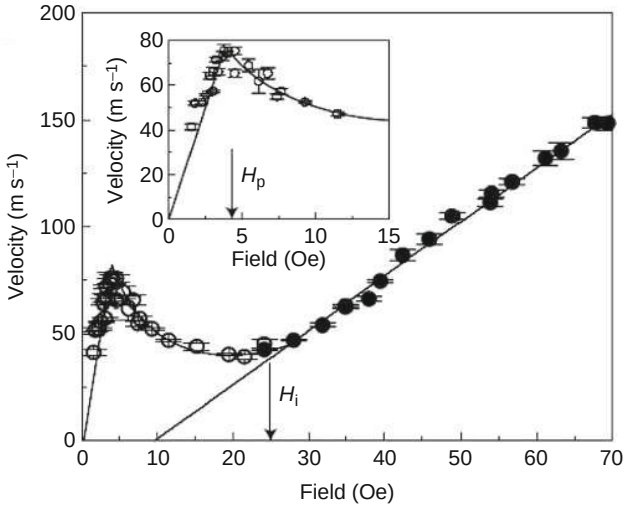

FIGURE 11 Average domain-wall velocity versus field step amplitude. The inset shows the details around the velocity peak [22].

thick $Ni_{80}Fe_{20}$ wire with 600 nm in width. One can recognize that there are three regimes: the high DW mobility regime of 25 m/s Oe below 5 Oe, the low DW mobility regime of 2.5 m/s Oe above 25 Oe and the transition regime with negative differential mobility between 5 and 25 Oe. These results are in accord with theoretical predictions that, above a threshold field (so-called Walker field), uniform wall movement gives way to turbulent wall motion, leading to a substantial drop in wall mobility [23–28].

The DW mobilities for low and high fields in Fig. 11 are very close to those reported in Ref. [21] and in Ref. [19], respectively. Thus, it can be concluded that the measurements in Ref. [19] were performed above the Walker field and those in Ref. [21] were carried out below the Walker field. So, the discrepancy between two experiments was resolved. The high DW mobility in the relatively large external magnetic field in Ref. [21] can be understood by the micromagnetic simulation which suggests that Walker breakdown in nanowires involves the nucleation and motion of Bloch lines (vortices) in the wall, and that finite roughness inhibits this process, pushing the breakdown field higher [23]. In the thinner nanowire of Ref. [21], this effect might become more prominent than in wider nanowires, pushing the breakdown field to the higher value.

3. CURRENT-DRIVEN DW MOTIONS

3.1. Concept of current-driven DW motion

Figure 12A is an illustration of a DW between two domains in a magnetic wire. Here, arrows show the direction of magnetic moments. The magnetic DW is a transition region of the magnetic moments between domains, and the direction of

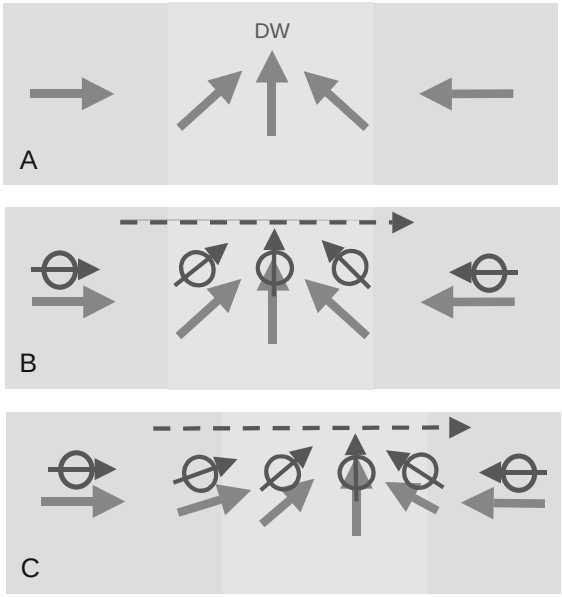

FIGURE 12 Schematic illustration of current-driven DW motion. (A) A DW between two domains in a magnetic wire. The arrows show the direction of magnetic moments. The magnetic DW is a transition region of the magnetic moments between domains, and the direction of moments gradually changes in the DW. (B) The spin of conduction electron follows the direction of local magnetic moments because of the *s–d* interaction. (C) As a reaction, the local magnetic moments rotate reversely, and in consequence, the electric current displaces the DW.

moments gradually changes in the DW. What will happen if an electric current flows through a DW? Suppose a conduction electron passes though the DW from left to right. During this travel, the spin of conduction electron follows the direction of local magnetic moments because of the *s–d* interaction (Fig. 12B). As a reaction, the local magnetic moments rotate reversely (Fig. 12C), and, in consequence, the electric current can displace the DW. This current-driven DW motion was first predicted by Berger [29, 30], and his group performed several experiments on magnetic films [31, 32]. It needed huge currents to move a DW in a magnetic film due to the large cross section. Recent developments in nanolithography techniques make it possible to prepare nanoscale magnetic wires, resulting in the review of their pioneering works. The current-driven DW motion provides a new strategy to manipulate a magnetic configuration without an assistance of magnetic field, and will improve drastically the performance and functions of recently proposed spintronic devices, whose operation is based on the motion of a magnetic DW [33–36]. Reports on this subject have been increasing in recent years from both theoretical [37–42] and experimental [43–68] points of view because of its scientific and technological importance. However, most of the results cannot be reviewed here due to the limitation of space. The reader may be referred to Chapter 7 by H. Ohno for the current-driven DW experiments in ferromagnetic semiconductor (Ga,Mn)As [50, 62].

3.2. MFM direct observations

In this section, results of the direct observation of the current-driven DW motion in a micro-fabricated magnetic wire are presented [47]. Magnetic force microscopy (MFM) is used to show that a single DW can be displaced back and forth by positive and negative pulsed currents.

An L-shaped magnetic wire with a round corner, as schematically illustrated in Fig. 13, was prepared for the experiments. One end of the L-shaped magnetic wire is connected to a diamond-shaped pad, which acts as a DW injector [4], and the other end is sharply pointed to prevent a nucleation of a DW from this end. L-shaped magnetic wires of 10-nm-thick $Ni_{81}Fe_{19}$ were fabricated onto thermally oxidized Si substrates by means of an e-beam lithography and a lift-off method. The width of the wire is 240 nm.

To introduce a DW positioned in the vicinity of the corner, the direction of the external magnetic field was tilted from the wire axis in the substrate plane as shown in Fig. 13. In the initial stage, a magnetic field of +1 kOe was applied to align the magnetization in one direction along the wire. Then, a single DW was introduced by applying a magnetic field of −175 Oe. After that, the MFM observations were carried out in the absence of a magnetic field. The existence of the single DW in the vicinity of the corner was confirmed as shown in Fig. 14A. The DW is imaged as a bright contrast, which corresponds to the stray field from positive magnetic charge. In this case, a head-to-head DW is realized as illustrated schematically in Fig. 14D. The position and the shape of the DW were unchanged after several MFM scans, indicating that the DW was pinned by a local structural

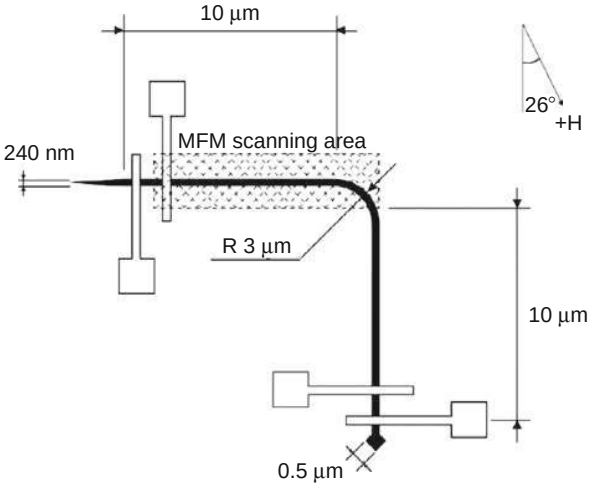

FIGURE 13 Schematic illustration of a top view of the sample. One end of the L-shaped wire is connected to a diamond-shaped pad which acts as a DW injector, and the other end is sharply pointed to prevent a nucleation of a DW from this end. The wire has four electrodes made of Cu. MFM observations were performed for the hatched area at room temperature [47].

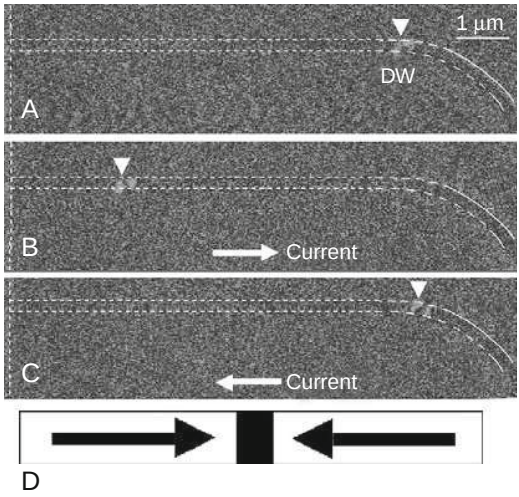

FIGURE 14 (A) MFM image after the introduction of a head-to-head DW. The DW is imaged as a bright contrast, which corresponds to the stray field from positive magnetic charge. (B) MFM image after an application of a pulsed current from left to right. The current density and pulse duration are 7.0×10^{11} A/m^2 and 5 μs, respectively. DW is displaced from right to left by the pulsed current. (C) MFM image after an application of a pulsed current from right to left. The current density and pulse duration are 7.0×10^{11} A/m^2 and 5 μs, respectively. The DW is displaced from left to right by the pulsed current. (D) Schematic illustration of a magnetic domain structure inferred from the MFM image. The DW has a head-to-head structure [47].

defect, and that a stray field from the probe was too small to change the magnetic structure and the position of the DW.

After the observation of Fig. 14A, a pulsed current was applied through the wire in the absence of a magnetic field. The current density and the pulse duration were 7.0×10^{11} A/m^2 and 5 μs, respectively. Figure 14B shows the MFM image after an application of the pulsed current from left to right. The DW, which had been in the vicinity of the corner (Fig. 14A), was displaced from right to left by the application of the pulsed current. Thus, the direction of the DW motion is opposite to the current direction. Furthermore, the direction of the DW motion can be reversed by switching the current polarity as shown in Fig. 14C. These results are consistent with the spin-transfer mechanism.

The same experiments for a DW with different polarities, a tail-to-tail DW, were performed to examine the effect of a magnetic field generated by the electric current (Oersted field). The tail-to-tail DW was generated by the following procedures. A magnetic field of −1 kOe was applied to align the magnetization in the direction opposite to that in the previous experiment. Then, a tail-to-tail DW was introduced by applying a magnetic field of +175 Oe. The introduced DW is imaged as a dark contrast in Fig. 15A, which indicates that a tail-to-tail DW is formed as schematically illustrated in Fig. 15D. Figure 15A–C shows that the direction of the tail-to-tail DW displacement is also opposite to the current

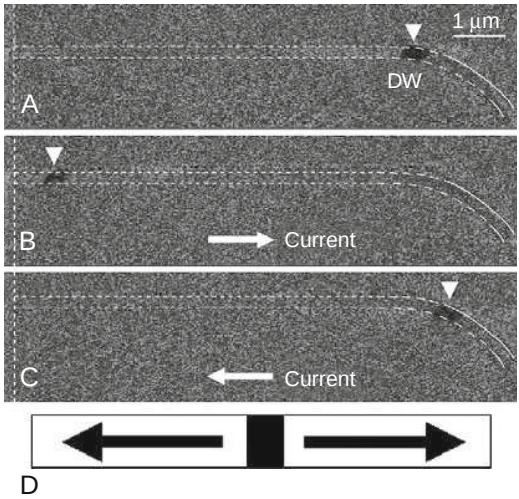

FIGURE 15 (A) MFM image after the introduction of a tail-to-tail DW. The DW is imaged as a dark contrast, which corresponds to the stray field from negative magnetic charge. (B) MFM image after an application of a pulsed current from left to right. The current density and pulse duration are 7.0×10^{11} A/m^2 and 5 μs, respectively. DW is displaced from right to left by the pulsed current. (C) MFM image after an application of a pulsed current from right to left. The current density and pulse duration are 7.0×10^{11} A/m^2 and 5 μs, respectively. The DW is displaced from left to right by the pulsed current. (D) Schematic illustration of a magnetic domain structure inferred from the MFM image. The DW has a tail-to-tail structure [47].

direction. The fact that both head-to-head and tail-to-tail DWs are displaced opposite to the current direction indicates clearly that the DW motion is not caused by the Oersted field.

Figure 16A–K are successive MFM images with one pulsed current applied between each consecutive image. The current density and the pulse duration were 7.0×10^{11} A/m^2 and 0.5 μs, respectively. Each pulse displaced the DW opposite to the current direction. The difference in the displacement for each pulse is possibly due to the pinning by randomly located defects. The average displacement per one pulse did not depend on the polarity of the pulsed current. The average DW displacement per one pulse as a function of the pulse duration under the condition of constant current density of 7.0×10^{11} A/m^2 is shown in Fig. 17. The average DW displacement is proportional to the pulse duration, which indicates that the DW has a constant velocity of 3.0 m/s. It was also confirmed that the DW velocity increases with the current density.

3.3. Towards applications of current-driven DW motion

It was shown that a DW position in a wire can be controlled by tuning the intensity, the duration and the polarity of the pulsed current, and thus the current-driven DW motion has the potentiality for spintronic device applications

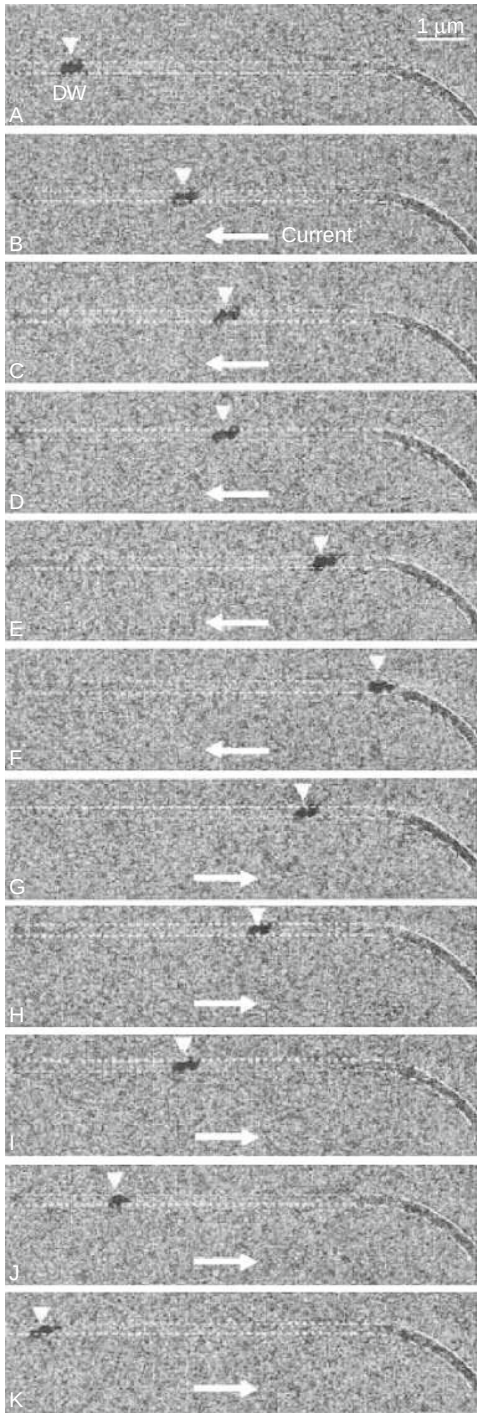

FIGURE 16 Successive MFM images with one pulse applied between each consecutive image. The current density and the pulse duration were 7.0 $\times$ 10^{11} A/m^2 and 0.5 μs, respectively. Note that a tail-to-tail DW is introduced, which is imaged as a dark contrast [47].

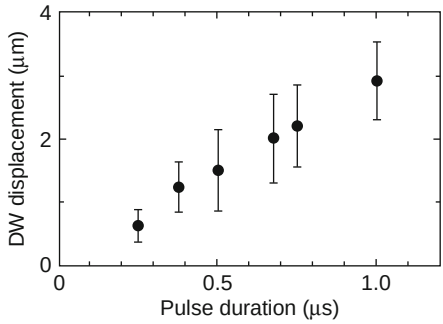

FIGURE 17 Average DW displacement per one pulse as a function of the pulse duration under a condition of constant current density of 7.0 $\times$ 10^{11} A/m^2 [47].

such as novel memory and storage devises [33–36]. However, there are following issues to be overcome for the practical applications: (1) low threshold current density, (2) high DW velocity and (3) stability of DW position. These three conditions should be simultaneously satisfied in the operations of real devices.

The experimentally obtained threshold current densities in the absence of a magnetic field are the order of 10^{11}–10^{12} A/m^2 [47, 52]. These values are more than an order smaller than the theoretical value and also much smaller than that obtained from the micromagnetic simulation [37, 41, 42]. Several possibilities to solve this strong discrepancy have been proposed: sample heating by the current, inclusion of new term to the model and the use of Landau–Lifshitz equation instead of Landau–Lifshitz–Gilbert (LLG) equation. The reader may be referred to Chapter 5 by H. Kohno and G. Tatara for an approach by an analytical model, and also to Chapter 6 by A. Thiaville and Y. Nakatani for an approach by micromagnetics. In real experiments, the application of the high current density of 10^{11} A/m^2 results in the severe increase of sample temperature up to reaching the Curie temperature [54, 65]. Figure 18 shows the estimated sample

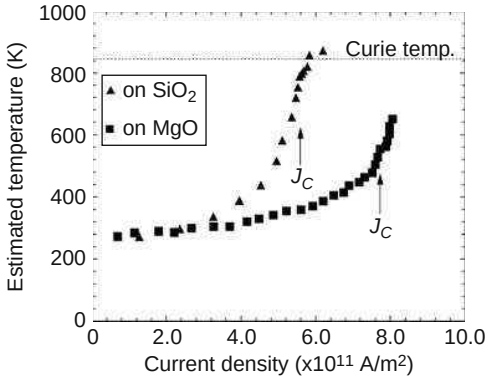

FIGURE 18 Estimated sample temperatures as a function of current density for two samples with the same dimension prepared on different substrates (SiO_2/Si and MgO) [56].

temperatures as a function of current density for two samples with the same dimension prepared on different substrates (SiO_2/Si and MgO) [56]. One can recognize at a glance that the Joule heating effect strongly depends on the substrate; the lower thermal conductance of SiO_2 leads to the rapid increase of the sample temperature. Thus, the sample heating depends on the sample architecture (dimension, composition, substrate, etc.). More important message from Fig. 18 is the large difference of the threshold current densities J_c in two samples with the same dimension. The higher sample temperature of the sample on the thermally oxidized Si substrate results in the lower threshold current density. This clearly suggests the importance of the thermal effect on the current-driven DW motion.

In a simple model in which the transferred spin angular momentum from conduction electrons is fully used to the DW motion, the DW velocity is expected to be $jPg\mu_B/(2eM_s)$, where j is the current density, P the spin polarization of the current, g the g-value of an electron, μ_B the Bohr magneton, e the electronic charge and M_s the saturation magnetization. This predicts about an order larger DW velocity than typical experimental values of several m/s in the absence of a magnetic field at the current density of 10^{11} A/m^2 [47, 52]. Thus, the efficiency of the current-driven DW motion is about 10%, and most of the transferred momentum seems to dissipate by local excitations rather than being used to drive a DW. However, recent experiments show that high velocity of about 100 m/s can be obtained with the current density of 1.5×10^{12} A/m^2 for NiFe in the case of very low DW depinning field less than 10 Oe [68]. Thus, the low efficiency in the pioneering studies can be attributable to the pinning effect of a DW due to the defects such as surface and/or edge roughness.

Although the high velocity has been demonstrated for NiFe nanowires as mentioned above, it has also been shown that the threshold current density increases with the DW pinning field. This could become a problem in the application, because DW position should be stabilized by using such as notch structures against the thermal agitation. Recently very attractive simulation results has been coming out, which suggest that it is possible to reduce the threshold current density with keeping the high thermal stability of the DW position for nanowires with perpendicular magnetic anisotropy [69, 70]. The promising experimental results, which support these simulations, have been reported [71, 72]. It was shown that a single nanosecond current pulse can control precisely the DW position from notch to notch in a Co/Ni wire with perpendicular magnetic anisotropy in spite of the large DW depinning field from the notch of 400 Oe [72].

Can we have higher DW velocity with lower current density? The straight forward way is to reduce the magnetization because the DW velocity is given by $jPg\mu_B/(2eM_s)$ in a simple model. Because NiFe already has relatively high spin polarization $P = 0.7$, it seems more effective to make effort to reduce the magnetization. Alternative way is to rely on so-called non-adiabatic torque [42]. It has been shown theoretically that the DW velocity is proportional to β/α, where β is the coefficient of non-adiabatic torque term and α is the Gilbert damping constant.

4. TOPICS ON NANODOT SYSTEMS

4.1. MFM studies on magnetic vortices in dot systems

As mentioned in Section 1, ferromagnetic materials generally form domain structures to reduce their magnetostatic energy. In very small ferromagnetic systems, however, the formation of DWs is not energetically favoured. Specifically, in a dot of ferromagnetic material of micrometre or submicrometre size, a curling spin configuration – that is, a magnetization vortex (Fig. 19) – has been proposed to occur in place of domains. When the dot thickness becomes much smaller than the dot diameter, usually all spins tends to align in-plane. In the curling configuration, the spin directions change gradually in-plane so as not to lose too much exchange energy, but to cancel the total dipole energy. In the vicinity of the dot centre, the angle between adjacent spins then becomes increasingly larger when the spin directions remain confined in-plane. Therefore, at the centre of the vortex structure, the magnetization within a small spot will turn out-of-plane and parallel to the plane normal [73].

Cowburn *et al.* [74] reported magneto-optical measurements on nanoscale supermalloy ($Ni_{80}Fe_{15}Mo_5$) dot arrays. From the profiles of the hysteresis loops, they concluded that a collinear-type single domain phase is stabilized in dots with diameters smaller than a critical value of about 100 nm and a vortex phase likely occurs in dots with larger diameters. Figure 20 shows the hysteresis loop for the dot with a diameter of 300 nm and a thickness of 10 nm under an external magnetic field in the sample plane [74]. The magnetic field increases the area where the magnetization aligns parallel and decreases the area where the magnetization aligns antiparallel to the magnetic field. The gradual increase of magnetization corresponds to the moving of the vortex core from the centre to the outside and the jump of magnetization corresponds to the annihilation of the magnetization vortex. The relatively sudden loss in the course of field reducing corresponds to the nucleation of the vortex.

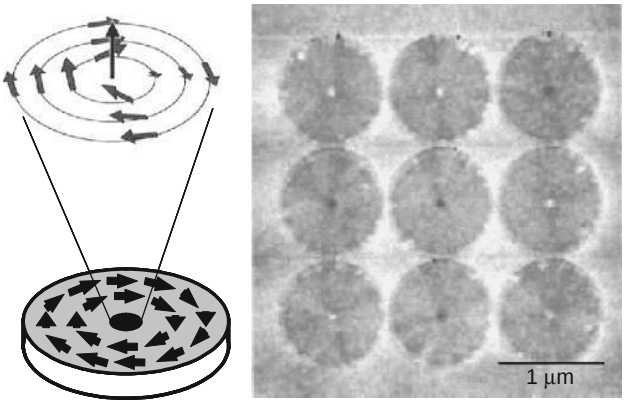

FIGURE 19 MFM image of an array of permalloy dots 1 μm in diameter and 50-nm thick with the schematic spin structure (magnetic vortex and vortex core) in a dot [72].

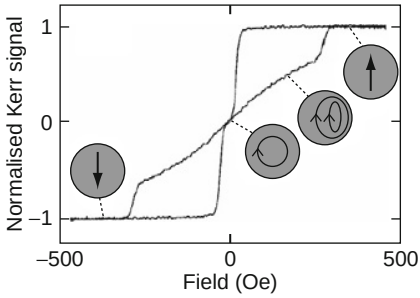

FIGURE 20 Hysteresis loop for the circular dot with a diameter of 300 nm and a thickness of 10 nm under an external magnetic field in the sample plane. The schematic annotation shows the magnetization within a circular dot.

Figure 19 is the first proof of such a vortex structure with a nanometre-scale core where the magnetization rises out of the dot plane [75]. The sample is an array of 3 × 3 dots of permalloy ($Ni_{81}Fe_{19}$) with 1 μm in diameter and 50-nm thickness. At the centre of each dot, bright or dark contrast is observed, which corresponds to the positive or negative stray field from the vortex core. The direction of the magnetization at the centre turns randomly, either up or down, as reflected by the different contrast of the centre spots. This is reasonable since up and down magnetizations are energetically equivalent without an external applied field and do not depend on the vortex orientation: clockwise or counter-clockwise. MFM observations were performed also for an ensemble of permalloy dots with varying diameters, nominally from 0.3 to 1 μm (Fig. 21). The image in Fig. 21A was taken after applying an external field of 1.5 T along an in-plane direction. Again, the two types of vortex core with up and down

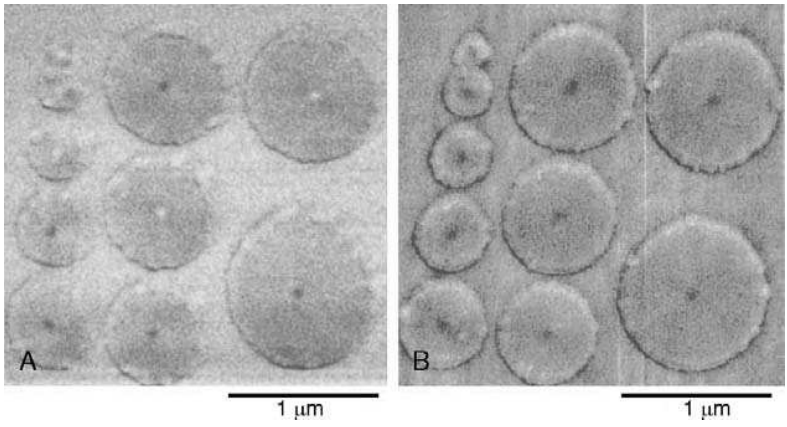

FIGURE 21 MFM images of an ensemble of 50-nm-thick permalloy dots with diameters varying from 0.3 to 1 μm: (A) after applying an external field of 1.5 T along an in-plane direction and (B) parallel to the plane normal, respectively [72].

magnetization are observed. In contrast, after applying an external field of 1.5 T normal to the substrate plane, centre spots exhibit the same contrast (Fig. 21B) indicating that all the vortex core magnetizations have been oriented into the field direction. The size of the core cannot be determined from the images since the spatial resolution of MFM is much larger than the theoretical core size. The core size was determined to be 9 nm by using spin-polarized scanning tunnelling microscopy which has an atomic-scale resolution [76].

Since the size of the perpendicular magnetization at the vortex core is very small, conventional magnetization measurements cannot detect switching of the vortex core under magnetic field. For the measurement of switching field of core magnetization, arrays of circular dots of permalloy with the diameter of 0.2, 0.4 and 1 μm and the thickness of 50 nm were prepared [77]. The sample consists of sets of permalloy dots arrays of square lattice 5×5. First, a strong magnetic field (1.5 T) normal to the sample plane was applied in order to align all the core magnetizations in one direction. The perpendicular magnetization turning to this direction shows dark contrast in MFM image as shown Fig. 22A. Second, a certain magnetic field H_t was applied to the counter direction for 5 min. Finally, one 5×5 array which was chosen randomly in the sample was observed by MFM in the absence of a magnetic field. The MFM images for the cases of H_t of 3500 Oe are shown in Fig. 22B. A bright spot corresponds to core magnetization switched by H_t, while a dark spot represents the core magnetization with its initial direction. The number of bright spots in the MFM images after applying various values of H_t gives the switching probability for each field. The results for the three samples are shown in Fig. 23. The average switching field is 4100, 3900 and 3650 Oe in the sample of 0.2, 0.4 and 1 μm in diameter, respectively.

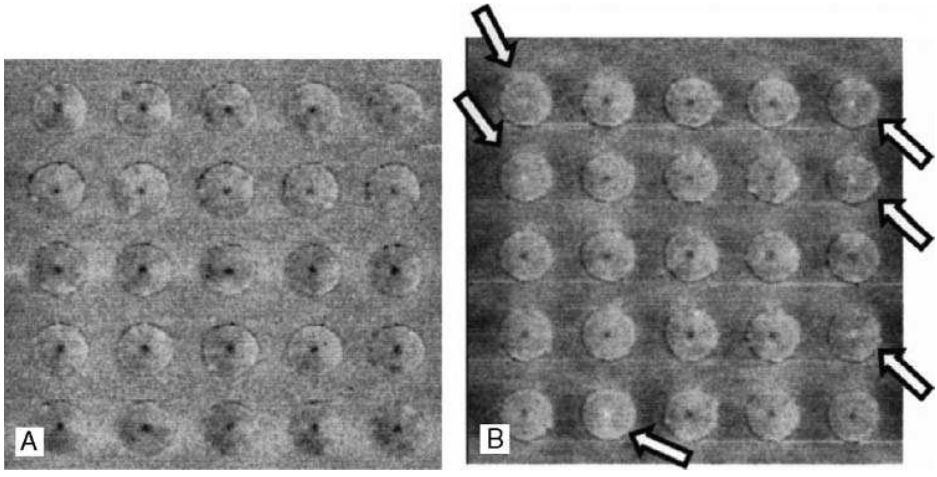

FIGURE 22 MFM images of an array composed of 5×5 circular permalloy dots with the diameter of 0.4 μm: (A) after applying a magnetic field of 1.5 T and (B) after applying a magnetic field $H_t = -0.35$ T [74].

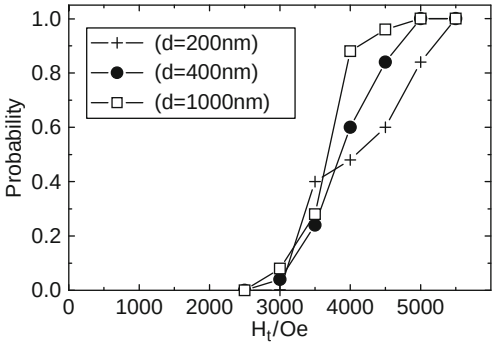

FIGURE 23 Switching probability of core magnetization in circular dots with the diameter of 0.2, 0.4 and 1 μm as a function of magnetic field normal to the sample plane. The average switching fields are 4100, 3900 and 3650 Oe in the samples of 0.2, 0.4 and 1 μm in diameter, respectively [74].

The experimental confirmation of the existence of the vortex core by MFM study [75] stimulated the subsequent intensive studies on the dynamics of the vortex core. It has been clarified that a vortex core displaced from the stable position (dot centre) exhibits a spiral precession around it during the relaxation process [78–80]. This motion has a characteristic frequency which is determined by the shape of the dot. Thus, the nanodot functions as a resonator for vortex core motion.

4.2. Current-driven resonant excitation of magnetic vortex

As is clear from Fig. 12, the underlying physics of the current-driven DW motion is that spin currents can apply a torque on the magnetic moment when the spin direction of the conduction electrons has a relative angle to the local magnetic moment. This leads us to the hypothesis that any type of spin structure with spatial variation can be excited by a spin-polarized current in a ferromagnet.

The ideal example of such a non-collinear spin structure is a curling magnetic structure ("magnetic vortex") realized in a ferromagnetic circular nanodot described in the previous section. In this section, current-induced dynamics of a vortex core in a ferromagnetic dot will be discussed. It is shown that a magnetic vortex core can be resonantly excited by an AC current through the dot when the current frequency is tuned to the resonance frequency originating from the confinement of the vortex core in the dot [81]. The core is efficiently excited by the AC current due to the resonant nature and the resonance frequency is tunable by the dot shape. It is also demonstrated that the direction of a vortex core can be switched by utilizing the current-driven resonant dynamics of the vortex.

The current-induced dynamics of the vortex core was calculated by the micromagnetic simulations based on the LLG equation,

$$\frac{\partial \boldsymbol{m}}{\partial t} = -\gamma_0 \boldsymbol{m} \times \boldsymbol{H}_{\text{eff}} + \alpha \boldsymbol{m} \times \frac{\partial \boldsymbol{m}}{\partial t} - (\boldsymbol{u} \cdot \nabla)\boldsymbol{m}, \tag{3}$$

with modifications due to electric/spin current [41, 42]. Here $\boldsymbol{m}$ is a unit vector along the local magnetization, γ_0 is the gyromagnetic ratio, $\boldsymbol{H}_{\text{eff}}$ is the effective magnetic field including the exchange and the demagnetizing fields and α is the Gilbert damping constant. The third term on the right-hand side represents the spin-transfer torque, which describes the effect of spin transfer from conduction electrons to localized spins. This spin-transfer effect is a combined effect of the spatial non-uniformity of magnetization and the current flow. The vector $\boldsymbol{u} = -jPg\mu_B/(2eM_s)$, which has the dimension of velocity, is essentially the spin current associated with the electric current in a ferromagnet, where j is the current density, P the spin polarization of the current, g the g-value of an electron, μ_B the Bohr magneton, e the elementary charge and M_s the saturation magnetization.

First, we determined the eigenfrequency f_0 of the vortex core precession in the dot by calculating the free relaxational motion of the vortex core from the off-centred position. The eigenfrequency depends on the aspect ratio h/r (the height h to the radius r) of the dot [78]. Then, the simulations were performed by applying an AC current at a given frequency f in the absence of a magnetic field. Figure 24A shows the time evolution of the core position when an AC current ($f = f_0 = 380$ MHz and $J_0 = 3 \times 10^{11}$ A/m^2) is applied to a dot with $r = 410$ nm and

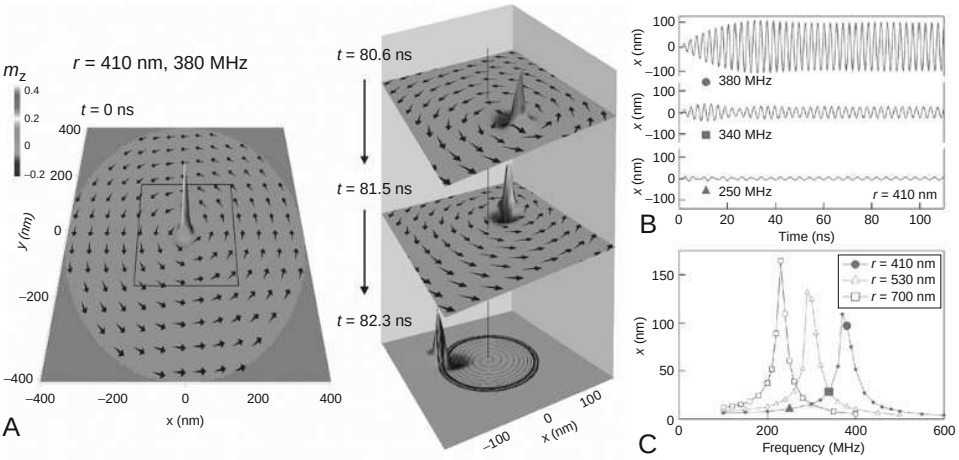

FIGURE 24 (A) Time evolution of the vortex under the AC current application. Magnetization direction $\boldsymbol{m} = (m_x, m_y, m_z)$ inside the dot on the xy-plane was obtained by micromagnetic simulation. The 3D plots indicate m_z with the $m_x - m_y$ vector plots superimposed. The plot on the left represents the initial state of the vortex core situated at the centre of the dot with $r = 410$ nm. The 3D plots on the right show the vortex on the steady orbital at $t = 80.6$, 81.5 and 82.3 ns after applying the AC current ($f_0 = 380$ MHz and $J_0 = 3 \times 10^{11}$ A/m^2). These plots are close-ups of the square region around the dot centre indicated by the black square in the plot on the left. The time evolution of the core orbital from $t = 0$ to 100 ns is superimposed only on the $t = 82.3$ ns plot. (B) Time evolutions of the vortex core displacement (x) for three excitation frequencies $f = 250$, 340 and 380 MHz ($r = 410$ nm and $J_0 = 3 \times 10^{11}$ A/m^2). (C) Radius of the steady orbital as a function of the frequency for the dots with $r = 410$, 530 and 700 nm [81].

$h = 40$ nm. Once the AC current is applied, the vortex core first moves in the direction of the electron flow or spin current. This motion originates from the spin-transfer effect. The off-centred core is then subjected to a restoring force towards the dot centre. However, because of the gyroscopic nature of the vortex (i.e. a vortex moves perpendicularly to the force), the core makes a circular precessional motion around the dot centre [78]. The precession is amplified by the current to reach a steady orbital motion where the spin transfer from the current is balanced with the damping, as depicted in Fig. 24A. The direction of the precession depends on the direction of the core magnetization as in the motion induced by the magnetic field [78, 82]. It should be noted that the radius of the steady orbital on resonance is larger by more than an order of magnitude as compared to the displacement of the vortex core induced by a DC current of the same amplitude [83]. Thus, the core is efficiently excited by the AC current due to resonance.

Figure 24B shows the time evolutions of the x position of the vortex core for three different excitation frequencies $f = 250$, 340 and 380 MHz. The steady state appears after around 30 ns on resonance ($f = 380$ MHz). For $f = 340$ MHz slightly off the resonance, the amplitude beats first, and then the steady state with smaller amplitude appears. The vortex core shows only a weak motion for $f = 250$ MHz, which is quite far from the resonance. Figure 24C shows the radii of the steady orbitals as a function of the current frequency for the dots with $r = 410$, 530 and 700 nm. Each dot exhibits the resonance at the eigenfrequency of the vortex motion.

To experimentally detect the resonant excitation of a vortex core predicted by the micromagnetic simulation, we measured the resistance of the dot while an AC excitation current was passed through it at room temperature in the configuration shown in Fig. 25. A scanning electron microscope image of the sample is shown in Fig. 25. Two wide Au electrodes with 50-nm thickness, through which an AC

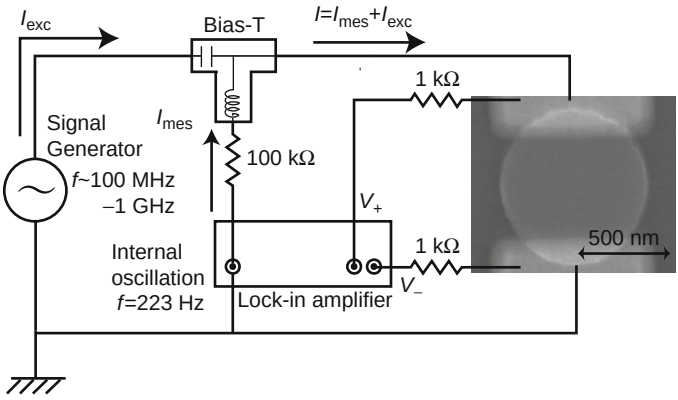

FIGURE 25 Scanning electron microscope image of the sample along with a schematic configuration used for the measurements. The detection of the vortex excitation was performed by resistance measurements with a lock-in technique (223 Hz and current $I_{mes} = 15$ μA) under the application of an AC excitation current $I_{exc} = 3 \times 10^{11}$ A/m^2 [81].

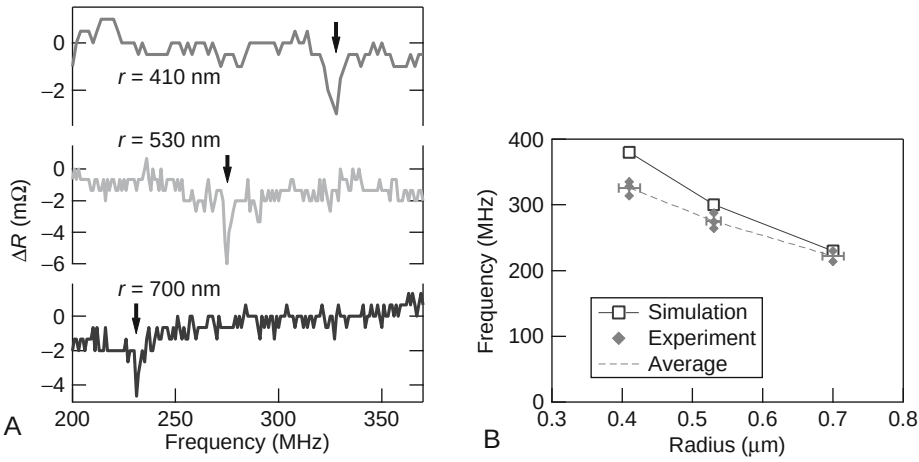

FIGURE 26 (A) Experimental detection of the current-driven resonant excitation of a magnetic vortex core. The resistances are indicated as a function of the frequency of the AC excitation current for the dots with three different radii $r = 410$, 530 and 700 nm. (B) Radius dependence of the resonance frequency. The blue rectangles and the red circles indicate the simulation and the experimental results, respectively. The experimental results for eight samples are plotted. The red dashed line is the averaged value of the experimental data [81]. (For interpretation of the references to colour in this figure legend, the reader is referred to the web version of this chapter.)

excitation current is supplied, are also seen. The amplitude of the AC excitation current was 3×10^{11} A/m^2. Figure 26A shows the resistances as a function of the frequency of the AC excitation current for the dots with three different radii $r = 410$, 530 and 700 nm. A small but clear dip is observed for each dot; this signifies the resonance. The radius dependence of the resonance frequency is well reproduced by the simulation, as shown in Fig. 26B.

4.3. Switching a vortex core by electric current

During the study on the current-driven resonant excitation of magnetic vortex, we found that higher excitation currents induce even the switching of the core magnetization during the circular motion [84]. Figure 27A–F are successive snapshots of the calculated results for the magnetization distribution during the process of core motion and switching, showing that the reversal of the core magnetization takes place in the course of the circular motion without going out of the dot. Noteworthy is the development of an out-of-plane magnetization (dip) which is opposite to the core magnetization (Figs 27A–D). Figure 29A displays the vortex core trajectory corresponding to Fig. 27. One sees that, after switching, the core steps towards the disc centre and starts rotating in the opposite sense, again evidencing the core switching.

We confirmed the predicted current-induced switching of the vortex core by the MFM observation as described below [84]. First, the direction of a core magnetization was determined by MFM observation. A dark spot at the centre

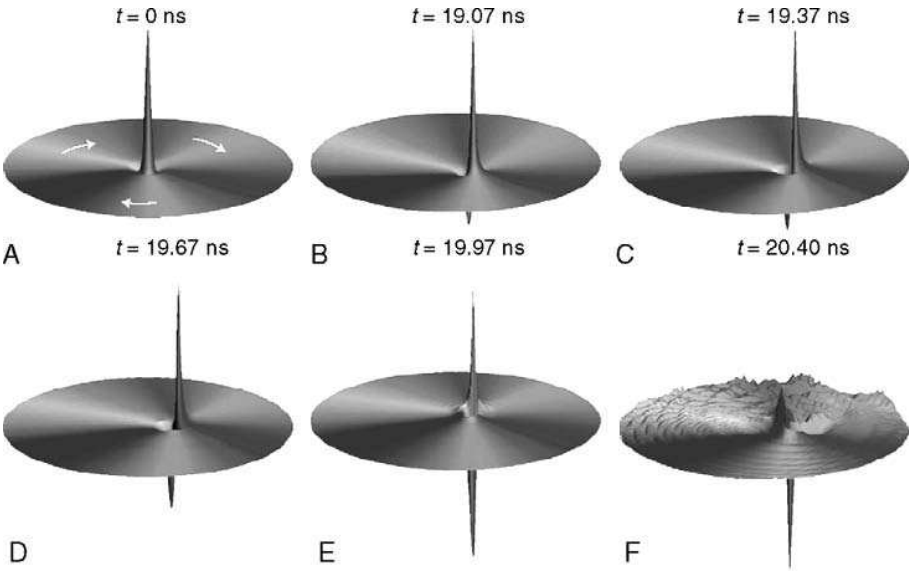

FIGURE 27 Perspective view of the magnetization with a moving vortex structure. The height is proportional to the out-of-plane (z) magnetization component. Rainbow colour indicates the in-plane component as exemplified by the white arrows in (A). (A) Initially, a vortex core magnetized upward is at rest at the disc centre. (B) On application of the AC current, the core starts to make a circular orbital motion around the disc centre. There appears a region with downward magnetization (called "dip" here) on the inner side of the core. (C–E) The dip grows slowly as the core is accelerated. When the dip reaches the minimum, the reversal of the initial core starts. (F) After the completion of the reversal, the stored exchange energy is released to a substantial amount of spin waves. A positive "hump" then starts to build up, which will trigger the next reversal. Calculation with $h = 50$ nm, $R = 500$ nm and $J_0 = 4 \times 10^{11}$ A/m^2 [81]. (For interpretation of the references to colour in this figure legend, the reader is referred to the web version of this chapter.)

of the disc in Fig. 28B indicates that the core magnetization directs upward with respect to the paper plane. The core direction was checked again after the application of an AC excitation current of frequency $f = 290$ MHz and amplitude $J_0 = 3.5 \times 10^{11}$ A/m^2 through the disc, with the duration of about 10 s. Here, the current densities were evaluated by dividing current by the disc diameter times thickness. As shown in Fig. 28C, the dark spot at the centre of the disc changed into bright after the application of the excitation current, indicating that the core magnetization has been switched. Figure 28B–L are successive MFM images with an excitation current applied between each consecutive image. It was observed that the direction of the core magnetization after application of the excitation current was changed randomly. This indicates that the switching occurred frequently compared to the duration of the excitation current (about 10 s) and the core direction was determined at the last moment when we turned off the excitation current.

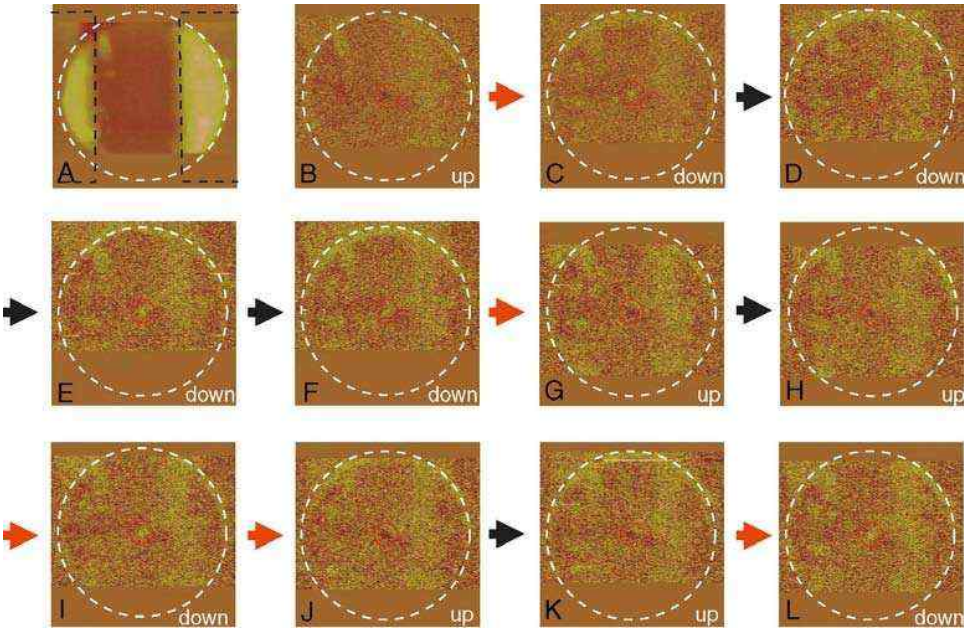

FIGURE 28 MFM observation of electrical switching of vortex core. (A) AFM image of the sample. A permalloy disc fills inside the white circle. The thickness of the disc is 50 nm and the radius is 500 nm. Two wide Au electrodes with 50-nm thickness, through which an AC excitation current is supplied, are also seen. (B) MFM image before the application of the excitation current. A dark spot at the centre of the disc (inside the red circle) indicates that the core magnetization directs upward with respect to the paper plane. (C) MFM image after the application of the AC excitation current at a frequency $f = 290$ MHz and amplitude $J_0 = 3.5 \times 10^{11}$ A/m^2 through the disc with the duration of about 10 s. The dark spot at the centre of the disc in (B) changed into the bright spot, indicating the switching of the core magnetization from up to down. (B–L) Successive MFM images with excitation current applied similarly between consecutive images. The switching of the core magnetization occurs from (B) to (C), (F) to (G), (H) to (I), (I) to (J) and (K) to (L) [81]. (For interpretation of the references to colour in this figure legend, the reader is referred to the web version of this chapter.)

Figure 29B shows the core velocity as a function of excitation time which was obtained by the micromagnetic simulation. The sudden decreases of velocity correspond to the repeated core-switching events. Worth noting is that the core switches when its velocity reaches a certain value, $v_{\text{switch}} \approx 250$ m/s here, regardless of the value of the excitation current density. This is the crucial key to understand the switching mechanism together with the existence of the dip structure which appears just before the core switching. The rotational motion of the core is accompanied by the magnetization dynamics in the vicinity of the core. This magnetization dynamics in the dot plane produces so-called damping torque perpendicular to the plane according to the second term of Eq. (3), which generates the dip structure seen in Figs 27B–E. The higher core velocity leads to the stronger damping torque, and eventually the core switching occurs at the

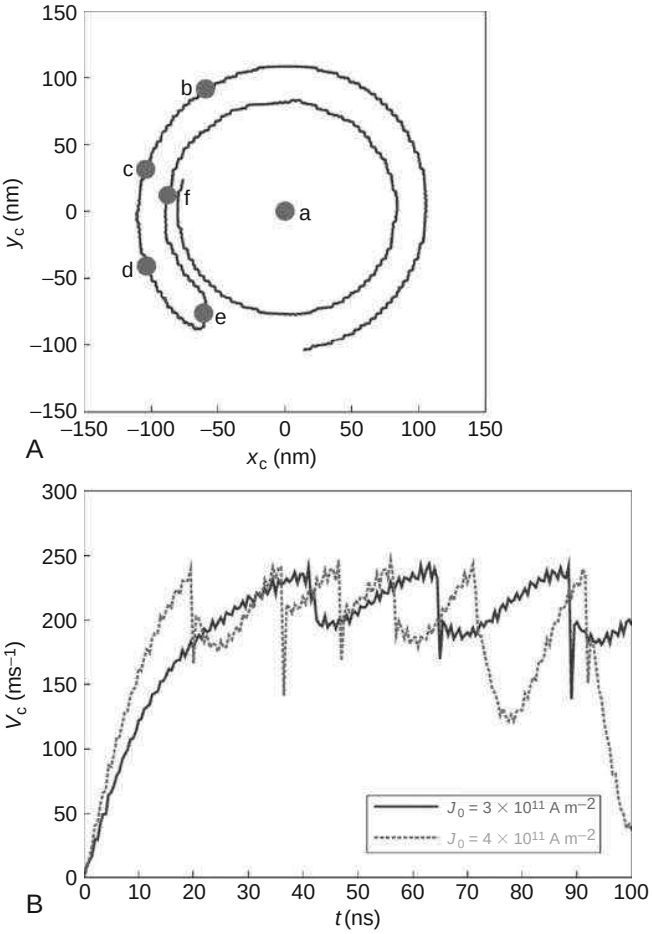

FIGURE 29 Core dynamics under AC spin-polarized current. The calculation was performed for the same disc as in Fig. 27. (A) In-plane trajectory of the core motion of Fig. 27 ($J_0 = 4 \times 10^{11}$ A/m^2), from $t = 17.5$ to 23 ns with the snapshot points indicated. (B) Magnitude of the core velocity as a function of time, for two choices of the current density, showing that the maximum velocity is the same [81].

threshold core velocity. If the core switching is governed by the core velocity, the switching should occur regardless of how the core has the threshold velocity. In fact, the core switching was also observed by the resonant excitation with AC magnetic field [85].

It has been shown that an electric current can switch the direction of a vortex core in a magnetic disc. The current necessary for the switching is only several mA, while the core switching by an external magnetic field needs a large magnetic field of several kOe as described in Section 4.1 [77]. Although the repeated vortex core switching by a continuous AC current was presented here, it will be possible

to control the core direction by a current with an appropriate waveform. The quantitative agreement between experiment and micromagnetic simulation demonstrates the validity of the micromagnetic description of the spin-transfer torque. Given the presently observed discrepancies between measured and calculated results on the current-induced domain-wall motion, the agreement obtained here, on a non-trivial physical effect, is very important. The current-induced vortex core switching can be used as an efficient data writing method for a memory device in which the data are stored in a nanometre size core.

It was shown very recently that a nanosecond single current pulse can switch the core magnetization [86]. This method has advantages over the core switching by using the resonance effect described above; it gives short switching time as well as controllability of the core direction which is indispensable in the applications, although the pulse method requires an order higher current density.

ACKNOWLEDGEMENTS

This work was partly supported by NEDO, MEXT and JSPS of Japan. The authors thank S. Kasai, K. Kobayashi, K. Mibu, N. Nakatani, A. Thiaville, G. Tatara and H. Kohno for fruitful discussions.

REFERENCES

[1] Weiss, P. (1907). *J. Phys.* **6**, 661.
[2] Baibich, M. N., Broto, J. M., Fert, A., Nguyen Van Dau, F., Petroff, F., Etienne, P., Creuzet, G., Friederich, A., and Chazelas, J. (1988). *Phys. Rev. Lett.* **61**, 2472.
[3] Ono, T., Miyajima, H., Shigeto, K., and Shinjo, T. (1998). *Appl. Phys. Lett.* **72**, 1116.
[4] Shigeto, K., Shinjo, T., and Ono, T. (1999). *Appl. Phys. Lett.* **75**, 2815.
[5] Himeno, A., Ono, T., Nasu, S., Shigeto, K., Mibu, K., and Shinjo, T. (2003). *J. Appl. Phys.* **93**, 8430.
[6] Himeno, A., Okuno, T., Ono, T., Mibu, K., Nasu, S., Shinjo, T., and Magn, J. (2005). *Magn. Mater.* **286**, 16.
[7] Grollier, J., Boulenc, P., Cros, V., Hamzic, A., Vaures, A., Fert, A., and Faini, G. (2003). *Appl. Phys. Lett.* **83**, 509.
[8] Astumian, R. D., *et al.* (1997). *Science* **276**, 917.
[9] Reimann, P. (2002). *Phys. Rep.* **361**, 57.
[10] Astumian, R. D., and Hänggi, P. (2002). *Phys. Today* **55**, 33.
[11] Linke, H., Humphrey, T. E., Löfgren, A., Sushkov, A. O., Newbury, R., Taylor, R. P., and Omling, P. (1999). *Science* **286**, 2314.
[12] Linke, H. (ed.) (2002). Special issue on "Ratchets and Brownian Motors: Basics, Experiments and Applications". *Appl. Phys. A* **75**(2).
[13] Hayashi, N., Hsu, C., Romankiw, L., and Krongelb, S. (1972). *IEEE Trans. Magn.* **8**, 16.
[14] Hayashi, N. (1972). *IBM Res.* **March 1**, RC3754.
[15] Himeno, A., Okuno, T., Kasai, S., Ono, T., Nasu, S., Mibu, K., and Shinjo, T. (2005). *J. Appl. Phys.* **97**, 066101.
[16] Allwood, D. A., Xiong, G., and Cowburn, R. P. (2005). *Appl. Phys. Lett.* **85**, 2848.
[17] Himeno, A., Kasai, S., and Ono, T. (2005). *Appl. Phys. Lett.* **87**, 243108.
[18] Sixtus, K. J., and Tonks, L. (1931). *Phys. Rev.* **37**, 930.
[19] Ono, T., Miyajima, H., Shigeto, K., Mibu, K., Hosoito, N., and Shinjo, T. (1999). *Science* **284**, 468–470.
[20] Himeno, A., Ono, T., Nasu, S., Okuno, T., Mibu, K., Shinjo, T., and Magn, J. (2004). *Magn. Mater.* **272–276**, 1577.

[21] Atkinson, D., Allwood, D. A., Xiong, G., Cooke, M. D., Faulkner, C. C., and Cowburn, R. P. (2003). *Nat. Mater.* **2**, 85.
[22] Beach, G. S. D., Nistor, C., Knutson, C., Tsoi, M., and Erskine, J. L. (2005). *Nat. Mater.* **4**, 741.
[23] Nakatani, Y., Thiaville, A., and Miltat, J. (2003). *Nat. Mater.* **2**, 521.
[24] Schryer, N. L., and Walker, L. R. (1974). *J. Appl. Phys.* **45**, 5406.
[25] Slonczewski, J. C. (1972). *Int. J. Magn.* **2**, 85.
[26] Slonczewski, J. C. (1974). *J. Appl. Phys.* **45**, 2705.
[27] Malozemoff, A. P., and Slonczewski, J. C. (1979). "Magnetic Domain Walls in Bubble Materials." Academic Press, New York.
[28] Redjdal, M., Giusti, J., Ruane, M. F., and Humphrey, F. B. (2002). *J. Appl. Phys.* **91**, 7547.
[29] Berger, L. (1984). *J. Appl. Phys.* **55**, 1954.
[30] Berger, L. (1992). *J. Appl. Phys.* **71**, 2721.
[31] Freitas, P. P., and Berger, L. (1985). *J. Appl. Phys.* **57**, 1266.
[32] Hung, C. Y., and Berger, L. (1988). *J. Appl. Phys.* **63**, 4276.
[33] Allwood, D. A., Xiong, G., Cooke, M. D., Faulkner, C. C., Atkinson, D., Vernier, N., and Cowburn, R. P. (2002). *Science* **296**, 2003.
[34] Versluijs, J. J., Bari, M. A., and Coey, J. M. D. (2001). *Phys. Rev. Lett.* **87**, 026601.
[35] Parkin, S. S. P. (2004). U.S. Patent No. 6834005.
[36] Numata, H., Suzuki, T., Ohshima, N., Fukami, S., Ishiwata, K., and Kasai, N. (2007). "Symposium on VLSI Technical Digest", pp. 232–233.
[37] Tatara, G., and Kohno, H. (2004). *Phys. Rev. Lett.* **92**, 086601.
[38] Li, Z., and Zhang, S. (2004). *Phys. Rev. Lett.* **92**, 207203.
[39] Zhang, S., and Li, Z. (2004). *Phys. Rev. Lett.* **93**, 127204.
[40] Waintal, X., and Viret, M. (2004). *Europhys. Lett.* **65**, 427.
[41] Thiaville, A., Nakatani, Y. Miltat, J., and Vernie, N. (2004). *J. Appl. Phys.* **95**, 7049.
[42] Thiaville, A., Nakatani, Y. Miltat, J., and Suzuki, Y. (2005). *Europhys. Lett.* **69**, 990.
[43] Koo, H., Krafft, C., and Gomez, R. D. (2002). *Appl. Phys. Lett.* **81**, 862.
[44] Tsoi, M., Fontana, R. E., and Parkin, S. S. P. (2003). *Appl. Phys. Lett.* **83**, 2617.
[45] Klaui, M., Vaz, C. A. F., Bland, J. A. C., Wemsdorfer, W., Fani, G., Cambril, E., and Heyderman, L. J. (2003). *Appl. Phys. Lett.* **83**, 105.
[46] Kimura, T., Otani, Y., Tsukagoshi, K., and Aoyagi, Y. (2003). *J. Appl. Phys.* **94**, 07947.
[47] Yamaguchi, A., Ono, T., Nasu, S., Miyake, K., Mibu, K., and Shinjo, T.(2004). *Phys. Rev. Lett.* **92**, 077205; *Phys. Rev. Lett.* **96**, 179904(E) (2006).
[48] Lim, C. K., Devolder, T., Chappert, C., Grollier, J., Cros, V., Vaures, A., Fert, A., and Faini, G. (2004). *Appl. Phys. Lett.* **84**, 2820.
[49] Vernier, N., Allwood, D. A., Atkinson, D., Cooke, M. D., and Cowburn, R. P. (2004). *Europhys. Lett.* **65**, 526.
[50] Yamanouchi, M., Chiba, D., Matsukura, F., and Ohno, H. (2004). *Nature* **428**, 539.
[51] Saitoh, E., Miyajima, H., Yamaoka, T., and Tatara, G. (2004). *Nature* **432**, 203.
[52] Klaui, M., Vaz, C. A. F., Bland, J. A. C., Wernsdorfer, W., Faini, G., Cambril, E., Heyderman, L. J., Nolting, F., and Rüdiger, U. (2005). *Phys. Rev. Lett.* **94**, 106601.
[53] Klaui, M., Jubert, P. O., Allenspach, R., Bischof, A., Bland, J. A. C., Faini, G., Rüdiger, U., Vaz, C. A. F., Vila, L., and Vouille, C. (2005). *Phys. Rev. Lett.* **95**, 026601.
[54] Yamaguchi, A., Nasu, S., Tanigawa, H., Ono, T., Miyake, K., Mibu, K., and Shinjo, T. (2005). *Appl. Phys. Lett.* **86**, 012511.
[55] Ravelosona, D., Lacour, D., Katine, J. A., Terris, B. D., and Chapper, C. (2005). *Phys. Rev. Lett.* **95**, 117203.
[56] Yamaguchi, A., Yano, K., Tanigawa, H., Kasai, S., and Ono, T. (2006). *Jpn. J. Appl. Phys.* **45**, 3850.
[57] Beach, G. S. D., Knutson, C., Nistor, C., Tsoi, M., and Erskine, J. L. (2006). *Phys. Rev. Lett.* **97**, 057203.
[58] Hayashi, M., Thomas, L., Bazaliy, Y. B., Rettner, C., Moriya, R., Jiang, X., and Parkin, S. S. P. (2006). *Phys. Rev. Lett.* **96**, 197207.
[59] Fukumoto, K., Kuch, W., Vogel, J., Romanens, F., Pizzini, S., Camarero, J., Bonfim, M., and Kirschner, J. (2006). *Phys. Rev. Lett.* **96**, 097204.
[60] Laufenberg, M., Bührer, W., Bedau, D., Melchy, P. E., Kläui, M., Vila, L., Faini, G., Vaz, C. A. F., Bland, J. A. C., and Rüdiger, U. (2006). *Phys. Rev. Lett.* **97**, 046602.

[61] Thomas, L., Hayashi, M., Jiang, X., Moriya, R., Rettner, C., and Parkin, S. S. P. (2006). *Nature* **443**, 197.
[62] Yamanouchi, M., Chiba, D., Matsukura, F., Dietl, T., and Ohno, H. (2006). *Phys. Rev. Lett.* **96**, 096601.
[63] Klaui, M., Laufenberg, M., Heyne, L., Backes, D., and Rüdiger, U. (2006). *Appl. Phys. Lett.* **88**, 232507.
[64] Togawa, Y., Kimura, T., Harada, K., Akashi, T., Matsuda, T., Tonomura, A., and Otani, Y. (2006). *Jpn. J. Appl. Phys.* **45**, L683.
[65] Togawa, Y., Kimura, T., Harada, K., Akashi, T., Matsuda, T., Tonomura, A., and Otani, Y. (2006). *Jpn. J. Appl. Phys.* **45**, L1322.
[66] Hayashi, M., Thomas, L., Rettner, C., Moriya, R., Bazaliy, Y. B., and Parkin, S. S. P. (2007). *Phys. Rev. Lett.* **98**, 037204.
[67] Thomas, L., Hayashi, M., Jiang, X., Moriya, R., Rettner, C., and Parkin, S. S. P. (2007). *Science* **315**, 1553.
[68] Parkin, S. S. P., *et al.* (2008). *Science* **320**, 190.
[69] Fukami, *et al.* (2008). *J. Appl. Phys.* **103**, 07E718.
[70] Jung, S. W., *et al.* (2008). *Appl. Phys. Lett.* **92**, 202508.
[71] Tanigawa, H., *et al.* (2008). *Appl. Phys. Express* **1**, 011301.
[72] Koyama, T., *et al.* (2008). *Appl. Phys. Express* **1**, 101303.
[73] Hubert, A., and Schafer, H. (1998). "Magnetic Domains." Springer, Berlin.
[74] Cowburn, R. P., Koltsov, D. K., Adeyeye, A. O., and Welland, M. E. (1999). *Phys. Rev. Lett.* **83**, 1042.
[75] Shinjo, T., Okuno, T., Hassdorf, R., Shigeto, K., and Ono, T. (2000). *Science* **289**, 930.
[76] Wachowiak, A., Wiebe, J., Bode, M., Pietzsch, O., Morgenstern, M., and Wiesendanger, R. (2002). *Science* **298**, 577.
[77] Okuno, T., Shigeto, K., Ono, T., Mibu, K., Shinjo, T., and Magn, J. (2002). *Magn. Mater.* **240**, 1.
[78] Guslienko, K. Yu., Ivanov, B. A., Novosad, V., Otani, Y., Shima, H., and Fukamichi, K. (2002). *J. Appl. Phys.* **91**, 8037.
[79] Park, J. P., Eames, P., Engebretson, D. M., Berezovsky, J., and Crowell, P. A. (2003). *Phys. Rev. B* **67**, 020403.
[80] Choe, S. B., Acremann, Y., Scholl, A., Bauer, A., Doran, A., Stöhr, J., and Padmore, H. A. (2004). *Science* **304**, 420.
[81] Kasai, S., Nakatani, Y., Kobayashi, K., Kohno, H., and Ono, T. (2006). *Phys. Rev. Lett.* **97**, 107204.
[82] Shibata, J., Nakatani, Y., Tatara, G., Kohno, H., and Otani, Y. (2006). *Phys. Rev. B* **73**, 020403.
[83] Ishida, T., Kimura, T., and Otani, Y. (2006). *Phys. Rev. B* **74**, 014424.
[84] Yamada, K., Kasai, S., Nakatani, Y., Kobayashi, K., Kohno, H., Thiaville, A., and Ono, T. (2007). *Nat. Mater.* **6**, 269.
[85] Waeyenberge, B. V., Puzic, A., Stoll, H., Chou, K. W., Tyliszczak, T., Hertel, R., Fähnle, M., Brückl, H., Rott, K., Reiss, G., Neudecker, I., Weiss, D., Back, C. H., and Schütz, G. (2006). *Nature* **444**, 461.
[86] Yamada, K., *et al.* (2008). *Appl. Phys. Lett.* **93**, 152502.

CHAPTER 5

Theoretical Aspects of Current-Driven Magnetization Dynamics

H. Kohno* and **G. Tatara†**

Contents

Abstract

Current-driven domain-wall motion and related phenomena are reviewed from a theoretical point of view. In the first part, the dynamics of a rigid domain wall is described based on the collective-coordinate method. After an elementary introduction, the equations of motion are derived for the position and the polarization of the wall, where the effect of the current enters as spin transfer and momentum transfer (or force). The wall motion is studied in the presence of magnetic anisotropy and extrinsic pinning, and several depinning mechanisms are found. The depinning current is determined in each case. The second part is concerned with the microscopic derivation of the spin torques for slowly varying magnetization dynamics as described by

*Graduate School of Engineering Science, Osaka University, Toyonaka 560-8651, Japan
†Graduate School of Science, Tokyo Metropolitan University, Hachioji, Tokyo 192-0397, Japan

Nanomagnetism and Spintronics
DOI: 10.1016/B978-0-444-53114-8.00005-4

the Landau–Lifshitz–Gilbert equation. In addition to the well-established spin-transfer torque, two new torques are shown to arise from the spin-relaxation process and the non-adiabatic process (reflection) of conduction electrons. These new torques act as the momentum transfer on a rigid wall, and can be important in domain-wall dynamics. Some related topics are described in the third part, which includes current-driven dynamics of magnetic vortices, and the current-induced spin-wave instability and domain-wall nucleation.

Key Words: Magnetic domain wall, Field-driven motion, Current-driven motion, Spin current, Spin-transfer effect, Momentum-transfer effect, Force, Magnetotransport, Magnetic anisotropy, Intrinsic pinning, Extrinsic pinning, Threshold current, Döring mass, Landau–Lifshitz–Gilbert equation, Spin torque, Gilbert damping, Adiabatic spin torque, Non-adiabatic spin torque, Spin relaxation, Kubo formula, Gauge field, s–d exchange interaction, s–d model, Stoner model, Spin chirality, Magnetic vortex, Spin-wave instability, Nucleation, Permalloy, Ferromagnetic semiconductor.

1. INTRODUCTION

Magnetization dynamics driven by electric/spin current in submicron-scale ferromagnets has been a subject of active study for a decade in the field of spintronics [1, 2]. It includes magnetization reversal in multilayer systems, displacive and resonant motions of domain walls in thin wires, and those of magnetic vortices realized in disks. These phenomena are understood as caused by spin torques, the effect that conduction electrons exert on magnetization through the microscopic s–d exchange interaction.

Recent activity on this subject was triggered by the concept of "spin-transfer effect" introduced by Slonczewski [3] and Berger [4]. On the other hand, it should be remembered that the idea of driving domain walls by electric current was proposed long ago by Berger. He recognized that the s–d exchange interaction should be the main origin of the driving in thin samples [5], and proposed the driving mechanisms that are called s–d exchange force (momentum-transfer effect) [5] and s–d exchange torque (spin-transfer effect) [6–8]. Experimental demonstration is also made by him and collaborators using semi-macroscopic samples [9, 10].

The continuous progress during this decade is of course rests on the experimental achievements. The development of fabrication and observation techniques has enabled us to study submicron-scale magnets having simple domain structure, which are suitable for scientific studies under well-controlled conditions, notwithstanding for technological applications. On a theoretical side, modern techniques and viewpoints in solid-state or condensed-matter physics started to be applied, which will hopefully develop further microscopic understanding.

In this chapter, we review some basic aspects of the theory of current-driven magnetization dynamics. We are concerned with magnetization dynamics which are smoothly varying in space and time compared with the microscopic electronic scales. Magnetization is thus treated as a continuous function, $\boldsymbol{n}(\boldsymbol{r}, t)$, of space and

time, and the dynamics is described by the Landau–Lifshitz–Gilbert (LLG) equation. Most prototypical phenomenon is the domain-wall motion. In spite of tremendous amount of works on multilayer (pillar) systems [11], they are outside the scope of this chapter simply because of our lack of ability.

In Section 2, a theoretical treatment is given for the domain-wall motion driven by electric current. We start with an elementary introduction to a theoretical description of domain-wall dynamics, by taking the (magnetic) field-driven case as an example. The effect of electric current will then be introduced to study the main subject of the current-driven domain-wall motion. In Section 3, microscopic calculation of spin torques is described in a more general framework of the LLG equation. Generalization of the force to arbitrary magnetization texture, as well as its relation to transport coefficients are also studied. In Section 4, two related topics, current-driven motion of a magnetic vortex and current-induced spin-wave instability, are surveyed.

2. DYNAMICS OF A RIGID DOMAIN WALL

In this section, we study the dynamics of rigid domain walls by neglecting their deformation. The validity of this approximation will be discussed at the end of this section.

2.1. Field-driven domain-wall motion

Suppose we have two nails made of iron. We know that they are ferromagnets at room temperature, but they do not attract each other. The reason is the existence of the magnetic domain structure, which is formed to lower the magnetostatic energy due to long-range dipole–dipole interaction. The typical size of domains is ∼1–10 μm, and any semi-macroscopic sample inevitably has a multi-domain structure with vanishing total moment in zero field (if, e.g. it is prepared by cooling from above the Curie temperature). On the other hand, nanoscale magnets have simple domain structures suitable for application and basic studies. The transition region between two neighbouring domains, as illustrated in Fig. 1E, is the magnetic domain wall.

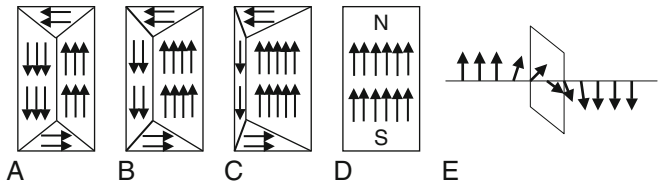

FIGURE 1 (A) Magnetic domain structure with lowest energy in zero external magnetic field. (B–D) The magnetization process due to domain-wall motion. Conventionally, this is induced by applying magnetic field, but also by applying electric current, the latter being the main subject here. (E) An example of magnetic domain wall (Bloch wall).

If we apply an external magnetic field, magnetic domains with lowered magnetic energy grow at the expense of other domains (Fig. 1A–D). This magnetization process occurs as the movement of domain walls. In this section, we shall consider how to describe this field-driven domain-wall motion [12–15]. We assume that the magnetization profile of the wall is rigid, and treat it by the method of collective coordinates.

2.1.1. Phenomenological equation of motion

Consider a ferromagnetic wire containing a single domain wall (Fig. 2), and let the position of the domain wall be X. If we apply an external magnetic field, B, in the easy-axis direction, the energy of the whole magnet depends on X as

$$E_{\mathrm{B}} = -2\gamma_0 \hbar SB \frac{AX}{a^3} + \text{constant}. \tag{1}$$

Here, we are considering magnetic moments due to localized spins of magnitude S and gyromagnetic ratio γ_0 [16]. A is the cross-sectional area of the wire and a^3 is the volume per spin. If we regard the domain wall as a particle, whose position is X, Eq. (1) represents a potential energy of this particle. This means that this particle feels a force,

$$F_{\mathrm{B}} = 2\gamma_0 \hbar SB \frac{A}{a^3}, \tag{2}$$

proportional to B. One may then expect, naively, that the motion of this particle may be described by an equation something like

$$M_{\mathrm{w}} \ddot{X} = F_{\mathrm{B}} - \eta \dot{X}. \tag{3}$$

Here, the dot represents time derivative and η is a friction constant. This is indeed a very naive expectation, but it is known that Eq. (3) holds under certain circumstances. In particular, a domain wall has inertial mass, M_{w}, known as the Döring mass [17]. To see this, and to derive the correct equations of motion for a domain wall, let us next look into the dynamics of individual spins in the domain wall.

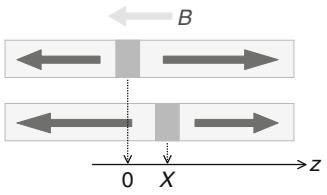

FIGURE 2 A ferromagnetic wire containing a single domain wall. The position of the domain wall is denoted by X. Thick arrows represent magnetization direction rather than spin direction [16].

2.1.2. Equations of motion from microscopic spin dynamics

To see how the domain-wall motion occurs at the microscopic spin level, let us first set up a microscopic model. We assume that the magnetization is carried by localized spins, $\boldsymbol{S}_i$, located at each site i on a lattice, which are described by the following spin Hamiltonian:

$$H_{\mathrm{S}} = -\tilde{J}\sum_{\langle i,j\rangle}\boldsymbol{S}_i\cdot\boldsymbol{S}_j + \frac{1}{2}\sum_i (K_\perp S_{i,y}^2 - KS_{i,z}^2). \tag{4}$$

Here, $\tilde{J}$ is the exchange coupling constant, and K and $K_\perp$ represent easy- and hard-axis anisotropy constants, respectively. We have chosen the easy axis to be z-axis, and the hard axis to be y-axis ($K > 0, K_\perp \geq 0$). In the ground state of a domain wall, the spins lie in the xz-plane, called easy plane (see Fig. 4A).

Each spin obeys a simple law of angular-momentum dynamics. It continues precessing around an effective field $\boldsymbol{H}_{\mathrm{eff}}$ if there is no damping (Fig. 3A). In the presence of damping, the precession will decay and the spin (or, precisely speaking, the associated magnetic moment) eventually points to the direction of $\boldsymbol{H}_{\mathrm{eff}}$ (Fig. 3B). These are described by the equation [12, 18]

$$\frac{\mathrm{d}\boldsymbol{S}}{\mathrm{d}t} = -\gamma_0\boldsymbol{S}\times\boldsymbol{H}_{\mathrm{eff}} - \alpha\frac{\boldsymbol{S}}{S}\times\frac{\mathrm{d}\boldsymbol{S}}{\mathrm{d}t}. \tag{5}$$

The first term on the right-hand side describes precession. The second term represents damping, called Gilbert damping, with α being a dimensionless damping constant. In this section, we consider the case of no damping ($\alpha = 0$) for simplicity.

Back to the domain-wall solution of Eq. (4), suppose a magnetic field $\boldsymbol{B} = (0, 0, -B)$ is applied along the easy axis. It is represented by the additional term

$$H_{\mathrm{B}} = -\gamma_0\hbar B\sum_i S_{i,z} \tag{6}$$

in the Hamiltonian. Then, what happens for spins? Since the spins in the domain wall are not parallel to the field $\boldsymbol{B}$, they will precess around $\boldsymbol{B}$, that is, around the

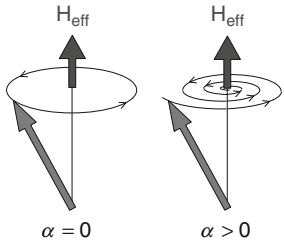

FIGURE 3 Dynamics of a single spin (or precisely, magnetic moment [16]) in an effective field $\boldsymbol{H}_{\mathrm{eff}}$. (A) Without damping. (B) With damping. As for the direction of motion, please note Ref. [16].

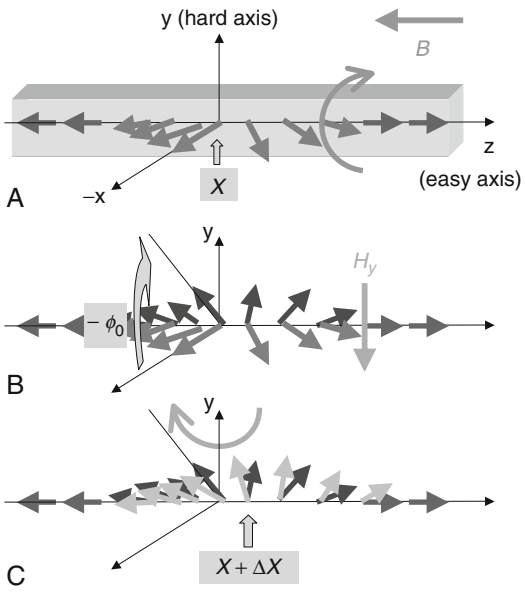

FIGURE 4 Dynamics of spins (actually, arrows shown here are magnetic moments rather than spins [16]) in the domain wall under applied magnetic field $\boldsymbol{B} = (0, 0, -B)$. Spins in the domain wall rotate around the applied field (A), deviate from the easy plane (B) and rotate around the hard axis (C). As a whole, the domain wall makes a translational motion.

easy axis (see Fig. 4B); therefore, they deviate from the easy (xz-) plane and acquire a hard-axis component, S_y. The associated energy increase is given by

$$E_\perp = \frac{1}{2} K_\perp S_y^2 \tag{7}$$

per spin. Then the spins feel an effective field [19]

$$H_y = \frac{1}{\gamma_0 \hbar} \frac{\partial E_\perp}{\partial S_y} = \frac{1}{\gamma_0 \hbar} K_\perp S_y \tag{8}$$

in the hard-axis direction, and will precess around this field (Fig. 4C). Namely, the spins in the domain wall rotate in the easy plane, and this is nothing but the translational motion of the domain wall. The direction of the translation is, as you see, in the correct direction, so that the magnetization occurs in the correct direction.

Let us describe these processes a little more quantitatively. First, the applied $\boldsymbol{B}$ induces a rotation around the easy axis. If we denote the rotation angle by ϕ_0, it obeys the equation

$$\dot{\phi}_0 = -\gamma_0 B. \tag{9}$$

Now we have finite ϕ_0 (hence finite $S_y = S \sin \phi_0$), and the associated increase in energy, $E_\perp = \frac{1}{2} K_\perp S^2 \sin^2 \phi_0$, due to hard-axis anisotropy. This causes a torque

$$T_z = -\frac{\partial E_\perp}{\partial \phi_0} = -K_\perp S^2 \sin\phi_0 \cos\phi_0 \tag{10}$$

in the easy-axis direction, and this torque induces a change of $S^z_{\rm tot} = \sum_i S^z_i$, which is nothing but the domain-wall motion. This process is quantified as

$$\frac{A\dot{X}}{a^3} 2\hbar S = -N\left(\frac{1}{2} K_\perp S^2 \sin 2\phi_0\right) \tag{11}$$

or

$$\frac{\dot{X}}{\lambda} = -\frac{K_\perp S}{2\hbar} \sin 2\phi_0, \tag{12}$$

where $\lambda = a\sqrt{\tilde{J}/K}$ is the domain-wall width [see Eq. (22)], and $N = 2A\lambda/a^3$ is the number of spins in the wall. In Eq. (11), the left-hand side represents the change of angular momentum $S^z_{\rm tot}$ per unit time, and the right-hand side represents a torque acting on N spins [20]. Equations (9) and (11) [or Eq. (12)] describe the domain-wall motion under $\boldsymbol{B}$ applied in the easy-axis direction. The former equation (9) corresponds to the x-, y-components of Eq. (5), and the latter equation (11) corresponds to the z-component, with [21]

$$\boldsymbol{H}_{\rm eff} = \boldsymbol{B} + \frac{1}{\gamma_0 \hbar} \frac{\partial E_\perp}{\partial \boldsymbol{S}}. \tag{13}$$

In Eq. (9), the magnetic field B appears on the right-hand side, which is essentially the force in the particle picture [see Eq. (2)]. According to Newton's equation of motion, it should be equal to the time derivative of "momentum". In this sense, ϕ_0 may be regarded as a momentum of the domain wall [22]. In fact, if $|\phi_0| \ll 1$, we may linearize the sine-term of Eq. (12) as $\dot{X} \simeq -(K_\perp S\lambda/\hbar)\phi_0$, and see that ϕ_0 is proportional to $\dot{X}$, the domain-wall velocity. From the coefficient, one may read the mass of the domain wall as [23]

$$M_{\rm w} = \frac{\hbar^2 N}{\lambda^2} \frac{1}{K_\perp}. \tag{14}$$

This is the inertial mass, known as the Döring mass [17, 24]. This shows a remarkable property of a domain wall that it has inertia. Even if there is no force ($B = 0$) applied, there is a moving solution, $\phi_0 =$ constant and $\dot{X} =$ constant $\neq 0$ (if there is no damping as assumed here). For $|\phi_0| \ll 1$, the energy increase associated with ϕ_0 (hence $\dot{X}$) is written as

$$NE_\perp \simeq \frac{1}{2} M_{\rm w} \dot{X}^2, \tag{15}$$

and the equation of motion takes the form of Eq. (3).

It is noted that $M_{\rm w}$ is inversely proportional to $K_\perp$; if $K_\perp = 0$, the mass $M_{\rm w}$ is divergent, and the domain wall cannot move even if it feels a force. This is a consequence of the conservation of angular momentum $S^z_{\rm tot}$ [25, 26]. Thus, $K_\perp$ works as a source of angular momentum, and, in this sense, $K_\perp$ assists the

domain-wall motion. This feature is characteristic to the field-driven (or more generally, force-driven) motion. Later, we shall see that $K_\perp$ tends to prevent the domain-wall motion if it is driven by the spin-transfer effect.

2.1.3. Lagrangian formulation

Now, we proceed to a little more theoretical treatment and put the analysis into Lagrangian formalism. The Lagrangian formalism is a very convenient method to focus on a few degrees of freedom (such as X and ϕ_0) out of many degrees of freedom. But let us start with a single spin.

The equation of motion of a single spin is given by the LLG equation (5). Apart from the damping term, it is derived from the Lagrangian [16],

$$L = \hbar S\dot{\phi}(\cos\theta - 1) - \gamma_0 \hbar \boldsymbol{S}\cdot\boldsymbol{B} - V_{\rm ani}(\theta,\phi), \tag{16}$$

with $\boldsymbol{H}_{\rm eff} = \boldsymbol{B} + (1/\gamma_0\hbar)(\partial V_{\rm ani}/\partial \boldsymbol{S})$ in Eq. (5). We have parametrized the spin orientation as

$$\boldsymbol{S}(t) = S(\sin\theta\cos\phi,\ \sin\theta\sin\phi,\ \cos\theta), \tag{17}$$

where $\theta = \theta(t)$ and $\phi = \phi(t)$ are dynamical variables. (We assume S is constant.) In Eq. (16), the first term is the kinetic term; this form is known as the spin Berry phase in quantum mechanics [27, 28]; it is important also in classical mechanics in that it leads to the equation of motion characteristic to the angular momentum. (In the present study, we treat the magnetization and domain wall as classical objects.) One can check that the Euler–Lagrange equations

$$\frac{\mathrm{d}}{\mathrm{d}t}\frac{\partial L}{\partial \dot{q}} - \frac{\partial L}{\partial q} = 0 \tag{18}$$

for $q = \theta$ and $q = \phi$, lead to Eq. (5) with $\alpha = 0$.

The Euler–Lagrange formalism does not include damping effects: it conserves energy (if L is not explicitly time dependent). The damping can be included by the Rayleigh's method [29]. With a so-called dissipation function

$$W = \frac{\alpha}{2}\frac{\hbar}{S}\dot{\boldsymbol{S}}^2 = \frac{\alpha}{2}\hbar S(\dot{\theta}^2 + \sin^2\theta\dot{\phi}^2), \tag{19}$$

the Euler–Lagrange equation is now modified as

$$\frac{\mathrm{d}}{\mathrm{d}t}\frac{\partial L}{\partial \dot{q}} - \frac{\partial L}{\partial q} = -\frac{\partial W}{\partial \dot{q}}. \tag{20}$$

One can show that $\mathrm{d}H/\mathrm{d}t = -2W$, where $H = \dot{q}(\partial L/\partial\dot{q}) - L$ is the Hamiltonian; therefore, the quantity $2W$ has a physical meaning as the energy dissipation rate [30]. Equation (20), with (16) and (19), then reproduces the full equation (5).

It is straightforward to extend the above description for a single spin to many-spin systems. Here, we restrict ourselves to spin configurations which are slowly varying in space and time, and adopt a continuum description, $\boldsymbol{S}_i(t) \to \boldsymbol{S}(\boldsymbol{r}, t)$, and write it as Eq. (17) with $\theta = \theta(\boldsymbol{r}, t)$ and $\phi = \phi(\boldsymbol{r}, t)$ now describing spin configurations in a continuum space $\boldsymbol{r}$ and time t. The Lagrangian is then given by

$$L_S = \int \frac{d^3x}{a^3}\left[\hbar S\dot{\phi}(\cos\theta - 1) + \gamma_0 \hbar BS\cos\theta - \frac{S^2}{2}\{J((\nabla\theta)^2 + \sin^2\theta(\nabla\phi)^2) + \sin^2\theta(K + K_\perp \sin^2\phi)\}\right], \tag{21}$$

where $J = \tilde{J}a^2$.

We now restrict ourselves to a fixed magnetization profile representing a single domain wall [31–33]. The Euler–Lagrange equation derived from Eq. (21) has a static domain-wall solution $\theta = \theta_{dw}(x - X)$, $\phi = 0$, where

$$\cos\theta_{dw}(x) = \pm\tanh(x/\lambda), \tag{22}$$

or $\sin\theta_{dw}(x) = (\cosh(x/\lambda))^{-1}$, and X is a constant. (We consider an effectively one-dimensional magnet, and neglect transverse variations.) We then "elevate" the domain-wall position X to a dynamical variable and allow its time dependence, $X = X(t)$. Using this domain-wall solution in Eq. (21), we obtain the Lagrangian for a "rigid" domain wall as

$$L_{dw} = \pm\frac{\hbar NS}{\lambda}\dot{X}\phi_0 - \frac{1}{2}K_\perp NS^2\sin^2\phi_0 \mp F_B X - V_{pin}(X), \tag{23}$$

up to total time derivative. Here

$$\phi_0(t) \equiv \int \frac{dx}{2\lambda}\phi(x,t)\sin^2\theta_{dw}(x - X(t)) \tag{24}$$

is essentially the angle $\phi(x, t)$ at the domain-wall centre. We have introduced a pinning potential $V_{pin}(X)$ for the domain wall coming from spatial irregularities of the sample. The first term of Eq. (23) means that, except for a proportionality constant, X and ϕ_0 are canonical conjugate to each other; namely, ϕ_0 is the canonical momentum conjugate to X. We have noted this fact before by an intuitive argument, but now have shown it mathematically [33]. Similarly, the dissipation function becomes

$$W_{dw} = \alpha\hbar S\frac{A}{a^3}\left(\frac{\dot{X}^2}{\lambda} + \lambda\dot{\phi}_0^2\right). \tag{25}$$

Taking variations with respect to X and ϕ_0, respectively, we obtain the equations of motion for a domain wall as follows:

$$\frac{\hbar NS}{\lambda}\left(\pm\dot{\phi}_0 + \alpha\frac{\dot{X}}{\lambda}\right) = \mp F_B + F_{pin}, \tag{26}$$

$$\frac{\hbar NS}{\lambda}(\pm\dot{X} - \alpha\lambda\dot{\phi}_0) = \frac{NS^2K_\perp}{2}\sin 2\phi_0. \tag{27}$$

These equations (especially, with the lower sign [34]) are equivalent to Eqs (9) and (11), but now include damping effects. The magnetic field acts as a force, $F_B = \gamma_0\hbar(NS/\lambda)B$ [Eq. (2)], and promotes ϕ_0 (i.e. spin rotation around the easy

axis), and the hard-axis anisotropy $K_\perp$ acts as a torque and drives X (i.e. translation of the domain wall). If the system is not spatially uniform, we have a pinning force $F_{\rm pin} = -(\partial V_{\rm pin}/\partial X)$. Note that X and ϕ_0 have opposite time-reversal properties, and their mixing (α-terms) means breaking of time-reversal symmetry and leads to damping. For $|\phi_0| \ll 1$, Eqs (26) and (27) reduce to Eq. (3) with $\eta = \alpha(\hbar NS/\lambda^2)$ [35].

2.2. Current-driven domain-wall motion

In the previous section, we have reviewed the domain-wall motion driven by a magnetic field. The contents presented there will be well-known results; in particular, the theoretical descriptions are equivalent to the LLG equation under the constraint that the magnetization profile is fixed to that of a single domain wall (hence a rigid wall). In this section, we proceed to the main topic of current-driven domain-wall motion [36–51]. We introduce the effect of electric current (due to conduction electrons) into the same formalism. We treat conduction electron and magnetization degrees of freedom as mutually independent [52]. In the following, "magnetization" means that of localized spins. Also, we refer to conduction electrons simply as "electrons".

2.2.1. Interaction of domain wall and electron flow: An intuitive picture

How does the electric current affect the domain-wall motion? The relevant microscopic interaction is the s–d exchange interaction

$$H_{\rm sd} = -J_{\rm sd}\int {\rm d}^3x \boldsymbol{S}(\boldsymbol{r})\cdot\boldsymbol{\sigma}(\boldsymbol{r}) \tag{28}$$

between localized spins $\boldsymbol{S}(\boldsymbol{r})$ and electron spins. Here, $\boldsymbol{\sigma}(\boldsymbol{r}) = c^\dagger(\boldsymbol{r})\boldsymbol{\sigma}c(\boldsymbol{r})$ represents (twice) the spin density of conduction electrons, with $c^\dagger = (c_\uparrow^\dagger, c_\downarrow^\dagger)$ being the electron creation operator. There are certainly other possible effects, such as hydromagnetic or electromagnetic, but they are ineffective in small or thin systems [6], or can be excluded experimentally.

The s–d interaction affects the domain-wall motion in two different ways. One is the momentum transfer, or force, and the other is the spin transfer, or torque.

Consider a metallic ferromagnet containing a single domain wall, and suppose there is an electron flow from left to right (Fig. 5). If an electron is reflected by the domain wall, its momentum is changed (Fig. 5A). This process acts as a force

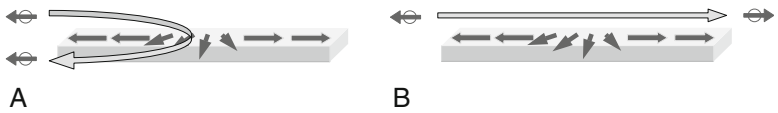

FIGURE 5 Two effects of electric current on the domain wall via the s–d exchange interaction. (A) Reflected electron has transferred linear momentum to the domain wall. (B) Adiabatically transmitted electron has transferred spin angular momentum to the domain wall.

on the domain wall by transferring the linear momentum from the electron to the domain wall. (Note that the s–d interaction (28) is translationally invariant and conserves the total momentum of electrons and magnetization.) This force is proportional to the charge current, j, and domain-wall resistivity, ρ_{w}, as we will show later.

On the other hand, if the electron is transmitted through the domain-wall *adiabatically*, namely, by keeping its spin direction closely parallel to the local magnetization, the spin angular momentum of the electron is changed (Fig. 5B). This process acts as a torque on the domain wall by transferring the spin angular momentum from the electron to the domain wall. (Note that the s–d interaction (28) also conserves the total spin angular momentum of the electrons and magnetization.) In other words, this change of the electron spin should be absorbed by the magnetization, leading to a translational motion of the domain wall. This torque can be shown to be proportional to the spin current, j_{s}, in the adiabatic limit. This is the spin-transfer effect; a conduction electron exerts a (spin-transfer) torque on the domain wall. These two effects were originally found by Berger long ago [5, 6, 8]. The spin-transfer effect is now familiar through recent studies on multilayer or pillar systems [3, 4].

These two effects enter the equations of motion as follows [34]:

$$\frac{\hbar NS}{\lambda}\left(\dot{\phi}_0 + \alpha\frac{\dot{X}}{\lambda}\right) = F_{\mathrm{el}} + F_{\mathrm{B}} + F_{\mathrm{pin}}, \tag{29}$$

$$\frac{\hbar NS}{\lambda}(\dot{X} - \alpha\lambda\dot{\phi}_0) = \frac{NS^2K_{\perp}}{2}\sin 2\phi_0 + T_{\mathrm{el},z}, \tag{30}$$

where F_{el} is the force and $T_{\mathrm{el},z}$ is the torque, both from electrons [8, 53]. One might easily convince oneself that the force F_{el} from electrons appears in the equations in exactly the same way as the other forces (F_{B} and F_{pin}) already considered. As for the torque $T_{\mathrm{el},z}$, we may understand it as follows.

Suppose a spin current I_{s} (in unit of $\hbar/2$, the dimension being, e.g. [Ampere]) is flowing in the left far region to the domain wall. In the adiabatic case, the spin current flowing in the right far region to the domain wall is given by $-I_{\mathrm{s}}$. Since the change of angular momentum of a single electron is $\hbar$ after a passage through the domain wall, the total angular momentum of electrons is changing at a rate $\hbar I_{\mathrm{s}}/(-e)$, which is transferred to the domain wall, and acts as a torque

$$T_{\mathrm{el},z} = -\frac{\hbar}{e}I_{\mathrm{s}} \tag{31}$$

on the domain wall. This torque is now added to the right-hand side of Eq. (11), leading to Eq. (30).

To derive the expression of the force, consider a situation that the electrons are accelerated by an applied electric field E, and a steady-current state is maintained by reflections from the domain wall. We assume that only the domain wall scatters electrons. Then, the electrons acquire momentum $-eN_{\mathrm{el}}E$ per unit time (N_{el} is the total number of electrons and $e > 0$ is the elementary charge), which is nothing but the force, and the whole of this momentum is released to the domain

wall under the stationarity condition assumed here. Thus the domain wall feels a force $F_{\rm el} = -eN_{\rm el}E$ from the electrons. The current density j is related to E as

$$E = \rho_{\rm w} j \tag{32}$$

via the resistivity $\rho_{\rm w}$ due to a single domain wall. By eliminating E from these two relations, we obtain

$$F_{\rm el} = -eN_{\rm e}\rho_{\rm w} j. \tag{33}$$

For thick walls as realized in metallic wires, the reflection probability (or domain-wall resistivity) will be vanishingly small, and the spin-transfer effect will be the dominant driving mechanism. (It turns out that this is not the case for AC current [42].) The momentum-transfer effect is considered to be effective only for thin walls, as in nanocontacts and possibly in magnetic semiconductors. However, as described in Section 2.2.3, it should also be noted that there is another contribution to the force from spin-relaxation processes, which can be effective even for thick walls.

2.2.2. Mathematical derivation

Mathematically, what is new compared to the field-driven case is the s–d exchange term $H_{\rm sd}$. Supplementing the electron part by, for example, that of a free-electron system

$$L^0_{\rm el} = \sum_{\boldsymbol{k}} c^\dagger_{\boldsymbol{k}} (\mathrm{i}\hbar\partial_t - \varepsilon_{\boldsymbol{k}}) c_{\boldsymbol{k}} \tag{34}$$

with $\varepsilon_{\boldsymbol{k}} = \hbar^2\boldsymbol{k}^2/2m$, we consider the total Lagrangian $L_{\rm tot} = L_{\rm dw} + L^0_{\rm el} - H_{\rm sd}$, and derive the equations of motion by taking variations with respect to X and ϕ_0.

The s–d coupling introduces two new terms into the equations of motion [53]. One comes from the X derivative, which is force

$$F_{\rm el} \equiv -\left\langle \frac{\partial H_{\rm sd}}{\partial X} \right\rangle = -J_{\rm sd} \int \mathrm{d}^3x \nabla_x \boldsymbol{S}_{\rm dw}(x - X) \cdot \langle \boldsymbol{\sigma}(x) \rangle_{\rm ne}, \tag{35}$$

where $\boldsymbol{S}_{\rm dw}(x)$ is the domain-wall spin configuration and $\langle \boldsymbol{\sigma}(x) \rangle_{\rm ne}$ represents spin density of electrons under the current and/or a moving domain wall. The other comes from the ϕ_0 derivative, which is torque (force on $-\phi_0$)

$$T_{{\rm el},z} \equiv +\left\langle \frac{\partial H_{\rm sd}}{\partial \phi_0} \right\rangle = -J_{\rm sd} \int \mathrm{d}^3x [\boldsymbol{S}_{\rm dw}(x - X) \times \langle \boldsymbol{\sigma}(x) \rangle_{\rm ne}]_z. \tag{36}$$

As seen above, the torque $T_{{\rm el},z}$ is proportional to the spin current flowing in the bulk (far from the domain wall) in the adiabatic case.

The force comes from the gradient of magnetization; electrons are scattered by this spatial non-uniformity, and there occurs an exchange of linear momentum between electrons and the domain wall. The torque comes from the mismatch in direction between the domain-wall magnetization and electron spin polarization; they precess around each other, and exchange spin angular momentum with each other.

Force and torque both vanish if there is no current (and if the domain wall is at rest). They can be finite if there is a current (or the domain wall is in motion). In this sense, the calculation of force and torque resembles that of transport coefficients, and we can use the techniques developed for transport coefficients, such as those named after the great physicists, Boltzmann, Kubo, Landauer, Keldysh and others. We will outline some calculations based on the Kubo formula in the next section.

The equations of motion are obtained as Eqs (29) and (30). These equations are directly obtained from the effective Lagrangian

$$L_{\rm eff} = -\frac{\hbar NS}{\lambda} X\dot{\phi}_0 - \frac{1}{2}K_\perp NS^2 \sin^2\phi_0 + (F_{\rm B} + F_{\rm el})X - T_{{\rm el},z}\phi_0 - V_{\rm pin}(X), \tag{37}$$

together with the dissipation function (25). Among others, there is a direct linear coupling between ϕ_0 and spin current (or spin-transfer torque, $T_{{\rm el},z}$). As noted in Section 2.2.3, the spin S in the first term of Eq. (37) gets renormalized to $S_{\rm tot} = S + \delta S$ with δS being the contribution from conduction electrons (see also Section 3.1).

2.2.3. Supplementary remarks

In deriving the expressions (31) and (33), for the torque and the force, we have considered an idealized situation that there are no spin- and momentum-relaxation processes in the electron system. This is certainly not the case in real systems. The effect of spin- and momentum-relaxation processes will be examined in the next section in the more general framework of the LLG equation. According to that, the spin-transfer torque (31) is not modified by the normal impurities (momentum-relaxation process) and weak magnetic impurities (spin-relaxation process) [Eq. (88)]. On the other hand, we will see that spin-relaxation process will induce a new type of current-induced torque, called β-term [see Eq. (90)], which acts as a force

$$F_\beta = -\beta\frac{\hbar}{2e}j_{\rm s}\frac{Na^3}{\lambda^2} = \beta\frac{\hbar SN}{\lambda^2}v_{\rm s} \tag{38}$$

on a rigid wall. Here, $j_{\rm s} = I_{\rm s}/A$ is the spin-current density, $v_{\rm s} = -(a^3/2eS)j_{\rm s}$ is the corresponding drift velocity and β is a dimensionless parameter characterizing the degree of spin relaxation. The current-induced force thus consists of two contributions, $F_{\rm el} = F_\beta + F_{\rm na}$, where we have written the right-hand side of Eq. (33) as $F_{\rm na}$ (the subscript "na" means non-adiabatic). The spin-relaxation process also gives an additional contribution to the Gilbert damping. These issues will be elucidated systematically in the next section (Section 3).

Actually, even in the absence of spin- and momentum-relaxation processes, the coupling to electrons modifies Eqs (29) and (30) in one more way. Namely, it modifies the magnitude of spin from that of the localized spin, S, to the total one, $S_{\rm tot} = S + \delta S$, where δS is the contribution from conduction electrons. This applies to the coefficients of $\dot{\phi}_0$ and $\dot{X}$ on the left-hand side of Eqs (29) and (30). Let us see their physical implications.

In the above argument that led to Eq. (31), we should have been a little more careful about the fact that, when the domain wall is moving, the spin current

flowing into the domain wall is modified. To see this, let us write the spin-current density as $-e\sum_\sigma \sigma n_\sigma v_\sigma = -e(n_\uparrow v_\uparrow - n_\downarrow v_\downarrow)$, where n_σ and v_σ are the density and drift velocity of spin-σ electrons, respectively. When the domain wall is moving, v_σ should be measured relative to the domain-wall velocity, $\dot{X}$, hence the effective spin-current density seen by the domain wall is given by $-e\sum_\sigma \sigma n_\sigma (v_\sigma - \dot{X})$, and the above torque (31) is modified to

$$T_{\mathrm{el},z} = -\frac{\hbar}{e} I_\mathrm{s} - \frac{\hbar N}{\lambda}\left(\frac{1}{2}a^3\rho_\mathrm{s}\right)\dot{X}, \tag{39}$$

where $\rho_\mathrm{s} = \sum_\sigma \sigma n_\sigma = n_\uparrow - n_\downarrow$ is the electron spin density. If the second term of Eq. (39) is transposed to the left-hand side of Eq. (30), it amounts to renormalize the spin S in the coefficient of $\dot{X}$ to

$$S_\mathrm{tot} = S + \frac{1}{2}a^3\rho_\mathrm{s}. \tag{40}$$

This effect is expressed as the renormalization $S \to S_\mathrm{tot}$ in the first term of the effective Lagrangian (37). Therefore, the factor S in front of $\dot{\phi}_0$ of Eq. (29) should also be modified to S_tot. It is thus concluded that a similar term should appear also in the force, Eq. (33), as

$$F_\mathrm{el} = -eN_\mathrm{e}\rho_\mathrm{w} j - \frac{\hbar N}{\lambda}\left(\frac{1}{2}a^3\rho_\mathrm{s}\right)\dot{\phi}_0. \tag{41}$$

The second term can be obtained if we replace Eq. (32) by

$$E = \rho_\mathrm{w} j + \frac{V'}{L}, \tag{42}$$

where L is the length of the wire, and

$$V' = \frac{\hbar}{e}\cdot\frac{\rho_\mathrm{s}}{n}\dot{\phi}_0 \tag{43}$$

with $n = n_\uparrow + n_\downarrow$ being the electron density. Equation (42) indicates that the domain-wall motion (with $\dot{\phi} \neq 0$) is accompanied by a voltage generation, or the electromotive force, V'. This voltage V' may be considered as originating from the more fundamental "spin motive force" or "spin voltage"

$$V_\mathrm{s} = \frac{\hbar}{e}\dot{\phi}_0 \tag{44}$$

associated with the domain-wall motion. The two quantities are mutually related via $V' = \langle\sigma\rangle V_\mathrm{s}$ with $\langle\sigma\rangle = (n_\uparrow - n_\downarrow)/(n_\uparrow + n_\downarrow) = \rho_\mathrm{s}/n$ being the s-electron spin polarization [54].

Berger predicted the existence of motive force $V = (\hbar/e)\dot{\phi}_0$ from the analogy to the Josephson effect in superconductors [7]. His motive force is, however, in the charge channel, in contrast to the spin motive force of Eq. (44) in the spin channel. The concept of motive force associated with time-dependent inhomogeneous magnetic (spin Zeeman) field was also proposed by Stern [55] through the

study of the (time-dependent) Berry's phase, and discussed recently by Barnes *et al.* [54, 56] again in the context of domain-wall motion, which are followed by further theoretical studies [57–61]. Detecting the spin motive force is currently an experimental challenge [62]. Conceptually, the same phenomenon ("spin battery") had been proposed in ferromagnet/normal metal junction systems [63].

2.3. Dynamics

In this section, we study the dynamics of a domain wall on the basis of Eqs (29) and (30). We introduce a pinning potential (see the inset of Fig. 6A)

$$V_{\rm pin} = \frac{NV_0}{\xi^2}(X^2 - \xi^2)\Theta(\xi - |X|). \tag{45}$$

Here, $\Theta(x)$ is the Heaviside step function, V_0 is the pinning strength and ξ is the pinning range. We rewrite Eqs (29) and (30) in the form

$$\dot{\phi}_0 + \alpha\frac{\dot{X}}{\lambda} = f - v_{\rm pin}\frac{X}{\lambda}\Theta(\xi - |X|), \tag{46}$$

$$\frac{\dot{X}}{\lambda} - \alpha\dot{\phi}_0 = \kappa_\perp \sin 2\phi_0 + v_{\rm s}, \tag{47}$$

where all parameters, except for α, have dimensions of frequency: $v_{\rm pin} = 2V_0/\hbar S$, $\kappa_\perp = SK_\perp/2\hbar$, $v_{\rm s} = T_{{\rm el},z}/(\hbar NS) = -I_{\rm s}/(eNS)$ and $f = (\lambda/\hbar NS)(F_{\rm el} + F_{\rm B})$. Explicitly, we have

$$f = \beta'\frac{v}{\lambda} + \gamma_0 B \tag{48}$$

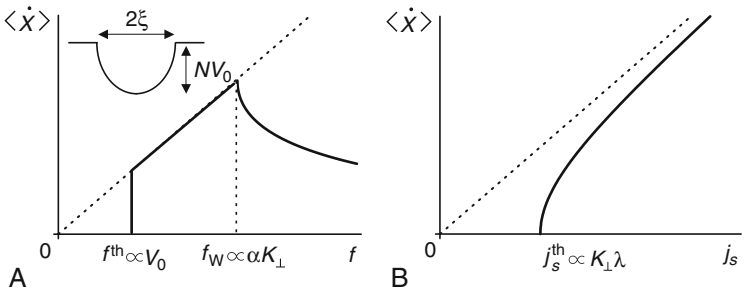

FIGURE 6 Time-averaged domain-wall velocity, $\langle\dot{X}\rangle$. (A) Force-driven case. As a function of $f = (\lambda/\hbar NS)F$, where $F = F_{\rm el} + F_{\rm B}$ is the driving force. Inset illustrates model pinning potential. (B) Current-driven case. As a function of spin-current density j_s. The dotted line represents $\langle\dot{X}\rangle = v_{\rm s}$ corresponding to the case of complete spin transfer ($K_\perp = 0$).

with

$$\beta' = \beta \frac{P}{2S} + \beta_{\rm na}, \tag{49}$$

$$\beta_{\rm na} = \frac{e^2 n \lambda}{2\hbar S} R_{\rm w} A, \tag{50}$$

where $P = j_{\rm s}/j$ is the degree of spin polarization of the current, and we defined $v \equiv -(a^3/e)j$. Note that the effects of (easy-axis) magnetic field, momentum transfer ($\sim\beta_{\rm na}$), and the β-term enter the equation through f defined above.

2.3.1. Dynamics driven by force

First, we study the domain-wall dynamics driven by force by setting $v_{\rm s} = 0$.

In the absence of a pinning potential ($v_{\rm pin} = 0$), Eqs (46) and (47) have a stationary solution describing a moving domain wall with constant velocity $\dot{X} = \lambda f/\alpha$ and constant ϕ_0 (i.e. $\dot{\phi}_0 = 0$). The value of ϕ_0 is determined by Eq. (27). This stationary solution exists only if $|\dot{X}| < \kappa_\perp \lambda$, namely, $|f| < \alpha\kappa_\perp \equiv f_{\rm W}$. For $|f| > f_{\rm W}$, ϕ_0 also becomes time dependent, and the wall motion acquires oscillatory components. This is known as the Walker breakdown.

In the presence of a pinning potential, the domain wall is pinned below the threshold $f^{\rm th} = v_{\rm pin}\xi/\lambda$. This corresponds to the threshold field, $\gamma_0 B^{\rm th} = 2V_0\xi/(\hbar S\lambda)$, or the threshold (charge) current,

$$j^{\rm th} = \frac{e}{a^3} \cdot \frac{2V_0}{\hbar S} \cdot \frac{\xi}{\beta'}, \quad v^{\rm th} = \frac{2V_0}{\hbar S} \cdot \frac{\xi}{\beta'}. \tag{51}$$

The domain-wall velocity as a function of force (B or j) is shown in Fig. 6A.

2.3.2. Dynamics driven by spin transfer

Next, we focus on the spin-transfer effect by setting $f = 0$. We consider only the case of DC current, and assume $v_{\rm s}$ is time independent. (This also includes the case of a pulsed current.)

We first consider the case without pinning potential, $v_{\rm pin} = 0$. In Eq. (47), the spin-transfer torque enters as a source to the domain-wall velocity $\dot{X}$; it tries to drive $\kappa_\perp$ directly. However, there is also a hard-axis anisotropy ($\kappa_\perp$) term, which tends to absorb the transferred angular momentum. In fact, if $|v_{\rm s}|$ is smaller than $\kappa_\perp$, spin transfer $v_{\rm s}$ is completely absorbed by the $\kappa_\perp$-term, that is, transferred to the lattice, and is not used for the translational motion ($\dot{X}$) of the domain wall: domain wall is apparently pinned and not driven to a stream motion even in the absence of any extrinsic pinning potential [53]. This is called intrinsic pinning.

The time dependence of X and ϕ_0 are shown in Fig. 7A. The domain wall approaches a static state with finite displacements of X and ϕ_0. If $|v_{\rm s}|$ exceeds $\kappa_\perp$, the domain wall moves with constant average velocity $\langle\dot{X}\rangle$ with oscillating components superposed (Fig. 7B). This oscillation is due to the alternating exchange of angular momentum between X and ϕ_0 degrees of freedom. (ϕ_0 also varies with some constant average angular velocity $\langle\dot{\phi}_0\rangle$, which is smaller than $\langle\dot{X}\rangle$ by a factor of α.) Therefore, for the domain-wall motion driven by the spin-transfer effect, there is a finite threshold spin current,

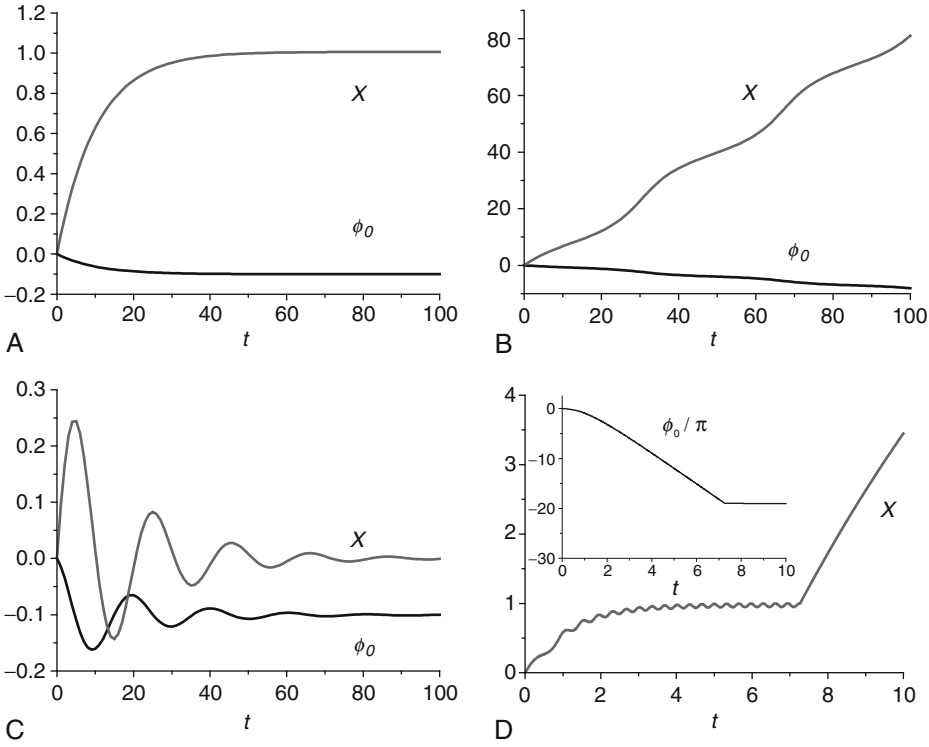

FIGURE 7 Time dependence of X/λ and ϕ_0 under spin current v_s, without pinning potential $v_{pin} = 0$ (A, B) and with pinning potential $v_{pin} > 0$ (C, D), for $\kappa_\perp = 0.5$, $\xi = \lambda$ and $\alpha = 0.1$. (A) Below the threshold $j_s^{th(1)}$ ($v_s < \kappa_\perp$; $v_s = 0.1$). (B) Above the threshold $j_s^{th(1)}$ ($v_s > \kappa_\perp$; $v_s = 1$). (C) Below $j_s^{th(1)}$, pinned regime ($v_s < \kappa_\perp$; $v_s = 0.1$, $v_{pin} = 0.1$). (D) Above $j_s^{th(1)}$, and close to but slightly above $j_s^{th(2)}$ ($v_s > \kappa_\perp$; $v_s = 0.977$, $v_{pin} = 10$), the depinning is seen. For a more realistic value of $\alpha = 0.01$, characteristic features of the domain-wall motion are modified as follows. (A, B) Time scale for both X and ϕ_0 becomes longer in proportion to α^{-1}. Magnitude of X is enhanced ($\propto \alpha^{-1}$) according to $\dot{X}/\lambda = -\alpha^{-1} \cdot \phi_0$. (C) Decay time becomes long ($\sim\alpha^{-1}$) whereas the oscillation period ($\Delta t \sim 20$) is unchanged, therefore, X and ϕ_0 oscillate many times ($\sim$30–40) before the decay. (D) The oscillation amplitude of X in the pinned state is much reduced.

$$j_s^{th(1)} = \frac{eS^2}{a^3\hbar} K_\perp \lambda, \quad v_s^{th(1)} = \frac{S}{2\hbar} K_\perp \lambda = \kappa_\perp \lambda, \tag{52}$$

essentially determined by $K_\perp$. This threshold is finite even if there is no pinning potential. This is intrinsic pinning due to $K_\perp$. Here, $K_\perp$ tends to prevent the domain-wall motion by absorbing the transferred spin angular momentum, in contrast to the force-driven case, where, as we have seen before, $K_\perp$ helps the domain-wall motion by supplying angular momentum. Above the threshold, the time-averaged domain-wall velocity is given by (Fig. 6B)

$$\langle \dot{X} \rangle = \frac{1}{1+\alpha^2} \sqrt{v_s^2 - (v_s^{th(1)})^2}. \tag{53}$$

We next consider the case with extrinsic pinning potential, $v_{\rm pin} > 0$. For $|v_{\rm s}| < \kappa_\perp$, after the initial transient period with oscillatory behaviour, the domain wall is eventually pulled back to the pinning centre ($X = 0$) and ϕ_0 approaches a constant value (Fig. 7C). For $|v_{\rm s}| > \kappa_\perp$, the domain wall makes a finite displacement ΔX and oscillates around the mean position (Fig. 7D). This is the (extrinsically) pinned state. In this pinned state, transferred spin is solely used to drive ϕ_0, and ϕ_0 continues to vary rapidly. Here, AC noise or electromagnetic radiation may be expected due to this ϕ_0 motion. If X happens to "step over" the pinning range, the domain wall is depinned. After depinning, the ϕ_0-motion slows down, and the transferred spin is mainly used for the translational motion of the domain wall.

Let us examine the depinning condition for the latter case (Fig. 7D). In the pinned state ($\dot{X} \sim 0$), the average displacement may be estimated from Eq. (46) as $\Delta X \sim -\lambda \dot{\phi}_0 / v_{\rm pin}$, whereas $\dot{\phi}_0 \sim -v_{\rm s}/\alpha$ from Eq. (47). The condition for depinning, $|\Delta X| > \xi$, thus leads to the second threshold

$$j_{\rm s}^{\rm th(2)} = \frac{4e}{a^3 \hbar} \alpha V_0 \xi, \quad v_{\rm s}^{\rm th(2)} = \frac{2}{\hbar S} \alpha V_0 \xi = \alpha v_{\rm pin} \xi \tag{54}$$

for the spin-current density $j_{\rm s}$.

The actual threshold spin-current density $j_{\rm s}^{\rm th}$ is given by the larger of $j_{\rm s}^{\rm th(1)}$ and $j_{\rm s}^{\rm th(2)}$. Since $j_{\rm s}^{\rm th(2)}$ contains a factor of α, which is considered to be very small ($\sim$0.01), $j_{\rm s}^{\rm th}$ will be determined by the hard-axis anisotropy if the pinning potential is not extremely strong [53]. For this case, the time-averaged domain-wall velocity $\langle \dot{X} \rangle$ is plotted as a function of spin current $j_{\rm s}$ in Fig. 6B.

So far, experimental studies on the domain-wall motion have been focussed on the X motion. It will be interesting to detect the motion of ϕ_0 as well.

2.3.3. Dynamics driven by both spin transfer and force

We have seen that, even in the absence of extrinsic pinning ($V_0 = 0$), there exists a threshold current density for the domain-wall motion if it is driven solely by the spin-transfer effect. This threshold is due to the hard-axis anisotropy, and is called of intrinsic origin. This intrinsic pinning is expected to be removed by any small amount of force (momentum-transfer effect, or the β-term), but then the extrinsic pinning will play essential roles [64–66].

Threshold current for depinning as a function of pinning strength is shown in Fig. 8A. It reveals several depinning mechanisms depending on the following parameter regimes:

(I) Weak pinning regime ($\tilde{\Omega} < O(1)$): $\tilde{j}_{\rm c}$ grows with $\tilde{\Omega}$.
(II) Intermediate regime ($O(1) < \tilde{\Omega} < O(\alpha^{-1/2})$): $\tilde{j}_{\rm c} \simeq$ constant $\simeq 0.7 - 0.8$.
(III) Strong pinning regime ($\tilde{\Omega} > O(\alpha^{-1/2})$): $\tilde{j}_{\rm c} \propto \tilde{\Omega}^2 \propto V_0$.

As seen from Fig. 8A, the β' affects $\tilde{j}_{\rm c}$ only in regime I, which can be further divided into two subregimes:

(I-a) Small $\beta'/\tilde{\Omega}$: $\tilde{j}_{\rm c} \propto \tilde{\Omega} \propto \sqrt{V_0}$.
(I-b) Large $\beta'/\tilde{\Omega}$: $\tilde{j}_{\rm c} \propto \tilde{\Omega}^2/\beta' \propto V_0/\beta'$.

In regime I, ϕ_0 does not grow because of low current, and the dynamics is described by X. In regime I-a, β' is negligible and the depinning is due to spin

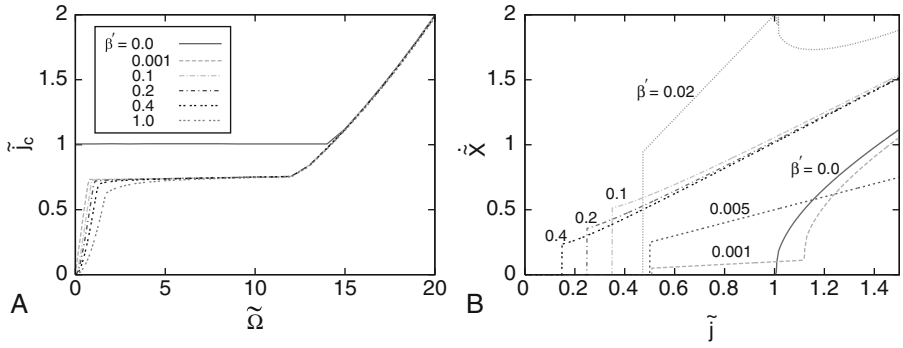

FIGURE 8 (A) Threshold current as a function of pinning frequency. Both quantities are given in dimensionless forms: $\tilde{j} = (a^3/ev_c)j$ for current density j, and $\tilde{\Omega} = \Omega\lambda/v_c$ for pinning frequency Ω defined by $NV_0 = \frac{1}{2}M_w\Omega^2$. (B) Time-averaged domain-wall velocity as a function of (dimensionless) current density, $\tilde{j}$, for $\tilde{\Omega} = 0.5$ and $\alpha = 0.01$. A jump in wall velocity is seen at the threshold $\tilde{j} = \tilde{j}_c$ (except for $\beta' = 0$). Crossover from regime I-a ($\tilde{j}_c \sim \tilde{\Omega}/\beta'$) to regime I-b ($\tilde{j}_c \sim \tilde{\Omega}$) is seen near $\beta' \approx \tilde{\Omega}/4 \sim 0.1$. After Ref. [66].

transfer. Namely, spin-transfer term gives a finite velocity, $\dot{X} = v_s\lambda = v_s$ [see Eq. (47)], to the wall, and if the corresponding kinetic energy $\frac{1}{2}M_w v_s^2$ exceeds NV_0, the domain wall will be depinned. This determines the third threshold:

$$j_s^{\mathrm{th}(3)} = \frac{2eS\lambda}{a^3\hbar}\sqrt{2K_\perp V_0}, \quad v_s^{\mathrm{th}(3)} = \frac{\lambda}{\hbar}\sqrt{2K_\perp V_0}. \tag{55}$$

In regime I-b, the depinning is governed by the force, and the corresponding threshold current is given by Eq. (51).

Dynamics in regimes II and III are determined by ϕ_0. In regime II, the depinning is due to spin transfer, but the terminal velocity is determined by β'. The depinning mechanism here is the same as that discussed around Eq. (52), but the lowering of j_c by a factor of 0.7–0.8 is due to the β'-term eliminating the intrinsic pinning. This is the reason why j_c looks different for $\beta' = 0$ and $\beta' \neq 0$ in Fig. 8A. The regime III corresponds to the strong pinning regime already studied; the threshold is given by Eq. (54). In both regimes II and III, the depinning is due to the spin-transfer effect, and β' does not affect the threshold current.

The domain-wall velocity after depinning is shown in Fig. 8B. It is noted that the wall velocity at the extrinsic threshold is discontinuous. This is because the wall as soon as depinned feels a tilted potential due to β' and has finite velocity. The velocity jump is estimated as

$$\Delta v^{\mathrm{Ia}} = \frac{\beta'}{\alpha}\frac{2S}{P}\frac{\sqrt{2K_\perp V_0}}{\hbar}\lambda, \tag{56}$$

$$\Delta v^{\mathrm{Ib}} = \frac{1}{\alpha}\frac{SV_0}{\hbar}\frac{\lambda^2}{\xi} \tag{57}$$

for regime I-a and regime I-b, respectively.

The wall velocity above the threshold is given by

$$\langle \dot{X} \rangle = \frac{\beta'}{\alpha} v \quad (v > v_a), \tag{58}$$

$$\langle \dot{X} \rangle = \frac{\beta'}{\alpha} v - \frac{v}{1+\alpha^2} \sqrt{1 - \left(\frac{v_a}{v}\right)^2} \quad (v > v_a), \tag{59}$$

where $v = -(a^3/e)j$ (as before) and $v_a = v_s^{th(1)}/|(P/2S) - (\beta'/\alpha)|$. The v_a corresponds to the Walker breakdown above which ϕ_0 increases with time continuously.

2.3.4. Discussion

The present description in terms only of X and ϕ_0 out of many degrees of freedom, called "collective-coordinate" description, will be a good approximation if the energy scale of the domain-wall motion ($\sim K_\perp$, V_0) is much smaller than the lowest energy of any other modes. The latter may be estimated as the spin-wave gap $\sim S\sqrt{K(K+K_\perp)}$ (see Section 4.2). Thus, a necessary condition is $K_\perp \ll K$.

The present analysis assumes a wall structure which is uniform in the width direction (called transverse wall), and applies to thin wires (one-dimensional limit). For wider wires, the wall contains a vortex as the most stable structure (called vortex wall [65]), and actually most experiments are done with such vortex walls [41, 45–51]. While the present analysis loses justice for such vortex walls, proper interpretation of the vortex motion in terms of ϕ_0-motion reveals a surprising usefulness of the present "one-dimensional model", as pointed out in micromagnetic simulations [67] and in experiments [47–51].

2.3.5. Further references

The analysis presented above applies to absolute zero temperature. Effects of finite temperature (thermally assisted process) are studied in Refs [68, 69]. Creep-like motion below the threshold is suggested experimentally in magnetic semiconductors [44], whose behaviour was recently explained in Ref. [70]. Analytical treatment of vortex walls is attempted in Ref. [71].

As for spin torques, effects of non-adiabaticity on the spin-transfer torque is studied in Ref. [72]. Conduction electrons are numerically treated with full account of non-adiabaticity in a mesoscopic system in Ref. [73].

3. MICROSCOPIC CALCULATION OF SPIN TORQUES

In this section, we describe the present theoretical status of the microscopic derivation of spin torques. We focus on magnetization dynamics which is slowly varying in space and time, as described by the LLG equation. Here "slow" means slow compared to the electronic scales, so it is satisfied quite well in most cases for metallic systems. Throughout this section, we consider general spin texture (magnetic configurations).

3.1. General

The LLG equation is given by

$$\frac{\mathrm{d}\boldsymbol{M}}{\mathrm{d}t} = \gamma_0 \boldsymbol{H}_{\mathrm{eff}} \times \boldsymbol{M} + \frac{\alpha_0}{M}\boldsymbol{M} \times \frac{\mathrm{d}\boldsymbol{M}}{\mathrm{d}t} + \boldsymbol{T}_{\mathrm{el}}, \tag{60}$$

in terms of magnetization vector $\boldsymbol{M}$. The first term on the right-hand side represents precessional torque around the effective field $\boldsymbol{H}_{\mathrm{eff}}$, with γ_0 being the gyromagnetic ratio. The effective field includes the ferromagnetic exchange (gradient energy) field, the magnetocrystalline anisotropy field and the demagnetizing field. The second term represents the Gilbert damping, coming from processes which do not involve conduction electrons, and is thus present even in the insulating ferromagnets. The effects of conduction electrons are contained in the third term, $\boldsymbol{T}_{\mathrm{el}}$, called spin torque in particular. This term comes from the s–d exchange coupling $\boldsymbol{H}_{\mathrm{sd}}$ to conduction electrons, and is given by

$$\boldsymbol{T}_{\mathrm{el}} = -M\boldsymbol{n}(\boldsymbol{r}) \times \langle \sigma(\boldsymbol{r}) \rangle_{\mathrm{ne}}. \tag{61}$$

For notational convenience, we introduce a unit vector, $\boldsymbol{n}$, whose direction is in the d-spin direction, hence is opposite to magnetization direction,

$$\boldsymbol{M} = -\gamma_0 \frac{\hbar S}{a^3}\boldsymbol{n}. \tag{62}$$

Note that the magnetization is, by definition, the magnetic moment per unit volume, hence $|\boldsymbol{M}| = \gamma_0 \hbar S/a^3$. In terms of $\boldsymbol{n}$, the LLG equation is written as

$$\dot{\boldsymbol{n}} = \gamma_0 \boldsymbol{H}_{\mathrm{eff}} \times \boldsymbol{n} + \alpha_0 \dot{\boldsymbol{n}} \times \boldsymbol{n} + \boldsymbol{t}'_{\mathrm{el}}, \tag{63}$$

where we have put $\boldsymbol{T}_{\mathrm{el}}(\boldsymbol{M}) = -(\hbar S/a^3)\boldsymbol{t}'_{\mathrm{el}}(\boldsymbol{n})$. The dot represents time derivative.

For long-wavelength, low-frequency dynamics, it may be sufficient to consider spin torques which are first order in space/time derivative. Let us call such torques as *adiabatic torques*. In the presence of rotational symmetry in spin space, they are expressed as

$$\boldsymbol{\tau}^{0'}_{\mathrm{ad}} = -(\boldsymbol{v}^0_{\mathrm{s}}\cdot\nabla)\boldsymbol{n} - \beta_{\mathrm{sr}}\boldsymbol{n} \times (\boldsymbol{v}^0_{\mathrm{s}}\cdot\nabla)\boldsymbol{n} - \alpha_{\mathrm{sr}}(\boldsymbol{n} \times \dot{\boldsymbol{n}}) - \frac{\delta S}{S}\dot{\boldsymbol{n}}. \tag{64}$$

The first term on the right-hand side is the celebrated spin-transfer torque [74–78], where

$$\boldsymbol{v}^0_{\mathrm{s}} = -\frac{a^3}{2eS}\boldsymbol{j}_{\mathrm{s}} \tag{65}$$

is the (unrenormalized) "spin-transfer velocity", with $\boldsymbol{j}_{\mathrm{s}}$ being the spin-current density. The second term, sometimes called "β-term", comes from spin-relaxation processes of electrons [64, 65, 79–84]. Here, β_{sr} is a dimensionless constant. The third term is the Gilbert damping, which also results from spin relaxation of electrons. The fourth term contributes as a "renormalization" of spin, as seen below.

If the magnetization varies rapidly in space, we have in addition a *non-adiabatic torque*, $\boldsymbol{\tau}^0_{\rm na}$, which is oscillatory and non-local (see Section 3.3). The total torque may thus be given by the sum of the two:

$$\boldsymbol{t}'_{\rm el} = \boldsymbol{\tau}^{0'}_{\rm ad} + \boldsymbol{\tau}^{0'}_{\rm na}. \tag{66}$$

The LLG equation (63) is then written as

$$\left(1 + \frac{\delta S}{S}\right)\dot{\boldsymbol{n}} = \gamma_0 \boldsymbol{H}_{\rm eff} \times \boldsymbol{n} - (\boldsymbol{v}^0_{\rm s}\cdot\nabla)\boldsymbol{n} - \beta_{\rm sr}\boldsymbol{n} \times (\boldsymbol{\nu}^0_{\rm s}\cdot\nabla)\boldsymbol{n} - (\alpha_0 + \alpha_{\rm sr})\boldsymbol{n} \times \dot{\boldsymbol{n}} + \boldsymbol{\tau}^{0'}_{\rm na}. \tag{67}$$

Here, we have transposed the "spin renormalization" term to the left-hand side. We define the total ("renormalized") spin as

$$S_{\rm tot} = S + \delta S, \tag{68}$$

with δS being the contribution from conduction electrons, and divide both sides of Eq. (67) by $S_{\rm tot}/S$. Then we arrive at

$$\dot{\boldsymbol{n}} = \gamma \boldsymbol{H}_{\rm eff} \times \boldsymbol{n} - (\boldsymbol{v}_{\rm s}\cdot\nabla)\boldsymbol{n} - \beta \boldsymbol{n} \times (\boldsymbol{v}_{\rm s}\cdot\nabla)\boldsymbol{n} - \alpha(\boldsymbol{n} \times \dot{\boldsymbol{n}}) + \boldsymbol{\tau}'_{\rm na}, \tag{69}$$

where $\gamma = (S/S_{\rm tot})\gamma_0$, $\alpha = (S/S_{\rm tot})(\alpha_0 + \alpha_{\rm sr})$, $\beta = \beta_{\rm sr}$, $\boldsymbol{\tau}'_{\rm na} = (S/S_{\rm tot})\boldsymbol{\tau}^{0'}_{\rm na}$ and

$$\boldsymbol{v}_{\rm s} = \frac{S}{S_{\rm tot}}\boldsymbol{v}^0_{\rm s} = -\frac{a^3}{2eS_{\rm tot}}\boldsymbol{j}_{\rm s}, \tag{70}$$

is the "renormalized" spin-transfer velocity. Thus, within the LLG equation of Eq. (69), the current-driven dynamics is specified by the parameters, $\boldsymbol{\nu}_{\rm s}$, α and β, and a functional $\boldsymbol{\tau}'_{\rm na}$ of $\boldsymbol{n}$ [85].

In the parameter space of the LLG equation, the manifold of $\alpha = \beta$ (with $\boldsymbol{\tau}'_{\rm na} = \boldsymbol{0}$) provides a very special case for the dynamics, and there has been a controversy whether the relation $\alpha = \beta$ holds generally or not. If $\alpha = \beta$, the following peculiar dynamics are expected:

(1) Any static solution, $\boldsymbol{n}(\boldsymbol{r})$, in the absence of spin current is used to construct a solution, $\boldsymbol{n}(\boldsymbol{r} - \boldsymbol{v}_{\rm s}t)$, in the presence of spin current $\boldsymbol{\nu}_{\rm s}$.
(2) Gilbert damping α does not affect the current-driven motion.
(3) Current-induced spin-wave instability does not occur (see Section 4.2) [80].

The relation $\alpha = \beta$ was originally suggested in Refs [79, 84] based on the Galilean invariance of the system. Although one may argue that the Galilean invariance should be valid for the long-wavelength and low-frequency dynamics in which the underlying lattice structure is irrelevant, the α and β comes from spin-relaxation processes [64], which are usually intimately related to the lattice, for example, through the spin–orbit coupling. The problem is thus subtle, and one has to go beyond the phenomenological argument such as the one based on the Galilean invariance. Instead, a fully microscopic calculation, which starts from a definite microscopic model and does not introduce any phenomenological assumptions, is desired. The present section is devoted to outline such attempts.

At present, only a single model, where spin-relaxation processes are introduced by magnetic impurities, has been examined, with a result that $\alpha \neq \beta$ (even

for single-band itinerant ferromagnets) in general. This will be surveyed in Sections 3.2 and 3.3. Studies on other models, hopefully with more realistic spin-relaxation mechanisms, are left to future studies. Readers who are not interested in theoretical details but the results can jump to Section 3.2.3.

Intuitive picture

Before going into serious calculations, we here present as preliminary considerations an intuitive picture of the spin-transfer torque and the β-term. It also serves to motivate us more serious calculations.

A nice picture of the spin-transfer torque was given by Xiao *et al.* [78]. It is in terms of the Aharonov–Stern effect [86], stating that a magnetic moment, or a spin $\boldsymbol{\sigma}$, moving in an inhomogeneous magnetization $\boldsymbol{n}(\boldsymbol{r})$ [or an external magnetic field, $\gamma\hbar\boldsymbol{B}(\boldsymbol{r}) \equiv M\boldsymbol{n}(\boldsymbol{r})$, see Fig. 9A], sees an effective field,

$$\gamma\hbar\boldsymbol{B}_{\rm eff}(t) = M\boldsymbol{n}(\boldsymbol{r}(t)) + \frac{\hbar}{2}\boldsymbol{n}\times(\boldsymbol{v}\cdot\nabla)\boldsymbol{n}, \tag{71}$$

where $\boldsymbol{r} = \boldsymbol{r}(t)$ is the trajectory of the particle, and $\boldsymbol{v} = \dot{\boldsymbol{r}}(t)$ its velocity. Then, the spin $\boldsymbol{\sigma}$ will tend to align this effective field, and acquires a component $\propto \boldsymbol{n}\times(\boldsymbol{v}\cdot\nabla)\boldsymbol{n}$. The torque, $M\boldsymbol{n}\times\boldsymbol{\sigma}$, that $\boldsymbol{\sigma}$ exerts on the magnetization $\boldsymbol{n}$ thus has a component, $\propto(\boldsymbol{v}\cdot\nabla)\boldsymbol{n}$, which is nothing but the spin-transfer torque. They proceeded to argue that the β-term is not induced by the presence of spin-relaxation processes, since the above argument is already based on the relaxation of $\boldsymbol{\sigma}$ to $\boldsymbol{B}_{\rm eff}$. However, we note that the field $\boldsymbol{B}_{\rm eff}$ is not a simple static field but contains a field of dynamical origin [second term of Eq. (71)], and the effect of relaxation needs to be carefully examined.

Here, we reformulate the above picture by solving the spin dynamics explicitly. We consider the following two cases:

(a) A spin in a time-dependent magnetization
(b) A spin moving in a static but spatially varying magnetization (Fig. 9A)

In both cases, the spin feels a time-dependent field (or magnetization). The essential physics of the spin torque lies in the response of the spin to such

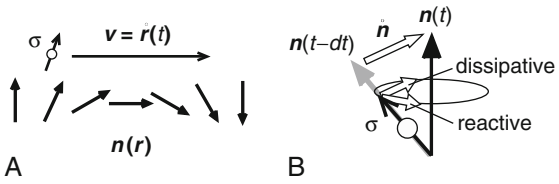

FIGURE 9 Illustration of the response of a spin moving in magnetization texture, $\boldsymbol{n}(\boldsymbol{r})$. (A) A moving spin in inhomogeneous magnetization feels a time-dependent magnetization, $\boldsymbol{n}(t) \equiv \boldsymbol{n}(\boldsymbol{r}(t))$, where $\boldsymbol{r}(t)$ is the real-space trajectory of the spin. (B) Two kinds of response of the spin to the time-dependent field. One is the reactive response as a precession around $\boldsymbol{n}(t)$. The other is the dissipative response, as a tendency to orient to $\boldsymbol{n}(t)$. The former gives rise to the spin-transfer torque, and the latter to the β-term.

time-dependent field (or magnetization). So, let us study the motion of a single spin in a time-dependent field $M\boldsymbol{n}(t)$ on the basis of the equation

$$\frac{\mathrm{d}\boldsymbol{\sigma}}{\mathrm{d}t} = \frac{2M}{\hbar}\boldsymbol{n}(t) \times \boldsymbol{\sigma} + \alpha_1 \boldsymbol{\sigma} \times \frac{\mathrm{d}\boldsymbol{\sigma}}{\mathrm{d}t}. \tag{72}$$

We have phenomenologically introduced the damping (spin-relaxation) term with α_1 being its strength. Assuming that the time variation of $\boldsymbol{n}(t)$ is very slow, we solve Eq. (72) from the adiabatic limit, and calculate the solution as an expansion with respect to the number of time derivative as

$$\boldsymbol{\sigma} = \boldsymbol{n} + \frac{\hbar}{2M}(\dot{\boldsymbol{n}} \times \boldsymbol{n} + \alpha_1 \dot{\boldsymbol{n}}) + \ldots. \tag{73}$$

On the right-hand side, the first term is the "static" solution in the sense that it is static in the spin frame co-rotating with $\boldsymbol{n}$. (Namely, the frame in which $\boldsymbol{n}$ is static. In Section 3.3, this frame will be called "adiabatic frame".) The next two terms which are first order in time derivative are "adiabatic" contributions (Fig. 9B). The ... represents terms which are higher order in time derivative, and are thus "non-adiabatic" contributions. The torque is obtained as $\boldsymbol{t}_{\mathrm{el}} = M\boldsymbol{n} \times \boldsymbol{\sigma}$:

$$\boldsymbol{t}_{\mathrm{el}} = \frac{\hbar}{2}(\dot{\boldsymbol{n}} + \alpha_1 \boldsymbol{n} \times \dot{\boldsymbol{n}}). \tag{74}$$

Note that the same solution is obtained even if we start from the Landau–Lifshitz damping [$\sim 2M\alpha_1 \boldsymbol{n} \times (\boldsymbol{n} \times \boldsymbol{\sigma})$] instead of the Gilbert type. The second term of Eq. (74) gives a damping torque on $\boldsymbol{n}$ for the situation (a).

For case (b), the time dependence of $\boldsymbol{n}(\boldsymbol{r}(t))$ arises from that of $\boldsymbol{r}(t)$. Hence, the result in this case may be obtained from Eq. (74) by the replacement,

$$\partial/\partial t \to \boldsymbol{v}\cdot\nabla \quad (?) \tag{75}$$

as

$$\boldsymbol{t}_{\mathrm{el}} = \frac{\hbar}{2}[(\boldsymbol{v}\cdot\nabla)\boldsymbol{n} + \beta_1 \boldsymbol{n} \times (\boldsymbol{v}\cdot\nabla)\boldsymbol{n}], \tag{76}$$

with $\beta_1 = \alpha_1$. The first term represents the spin-transfer torque and the second term corresponds to the β-term. As noted above, both torques may be classified as adiabatic torques. Torques of higher order (in space/time derivative) would be called non-adiabatic. For example, electrons scattered (reflected) by some magnetization texture feel a sudden change of the field, and respond in a way to produce non-adiabatic torques.

In a similar way that we "derived" $\beta_1 = \alpha_1$ here, one may "derive" a relation $\beta = \alpha$ quite generally. However, we should note that an implicit assumption was made there that the damping constant α_1 is unchanged (Galilean invariance) under the replacement (75). In reality, the spin-relaxation processes are often related to the underlying lattice (such as spin–orbit coupling), and the Galilean invariance cannot be expected in general. Also, for many-electron systems having Fermi surfaces, the Galilean invariance is not an obvious property. This problem therefore needs a careful study. In particular, to see, for example, whether the

relation $\alpha = \beta$ holds or not, one needs to perform microscopic calculations without introducing any phenomenological assumptions. For this purpose, it is necessary to set up a microscopic model for the spin-relaxation mechanism. Such calculations will be outlined in the following two sections [81, 87].

3.2. Small-amplitude method

3.2.1. Microscopic model

Let us first set up a microscopic model. We take a localized picture for ferromagnetism, and consider the so-called s–d model. It consists of localized d-spins, $\boldsymbol{S}$, and conducting s-electrons, which are coupled via the s–d exchange interaction. The total Lagrangian is given by $L_{\rm tot} = L_{\rm S} + L_{\rm el} - H_{\rm sd}$, where $L_{\rm S}$ is the Lagrangian for d spins [Eq. (21)],

$$L_{\rm el} = \int {\rm d}^3 x c^\dagger \left[{\rm i}\hbar \frac{\partial}{\partial t} + \frac{\hbar^2}{2m}\nabla^2 + \epsilon_{\rm F} - V_{\rm imp} \right] c \tag{77}$$

is the Lagrangian for s-electrons and

$$H_{\rm sd} = -M \int {\rm d}^3 x \boldsymbol{n}(\boldsymbol{r}) \cdot \boldsymbol{\sigma}(\boldsymbol{r}) \tag{78}$$

is the s–d exchange coupling [Eq. (28)]. Here, $c^\dagger = (c_\uparrow^\dagger, c_\downarrow^\dagger)$ is the spinor of electron creation operators, $\boldsymbol{\sigma}(\boldsymbol{r}) = c^\dagger(\boldsymbol{r})\boldsymbol{\sigma}c(\boldsymbol{r})$ represents (twice) the s-electron spin density, with $\boldsymbol{\sigma}$ being a vector of Pauli spin matrices. We have put $\boldsymbol{S} = S\boldsymbol{n}$ with the magnitude of spin, S, and a unit vector $\boldsymbol{n}$ [88], and $M = J_{\rm sd}S$ with $J_{\rm sd}$ being the s–d exchange coupling constant.

The s-electrons are treated as a free-electron gas in three dimensions subject to the impurity potential

$$V_{\rm imp} = u \sum_i \delta(\boldsymbol{r} - \boldsymbol{R}_i) + u_{\rm s} \sum_j \boldsymbol{S}_j \cdot \boldsymbol{\sigma} \delta(\boldsymbol{r} - \boldsymbol{R}_j'). \tag{79}$$

The first term describes potential scattering. The second term represents quenched magnetic impurities, which is aimed at introducing spin-relaxation processes. The averaging over the impurity spin direction is taken as $\overline{S_i^\alpha} = 0$ and

$$\overline{S_i^\alpha S_j^\beta} = \frac{1}{3} S_{\rm imp}^2 \delta_{ij} \delta^{\alpha\beta}. \tag{80}$$

The damping rate of s-electrons is then given by

$$\gamma_\sigma = \frac{\hbar}{2\tau_\sigma} = \pi n_{\rm i} u^2 \nu_\sigma + \frac{\pi}{3} n_{\rm s} u_{\rm s}^2 S_{\rm imp}^2 (2\nu_{\overline{\sigma}} + \nu_\sigma). \tag{81}$$

Here $n_{\rm i}$ ($n_{\rm s}$) is the concentration of normal (magnetic) impurities, and $\nu_\sigma = mk_{{\rm F}\sigma}/2\pi^2\hbar^2$ (with $\hbar k_{{\rm F}\sigma} = \sqrt{2m\epsilon_{{\rm F}\sigma}}$) is the density of states at energy $\epsilon_{{\rm F}\sigma} \equiv \epsilon_{\rm F} + \sigma M$. (The subscript $\sigma = \uparrow, \downarrow$ corresponds, respectively, to $\sigma = +1, -1$ in the formula, and to $\overline{\sigma} = \downarrow, \uparrow$ or $-1, +1$.) We assume that $\gamma_\sigma \ll \epsilon_{{\rm F}\sigma}$ and $\gamma_\sigma \ll M$, and calculate the torques in the lowest non-trivial order in $\gamma_\sigma/\epsilon_{{\rm F}\sigma}$ and γ_σ/M.

3.2.2. General framework

The spin torque from $H_{\rm sd}$ is given by

$$\boldsymbol{t}_{\rm el}(\boldsymbol{r}) \equiv M\boldsymbol{n}(\boldsymbol{r}) \times \langle \boldsymbol{\sigma}(\boldsymbol{r}) \rangle_{\rm ne}. \tag{82}$$

This is related to $\boldsymbol{T}_{\rm el}$ of Eq. (61) via $\boldsymbol{t}_{\rm el}[\boldsymbol{n}] = -\boldsymbol{T}_{\rm el}[\boldsymbol{M}]$, and to $\boldsymbol{t}'_{\rm el}$ of Eq. (66) via

$$\boldsymbol{t}_{\rm el} = \frac{\hbar S}{a^3} \boldsymbol{t}'_{\rm el} \tag{83}$$

with a^3 being the volume per d-spin.

The calculation of spin torque is thus equivalent to that of s-electron spin polarization, $\langle \boldsymbol{\sigma}(\boldsymbol{r}) \rangle_{\rm ne}$, or precisely speaking, its orthogonal projection [89] $\langle \boldsymbol{\sigma}_\perp(\boldsymbol{r}) \rangle_{\rm ne}$ to $\boldsymbol{n}$. The expectation value $\langle \ldots \rangle_{\rm ne}$ is taken in the following non-equilibrium states depending on the type of the torque:

(a) Non-equilibrium states under the influence of uniform but *time-dependent magnetization*. This leads to torques with time derivative of $\boldsymbol{n}$, namely, Gilbert damping and spin renormalization.
(b) Non-equilibrium states with *current flow* under static but *spatially varying magnetization*. This leads to current-induced torques, namely, spin-transfer torque and the β-term.

In the presence of spin rotational symmetry for electrons, adiabatic spin torques, which are first order in space/time derivative, are expressed as

$$\boldsymbol{\tau}^0_{\rm ad} = a_0 \dot{\boldsymbol{n}} + (\boldsymbol{a}\cdot\nabla)\boldsymbol{n} + b_0(\boldsymbol{n} \times \dot{\boldsymbol{n}}) + \boldsymbol{n} \times (\boldsymbol{b}\cdot\nabla)\boldsymbol{n}. \tag{84}$$

The corresponding s-electron spin polarization is given by [89]

$$\langle \boldsymbol{\sigma}_\perp \rangle_{\rm ne} = \frac{1}{M}[b_0 \dot{\boldsymbol{n}} + (\boldsymbol{b}\cdot\nabla)\boldsymbol{n} - a_0(\boldsymbol{n} \times \dot{\boldsymbol{n}}) - \boldsymbol{n} \times (\boldsymbol{a}\cdot\nabla)\boldsymbol{n}]. \tag{85}$$

To calculate the coefficients a_μ and b_μ microscopically, it is sufficient to consider small transverse fluctuations, $\boldsymbol{u} = (u^x, u^y, 0), |\boldsymbol{u}| \ll 1$, around a uniformly magnetized state, $\boldsymbol{n} = \hat{z}$, such that $\boldsymbol{n} = \hat{z} + \boldsymbol{u} + O(u^2)$ [80, 90]. Then, up to $O(u)$, Eq. (85) becomes

$$\langle \boldsymbol{\sigma}_\perp \rangle_{\rm ne} = \frac{1}{M}[b_0 \dot{\boldsymbol{u}} + (\boldsymbol{b}\cdot\nabla)\boldsymbol{u} - a_0(\hat{z} \times \dot{\boldsymbol{u}}) - \hat{z} \times (\boldsymbol{a}\cdot\nabla)\boldsymbol{u}]. \tag{86}$$

This equation can be regarded as a linear response of $\boldsymbol{\sigma}_\perp$ to $\boldsymbol{u}$, and the coefficients, a_μ and b_μ, are obtained as linear-response coefficients. (Precisely speaking, $\langle \boldsymbol{\sigma}_\perp \rangle_{\rm ne}$ due to current is calculated as a linear response to the applied electric field.)

3.2.3. Results

The results are given by

$$\delta S = \frac{1}{2}\rho_{\rm s} a^3, \tag{87}$$

$$\boldsymbol{v}_{\rm s} = -\frac{a^3}{2e(S + \delta S)} \boldsymbol{j}_{\rm s}, \tag{88}$$

$$\alpha = \frac{a^3 v_+}{4(S+\delta S)} \cdot \frac{\hbar}{\tau_s} + \frac{S}{S+\delta S}\alpha_0, \tag{89}$$

$$\beta = \frac{\hbar}{2M\tau_s}, \tag{90}$$

where $\rho_s = n_\uparrow - n_\downarrow$, $v_+ = v_\uparrow + v_\downarrow$, and $\boldsymbol{j}_s = \sigma_s \boldsymbol{E} = \boldsymbol{j}_\uparrow - \boldsymbol{j}_\downarrow$ is the spin current, with $\sigma_s = (e^2/m)(n_\uparrow\tau_\uparrow - n_\downarrow\tau_\downarrow)$ being the "spin conductivity". (n_σ is the density of spin-σ electrons.) We have defined the spin-relaxation time τ_s by

$$\frac{\hbar}{\tau_s} = \frac{4\pi}{3} n_s u_s^2 S_{\rm imp}^2 v_+. \tag{91}$$

As expected, only the spin scattering ($\sim \tau_s^{-1}$) contributes to α and β, and the potential scattering ($\sim n_i u^2$) does not. (For α, the second term on the right-hand side of Eq. (89) comes from processes which do not involve s-electrons.)

The ratio β/α cannot be unity in general for the two-component s–d model, since it contains mutually independent quantities, for example, S for d-electrons and δS for s-electrons. For a single-band itinerant ferromagnet (as described by, e.g. the Stoner model), the results are obtained by simply putting $S = 0$ and $\alpha_0 = 0$ in Eqs (87)–(90), and by using the spin polarization of itinerant electrons for δS [81]. We still see that $\alpha \neq \beta$, but it was pointed out that the ratio

$$\frac{\beta}{\alpha} = \frac{\rho_s}{M v_+} \simeq 1 + \frac{1}{12}\left(\frac{M}{\varepsilon_F}\right)^2 \tag{92}$$

is very close to unity [80]. Even so, if we generalize Eq. (80) to the anisotropic one,

$$\overline{S_i^\alpha S_j^\beta} = \delta_{ij}\delta_{\alpha\beta} \times \begin{cases} \overline{S_\perp^2} & (\alpha,\beta = x,y) \\ \overline{S_z^2} & (\alpha,\beta = z) \end{cases}, \tag{93}$$

we have

$$\frac{\beta}{\alpha} = \frac{3\overline{S_\perp^2} + \overline{S_z^2}}{2(\overline{S_\perp^2} + \overline{S_z^2})}, \tag{94}$$

which ranges from 1/2 (for $\overline{S_\perp^2} \ll \overline{S_z^2}$) to 3/2 (for $\overline{S_\perp^2} \gg \overline{S_z^2}$). Therefore, we conclude that $\alpha \neq \beta$ in general, and that the value β/α is very sensitive to the details of the spin-relaxation mechanism.

The results obtained based on phenomenological spin-diffusion equations by Zhang and Li [64] can be written in the form

$$\alpha_{\rm ZL} = \frac{\delta S}{S+\delta S} \cdot \frac{\hbar}{2M\tau_s}, \tag{95}$$

whereas $\beta_{\rm ZL} = \beta$ is the same as Eq. (90). Thus, it predicts $\alpha = \beta$ for single-band itinerant ferromagnets, $S = 0$, which is, however, in disagreement with the present microscopic calculation. So far, all phenomenological theories predict $\alpha = \beta$, in contrast to the present microscopic results showing $\alpha \neq \beta$ in general.

3.3. Gauge field method

In the previous section, we considered small-amplitude fluctuations of magnetization, and calculated the torques in the first order with respect to these small fluctuations. In this sense, the spin torques calculated there are limited to small-amplitude dynamics. (Only for systems with rotational symmetry in spin space, where the form of the torque is known as Eq. (84), this small-amplitude method is sufficient to determine the coefficients, hence the torque.) In this section, we describe a theoretical formalism which is not restricted to small-amplitude dynamics, but can treat finite-amplitude (arbitrary) dynamics directly [87].

3.3.1. Adiabatic spin frame and gauge field

To treat finite-amplitude dynamics of magnetization, we work with a local/instantaneous spin frame (called "adiabatic frame" in the following) for s-electrons whose spin quantization axis is taken to be the local/instantaneous d-spin direction, $\boldsymbol{n}$ [91–93]. The electron spinor $a(x)$ in the new frame is related to the original spinor $c(x)$ as $c(x) = U(x)a(x)$, where U is a 2×2 unitary matrix satisfying $c^\dagger(\boldsymbol{n}\cdot\boldsymbol{\sigma})c = a^\dagger\sigma^z a$. It is convenient to choose U satisfying $U^2 = 1$.

Since $\partial_\mu c = U(\partial_\mu + U^\dagger\partial_\mu U)a \equiv U(\partial_\mu + \mathrm{i}A_\mu)a$, the a-electrons satisfy the Schrödinger equation

$$\mathrm{i}\hbar\left(\frac{\partial}{\partial t} + \mathrm{i}A_0\right)a(x) = \left[-\frac{\hbar^2}{2m}(\nabla_i + \mathrm{i}A_i)^2 - M\sigma_z + \tilde{V}_{\mathrm{imp}}\right]a(x). \tag{96}$$

The original electrons moving in time-dependent/inhomogeneous magnetization is thus mapped to new electrons moving in a uniform and static magnetization $M\sigma_z$ but there arises a coupling to an SU(2) gauge field [94]:

$$A_\mu = -\mathrm{i}U^\dagger(\partial_\mu U) = A_\mu^\alpha\sigma^\alpha \equiv \boldsymbol{A}_\mu\cdot\boldsymbol{\sigma}. \tag{97}$$

Here $\boldsymbol{A}_\mu$ is a measure of temporal ($\mu = 0$) or spatial ($\mu = 1, 2, 3$) variation of magnetization.

Let us introduce a 3×3 orthogonal matrix $\mathcal{R}$, representing the same rotation as U but in a three-dimensional vector space, and satisfying $\det \mathcal{R} = 1$. Note that $\mathcal{R}\hat{z} = \boldsymbol{n}$, $\mathcal{R}\boldsymbol{n} = \hat{z}$, $c^\dagger\boldsymbol{\sigma}c = \mathcal{R}(a^\dagger\boldsymbol{\sigma}a)$ and that $\mathcal{R}(\boldsymbol{a}\times\boldsymbol{b}) = (\mathcal{R}\boldsymbol{a})\times(\mathcal{R}\boldsymbol{b})$ for arbitrary vectors $\boldsymbol{a}$ and $\boldsymbol{b}$. Then the spin-torque density, Eq. (82), is written as

$$\boldsymbol{t}_{\mathrm{el}}(x) = M\mathcal{R}(\hat{z}\times\langle\tilde{\boldsymbol{\sigma}}(x)\rangle_{\mathrm{ne}}), \tag{98}$$

where $\tilde{\boldsymbol{\sigma}}(x) = (a^\dagger\boldsymbol{\sigma}a)_x$.

Since the gauge field $\boldsymbol{A}_\mu$ contains a space/time derivative of magnetization, one may naturally formulate a gradient expansion in terms of $\boldsymbol{A}_\mu$ to calculate, for example, the torque (or spin polarization). In particular, the adiabatic torques are obtained as the first-order terms in $\boldsymbol{A}_\mu$:

$$\langle\tilde{\boldsymbol{\sigma}}_\perp\rangle_{\mathrm{ne}} = \frac{2}{M}[a_\mu\boldsymbol{A}_\mu^\perp + b_\mu(\hat{z}\times\boldsymbol{A}_\mu^\perp)]. \tag{99}$$

Here, $\tilde{\boldsymbol{\sigma}}_\perp = \tilde{\boldsymbol{\sigma}} - \hat{z}(\hat{z}\cdot\tilde{\boldsymbol{\sigma}})$ and $\boldsymbol{A}_\mu^\perp = \boldsymbol{A}_\mu - \hat{z}(\hat{z}\cdot\boldsymbol{A}_\mu)$ are the respective transverse components [94], and the sums over $\mu = 0, 1, 2, 3$ are understood. From the identities,

$$\mathcal{R}\boldsymbol{A}_\mu^\perp = -\frac{1}{2}\boldsymbol{n}\times(\partial_\mu \boldsymbol{n}), \quad \mathcal{R}(\hat{z}\times\boldsymbol{A}_\mu^\perp) = \frac{1}{2}\partial_\mu \boldsymbol{n}, \tag{100}$$

together with Eq. (98), we see that Eq. (99) leads to the adiabatic torque density $\boldsymbol{\tau}_{\rm ad}^0$ of Eq. (84).

3.3.2. Results

If we regard Eq. (99) as a linear response to the gauge field $\boldsymbol{A}_\mu$ appearing in Eq. (96), the coefficients a_μ and b_μ are calculated as linear-response coefficients, and δS, $\boldsymbol{\nu}_{\rm s}$ and β thus obtained coincide with those obtained by the small-amplitude method, Eqs (87), (88) and (90). However, it predicts $\alpha_{\rm sr} = 0$, namely, fails to reproduce the Gilbert damping.

3.3.3. Gilbert damping

The above difficulty that the gauge field method apparently fails to reproduce the Gilbert damping term has been resolved [87] by noting that the impurity spins, which are static (quenched) in the original frame, become time dependent in the adiabatic frame (see Fig. 10). Namely, the spin part of $V_{\rm imp}$ is expressed as

$$\boldsymbol{S}_j\cdot c^\dagger \boldsymbol{\sigma} c = \tilde{\boldsymbol{S}}_j(t)\cdot a^\dagger \boldsymbol{\sigma} a, \tag{101}$$

where

$$\tilde{\boldsymbol{S}}_j(t) = \mathcal{R}(t)\boldsymbol{S}_j \tag{102}$$

is the impurity spin in the adiabatic frame, which is time dependent. (This fact has been expressed by $\tilde{V}_{\rm imp}$ in Eq. (96).) Actually, we can obtain the gauge field from this time dependence as

$$[\mathcal{R}(t)\dot{\mathcal{R}}(t)]^{\alpha\beta} = 2\varepsilon^{\alpha\beta\gamma}A_0^\gamma. \tag{103}$$

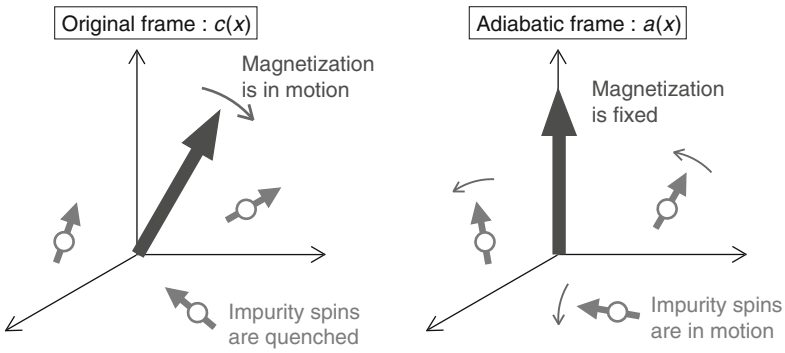

FIGURE 10 Left: magnetization vector $\boldsymbol{n}(t)$ and impurity spins $\boldsymbol{S}_j$ in the original frame. Right: magnetization vector $\hat{z}$ and impurity spins $\tilde{\boldsymbol{S}}_j(t)$ in the adiabatic frame.

Explicit calculation of $\langle\tilde{\boldsymbol{\sigma}}_\perp\rangle_{\rm ne}$ in the second order in $\tilde{\boldsymbol{S}}_j(t)$ (nonlinear response) gives

$$\langle\tilde{\boldsymbol{\sigma}}_\perp(t)\rangle_{\rm ne} = -\frac{2\pi\hbar}{3M} n_{\rm s} u_{\rm s}^2 S_{\rm imp}^2 v_+^2 (\hat{z}\times \boldsymbol{A}_0^\perp(t)), \tag{104}$$

leading to the Gilbert damping, with damping constant exactly the same as Eq. (89).

The present calculation provides us a new picture of Gilbert damping. While the s-electron spin tends to follow the instantaneous d-spin direction $\boldsymbol{n}(t)$, it is at the same time pinned by the quenched impurity spins. These two competing effects are expressed by the time dependence of $\tilde{\boldsymbol{S}}_j(t)$ in the adiabatic frame, and this effect causes Gilbert damping. Namely, the Gilbert damping arises since spins of s-electrons are "dragged" by impurity spins.

Generally, any terms in the Hamiltonian leading to spin relaxation break spin rotational symmetry of s-electrons, and thus acquire time dependence in the adiabatic frame. Therefore, the same scenario as presented here is expected to apply to other type of spin-relaxation processes quite generally.

3.3.4. Non-adiabatic torque

The non-adiabatic torques come from large-momentum processes, so let us put $V_{\rm imp} = 0$ for simplicity. If we retain the full $\boldsymbol{q}$-dependence in the response function, we have, among others, a contribution

$$\langle\tilde{\boldsymbol{\sigma}}_\perp(\boldsymbol{q})\rangle_{\rm ne} = \chi_{ij}(\boldsymbol{q}) E_i (\hat{z}\times \boldsymbol{A}_{q,j}^\perp) + \dots, \tag{105}$$

where the function $\chi_{ij}(\boldsymbol{q})$ is non-zero only when $|k_{\rm F\uparrow} - k_{\rm F\downarrow}| < q < k_{\rm F\uparrow} + k_{\rm F\downarrow}$. In particular, $\chi_{ij}(\boldsymbol{q}) = 0$ in the vicinity of $\boldsymbol{q} = \boldsymbol{0}$, and hence the long-wavelength approximation cannot be applied. The resulting torque

$$\boldsymbol{\tau}_{\rm na}^0(x) = -ME_i \int {\rm d}^3x' \chi_{ij}(\mathbf{r}-\mathbf{r}')\mathcal{R}(x)\boldsymbol{A}_j^\perp(x') \tag{106}$$

is characterized by an oscillatory function $\chi_{ij}(\boldsymbol{r}-\boldsymbol{r}')$ in real space, and is essentially non-local [53, 78, 95–97]. This is the non-adiabatic, momentum-transfer torque due to electron reflection [53], generalized here to arbitrary magnetization texture. For details, see [96].

3.4. Force

We have seen in Section 2.2 that electrons reflected by a domain wall exert a force on the (rigid) domain wall as a back reaction. It was also recognized that the adiabatic β-term also acts as a force on a domain wall [64, 65]. Here, we consider a generalization of the concept of force to a fixed but arbitrary magnetization texture, and derive a general expression of the force acting on the texture.

From $\boldsymbol{t}_{\rm el} = M\boldsymbol{n}\times\langle\boldsymbol{\sigma}_\perp\rangle_{\rm ne}$ and $F_{{\rm el},i} = -M\int {\rm d}^3x(\partial_i\boldsymbol{n})\cdot\langle\boldsymbol{\sigma}_\perp\rangle_{\rm ne}$ [Eq. (35)] [53, 98], one can eliminate $\langle\boldsymbol{\sigma}_\perp\rangle_{\rm ne}$ to obtain

$$F_{{\rm el},i} = -\int {\rm d}^3x(\boldsymbol{n}\times\partial_i\boldsymbol{n})\cdot\boldsymbol{t}_{\rm el}. \tag{107}$$

This is a general formula relating the force to the torque [99].

Each term of the spin torque (84) corresponds to a different type of force. The spin-transfer torque exerts a "transverse" force

$$F_{\mathrm{ST},i} = -\frac{\hbar}{2e} j_{\mathrm{s},\ell} \int \mathrm{d}^3x (\partial_i \boldsymbol{n} \times \partial_\ell \boldsymbol{n}) \cdot \boldsymbol{n}, \tag{108}$$

for a magnetic configuration $\boldsymbol{n}$ subtending a finite solid angle (spin chirality). An example is given by the magnetic vortex in a ferromagnetic dot, whose dynamics driven by electric/spin current will be studied in Section 4.2. The β-term leads to the force

$$F_{\beta,i} = -\beta \frac{\hbar}{2e} j_{\mathrm{s},\ell} \int \mathrm{d}^3x (\partial_i \boldsymbol{n}) \cdot (\partial_\ell \boldsymbol{n}). \tag{109}$$

The non-adiabatic torque, $\boldsymbol{\tau}_{\mathrm{na}}$, gives a force,

$$F_{\mathrm{na},i} = -2ME_i \int \mathrm{d}^3x \int \mathrm{d}^3x' \chi_{ij}(\boldsymbol{r} - \boldsymbol{r}') \boldsymbol{A}_i^\perp(\boldsymbol{r}) \cdot \boldsymbol{A}_j^\perp(\boldsymbol{r}'). \tag{110}$$

This force is due to the reaction to the electron reflection, and is closely related to the resistivity as noted in the domain-wall case [53], and also shown below.

3.4.1. Relation to transport coefficients

Since the force is, by definition, the momentum transfer from s-electrons to magnetization, its back reaction will affect the s-electrons' orbital motion, hence their transport. Therefore, it is expected that the force and the transport coefficients are closely related with each other. In fact, we have observed a relation, Eq. (33) or Eq. (41), for a domain wall in an idealized situation that there are no spin- and momentum-dissipation processes (other than the domain wall) for s-electrons. Explicit calculation shows that these relations are not modified by the presence of normal impurities (momentum-dissipation processes) [53]. Here we extend such relations to more general magnetization texture, and to the case that the s-electron transport is diffusive [96, 97]. The texture is assumed static here.

For simplicity, we neglect the spin-relaxation processes, and calculate the transport coefficients by using Mori formula (memory function formalism) [100, 101]. The electrical resistivity due to (static) magnetization texture is obtained as

$$\rho_{ij} = \left(\frac{2M}{enV}\right)^2 \sum_{\boldsymbol{q}} \left[\chi^{(0)}(\boldsymbol{q})(\boldsymbol{A}_{-\boldsymbol{q},i}^\perp \cdot \boldsymbol{A}_{-\boldsymbol{q},j}^\perp) + \chi^{(1)}(\boldsymbol{q})(\boldsymbol{A}_{-\boldsymbol{q},i}^\perp \times \boldsymbol{A}_{-\boldsymbol{q},j}^\perp)^z\right], \tag{111}$$

$$\equiv \rho_{ij}^{\mathrm{refl}} + \rho_{ij}^{\mathrm{Hall}}, \tag{112}$$

where

$$\chi^{(0)}(\boldsymbol{q}) = \frac{2\hbar}{V} \sum_k \delta(\xi_{\boldsymbol{k}+\boldsymbol{q}/2}^\sigma) \delta(\xi_{\boldsymbol{k}-\boldsymbol{q}/2}^{\overline{\sigma}}) = \frac{m^2}{2\pi\hbar^3} \cdot \frac{1}{q} \Theta_{\mathrm{st}}(q), \tag{113}$$

$$\chi^{(1)}(\boldsymbol{q}) = \frac{\hbar}{V} \sum_\sigma \sigma \sum_k \frac{f_{\boldsymbol{k}+\boldsymbol{q}/2}^\sigma - f_{\boldsymbol{k}-\boldsymbol{q}/2}^{\overline{\sigma}}}{(\xi_{\boldsymbol{k}+\boldsymbol{q}/2}^\sigma - \xi_{\boldsymbol{k}-\boldsymbol{q}/2}^{\overline{\sigma}})^2} = \frac{\hbar}{2M^2} \rho_{\mathrm{s}} + O(q^2), \tag{114}$$

with $\xi_{\boldsymbol{k}}^{\sigma} = \varepsilon_{\boldsymbol{k}} - \varepsilon_{\mathrm{F}\sigma} = \hbar^2(\boldsymbol{k}^2 - k_{\mathrm{F}\sigma}^2)/2m$, and $\Theta_{\mathrm{st}}(q) = 1$ for $|k_{\mathrm{F}\uparrow} - k_{\mathrm{F}\downarrow}| < q < k_{\mathrm{F}\uparrow} + k_{\mathrm{F}\downarrow}$, and $\Theta_{\mathrm{st}}(q) = 0$ otherwise. In deriving Eq. (111), we have used the same model as used in Section 3.3, and neglected the difference, $\tau_\uparrow - \tau_\downarrow \simeq 0$, in the s-electron lifetimes. We define the symmetric part as $\rho_{ij}^{\mathrm{refl}}$, and the anti-symmetric part as $\rho_{ij}^{\mathrm{Hall}}$.

Let us first consider the anti-symmetric part, $\rho_{ij}^{\mathrm{Hall}}$. Since the kernel $\chi^{(1)}(\boldsymbol{q})$ is non-zero in the adiabatic limit, $q \to 0$, one may make a long-wavelength approximation as

$$\rho_{ij}^{\mathrm{Hall}} = \frac{2\hbar\rho_{\mathrm{s}}}{e^2 n^2 V}\int \mathrm{d}^3x [\boldsymbol{A}_i^{\perp}(\boldsymbol{r}) \times \boldsymbol{A}_j^{\perp}(\boldsymbol{r})]^z, \tag{115}$$

$$= \frac{\hbar\rho_{\mathrm{s}}}{2e^2 n^2 V}\int \mathrm{d}^3x \boldsymbol{n}\cdot(\partial_i \boldsymbol{n} \times \partial_j \boldsymbol{n}). \tag{116}$$

In the second line, we have used Eq. (100). By comparing with the spin-transfer force of Eq. (108), we see the relation

$$\begin{aligned} F_{\mathrm{ST},i} &= -\frac{en^2V}{\rho_{\mathrm{s}}}\sum_{\ell}\rho_{i\ell}^{\mathrm{Hall}} j_{\mathrm{s},\ell} \\ &\simeq -eN_{\mathrm{e}}\sum_{\ell}\rho_{i\ell}^{\mathrm{Hall}} j_{\ell}. \end{aligned} \tag{117}$$

Here, $n = n_\uparrow + n_\downarrow$ is the s-electron density, $N_{\mathrm{e}} = nV$ is the total number of s-electrons, and $\boldsymbol{j}$ is the electric (charge) current. In the second line, we have used the same approximation ($\tau_\uparrow \simeq \tau_\downarrow$) as used above, and put $(n/\rho_{\mathrm{s}})\boldsymbol{j}_{\mathrm{s}} \simeq \boldsymbol{j}$.

For the symmetric part, $\rho_{ij}^{\mathrm{refl}}$, the kernel $\chi^{(0)}(\boldsymbol{q})$ is finite only for $|k_{\mathrm{F}\uparrow} - k_{\mathrm{F}\downarrow}| \le q \le k_{\mathrm{F}\uparrow} + k_{\mathrm{F}\downarrow}$, and vanishes near $q = 0$, hence one cannot make a long-wavelength approximation. This term is due to the electron reflection. The force due to non-adiabatic torque is obtained as

$$F_{\mathrm{na},i} = -\sum_{\ell} R_{i\ell} j_{\ell}, \tag{118}$$

where

$$R_{i\ell} = \frac{(2M)^2}{enV}\sum_{q,j}\frac{q_j q_\ell}{q^2}\chi^{(0)}(\boldsymbol{q})(\boldsymbol{A}_{\boldsymbol{q},i}^{\perp}\cdot\boldsymbol{A}_{-\boldsymbol{q},j}). \tag{119}$$

There seems no exact relation between $\rho_{ij}^{\mathrm{refl}}$ and R_{ij} in general. However, if the magnetization texture is one-dimensional, namely, if it depends on only one Cartesian coordinate, say x, the gauge field $\boldsymbol{A}_i$ is non-zero only for this component, $i = x$, and $R_{i\ell}$ is non-zero only for $i = \ell = x$. In this case, we see that $R_{xx} = enV\rho_{xx}^{\mathrm{refl}} = eN_{\mathrm{e}}\rho_{xx}^{\mathrm{refl}}$, and hence

$$F_{\mathrm{na},x} = -eN_{\mathrm{e}}\rho_{xx}^{\mathrm{refl}} j_x. \tag{120}$$

Namely, the x-component of the current exerts a force in the x-direction. (The relative minus sign is due to the fact that the direction of electron flow is opposite to that of the electric current.)

3.4.2. Further references

The spin-transfer torque in the form of Eq. (64) was first derived by Bazaliy *et al.* [74]. The β-term was first derived by Zhang and Li [64] based on a spin-diffusion equation with a spin-relaxation term included, and by Thiaville *et al.* [65] as a continuum limit of a special type of torque known in multilayer systems [102].

Duine *et al.* [83] put the present microscopic (small-amplitude) calculation into the Keldysh formalism, and developed a functional description of spin torques, which will be used for finite-temperature and/or fluctuation dynamics. Some attempts with the Boltzmann equation are done in Ref. [82]. Some developments in the treatment of Gilbert damping can be seen in Refs [90, 103, 104]. Phenomenological theory [105, 106] based on irreversible thermodynamics is also developed, which, however, needs to be reconciled with the microscopic theory.

The non-adiabatic torque is studied in Refs [53, 78, 95, 96]. The domain-wall resistivity is studied in Refs [93, 107]. The effects of spin–orbit coupling are studied on domain-wall resistance [108] and domain-wall mobility [109] in a model of ferromagnetic semiconductors.

4. RELATED TOPICS

In this section, we present two topics on the current-driven magnetization dynamics.

The first topic is the current-driven motion of a magnetic vortex. It is mainly governed by the spin-transfer torque, and nicely exemplifies the "spin-transfer force", $\boldsymbol{F}_{\mathrm{ST}}$, of Eq. (108).

The second topic is related to another aspect of the spin-transfer torque. Namely, the spin-transfer torque favours, and even induces, a topologically non-trivial spin texture along the spin current [74–77], in quite a similar way that the spin Berry phase does in the time direction, namely, precession. It causes the Doppler shift and the softening of spin-wave frequency, and eventually leads to an instability of the uniformly magnetized state.

4.1. Current-driven motion of magnetic vortices

Just as the magnetic domain wall is a topologically stable structure in easy-axis magnets, such as thin wires of soft ferromagnets, a magnetic vortex is a topologically stable structure in easy-plane magnets such as films. In thin disks in particular, it is realized as the most stable structure for a certain range of parameters [110]. The current-driven dynamics of such magnetic vortices is the subject of this section [111–114].

A magnetic vortex realized in a disk is illustrated in Fig. 11A and B. It is characterized by circulating in-plane magnetization in the region away from the centre ($|\boldsymbol{r}| \gg \delta_{\mathrm{v}}$), and out-of-plane magnetization in the core (centre) region ($|\boldsymbol{r}| \leq \delta_{\mathrm{v}}$), where δ_{v} is the size of the core. Such a vortex configuration is characterized by two integers, p and C. The first one is the polarity, $p = \pm 1$, which specifies the

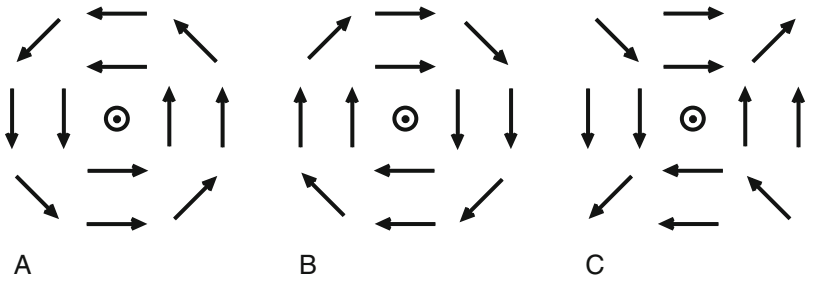

FIGURE 11 Schematic illustration of magnetic vortices. (A) A vortex with $q = 1$, $p = 1$ and $C = 1$. (B) A vortex with $q = 1$, $p = 1$ and $C = -1$. (C) An example of anti-vortex ($q = -1$). In each case, the magnetization in the centre (core) region rises out of the plane, either upward ($p = 1$) or downward ($p = -1$). In each figure, a vortex with $p = 1$ is shown, as indicated by a circle with a dot. In a ferromagnetic dot with suitable size, either (A) or (B) is realized, whereas in a film, free vortices and anti-vortices can appear.

direction of the out-of-plane component at the vortex centre. The second one is the chirality, C, which specifies the sense of circulation, namely, counterclockwise ($C = 1$) or clockwise ($C = -1$).

More generally, magnetic configurations illustrated in Fig. 11C are also called vortices. These new members are distinguished by introducing a third integer, $q = \pm 1, \pm 2, \ldots$, called vorticity. It represents the number of circulation of the in-plane magnetization component. A vortex constrained by the disk boundary condition corresponds to $q = 1$, but in other situations, vortices with $q \neq 1$ can also appear in general. In the latter case, the value of C may not be restricted to integers, but can take general real numbers. Magnetization pattern for a vortex specified by (p, q, C) is expressed as

$$-\boldsymbol{n}(\boldsymbol{r}) = \begin{cases} \hat{x}\cos(q\varphi + \pi C/2) + \hat{y}\sin(q\varphi + \pi C/2) & (|\,\boldsymbol{r}\,| \gg \delta_{\mathrm{v}}) \\ p\hat{z} & (\boldsymbol{r} \to \boldsymbol{0}) \end{cases}, \tag{121}$$

where $\varphi = \tan^{-1}(y/x)$ with $\boldsymbol{r} = (x, y, z)$. (The minus sign on the left-hand side indicates that we define the numbers (p, q, C) with respect to the direction of magnetization, not spin.)

In the following, we mainly consider a vortex realized in a disk, hence with $q = 1$. However, some of the equations have more generality, so we leave q to be a general integer in the equations.

4.1.1. Equation of motion

We focus on the position of the vortex centre, $\boldsymbol{X} = \begin{pmatrix} X \\ Y \end{pmatrix}$. The equation of motion for $\boldsymbol{X}$ is known as the Thiele equation [98, 111, 115],

$$-\boldsymbol{G} \times \dot{\boldsymbol{X}} - \alpha D \dot{\boldsymbol{X}} + \boldsymbol{F} = \boldsymbol{0}, \tag{122}$$

which is obtained as a force balance equation. The first term on the left-hand side is known as a gyroforce. A vector

$$\boldsymbol{G} = \hat{z}\frac{M_s d}{\gamma_0}\int_{\text{disk}} \mathrm{d}x\mathrm{d}y(\partial_x \boldsymbol{n} \times \partial_y \boldsymbol{n})\cdot\boldsymbol{n} \tag{123}$$

is called as the gyrovector, which is perpendicular to the disk (xy-) plane. Here the magnetization is assumed constant in the thickness (z-) direction, and the film thickness d is simply multiplied. The integral in Eq. (123), which is thus over the two-dimensional disk region, is a topological quantity equal to the solid angle subtended by the magnetization vector $\boldsymbol{n}$ over the disk, which is estimated to be $2\pi pq$ using Eq. (121). Thus,

$$\boldsymbol{G} = 2\pi pq\frac{M_s d}{\gamma_0}\hat{z}. \tag{124}$$

The second term of Eq. (122) represents the damping force, where α is the Gilbert damping constant and D is given by

$$D = \frac{M_s d}{\gamma_0}\int_{\text{disk}} \mathrm{d}x\mathrm{d}y(\nabla \boldsymbol{n})^2. \tag{125}$$

The third term, $\boldsymbol{F}$, represents any other forces acting on the vortex centre. The force due to electric/spin current is given by

$$\boldsymbol{F}_{\text{el}} = \boldsymbol{G} \times \boldsymbol{v}_s + \beta' D\boldsymbol{v}_s, \tag{126}$$

as seen in Section 3.4. Here β' includes contributions from the β-term due to spin relaxation, and also from the non-adiabatic torque due to electron reflection. Note that, in the absence of applied field, the chirality does not enter the equation of motion, and only p and q (contained in $\boldsymbol{G}$) are relevant for the current-driven dynamics.

The value of D will actually depend on the vortex position owing to the deformation of the vortex profile. On the other hand, the value of G is quite robust since it is a topological invariant; as far as the magnetization at the disk perimeter is along the surface ("disk boundary condition"), and the continuum approximation is valid, it is quantized as given above.

4.1.2. Current-driven dynamics

Let us study a current-driven motion of a vortex confined in a disk. The equation of motion is given by

$$\boldsymbol{G} \times (\dot{\boldsymbol{X}} - \boldsymbol{v}_s) + \alpha D\dot{\boldsymbol{X}} - \beta' D\boldsymbol{v}_s = -k\boldsymbol{X}. \tag{127}$$

Here the restoring force due to the confinement is approximated by $-k\boldsymbol{X}$ with a force constant k. We assume k and D to be constant for simplicity.

We first consider the case that a steady DC current, represented by $\boldsymbol{v}_s = (v_s, 0)$, is applied. The solution is easily obtained in terms of a complex coordinate, $Z = X + \mathrm{i}Y$, as

$$Z(t) = \mathrm{e}^{\mathrm{i}\zeta t}Z(0) + \mathrm{i}\frac{v_s}{\Omega}(1 - \mathrm{i}\tilde{\beta})(1 - \mathrm{e}^{\mathrm{i}\zeta t}), \tag{128}$$

where $\Omega = k/G$, $\zeta = \Omega/(1 - \mathrm{i}\tilde{\alpha}) = k/(G - \mathrm{i}\alpha D)$, $\tilde{\alpha} = \alpha D/G$ and $\tilde{\beta} = \beta' D/G$. In a vector notation, it reads

$$\boldsymbol{X}(t) = \mathcal{R}(\zeta' t)[\boldsymbol{X}(0) - \boldsymbol{X}(\infty)]\mathrm{e}^{-\zeta'' t} + \boldsymbol{X}(\infty), \tag{129}$$

where $\zeta' = \mathrm{Re}\,\zeta$, $\zeta'' = \mathrm{Im}\,\zeta > 0$ and

$$\mathcal{R}(\theta) = \begin{pmatrix} \cos\theta & -\sin\theta \\ \sin\theta & \cos\theta \end{pmatrix} \tag{130}$$

is the rotation matrix. Thus the vortex centre exhibits a spiral motion in clockwise (for $\zeta' < 0$, i.e. $pq = -1$) or counterclockwise (for $\zeta' > 0$, i.e. $pq = 1$) sense, and eventually approaches the equilibrium position

$$\boldsymbol{X}(\infty) = \frac{v_\mathrm{s}}{\Omega}\begin{pmatrix} \tilde{\beta} \\ 1 \end{pmatrix} = \frac{v_\mathrm{s}}{k}\begin{pmatrix} \beta' D \\ G \end{pmatrix} \tag{131}$$

as $t \to \infty$. Note that the vortex configuration is defined here in terms of magnetization direction, not spin direction, in contrast to Ref. [111].

For AC current, $v_\mathrm{s} = (v_\mathrm{s}\cos\omega t, 0)$, the solution is obtained as [114]

$$Z(t) = \mathrm{e}^{\mathrm{i}\zeta t}Z(0) + \frac{\mathrm{i}}{2}v_\mathrm{s}(1 - \mathrm{i}\tilde{\beta})\left[\frac{\mathrm{e}^{-\mathrm{i}\omega t} - \mathrm{e}^{\mathrm{i}\zeta t}}{\Omega + (1 - \mathrm{i}\tilde{\alpha})\omega} + \frac{\mathrm{e}^{\mathrm{i}\omega t} - \mathrm{e}^{\mathrm{i}\zeta t}}{\Omega - (1 - \mathrm{i}\tilde{\alpha})\omega}\right], \tag{132}$$

in the complex notation, or as

$$\boldsymbol{X}(t) = \mathcal{R}(\zeta' t)[\boldsymbol{X}(0) - \boldsymbol{X}_\omega - \boldsymbol{X}_{-\omega}]\mathrm{e}^{-\zeta'' t} + \mathcal{R}(\omega t)\boldsymbol{X}_\omega + \mathcal{R}(-\omega t)\boldsymbol{X}_{-\omega}, \tag{133}$$

in the vector notation, where

$$\boldsymbol{X}_{\pm\omega} = \frac{1}{2}\frac{v_\mathrm{s}}{(\Omega \mp \omega)^2 + (\tilde{\alpha}\omega)^2}\begin{pmatrix} \tilde{\beta}\Omega \pm (\tilde{\alpha} - \tilde{\beta})\omega \\ \Omega \mp (1 + \tilde{\alpha}\tilde{\beta})\omega \end{pmatrix}. \tag{134}$$

The first term of Eq. (133) represents eigenrotation [116], which will eventually decay, and the second and third terms represent forced rotation. Near the resonance, $\omega \simeq \pm\Omega$, it exhibits a steady circular motion,

$$\boldsymbol{X}(t) \simeq \mathcal{R}(\pm\omega t)\boldsymbol{X}_{\pm\omega} \simeq \mathcal{R}(\Omega t)\boldsymbol{X}_\Omega, \tag{135}$$

for $\zeta'' t \gg 1$. The amplitude just on resonance is given by

$$\boldsymbol{X}_\Omega = \frac{v_\mathrm{s}}{2\tilde{\alpha}\Omega}\begin{pmatrix} 1 \\ -\tilde{\beta} \end{pmatrix}, \tag{136}$$

which is enhanced by a factor of $\tilde{\alpha}^{-1}$ compared with the displacement (131) due to DC current.

4.1.3. Lagrangian formalism

The Lagrangian formalism for vortex dynamics with the spin-transfer effect has been developed by Shibata *et al.* [111]. They obtained the Lagrangian

$$L_\mathrm{v} = \frac{1}{2}\boldsymbol{G}\cdot(\dot{\boldsymbol{X}} \times \boldsymbol{X}) - \boldsymbol{G}\cdot(\boldsymbol{v}_\mathrm{s} \times \boldsymbol{X}) - U(\boldsymbol{X}), \tag{137}$$

which, together with the dissipation function

$$W_{\rm v} = \frac{1}{2}\alpha D\dot{\boldsymbol{X}}^2, \tag{138}$$

leads to Eq. (127) with $\beta' = 0$. The first term of Eq. (137), namely, $G(\dot{X}Y - \dot{Y}X)/2$, shows that X and Y are canonically conjugate each other. Note that these variables for the vortex are quite symmetric each other, in contrast to X and ϕ_0 for the domain-wall case.

4.2. Current-induced spin-wave instability

The spin-transfer torque is expressed by the term

$$H_{\rm ST} = \frac{\hbar}{2e}\int {\rm d}^3x(\boldsymbol{j}_{\rm s}\cdot\nabla\phi)(1-\cos\theta) \tag{139}$$

in the spin Hamiltonian [77]. The spin current couples to a gradient of magnetization. It thus favours spatial variation of magnetization. This leads to the softening, and even to instability, of spin waves [74–77]. It also lowers the domain-wall energy under spin current [77].

It has been known that a sufficiently large spin current leads to a spin-wave instability of the uniformly magnetized state. This was first shown by Bazaliy *et al.* [74] for a layered system with an interface between a normal metal and a ferromagnet, and later emphasized by Fernández-Rossier *et al.* [76] to be a bulk phenomenon. Indeed, Eq. (139) can be seen as a spatial-derivative version of the kinetic (Berry phase) term, and a kind of "precession" along the spin current may be expected.

Let us consider the LLG equation

$$\dot{\boldsymbol{n}} = S'(-J\nabla^2\boldsymbol{n} - Kn_z\hat{z} + K_\perp n_y\hat{y})\times\boldsymbol{n} + \alpha\dot{\boldsymbol{n}}\times\boldsymbol{n} + (\boldsymbol{v}_{\rm s}\cdot\nabla)\boldsymbol{n}, \tag{140}$$

where $S' = S^2/\hbar S_{\rm tot}$. The ground state is given by $\boldsymbol{n} = \hat{z}$, namely, uniformly magnetized in z-direction, which actually satisfies Eq. (140). Next, as an excited state, we consider a small fluctuation $\delta\boldsymbol{n}$ from the ground state, $\boldsymbol{n} = \hat{z}$, and put $\boldsymbol{n}(\boldsymbol{r},t) = \hat{z} + \delta\boldsymbol{n}(\boldsymbol{r},t)$. The spin-wave dispersion is obtained by assuming a solution of the form, $\delta\boldsymbol{n}(\boldsymbol{r},t) = (\delta n_x, \delta n_y, 0){\rm e}^{{\rm i}(\boldsymbol{q}\cdot\boldsymbol{r}-\omega t)}$. For $\alpha = 0$, it is given by

$$\Omega_{\boldsymbol{q}} = KS'\sqrt{\omega_q(\omega_q+\kappa)} + \boldsymbol{q}\cdot\boldsymbol{v}_{\rm s}, \tag{141}$$

where $\omega_q = q^2\lambda^2 + 1$, $\lambda = \sqrt{J/K}$, and $\kappa = K_\perp/K$. The first term represents the spin-wave energy in the absence of spin current, and has a spectral gap $S'\sqrt{K(K+K_\perp)}$ due to magnetic anisotropy. The second term represents the effect of spin current, called Doppler shift [117]. It reduces the spin-wave gap and shifts the energy-minimum point from $\boldsymbol{q} = \boldsymbol{0}$ to some finite wave vector. If the spin-current density exceeds a certain critical value, $v_{\rm s} > v_{\rm s}^{\rm cr}$, the spin-wave energy becomes negative for a range of $\boldsymbol{q}$ (spin-wave instability). This means that the uniformly magnetized state is not the ground state any more, and is energetically unstable.

In the presence of a domain wall, the spin-wave spectrum is modified to be [77]

$$\Omega_q = KS'\sqrt{\omega_q(\omega_q+\kappa) + 2\kappa^2\sin^2\phi_0\cos 2\phi_0} + q(v_{\rm s} - \dot{X}). \tag{142}$$

The spin-transfer velocity appears relative to the domain-wall velocity, and the above instability is reduced. There is a range of the spin current where the uniformly magnetized state is unstable whereas the domain-wall state is stable (at least locally in configuration space). It was then proposed that in such case the domain walls are created spontaneously. Indeed, for large $K_\perp$, the state with a domain wall is shown to have lower energy than that of the uniform ferromagnetic state under large current [77]. Current-induced formation of domain walls was observed in 1D micromagnetic simulations [118]. For films or wide wires having easy-plane magnetic anisotropy, the spin-wave instability is followed by the formation of magnetic vortices as found by simulations [119].

5. PROSPECTS

As for the domain-wall motion, identification of driving mechanism together with the origin of threshold current in each system/current density/temperature is the most important issue. At present, the experimental situation seems controversial for metallic systems. Since they are expected to be located in regime I (weak and extrinsic pinning), systematic studies by tuning extrinsic pinning and/or the β-term will clarify the issue. As for semiconductors, the spin-transfer mechanism seems to well fit the experimental results above the threshold [44], as well as the creep region below the threshold [70]. However, there remains a theoretical puzzle why the force (due to spin relaxation) does not seem to play any role in spite of strong spin–orbit coupling expected in this system.

Microscopic understanding of each spin torque is also an important issue. In particular, dissipative torques (α- and β-terms), coming from spin relaxation of electrons, should be understood as material-dependent quantities; for each real system, we need to identify the dominant spin-relaxation mechanism, and clarify the dependence of α and β on material parameters. Development of first-principles calculational methods for spin torques is also desired for the purpose of material/device design.

Inverse effects to spin torques such as electron transport coefficients and "spin motive force" also deserve closer study. These studies will lead to a unified picture of interplay between electric/spin current and magnetization.

ACKNOWLEDGEMENTS

We would like to express our deep thanks to J. Shibata for his fruitful contributions at every stage of our collaboration. H.K. is indebted to K. Miyake for his continual encouragement.

REFERENCES

[1] Maekawa, S. (ed.) (2006). *In* "Concepts in Spin Electronics." Oxford University Press, Oxford.
[2] Xu, Y. B., and Thompson, S. M. (eds.) (2007). *In* "Spintronic Materials and Technology." Taylor & Francis, New York.

[3] Slonczewski, J. C. (1996). *J. Magn. Magn. Mater.* **159**, L1.
[4] Berger, L. (1996). *Phys. Rev. B* **54**, 9353.
[5] Berger, L. (1984). *J. Appl. Phys.* **55**, 1954.
[6] Berger, L. (1978). *J. Appl. Phys.* **49**, 2156.
[7] Berger, L. (1986). *Phys. Rev. B* **33**, 1572.
[8] Berger, L. (1992). *J. Appl. Phys.* **71**, 2721.
[9] Freitas, P. P., and Berger, L. (1985). *J. Appl. Phys.* **57**, 1266.
[10] Salhi, E., and Berger, L. (1993). *J. Appl. Phys.* **73**, 6405.
[11] Tserkovnyak, Y., Brataas, A., Bauer, G. E. W., and Halperin, B. I. (2005). *Rev. Mod. Phys.* **77**, 1375.
[12] Chikazumi, S. (1997). "Physics of Ferromagnetism", 2nd edn. Oxford University Press, Oxford.
[13] Hubert, A., and Schäfer, R. (1998). "Magnetic Domains." Springer-Verlag, Berlin.
[14] de Leeuw, F. H., van den Doel, R., and Enz, U. (1980). *Rep. Prog. Phys.* **43**, 659.
[15] Slonczewski, J. C. (1972). *Int. J. Magn.* **2**, 85; (1974); *J. Appl. Phys.* **45**, 2705.
[16] We consider the case that the spin $\boldsymbol{S}$ and the associated magnetic moment $\boldsymbol{\mu}$ are opposite in direction, $\boldsymbol{\mu} = -\gamma_0 \hbar \boldsymbol{S}$ with $\gamma_0 > 0$, as is the case for a free electron.
[17] Döring, W. (1948). *Z. Naturforsch.* **3A**, 373.
[18] The equation for magnetization $\boldsymbol{M}$, instead of spin $\boldsymbol{S}$ [16], has a plus sign (instead of minus sign) in front of the damping (α-) term in Eq. (5).
[19] This may include the demagnetizing field from surface magnetic charges (as in nanowires) or from volume magnetic charges (as in moving Bloch walls [12, 31, 32]), as well as the effective field due to magnetocrystalline anisotropy.
[20] We may also estimate the torque as $T_z = -\gamma_0 \hbar (\boldsymbol{S} \times \boldsymbol{H}_{\rm eff})_z = -\gamma_0 \hbar S_x H_y = -K_\perp S_x S_y$ (from Eq. (8)), with $S_x = S \cos \phi_0$ and $S_y = S \sin \phi_0$.
[21] Effective fields coming from $\tilde{J}$ and K in the Hamiltonian (4) cancel each other thanks to the stationary property of the domain-wall solution.
[22] If we rewrite Eq. (9) as $-(\hbar SN/\lambda)\dot{\phi}_0 = F_{\rm B}$, with $F_{\rm B}$ given by Eq. (2), we see that $P = -(\hbar SN/\lambda)\phi_0$ is the corresponding momentum.
[23] From Eq. (12) and [22], we have $P = (\hbar^2 N/\lambda^2 K_\perp)\dot{X}$ for "momentum", which may be identified with $M_{\rm w}\dot{X}$.
[24] For a Bloch wall, the demagnetizing field from volume magnetic charges (due to non-uniform $\phi(x, t)$) contributes to $K_\perp$ by $2\pi M_0^2$, where $M_0 = \gamma_0 \hbar S/a^3$ is the magnetization. Retaining only this contribution leads to the original expression by Döring [17].
[25] The $K_\perp$ breaks spin rotational symmetry around the z-axis, and hence breaks the conservation of $S^z_{\rm tot}$. Note that the applied field $\boldsymbol{B}$ conserves $S^z_{\rm tot}$.
[26] Introduction of finite damping α also leads to non-conservation of $S^z_{\rm tot}$. In this case, it is possible to exchange angular momentum between X and ϕ_0, as seen from Eqs (26) and (27). Then, even if $K_\perp = 0$, there is a solution of a moving domain wall, where the angular momentum necessary for the domain-wall translation (X) is provided by ϕ_0.
[27] Auerbach, A. (1994). "Interacting Electrons and Quantum Magnetism." Springer-Verlag, Berlin (Chapter 10).
[28] Berry, M. V. (1984). *Proc. R. Soc. Lond. A* **392**, 45.
[29] Goldstein, H., Poole, C., and Safko, J. (2002). "Classical Mechanics", 3rd edn. Addison-Wesley, San Francisco, CA (Chapter 1, Section 5).
[30] Therefore, W is independent of the choice (parametrization) of dynamical variables, and one can check that Eq. (20) is covariant under general variable changes.
[31] Braun, H. B., Kyriakidis, J., and Loss, D. (1997). *Phys. Rev. B* **56**, 8129.
[32] Braun, H. B., and Loss, D. (1996). *Phys. Rev. B* **54**, 3237.
[33] Takagi, S., and Tatara, G. (1996). *Phys. Rev. B* **54**, 9920.
[34] If we take the upper sign in Eqs (26) and (27), and assume that the external field is applied in the positive z-direction, $\boldsymbol{B} = (0, 0, +B)$, they coincide with those of Ref. [53]. Note that Eqs (26) and (27) (and Eqs (9) and (11)) have been derived for $\boldsymbol{B} = (0, 0, -B)$.
[35] Precisely speaking, because of the special form of the damping (α-) terms, the mass and force are renormalized as $M_{\rm w} = (\hbar^2 N/\lambda^2 K_\perp)(1 + \alpha^2)$ and $F = f + \alpha(\hbar/SK_\perp)\dot{f}$, where $f = F_{\rm B} + F_{\rm pin}$.
[36] Grollier, J., Boulenc, P., Cros, V., Hamzic, A., Vaurés, A., Fert, A., and Faini, G. (2003). *Appl. Phys. Lett.* **83**, 509.

[37] Grollier, J., Lacour, D., Cros, V., Hamzic, A., Vaurés, A., Fert, A., Adam, D., and Faini, G. (2002). *J. Appl. Phys.* **92**, 4825.
[38] Tsoi, M., Fontana, R. E., and Parkin, S. S. P. (2003). *Appl. Phys. Lett.* **83**, 2617.
[39] Kläui, M., Vaz, C. A. F., Bland, J. A. C., Wernsdorfer, W., Faini, G., Cambriland, E., and Heyderman, L. J. (2003). *Appl. Phys. Lett.* **83**, 105.
[40] Vernier, N., Allwood, D. A., Atkinson, D., Cooke, M. D., and Cowburn, R. P. (2004). *Europhys. Lett.* **65**, 526.
[41] Yamaguchi, A., Ono, T., Nasu, S., Miyake, K., Mibu, K., and Shinjo, T. (2004). *Phys. Rev. Lett.* **92**, 077205.
[42] Saitoh, E., Miyajima, H., Yamaoka, T., and Tatara, G. (2004). *Nature* **432**, 203.
[43] Yamanouchi, M., Chiba, D., Matsukura, F., and Ohno, H. (2004). *Nature* **428**, 539.
[44] Yamanouchi, M., Chiba, D., Matsukura, F., Dietl, T., and Ohno, H. (2006). *Phys. Rev. Lett.* **96**, 096601.
[45] Kläui, M., Vaz, C. A. F., Bland, J. A. C., Wernsdorfer, W., Faini, G., Cambril, E., Heyderman, L. J., Nolting, F., and Rüdiger, U. (2005). *Phys. Rev. Lett.* **94**, 106601.
[46] Kläui, M., Jubert, P. O., Allenspach, R., Bischof, A., Bland, J. A. C., Faini, G., Rüdiger, U., Vaz, C. A. F., Vila, L., and Vouille, C. (2005). *Phys. Rev. Lett.* **95**, 026601.
[47] Hayashi, M., Thomas, L., Bazaliy, Ya. B., Rettner, C., Moriya, R., Jiang, X., and Parkin, S. S. P. (2006). *Phys. Rev. Lett.* **96**, 197207.
[48] Hayashi, M., Thomas, L., Rettner, C., Moriya, R., Jiang, X., and Parkin, S. S. P. (2006). *Phys. Rev. Lett.* **97**, 207205.
[49] Hayashi, M., Thomas, L., Rettner, C., Moriya, R., and Parkin, S. S. P. (2007). *Nat. Phys.* **3**, 21.
[50] Thomas, L., Hayashi, M., Jiang, X., Moriya, R., Rettner, C., and Parkin, S. S. P. (2006). *Nature* **443**, 197.
[51] Thomas, L., Hayashi, M., Jiang, X., Moriya, R., Rettner, C., and Parkin, S. S. P. (2007). *Science* **315**, 1553.
[52] This is not an essential assumption in the following part, but just for simplicity. No essential changes are needed in applying the following results to itinerant ferromagnets where magnetization and conduction are carried by same electrons, as described near the end of Section 3.2.
[53] Tatara, G., and Kohno, H. (2004). *Phys. Rev. Lett.* **92**, 086601; (2006). **96**, 189702.
[54] Barnes, S. E., and Maekawa, S. Chapter 7 of Ref. [1].
[55] Stern, A. (1992). *Phys. Rev. Lett.* **68**, 1022.
[56] Barnes, S. E., Maekawa, S., and Ieda, J. (2006). *Appl. Phys. Lett.* **89**, 122507.
[57] Barnes, S. E., and Maekawa, S. (2007). *Phys. Rev. Lett.* **98**, 246601.
[58] Duine, R. A. (2008). *Phys. Rev. B* **77**, 014409.
[59] Stamenova, M., Todorov, T. N., and Sanvito, S. cond-mat/0708.1167.
[60] Yang, S. A., Xiao, D., and Niu, Q. cond-mat/0709.1117.
[61] Tserkovnyak, Y., and Mecklenburg, M. cond-mat/0710.5193.
[62] Saitoh, E. (private communications).
[63] Brataas, A., Tserkovnyak, Y., Bauer, G. E. W., and Halperin, B. I. (2002). *Phys. Rev. B* **66**, 060404.
[64] Zhang, S., and Li, Z. (2004). *Phys. Rev. Lett.* **93**, 127204.
[65] Thiaville, A., Nakatani, Y., Miltat, J., and Suzuki, Y. (2005). *Europhys. Lett.* **69**, 990.
[66] Tatara, G., Takayama, T., Kohno, H., Shibata, J., Nakatani, Y., and Fukuyama, H. (2006). *J. Phys. Soc. Jpn.* **75**, 064708.
[67] Nakatani, Y. (unpublished results).
[68] Tatara, G., Vernier, N., and Ferre, J. (2005). *Appl. Phys. Lett.* **86**, 252509.
[69] Duine, R. A., Núñez, A. S., and MacDonald, A. H. (2007). *Phys. Rev. Lett.* **98**, 056605.
[70] Yamanouchi, M., Ieda, J., Matsukura, F., Barnes, S. E., Maekawa, S., and Ohno, H. (2007). *Science* **317**, 1726.
[71] He, J., Li, Z., and Zhang, S. (2006). *Phys. Rev. B* **73**, 184408.
[72] Falloon, P. E., Jalabert, R. A., Weinmann, D., and Stamps, R. L. (2004). *Phys. Rev. B* **70**, 174424.
[73] Ohe, J., and Kramer, B. (2006). *Phys. Rev. Lett.* **96**, 027204.
[74] Bazaliy, Ya. B., Jones, B. A., and Zhang, S. C. (1998). *Phys. Rev. B* **57**, R3213.
[75] Ansermet, J. Ph. (2004). *IEEE Trans. Magn.* **40**, 358.

[76] Fernández-Rossier, J., Braun, M., Núñez, A. S., and MacDonald, A. H. (2004). *Phys. Rev. B* **69**, 174412.
[77] Shibata, J., Tatara, G., and Kohno, H. (2005). *Phys. Rev. Lett.* **94**, 076601.
[78] Xiao, J., Zangwill, A., and Stiles, M. D. (2006). *Phys. Rev. B* **73**, 054428.
[79] Barnes, S. E. (2006). *Phys. Rev. Lett.* **96**, 189701.
[80] Tserkovnyak, Y., Skadsem, H. J., Brataas, A., and Bauer, G. E. W. (2006). *Phys. Rev. B* **74**, 144405.
[81] Kohno, H., Tatara, G., and Shibata, J. (2006). *J. Phys. Soc. Jpn.* **75**, 113706.
[82] Piéchon, F., and Thiaville, A. (2007). *Phys. Rev. B* **75**, 174414.
[83] Duine, R. A., Núñez, A. S., Sinova, J., and MacDonald, A. H. (2007). *Phys. Rev. B* **75**, 214420.
[84] Barnes, S. E., and Maekawa, S. (2005). *Phys. Rev. Lett.* **95**, 107204.
[85] There will also be contributions from electrons to $\boldsymbol{H}_{\text{eff}}$, such as the exchange field [92]. We do not discuss them here for simplicity.
[86] Aharonov, Y., and Stern, A. (1992). *Phys. Rev. Lett.* **69**, 3593.
[87] Kohno, H., and Shibata, J. (2007). *J. Phys. Soc. Jpn.* **76**, 063710.
[88] We define $\boldsymbol{n}$ to be a unit vector in the direction of spin, which is opposite to the direction of magnetization.
[89] We define $\hat{\boldsymbol{\sigma}}_{\perp} = \hat{\boldsymbol{\sigma}} - \boldsymbol{n}(\boldsymbol{n}\cdot\hat{\boldsymbol{\sigma}})$ and $\hat{\boldsymbol{\sigma}}'_{\perp} = \hat{\boldsymbol{\sigma}} - \hat{z}(\hat{z}\cdot\hat{\boldsymbol{\sigma}})$. Note that $\langle\hat{\boldsymbol{\sigma}}\rangle_{\text{ne}}$ in Eq. (82) can be replaced by $\langle\hat{\boldsymbol{\sigma}}_{\perp}\rangle_{\text{ne}}$.
[90] Tserkovnyak, Y., Fiete, G. A., and Halperin, B. I. (2004). *Appl. Phys. Lett.* **84**, 5234.
[91] Korenman, V., Murray, J. L., and Prange, R. E. (1977). *Phys. Rev. B* **16**, 4032.
[92] Tatara, G., and Fukuyama, H. (1994). *Phys. Rev. Lett.* **72**, 772; *J. Phys. Soc. Jpn.* **63**, 2538.
[93] Tatara, G., and Fukuyama, H. (1997). *Phys. Rev. Lett.* **78**, 3773.
[94] We use the vector (bold–italic) notation for the spin component. The space–time components are indicated by subscripts such as μ, ν (=0, 1, 2, 3) or i, j (=1, 2, 3).
[95] Waintal, X., and Viret, M. (2004). *Europhys. Lett.* **65**, 427.
[96] Tatara, G., Kohno, H., Shibata, J., Lemaho, Y., and Lee, K. J. (2007). *J. Phys. Soc. Jpn.* **76**, 054707.
[97] Kohno, H., Tatara, G., and Shibata, J. (unpublished note).
[98] Thiele, A. A. (1973). *Phys. Rev. Lett.* **30**, 230–233.
[99] Kohno, H., Tatara, G., Shibata, J., and Suzuki, Y. (2007). *J. Magn. Magn. Mater.* **310**, 2020.
[100] Mori, H. (1965). *Prog. Theor. Phys.* **33**, 423; **34**, 399.
[101] Götze, W., and Wölfle, P. (1972). *Phys. Rev. B* **6**, 1226.
[102] Heide, C., Zilberman, P. E., and Elliott, R. J. (2001). *Phys. Rev. B* **63**, 064424.
[103] Sakuma, A. preprint (cond-mat/0602075).
[104] Skadsem, H. J., Tserkovnyak, Y., Brataas, A., and Bauer, G. E. W. (2007). *Phys. Rev. B* **75**, 094416.
[105] Stiles, M. D., Saslow, W. M., Donahue, M. J., and Zhangwill, A. (2007). *Phys. Rev. B* **75**, 214423.
[106] Saslow, W. M. (2007). *Phys. Rev. B* **76**, 184434.
[107] Simánek, E., and Rebei, A. (2005). *Phys. Rev. B* **71**, 172405.
[108] Nguyen, A. K., Shchelushkin, R. V., and Brataas, A. (2006). *Phys. Rev. Lett.* **97**, 136603.
[109] Nguyen, A. K., Skadsem, H. J., and Brataas, A. (2007). *Phys. Rev. Lett.* **98**, 146602.
[110] Shinjo, T., Okuno, T., Hassdorf, R., Shigeto, K., and Ono, T. (2000). *Science* **289**, 930.
[111] Shibata, J., Nakatani, Y., Tatara, G., Kohno, H., and Otani, Y. (2006). *Phys. Rev. B* **73**, 020403(R).
[112] Ishida, T., Kimura, T., and Otani, Y. (2006). *Phys. Rev. B* **74**, 014424.
[113] Kasai, S., Nakatani, Y., Kobayashi, K., Kohno, H., and Ono, T. (2006). *Phys. Rev. Lett.* **97**, 107204.
[114] Yamada, K., Kasai, S., Nakatani, Y., Kobayashi, K., Kohno, H., Thiaville, A., and Ono, T. (2007). *Nat. Mater.* **6**, 269.
[115] Huber, D. L. (1982). *J. Appl. Phys.* **53**, 1899–1900.
[116] Guslienko, K. Yu., Ivanov, B. A., Novosad, V., Otani, Y., Shima, H., and Fukamichi, K. (2002). *J. Appl. Phys.* **91**, 8037.
[117] Lederer, P., and Mills, D. L. (1966). *Phys. Rev.* **148**, 542.
[118] Nakatani, Y. (unpublished results).
[119] Nakatani, Y., Shibata, J., Tatara, G., Kohno, H., Thiaville, A., and Miltat, J. (2008). *Phys. Rev. B* **77**, 014439.

CHAPTER 6

Micromagnetics of Domain-Wall Dynamics in Soft Nanostrips

André Thiaville* and **Yoshinobu Nakatani†**

Contents

Abstract

Spin-transfer torque (STT) manifests itself in two main geometries, either sub-micrometer diameter pillars composed of magnetic multilayers, flooded by a current perpendicular to plane (CPP), or nanowires with current flowing in their plane (CIP). The first situation can be described rather well, from the magnetic

*Laboratoire de Physique des Solides, CNRS, Université Paris-sud 11, 91405 Orsay Cedex, France
†Department of Computer Science, University of Electro-communications, Chofu, 182-8585 Tokyo, Japan

Nanomagnetism and Spintronics
DOI: 10.1016/B978-0-444-53114-8.00006-6

point of view, in the framework of the macrospin model (see Chapter 3 by Y. Suzuki). In the latter case however, the typical situation is that of a magnetic domain wall under CIP current, with many internal degrees of freedom. In Chapter 5 by H. Kohno and G. Tatara, a simplest model of the domain wall, called collective coordinates or 1D model, has been introduced to study this question.

In this chapter, we will address the entire manifold of the degrees of freedom in the domain wall by micromagnetic numerical simulations, and apply this to the physics of CIP spin transfer in magnetic domain walls. We will consider soft magnetic materials only, where domain-wall structures and dynamics are controlled by magnetostatics. This corresponds to experiments performed up to very recently, soft magnetic materials having generally lower coercive forces and domain-wall propagation fields. The experimental counterpart to this chapter can be found in Chapter 4 by T. Ono and T. Shinjo. After briefly introducing micromagnetics and the typology of domain walls in samples shaped into nanostrips, we start by reviewing the field-driven dynamics in such samples. This situation was indeed considered first, historically, and led to the introduction of several useful concepts. Prominent among them are the separation between linear and non-linear regimes, and the existence of a maximum velocity for a domain wall. STT-induced domain-wall dynamics will then be addressed, considering first the implementation of the CIP STT in micromagnetics, with several components as introduced by theory. Comparison will be made to the field-driven case, with similarities and differences highlighted.

In the nascent field of Nanomagnetism and Spintronics, micromagnetics can be considered to play the role of a translator. There are on one side experiments and on the other side theories about interaction between magnetization and spin-polarized electrical currents. Micromagnetics is a tool that translates the equations of the latter into quantitative predictions that can be compared to the former. Considering the present state of the subject of this book, with rapidly advancing experiments and theories, keeping in touch those two aspects of research is very important for its sound development. This is the objective of this chapter.

Key Words: Domain-wall structure, Domain-wall dynamics: by field, by current, by field and current, Bloch wall, Landau–Lifshitz (LL) and Landau–Lifshitz–Gilbert (LLG) equation, Spin transfer torque (STT): adiabatic and non-adiabatic, Transverse wall, Vortex wall, Thiele equation, Döring principle.

1. INTRODUCTION

1.1. Micromagnetics

The micromagnetic theory was introduced progressively (1930–1960) as a continuous theory of the magnetic structures, with William F. Brown, Jr. as the main contributor. By structures here, we mean those that spread across many atomic distances, so that the atomic nature of magnetism (ferromagnetism or ferrimagnetism, localized or itinerant magnetism) is not relevant. The preceding theory was the so-called domain theory that considers uniformly magnetized domains separated by magnetic walls of zero thickness, with a number of rules concerning the orientation of the magnetization in the domains and of the domain walls (DWs).

In micromagnetics, domains and walls are all described by a continuous function – the local magnetization – a classical vector that is the local average over a small volume of the magnetization density. Several hypotheses underlie the present formulation of micromagnetics:

- The small volume should contain many atoms, yet be smaller in size than any magnetic structure to be described.
- Temperature has to be low enough so that the thermodynamic equilibrium value of local magnetization $M_s(T)$ is attained everywhere, with negligible thermodynamic fluctuations, within this averaging volume.
- The time variation of magnetization should be slow enough to use the magnetostatic approximation for the computation of the electromagnetic interactions. This last hypothesis is not essential. However, the requirement that the local average of magnetization is the thermodynamic value limits dynamic phenomena to timescales much larger than femtoseconds.

The above points imply that the local magnetization density can then be written $\boldsymbol{M}(\boldsymbol{r},t) = M_s\boldsymbol{m}(\boldsymbol{r},t)$, where $\boldsymbol{m}$ is the unit vector indicating the local orientation of the magnetization (in this chapter, bold–italic symbols will be used for denoting vectors). The evolution in space and time of this vector is ruled by an energy functional and a dynamic equation.

Micromagnetic energy is defined as the integral over the sample volume of a density E composed of several terms (we use SI units throughout). The exchange term, written $A\Sigma_{i,j}\,(\partial m_j/\partial r_i)^2$ (where i and j refer to the spatial components), is the continuous form of the Dirac–Heisenberg exchange energy. The Zeeman term, written as $-\mu_0 M_s \boldsymbol{H}_{app}\cdot\boldsymbol{m}$, expresses the action of an external field $\boldsymbol{H}_{app}$. The anisotropy term, accounting for preferred orientations of the magnetization, is written generally as $KG(\boldsymbol{m})$, where G is an angular function and K is the anisotropy constant. The magnetostatic interaction results in a term reading $-(1/2)\mu_0 M_s \boldsymbol{H}_d \cdot \boldsymbol{m}$, where $\boldsymbol{H}_d$ is the demagnetizing field given by the solution of the magnetostatic problem.

The magnetization dynamics is governed by the Landau–Lifshitz–Gilbert (LLG) equation

$$\frac{\partial \boldsymbol{m}}{\partial t} = \gamma_0 \boldsymbol{H}_{eff} \times \boldsymbol{m} + \alpha \boldsymbol{m} \times \frac{\partial \boldsymbol{m}}{\partial t}, \tag{1}$$

where the effective field is defined by the functional derivative ∇ of the energy density with respect to magnetization orientation:

$$\boldsymbol{H}_{eff} = -\frac{1}{\mu_0 M_s}\frac{\delta E}{\delta \boldsymbol{m}}, \tag{2}$$

$\gamma_0 = \mu_0\,|\gamma|$ is the gyromagnetic ratio and α is the Gilbert damping constant. When solved, the LLG equation (1) becomes of the form put forward by Landau and Lifshitz (LL):

$$\frac{\partial \boldsymbol{m}}{\partial t} = \frac{\gamma_0}{1+\alpha^2}\boldsymbol{H}_{eff} \times \boldsymbol{m} + \frac{\alpha\gamma_0}{1+\alpha^2}\boldsymbol{m} \times (\boldsymbol{H}_{eff} \times \boldsymbol{m}). \tag{3}$$

For recent reviews about micromagnetics, the reader should consult Refs [1–3].

1.2. Numerical micromagnetics

Exact solutions of the equations of micromagnetics are very rare, as the problem is non-linear ($|\boldsymbol{m}| = 1$) and integro-differential (magnetostatic and exchange energy terms). For finite samples in particular, the magnetostatic problem cannot be circumvented. With the increase of computers power and the recent availability of micromagnetic codes [4–7], numerical micromagnetics has become a widely spread tool for the analysis of the magnetic structures in small samples as fabricated nowadays.

Most codes discretize the sample volume into equal cells, with a finite differences implementation of the equations. This works perfectly and very efficiently for idealized samples with straight edges. For complex sample shapes, the finite elements formulation is better suited in principle as it allows any polyhedral sample shape [8]. For both methods, the cell size should be smaller than the characteristic lengths of the material [1], defined as the exchange length:

$$\Lambda = \sqrt{2A/\left(\mu_0 M_s^2\right)} \tag{4}$$

or, in cases where anisotropy is large, the Bloch wall width parameter:

$$\Delta = \sqrt{A/K}. \tag{5}$$

A large part of the numerical calculation time is devoted to the solution of the magnetostatic problem. The demagnetizing field obeys the same equations as the electric field in electrostatics, with "magnetic" charges spread in the sample volume (density $-M_s \mathrm{div}\, \boldsymbol{m}$) and on the sample surface (density $M_s \boldsymbol{m} \cdot \boldsymbol{n}$, with $\boldsymbol{n}$ the outward-oriented normal to the surface). Thus, the demagnetizing field can be computed directly as a convolution product of the charges with a kernel function. In the finite differences method where all cells are identical, this operation is a discrete convolution product that can be evaluated through fast Fourier transformation, much more rapidly than by direct summation (the cost being $N \log N$ instead of N^2, where N is the number of mesh cells). This is the main advantage of the finite differences method. For the finite elements technique, the calculation is more complex as the magnetostatic problem needs to be solved on the same sample mesh, but involves the field outside the sample (see the recent review [8] for more details). For samples shaped as nanowires where the dynamics of one DW is investigated, some additional points need to be considered:

- Nanowires may be very long, thus impossible to mesh entirely. Moreover, far from the DW and from the wire ends, the magnetization is invariant along the wire length. In such a case, a restricted calculation region can be used, centred on the DW and moving with it (Fig. 1). An infinitely long wire can be mimicked by cancelling the magnetostatic charges at the ends – within the wire – of the calculation region [this applies to a soft nanostrip as considered through all this chapter, the charges are different for domains magnetized vertically (z) or transversally (y)]. The length of the calculation region along the wire has of

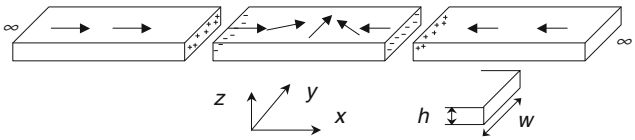

FIGURE 1 Sketch of a calculation region in an infinite nanostrip made out of a material with no anisotropy. The magnetic charges at the wire ends are drawn (+ and − signs). The separation between the calculation region and the rest of the sample was increased for the sake of drawing. The coordinates system is also defined, as well as the sample dimensions.

course to be well above the static DW width, and for dynamics one should always check that no structure propagates to its ends.

- The total energy of an isolated DW in the wire is not that of the calculation region alone, because the stray field of the DW extends to infinity. Indeed, the DW in nanowires considered here bear a non-zero magnetostatic charge, contrarily to most DW in bulk samples (so that the prohibition of charged DW was one of the rules of the old domain theory).

The representative calculations to be discussed below were performed with parameters characteristic of the soft alloy $Ni_{80}Fe_{20}$ that has been used in many experiments, namely $M_s = 8 \times 10^5$ A/m, $A = 10^{-11}$ J/m, $K = 0$, $\alpha = 0.02$ and $\gamma_0 = 2.21 \times 10^5$ m/(A s). They were performed using a 2D mesh, with mesh size 4 nm (x) × 4 nm (y) × h (z), where $h = 5$ nm, mostly.

1.3. Domain-wall structures in soft nanostrips

As all experiments performed up to now use samples patterned by lithography techniques out of thin magnetic films, we shall consider flat nanowires of rectangular cross section (width w and thickness h, the area of the cross section will be called $S = wh$) that are referred to as nanostrips. Starting from a schematic DW configuration, the numerical calculations (no applied field, damping set to $\alpha = 0.5$ in order to reach equilibrium rapidly) show the existence of several stable structures [9, 10] that are displayed in Fig. 2.

1.3.1. The symmetric transverse wall (STW)

In this structure, closest to what is expected for a one-dimensional magnetic wire, the DW average magnetic moment is oriented along the wire transverse axis. To quantify the DW transverse moments, we define for $i = y, z$

$$\mu_i = \frac{1}{\pi S} \int m_i \mathrm{d}^3 \boldsymbol{r} \tag{6}$$

that has the dimensions of a length (for a Bloch wall profile with $m_i = 1/\cosh(x/\Delta)$ one gets $\mu_i = \Delta$). As the cross section is very flat ($w \gg h$), this moment is oriented in the plane of the magnetic film. The DW region has the shape of a triangle. In the framework of the domain theory, the avoidance of magnetic charges inside the strip would indeed lead to 45° inclined boundaries

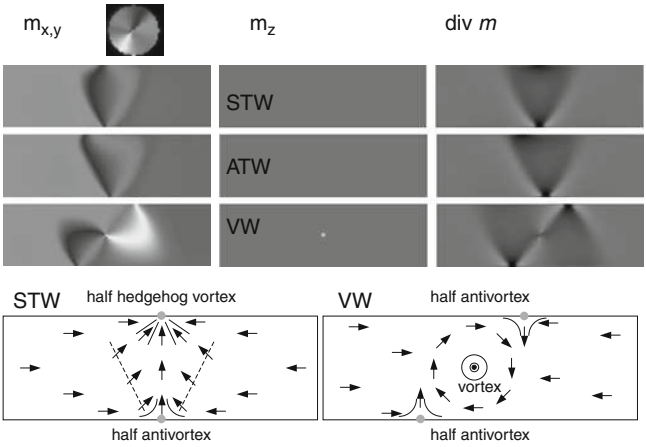

FIGURE 2 Computed domain-wall structures in permalloy nanostrip of cross section $w = 300$-nm wide and $h = 5$-nm thick. Each structure is shown by the in-plane (x, y) magnetization components (left) with circular colour coding (map shown on top), by the perpendicular (z) component in black and white (centre), and finally by the volume charge (div $\boldsymbol{m}$), in black and white (right). Schematic drawings of the two basic structures are also included. The ATW can exist in two variants with left and right inclination, only the left one being shown here. Images are 1-μm wide, one half the width of the calculation region. All walls are of head-to-head type, with a positive total magnetostatic charge (coded as black on the right column of images). For tail-to-tail walls, the magnetostatic charge is reversed, but the structures are the same ($\boldsymbol{m} \rightarrow -\boldsymbol{m}$ transformation).

between the "domains" and "wall" blocks. The structure is also characterized by two topological objects, located on the edges of the nanostrip [11], as depicted by the schematic drawing included in Fig. 2. At the triangle apex, a half-antivortex is present. A full antivortex (entirely contained inside the sample) would show a magnetization perpendicular to the film plane at his core. Here, as shown in the picture coded with the z-component, there is no trace of a perpendicular magnetization in statics. However, the in-plane magnetization component conforms that of a half-antivortex. Thus, the topological charge (winding number of the in-plane magnetization) of this object is $q = -1/2$ [11].

At the strip edge opposite to the apex, another topological structure exists. It is a half-hedgehog vortex, again with no core, that is topologically equivalent to a half-vortex hence with a topological charge $q = +1/2$. The half-hedgehog vortex bears, contrarily to the half-vortex, a magnetostatic charge. In the block structure discussed above, all the DW charge would be transferred to this edge, at the base of the triangle. In the magnetostatic limit (no role of exchange energy), all the DW charge would be concentrated on the half-hedgehog vortex. The numerical simulations show that, depending on the sizes of the wire cross section, the charge is spread all over the DW region (Fig. 2). The charge image, in a first approximation [12], corresponds to the image of the DW structure obtained by magnetic force microscopy.

1.3.2. The vortex wall (VW)

This DW structure does not show any transverse magnetic moment. However, due to the presence of the vortex core, a perpendicular magnetization component exists locally. As the vortex core is small (a few Λ [1]), the average perpendicular moment is much smaller than the transverse moment of the STW.

Topologically, the structure consists in a vortex ($q = 1$) with two half-antivortices, one at each edge of the nanostrip, as drawn in the schematic drawing included in Fig. 2.

In terms of magnetic charges, this structure spreads the DW charge more than the STW and thus reduces the magnetostatic energy, at the expense of larger exchange energy.

1.3.3. The asymmetric transverse wall (ATW)

This structure is a variant of the STW that becomes stable at larger film thickness h. The half-hedgehog vortex is no longer aligned with the half-antivortex along the transverse direction, but shows some offset (mainly visible on the volume charge pictures in Fig. 2).

1.3.4. Energies and phase diagram

These three DW structures can be absolutely stable or metastable, depending on the wire sizes w and h.

The equal energy line between VW and TW was found to lie at $wh \approx 61.3\ \Lambda^2$ ($1500\ \text{nm}^2$ for NiFe) [9, 10]. However, as shown experimentally and by micromagnetic calculations, in the case where the DW is nucleated by application of a field transverse to the wire, the TW can be found well above this line [13]. This metastability is due to the existence of an energy barrier. Indeed, in order to transform a VW into a TW, the vortex has to be expelled at one of the strip edges, leaving the centre where its energy is lowest. Similarly, in order to transform a TW into a VW, the half-hedgehog vortex has to leave the strip edge, thus creating the vortex core with perpendicular magnetization that makes most of the vortex energy. If it were possible to vary continuously the film thickness h, one could say that the TW–VW transition is first order.

In addition, above some thickness, the STW transforms to an ATW. An energy barrier for this process has not been seen in the numerical calculations, although the STW state can be obtained above this second transition line by symmetry. Indeed, this transition can be realized continuously (a shift of DW centre along the strip length that depends on position across the strip width). Thus, the STW–ATW transition can be described as second order, and we shall use the symbol TW to denote both structures.

Figure 3A plots these two equal energy lines, as obtained from the numerical calculations. One should note that, as these calculations were performed with one cell in the film thickness (2D calculations), the "phase diagram" thus obtained is limited to low thicknesses. A deformation of the transition lines is anticipated at larger thicknesses. This phase diagram was confirmed by experiments where the most stable DW structure was obtained by thermal annealing [14]. This study also

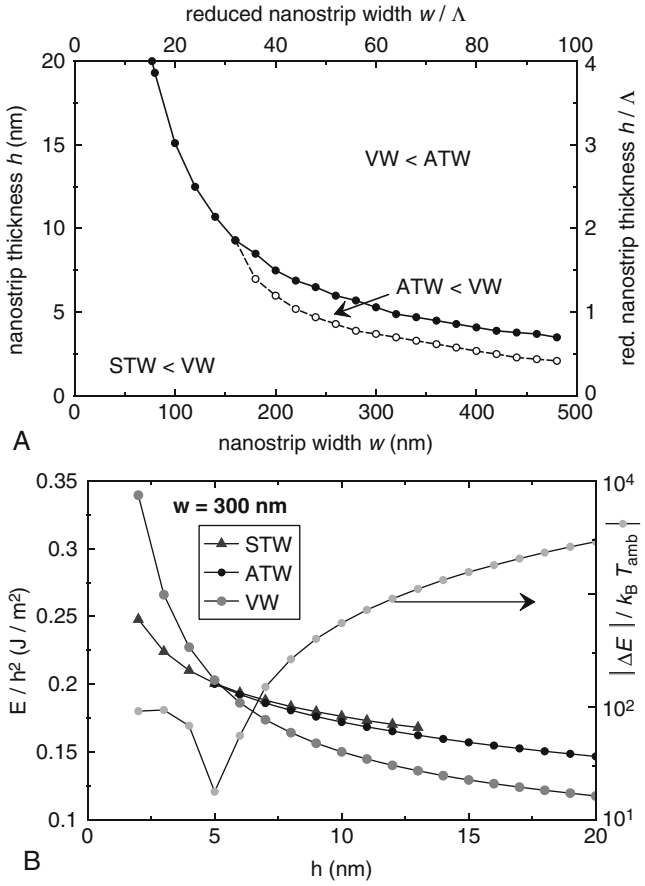

FIGURE 3 Comparison of the energies of the different DW structures upon variation of the nanostrip dimensions. (A) "Phase diagram" mapping the lowest energy structures [10]. (B) Energies of the three DW structures in permalloy nanostrips of cross section $w = 300$-nm wide and varying thickness, summed over the 2-μm calculation region. VW and TW have very close energies at the thickness $h = 5$ nm, a value that applies to all numerical results shown in this chapter. Because of its symmetry, the STW structure can be obtained above the thickness for transition to ATW, but in an unstable state. In addition, the energy difference (absolute value) between VW and TW is compared to the thermal energy at room temperature (note the log scale). These calculations were performed with a 2D mesh.

revealed the role of sample imperfections that may hinder the DW conversion and even lead to a re-entrant VW phase at very low thickness.

The variation with film thickness of the energies of the three DW types presented here is plotted in Fig. 3B, for one value of the wire width, namely $w = 300$ nm.

These are the simplest DW structures, corresponding to the small sizes of the nanostrips. The micromagnetic parameters that characterize these three structures are shown in the Table 1.

Table 1 Main micromagnetic parameters for the three simplest DW structures in a 300-nm wide and 5-nm thick NiFe nanostrip

Parameter	STW	ATW	VW
DW energy (10^{-18} J)	5.014	5.001	5.071
Δ_T ($v = 0$) (nm)	52.2	49.5	25.4
DW y-moment μ_y (nm)	53.06	53.62	−0.53
DW z-moment μ_z (nm)	0	0	0.19
$\alpha\tau_{DW}$ (ps)	6.3		400
v_{max} (m/s)	644.7		61.1
Δ_T (v_{max}) (nm)	31.8		26.1

Symbols: Δ_T, the Thiele domain-wall width (8); v_{max}, the DW maximum velocity; τ_{DW}, the characteristic time for DW structure relaxation; μ_i, the DW transverse magnetization moments (6). DW energies were evaluated in a 2-μm long calculation box. Note that the dynamic parameters (lower half) are identical for the STW and ATW as the STW is unstable at this nanostrip size.

For much larger thicknesses, comparable to the nanostrip width, it has been shown, for example, that another type of DW exists, called Bloch point wall [15, 16]. At large width and small thickness, cross-tie walls and diamond structures appear [14]. Eventually, the benefit of the reduced dimensions disappears and we recover the full complexity of the bulk domain structures.

2. FIELD DYNAMICS OF DOMAIN WALLS

Domain-wall dynamics under an applied field is a rather old subject [17]. The early studies, however, concerned bulk samples, and only more recently thin films. We will address here DW dynamics in soft nanostrips, where the DWs are confined and their dynamics simpler. This research field is rather recent, as more and more high-quality samples have been fabricated in the last 10 years only.

2.1. Panorama

Let a field be applied along the nanostrip axis (x-direction) so as to displace the DW. Far away from the DW, the field exerts no torque as $\boldsymbol{m}$ and $\boldsymbol{H}_{app}$ are collinear, so that the magnetization in the left and right domains does not change. This mathematical evidence is in fact correct only for low fields: in real samples some deviations of magnetization are always present (the ripple structure [1]) that become exacerbated under a reverse applied field, eventually leading to the nucleation of domains of magnetization aligned with the field before sufficient DW motion may take place. Thus, the dynamics of one DW can be properly calculated (and measured) only under low fields.

It is not possible here to describe what is obtained for all points in the phase diagram of Fig. 3A. The reader is referred to Chapter 5 by H. Kohno and G. Tatara for an approach of this physics by a simple analytical model. In addition, a chapter

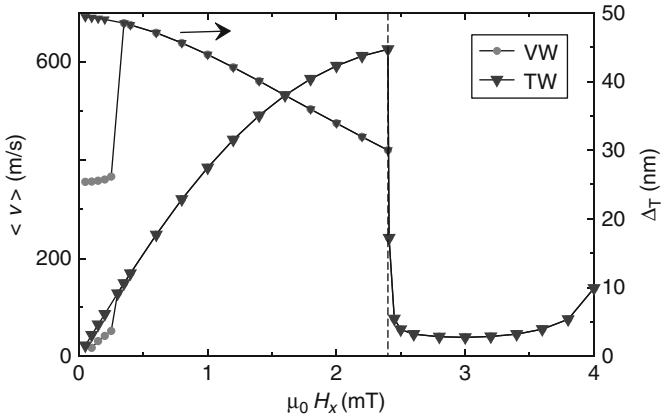

FIGURE 4 Computed velocity v of domain walls, under a field applied along the axis of a nanostrip with a cross section $w = 300$-nm wide and $h = 5$-nm thick. The damping constant is $\alpha = 0.02$. A transverse wall (TW, in fact an asymmetric transverse wall) and a vortex wall (VW) are compared, the latter existing only up to a velocity of about 60 m⁄s. In the steady-state regime (up to the dashed line), the Thiele domain-wall width Δ_T is also plotted. The velocity in non-steady state is a time-averaged value.

devoted to field dynamics of DW in soft nanowires and nanostrips was written recently by us [15], where the 1D model of DW dynamics is discussed in detail and compared to numerical calculations. We shall here recall the main features of these dynamics as revealed by numerical calculations, keeping the nanostrip size constant (width $w = 300$ nm and thickness $h = 5$ nm). One interest of this size is that the TW and VW have very similar energies, as just shown.

Figure 4 shows the velocity versus field curves for this sample, for an (A)TW and a VW. The values were obtained from a collection of time-dependent calculations where a DW at rest is submitted at time $t = 0$ to an applied field. Two very distinct regions can be seen that correspond to different regimes of motion.

2.2. Linear regime (steady state)

For all DW structures, a first regime, beginning at zero field, shows a linear – or slightly curved – increase of velocity with field. This behaviour is to be expected as the field supplies energy and the damping term in LLG is akin to a viscous friction. This regime of motion is called linear. Were the DW width in motion the same as at rest, the $v(H)$ curve would be perfectly linear. Indeed, Thiele [18] has shown that for a stationary DW motion [a motion where the DW structure does not change when seen in the moving frame, so that $\boldsymbol{m}(\boldsymbol{r},t) = \boldsymbol{m}_0(\boldsymbol{r} - \boldsymbol{Q}(t))$], the DW velocity v obeys the famous Walker relation:

$$v = \frac{\gamma_0 \Delta_T}{\alpha} H, \tag{7}$$

where the Thiele DW width Δ_T is defined as an integral over the moving DW structure $\boldsymbol{m}_0$:

$$\frac{2}{\Delta_T} = \frac{1}{S}\int\left(\frac{\partial \boldsymbol{m}_0}{\partial x}\right)^2 \mathrm{d}^3\boldsymbol{r}. \tag{8}$$

Thus, it is more precise to call this regime steady state.

The corresponding time-dependent evolution for a TW is plotted in Fig. 5A for a representative field applied abruptly at time $t = 0$. It shows that the DW reaches a constant structure after some time, and that this structure differs from the one at rest. The exponential relaxation of DW structure involves the characteristic time τ_{DW}. The deformation of the DW structure expresses magnetization precession under the applied field (a m_z-component appears for the TW, and a m_y-component for the VW, see Fig. 5D).

Figure 5A shows the initial decrease of Δ_T, more pronounced as H becomes larger, that explains the downward curvature of the $v(H)$ curve for the TW. The change of the Thiele DW width reflects the higher energy of the moving DW structure when compared to the structure at rest. As for small field (hence velocity) this energy increase scales as v^2, the factor in front of v^2 may be called a mass, known as the Döring mass [15, 19]. The existence of this mass explains the transient dynamics of the DW when the field is applied abruptly.

Figure 6 shows a series of snapshots of DW structures in steady-state motion, under increasing fields. For the TW (Fig. 6A), all structures are ATW. Magnetization rotation (as shown by the charge image) peaks at the leading edge of the DW as well as at the half-hedgehog vortex and half-antivortex on the sample edges, increasing with DW velocity. The m_z-component also increases in this region as field and velocity get larger (not shown). For the VW (Fig. 6B), the main deformation under motion is the progressive shift of the vortex core in the transverse y-direction that causes the change of the y-moment of the VW.

The comparison of the results for the TW and VW (Fig. 4) reveals that the VW moves more slowly than the TW, at the same field. The Thiele DW width is indeed smaller for the VW, due to the larger magnetization gradients that occur because of the existence of a vortex core (Table 1). Note that this result is opposite to the naïve appreciation of the DW width from the magnetization pictures (Fig. 2). More quantitatively, if the magnetization profile averaged over the transverse variables y and z were fitted by the profile of a Bloch wall ($m_x = \tanh(x/\Delta_x)$), the resulting Δ_x would indeed be larger for the VW. The reason for this difference is that the Thiele DW width derives from the energy dissipation in LLG, and one should rather think of the DW width that governs DW dynamics in the linear regime as a measure of energy dissipation. The existence of this "dynamic" DW width shows that a straightforward application of the Bloch wall dynamics solution to DW in nanostrips may turn out to be very far from reality.

Starting from a VW, two steady-state regimes can be seen (see Fig. 4), the second steady-state regime being identical to that of a TW. The reason is that the breakdown marking the end of the first steady-state regime leads to a TW structure that can move in steady-state conditions up to higher fields. Indeed, in the first regime,

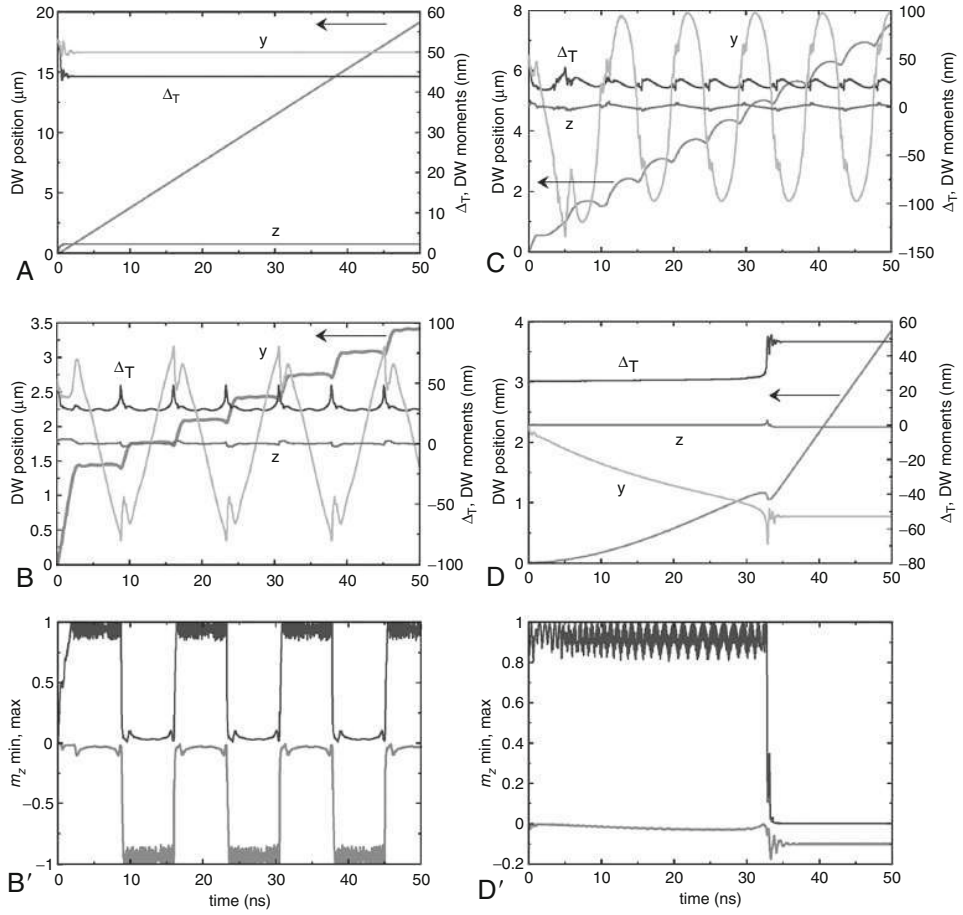

FIGURE 5 Computed motion of domain walls, under a field applied along the axis of a nanostrip with a cross section $w = 300$-nm wide and $h = 5$-nm thick. The damping constant is $\alpha = 0.02$. The starting structure is either a TW, with applied fields $\mu_0 H_x = 1$, 2.6 and 4 mT [panels (A), (B) and (C), respectively] or a VW [0.4 mT, panel (D)]. The figures show the DW position (left axis) and, on the right axis, the Thiele DW width (Δ_T) as well as the two transverse moments, along y and z – see labels, of the DW magnetization [Eq. (6)]. For cases (B) and (D), supplementary graphs (B′, D′) plot the time evolution of the maximum and minimum perpendicular magnetization component. When these last values reach the vicinity of ± 1, a localized structure (V, AV) is present. The fluctuations seen below $+1$ or above -1 are due to the discreteness of the mesh. The applied field for the VW is just above the first Walker threshold, so that the VW is seen to transform to a TW during the calculation.

magnetization precession inside the VW leads to the apparition of a m_y-component, linked to the displacement of the vortex core in the y-direction from the nanostrip centre (Fig. 6B). This displacement increases with field (thus, and more appropriately in fact, with DW velocity, see later) up to a point where the vortex core is expelled from the sample. This transforms the VW into a TW (see Fig. 5D and D′).

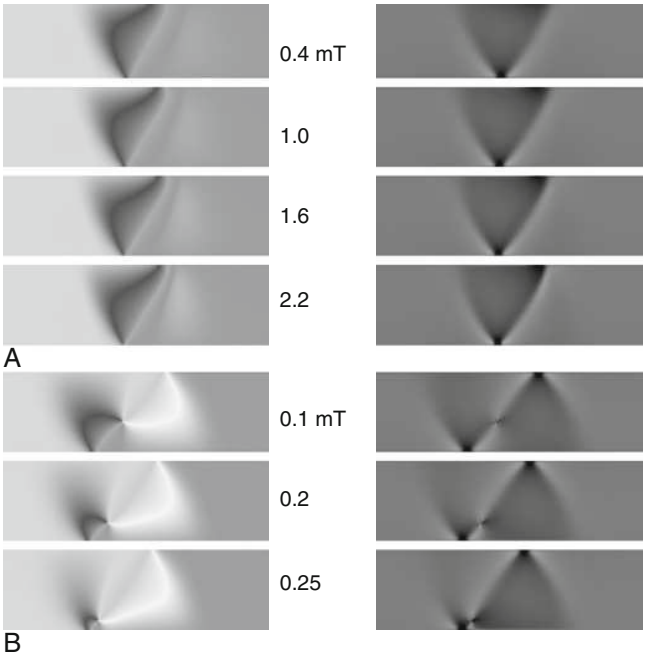

FIGURE 6 Snapshots of DW structures in steady-state motion (towards the right of the pictures) under different fields (values of $\mu_0 H_x$ are indicated), starting from a TW (A) and a VW (B). The nanostrip size is $w = 300$ nm and $h = 5$ nm. The left images display the in-plane magnetization orientation with the same colour code as in Fig. 2, and the right images map the magnetization in-plane divergence (the magnetic volume charge). Images are 1-μm wide, one half of the calculation region. The corresponding velocities are 169, 385, 532 and 612 m/s for the TW and 19, 41 and 52 m/s for the VW.

In all cases, the end of the (last) steady-state regime is characterized by a velocity that reaches a maximum. More precisely, due to the curvature of the $v(H)$ curve, the maximum may be even reached slightly before the end the steady-state regime (the 1D model predicts that this is possible [15]).

All this phenomenology was uncovered by Walker in the case of the 1D Bloch wall in an infinite sample with uniaxial anisotropy [20], so that the end of the steady-state regime may be described as Walker field and Walker velocity. These terms are kept here, even if the walls existing in the nanostrips have nothing to do with a Bloch wall.

2.3. Motion above the Walker field

When the steady-state regime ends, the average velocity drops abruptly as shown in Fig. 4 (this is called the Walker breakdown). The time traces for this case (Fig. 5B) show that some regularity in time however exists, where the DW magnetization components oscillate as well as DW width and velocity. Thus, an

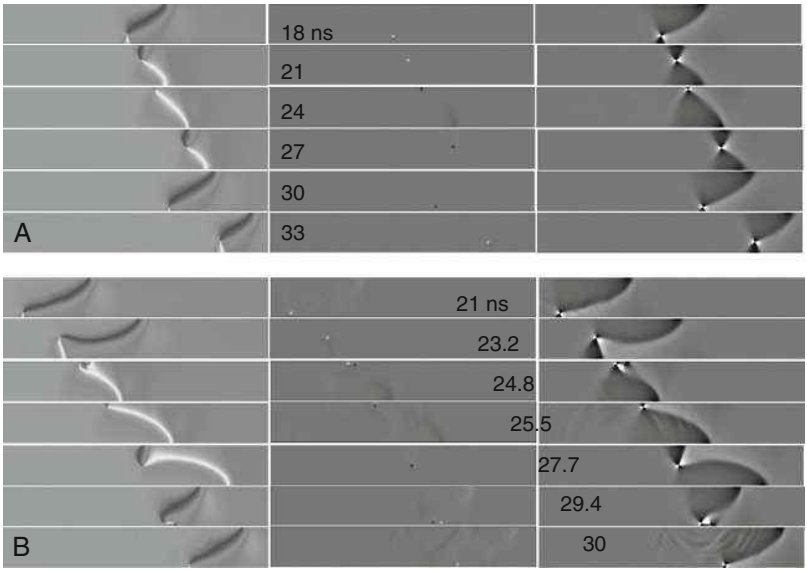

FIGURE 7 Snapshots of a TW set into motion by fields larger than the Walker value, namely $\mu_0 H_x = 2.6$ mT (A) and 4.0 mT (B). The nanostrip size is $w = 300$ nm and $h = 5$ nm, and the same part of the nanostrip is shown in each series. The left images display the magnetization in-plane component, the out-of-plane component is displayed in the centre images and the right images map the magnetization divergence. For a field weakly larger than the Walker value (A), the DW structure changes by continuous injection of an AV at one strip edge that crosses the sample width to disappear at the other edge, followed by the injection of an AV with opposite core magnetization at that edge and so on. For a larger field (B), the AV annihilates with a V of opposite core magnetization that is injected before it reaches the other edge of the sample. Note the increasing DW *x* extension as field gets larger, and the "anchoring" role played by the AV core.

average velocity can be defined that has been plotted in Fig. 4. The snapshots of the DW structures (Fig. 7), as well as the plot of the maximum and minimum of the perpendicular component of magnetization (Fig. 5B′), reveal the now well-known continuous transformation of the DW structures, by the injection, displacement across the nanostrip width and expulsion of single antivortices (AV) and vortices (V). Note that the breakdown mechanism with the apparition of these very localized structures is rather different from the predictions of the 1D model, where a precession of the DW magnetization is expected (this is also reflected in the very different oscillation amplitudes of the y- and z-DW moments, whereas in the 1D model they would be equal). The topological analysis presented above is useful for understanding what structures do appear and where [21]. Note that the above-described mechanism is specific for soft materials.

At still larger fields, the regularity progressively disappears (Figs 5C and 7B) because more than one AV or V is present. Consequently, the evaluation of an average velocity is not so easy, and the numerical data show some scatter. In this regime the velocity appears to increase again with field. Thus, the $v(H)$ curve

shows a minimum value slightly above the Walker field that we will denote by v_{min}. As the processes become rather complex, calculations should be checked for mesh independence and robustness to disorder (see next section) before attempting to compare these results to experiments. In this regime, it is obvious that the 1D model will not work. Too many degrees of freedom exit in the nanostrip considered in this example (the stripe width is about 60 Λ) that can be excited.

2.4. Imperfect samples

2.4.1. Propagation field

One important characteristic of the DW dynamics in the perfect samples considered up to now is the existence of a linear regime at small applied fields, down to zero. In real samples, however, a minimum field has to be applied in order to displace an existing DW that is therefore called propagation field, H_P. This field is different from the coercive field of the sample, H_c, that can be measured by magnetometry, as the latter involves in general DW nucleation, propagation and disappearance. One advantage of the nanowires is to allow separating propagation of DWs from their nucleation, as recognized early [22]. The propagation field may originate from many types of defects, so that its faithful micromagnetic modelling is difficult. The defect type most considered for nanostrips is edge roughness [23–25], but local variation of the micromagnetic parameters (A, M_s or even h) has also been considered. The edge roughness mechanism is anticipated to be dominant among the microfabrication-induced defects, and microfabrication plays indeed a big role as, very often, $H_P > H_c$. This is also consistent with the experimental observation that H_P increases as the nanostrip width decreases. Values of H_P are rarely given in the literature, the published numbers ranging from ≈1.5 [26] to 100 Oe [27] ($\mu_0 H_P = 0.15$–10 mT). For comparison, a good NiFe film has $H_c \approx 1$ Oe ($\mu_0 H_c = 0.1$ mT). We will therefore discuss now the effects of edge roughness on DW dynamics by field.

Periodic roughness was first tried [23], but is not realistic at least for cases where roughness is not intentional. Random roughness is therefore preferred. Its generation is inspired by the existence of nanocrystals inside the sample. A random grain pattern can be generated as the Voronoi cells for a random distribution of points [25]. The rough edge is then obtained as the boundary of the grains contained within a nominal nanostrip width with, if necessary, some regularization to eliminate excessive roughness. The parameter of such a roughness is the point density or, equivalently, the mean grain diameter $\langle D \rangle$. To implement the moving calculation region technique, a sufficiently long rough nanostrip has to be generated first. As the magnetization in a rough nanostrip deviates from strict uniformity, this should be taken into account at the x boundaries of the calculation region. However, as the roughness considered here is small, of the order of the exchange length, these deviations are neglected for simplicity.

The calculated DW dynamics with such a roughness is shown in Fig. 8, to be compared with Fig. 4 in the perfect case. The figure depicts one of the problems of the numerical micromagnetics of imperfect samples. For a given field, there is

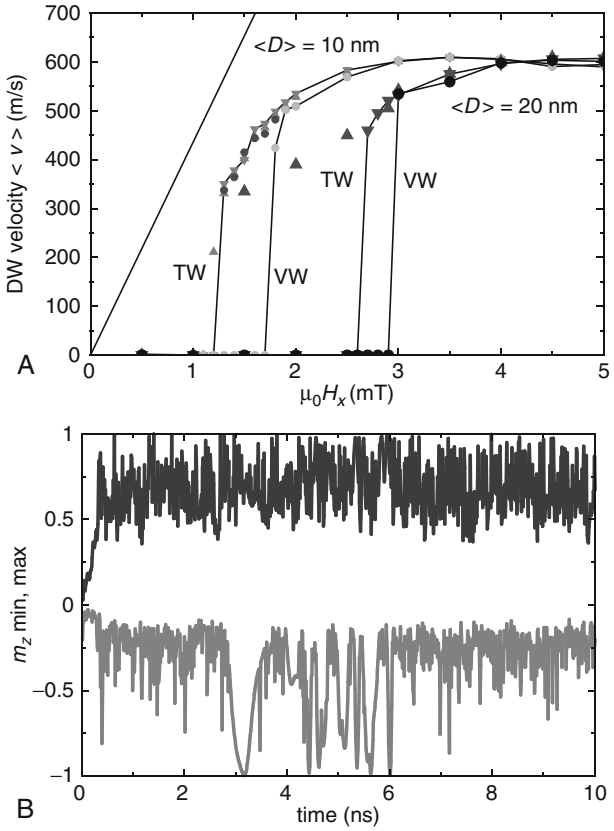

FIGURE 8 Motion of domain walls by field in a nanostrip with rough edges, of cross section $w = 300$-nm wide in average and $h = 5$-nm thick. The damping constant is $\alpha = 0.02$. (A) Computed velocity of domain walls. A transverse wall (TW, in fact an asymmetric transverse wall, triangular symbols) and a vortex wall (VW, circles) are compared. Two values of the average size of grains that are used to define the nanostrip edges are shown, $\langle D \rangle = 10$ (smaller symbols) and 20 nm (larger symbols). For each case, the velocity in linear motion and the final velocity are indicated (calculations last 50 ns), showing the field window in which the DW motion is stochastic. The straight line shows the linear mobility of the TW extracted from Fig. 4. Lines link the data points with the lower velocities. (B) Time evolution of the maximum and extremum m_z-magnetization components for a TW, under field $\mu_0 H_x = 4$ mT for the smaller edge roughness $\langle D \rangle = 10$ nm.

some probability that a DW stops at some place where the pinning potential induced by roughness is too large. This is true especially as calculations are performed without thermal fluctuations. In the absence of a better statistical analysis, criteria have to be adopted for deciding whether the DW moves or not, so as to compute its velocity. In the case of Fig. 8, motion was declared to take place when the DW moved for more than 1 μm, and in cases it eventually stopped the velocity during the motion phase was evaluated, together with a zero value indicating DW stopping. Thus, in a certain field range (that depends on the

calculation total time and on the 1-μm criterion), DW motion and stop can occur. This corresponds to the experimental behaviour.

Figure 8 shows that propagation fields $H_P \approx 10$–30 Oe ($\mu_0 H_P = 1$–3 mT) can be simulated by this technique. The grain size $\langle D \rangle$ is, however, limited by the numerical mesh size, so that for lower H_P smaller $\langle D \rangle$, hence smaller mesh sizes, are required. As a consequence, small velocities of DW motion are not observed when using standard mesh sizes of micromagnetics (below, but comparable to the exchange length Λ). The approach to zero velocity in the vicinity of H_P is also not computed, as it would require the introduction of thermal fluctuations and extremely long calculation times [28].

In the case chosen for Fig. 8, it appears that a VW is more pinned than a TW. This is, however, not a general conclusion, as for other sizes the opposite was seen. The DW pinning is also quite sensitive to the type of defects. For example, film thickness reduction (up to zero) for randomly chosen cells is very effective on a VW, as this DW structure bears a large energy localized at the vortex core [1].

2.4.2. Walker breakdown

Apart from the apparition of a propagation field, disorder as introduced here has a striking consequence: the Walker breakdown is pushed to much higher fields (not even visible in the field range of this plot). Therefore, already little above the propagation field the DW travels at an average velocity clipped to the maximum velocity of the perfect case [25]. This was shown to result from energy dissipation at the nanostrip edge, in the form of spin waves emission, preventing the apparition of localized structures (V and AV) seen in the perfect case. This is demonstrated in Fig. 8B plotting the evolution of the maximum and minimum of the perpendicular magnetization for one case: comparison with Fig. 5B′ and D′ shows variations of these extremum values that are much larger than the fluctuations seen when a V or AV is present, due to mesh discreteness.

It should be noted finally that the best samples fabricated nowadays are better than those of this calculation (Section 2.5), so that predictions for perfect samples may not be so unrealistic.

2.5. Comparison to experiments

The experimental investigation of DW dynamics by field in nanostrips has started only recently, once samples have become available (the reader should consult Chapter 4 by T. Ono and T. Shinjo).

The main observable was, initially, the DW velocity and its dependence on field. In the first experiments [22, 29] only one regime was seen, and the propagation fields were rather high.

More recently however, Walker breakdown could be experimentally seen in a few cases [26, 30] where the propagation field was very low, 1.5 and 5 Oe, the Walker breakdown occurring at 6 and 10 Oe, respectively. The other signature of Walker breakdown is the oscillation with time of the DW structure, velocity, etc., as shown in Fig. 5. In one experiment [26], oscillations of DW velocity were indeed detected, however as a function of DW position rather than of time, so that these

data are still non-understood. Still more recently, oscillations of the DW width have been inferred from time-resolved measurements of the anisotropic magnetoresistance (AMR) of a nanostrip sample [31] for large enough applied fields. The variation of the resistance R of the sample due to AMR reads

$$\Delta R = -\frac{\Delta\rho}{S^2}\int (m_y^2 + m_z^2)\mathrm{d}^3\boldsymbol{r}, \tag{9}$$

where $\Delta\rho$ is the change of resistivity by AMR. Thus, AMR is sensitive to a geometric DW width and not to the dynamic DW width of Thiele. Nevertheless, an oscillation of AMR due to DW dynamics above the Walker threshold is also anticipated, similar to that of Δ_T (see Fig. 5). The non-observation of this phenomenon in earlier experiments may be due to insufficient sample quality masking the regularity of the DW dynamics slightly over the Walker field. Indeed, as shown in the previous section, the Walker breakdown may even be suppressed at large roughness [25].

Thus, we may say that the micromagnetic predictions fit with experiments, qualitatively at least. It is anticipated that a detailed comparison between experiments and micromagnetic calculations will eventually boil down to a value of damping α and a suitable imperfection model.

We finally note that, for applications requiring fast DW motion, the control of the breakdown will become a very important topic.

3. DOMAIN-WALL MOTION BY SPIN-POLARIZED CURRENT

This section is intended to describe the status of research about spin-polarized current-induced DW motion, and, more generally, current in-plane (CIP) spin transfer, from a micromagnetic point of view. We stress that the final understanding of this question is yet to be reached. Nevertheless, the subject being very active presently, an attempt towards a synthesis may be worthwhile. As most of the controversy concerns the introduction of CIP spin transfer in micromagnetics (see a recent chapter [32] and related papers [33, 34]), we start by considering this point before showing numerical results and comparing them to experiments. Analytic results, using schematic DW models, are presented in Chapter 5 by H. Kohno and G. Tatara.

3.1. CIP spin transfer in micromagnetics

In the early theoretical work by Luc Berger [35, 36], spin-transfer torque (STT) on a DW was considered in a space-integrated form, from the change of conduction electrons angular momentum after crossing the DW. Bazaliy *et al.* [37] were the first to propose an expression for the local torque due to spin transfer inside a DW. This expression applies to the situation of wide walls, when the DW width δ (for the Bloch wall profile one has $\delta = \pi\Delta$, so that Δ is called the wall width parameter) is large compared to the so-called Larmor length:

$$\delta \gg \frac{\hbar v_F}{E_{sd}}. \tag{10}$$

In this expression pertaining to free "s"-electrons exchange-coupled to localized "d"-electrons responsible for the material's magnetization, v_F is the Fermi velocity and E_{sd} is the energy splitting of the s-electrons' up and down bands. For wide walls, and in similarity to neutrons travelling inside a polarization rotation device [38], the conduction electrons' spin is expected to closely follow the local d-electrons spin direction. This is called the adiabatic limit. STT is then obtained as the differential change of the angular momentum of all conduction electrons. For a sample slice of thickness dx (along the electron flow), the time evolution of the angular momentum associated to the local magnetization can be evaluated by both the evolution of the local magnetization and the amount of angular momentum deposited by the conduction electrons:

$$\begin{aligned} \mathrm{d}\left(\frac{\mathrm{d}\boldsymbol{L}}{\mathrm{d}t}\right) &= -\frac{\mu_0 M_s}{\gamma_0}\frac{\partial \boldsymbol{m}}{\partial t}\mathrm{d}x \\ &= \frac{J}{e}P\frac{\hbar}{2}[\boldsymbol{m}(x+\mathrm{d}x) - \boldsymbol{m}]. \end{aligned} \tag{11}$$

As the time derivative of an angular momentum is a torque, this effect is called spin transfer torque. Therefore, the spin-polarized current leads to a time evolution of the magnetization that can be expressed as

$$\left.\frac{\partial \boldsymbol{m}}{\partial t}\right|_{STT} = -\frac{Jg \mid \mu_B \mid P}{2eM_s}\frac{\partial \boldsymbol{m}}{\partial x} \equiv -(\boldsymbol{u}\cdot\nabla)\boldsymbol{m}. \tag{12}$$

In this equation, e is the absolute value of the electron charge and the sign of the current density J corresponds to the direction of motion of the electrons. We denote this form of STT as CIP STT, since the current flows along the magnetic layer with non-uniform magnetization. Adiabatic CIP spin transfer can thus be represented by an equivalent velocity $\boldsymbol{u}$. This velocity is proportional to the current density J and its polarization ratio P and, importantly, inversely proportional to the magnetization M_s. The velocity u may be compared to the classical drift velocity v_d associated to the current by $J = n_e e v_d$, where n_e is the conduction electrons density. One obtains

$$u = v_d P\frac{n_e}{n_s}, \tag{13}$$

where n_s is the density of Bohr magnetons. For NiFe, the prefactor $g|\mu_B|/(2eM_s)$ is numerically equal to 7×10^{-11} m^3/C. Thus, a typical current density $J = 10^{12}$ A/m^2 with a polarization $P = 0.7$ corresponds to $u = 50$ m/s. This form of the adiabatic CIP STT is well accepted, with u also denoted by b_J [39, 40] (but the double vector product form $\boldsymbol{m}\times(\partial_x\boldsymbol{m}\times\boldsymbol{m})$ is unnecessarily complicated as it is always equal to $\partial_x\boldsymbol{m}$ because $|\boldsymbol{m}| = 1$).

A first issue of controversy appears when this torque has to be incorporated into the dynamics equation of micromagnetics. One may add this term to the

right-hand side of the LLG equation (1) [39, 41, 42] or of its LL form (3) [32, 33, 43]. The first procedure, namely

$$\dot{\boldsymbol{m}} = \gamma_0 \boldsymbol{H}_{\text{eff}} \times \boldsymbol{m} + \alpha m \times \dot{\boldsymbol{m}} - (\boldsymbol{u}\cdot\nabla)\boldsymbol{m} \tag{14}$$

(where from now on an overdot is used to denote a time derivative), has a solved form that reads

$$\begin{aligned} \dot{\boldsymbol{m}} \quad &= \frac{\gamma_0}{1+\alpha^2}\boldsymbol{H}_{\text{eff}} \times \boldsymbol{m} + \frac{\alpha\gamma_0}{1+\alpha^2}\boldsymbol{m} \times (\boldsymbol{H}_{\text{eff}} \times \boldsymbol{m}) \\ &\quad - \frac{1}{1+\alpha^2}(\boldsymbol{u}\cdot\nabla)\boldsymbol{m} - \frac{\alpha}{1+\alpha^2}\boldsymbol{m} \times [(\boldsymbol{u}\cdot\nabla)\boldsymbol{m}]. \end{aligned} \tag{15}$$

In this last equation, two terms derived from the spin-polarized current appear, whereas if the STT is added directly to the solved (or LL) form (3) one gets

$$\begin{aligned} \dot{\boldsymbol{m}} \quad &= \frac{\gamma_0}{1+\alpha^2}\boldsymbol{H}_{\text{eff}} \times \boldsymbol{m} + \frac{\alpha\gamma_0}{1+\alpha^2}\boldsymbol{m} \times (\boldsymbol{H}_{\text{eff}} \times \boldsymbol{m}) \\ &\quad - (\boldsymbol{u}\cdot\nabla)\boldsymbol{m}. \end{aligned} \tag{16}$$

One presentation of the difference of conceptions leading to these two equations is that Eq. (14) considers damping as a viscosity with respect to the lattice that creates a friction field proportional to the magnetization velocity, whatever its origin. On the other hand, a motivation behind Eq. (16) is that damping always decreases the energy of the sample and, as the adiabatic STT cannot be derived from an energy term, only the magnetic energy of the sample is considered for damping [33].

It should also be noted that Eq. (16) has a straightforward solution for a sample with translation invariance, like a wire without any defect. Indeed, if $\boldsymbol{m}_0(\boldsymbol{r})$ is a solution of this equation with $\boldsymbol{u} = 0$, for example, a DW, then the solution for an arbitrary $\boldsymbol{u}(t)$ is

$$\boldsymbol{m}(\boldsymbol{r}, t) = \boldsymbol{m}_0\left(\boldsymbol{r} - \int_{-\infty}^{t} \boldsymbol{u}(\tau)\mathrm{d}\tau\right). \tag{17}$$

Such is not the case with Eq. (14), as explained hereafter.

The second point of controversy concerns the presence or not of a CIP STT term beyond that of the adiabatic approximation. Domain walls, even if they are wide in nanowires made of soft materials (because the DW width is determined by the wire size and not by anisotropy), are never infinitely wide so that a deviation to adiabaticity has to occur. From a mathematical point of view, the only possible other torque term linear in the spatial gradient of $\boldsymbol{m}$ is of the form $\boldsymbol{m}\times[(\boldsymbol{u}\cdot\nabla\boldsymbol{m})]$, as $\dot{\boldsymbol{m}}$ has to be orthogonal to $\boldsymbol{m}$ because $|\boldsymbol{m}| = 1$. From the micromagnetic results to be shown below, such a term has a great impact on DW dynamics. Therefore, the equation often considered in LLG form is [44, 45]

$$\begin{aligned} \dot{\boldsymbol{m}} \quad &= \gamma_0 \boldsymbol{H}_{\text{eff}} \times \boldsymbol{m} + \alpha \boldsymbol{m} \times \dot{\boldsymbol{m}} \\ &\quad - (\boldsymbol{u}\cdot\nabla)\boldsymbol{m} + \beta \boldsymbol{m} \times [(\boldsymbol{u}\cdot\nabla)\boldsymbol{m}], \end{aligned} \tag{18}$$

where $\beta \ll 1$ expresses a small deviation to adiabaticity (the denomination $c_{\text{J}} \equiv \beta u$ is also used). The solved form of Eq. (18) is

$$\begin{aligned}\dot{\boldsymbol{m}} &= \frac{\gamma_0}{1+\alpha^2}\boldsymbol{H}_{\text{eff}} \times \boldsymbol{m} + \frac{\alpha\gamma_0}{1+\alpha^2}\boldsymbol{m} \times (\boldsymbol{H}_{\text{eff}} \times \boldsymbol{m}) \\ &\quad - \frac{1+\alpha\beta}{1+\alpha^2}(\boldsymbol{u}\cdot\nabla)\boldsymbol{m} + \frac{\beta-\alpha}{1+\alpha^2}\boldsymbol{m} \times [(\boldsymbol{u}\cdot\nabla)\boldsymbol{m}].\end{aligned} \tag{19}$$

This expression shows that, when the CIP STT terms are added to the LLG equation, the equation is equivalent to a LL form to which a slightly renormalized adiabatic term $u(1+\alpha\beta)/(1+\alpha^2)$ and a non-adiabatic term $u(\beta-\alpha)/(1+\alpha^2)$ have been added. In this sense, the various points of view presented above end up into different expectations for the value of β.

In this chapter, we will describe results in the framework of the LLG formulation (18). Results can be transformed back to the LL formulation by replacing β in LLG by $\beta - \alpha$ in LL. To be specific and allow for direct comparison with the field-driven case, the nanostrip of $300 \times 5\ \text{nm}^2$ cross section will be kept. Starting from the simplest situation, complexity will be added step by step in the models.

3.1.1. Other terms

Apart from the spin-transfer effect, the large current flowing inside the nanostrip gives rise to two other effects that affect magnetization dynamics: the Œrsted field created by the current and the rise of sample temperature.

3.1.1.1. The Œrsted field The existence of this field is the reason for which sample width and thickness have to be small. For a nanostrip with flat rectangular cross section $h \ll w$, the field has only a perpendicular z-component that is maximum at the strip edges, and reads (for an infinitely long straight strip, J being the current density)

$$H_{z,\max} = \frac{J}{4\pi}\left[h \ln\left(1 + \left(\frac{2w}{h}\right)^2\right) + 4w\text{Atan}\frac{h}{2w}\right]. \tag{20}$$

This value is roughly proportional to the nanostrip thickness h. The y-field component [obtained from Eq. (20) by exchanging h and w] is slightly smaller, and changes sign across the strip thickness so that for thin nanostrips (a few exchange lengths thick) this field should have virtually no effect. Note that a non-zero average for the y-field exists if the sample consists of several metallic layers, as in spin-valve structures [46]. For a straight wire the axial (x) field component is zero, so that there is no direct effect on the DW position.

The maximum values of the Œrsted field are not large for usual current densities. For example, in a $300 \times 5\ \text{nm}^2$ nanostrip with a typical current density $J = 10^{12}\ \text{A/m}^2$, one gets $\mu_0 H_{z,\max} = 5.8\ \text{mT}$. This field has to be compared to the demagnetizing field opposing an out-of-plane component, so that neglecting exchange effects one expects a local $m_z \approx H_z/M_s$, here less than 1%. A profile of this field is plotted in Fig. 9, together with the m_z-component that results from a micromagnetic calculation under this non-homogeneous field.

The presence of this perpendicular field component may affect the processes that occur at the sample edges. As seen in the field-driven case, V and AV are

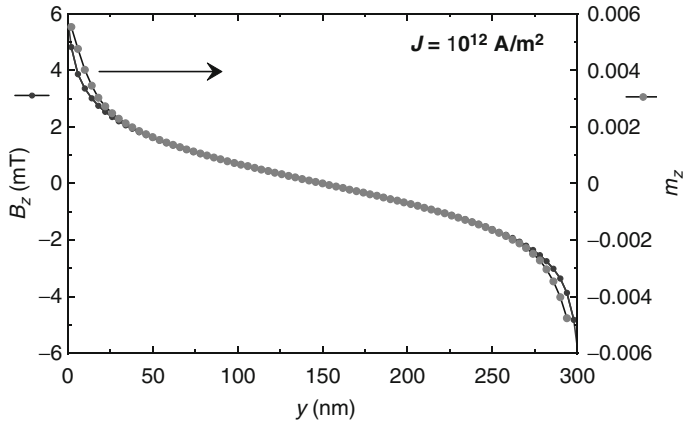

FIGURE 9 Œrsted field in a nanostrip 300×5 nm^2 under a uniform current density $J = 10^{12}$ A/m^2. The field component perpendicular to the film plane is evaluated at the centre of the thickness, and has the expression

$$H_z(y) = \frac{J}{4\pi}\left[h \ln\left(\frac{(w-y)^2 + (h/2)^2}{y^2 + (h/2)^2}\right) + 4(w-y)\mathrm{Atan}\frac{h/2}{w-y} - 4y\mathrm{Atan}\frac{h/2}{y}\right].$$

The perpendicular magnetization component m_z induced by this field in the uniformly magnetized nanostrip is also shown. The scales of both curves are such that the approximate expression $m_z \approx H_z/M_s$ can be visually tested: a larger out-of-plane magnetization component is seen close to the edges, due to the reduced local perpendicular demagnetizing field.

injected and disappear at the edges, and their core has a perpendicular magnetization. Thus, a dissymmetry of dynamic processes is to be expected, in principle. However, the smallness of this field component in comparison to the typical demagnetizing field within the core, of the order of M_s, lets anticipate weak effects. One report, however, has evidenced calculated oscillations in the transient response of a DW to a current step due to the influence of the Œrsted field [47].

The influence of this field for unperfect samples, for example, with an edge roughness or even a notch that reduces locally the nanostrip width, should be investigated in each precise case. For this purpose, the current density cannot be assumed as uniform, and requires a separate evaluation.

3.1.1.2. Sample temperature Due to the sample resistivity $\rho(T)$, to a current density J is associated a volumic heating power ρJ^2. For $\rho = 10\ \mu\Omega$ cm and $J = 10^{12}$ A/m^2 this power is 10^{17} W/m^3. Without sample cooling, such a power would rapidly destroy the sample: the volumic heat capacity of Iron is, for example, $C = 3.5 \times 10^6$ J/(m^3 K) so that sample heating would proceed at the tremendous rate of 30 K/ns. An analysis of heat flow in an infinitely long nanostrip on top of an infinitely thick substrate was performed analytically and by finite elements solution of the heat diffusion equation [48]. The result is that, if λ_S denotes the thermal conductivity of the substrate, C_S its volumic heat capacity and hence $D_S = \lambda_S/C_S$

the heat diffusion constant in the substrate, the heating power applies at long times t (i.e. $\sqrt{D_S t} \gg w$) to a cross section of the substrate that increases by diffusion as $\approx D_S t$, so that temperature rises much more slowly than linearly, as

$$T(t) = \frac{\rho J^2}{\lambda_S} \frac{wh}{\pi} \ln\left(\frac{4\sqrt{D_S t}}{w_G}\right) \tag{21}$$

(the symbol w_G is the width of the Gaussian profile matched to the nanostrip width for simplicity of the formula, it is of order $w_G \approx 0.5w$). Taking Silicon as substrate [$C_S = 1.66 \times 10^6$ J/(m^3 K) and $\lambda_S = 148$ W/(m K) so that $D_S = 8.92 \times 10^{-5}$ m^2/s, at room temperature], the calculated temperature increase in the same conditions as before is 2.7, 5.6 and 8.6 K for times 1 ns, 100 ns and 10 μs, respectively. But with SiO_2 the values become roughly 100 times larger. The first values are very conservative estimates: the resistivity of NiFe is 2–3 times larger than the value used here, there is an insulating layer below the sample, the substrate may be thin, and the resistivity of metals increases with temperature. The second values correspond to some experimental situations [49, 50] (as described in Chapter 4 by T. Ono and T. Shinjo, temperature can be monitored experimentally through the sample resistance). The heat diffusion analysis was extended recently to the case where an insulating layer separates the nanostrip from the substrate [51].

Thus, to describe all possible experiments, simulations should incorporate thermal effects. In micromagnetics, temperature has two influences:

- All micromagnetic parameters, as they derive from the magnetic free energy of the material, are temperature dependent. One has thus to consider $M_s(T)$, $A(T)$, $\alpha(T)$ and, for the current polarization, $P(T)$. The temperature dependence of magnetization is well known experimentally. The calculation of the exchange constant from the Dirac–Heisenberg Hamiltonian provides $A(T) \propto M_s^2(T)$. Measurements of damping versus temperature show virtually no effect [52, 53]. Finally, it seems reasonable to assume $P \propto M_s(T)$. Thus, from the definition (12), we expect that the equivalent velocity u does not change upon heating (this holds true provided the current is maintained constant despite the rise of the sample resistance), as well as the exchange length (4). The overall effect of temperature can be better appreciated by transforming the equations to non-dimensioned quantities, defined by

$$\begin{aligned} \tau &= \gamma_0 M_s t, \\ \boldsymbol{h} &= \boldsymbol{H}/M_s, \\ \boldsymbol{\rho} &\equiv (\xi, \eta, \zeta) = \boldsymbol{r}/\Lambda, \end{aligned} \tag{22}$$

  so that, for example, $\boldsymbol{h}_{\text{eff}} = \partial^2 \boldsymbol{m}/\partial \rho^2 + \boldsymbol{h}_d$. With these definitions, the LLG equation with adiabatic term becomes

$$\frac{\partial \boldsymbol{m}}{\partial \tau} = \boldsymbol{h}_{\text{eff}} \times \boldsymbol{m} + \alpha \boldsymbol{m} \times \frac{\partial \boldsymbol{m}}{\partial \tau} - \frac{u}{\gamma_0 M_s \Lambda} \frac{\partial \boldsymbol{m}}{\partial \xi}. \tag{23}$$

  This form shows clearly that the effect of temperature rise is to increase the current efficiency, as $u/(\gamma_0 M_s \lambda)$ varies like $1/M_s$ and M_s decreases with

temperature. Note that also the real-time dynamics slows down as T increases, a phenomenon well known close to the Curie point.

No systematic analysis of the effect, on current-induced DW dynamics, of a temperature elevation-induced change of the micromagnetic parameters has been performed up to now, with the exception of one paper [54] that used the finite size scaling technique for changing the micromagnetic parameters [55] and found that indeed DW could be displaced with lower currents when T rose close to T_c.

- Superparamagnetic fluctuations increase when temperature rises. These can, following Brown [56], be introduced into standard micromagnetics by adding to the effective field a random field $\boldsymbol{H}_{th}$ with zero mean and whose variance obeys (beware that delta functions have dimensions)

$$\langle H^i_{th}(\boldsymbol{r},t)H^j_{th}(\boldsymbol{r}',t')\rangle = \frac{2\alpha k_B T}{\gamma_0\mu_0 M_s}\delta_{ij}\delta(\boldsymbol{r}-\boldsymbol{r}')\delta(t-t'). \tag{24}$$

Calculations incorporating these fluctuations have shown a very weak effect of temperature, at least for metallic samples. In fact, the energy barriers between different structures of a DW are most of the time very high compared to the thermal energy [42, 57] (see, e.g. Fig. 3B). Note finally that when combining both aspects of temperature rise, the scaled typical thermal field is reinforced as it varies with temperature as $\sqrt{T}/M_s(T)$.

3.2. Perfect case with adiabatic STT

An ideal situation will be discussed first: the nanostrip is assumed to be perfectly straight, with no defect, and contains a DW at rest, the current is switched on instantaneously at time $t = 0$, and only the adiabatic term exists in LLG (14). The Œrsted field is not included either.

3.2.1. Transverse wall

Starting from a STW solution at rest, the time evolution of several quantities that allow monitoring the DW dynamics is plotted in Fig. 10, for various values of the velocity u representing the spin-polarized current torque.

For currents below a threshold ($u_{c,TW} \approx 645$ m/s here), the DW displaces a little along the wire and finally comes to rest under current (Fig. 10A). The DW initial velocity is equal to u, as remarked early [39]. The structure at rest under current differs from the initial one: the DW transverse moments μ_y and μ_z have changed (Fig. 10B), similarly in fact to the steady-state solution under field, as the y-moment decreases and the z-moment increases. In addition, the maximum z-component of the magnetization reaches higher and higher values as current becomes larger (Fig. 10C). The characteristic time for the equilibration of the DW structure is short (≈0.5 ns), with some clear oscillations. These are due to the conversion during motion of the STW into the ATW structure (i.e. the stable form of TW at this nanostrip size, see Table 1 and Fig. 3), as proved in Fig. 10C.

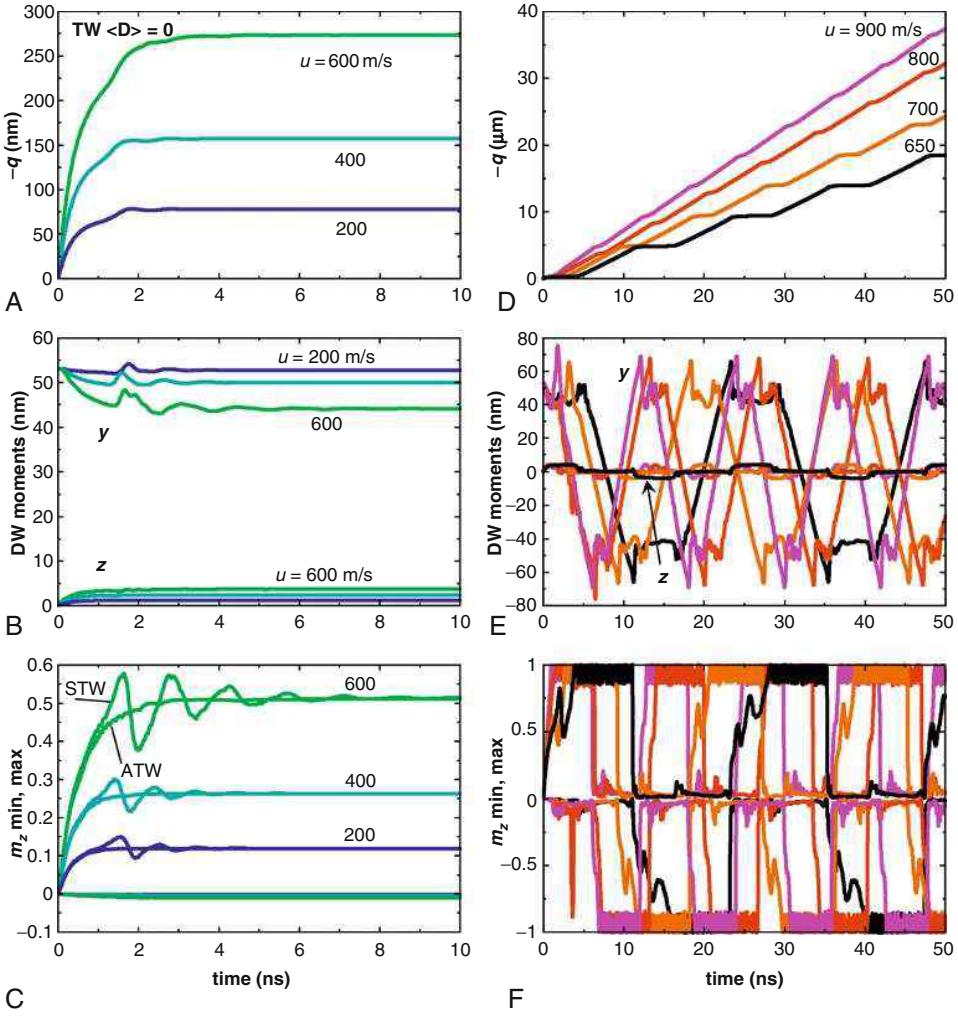

FIGURE 10 Time-resolved dynamics of a STW in a 300 × 5 nm^2 perfect nanostrip submitted at $t = 0$ to a constant spin-polarized current, in the adiabatic model. The low-current regime $u < u_{c,TW}$ is shown on the left figures (A–C) and the high-current regime on the right (D–F), with different scales at left and right. The DW position is shown in the top (A, D) panels, then (B, E) the y- and z-moments of DW magnetization [Eq. (6)], and finally the values of the maximum and minimum perpendicular component m_z of magnetization (C, F). The electric current is along the positive x-direction, so that electrons move in the negative x-direction. Panel (C) contains in addition the data obtained when starting from the stable ATW structure, where the oscillations seen for the STW are absent.

The fact that the DW eventually stops implies that the CIP STT has to be compensated by another torque. Such a torque is provided by the deformation of the DW structure. To understand this deformation, we reduce the TW structure to the central moment in the DW (i.e. the moment oriented along the transverse y-direction, at equilibrium). The CIP STT on this moment, starting from equilibrium, is the same as that resulting from a field applied along the perpendicular z-direction. Therefore, at equilibrium under current, this moment will have precessed towards the z-direction, leading to an effective field (of demagnetizing origin, mostly) also along the z-direction that compensates the spin transfer. Although their full spatial form and dependence on magnetization orientation are different, the fact that initially spin transfer is equivalent to a perpendicular field helps understanding why no continuous DW motion under current should be expected. Note finally that DW transient displacement and DW structural transformation are intimately related, as shown recently [58] using the concept of DW angle (or momentum [59–61]).

For $u > u_{c,TW}$, the DW is set into continuous motion (Fig. 10D), and the DW velocity reaches, in a small current interval, values of the order of several times 100 m/s. This motion is not a mere DW translation, but occurs under rotation of the DW moment (Fig. 10E), realized through the injection, displacement across the nanostrip width, and expulsion of AVs, as shown by the plots of the maximum and minimum of the perpendicular magnetization component (Fig. 10F), as well as by looking at the movie of the magnetization evolution. This is fully similar to the field-driven case. The comparison of Fig. 10D and F reveals that DW motion occurs only when the AV is present; another illustration of the relation between DW displacement and DW structure transformation.

These phenomena have been recognized early [39, 40, 42]. Composite models of DW dynamics based on AV and V energetics and dynamics are being constructed presently [21, 62] that provide simple and efficient explanations of this behaviour. The basic ingredient of these models is the Thiele equation that is introduced in Chapter 5 by H. Kohno and G. Tatara and discussed later.

3.2.2. Vortex wall

The case of the VW structure is similarly illustrated in Fig. 11. At very low currents, the VW structure is conserved. Similar to the TW case, the DW first moves but finally stops (Fig. 11A), adopting a deformed structure (Fig. 11B) under current. The quantitative difference with the TW case is that the VW is displaced much more (for the same current) than the TW. This is in fact related to the much larger structural characteristic time of this structure, equal to ≈20 ns in this case (see Table 1). The deformation of the VW structure is mainly apparent by the change of the y-DW moment that corresponds to an offset of the vortex core (Fig. 11C). The other quantitative difference with the TW is the magnitude of the currents involved: the VW structure is maintained only for $u < u_{c,VW} \approx 60$ m/s.

For intermediate currents, the VW transforms to a TW by expulsion of the V core, as shown by Fig. 11E and F. This transformation is accompanied by a sizeable displacement of the DW position that is in fact "quantized" [58]. The intermediate regime, defined by $u_{c,VW} < u < u_{c,TW}$, is such that even after

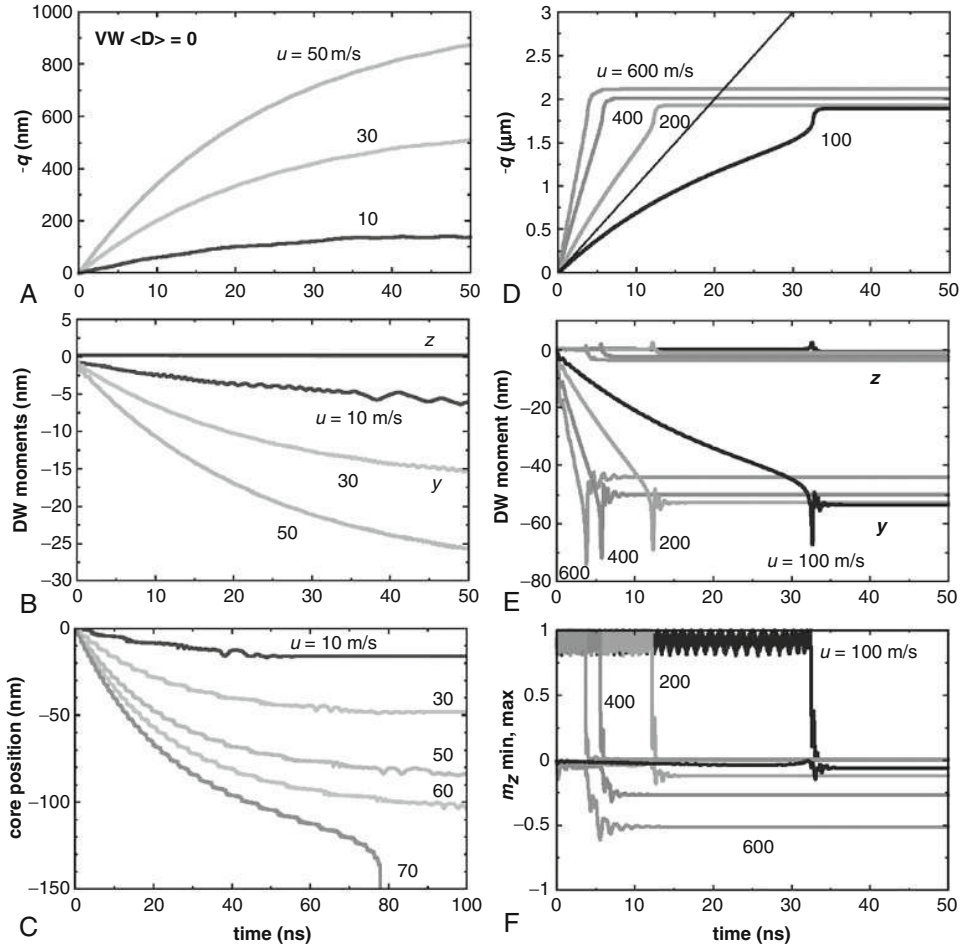

FIGURE 11 Time-resolved dynamics of a VW in a 300×5 nm^2 perfect nanostrip submitted at $t = 0$ to a constant spin-polarized current, in the adiabatic model. The low-current regime $u < u_{c,VW}$ is shown on the left figures (A–C, $u = 10$, 30, 50 m/s) and the intermediate current regime on the right (D–F, $u = 100$, 200, 400, 600 m/s). The electric current is along the positive x-direction, so that electrons move in the negative x-direction. The DW transverse moments (B, E) are the scaled integrals of the transverse (y and z) magnetization components [Eq. (6)]. The vortex core y-position is shown (C) for long times and low currents, including in addition those close to the transition to the TW ($u = 60$, 70 m/s). The straight line in (D) shows that for $u = 100$ m/s, the DW initial velocity is indeed $v = u$.

conversion to a TW the wall eventually stops. The total DW displacement incurred by the current application is then the algebraic sum of the "quantized" displacement due to the structure conversion and the displacement of the TW when submitted to the current.

At large currents $u > u_{c,TW}$ we recover the DW continuous motion seen before.

3.2.3. Comparison to experiments

From the study of these two cases, we conclude that in the perfect and adiabatic situation there is no continuous DW displacement under constant current, except for very large values of the current where DW motion occurs at the price of a continuous transformation of the DW structure, with a large velocity. Thus, an intrinsic current threshold for DW motion is predicted in this framework [41, 42]. For other nanostrip sizes, results are similar with only a change in numerical values. Some plots of the important quantities in the (w, h) plane are provided in Ref. [58].

These conclusions are in strong disagreement with experiments. Indeed, with a polarization $P = 0.7$ for NiFe, a current equivalent velocity $u_c = 650$ m/s corresponds to $J_c = 13 \times 10^{12}$ A/m^2, a value 20 times larger than the experimental results for close sizes [63–65]. Moreover, the current threshold for DW motion has been shown to be proportional to the DW propagation field, and is therefore extrinsic [66]. Several ways to lift this paradox, whereby the current appears to be much more efficient in reality than in models, have been proposed: the inclusion of a non-adiabatic term, the use of the LL equation with adiabatic term only, and the increase of sample temperature:

(i) In Section 3.1, we have shown that sample heating depends enormously on sample architecture, and varies very rapidly with current density J (faster than J^2). From the micromagnetic analysis of the temperature dependence of the material parameters, it has also been shown that the CIP spin transfer is expected to be amplified by an increase of temperature. Therefore, the rise of T up to the vicinity of T_c may give rise to DW motion in the perfect case, at values of current compatible with those of the experiments. However, first, the current window for such DW motion should be very narrow, as with just a little more current the sample reaches T_c. There are indeed many reports [49, 50, 67, 68] that T_c could be reached in experiments, as the nucleation of structures such as pairs of domain walls, was observed. Even without reaching the Curie temperature, the transformation of the DW structure is also often observed: change of chirality of the DW [69], or change between TW and VW [70, 71] (but DW structure transformations can also be ascribed to STT) Second, there exist also experiments with different sample structures and experimental conditions where heating was measured to be relatively small, and nevertheless DW motion observed, so that alternatives to heating have to be considered.

(ii) The introduction of adiabatic CIP spin transfer into the LL equation [see Eq. (16)] changes the situation completely. Indeed, as explained in Section 3.1, the solution for a DW under current is then trivial: a translation as a whole without any deformation, with instantaneous velocity $v(t) = u(t)$. There would therefore be no current threshold for DW motion.

From the field-driven case however, we know that DW propagation is hindered by many sorts of defects. The existence of these defects breaks the translation invariance of the nanostrip, so that the analytic solution just discussed no longer applies and micromagnetic models with disorder have to be employed. These show the apparition of a threshold current,

depending on the disorder model and magnitude, so that the very existence of a threshold current is not a sensitive test of the models.

Another prediction of the model is the velocity relation $v = u$. Velocities measured were initially much smaller, of the order of a few m/s [63, 72], but recently much higher values were measured with shorter current pulses [65, 68] that do not always obey $v = u$.

The other strong prediction of the adiabatic LL formulation is the displacement without change of structure. Several experiments with a VW have shown a lateral y shift of the vortex core following current pulses [68, 70, 71] (due to defects that prevent the core from returning to the nanostrip centre) that contradicts the rigid translation model. This may well be the most sensitive experimental test of the CIP spin-transfer micromagnetic models. However, all conclusions of this model should be tested for robustness to disorder.

(iii) The third alternative is to stick to LLG and add a non-adiabatic term (18), with coefficient β. This encompasses the previous idea as a special case, namely $\beta = \alpha$ (up to a very small renormalization of u by a factor $1 + \alpha^2$). Therefore, we will in the following discuss the micromagnetic numerical results obtained in this framework. An analytic description can be found in Chapter 5 by H. Kohno and G. Tatara.

3.3. Perfect case with non-adiabatic STT

The equation governing magnetization dynamics considered now is (18) and (19). We will discuss first the results for the transverse wall before analyzing those for the vortex wall and comparing them.

3.3.1. Transverse wall

The dependence of the TW velocity on current u as a function of the non-adiabaticity parameter β is shown in Fig. 12 that also incorporates the results of Section 3.2. The velocity here is the velocity measured at long times, the current being applied in a step-like way at time $t = 0$ on the TW structure at rest. In the case where DW motion is not stationary, as it is still periodical once the transients are over, the velocity is the average value over one period.

The first striking result is that, as soon as $\beta > 0$, DW motion is obtained under infinitely small currents. Thus, there is no longer an intrinsic threshold current for DW motion, and small DW velocities can be easily reached. The reason for DW motion as soon as $\beta \neq 0$ can be "read" from (19): to avoid the full cancellation of the CIP STT, the ratio of both spin-transfer terms $[(\alpha - \beta)/(1 + \alpha\beta)$ here] has to differ from the corresponding ratio for the effective field (α).

3.3.1.1. Linear regime The linear regime found at low currents does not show any curvature, at variance with the field-driven case. The 1D model of DW (see Chapter 5 by H. Kohno and G. Tatara) predicts indeed that

$$v = \frac{\beta}{\alpha} u \tag{25}$$

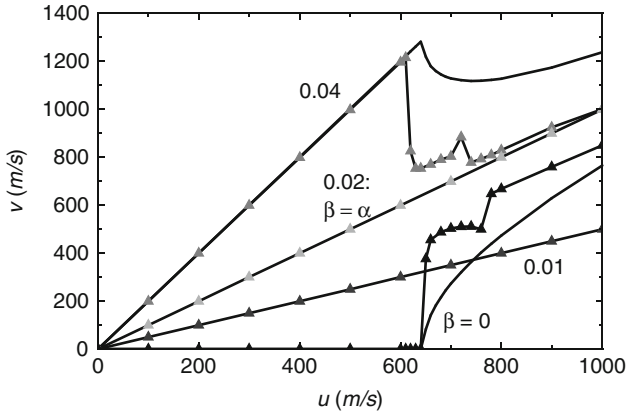

FIGURE 12 Velocities of a TW in a 300 × 5 nm^2 nanostrip without any defect under constant current represented by the equivalent velocity u, with the non-adiabaticity coefficient β as a parameter (material is NiFe with damping $\alpha = 0.02$). Continuous curves are the prediction of the 1D model with constant DW width [45], with $u_c = 644.7$ m/s. As explained in the text, the figure applies also to the VW.

(note that for $\beta = \alpha$ we recover $v = u$ as seen above). In fact, this relation has a much greater range of validity, as it has been shown to hold as soon as there is a steady-state DW motion, whatever the DW structure [45]. In stationary conditions indeed, time derivatives are space derivatives and by integration general relations can be obtained, known as the Thiele equation [18, 61] and its generalization to the current-driven case [45]. The slopes in Fig. 12 are perfectly reproduced by Eq. (25).

However, this does not mean that the DW structure is unchanged. The evolution with time of the parameters of the TW is shown in Fig. 13A–C for some values of the parameters β and for a realistic current $u = 100$ m/s. From that figure (panels B and C) the evolution of the DW transverse magnetization moment is apparent. It should be noted that the evolutions for $\beta = 0$ and 0.04 are opposite to each other, that for $\beta = 0.01$ being one half of that for $\beta = 0$ and that for $\beta = 0.02 \equiv \alpha$ being nil (except for the STW to ATW transition shown in Fig. 13B by the Thiele DW width, due to the unstability of the STW).

More quantitatively, DW structures in steady-state motion under current are virtually undiscernable from those obtained under field (shown in Fig. 6), provided they are compared at the same *relative velocity* v_R defined as $\boldsymbol{v}_R = \boldsymbol{v} - \boldsymbol{u}$. This comes directly from the Lagrangian formulation of the LLG equation (see Chapter 5 by H. Kohno and G. Tatara), and its extension to include CIP spin transfer.

3.3.1.2. Lagrangian formulation of micromagnetics under CIP STT In micromagnetics, the concept of Lagrangian was introduced by Döring [19], who used it to show that any DW structure has a maximum velocity, and to compute the moving DW structure to first order in damping (see the discussion in [15]; values of these

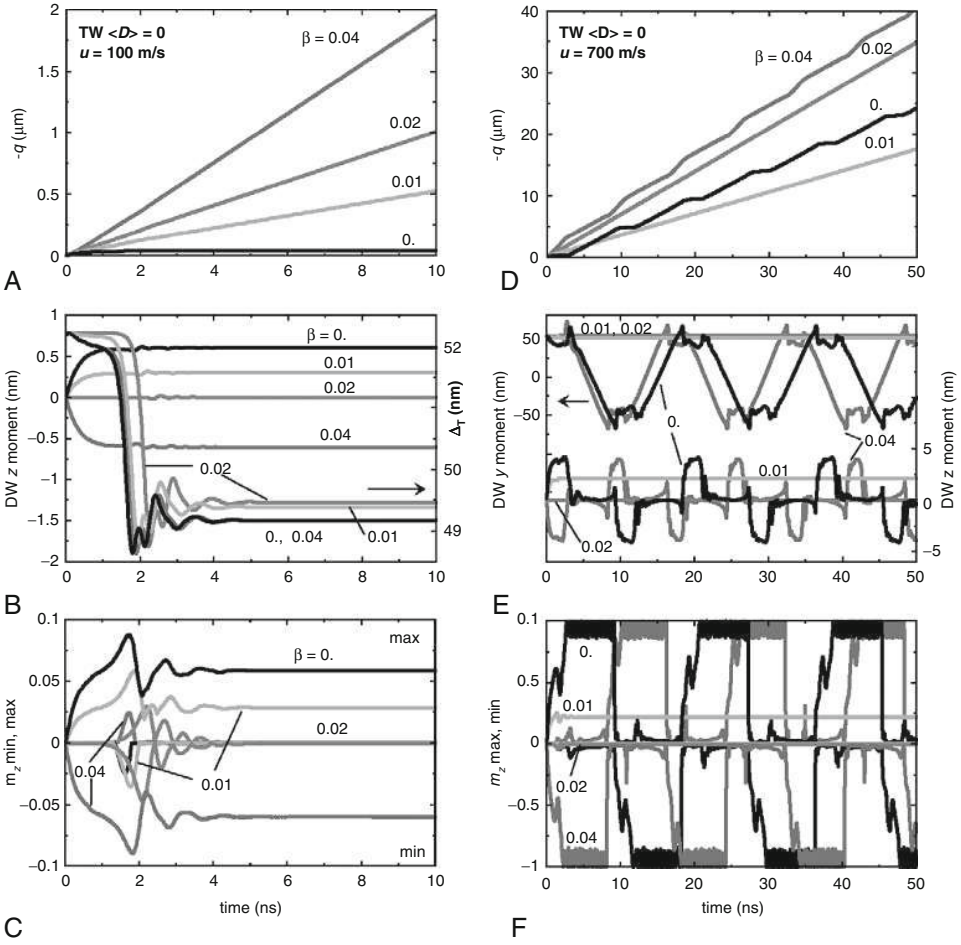

FIGURE 13 Time-dependent response of a STW in a 300 × 5 nm^2 nanostrip without any defect ($\langle D \rangle = 0$) submitted at time 0 to a current represented by the equivalent velocity u, with the non-adiabaticity coefficient β as a parameter ($\alpha = 0.02$). Two values of current are shown, $u = 100$ m/s (A–C) in the linear regime and $u = 700$ m/s (D–F) above the Walker threshold, for some values of β.

velocities for TW and VW are given as a function of w and h in [58]). In the presence of CIP spin transfer the Lagrangian incorporates a term due to adiabatic spin transfer, whereas the non-adiabatic term plays no role as it belongs to the terms that do work, like damping and applied field along the strip axis. For steady-state motion, the Lagrangian is found to depend on the relative velocity $\boldsymbol{\nu}_{\mathrm{R}}$ only. Thus, steady-state motion at velocity v under STT described by the equivalent velocity u obeys

$$|v - u| < v_{\max}. \tag{26}$$

As a consequence, the regime where the DW does not move ($v = 0$) can exist only for $|u| < v_{\mathrm{max}}$, as seen above. In the case $\beta = 0$ where this solution exists, we have the following important relation between the field- and current-driven regimes:

$$u_{\mathrm{c,TW}} = v_{\mathrm{max,TW}}. \tag{27}$$

This equation shows that two quantities apparently unrelated are in fact equal (this is one of the motivations for describing DW dynamics by field and by current together in this chapter).

When $\beta \neq 0$, the steady-state relation (25) implies that the steady state ends at $u = \boldsymbol{u}^*$ (with a DW velocity v^*) given by

$$\begin{aligned} u^* &= \frac{\alpha}{|\,\beta - \alpha\,|}\, v_{\mathrm{max}}, \\ v^* &= \frac{\beta}{|\,\beta - \alpha\,|}\, v_{\mathrm{max}}. \end{aligned} \tag{28}$$

For the values of β considered in the figures, we obtain the following analytical predictions for $\alpha = 0.02$: $u^* = 2v_{\mathrm{max,TW}}$ and $v^* = v_{\mathrm{max,TW}}$ for $\beta = 0.01$; $u^* = v_{\mathrm{max,TW}}$ and $v^* = 2v_{\mathrm{max,TW}}$ for $\beta = 0.04$ and $u^* = \infty$ for $\beta = 0.02$ (the meaningful parameter being β/α). With the value of $v_{\mathrm{max,TW}}$ given in Table 1, we see that the analytical predictions for the end of the linear regime are well obeyed. The agreement is not perfect as the "Döring principle" is in fact a low damping approximation [15].

The dependence on $\boldsymbol{\nu}_{\mathrm{R}}$ only of the Lagrangian in the stationary regime, together with the expression of DW velocity (25) in that regime, show that the modification of the DW structure in the stationary regime depends on $(\beta - \alpha)u/\alpha$. This explains the magnitudes and signs of the DW structural deformations seen in Fig. 13.

3.3.1.3. Beyond the Walker regime For currents above u^*, DW motion is no longer stationary, as shown in Fig. 13D–F in the particular case $u = 700$ m/s. The dynamics is very similar to that seen under field (Fig. 5) with precession of the DW magnetization through the injection and displacement of isolated antivortices (moderately above u^*), followed by vortices and multiple localized structures at larger and larger currents.

A notable difference with the field case is that, depending on the value of β, the velocity can increase (if $\beta < \alpha$) or decrease (if $\beta > \alpha$) compared to the linear regime (Fig. 12). To explain this, we may remark from Fig. 13D that DW velocity is lower when there are no localized structures for $\beta < \alpha$, and higher when $\beta > \alpha$, generalizing the observation made in the case $\beta = 0$ (Fig. 10). In all cases velocities converge to $v = u$ at very large currents (Fig. 12), as predicted by the 1D model.

In addition, although this is not a general feature as it depends on nanostrip size, we see two regions in the above Walker regime with a velocity jump between them. Examination of the associated movies shows that this is due to the time required to inject the AV. The peaks at $u = 760$ m/s for $\beta = 0$ and $u = 720$ m/s at $\beta = 0.04$ are characterized by the injection and motion of an isolated V (instead of

an AV). In fact, there appears to be a competition between injection of an AV at one edge of the nanostrip and the injection of a V at the opposite edge. This competition depends on the aspect ratio of the nanostrip [21].

3.3.2. Vortex wall

The DW velocities evaluated at long times (stationary regime, or periodic average above) for a VW are identical to those found for the TW and displayed in Fig. 12. In the stationary regime, this result is proved directly by the Thiele approach recalled earlier that gives Eq. (25) independently of the DW structure. Above this regime, as the DW structural transformation starts by the expulsion of the vortex core and transformation to a TW, the similarity of TW and VW is also understood.

3.3.2.1. Linear regime The time evolution of the VW under two values of current is illustrated in Fig. 14. The first value $u = 50$ m/s (panels A–C) was chosen such that for all values of β the current is in the linear region for the VW, whereas for $u = 100$ m/s only $\beta = 0.01$ and 0.02 belong to it. Similar to the TW, the linear regime features a progressive VW structural transformation despite the perfect linearity of the $v(u)$ relation. The transformation is displayed, for example, by the DW y-moment (Fig. 14B and E), or by the vortex core y-position (Fig. 14C). As already seen for the TW, there is no change when $\beta = \alpha$, the change for $\beta = 0.01$ is one half of that for $\beta = 0$ and that for $\beta = 0.04$ is opposite to that for $\beta = 0$.

This was well understood with the Lagrangian formulation of micromagnetics under CIP STT. Equivalently, the study of the VW dynamics by simple analytical models rests on the application of the Thiele equation to the AV and V. As explained in Chapter 5 by H. Kohno and G. Tatara, this equation shows that AV and V are submitted to a "gyrotropic" force that is orthogonal to $\boldsymbol{\nu}_R$ and changes sign with the core z-polarization direction and between AV and V.

The big difference between TW and VW that appears in the time-dependent results comes from the very different characteristic times of these two DW structures (see Table 1). The calculations show that the structural deformations under current have not yet reached their steady-state values after 50 ns (Fig. 14B). Consequently, the DW velocities are still off from the steady-state values, as shown in Fig. 14A where the lines corresponding to Eq. (25) were added. As the DW initial velocity is u, the transient DW velocities deduced from Fig. 14A and D lie between $v = u$ and $v = (\beta/\alpha)u$.

This figure also shows that the DW displacements converge to this analytic relation with an offset, itself varying like $\beta - \alpha$. This offset is of the same nature as the transient displacement seen in the $\beta = 0$ case previously (Fig. 11), and is directly related to the change of DW angle of the VW structure (the DW angle for a VW is defined precisely from the general definition in Ref. [58]).

The values of current at which the linear regime for the VW ends are given by the analytical prediction (28), with the micromagnetic value of $v_{max,VW}$ given in Table 1, hence $u^* = 122$ m/s for $\beta = 0.01$ and 61 m/s for $\beta = 0.04$ and 0. This is in agreement with the results shown in Fig. 14 for $u = 50$ and 100 m/s.

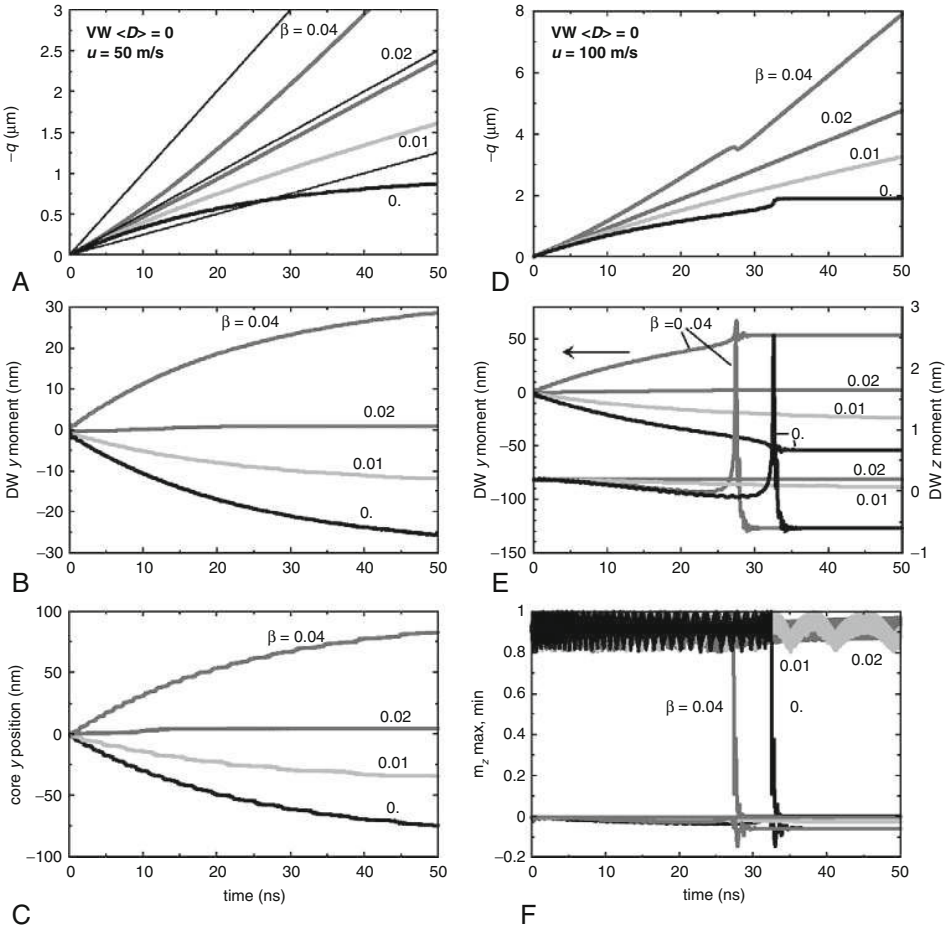

FIGURE 14 Time-dependent response of a VW in a 300 × 5 nm^2 nanostrip without any defect ($\langle D \rangle = 0$) submitted at time 0 to a current represented by the equivalent velocity u, with the non-adiabaticity coefficient β as a parameter ($\alpha = 0.02$). Two values of current are shown, $u = 50$ m/s (A–C) in the VW linear regime and $u = 100$ m/s (D–F) above the VW Walker threshold for some values of β. The lines in (A) express the analytical relation (25).

3.3.2.2. Above the VW linear regime The end of the linear regime for the VW is marked by the vortex expulsion (Fig. 14F). As shown in Fig. 14D, the DW velocity subsequently rapidly adopts the analytical value (25), as the characteristic time of the TW is short (see Table 1) and $u < u^*$ for the TW. This explains why Fig. 12, that plots the long time velocity, is identical for TW and VW.

3.3.3. Comparison to experiments

Remembering that the experimental values of u are at most 100 m/s, we see that the steady-state regime should apply, the DW velocity being thus directly linked to the β-parameter, independent of the DW structure, and with no current threshold.

The steady-state DW velocity is, however, not the only data that should be compared to experiments. Indeed, as explained in Section 3.1, the sample heating can be very important, and the high-current densities can lead to sample destruction by electromigration, so that sample damage is reduced by applying the current in pulses. Many experiments are thus now performed with short pulses, with sub-nanosecond [73], nanosecond [65, 68] up to microsecond [63, 70] duration. In such a situation, the characteristic time of the DW structure plays a role, especially for the VW where it can be very large (a map of this time as a function of nanostrip width and thickness is given in Ref. [58]). Figure 11A has shown that, even with $\beta = 0$, a VW transient displacement as large as 1 μm can be obtained under a reasonable current $u = 50$ m/s. This displacement is roughly linear with time up to 50 ns, and also with current. However, if the current is switched off the VW will come back to its original position.

This phenomenon has been discussed a long time ago, when studying the "gyrotropic" propagation of vertical Bloch lines (VBLs) inside the Bloch walls of bubble garnet films with perpendicular anisotropy, so as to realise a solid state memory known at the time as Bloch line memory [74]. The correspondence is between VW and VBL x-position, and V core and Bloch wall y-position. To retain a non-zero VBL displacement after a z-field pulse, the strategy was to apply a field pulse with long fall time, and to stabilize VBL position by an artificial potential well or pinning.

In the case of the VW discussed here, a long current fall time together with pinning of the V would lead to a non-zero VW displacement after a current pulse. We note that direct imaging experiments have indeed shown off-centred vortex cores after current pulses [68, 70] that support this mechanism. The additional observation that, once a VW was converted to TW, no motion could be seen [70] supports also this view. However, experimental pulse durations may be much longer (20 μs [72]) than the VW typical characteristic times, so that this explanation does not apply to all cases.

More generally, we have already mentioned that imperfections exist in real samples, so that the conclusions reached on perfect samples have to be checked in their presence. This is the object of the next section.

3.4. Imperfect case

As discussed for field-driven dynamics, imperfections can be introduced in micromagnetic calculations by some roughness of the nanostrip edge. Edge roughness has the additional consequence that the current density becomes non-uniform, and has to be calculated at every point. This involves solving the Poisson equation in the rough nanostrip, a calculation to perform only once, before the micromagnetic calculations. We consider here the case where the average grain diameter is $\langle D \rangle = 10$ nm only (propagation field $\mu_0 H_P \approx 1.5$ mT).

3.4.1. Transverse wall

Results obtained for a TW are shown in Fig. 15, for several values of the parameter β. This figure should be compared to Fig. 12.

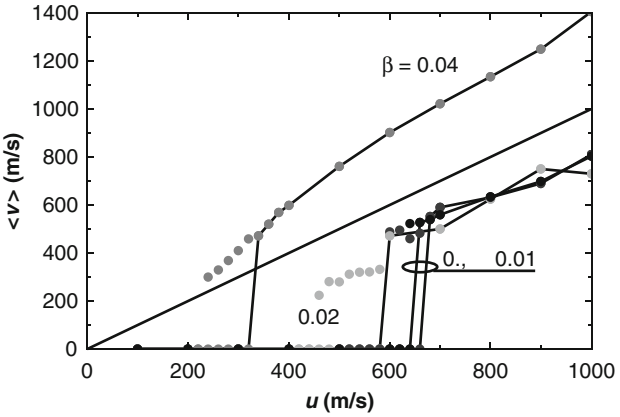

FIGURE 15 Velocities of a TW in a 300 × 5 nm^2 nanostrip without rough edges ($\langle D \rangle = 10$ nm) under constant current represented by the equivalent velocity u, with the non-adiabaticity coefficient β as a parameter (material is NiFe with damping $\alpha = 0.02$). In the case of stochastic DW displacement, two velocities are shown for the same current, and the points with lower velocity are linked together. The straight line plots the $v = u$ relation, for comparison.

In the adiabatic case $\beta = 0$, there is little change compared to the perfect case: DW motion occurs with transformation of the DW structure, starting at $u \approx u_c$.

When $\beta \neq 0$, no DW propagation is seen unless the velocity u is large enough, similar to field case. It can therefore be said that roughness leads to the apparition of a current threshold for DW motion. This threshold is not an intrinsic quantity, but linked to disorder (and indeed calculations with a larger roughness lead to a larger current threshold). Similar to the field case also (Fig. 8), DW motion in a certain range of currents above this threshold is stochastic, as the DW may move and stop at some places. The plot shows therefore two values of velocity in such range, namely 0 and the velocity derived from the period of DW motion.

The data with $\beta = 0.01$ are very similar to those at $\beta = 0$, so that this amount of adiabatic torque has no visible influence on DW motion, for the magnitude of imperfection considered in this calculation.

In the case $\beta = 0.02 = \alpha$, two regimes are seen. At the lower currents, the TW moves without notable change of structure (apart from the fluctuations of width, asymmetry, etc., due to roughness). This corresponds to what is expected in the perfect wire case. However, a relation $u \approx u - 200$ m/s is measured, instead of the expected $v = u$ rule. In this regime, the wall moves and may stop. At $u > 600$ m/s (the value of u_c in the perfect case), the continuous transformation of DW structure sets in, with the successive motion of AV across the nanostrip width (at least moderately above the threshold). The DW velocity increases and becomes similar to the velocity obtained under DW structure transformation at lower values of β. The $v(u)$ relation has still the slope 1, but the offset has diminished slightly.

Finally, in the case $\beta = 0.04 > \alpha$, the low u regime with DW motion without structure transformation is also found. The perfect case relation (25) is obeyed,

but again with an offset. In the higher current regime, the breakdown expected at $u = u_c$ (see Fig. 12) does not occur, and the DW structure does not process at least for the currents shown. Only a gradual reduction of the $v(u)$ slope occurs, towards unity (as found for a perfect nanostrip, but again with an offset).

This example shows that the influence of imperfections is (i) to mask the effect on DW motion of too small β-parameters, (ii) to introduce offsets in the linear regime and (iii) to suppress velocity breakdown (as already seen in the field-driven case). Note that, for this sample, the analytic slopes of the linear regime are preserved, whereas for a less wide nanostrip with the same roughness parameter $\langle D \rangle$ they were even reduced [45].

3.4.2. Vortex wall

As we have seen in the perfect nanostrip case, the VW dynamics under current is dominated by the presence of the vortex, with the long relaxation time of its y-position. This y-position will be controlled by the relative DW velocity $\boldsymbol{\nu}_R$.

Figure 16 depicts the dynamics of the VW, for two values of the current and various non-adiabaticity parameters. The data show, similar to the results obtained for perfect nanostrips, a transient VW motion at lower currents than for the TW that lasts as long as the V is present. As the initial V core z-magnetization is always the same, the V transverse motion direction is determined by v_R only.

The first value $u = 100$ m/s (panels A–C) should be compared to the perfect nanostrip situation, shown in Fig. 14A–C. We see that in the rough case, since $v < u$ is calculated, the DW y-moment always decreases and the vortex core y-position becomes negative. In the case $\beta = 0.04$ where v is close to u, the gyrotropic force on the vortex core is weak and the vortex core remains close to the nanostrip centre. Thus, this calculation provides an example where microscopically $\beta = 0.04 = 2\alpha$ whereas the apparently steady-state DW motion corresponds to $v = 85.4$ m/s thus $\beta = 0.85\alpha$. This behaviour exists in a certain range of currents, and the DW velocities measured in that range are plotted in Fig. 17. Each of the measured DW velocities could be translated into a value of an effective β/α that would vary between 0.55 and 1.13. The figure, however, shows that a slope of $v(u)$ can be defined in this regime (equal to 1.4 here) that lies between the values 1 and $\beta/\alpha = 2$. An offset in the $v(u)$ relation appears in addition. More generally, Fig. 16A shows that the DW velocities in the transient regime, that in the perfect situation ranged between u and $(\beta/\alpha)u$, are reduced when roughness is present. The results for $\beta = \alpha$ are remarkable, as the DW velocity is significantly smaller than u so that the vortex is expelled and the DW stops.

For the higher value of current $u = 300$ m/s (Fig. 16D–F), the DW velocity with $\beta = 0.04$ is now sufficiently larger than u so that the V moves upwards in y and is finally expelled, bringing the DW into a TW that stops later, as the value of u is in the region of stochastic DW motion for the TW at $\beta = 0.04$. The other cases, with lower β values, show DW velocities lower than u and thus a downwards expulsion of the V. The transient DW velocities are, as seen already for $u = 100$ m/s, also smaller than in the perfect case. From the figures, it can be expected that for an intermediate value $\beta \approx 0.03$, the vortex is kept and the DW continuously moves at $\langle v \rangle \approx u$, that is, an apparent $\beta \approx \alpha$.

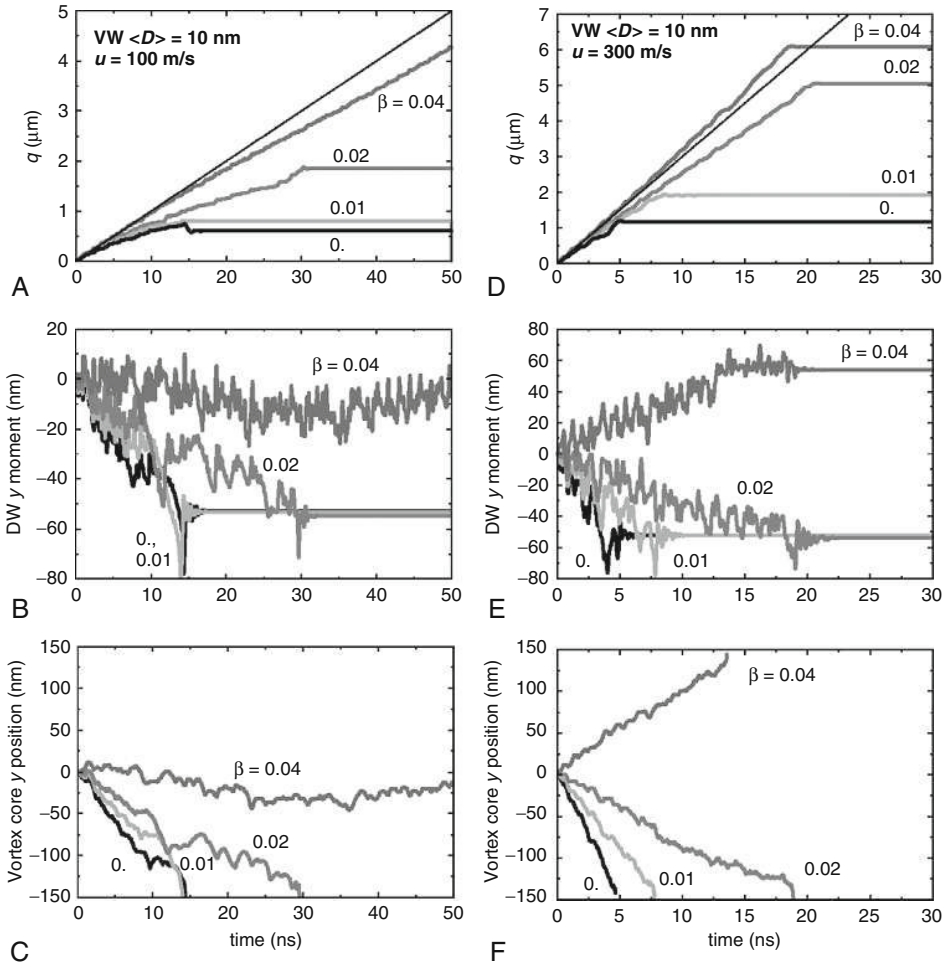

FIGURE 16 Time-dependent response of a VW in a 300 × 5 nm^2 nanostrip with roughness (average grain size $\langle D \rangle = 10$ nm) submitted at time 0 to a current represented by the equivalent velocity u, with the non-adiabaticity coefficient β as a parameter ($\alpha = 0.02$). Two values of current are shown, $u = 100$ m/s (A–C) and $u = 300$ m/s (D–F) (note the different timescales), for some values of β. The straight lines in (A, D) display the $v = u$ relation.

Summarizing, it appears that the VW can move more easily under current than a TW, in the presence of imperfections of the sample edge [75]. This feature is clearly consistent with experiments [66, 71]. The possible reason for this behaviour is that the vortex core, the region with the largest magnetization gradient hence the largest CIP STT, is far from the rough edges (note that defects in the form of holes give the opposite result that the TW moves more easily than the VW [76]). In addition, a non-trivial effect of imperfections was seen, namely a general reduction of DW velocity, leading to apparent β/α ratios close to unity, and that depend

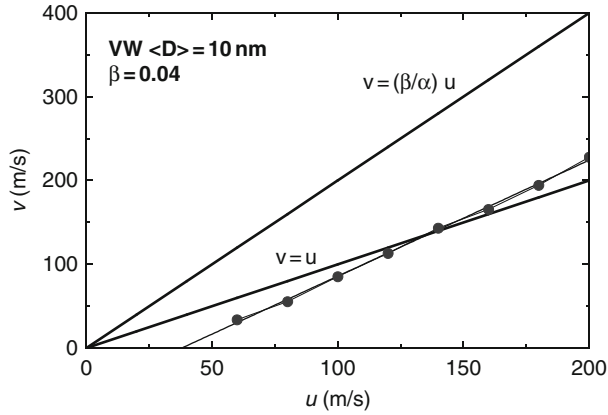

FIGURE 17 Transient velocity of a VW in a rough nanostrip (same parameters as in the previous figures) for $\beta = 0.04$, in a range of currents where the V is not expelled. The $v(u)$ slope is lower than the analytical value, with an offset, so that the relative velocity $(v - u)$ changes sign with increasing current.

on the current magnitude. This is also in qualitative agreement with experiments: many show that apparently $\beta \approx \alpha$ [30, 68, 77], but for similar samples other experiments require apparent $\beta/\alpha \approx 1$–10 [65, 71, 78]. Although the form and amount of disorder considered in these calculations result in clearly larger imperfections than what should exist in the best samples, these results show that the identification of the β-parameter by DW velocity measurements in real samples may not be straightforward.

4. DYNAMICS UNDER COMBINED FIELD AND CURRENT

As many experiments have considered how the CIP STT affects the field-induced DW dynamics, we will discuss this topic too.

4.1. Perfect samples

The results for a perfect wire are summarized in Fig. 18 where several values of u and β are compared. The calculations were performed for a TW. The results for a VW differ only close to the origin, precisely speaking when $|v-u|<v_{\max,\mathrm{VW}}$.

4.1.1. Linear regime

The linear regime has been theoretically studied in several papers [39, 40, 42, 44, 45]. The DW velocity in steady state reads

$$v = \frac{\gamma_0 \Delta_\mathrm{T}}{\alpha} H_x + \frac{\beta}{\alpha} u, \tag{29}$$

with as usual Δ_T the Thiele DW width of the moving domain structure (8). This relation, initially derived with the 1D model for a TW, holds in fact for any DW

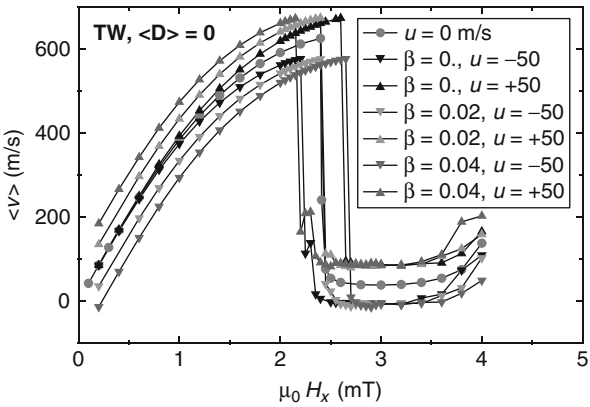

FIGURE 18 Velocity at long times of a TW in a perfect 300 × 5 nm^2 nanostrip under an applied field, superposed to a DC current with adiabatic and non-adiabatic spin-transfer torque. For each value of β, two opposite values of current $u = \pm 50$ m/s are injected.

structure and results only from the hypothesis of steady state. Similar to the field case, this relation has an intrinsic non-linearity due to the variation of the Thiele DW width (the accurate Döring approximation being that Δ_T depends only on the DW velocity v).

The end of the linear regime can be obtained, in the low dissipation approximation of the Döring principle, from the point where with Eq. (29) the maximum velocity v_{max} is reached, with a corresponding Thiele DW width $\Delta_T(v_{max})$. Thus, we get a dependence of Walker field on current as

$$\pm H_W(u) = \frac{\pm \alpha v_{max} - (\beta - \alpha)u}{\gamma_0 \Delta_T(v_{max})}. \tag{30}$$

This gives a relative variation $\Delta H_W / H_W$ of the Walker field at small u where the Thiele DW width has disappeared, reading

$$\frac{\Delta H_W}{H_W} = \frac{\beta - \alpha}{\alpha} \frac{u}{v_{max}}. \tag{31}$$

The numerical micromagnetic results displayed in Fig. 18 are in good agreement with Eq. (31), using the micromagnetic value of the maximum velocity given in Table 1. Therefore, at first sight, this analytic relation provides a very direct experimental measurement of β.

4.1.1.1. Above the Walker breakdown regime For fields larger than $H_W(u)$, velocity decreases abruptly, similar to the dynamics driven by field only. Figure 18 shows that the velocity slightly above the Walker field, in the region where $v(H)$ is flat, becomes also independent of the value of β. Moreover, the data are well described in this region by the very simple relation

$$v = v_{min} + u, \tag{32}$$

where the minimum velocity v_{min} was defined in Section 2.3. This result that depends only on the relative velocity v_R is very probably related to the Lagrangian description of the effect of CIP STT. Note that, if the steady-state relation were (erroneously) applied to such a result, a value $\beta/\alpha = 1$ would be deduced.

For higher fields where velocity increases again, however, a dependence on β reappears.

4.2. Imperfect nanostrip case

From the previous sections of this chapter, we know that imperfections may modify the conclusions reached on perfect samples. Nanostrip imperfection was mimicked here by an edge roughness as previously explained, with the same value (average diameter of the grains equal to 10 nm) used for the study of field-induced DW propagation (Section 2.4).

The results for TW motion under combined field and current obtained in such a nanostrip are shown in Fig. 19. Similar to the pure field case (Fig. 8), the disappearance of the Walker breakdown in the range of fields investigated is found.

For fields much larger than the propagation field, it is found that, remarkably, DW velocity is independent of the non-adiabaticity parameter β and obeys the simple relation

$$v = v_{max} + u. \tag{33}$$

This relation that mimics Eq. (32) corresponds to an effective ratio $\beta/\alpha = 1$. In terms of the Döring principle, relation (33) means simply that v_R is clipped to v_{max}. In the absence of a statistical treatment of imperfections, however, this statement should be considered just as an analogy, as there is no mathematically steady-state

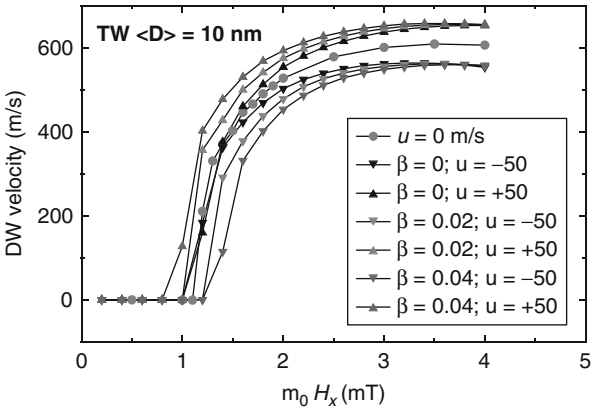

FIGURE 19 Velocity at long times of a TW, in a 300 × 5 nm^2 nanostrip having rough edges (mean grain diameter $\langle D \rangle = 10$ nm), under an applied field superposed to a DC spin-polarized current with both adiabatic and non-adiabatic CIP STT. For each value of β, two opposite values of current $u = \pm 50$ m/s are injected.

DW motion in a rough nanostrip. As expected, the behaviour in that field range is exactly the same for a VW.

We will not comment in detail the vicinity of the propagation field, as the approach used with no thermal fluctuations and relatively short calculation times is not very pertinent.

4.3. Comparison to experiments

4.3.1. Measurements of DW velocity

The DW mobility under field and current in samples where the Walker breakdown could be seen has been measured in only two cases up to now [30, 77], with nanostrip cross sections equal to 300×10 and $600 \times 20\,\mathrm{nm}^2$, respectively. Both experiments have seen mainly a vertical translation of the $v(H)$ curve under current, and conclude that $\beta \approx \alpha$ in their samples, based on the expressions established in the perfect nanostrip case.

The micromagnetic calculations performed with a large roughness (Section 4.2) have, however, shown that a vertical translation was obtained, irrespective of β. But this roughness was so large that it wiped out the Walker breakdown. Therefore, a milder imperfection model, that gives rise to propagation fields as low as those of samples where the Walker breakdown has been observed, is very much needed.

4.3.2. Depinning of a DW

In addition to the measurement of DW velocity under field and current, the variation of the propagation field under current has attracted a lot of attention experimentally [69, 78–81]. Samples with artificial defects (notch) pinning the DW, or just with natural defects, have been used.

For weak (natural) DW pinning, a rather linear variation of H_P with u has been measured once thermal (or thermal-like) effects were subtracted [79, 82]. Keeping in mind that this field is not confidently evaluated by current micromagnetic simulations, the trend seen in Fig. 19 proves qualitatively in agreement with these results.

4.4. AC effects

Spectacular results have been obtained by setting the DW into oscillation inside a pinning potential well [78, 81]. The 1D DW model was very efficient to understand the results obtained that were partly counter-intuitive.

A related experiment devised a nanostrip with small curvature under a field applied in the transverse direction so as to create a potential well for the DW [83], and resonant effects where the oscillation frequency was controlled by field were indeed observed.

Briefly stated, the interest of measurements at resonance is to avoid pinning effects and to detect weaker effects (see also Chapter 3 by Y. Suzuki). The micromagnetic analysis of data obtained in the situation of a vortex displaced inside a disc [84, 85] has shown that, importantly, the adiabatic CIP STT model was

quantitatively correct. However, no conclusion could be drawn about the non-adiabatic contribution up to now, as it did not influence the results in a measurable way.

The study of AC effects in CIP STT is developing very rapidly now, not only in the situation with a DW, but also with an isolated vortex, or even just field-dependent magnetization ripple (see Chapters 4 and 5 by T. Ono and T. Shinjo as well as by H. Kohno and G. Tatara).

5. CONCLUSIONS AND OUTLOOK

In this chapter, we have tried to present a unified view of DW dynamics in soft magnetic nanostrips, under the effect of field and/or spin-polarized current flowing along the nanostrip and across the domain wall. This view was based on micromagnetic simulations and their comparison to experiments.

A number of concepts have been shown to apply to both cases: the steady-state motion of the domain wall, the Walker breakdown, the maximum velocity of a DW structure, the Thiele DW width, for example. This justifies our choice to describe both driving mechanisms, even if one may appear as "old" and the other as "new". In fact, both mechanisms are only now becoming experimentally checked as better samples and experimental techniques are devised.

A few lessons can be taken from the synthesis presented here:

(1) Analytic results can be obtained that apply not just to the 1D model of the domain wall, but to the full micromagnetic situation. They hold true only in the limit of small damping and spin-transfer torque, similarly in fact to results derived recently for pillars owing to the macrospin model [86, 87]. It may even prove possible to extend these results to the above breakdown case, and to imperfect nanostrips.
(2) Effects of sample imperfections can be very important, up to destroying the rules obtained in the perfect case. As many models of imperfections can be thought of, it seems important now to find out which one fits best and most simply the experiments. The extension of analytic results to the imperfect situation would be a great step.
(3) It seems that the value of the apparent β/α ratio is reduced towards 1 by imperfections. A number of cases where the analytical prediction for a perfect sample turned to $\beta/\alpha \sim 1$ in a rough sample were shown. Thus, to answer the controversies about the proper incorporation of the STT in a continuous configuration crossed by current, experimental situations where the results are not affected by imperfections should be invented.

Finally, this chapter has not covered all possible applications of micromagnetics to the effect of STT within continuous magnetic structures, partly for lack of space. We have thus deliberately left aside:

(1) Nanostrips made out of hard materials with perpendicular anisotropy. Simulations [88, 89] and experiments [90] have appeared very recently. Briefly said, the interest of such materials is twofold: they allow controlling the DW width

by the anisotropy, and the Walker field and maximum velocity by the anisotropy and nanostrip geometry. In well-chosen cases, the intrinsic threshold for current-induced DW motion can be drastically reduced.

(2) Spin-valve nanostrips with two magnetic layers, where the magnetic structures are coupled and the spin-polarized current flows more complex to describe, despite many interesting results [46, 73, 80, 91].

(3) Nanostrips made out of magnetic semiconductors, prominently GaAs:Mn where large effects have been observed (see Chapter 7 by H. Ohno). There are indeed major issues like the effect of temperature and carrier-mediated ferromagnetism that cast warnings on the application of standard micromagnetics to this situation.

(4) The cases with no DW, but more generally just a non-uniform structure like a vortex or magnetization fluctuations (remember that the torque is proportional to the magnetization gradient). This field is more recent and extremely promising.

We hope nevertheless that the material presented in this chapter will be helpful to tackle these other subjects.

ACKNOWLEDGEMENTS

The work of Y.N. was partly supported by New Energy and Industrial Technology Development Organization (NEDO) of Japan. The work of A.T. was supported by the French Action Concertée Incitative NR 216 PARCOUR and ANR PNANO project DYNAWALL, and the European network MRTN-CT-2006-035327 SPINSWITCH. He also benefited from a JSPS fellowship for a stay at the Institute for Chemical Research, Kyoto University, Uji, Japan, in the summer 2006. Both thank T. Ono, S. Kasai, J. Shibata, G. Tatara, H. Kohno, M. Kläui and J. Miltat for fruitful discussions, and J. Miltat for a critical reading of the manuscript.

REFERENCES

[1] Hubert, A., and Schäfer, R. (1998). "Magnetic Domains." Springer-Verlag, Berlin.
[2] Aharoni, A. (1996). "Introduction to the Theory of Ferromagnetism." Clarendon Press, Oxford.
[3] Miltat, J., Albuquerque, G., and Thiaville, A. (2002). *In* "Spin Dynamics in Confined Magnetic Structures I" (B. Hillebrands, and K. Ounadjela, eds.), pp. 1–33. Springer-Verlag, Berlin.
[4] OOMMF is a free software (in fact, an open framework for micromagnetics routines) developed by M. J. Donahue and D. Porter mainly, from NIST. It is available at http://math.nist.gov/oommf.
[5] The commercial LLG Micromagnetics Simulator software is developed by M. R. Scheinfein. See the Web site http://llgmicro.home.mindspring.com.
[6] The commercial MicroMagus software is developed by D. V. Berkov, Innovent Technology Development e.V., Jena, Germany. See the Web site http://math.micromagus.de.
[7] The commercial finite elements micromagnetic simulator FEMME, from Vienna University of Technology, is being developed by D. Süss. See the Web site http://www.suessco.com.
[8] Fidler, J., and Schrefl, T. (2000). *J. Phys. D Appl. Phys.* **33**, R135.
[9] McMichael, R., and Donahue, M. J. (1997). *IEEE Trans. Magn.* **33**, 4167.
[10] Nakatani, Y., Thiaville, A., and Miltat, J. (2005). *J. Magn. Magn. Mater.* **290–291**, 750.
[11] Tchernyshyov, O., and Chern, G. (2005). *Phys. Rev. Lett.* **95**, 197204.
[12] Hubert, A., Rave, W., and Tomlinson, S. (1997). *Phys. Status Solidi B* **204**, 817.

[13] Kläui, M., Vaz, C. A. F., Bland, J. A. C., Heyderman, L. J., Nolting, F., Pavlovska, A., Bauer, E., Cherifi, S., Heun, S., and Locatelli, A. (2004). *Appl. Phys. Lett.* **85**, 5637.
[14] Laufenberg, M., Backes, D., Bührer, W., Bedau, D., Kläui, M., Rüdiger, U., Vaz, C. A. F., Bland, J. A. C., Heyderman, L. J., Nolting, F., Cherifi, S., Locatelli, A., Belkhou, R., Heun, S., and Bauer, E. (2006). *Appl. Phys. Lett.* **88**, 052507.
[15] Thiaville, A., and Nakatani, Y. (2006). *In* "Spin Dynamics in Confined Magnetic Structures III" (B. Hillebrands, and A. Thiaville, eds.), pp. 161–206. Springer-Verlag, Berlin.
[16] Hertel, R., and Kirschner, J. (2004). *Physica B* **343**, 206.
[17] Sixtus, K., and Tonks, L. (1931). *Phys. Rev.* **37**, 930.
[18] Thiele, A. A. (1973). *Phys. Rev. Lett.* **30**, 230.
[19] Döring, W. (1948). *Z. Naturforsch.* **3a**, 373.
[20] Schryer, N. L., and Walker, L. R. (1974). *J. Appl. Phys.* **45**, 5406.
[21] Lee, J. Y., Lee, K. S., Choi, S., Guslienko, K. Yu., and Kim, S. K. (2007). *Phys. Rev. B* **76**, 184408.
[22] Ono, T., Miyajima, H., Shigeto, K., Mibu, K., Hosoito, N., and Shinjo, T. (1999). *Science* **284**, 468.
[23] Gadbois, J., and Zhu, J. G. (1995). *IEEE Trans. Magn.* **31**, 3802.
[24] Cowburn, R. P., Koltsov, D., Adeyeye, A. O., and Welland, M. E. (2000). *J. Appl. Phys.* **87**, 7067.
[25] Nakatani, Y., Thiaville, A., and Miltat, J. (2003). *Nat. Mater.* **2**, 521.
[26] Beach, G. S. D., Nistor, C., Knutson, C., Tsoi, M., and Erskine, J. L. (2005). *Nat. Mater.* **4**, 741.
[27] Yamaguchi, A., Yano, K., Tanigawa, H., Kasai, S., and Ono, T. (2006). *Jpn. J. Appl. Phys.* **45**, 3850.
[28] Ferré, J. (2002). *In* "Spin Dynamics in Confined Magnetic Structures I" (B. Hillebrands, and K. Ounadjela, eds.), pp. 127–165. Springer-Verlag, Berlin.
[29] Atkinson, D., Allwood, D. A., Xiong, G., Cooke, M. D., Faulkner, C. C., and Cowburn, R. P. (2003). *Nat. Mater.* **2**, 85.
[30] Hayashi, M., Thomas, L., Bazaliy, Y. B., Rettner, C., Moriya, R., Jiang, X., and Parkin, S. S. P. (2006). *Phys. Rev. Lett.* **96**, 197207.
[31] Hayashi, M., Thomas, L., Rettner, C., Moriya, R., and Parkin, S. S. P. (2006). *Nat. Phys.* **3**, 21.
[32] Barnes, S. E., and Maekawa, S. (2006). *In* "Concepts in Spin Electronics" (S. Maekawa, ed.). Oxford University Press, Oxford.
[33] Stiles, M., Saslow, W. M., Donahue, M. J., and Zangwill, A. (2007). *Phys. Rev. B* **75**, 214423.
[34] Smith, N. cond-mat/0706.1736 (unpublished data).
[35] Berger, L. (1978). *J. Appl. Phys.* **49**, 2156.
[36] Berger, L. (1984). *J. Appl. Phys.* **55**, 1954.
[37] Bazaliy, Y. B., Jones, B., and Zhang, S. C. (1998). *Phys. Rev. B* **57**, R3213.
[38] Waintal, X., and Viret, M. (2004). *Europhys. Lett.* **65**, 427.
[39] Li, Z., and Zhang, S. (2004). *Phys. Rev. Lett.* **92**, 207203.
[40] Li, Z., and Zhang, S. (2004). *Phys. Rev. B* **70**, 024417.
[41] Tatara, G., and Kohno, H. (2004). *Phys. Rev. Lett.* **92**, 086601.
[42] Thiaville, A., Nakatani, Y., Miltat, J., and Vernier, N. (2004). *J. Appl. Phys.* **95**, 7049.
[43] Barnes, S. E., and Maekawa, S. (2005). *Phys. Rev. Lett.* **95**, 107204.
[44] Zhang, S., and Li, Z. (2004). *Phys. Rev. Lett.* **93**, 127204.
[45] Thiaville, A., Nakatani, Y., Miltat, J., and Suzuki, Y. (2005). *Europhys. Lett.* **69**, 990.
[46] Grollier, J., Boulenc, P., Cros, V., Hamzić, A., Vaurès, A., and Fert, A. (2003). *Appl. Phys. Lett.* **83**, 509.
[47] Kim, W., Seo, S. M., Lee, T., and Lee, K. (2007). *J. Magn. Magn. Mater.* **310**, 2032.
[48] You, C. Y., Sung, I., and Joe, B. (2006). *Appl. Phys. Lett.* **89**, 222513.
[49] Yamaguchi, A., Nasu, S., Tanigawa, H., Ono, T., Miyake, K., Mibu, K., and Shinjo, T. (2005). *Appl. Phys. Lett.* **86**, 012511.
[50] Togawa, Y., Kimura, T., Harada, K., Akashi, T., Matsuda, T., Tonomura, A., and Otani, Y. (2006). *Jpn. J. Appl. Phys.* **45**, L683.
[51] You, C. Y., and Ha, S. S. (2007). *Appl. Phys. Lett.* **91**, 022507.
[52] Cochran, J., Rudd, J., Muir, W., Trayling, G., and Heinrich, B. (1991). *J. Appl. Phys.* **70**, 6545.
[53] Counil, G., Devolder, T., Kim, J. V., Crozat, P., Chappert, C., Zoll, S., and Fournel, R. (2006). *IEEE Trans. Magn.* **42**, 3323.
[54] Seo, S. M., Lee, K. J., Kim, W., and Lee, T. D. (2007). *Appl. Phys. Lett.* **90**, 252508.
[55] Grinstein, G., and Koch, R. H. (2003). *Phys. Rev. Lett.* **90**, 207201.
[56] Brown, W. Jr. (1963). *Phys. Rev.* **130**, 1677.

[57] Duine, R. A., Núñez, A., and MacDonald, A. H. (2007). *Phys. Rev. Lett.* **98**, 056605.
[58] Thiaville, A., Nakatani, Y., Piéchon, F., Miltat, J., and Ono, T. (2007). *Eur. Phys. J. B* **60**, 15.
[59] Thiele, A. A. (1976). *J. Appl. Phys.* **47**, 2759.
[60] Slonczewski, J. C., and Magn, J. (1979). *Magn. Mater.* **12**, 108.
[61] Malozemoff, A. P., and Slonczewski, J. C. (1979). "Magnetic Domain Walls in Bubble Materials." Academic Press, New York.
[62] Tretiakov, O., Clarke, D., Chern, G., Bazaliy, Y. B., and Tchernyshyov, O. (2008). *Phys. Rev. Lett.* **100**, 127204.
[63] Yamaguchi, A., Ono, T., Nasu, S., Miyake, K., Mibu, K., and Shinjo, T. (2004). *Phys. Rev. Lett.* **92**, 077205.
[64] Kläui, M., Vaz, C. A. F., Bland, J. A. C., Wernsdorfer, W., Faini, G., Cambril, E., Heyderman, L. J., Nolting, F., and Rüdiger, U. (2005). *Phys. Rev. Lett.* **94**, 106601.
[65] Hayashi, M., Thomas, L., Rettner, C., Moriya, R., Bazaliy, Y. B., and Parkin, S. S. P. (2007). *Phys. Rev. Lett.* **98**, 037204.
[66] Parkin, S. S. P., Hayashi, M., and Thomas, L. (2008). *Science* **320**, 190.
[67] Junginger, F., Kläui, M., Backes, D., Rüdiger, U., Kasama, T., Dunin-Borkowski, R., Heyderman, L. J., Vaz, C. A. F., and Bland, J. A. C. (2007). *Phys. Rev. Lett.* **90**, 132506.
[68] Meier, G., Bolte, M., Eiselt, R., Krüger, B., Kim, D. H., and Fischer, P. (2007). *Phys. Rev. Lett.* **98**, 187202.
[69] Hayashi, M., Thomas, L., Rettner, C., Moriya, R., Jiang, X., and Parkin, S. S. P. (2006). *Phys. Rev. Lett.* **97**, 207205.
[70] Kläui, M., Jubert, P. O., Allenspach, R., Bischof, A., Bland, J. A. C., Faini, G., Rüdiger, U., Vaz, C. A. F., Vila, L., and Vouille, C. (2005). *Phys. Rev. Lett.* **95**, 026601.
[71] Heyne, L., Kläui, M., Backes, D., Moore, T., Krzyk, S., Rüdiger, U., Heyderman, L. J., Rodrìguez, A. F., Nolting, F., Mentes, T., Niño, M., Locatelli, A., Kirsch, K., and Mattheis, R. (2008). *Phys. Rev. Lett.* **100**, 066603.
[72] Jubert, P. O., Kläui, M., Bischof, A., Rüdiger, U., and Allenspach, R. (2006). *J. Appl. Phys.* **99**, 08G523.
[73] Lim, C., Devolder, T., Chappert, C., Grollier, J., Cros, V., Vaurès, A., Fert, A., and Faini, G. (2004). *Appl. Phys. Lett.* **84**, 2820.
[74] Konishi, S., Matsuyama, K., Chida, I., Kubota, S., Kawahara, H., and Ohbo, M. (1984). *IEEE Trans. Magn.* **20**, 1129.
[75] He, J., Li, Z., and Zhang, S. (2006). *Phys. Rev. B* **73**, 184408.
[76] Nakatani, Y. "ICMFS'06 Conference", Sendai, Japan (unpublished data).
[77] Beach, G. S. D., Knutson, C., Nistor, C., Tsoi, M., and Erskine, J. L. (2006). *Phys. Rev. Lett.* **97**, 057203.
[78] Thomas, L., Hayashi, M., Jiang, X., Moriya, R., Rettner, C., and Parkin, S. S. P. (2006). *Nature* **443**, 197.
[79] Vernier, N., Allwood, D. A., Atkinson, D., Cooke, M. D., and Cowburn, R. P. (2004). *Europhys. Lett.* **65**, 526.
[80] Grollier, J., Boulenc, P., Cros, V., Hamzić, A., Vaurès, A., Fert, A., and Faini, G. (2004). *J. Appl. Phys.* **95**, 6777.
[81] Thomas, L., Hayashi, M., Jiang, X., Moriya, R., Rettner, C., and Parkin, S. S. P. (2007). *Science* **315**, 1553.
[82] Laufenberg, M., Bührer, W., Bedau, D., Melchy, P. E., Kläui, M., Vila, L., Faini, G., Vaz, C. A. F., Bland, J. A. C., and Rüdiger, U. (2006). *Phys. Rev. Lett.* **97**, 046602.
[83] Saitoh, E., Miyajima, H., Yamaoka, T., and Tatara, G. (2004). *Nature* **432**, 203.
[84] Kasai, S., Nakatani, Y., Kobayashi, K., Kohno, H., and Ono, T. (2006). *Phys. Rev. Lett.* **97**, 107204.
[85] Yamada, K., Kasai, S., Nakatani, Y., Kobayashi, K., Kohno, H., Thiaville, A., and Ono, T. (2007). *Nat. Mater.* **6**, 270.
[86] Stiles, M., and Miltat, J. (2006). *In* "Spin Dynamics in Confined Magnetic Structures III" (B. Hillebrands, and A. Thiaville, eds.), pp. 225–308. Springer-Verlag, Berlin.
[87] Serpico, C., d'Aquino, M., Bertotti, G., and Mayergoyz, I. (2004). *J. Appl. Phys.* **95**, 7052.
[88] Fukami, S., Suzuki, T., Ohshima, N., Nagahara, K., and Ishiwata, N. (2008). *J. Appl. Phys.* **103**, 07E718.
[89] Jung, S. W., Kim, W., Lee, T. D., Lee, K. J., and Lee, H. W. (2008). *Appl. Phys. Lett.* **92**, 202508.
[90] Koyama, T., Yamada, G., Tanigawa, H., Kasai, S., Ohshima, N., Fukami, S., Ishiwata, N., Nakatani, Y., and Ono, T. (2008). *Appl. Phys. Express* **1**, 101303.
[91] Laribi, S., Cros, V., Muñoz, M., Grollier, J., Hamzić, A., Deranlot, C., Fert, A., Martínez, E., López-Díaz, L., Vila, L., Faini, G., Zoll, S., and Fournel, R. (2007). *Appl. Phys. Lett.* **90**, 232505.

CHAPTER 7

III–V-Based Ferromagnetic Semiconductors

Fumihiro Matsukura[*,†] and **Hideo Ohno**[*,†]

Contents

Abstract

III–V compound semiconductors such as GaAs and InAs alloyed with Mn exhibit ferromagnetism. The magnetic, electrical and optical properties of ferromagnetic III–V semiconductors are first compiled along with the way to prepare the epitaxial films and the effect of post-growth annealing. Theories available to explain the magnetism in these alloys are then presented. Because

*Laboratory for Nanoelectronics and Spintronics, Research Institute of Electrical Communication, Tohoku University, 2-1-1 Katahira, Aoba-ku, Sendai 980-8577, Japan
†ERATO Semiconductor Spintronics Project, Japan Science and Technology Agency, Sendai, Japan

Nanomagnetism and Spintronics
DOI: 10.1016/B978-0-444-53114-8.00007-8

the ferromagnetic semiconductors are compatible with epitaxial III–V heterostructures, a number of device structures have been examined and shown to reveal a wide variety of phenomena that either cannot be realized or are very difficult to observe in ferromagnetic metal structures. The unique properties revealed by ferromagnetic semiconductor structures, ranging from reversible electric field control of ferromagnetic phase transition to generating velocity versus current-density curves of current-induced domain wall motion, are then reviewed. The prospect of realizing high-transition temperature is discussed in the last section.

Key Words: Ferromagnetic semiconductor, (Ga,Mn)As, (In,Mn)As, Molecular beam epitaxy, *p–d* Zener model, Strain and temperature dependence of magnetocrystalline anisotropy, Low-temperature annealing, Current-induced magnetization switching, Electric field control of ferromagnetism, Current-induced domain wall motion.

1. INTRODUCTION

In magnetic semiconductors, one can make use of a variety of spin-related phenomena, not readily available in other materials. The spin-related properties are brought about by the exchange interaction among band carriers and magnetic moments. The study of magnetic semiconductors was initiated by a series of experimental and theoretical studies on compound materials like rare-earth chalcogenides and chromite spinels (e.g. $CdCr_2Se_4$). A number of exotic properties were observed in these magnetic semiconductors, such as colossal magnetoresistance and magneto-optical properties, originating from the interplay between ferromagnetism and semiconducting properties [1–3]. Although these ferromagnetic semiconductors inspired new concepts using semiconductors with utilizing the spin degree of freedom, difficulties associated with material preparation hindered further progress in experimental studies.

Today, majority of the studies on magnetic semiconductor involve alloy semiconductors, in which magnetic elements substitute a part of lattice sites in non-magnetic semiconductor materials. Here, the host semiconductors include II–VI, III–VI, IV–VI, IV and II–VI–V_2. These magnetic alloy semiconductors are known as diluted magnetic semiconductors (DMSs) or semimagnetic semiconductors. Since DMSs and their heterostructures can readily be grown by modern epitaxial techniques such as molecular beam epitaxy (MBE), many of the studies conducted today on magnetic semiconductors are focusing on thin films and multilayered heterostructures prepared by epitaxy. The most extensively studied DMSs are II–VIs and III–Vs alloyed with Mn, such as (Cd,Mn)Te and (Ga,Mn)As.

Since the early stage, paramagnetic II–VI DMSs have been studied extensively [4–7]. Because Mn substitutes II-group cation in divalent state, II–VI DMS is isoelectronic and if carriers are needed they have to be provided by extrinsic means as doping or controlling defects. The *d*-electrons of transition metals provide localized magnetic moments. Owing to the antiferromagnetic superexchange coupling among Mn, most of II–VI DMSs show spin-glass phase or antiferromagnetic phase at low temperatures, depending on the concentration of the transition metal ions. In addition to the superexchange coupling, strong spin-dependent coupling (*sp–d*

exchange interaction) between the band of host semiconductors (*sp*-state) and magnetic moments (*d*-state) exists in DMSs. Because of the *sp–d* exchange, aligning the direction of magnetic moments by external magnetic fields induces giant Zeeman splitting in the band structure, resulting in large magneto-optical effects [8]. By injecting the carriers into II–VI DMSs by optical means, bound magnetic polarons (BMPs) can be formed [9]. In BMP, electrons trapped in a shallow impurity states align locally the surrounding magnetic moments by the *sp–d* exchange interaction. This implies that electronic states of carriers are delocalized and extended, and when the concentration exceeds a certain value, ferromagnetism may be expected. This type of carrier-induced ferromagnetism was reported in IV–VI [10] and III–Vs [11, 12] and later in II–VI compounds; the ferromagnetism in III–Vs is the subject of this chapter and is discussed in detail in the following sections.

In II–VI compounds, doping of delocalized *holes* in II–VI DMSs was predicted to result in the ferromagnetic order by the Ruderman–Kittel–Kasuya–Yosida (RKKY) type interaction [13] due to greater magnitude of the *p–d* exchange than that of the *s–d* exchange. This approach was taken in the experimental works and led to the observation of the ferromagnetic order in p-(Cd,Mn)Te quantum wells [14] and in p-(Zn,Mn)Te [15]. Another approach to obtain ferromagnetic II–VI DMSs is to select Cr as magnetic elements, among which the ferromagnetic superexchange interaction is predicted by the theoretical calculation [16].

In III–V DMSs, Mn acts simultaneously as the source of localized magnetic moments and as an acceptor. Thus, without additional doping, these materials show strong p-type conduction, which provides a strong exchange interaction mediated by *p–d* exchange among Mn ions. Synthesis [17] and subsequent discovery of ferromagnetism in III–V-based DMSs, (In,Mn)As and (Ga,Mn)As in 1990s [11, 12], added a new dimension to the magnetic semiconductor research, because it allowed seamless integration of ferromagnetism with established III–V heterostructures and devices. (Ga,Mn)As and (In,Mn)As are now the most well-investigated and well-understood ferromagnetic semiconductors among all and the material and their heterostructures provide an ideal test bench for demonstrating new concepts in physics as well as for spintronic device operations [18–20]. The *p–d* Zener model [21, 22], in which hole repopulation among *p–d* exchange split bands stabilizes ferromagnetism, has been shown to describe qualitatively and in many cases even quantitatively a number of experimental results on these materials.

Owing to the additional spin degree of freedom, ferromagnetic semiconductors can combine semiconductor heterostructure physics and ferromagnetism, which may lead us to new spintronic functionalities [23–26]. In this chapter, we summarize the present state of the research on ferromagnetic semiconductors focusing primarily on the prototypical (Ga,Mn)As and (In,Mn)As and their device structures.

2. MOLECULAR BEAM EPITAXY

For the observation of a ferromagnetic phase in DMS systems, one needs to introduce a sizable amount of magnetic elements (a few percent or more), which is usually beyond the solubility limit; of the order of 10^{18}–10^{19} cm^{-3} in III–V

semiconductors [27, 28]. For III–V DMSs which require growth far from equilibrium, MBE is so far the only established method for preparation. Under ordinary MBE growth conditions for high quality of III–Vs, such a high concentration of magnetic impurities (transition metals in most cases) results in segregation of impurity atoms and subsequent formation of unwanted compounds at the growth front, which prevents synthesis of alloy semiconductors with high concentration of transition metals. However, MBE growth can proceed under conditions far from equilibrium, especially at low growth temperatures, at which segregation and formation of unwanted compounds can be minimized or suppressed. Using low-temperature MBE (LT-MBE), preparation of uniform paramagnetic III–V DMS, (In,Mn)As, with Mn composition $x < 0.18$ was shown to be possible [17]. Here, the growth temperature T_S was reduced slightly below 300 °C (typical T_S for non-magnetic InAs is ∼500 °C). This T_S was high enough to provide metastable single-crystal epitaxial growth, yet low enough to suppress segregation of Mn and formation of thermodynamically more stable second phases such as MnAs. This initial success of (In,Mn)As was followed by the growth of uniform (Ga,Mn)As [12, 29]. When growth conditions are right, majority of Mn substitutes III-group cation site [30, 31], which is the reason these alloys are expressed as (III,Mn)V. Mn in cation site is an acceptor providing a hole. It also provides localized spins.

Growth of III–V DMSs is summarized in the following using (Ga,Mn)As as an example. (In,Mn)As can be prepared in a similar way. LT-MBE of (Ga,Mn)As is carried out in an ultra-high vacuum MBE chamber with Ga, Mn and As atoms impinging on GaAs(001) substrates having As stabilized surface conditions. After removal of surface oxide and growth of buffer layer for preparation of atomically flat starting surface, growth of (Ga,Mn)As is initiated by commencing the Mn flux during the LT-GaAs growth while keeping T_S constant at ∼250 °C. Reflection high-energy electron diffraction (RHEED) pattern is a common tool to monitor the growth front. The RHEED pattern of (Ga,Mn)As is streaky (1 × 2) confirming growth of (Ga,Mn)As with zincblende structure. The details of this surface reconstruction are not understood. The Mn composition x that can be introduced in GaAs depends on T_S; the maximum x at $T_S = 250$ °C is roughly 0.07 and the highest nominal x so far reported is 0.21 obtained at T_S of 150 °C and only with very thin thickness less than 10 nm [32, 33]. Even in such a thin (Ga,Mn)As layer with high x, uniform ferromagnetic phase is observed, confirmed by magnetization, magnetotransport and magneto-optical signals. When T_S and/or Mn flux is too high, formation of hexagonal MnAs phase is detected by a spotty RHEED pattern [34].

We note that accurate determination of T_S is critical in growth of (Ga,Mn)As. T_S of MBE is monitored by a thermocouple placed behind the substrate holder: T_S monitored this way can be different from the actual substrate temperature by 50 °C or even more, which has been shown by comparison of T_S monitored by thermocouple and by the band edge spectroscopy during (Ga,Mn)As growth. In addition, due to the high concentration of Mn acceptors in (Ga,Mn)As, the free carrier absorption in the near-infrared becomes significant and contributes to the increase of T_S after starting growth, that is, under radiation from Ga and Mn effusion cells. The effect depends on the thermal contact between the substrate

and its holder as well as the distance between the substrate and the effusion cells [35]; thus, it is critical to carefully establish the often machine-dependent growth temperature for (Ga,Mn)As growth.

When growth conditions are appropriate, a clear RHEED intensity oscillation is observed at the initial stage of growth [34], where surfactant effect of Mn and excess As is thought to be responsible for the two-dimensional growth at low T_S [36–38]. Magnetic and electrical properties of (Ga,Mn)As are strongly affected by the growth condition, such as V/III beam flux ratio and T_S as well as x [39–42], which is related to the degree of compensation due to the existence of As antisites and Mn interstitials, both known as donors in GaAs.

Mn composition in the epitaxial films can be calculated from beam equivalent pressure (BEP) measured by an ion gauge inserted in the path of the beam flux and later calibrated to relate BEP to the composition of the grown films and/or from the periods of the RHEED intensity oscillation observed at the initial stage of growth [12, 43]. Conventional analyses are also employed to establish the composition, such as Auger electron spectroscopy (AES), electron probe micro-analysis (EPMA) and secondary ion mass spectroscopy (SIMS) [12, 44]. The most widely used method is the use of lattice constant a determined by X-ray diffraction (XRD) as the measure of x due to its experimental simplicity, although it is affected by the presence of species other than Mn such as As antisites [41, 42, 45–48]. MBE growth of (Ga,Mn)As on high-index substrates (411) and (311) has also been explored [49–51].

Most of the synthesis techniques for semiconducting materials are applicable to prepare single crystals of II–VI DMSs with high quality, largely owing to the isoelectronic nature of transition metals in II–VI semiconductors [4]. Among them, MBE growth has been adopted for many heterostructures and low-dimensional structures based on II–VI materials.

3. STRUCTURAL AND MAGNETIC PROPERTIES

3.1. Structural characterization of (Ga,Mn)As

Zincblende structure of (Ga,Mn)As is confirmed by RHEED patterns during growth as well as post-growth XRD measurements, which show that the lattice constant a of (Ga,Mn)As is greater than that of GaAs and depends linearly on x. Asymmetric XRD showed that pseudomorphic growth of (Ga,Mn)As on GaAs substrate takes place without strain relaxation at least up to 2-μm thickness [52]. Pseudomorphic growth is also confirmed from the reciprocal space mapping on (115) and (224) planes as shown in Fig. 1. The freestanding lattice constant a of (Ga,Mn)As is calculated under the assumption that (Ga,Mn)As has the same elastic constants as those of GaAs (Poisson ratio = 0.311) [12]. Thus obtained x dependence of a follows the Vegard's law, $a = a_{\mathrm{LT-GaAs}}(1-x) + a_{\mathrm{ZB-MnAs}}x$, where $a_{\mathrm{LT\text{-}GaAs}}$ and $a_{\mathrm{ZB\text{-}MnAs}}$ are the lattice constants of low-temperature-grown GaAs (LT-GaAs) $\sim$ 0.566 nm and hypothetical zincblende MnAs $\sim$ 0.598 nm [12]; this value is close to the theoretically predicted value of 0.59 nm [53]. Note that

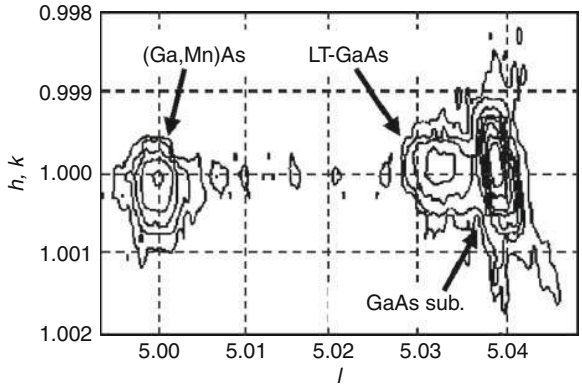

FIGURE 1 (115) asymmetric reciprocal space map for $Ga_{0.93}Mn_{0.07}As$ (150 nm)/LT-GaAs (50 nm)/GaAs(001) substrate measured at room temperature.

this way of determining a is known to suffer from uncertainties due to the degree of incorporation of defects like As antisites, As_{Ga}, and Mn interstitials, Mn_{int}, and gives inaccuracy of $x \pm 0.01$ and sometimes even more [41, 42, 45–48]. Theoretical calculation also shows that As antisites and/or Mn interstitials increase a of (Ga,Mn)As [54].

For Mn-doped GaAs with the doping level less than 10^{19} cm^{-3}, Mn substitutes Ga, which was confirmed by electron paramagnetic resonance (EPR) and cross-sectional scanning tunnelling microscopy (XSTM) [55–57]. For (Ga,Mn)As with a few percent of Mn, extended X-ray absorption fine structure (EXAFS) study revealed that the majority of Mn was at the substitutional site, that is, on the Ga sublattice of the zincblende lattice. The Mn–As bond length was determined to be 0.249 and 0.250 nm consistent with the XRD results, longer than 0.244 nm of the host Ga–As bond length [31]. Similarly, EXAFS showed that in (In,Mn)As, majority of Mn sits on the In sublattice [30]. The ion channelling measurements, Rutherford backscattering (RBS) and particle-induced X-ray emission (PIXE), later revealed that a part of Mn atoms (a few tens of percent of the introduced Mn atoms) were incorporated at interstitial sites [58]. Post-growth, low-temperature annealing (LT annealing) at or below the growth temperature [45] was found to decrease the number of Mn_{int} and simultaneously increases hole concentration p [59–61], indicating that Mn_{int} is unstable and mobile donor. The double-donor nature of Mn_{int} was also shown from ab initio calculations [62]. Further annealing above 350 °C results in the formation of MnAs nanoclusters having NiAs structure, which has Curie temperature T_C of ~310 K [29]. Disappearance of (Ga,Mn)As phase after annealing was indicated by the absence of corresponding XRD peaks [34]. Double-donor Mn_{int} was calculated not to participate in the ferromagnetic order and may form pairs with substitutional Mn, Mn_{Ga}. This results in superexchange antiferromagnetic coupling between Mn_{int} and Mn_{Ga}, which compensates the Mn moments of the two participating Mn atoms and reduces the net Mn moment [63].

Electron spin resonance (ESR) measurements [56] showed that neutral Mn_{Ga} in GaAs doped with Mn ($\sim 10^{17}$ cm^{-3}) is in the $A^0(d^5 + h)$ state, that is, the neutral acceptor Mn state (A^0) has an electronic structure of five d-electrons (Mn^{2+}) and a loosely bound hole. The charge state of a single Mn in GaAs was visualized by STM images, where switching between $A^0(d^5 + h)$ state and negatively ionized $A^-(d^5)$ state was observed by changing the bias polarity of the STM tip [64]. The hole binding energy of Mn acceptor is 0.11 eV [65, 66], and this moderate ionization energy results in the metal–insulator transition (MIT) in (Ga,Mn)As, which affects magnetic and transport properties. By measuring the STM spectra, the magnetic interaction between two Mn ions was shown to depend on the separation of the two; the positions of Mn ions were controlled by an atom by atom substitution using an STM chip [67]. The shape of the acceptor wave function was also shown to be distorted by local lattice strain, when the GaAs host lattice symmetry was broken by embedded InAs quantum dots [68]. These STM measurements showed that the nature of a single Mn ion is closely related to the magnetic and electrical properties of (Ga,Mn)As. Also, they showed the possibility of manipulating single magnetic spins in semiconductors.

3.2. Magnetic properties of (Ga,Mn)As

Magnetization M of (Ga,Mn)As is measured using a standard magnetometer such as superconducting quantum interference device (SQUID) magnetometer. The diamagnetic response of thick GaAs substrate determined by a separate measurement must be subtracted from the measured magnetization curve to obtain the response from thin epitaxial layers. This subtraction process together with the removal of the residual magnetic fields of the superconducting magnet becomes critical when the magnetic layer is very thin and/or the Mn concentration is low, because substrates themselves occasionally show paramagnetic response. When H is applied in the direction of magnetic easy axis, M of (Ga,Mn)As shows a sharp and clear hysteresis in its H dependence at low temperatures, which is one of the evidences of the presence of extended ferromagnetic order in the film [12]. T_C can be determined by measuring the temperature dependence of the remanent magnetization, from the Arrott plots and/or from the Curie–Weiss plot. The value of T_C has a strong correlation with the electrical conductivity, that is, for a given x higher T_C is observed for more metallic samples as shown in Fig. 2 [61]. This relationship can be traced using a single sample, because the conductivity of (Ga,Mn)As can be altered by annealing after sample preparation. Insulating samples, the resistance of which increases as temperature is reduced, often show a pronounced paramagnetic response in the M–H curve at high magnetic fields after closure of hysteresis loop. This also indicates correlation between magnetic and electrical properties [69]. The highest T_C reported so far is 185 K for a (Ga,Mn)As film with $x = 0.09$ after annealing [70]. The p–d Zener model discussed in Section 6 is capable of explaining the observed magnetic properties, including the magnitude of T_C and the temperature as well as the strain dependence of the magnetic easy axis [21, 22].

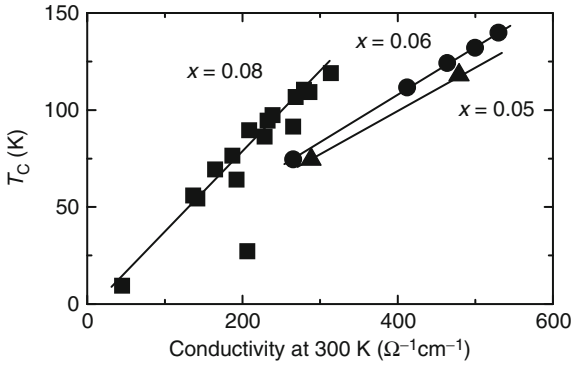

FIGURE 2 Room-temperature electrical conductivity dependence of the Curie temperature of (Ga,Mn)As. Straight lines are guide for the eye [61]. (Reused by permission of American Institute of Physics.)

3.2.1. Magnetic domain

Extended magnetic domain structure, which is an evidence of long-range magnetic interaction, was observed in (Ga,Mn)As samples with magnetic easy axis in-plane as well as those with easy axis perpendicular-to-plane by scanning Hall microscope, scanning SQUID microscope, magneto-optical microscope and Lorenz microscope as shown in Fig. 3, where the size of the domain is shown to range from a few microns to a millimetre [71–75]. The computed value of the domain width in (Ga,Mn)As by the *p–d* Zener model combined with micromagnetic theory [76] is in reasonable agreement with the experimental ones [71].

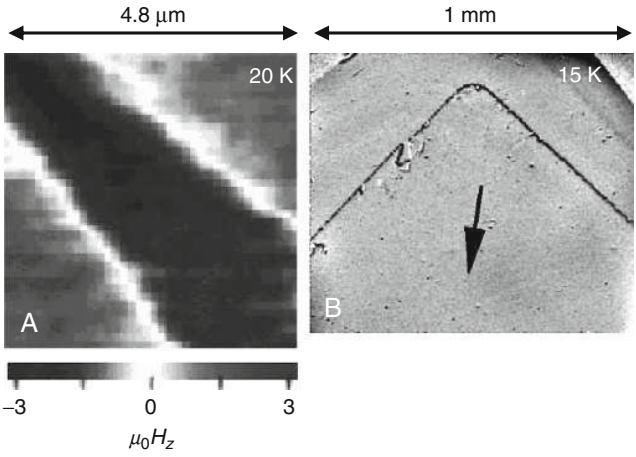

FIGURE 3 Magnetic domain structure observed for (Ga,Mn)As (A) with perpendicular easy axis by scanning Hall probe (after [71] and (B) with in-plan easy axis by magneto-optical microscope [73]. (Reproduced by permission of American Physical Society.)

3.2.2. Magnetic anisotropy

The direction as well as the magnitude of the magnetocrystalline anisotropy of (Ga,Mn)As can be tuned by the combination of direction and magnitude of lattice strain, and the hole concentration p. A number of methods have been employed to determine the magnetic anisotropy of (Ga,Mn)As, for example, direct magnetization measurement, ac-susceptibility, ferromagnetic resonance (FMR), anomalous Hall effect, planar Hall effect, anisotropic magnetoresistance (AMR), tunnelling magnetoresistance (TMR) and magneto-optical microscope [34, 73, 77–85]. Two measurements, FMR and transport, on the same sample, were shown to give nearly the same magnetic anisotropy constants as shown in Fig. 4 [86]. (Ga,Mn)As layers under compressive strain, for example, those grown directly on GaAs substrates, show in-plane magnetic easy axis as long as its carrier concentration is high, while the layers under tensile strain, like (Ga,Mn)As on (In,Ga)As, show magnetic easy axis perpendicular to the plane [34]. The single ion anisotropy of Mn in GaAs is confirmed to be too small to account for this sizable magnetic anisotropy [87]. The origin of this strain-dependent magnetic anisotropy can be explained in terms of the warped anisotropic valence band due to combined effect of spin–orbit interaction and the lattice stain in the framework of the p–d Zener model, which also predicts that the magnetic anisotropy is p dependent [21, 22, 88]. The p-dependent part has later been experimentally established in (Al,Ga,Mn)As, where Al reduces hole concentration; (Al,Ga,Mn)As shows perpendicular-to-plane magnetic easy axis under compressive strain as opposed to in-plane easy axis of usual (Ga,Mn)As with compressive strain [89]. In addition, the direction of magnetic easy axis was found to be temperature dependent; it was perpendicular at low temperatures and became in-plane as temperature increased as shown in Fig. 5 [77, 89, 90]. This peculiar temperature dependence is also in accordance with what has been predicted by the p–d Zener model for the low p case; this is due to the carrier redistribution among different spin-split states as spin splitting is M dependent which in turn is temperature dependent.

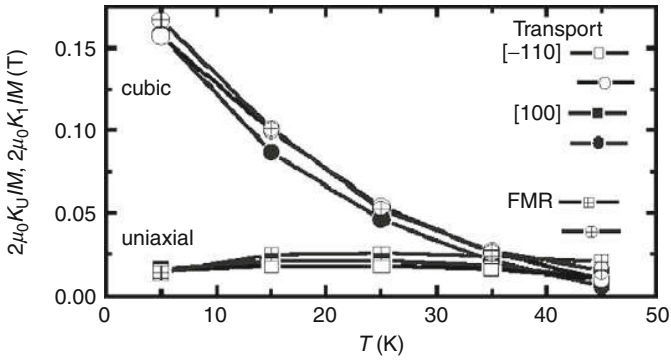

FIGURE 4 Temperature dependence of in-plane magnetic anisotropy fields determined from both magnetotransport (PHE in Hall bar along [−1 1 0] channel and AMR along [1 0 0] channel) and ferromagnetic resonance measurements [86].

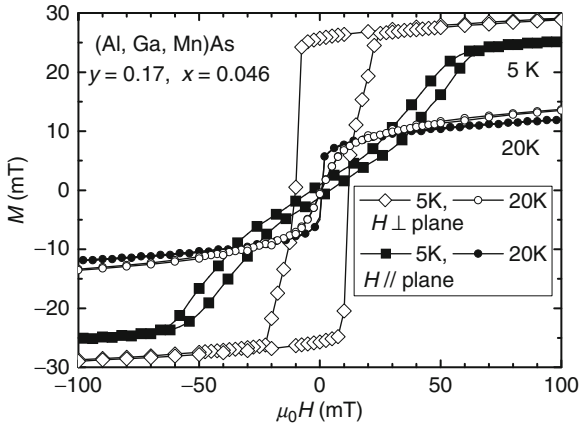

FIGURE 5 Magnetization curves of (Al,Ga,Mn)As with Al composition $y = 0.17$ and Mn composition $x = 0.046$ at 5 and 20 K. Magnetic field is applied in two different directions, showing that the easy axis of magnetization of the sample is perpendicular to the plane at 5 K and in-plane at 20 K [89].

Compressive (Ga,Mn)As shows fourfold in-plane easy axis along ⟨1 0 0⟩ and two uniaxial easy axes along [1 1 0] or [−1 1 0] [78, 91] and [1 0 0] or [0 1 0] [92]. The relative strength of these three anisotropic energies determined from planar Hall measurements is 100:10:1 [92]. The in-plane uniaxial anisotropy cannot be explained by the *p–d* Zener model without assuming the presence of shear strain, which has not yet been confirmed experimentally. Although a number of suggestions have been made, the origin of this in-plane uniaxial anisotropy remains unclear: suggestions include that it may be related to the anisotropic (1 × 2) surface reconstruction during MBE growth, the lack of top-bottom symmetry in epilayers, the existence of a trigonal distortion or the anisotropy of the strength of *p–d* hybridization [73, 77, 78, 93]. The magnetostriction measurements by resonant nanoelectromechanical system revealed the coupling between the magnetoelastic constants and in-plane magnetic anisotropic constants in compressive (Ga,Mn)As [94]. This makes it possible to control magnetization direction by application of external stress, which was demonstrated by the combination of (Ga,Mn)As with piezoelectric material; the direction of magnetization was manipulated through the change of stress by applying voltage to piezoelectric material [95].

The magnetic overlayers on (Ga,Mn)As can induce an additional anisotropy to (Ga,Mn)As. The pinning of the M direction or exchange bias of (Ga,Mn)As is shown to be possible with overlayers of spin-glass (Zn,Mn)Se, antiferromagnetic MnO and IrMn [96–98] as well as embedded nanosize-MnAs precipitates [99]. Another method to control the uniaxial anisotropy is lithographical nanopatterning of the (Ga,Mn)As layers. From the temperature dependence of the magnetic anisotropy, this lithography-induced anisotropy may be related to the strain relaxation and not to the classical shape magnetic anisotropy [100].

4. ELECTRICAL AND OPTICAL PROPERTIES

4.1. Electrical properties of (Ga,Mn)As

4.1.1. Hall effect and hole concentration

Since it has been shown that the presence of holes stabilize ferromagnetism in (Ga,Mn)As, it is important to measure the hole concentration p of the material. In conventional semiconductors, p can readily be determined by the Hall measurement. For ferromagnetic semiconductors, however, it is not straightforward due to the presence of the anomalous Hall effect, which may often be a significant portion of the Hall voltage even at room temperature. Hall resistance R_{Hall} in ferromagnetic materials is empirically expressed as the sum of the ordinary Hall resistance and anomalous Hall resistance, as $R_{\mathrm{Hall}} = (R_0/d)\mu_0 H + (R_{\mathrm{S}}/d)M$, where R_0 and R_{S} are the ordinary and the anomalous Hall coefficients, respectively, and d is the thickness of the ferromagnetic layer. Here, M is the component of the magnetization perpendicular to the sample surface. R_{S} is usually proportional to $R_{\mathrm{sheet}}^{\gamma}$ (R_{sheet} is the sheet resistance) with $\gamma = 1$ or 2 depending of the origin of the anomalous Hall effect; the skew scattering results in $\gamma = 1$, whereas the side jump in $\gamma = 2$ [101]. $\gamma = 2$ can also originate from scattering-independent topological contribution [102]. Although further compilation of the experimental data is necessary, $\gamma = 1$ for insulating and $\gamma = 2$ for metallic (Ga,Mn)As and (In,Mn)As have been reported [103, 104]. The dominance of the anomalous Hall term hinders straightforward determination of the carrier type and concentration from the ordinary Hall term; the carrier concentration is given as $1/(eR_0)$ (e is the elementary charge) and its positive (negative) sign corresponds to p-type (n-type) conduction. Only at low temperatures and under high H, the anomalous Hall term gradually saturates, so that R_0 can be determined with a reasonable accuracy from the remaining linear change of R_{Hall} in the H dependence [60, 105, 106]. Note that although M saturates at relatively low H, negative magnetoresistance (MR) persists to high H, and affects the H dependence of the anomalous Hall effect through the change of the anomalous Hall coefficient. Thus, this method is not applicable to insulating (Ga,Mn)As, because of the very large MR and resistance in insulating (Ga,Mn)As [69].

Another method for determining p is the electrochemical capacitance–voltage (ECV) profiling. The reliability of this method was confirmed by comparison of p obtained from the ECV and the Hall measurements for Be-doped LT-GaAs [107–109]. A gradient of p along the growth direction (higher p near surface) was also found [108]. Determination of p by other methods, such as thermoelectric power measurements [110] or the Raman scattering analysis of the coupled plasmon-LO-phonon modes, are also possible [111, 112].

These measurements revealed that p is often less than 10^{21} cm^{-3} (smaller than the nominal Mn composition x) for as-grown samples, and increases significantly to $p = x$, consistent with the acceptor nature of Mn, after appropriate annealing as long as x is below 0.07 and the film is thin enough [113].

4.1.2. Low-temperature annealing

Low-temperature (LT) annealing [45] is now a standard way to remove Mn interstitials in (Ga,Mn)As. An appropriate LT-annealing process increases the electrical conductivity (increase of p) and at the same time increases T_C. LT annealing allows us to measure the correlation between the electrical conductivity and T_C using a set of samples cleaved from the same wafer, where a monotonic positive dependence of T_C on the conductivity was observed (Fig. 2). This is one of the evidences of the hole-induced ferromagnetism [61]. The effect was initially attributed to the reduction of As antisites, which act as a double donor in GaAs. A series of subsequent studies established that the annealing effect is coming from the reduction of Mn_{int}. As shown by the EXAFS and the channelling measurements [31, 58], Mn occupies two distinct positions, Ga and interstitial sites, in zincblende host GaAs lattice. Mn_{Ga} acts as a single acceptor, while Mn_{int} as a double donor. Under the assumption that Mn is the only relevant dopant in the system, p can be expressed by the concentrations of Mn_{Ga} and Mn_{int}, as $p = [Mn_{Ga}] - 2[Mn_{int}]$. This relationship was confirmed experimentally by a combination of channelling and ECV measurements [114]. In addition, Mn_{Ga} and Mn_{int} can form antiferromagnetic pairs, in which the Mn moments are cancelled [63]. Thus, when all Mn_{int} form a pair with Mn_{Ga}, the effective Mn composition contributing to ferromagnetic order is the difference of compositions of Mn_{Ga} and Mn_{int}, $x_{eff} = ([Mn_{Ga}] - [Mn_{int}])/N_0$, where N_0 is the density of the cation sites. Assuming this relationship, magnetization data was shown to yield $\sim 5\mu_B$ per Mn atom in a wide range of x from 0.02 to 0.09 [113], consistent with the expected value for Mn^{2+}. Analysis of both as-grown and annealed samples also showed that the increase of T_C after LT annealing is a combined result of increased p and x_{eff} due to the reduction of $[Mn_{int}]$. Self-compensation of Mn is enhanced at higher x, and results in almost the same p for as-grown (Ga,Mn)As with x greater than 0.02. However, overcompensation has never been observed. Thus, the self-compensation is believed to be related to the Fermi level pinning [115]. This suggests that once the Fermi level reaches a certain position in the valence band, it becomes energetically favourable to form Mn_{int} as a counter dopant [116], which was explained theoretically by calculating the formation energy of Mn_{Ga} and Mn_{int} as a function of x and the concentration of various donors [117]. The calculated x dependence of $[Mn_{Ga}]$ and $[Mn_{int}]$ based on the argument of the formation energies is in good agreement with the experimental result as shown in Fig. 6 [118].

The effect of LT annealing is strongly structure dependent. The increase of T_C by LT annealing is greater for thinner (Ga,Mn)As and is observed only for the (Ga,Mn)As layers near the surface, that is, LT-annealing effect is suppressed with a cap GaAs layer with thickness beyond 10 monolayers [119, 120]. The surface Mn Auger signal increases after annealing, indicating that Mn out-diffuses and accumulates on the surface during the process [121]. This is shown to be modelled by a one-dimensional out-diffusion model as shown in Fig. 7 [121]. It has also been suggested that the diffusion of Mn to the substrate side may be limited electrostatically by a p–n junction formed by fast diffusing Mn_{int} (donor) and slowly, if any, diffusing Mn_{Ga} (acceptor). Mn_{int} at surface may become electrically inactive as a result of oxidation and p–n junction is perhaps not formed on the surface side.

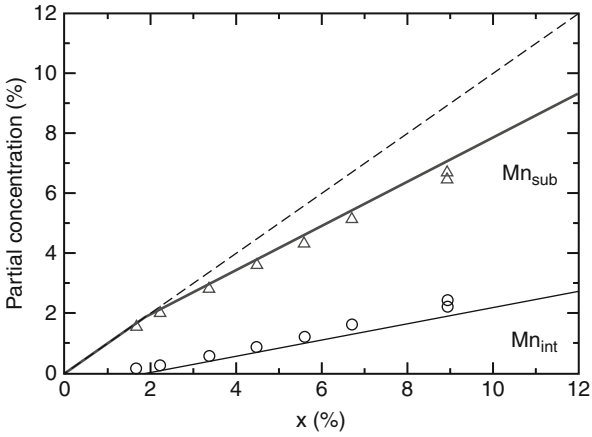

FIGURE 6 Solid lines show the partial compositions of substitutional Mn, Mn_{Ga}, and interstitial Mn, Mn_{int}, from the theoretical calculation. Symbols show the experimental results [20]. (Reproduced by permission of American Physical Society.)

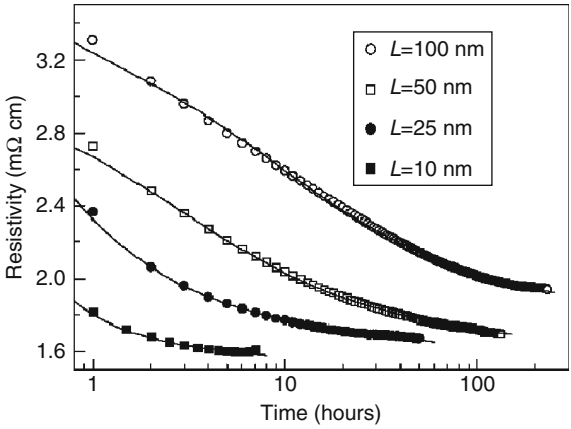

FIGURE 7 Time evolution of the resistivity change of (Ga,Mn)As with $x = 0.067$ and thickness L during annealing at 190 °C. Solid lines show the fitting by a 1D diffusion model [121]. (Reproduced by permission of American Physical Society.)

Thus, the LT annealing is expected to depend on the atmosphere and the layer on top of the magnetic layer. Efficient LT annealing is observed for (Ga,Mn)As annealed in O_2 and (Ga,Mn)As with an amorphous As cap layer, where the formation of Mn–O and Mn–As at the surface may have worked to reduce the number of Mn_{int} [122, 123]. The LT annealing was shown to produce a homogeneous magnetization depth profile than that of an as-grown sample, revealed by polarized neutron reflectometry measurements [124]. Post-growth hydrogenation of (Ga,Mn)As results in reduction of p from 10^{21} to 10^{17} cm^{-3} without changing Mn composition and is shown to lead to suppression of ferromagnetism [125].

The reduction of p by hydrogenation changes the direction of magnetic easy axis from in-plane to out-plane at low temperatures [126], consistent again with the prediction by the p–d Zener model [21, 22, 88].

4.1.3. Spin polarization

Spin polarization of holes P in (Ga,Mn)As at low temperatures has been measured directly by the Andreev reflection on $Ga/Ga_{0.95}Mn_{0.05}As$ junctions [127] and $Sn/Ga_{0.92}Mn_{0.08}As$ point contact [128] to be as high as ∼80%. Similar effective P value of 77% was obtained from the magnitude of TMR (290%) at low temperatures [129]. These results are consistent with the theoretical calculations of (Ga,Mn)As [22, 130]. The point contact Andreev reflection was measured in (Ga,Mn)Sb [131–133] and (In,Mn)Sb [134, 135], where $P \sim 50$–60% was obtained [136, 137].

4.1.4. Magnetotransport properties

The spin–orbit interaction together with the p–d exchange interaction manifests itself in magnetotransport phenomena including the anomalous Hall effect, anisotropic MR (AMR), and the planar Hall effect, which provide valuable information on the magnetism of (Ga,Mn)As. Because of the high sensitivity, the determination of magnetization behaviour from transport is an important technique for thin films of DMSs, where the total magnetic moments can be too small to be easily detected by other means. In addition, the sensitivity of transport measurements does not depend on the lateral size of the device with the fixed lateral aspect ratio.

Because R_{Hall} is dominated by the anomalous Hall effect, the temperature and magnetic field dependence of R_{Hall} reflects those of magnetization [138, 139]. From the same procedure as that for magnetization measurements, T_C can be determined by the Arrott plots and the Curie–Weiss plots [140]. Since (Ga,Mn)As layers grown directly on GaAs usually have in-plane magnetic easy axis, R_{Hall} measured in perpendicular H probes the magnetization process along the hard axis of the magnetization. One can also measure the planar Hall resistance, which is the transverse resistance measured by the same probes as R_{Hall} in an in-plane H [141], to obtain information about magnetization. For (Ga,Mn)As, the signal of the planar Hall resistance is greater than that of magnetic metals by several orders and can be used to detect the in-plane M reversal as well as the domain wall dynamics [82, 142, 143].

The temperature and magnetic field dependence of magnetization probed by the anomalous Hall effect, however, does not show exactly the same behaviour as those measured by direct magnetization measurements. The anomalous Hall effect scales with spin polarization of carriers, which is nearly proportional to the magnetization only when the spin splitting of the bands is smaller than the Fermi energy and the contribution of the hole magnetization to the total magnetization is negligible. Furthermore, transport measurements do not probe the magnetization of the entire sample but only the region visited by carriers, where carrier-mediated magnetic interaction is strong. Thus, near MIT in particular due to the non-uniform distribution of holes in (Ga,Mn)As [21, 22], transport and direct magnetization measurements may provide different information on magnetization.

4.1.5. Anisotropic magnetoresistance

It has been found that (Ga,Mn)As exhibits AMR, in which MR depends on the relative orientation of the current direction with respect to the magnetic field direction, and their direction with respect to crystal axes [91]. For metallic (Ga,Mn)As, the lowest resistance is observed when H is parallel to the current as shown in Fig. 8 [139, 144]. The direction of H for the highest resistance was predicted theoretically to be different for compressive and tensile lattice strain [145]. This is corroborated by experiments; for the sample with compressive strain, the highest resistance is measured when H is perpendicular to the surface, and for the sample with tensile strain it is observed when H is in in-plane perpendicular to the current [139].

4.1.6. Critical scattering

Resistance maximum observed at around T_C together with the negative MR associated with the maximum has been attributed to the critical scattering. The resistance maximum can be interpreted in terms of a spin-dependent scattering by magnetization fluctuation via exchange interaction [146]. The negative MR occurs because the H-induced spin alignment reduces the spin disorder scattering [138]. From the numerical fit to the data of the temperature dependence and H dependence of the resistance reproduces the data well and gives the magnitude of the p–d exchange interaction as $|N_0\beta| = 1.5 \pm 0.2$ eV [105], which compares favourably with that determined by photoemission experiments, $N_0\beta = -1.2$ eV [147].

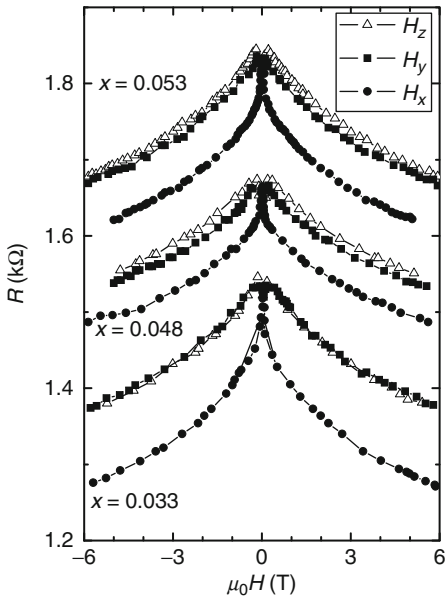

FIGURE 8 AMR of (Ga,Mn)As with different values of x. Magnetic field is applied three different direction, x is along current, y is in-plane and perpendicular to current and z is perpendicular to the plane [144]. (Reproduced by permission of American Institute of Physics.)

4.1.7. Weak localization and metal–insulator transition

At low temperatures, the negative MR extends to high magnetic fields, beyond the field at which magnetic spins are fully ordered ferromagnetically according to the anomalous Hall effect response. This cannot be accounted for by the suppression of spin disorder scattering. Here, the giant splitting of the valence bands makes both spin disorder and spin–orbit scattering ineffective. Under such conditions, weak localization which manifests itself in negative MR is expected to show up at low temperatures, where phase breaking scattering ceases to operate [148]. The weak localization MR formula [148] was shown to explain the observed negative MR data at 2 K quite well for samples under compressive as well as those under tensile strain [139]. This three-dimensional (3D) weak localization model predicts the temperature T dependence of the conductivity σ, as $\sigma \propto T^{1/2}$. In addition to the weak localization scenario, the possibility of the Kondo effect like temperature dependence, $\sigma \propto \ln T$, was suggested [149]. The $\sigma \propto T^{1/3}$ dependence observed in a metallic (Ga,Mn)As layer down to 30 mK was explained by the Aronov–Altshuler 3D scaling theory with spin scattering [150].

The universal conductance fluctuation in metallic (Ga,Mn)As submicron wires and rings was observed at low temperatures (<200 mK), indicating that the phase coherence length of electrons in (Ga,Mn)As is about 100 nm at 10 mK [151]. The MIT-associated anisotropic features can also be observed for insulating (Ga,Mn)As, which shows two orders of magnitude difference in resistance between the two directions along [1 1 0] and along [−1 1 0] below 1 K [152]. From the anisotropic tunnel conductance in (Ga,Mn)As/GaAs/(Ga,Mn)As tunnel junctions, the MIT behaviour is shown to be M direction dependent, which may be related to the formation of an Efros–Shklovskii gap induced by the change of density of states by M direction and the reduced screening effect of depletion layer at the interfaces [153]. As can be seen for the continued developments, III–V-based ferromagnetic semiconductors are providing new insights to the MIT, which is one of the most important topics in solid state physics.

4.1.8. Domain wall resistance

The Barkhausen noise caused by the scattering due to the presence of magnetic domain structure has been observed in the resistance measurement on (Ga,Mn)As [91]. The existence of magnetic domain wall (DW) is known to contribute to the electrical resistance, which is usually much smaller than the sample resistance and thus careful measurement is necessary. The DW resistance (DWR) of a single DW has been measured for (Ga,Mn)As; a negative sign of DWR was reported for (Ga, Mn)As with in-plane easy axis [142] and a positive one was reported for a sample with perpendicular easy axis [154]. The negative DWR may be explained by the destruction of quantum coherence of electrons at the DW [155] and/or by the AMR contribution [156]. In the latter experiment, the DW position was defined by using the coercivity H_C difference induced by the surface etching [157]. Using a series of samples having different sizes, the measured positive DWR was decomposed into extrinsic and intrinsic DWR components. Numerical evaluation of the zigzag current due to the alternating polarity of the anomalous Hall effect at DW [158] explained well the dominant extrinsic DWR. The remaining intrinsic DWR

was shown to be consistent with the mistracking of the carrier spins inside DW [159]. Here, the AMR contribution was shown to be 20 times smaller than the mistracking resistance.

4.1.9. Thermal transport

The Seebeck effect (the longitudinal thermopower) and the in-plane Nernst effect (the transverse thermopower) under in-plane H were measured on compressive (Ga,Mn)As. Both effects showed strong dependence on the direction of H, reflecting in-plane magnetization reversal process. These dependences indicate that the origin of the effect can be related to the anisotropic magnetoresistance and the planar Hall effect, which may provide useful information for further understanding of the origin of anisotropic scattering in (Ga,Mn)As [160]. For (Ga,Mn)As grown on (In,Ga)As buffer layer with perpendicular magnetic easy axis, the anomalous Hall effect and its thermoelectric counterpart, the anomalous Nernst effect, can be observed simultaneously [161]. The relationship between the two effects can be expressed through the Mott relation [162] with $\gamma = 2$, suggesting that the both effects share a common origin related to the spin–orbit interaction.

4.2. Magneto-optical properties

Magneto-optical properties have been studied to elucidate the origin of ferromagnetism of (Ga,Mn)As, because they can probe the spin-split band structures induced by the *sp–d* exchange interaction [163]. The absorption edge of (Ga,Mn)As is not sharp due to the disorder effect [164], and the absorption coefficient is 5×10^{-3} cm^{-1} at 1.2 eV which is a few orders greater than GaAs owing most likely to its free carrier absorption [165]. It was shown by spectroscopic ellipsometry [93] that the critical points of (Ga,Mn)As are essentially the same as those of GaAs in the photon energy range from 0.62 to 6 eV. When the ferromagnetism is intrinsic, one expects an enhanced magneto-optical response reflecting ferromagnetism at the critical points of the host zincblende semiconductors. This is the case for (Ga,Mn)As, in which a large Faraday rotation and magnetic circular dichroism (MCD) signals were observed at critical points E_0 and E_1, whose H dependence traces well the magnetization curves. Figure 9 shows the H dependence of the Faraday rotation of 2-μm thick $Ga_{0.957}Mn_{0.043}As$ at 10 and 300 K in the vicinity of the band gap, where the GaAs substrate was etched away to remove absorption of the GaAs substrate [166]. The magnitude of the Faraday rotation is proportional to the magnetization probed by AHE. The observed value of the Faraday rotation is 6×10^4 deg/cm under 0.1 T at 10 K (ferromagnetic phase) and the Verdet constant is 9×10^{-2} deg/G cm at room temperature (paramagnetic phase). An enhancement of MCD signals in (Ga,Mn)As at GaAs critical points was observed [167, 168]. The positive sign of the Faraday rotation and MCD at the band edge is opposite to most of the II–VI DMSs with negative *p–d* exchange, whereas theories predict negative *p–d* exchange for (Ga,Mn)As. This can be explained by a spin-dependent Burnstein–Moss shift caused by hole redistribution [22, 169]. In addition to the positive MCD, a negative contribution that increases with decreasing temperature was observed in the infrared spectrum [168]. This peculiar temperature

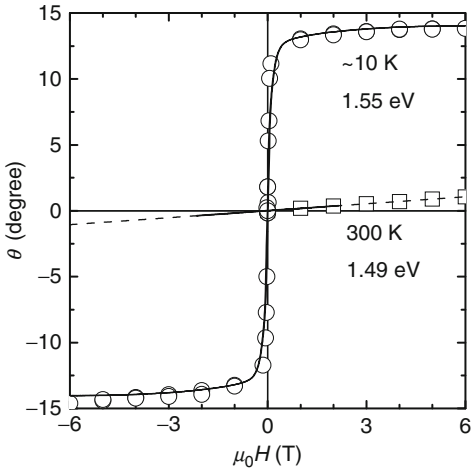

FIGURE 9 Faraday rotation as a function of magnetic field at 5 and 300 K near the absorption edge. Lines represent magnetization curves probed by anomalous Hall effect [166].

dependence was explained as a result of a non-linear dependence of MCD on magnetization at Moss–Burnstein edge again caused by the hole redistribution on the spin-split bands [22]. To understand the experimental data, the effect of disorder on the transition probability was noted [164]. The shift of peak positions in MCD spectra was observed with (Ga,Mn)As/AlAs superlattices depending on the layer thickness, and was interpreted as due to the quantum confinement in the (Ga,Mn)As quantum well layers [170]. The magnetic linear dichroism is also observed, reflecting the in-plane magnetization rotation in (Ga,Mn)As, whose spectrum is considered to be related to the electronic state in the vicinity of E_F responsible for the ferromagnetism [171].

When excited by 400-nm pump pulses, (Ga,Mn)As emits THz radiation. The radiation occurred only in the ferromagnetic phase and its strength and H dependence showed strong correlation with the magnetization. The radiation was explained by the influence of the magnetization on the photo-generated carrier acceleration path [172].

The summary of magneto-optical properties in (III,Mn)V and related phenomena can be found elsewhere [173].

5. THE *sp–d* EXCHANGE INTERACTION

The most prominent feature of magnetic semiconductors is the correlation among magnetic, electrical and optical properties, which is based on the presence of the *sp–d* exchange interaction in these materials [6, 174]. The *sp–d* exchange interaction gives a sizable spin splitting of bands in the conduction (*s*-state) as well as in the valence (*p*-state) bands, when the *d*-states of incorporated transition metals carry magnetization. This amplifies the spin properties of semiconductors in a number

of different ways; spin-dependent optical selection rules give rise to the giant magneto-optical effects and spin-polarized carriers modify the transport properties, as have seen in the previous sections. The magnitude of the *sp–d* interaction (expressed as $N_0\alpha$ for *s–d* and $N_0\beta$ for *p–d* exchange interaction, where N_0 is cation density) in II–VI magnetic semiconductors has been systematically investigated on various materials by photoemission and/or magneto-optical measurements. The *s–d* interaction is primarily due to potential interaction, which follows from the spin-dependent Coulomb interaction due to the Pauli exclusion principle between the band electrons and the localized *d*-electrons of transition metals. This potential interaction gives rise to ferromagnetic coupling between the delocalized *s*-state and the localized *d*-state. Because of the long-range nature of the Coulomb interaction, the magnitude of $N_0\alpha$ is nearly independent of the lattice constant a and is about 0.2 eV. The main part of the *p–d* exchange interaction, on the other hand, results from hybridization of the *p*- and the *d*-states. The sign of $N_0\beta$ is known to depend on the configuration of *d*-shell in the particular transition metal incorporated in semiconductor; for half-filled Mn 5*d*-state it is always negative. The magnitude of $N_0\beta$ is several times greater than $N_0\alpha$ due to hybridization. The chemical trend of $N_0\beta$ is summarized with respect to a for various II–VI magnetic semiconductors, and is found to be nearly inversely proportional to the unit cell volume as $N_0\beta \propto a^{-3}$, as shown in Fig. 10 [22].

For (Ga,Mn)As with percent order of Mn, the value of $N_0\beta$ is determined to be -1.2 ± 0.2 eV from the photoemission measurement [147]. By adopting this value, various experimental observations, including the magnitude of T_C, magnetic anisotropy, hole polarization and MCD spectra, can be reproduced by the *p–d* Zener model described in the following section. $N_0\beta$ of (In,Mn)As determined

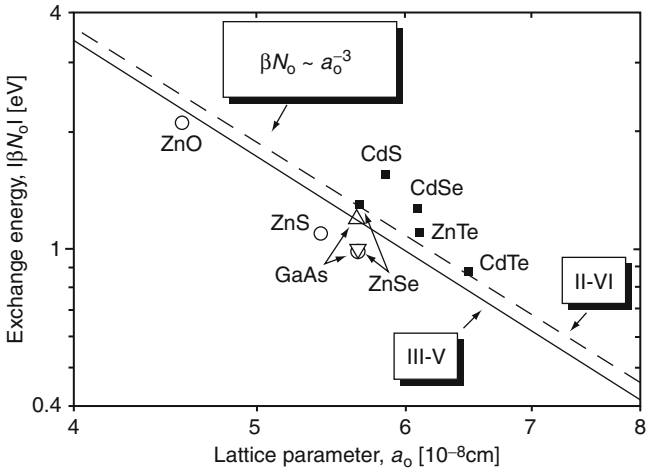

FIGURE 10 Energy of *p–d* exchange interaction for various materials with $x = 0.05$ as a function of lattice constant [22].

from the photoemission is -0.7 eV [175], which is consistent with the chemical trend complied for II–VI materials [22]. The paramagnetic Mn-doped GaAs with $x < 0.0005$ shows positive value of $N_0\beta$ about 2 eV from magneto-optical [176] and spin-flip Raman measurements [169]. The origin of the positive sign has not been understood.

The value of $N_0\alpha$ has been determined experimentally for paramagnetic Mn-doped GaAs. The spin-flip Raman experiments gives $N_0\alpha = 23$ meV for metal-organic vapour phase epitaxy grown Mn-doped GaAs [177]. This small value of $N_0\alpha$ has been attributed to the Coulomb repulsion between conduction band electrons and negatively charged magnetic ions [178]. For MBE-grown Mn-doped GaAs/(Al,Ga)As quantum wells (QWs) with QW width less than 10 nm and $x < 0.0003$, a negative $N_0\alpha$ down to -0.09 eV was observed by optical measurements [179]. This may be related to the confinement-induced p-symmetry in the conduction band of Mn-doped GaAs QWs [178, 180].

6. THE *p–d* ZENER MODEL OF FERROMAGNETISM

Because T_C goes to zero when holes are compensated and because T_C of (Ga,Mn)As is higher for higher hole concentrations, it is natural to consider that the ferromagnetism of (Ga,Mn)As is hole induced. Band carrier-induced ferromagnetism was noted first by Zener in 1950s, where the magnetic ordering is stabilized by the lowering carrier energy [181]. Because of the large p–d exchange interaction and high density of states (DOS) of the valence bands compared to the s–d exchange in the conduction band, the energy gain due to the hole redistribution among spin-split subbands is greater for p-type ferromagnetic semiconductors than n-type [21, 22, 88]. The model is now called the p–d Zener model, in which one uses realistic band structure with the p–d exchange interaction calculated by, for example, k·p description of the valence band to obtain magnetic properties of a ferromagnetic semiconductor. The model explains surprisingly well the experimentally obtained properties qualitatively and often even semiquantitatively. For example, T_C based on the p–d Zener model shows quantitative agreement with the experimental T_C for (Ga,Mn)As and (In,Mn)As as well as p-type II–VI (Zn,Mn)Te and (Cd,Mn)Te [15, 21, 22]. If one considers the biaxial strain in the calculation, the strain and hole concentration-dependent magnetic anisotropy can be obtained, which compares well with the experimental observations [21, 22, 88]. One can also explain many other experimental results on (Ga,Mn)As, for example, MCD spectra, conductance curves of the resonant tunnel diodes with a (Ga,Mn)As emitter, AMR effect and the magnetic domain width [19, 21, 22, 89].

It should also be noted that the p–d Zener model has limits, for example, it may not be applicable to the regime with extremely high hole concentration, where oscillatory carrier-mediated interaction (RKKY interaction) starts to work [182–184]. This situation may lead, thorough non-collinear spin arrangement, to spin-glass phase with the increase of hole concentration. The effect of disorder was shown to enhance T_C in the model whose starting point is the impurity band of holes localized by the Mn acceptors [185].

Standard calculation methods have also been employed to explain and to predict the magnetic phases and properties of (Ga,Mn)As as well as other magnetic semiconductors. Among them, the first-principle calculations have provided a number of insights to the electronic structure of the material. First-principle calculations with local-spin-density approximation (LSDA) predicted that E_F was at the Mn *d*-states [186, 187], which led to the suggestion that the origin of ferromagnetism was more of double exchange in nature, as opposed to the band-like picture of the *p–d* Zener model. Although care has to be taken to compare ground state electronic structure with excited state experiments, the calculated results do not appear to agree with the experimentally obtained DOS by photoemission, which shows very little mixture of Mn *d*-state at E_F. LDA + U [188] and self-interaction corrected (SIC) LSDA [189] are known to better describe the correlation, and have been used to calculate the band structure of (Ga,Mn)As. The results suggest the presence of a sizable portion of delocalized *p*-state at E_F, in accordance with the experimental results.

We note that the use of band picture for the description of ferromagnetism in magnetic III–V semiconductors (the *p–d* Zener model) is based on the past studies of doped non-magnetic semiconductors. A large number of studies in the past, dedicated to the understanding of the nature of the MIT in doped semiconductors, have shown that doped semiconductors near the MIT boundary exhibit duality, that is, these materials show metallic band-like nature on one type of measurement, whereas at the same time they can exhibit impurity band-like nature on another. These observations led to the proposal of the two-fluid model [190]. While whether conduction takes place in valence band or in impurity band is an unresolved issue in semiconductor physics at large [191–194], there are indications that thermodynamic properties such as specific heat can be described to a good approximation by band mass across the MIT [195]. Having these studies in mind, as pointed out in the earlier papers [21, 22], the band picture was employed to describe the magnetism in magnetic III–V semiconductors.

7. PROPERTIES REVEALED BY DEVICE STRUCTURES

To explore novel spin-dependent phenomena and their possibility for future applications, a number of ferromagnetic semiconductor-based heterostructures have been made and investigated both experimentally and theoretically. In this section, we review the results of heterostructures and device structures that exhibit properties not readily accessible in devices made only from non-magnetic semiconductors.

7.1. Electrical spin injection into non-magnetic semiconductors

Spontaneous magnetization in the ferromagnetic phase manifests itself in spin polarization of carriers below T_C. Ferromagnetic semiconductors that can be epitaxially grown on non-magnetic semiconductor heterostructures thus are a candidate for a source of spin-polarized carriers for electrical spin injection into

non-magnetic structures in the absence of magnetic field. Injection of spin-polarized carriers (spin injection), their transport and their detection are the building blocks of semiconductor spintronic devices. The first demonstration of electrical spin injection from a ferromagnet into non-magnetic semiconductor was done using a ferromagnetic (Ga,Mn)As semiconductor electrode as an emitter and a light-emitting diode (LED) as a spin detector (spin-LED) [196]. The employed structure was p-(Ga,Mn)As/i-GaAs/(In,Ga)As quantum well (QW)/n-GaAs. Spin polarization of injected holes from (Ga,Mn)As was detected by the circular polarization of electroluminescence (EL): the change in EL polarization was ±1%. Hysteresis loop of ΔP with respect to H and its temperature dependence traced the H dependence and temperature dependence of magnetization of (Ga,Mn)As.

For injection of spin-polarized *electrons*, an Esaki tunnel diode (ED) was employed as a spin emitter, where spin-polarized holes in the valence band of (Ga,Mn)As are injected into the conduction band of an adjacent n-GaAs by inter-band tunnelling [197, 198]. High spin polarization of the injected electrons (80%) has been reported [199]. A three-terminal device that can bias ED and LED independently was fabricated and used to examine the bias dependence and hence energy dependence of the injected electron spin polarization as shown in Fig. 11A [199]. EL polarization P_{EL} showed strong dependence on the biases: the highest P_{EL} of 32% (Fig. 11B) was obtained when the valence electrons near

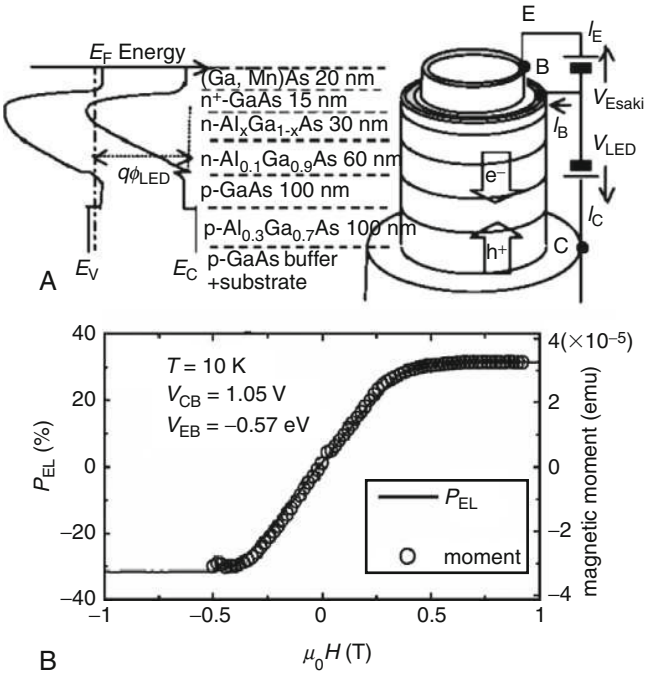

FIGURE 11 (A) Schematic band diagram and the three-terminal devices consisting of an Esaki diode and LED. (B) Magnetic field dependence of P_{EL}, which traces magnetization curve [199].

the Fermi level of (Ga,Mn)As dominated the tunnel current. The 32% polarization corresponds to injected electron spin polarization of 85%, when spin relaxation in the QW measured by the Hanlé effect is taken into account [199, 200]. The magnitude of the spin polarization as well as its bias dependence can be explained by the calculation based on Landauer–Büttiker formalism with tight-binding approximation for the ballistic transport regime [201].

7.2. Tunnel magnetoresistance (TMR) and current-induced magnetization switching (CIMS)

Magnetic tunnel junctions (MTJs) based on fully epitaxial (Ga,Mn)As ((Ga,Mn)As/(Al,Ga)As/(Ga,Mn)As) exhibit TMR [202, 203], where parallel and antiparallel configurations of the magnetization of the two (Ga,Mn)As layers result in low and high resistance (R_P and R_{AP}) states. Note here that GaAs acts as a barrier layer for holes in (Ga,Mn)As [204]. The highest TMR ratio [$=(R_{AP} - R_P)/R_P$] so far reported are 75% and 290% (Fig. 12) for AlAs and GaAs intermediary barrier layers, respectively [129, 205]. The latter corresponds to effective carrier spin polarization P of 77% according to the Julliere's formula, where TMR ratio $= 2P^2/(1 - P^2)$ [206]. The TMR ratio quickly decreases as the bias voltage increases, in a much faster way than seen in metallic MTJs [129]. This is understood as a result of small magnitude of band offset and the Fermi energy (~100 meV) in (Ga,Mn)As/GaAs [129, 201]. The anisotropic TMR behaviour has been observed in (Ga,Mn)As-based MTJs with in-plane magnetic easy axis, where TMR ratio depended on the direction of in-plane H [85, 129, 205], which reflects the in-plane magnetocrystalline anisotropy of (Ga,Mn)As (see Section 3.2).

Spontaneous spin splitting in the valence bands was observed in current–voltage (I–V) characteristics of AlAs/GaAs/AlAs p-type double-barrier resonant-tunnelling diodes (RTDs) having a (Ga,Mn)As emitter [207]. Here, the

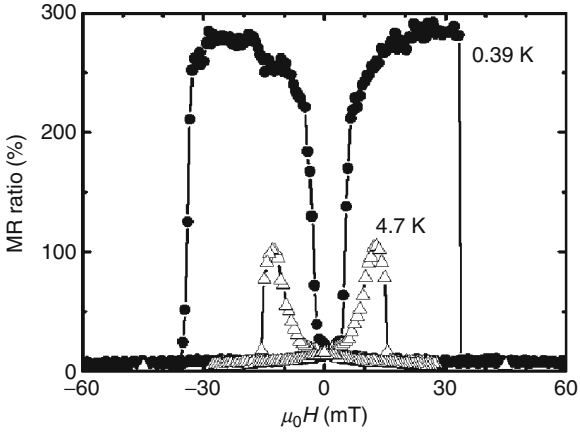

FIGURE 12 Tunnel magnetoresistance of (Ga,Mn)As/GaAs/(Ga,Mn)As under magnetic field along the [1 0 0] direction measured at low temperatures [129].

resonant levels in the GaAs QW act as an energy filter for hole transport, separating exchange split hole bands. In the experiment, the resonant peaks labelled HH2 and LH1 showed spontaneous splitting in the absence of magnetic field below T_C, when holes are injected from (Ga,Mn)As. This shows that RTD structure can be used to do spectroscopy of the spin splitting of the valence bands.

The interplay with the TMR effect and the quantum confinement in QWs was addressed utilizing integration of ferromagnetic semiconductor with semiconductor quantum structures. An RTD with (Ga,Mn)As emitter and collector showed the TMR effect as large as that of an MTJ with a single barrier, which was used to show the presence of spin accumulation in the QW [208]. A non-standard TMR behaviour was observed in an AlAs/(In,Ga)As/AlAs RTD with (Ga,Mn)As emitter and collector, in which an oscillatory TMR ratio was observed as a function of AlAs thickness [209]. Resonant tunnelling and TMR effect through the quantized levels in a QW made of (Ga,Mn)As was reported in AlAs/(Ga,Mn)As/AlAs RTD, where oscillation of TMR ratio was observed in its bias dependence when holes are injected from the non-magnetic p-GaAs:Be electrode as shown in Fig. 13 [210, 211].

Spin-dependent transport in a three-terminal device with a (Ga,Mn)As/AlAs/(Ga,Mn)As MTJ was also investigated. The device had three electrodes, emitter, base and collector, formed at the top (Ga,Mn)As, the bottom (Ga,Mn)As and p-type substrate, respectively [212]. The transistor was shown to exhibit current gain.

In submicron (Ga,Mn)As MTJs, CIMS has been observed [213, 214]. Starting from the parallel magnetization state (the R_P state), current pulse from the thick layer to the thin layer of (Ga,Mn)As induces magnetization reversal of the thin (Ga,Mn)As layer, resulting in the antiparallel state (the R_{AP} state). When the current polarity is reversed, reversal of the thinner (Ga,Mn)As layer takes place putting the MTJ into the R_P state. The critical current density J_C for switching is of

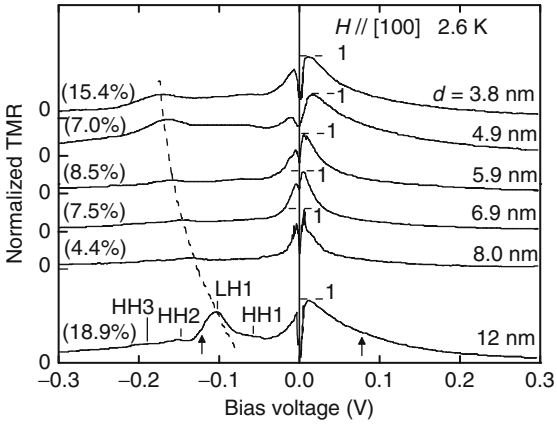

FIGURE 13 Bias dependence of normalized TMR ratio in p-type (Ga,Mn)As/AlAs/(Ga,Mn)As/AlAs/GaAs:Be RTD measured at 2.6 K with magnetic field along [1 0 0] direction. *d* represents the thickness of (Ga,Mn)As QWs. Negative bias corresponds to hole injection from GaAs:Be [211]. (Reproduced by permission of American Physical Society.)

the order of 10^4–10^5 A/cm^2 [213–215], two to three orders smaller than those observed in metal-based MTJs. Clear dependence of the switching on the current pulse direction shows that CIMS is neither due to the Oersted field nor the Joule heating. It can qualitatively be explained by the Slonczewski's spin-transfer torque model [216]. The orders of magnitude reduction of J_C compared to metal MTJs may be understood by the small magnetization of (Ga,Mn)As, although the model still predicts an order of magnitude greater J_C than the observed one. Possible effect of the large bias dependence of the TMR ratio in the CIMS process is not understood at the moment; that is, CIMS takes place at bias voltage, where the TMR ratio is almost zero. This may be related to the conservation of the total carrier spins despite reduction of the TMR ratio [214] and/or different trend in bias dependence between spin-transfer torque vector and the TMR ratio [217]. The role of possible incoherent switching processes, such as the formation of domain structures may also play a role in reversal [213–215, 218, 219].

A very large tunnel anisotropic magnetoresistance (TAMR) up to 150,000% has been reported in (Ga,Mn)As-based MTJs with vertical and lateral device structures [220–222]. The origin of TAMR [223] has been attributed to anisotropic valence band structure induced by the spin–orbit interaction and lattice strain in combination with the MIT [153].

7.3. Current-induced domain wall motion

The position of a magnetic domain wall (DW) before and after the motion induced by current can be detected by magneto-optical microscope. The motion can also be observed by transport measurements using AHE and PHE. The DW velocity induced by external H was measured for (Ga,Mn)As with in-plane magnetic easy axis utilizing PHE. The velocity was controlled over three decades from 10^{-5} to 10^{-2} m/s by varying H. The field-driven velocity increases with the increase of temperature [143].

By the application of a current pulse across the DW, it was found that the position of DW can electrically be manipulated in the absence of magnetic fields [157]. The channel made of (Ga,Mn)As used in the experiment has magnetic easy axis perpendicular to the surface by inserting an (In,Ga)As or (In,Al)As buffer layer. This easy axis direction is not only useful to monitor the DW position through the anomalous Hall effect and by the magneto-optical Kerr effect microscope (MOKE), but appears to play a role in observing the motion, as discussed later. The DW switching was observed in devices having a channel with three regions with different thicknesses, where the thinnest region was set to the centre of the channel. This double-step structure allowed patterning of H_C due to non-uniformity along the growth direction in the film. In addition, each step acted as a confinement potential for DW. The device was initialized by appropriately sweeping external magnetic field in such a way that a DW was placed at one of the stepped boundaries of the thinnest region. After setting $H = 0$, a current pulse of 10^5 A/cm^2 for 100 ms at 80 K (T_C of this film was 90 K) was applied. Both the anomalous Hall signals and MOKE images indicated that the DW moved to the other step boundary, in the direction opposite to the current direction. The

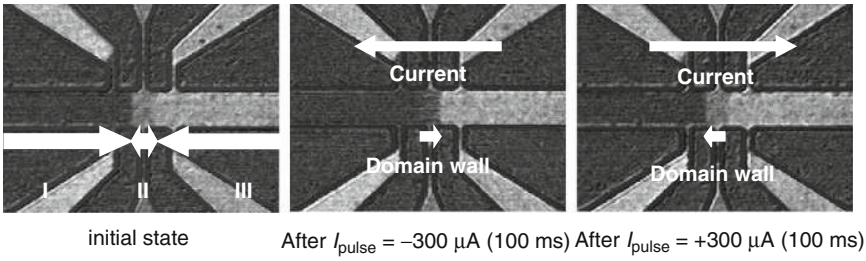

FIGURE 14 Current-induced DW motion in (Ga,Mn)As in stepped structure with central thinnest region II observed by MOKE. A DW prepared at the boundary of regions I and II (left) can be moved to the opposite boundary regions of II and III by a current pulse of −300 μA (middle) and be moved back to its original position by the current with the opposite direction (left) [157].

application of a subsequent current pulse in the opposite direction switched back the DW to its initial position as shown in Fig. 14.

Current density j as well as the temperature dependence of the DW velocity was systematically investigated using a 5-μm wide (Ga,Mn)As channel having a single step structure [224]. DW was formed at the step by a magnetic field sweep and then was moved by current pulses. The area swept by the DW was monitored by MOKE to obtain the DW speed, v. The DW displacement was calculated by dividing the area swept by the DW by the device width. The displacement was linearly dependent on the pulse width. The change of the device temperature by the Joule heating was monitored by measuring the device resistance during the pulse application and found to be constant during the pulse. Thus obtained j dependence of v under constant temperature showed that there were at least two regimes separated by a critical current density j_C, which is a few 10^5 A/cm^2 as shown in Fig. 15. Beyond j_C, v increased linearly with j, while a slow motion

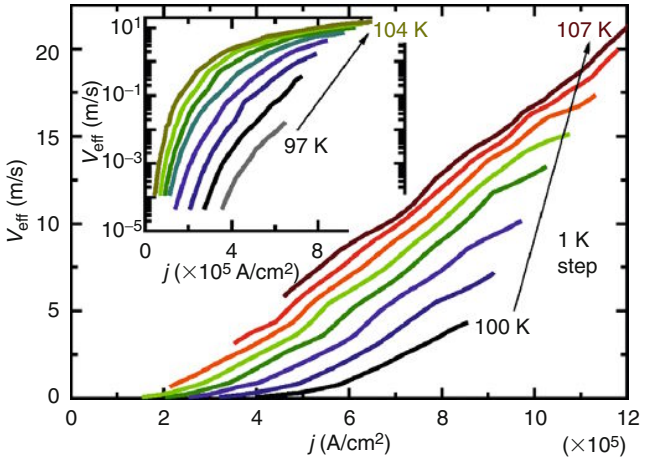

FIGURE 15 DW velocity as a function of current density at various device temperatures. The inset presents the same data but in logarithm plot to show the DW activity in subthreshold regime [224].

indicative of creep was observed below j_C. The quasi-linear dependence of v above j_C and its slope together with the direction of motion were found to be quantitatively consistent with the spin-transfer mechanism [225, 226]. The value of j_C can be reproduced by the spin-transfer mechanism assuming an intrinsic DW pinning due to hard-axis anisotropy [225]. DW motion by currents has so far not been observed in (Ga,Mn)As with in-plane axis. The intrinsic pinning model may offer an explanation for this observation: j_C is expected to be at least one order of magnitude higher in this case as the relevant anisotropy, magnetocrystalline anisotropy, is an order of magnitude higher than the hard-axis anisotropy (stray field) responsible for determining j_C in samples with perpendicular easy axis. An order of magnitude higher j_C is not easily accessible experimentally because of the associated Joule heating. Another important finding is the current-induced DW motion in the subthreshold regime, where the DW moves slowly (the inset of Fig. 15). The j dependence of v below j_C obeys an empirical scaling law, showing the existence of current-induced DW creep [227]. Comparison between current-induced and field-induced creep revealed that they could be scaled using the same functional form but with different scaling exponents, indicating that the current-induced creep is fundamentally different from the field-driven one. A model based on spin-transfer torque has been put forward to explain the current-induced creep, which describes the observed scaling exponents [228].

On the theory side, spin–orbit interaction in (Ga,Mn)As was pointed out to result in a spin accumulation and non-adiabaticity leading to a high mobility of DW above j_C when transport is ballistic [229]. Spin-transfer torque-assisted thermal activation process below j_C under rigid wall approximation [230, 231] indicated that the DW motion should follow a specific functional form with respect to j; the predicted temperature and/or j dependence of v appears to be different from the experimental findings. Further quantitative comparison between theory and experiment will reveal the rich physics involved in the DW motion of (Ga,Mn)As.

7.4. Control of magnetism and magnetization reversal by external means

Since the ferromagnetism in (Ga,Mn)As and (In,Mn)As is stabilized by holes, one can switch the magnetic phase without changing temperature by electrically controlling the value of p. This was shown possible using a metal–insulator–semiconductor field effect transistor structure (MISFET) with a thin (In,Mn)As layer ($\leq$5 nm) as the semiconductor channel [232]. The (In,Mn)As layer was grown on a GaAs substrate with a thick (Al,Ga)Sb buffer layer to relax the 7% lattice mismatch between (In,Mn)As and GaAs. To probe the magnetization through the anomalous Hall effect, Hall bar-shaped devices were prepared. Since the channel is p-type, application of positive (negative) gate electric-filed E_G decreases (increases) p; for the structure under discussion $|E_G| = 1.5$ MV/cm changes several percents of total p. In the vicinity of T_C, the magnetization curves show more square shape under negative E_G indicating enhanced ferromagnetic order, while paramagnetic-like response under positive E_G. This reversible

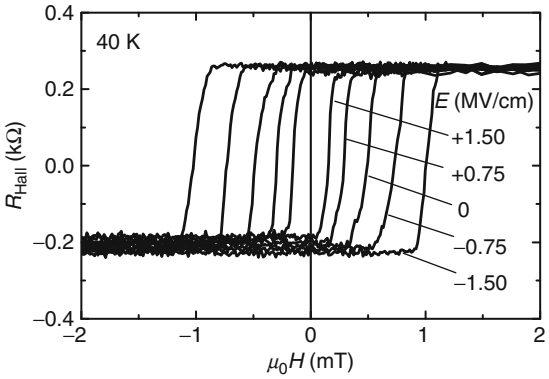

FIGURE 16 Isothermal control of coercivity of 5-nm thick (In,Mn)As with $x = 0.063$ by the application of external electric fields [233].

change of T_C by $E_G = \pm 1.5$ MV/cm determined using Arrott plots can be as large as 4 K for 4-nm thick (In,Mn)As [233]. Control of T_C by electrical means is also a proof that the ferromagnetism in this material is indeed carrier induced.

Another important effect of E_G is the change of the coercive force H_C below T_C; greater (smaller) H_C for negative (positive) E_G as shown in Fig. 16. It was shown that the temperature dependence of H_C under several E can be collapsed into a single curve, when H_C is plotted against the reduced T/T_C^*, where T_C^* is the temperature at which H_C becomes zero. The MOKE images during magnetization reversal of similar (In,Mn)As showed that the magnitude of H_C was determined by the nucleation field of domains [218]. These results suggest that the change of H_C by E is a result of the change of the nucleation field, whose temperature dependence is determined by the magnitude of T_C^*. By using this phenomenon, a new scheme of electrical magnetization reversal, electric field-assisted magnetization reversal, was demonstrated [233] in the following way. After saturation of magnetization at positive H under $E_G = -1.5$ MV/cm, H was reduced through zero to a small negative H but still less than the coercive force, H_C. Then, E_G was switched to zero, which reduced $|H_C|$ below $|H|$ and switching took place.

For (Ga,Mn)As, control of ferromagnetism by an electrical means was initially hindered by its insulating nature at thickness t below 5 nm [234]. To probe magnetic properties by AHE, metallic samples with $t > 5$ nm had to be employed. On the other hand, thick metallic samples made it difficult to observe the change in T_C because of the limited ratio of the modulated sheet hole concentration to the total sheet hole concentration. The first observation of T_C by electric fields in a GaAs-based system was done in Mn δ-doped GaAs, where holes were provided by modulation doping [235]. Later, the control of T_C by 5 K as well as H_C was shown to be possible in a 7-nm thick (Ga,Mn)As by the application of $|E_G| = 5$ MV/cm [236], where the high-quality Al_2O_3 gate insulator deposited by atomic layer deposition (ALD) [237] was used to increase the number of modulated holes by E_G. Later, a back-gate FET structure with an n-GaAs buffer layer as the back-gate was also used to modulate T_C in a (Ga,Mn)As FET, where no additional gate

insulator is necessary [238]. The non-volatile T_C modulation by E_G was also demonstrated for (Ga,Mn)As MISFETs by using ferroelectric as a gate insulator [239].

Because the magnitude of magnetic anisotropies of (Ga,Mn)As is p dependent [78], by applying E_G to (Ga,Mn)As in an MIS-FET structure, the magnetic anisotropy is expected to be manipulated, allowing electrical control of the M direction. This was demonstrated experimentally in a 4-nm thick (Ga,Mn)As layer with ALD-deposited ZrO_2 gate insulator, where the in-plane direction of M was probed by the planar Hall effect [240]. The application of E_G ranging from -4 to 4 MV/cm resulted in $\sim 10^\circ$ of in-plane M rotation; it was shown that the change of the sign and magnitude of in-plane uniaxial anisotropy is responsible for the observed M rotation. By using AMR as a probe to monitor out-of-plane M, the modulation of perpendicular magnetic anisotropy by E_G has also been observed.

Photo-generated carriers can also induce similar effects on magnetic properties. Illumination turned the magnetic state of (In,Mn)As with no H_C to a state with a clear hysteresis at 5 K, which was probed by both magnetization and magnetotransport measurements [241]. The photon energy needed to see the effect was greater than 0.8 eV, which indicated that the photo-generated carriers in the GaSb buffer layer below (In,Mn)As were responsible for the observed phenomena. The state after illumination with enhanced conductivity persisted after switching the illumination was turned off, suggesting that the interface electric filed at (In,Mn)As/GaSb spatially separated the photo-generated holes and electrons leading to hole accumulation on the (In,Mn)As side of the interface. Similar photo-induced effect was observed in (InMn)(AsSb)/InSb, where the effect showed up starting at low photon energy $\sim$0.6 eV because of the small band gap of the buffer semiconductor [242]. The photo-induced change of H_C was also observed in (In,Mn)As [243]. These results may partly be explained by the change of the magnetic anisotropy induced by the change of the hole concentration [244].

The magnetization enhancement of (Ga,Mn)As by circularly polarized light illumination was observed in (Ga,Mn)As thin films [245, 246] and in Mn δ-doped GaAs [247]. Time-resolved optical measurement showed the possibility of ultrafast control of magnetization in ferromagnetic semiconductors by photo-carrier injection. In addition, there have been reports on softening of hysteresis loops of (In,Mn)As during a short lifetime ($\sim$2 ps) of the photo-generated carries [248], demagnetization of (In,Mn)As within 100 ps [249], and the enhancement of the ferromagnetism of (Ga,Mn)As again within 100 ps [250].

It was shown that the application of hydrostatic pressure enhanced ferromagnetism of (In,Mn)Sb, which was explained by the increase of exchange coupling among Mn caused by the change of lattice constant [251].

The controllability of ferromagnetism by external means is not limited to III–V-based ferromagnetic semiconductors. The isothermal control of ferromagnetism was reported in II–VI (Cd,Mn)Te QW by electrical and optical means [252] and in IV GeMn by electric field [253].

Following these results obtained in ferromagnetic semiconductors, electric field control of H_C was demonstrated to be possible in metal ferromagnets, FePt and FePd immersed in an electrolyte [254].

8. PROSPECTS

Ferromagnetic semiconductors are providing an excellent test bench for exploring a variety of spin-dependent phenomena and to demonstrate new schemes of spintronic device operation. Although room-temperature application of well-established ferromagnetic semiconductors, such as (Ga,Mn)As and (In,Mn)As, and their devices are not yet possible due to their below room temperature T_C, the knowledge accumulated to date are of great importance for future development of spintronics in general, and in particular for semiconductor spintronics once material breakthrough in T_C is made. Initiated by theoretical predictions [21, 22, 255], a worldwide effort to synthesize ferromagnetic semiconductors with high T_C is currently underway.

According to the *p–d* Zener model, increase of effective Mn participating in ferromagnetic order and/or increase of hole concentration is the key to increase T_C of (Ga,Mn)As and (In,Mn)As [21, 22]. Although there exists no conclusive guide to overcome the solubility limit and the self-compensation effect, some strategies are proposed, ranging from codoping of donors to suppress the self-compensation [116], optimization of post-anneal condition, and use of high-index substrates other than (0 0 1) to increase Mn incorporation efficiency [50]. Introduction of heterostructures to increase local Mn composition and hole concentration simultaneously was shown to be promising; T_C of 250 K was observed in a Mn δ-doped GaAs-based structure with modulation doping to enhance the hole concentration [235].

Another direction is to synthesize ferromagnetic semiconductors based on a host semiconductor other than GaAs and InAs. Ferromagnetic semiconductors based on wide-gap semiconductors such as GaN and ZnO have extensively been investigated [256] as the chemical trend pointed out by the theoretical studies shows increase in exchange interaction. However, it has also been pointed out that high x is necessary to achieve high T_C in wide-gap materials due to the reduced range of exchange interaction among magnetic spins in these wide band-gap semiconductors [257, 258]. There are many reports on observation of room-temperature ferromagnetism in wide-gap materials doped with transition metals or rare earths. Some of them show correlation between magnetization and MCD signals at semiconductor critical points and/or the anomalous Hall effect [259–261]. To firmly establish the origin of the observed ferromagnetic order, it is now becoming increasingly clear that one needs to do a series of measurements to fully characterize the properties of the synthesized materials. Correlation among magnetization, magneto-optical and magnetotransport properties is one of the necessary conditions of intrinsic ferromagnetism, although large magneto-optical responses from materials with a small spin–orbit interaction cannot be expected. The presence of carrier spin polarization is another signature of having ferromagnetism in semiconductors, which results from spin-split states induced by the *sp–d* exchange interaction. Control of magnetism by changing carriers by external means is an important way to confirm that the ferromagnetism is carrier related.

Non-uniform distribution of magnetic ions in host semiconductor may result from nanoscale spinodal decomposition [262, 263], which is experimentally

confirmed in a number of "ferromagnetic" semiconductors [264–266]. Here, magnetically condensed nanometre regions have the same crystal structure as the host semiconductor. Each region behaves as a superparamagnetic cluster (even with antiferromagnetic interaction as there remain uncompensated spins) and can show ferromagnetic-like properties below blocking temperature [187, 267]. Since the presence of magnetic nanoparticles fully integrated in the host lattice can enhance the magnetotransport and magneto-optical properties of semiconductors [265, 268, 269], it is not an easy task to separate non-uniform magnetic semiconductors from uniform ones. It should also be noted that depending on what one is looking for, this non-uniform magnetic semiconductor may provide a solution as good as the uniform ferromagnetic semiconductors. Once percolated by increasing the concentration of magnetic ions, high T_C is predicted for these materials [262]. It has been suggested that the charge state of magnetic ions during crystal growth can change the way the nanoscale phase separation takes place [267, 270]. This has been experimentally verified by controllable aggregation of Cr in (Zn,Cr)Te by doping [266].

In an effort to intentionally integrate room-temperature ferromagnetic materials with non-magnetic semiconductor, ferromagnetic materials having the same crystal structure with the host semiconductor have also been investigated. Single-crystal zincblende CrAs and CrSb were grown by MBE and were confirmed to show ferromagnetism over 400 K [271, 272]. Theoretical calculation predicts that these materials are half-metallic [273].

Finally, it is important to consider how to apply the new schemes found using ferromagnetic semiconductors not only to new devices but to conventional ones using ferromagnetic metals [254], which will further enrich the field of spintronics.

ACKNOWLEDGEMENT

The authors thank Ms. Noriko Sato for her help with the list of references.

REFERENCES

[1] Methfessel, S., and Mattis, D. C. (1968). Magnetic semiconductors. *In* "Encyclopedia of Physics, vol. XVIII/1, Magnetism" (H. P. J. Wijn, ed.), pp. 389–562. Springer-Verlag, Berlin.
[2] Holtberg, F., von Molnár, S., and Coey, J. M. D. (1980). Rare earth magnetic semiconductors. *In* "Handbook on Semiconductors" (S. P. Ketler, ed.), vol. 3, pp. 803–856. North-Holland, Amsterdam.
[3] Mauger, A., and Godart, C. (1986). *Phys. Rep.* **141**, 51–176.
[4] Furdyna, J. K., and Kossut, J. (1988). "Semiconductors and Semimetals, vol. 25, Diluted Magnetic Semiconductors." Academic Press, London.
[5] Kossut, J., and Dobrowolski, W. (1993). Diluted magnetic semiconductors. *In* "Handbook of Magnetic Materials" (K. H. J. Bushchow, ed.), vol. 7, pp. 231–305. North-Holland, Amsterdam.
[6] Dietl, T. (1994). (Diluted) magnetic semiconductors. *In* "Handbook of Semiconductors" (S. Mahajan, ed.), Completely revised and enlarged edition, vol. 3B, pp. 1251–1342. North-Holland, Amsterdam.

[7] Dobrowolski, W., Kossut, J., and Story, T. (2003). II–VI and IV–VI diluted magnetic semiconductors – New bulk materials and low-dimensional quantum structures. *In* "Handbook of Magnetic Materials" (K. H. J. Buschow, ed.), vol. 15, pp. 289–377. North-Holland, Amsterdam.
[8] Gaj, J. A., Planel, R., and Fishman, G. (1979). *Solid State Commun.* **29**, 435.
[9] Nawrocki, M., Planel, R., Fishman, G., and Galazka, R. R. (1981). *Phys. Rev. Lett.* **46**, 735.
[10] Story, T., Gałazka, R. R., Frankel, R. B., and Wolf, P. A. (1986). *Phys. Rev. Lett.* **56**, 777.
[11] Ohno, H., Munekata, H., Penny, T., von Molnár, S., and Chang, L. L. (1992). *Phys. Rev. Lett.* **68**, 2664.
[12] Ohno, H., Shen, A., Matsukura, F., Oiwa, A., Endo, A., Katsumoto, S., and Iye, Y. (1996). *Appl. Phys. Lett.* **69**, 363.
[13] Dietl, T., Haury, A., and Merle d'Aubigné, Y. (1997). *Phys. Rev. B* **55**, R3347.
[14] Haury, A., Wasiela, A., Arnoult, A., Cibert, J., Tatarenko, S., Dietl, T., and Merle d'Aubigné, Y. (1997). *Phys. Rev. Lett.* **79**, 511.
[15] Ferrand, D., Cibert, J., Wasiela, A., Bourgognon, C., Tatarenko, S., Fishman, G., Andrearczk, T., Jarosyński, J., Koleśnik, S., Dietl, T., Barbara, B., and Dufeu, D. (2001). *Phys. Rev. B* **63**, 085201.
[16] Blinowski, J., Kacman, P., and Majewski, J. A. (1996). *Phys. Rev. B* **53**, 9524.
[17] Munekata, H., Ohno, H., von Molnar, S., Segmüller, A., Chang, L. L., and Esaki, L. (1989). *Phys. Rev. Lett.* **63**, 1849.
[18] Ohno, H. (1999). *J. Magn. Magn. Mater.* **200**, 110.
[19] Matsukura, F., Ohno, H., and Dietl, T. (2002). III–V ferromagnetic semiconductors. *In* "Handbook of Magnetic Materials" (K. H. J. Buschow, ed.), vol. 14, pp. 1–87. North-Holland, Amsterdam.
[20] Jungwirth, T., Sinova, S., Mašek, J., Kučera, J., and MacDonald, A. H. (2006). *Rev. Mod. Phys.* **78**, 809.
[21] Dietl, T., Ohno, H., Matsukura, F., Cibert, J., and Ferrand, D. (2000). *Science* **287**, 1019.
[22] Dietl, T., Ohno, H., and Matsukura, F. (2001). *Phys. Rev. B* **63**, 195205.
[23] Awschalom, D. D., Loss, D., and Samarth, N. (2002). "Semiconductor Spintronics and Quantum Computation." Springer-Verlag, Berlin.
[24] Žutić, I., Fabian, J., and Das Sarma, S. (2004). *Rev. Mod. Phys.* **76**, 323.
[25] Samarth, N. (2004). *Solid State Phys.* **58**, 1.
[26] Awschalom, D. D., and Flatté, M. E. (2007). *Nat. Phys.* **3**, 153.
[27] DeSimone, D., Wood, C. E. C., and Evans, C. A. Jr. (1982). *J. Appl. Phys.* **53**, 4938.
[28] Kordoš, P., Janšák, L., and Benč, V. (1975). *Solid State Electron.* **18**, 223.
[29] De Boeck, J., Oesterholt, R., Van Esch, A., Bender, H., Bruynseraede, C., Van Hoof, C., and Borghs, G. (1996). *Appl. Phys. Lett.* **68**, 2744.
[30] Soo, Y. L., Huang, S. W., Ming, Z. H., Kao, Y. H., Munekata, H., and Chung, L. L. (1996). *Phys. Rev. B* **63**, 195209.
[31] Shioda, R., Ando, K., Hayashi, T., and Tanaka, M. (1998). *Phys. Rev. B* **58**, 1100.
[32] Ohya, S., Ohno, K., and Tanaka, M. (2007). *Appl. Phys. Lett.* **90**, 112503.
[33] Chiba, D., Nishitani, Y., Matsukura, F., and Ohno, H. (2007). *Appl. Phys. Lett.* **90**, 122503.
[34] Shen, A., Ohno, H., Matsukura, F., Sugawara, Y., Akiba, N., Kuroiwa, T., Oiwa, A., Endo, A., Katsumoto, S., and Iye, Y. (1997). *J. Cryst. Growth* **175/176**, 1069.
[35] Novák, V., Olejník, K., Cukr, M., Smrčka, L., Remeš, Z., and Oswald, J. (2007). *J. Appl. Phys.* **102**, 083536.
[36] Shen, A., Horikoshi, Y., Ohno, H., and Guo, S. P. (1997). *Appl. Phys. Lett.* **71**, 1540.
[37] Yasuda, H., and Ohno, H. (1999). *Appl. Phys. Lett.* **74**, 3275.
[38] Guo, S. P., Shen, A., Yasuda, H., Ohno, Y., Matsukura, F., and Ohno, H. (2000). *J. Cryst. Growth* **208**, 799.
[39] Ohno, H. (1998). *Science* **281**, 951.
[40] Matsukura, F., Shen, A., Sugawara, Y., Omiya, T., Ohno, Y., and Ohno, H. (1999). "Institute of Physics, Conference Series No. 162", pp. 547–552.
[41] Shimizu, H., Hayashi, H., Nishinaga, Y., and Tanaka, M. (1999). *Appl. Phys. Lett.* **74**, 398.
[42] Myers, R. C., Sheu, B. L., Jackson, A. W., Gossard, A. C., Schiffer, P., Samarth, N., and Awschalom, D. D. (2006). *Phys. Rev. B* **74**, 155203.
[43] Sadowski, J., Domagała, J. Z., Bąk-Misiuk, J., Koleński, S., Sawicki, M., Świątek, U., Kanski, J., and Iveler, L. (2000). *J. Vac. Sci. Technol. B* **18**, 1697.

[44] Sadowski, J., Mathieu, R., Svendlindh, P., Domagała, J. Z., Bąk-Misiuk, J., Świątek, U., Karlsteen, M., Kanski, J., Ilver, L., Åsklund, H., and Södervall, U. (2001). *Appl. Phys. Lett.* **78**, 3271.
[45] Hayashi, T., Hashimoto, Y., Katsumoto, S., and Iye, Y. (2001). *Appl. Phys. Lett.* **78**, 1691.
[46] Schott, G. M., Faschinger, W., and Molenkamp, L. W. (2001). *Appl. Phys. Lett.* **79**, 1809.
[47] Schott, G. M., Schmidt, G., Karczewski, G., Molenkamp, L. W., Jakiela, R., Barcz, A., and Karczewski, G. (2003). *Appl. Phys. Lett.* **82**, 4678.
[48] Sadowski, J., and Domagala, J. Z. (2004). *Phys. Rev. B* **69**, 075206.
[49] Omiya, T., Matsukura, F., Shen, A., Ohno, Y., and Ohno, H. (2001). *Physica E* **10**, 206.
[50] Wang, K. Y., Edmonds, K. W., Zhao, L. X., Sawicki, M., Campion, R. P., Gallagher, B. L., and Foxon, C. T. (2005). *Phys. Rev. B* **72**, 115207.
[51] Reinwald, M., Wurstbauer, U., Döppe, M., Kipferl, W., Wagenhuber, K., Tranitz, H. P., Weiss, D., and Wegscheider, W. (2005). *J. Cryst. Growth* **278**, 690.
[52] Shen, A., Matsukura, F., Guo, S. P., Sugawara, Y., Ohno, H., Tani, M., Abe, H., and Liu, H. C. (1999). *J. Cryst. Growth* **201/202**, 679.
[53] Shirai, M., Ogawa, T., Kitagawa, I., and Suzuki, N. (1998). *J. Magn. Magn. Mater.* **177–181**, 1383.
[54] Mašek, J., Kudrnovský, J., and Máca, F. (2003). *Phys. Rev. B* **67**, 153203.
[55] Ilegrams, M., Dingle, R., and Rupp, L. W. Jr. (1975). *J. Appl. Phys.* **46**, 3059.
[56] Schneider, J., Kaufmann, U., Wilkening, W., Baeumler, M., and Köhl, F. (1987). *Phys. Rev. Lett.* **59**, 240.
[57] Tsuruoka, T., Tanimoto, R., Tachikawa, N., Ushioda, S., Matsukura, F., and Ohno, H. (2002). *Solid State Commun.* **121**, 79.
[58] Yu, K. M., Walukiewicz, W., Wojtowicz, T. J., Kuryliszyn, I., Liu, X., Sasaki, Y., and Furdyna, J. K. (2002). *Phys. Rev. B* **65**, 201303(R).
[59] Potashnik, S. J., Ku, K. C., Chun, S. H., Berry, J. J., Samarth, N., and Schiffer, P. (2001). *Appl. Phys. Lett.* **79**, 1495.
[60] Edmonds, K. W., Wang, K. Y., Campion, R. P., Neumann, A. C., Foxon, C. T., Gallagher, B. L., and Main, P. C. (2002). *Appl. Phys. Lett.* **81**, 3010.
[61] Edmonds, K. W., Wang, K. W., Campion, R. P., Neumann, A. C., Farley, N. R. S., Gallagher, B. L., and Foxon, C. T. (2002). *Appl. Phys. Lett.* **81**, 4991.
[62] Máca, F., and Mašek, J. (2003). *Phys. Rev. B* **66**, 235209.
[63] Blinowski, J., and Kacman, P. (2003). *Phys. Rev. B* **67**, 121204(R).
[64] Yakunin, A. M., Silov, A. Yu., Koenraad, P. M., Van Roy, W., De Boeck, J., Tang, J. M., and Flatté, M. E. (2004). *Phys. Rev. Lett.* **92**, 216806.
[65] Blakemore, J. S., Brown, W. Jr., Stass, M. L., and Woodbury, D. A. (1973). *J. Appl. Phys.* **44**, 3352.
[66] Linnarson, M., Janzén, E., Monemar, B., Kleverman, M., and Thilderkvist, A. (1997). *Phys. Rev. B* **58**, 6938.
[67] Kitchen, D., Richardella, A., Tang, J. M., Flatté, M., and Yazdani, A. (2006). *Nature* **442**, 436.
[68] Yakunin, A. M., Silov, A. Yu., Koenraad, P. M., Tang, J. M., Flatté, M. E., Primus, J. L., Van Roy, W., De Boeck, J., Monakhov, A. M., Romanov, K. S., Penaiotti, I. E., and Averkiev, N. S. (2007). *Nat. Mater.* **6**, 512.
[69] Oiwa, A., Katsumoto, S., Endo, A., Hirasawa, M., Iye, Y., Matsukura, F., Shen, A., and Sugawara, Y. (1997). *Solid State Commun.* **103**, 209.
[70] Novák, V., Olejník, E., Wunderlich, J., Cukr, M., Výborný, K., Rushforth, A. W., Edmonds, K. W., Campion, R. P., Gallagher, B. L., Sinova, J., and Jungwirth, T. (2008). *Phys. Rev. Lett.* **101**, 077201.
[71] Shono, T., Hasegawa, T., Fukumura, T., Matsukura, F., and Ohno, H. (2000). *Appl. Phys. Lett.* **77**, 1363.
[72] Fukumura, T., Shono, T., Inaba, K., Hasegawa, T., Koinuma, H., Matsukura, F., and Ohno, H. (2001). *Physica E* **10**, 135.
[73] Welp, U., Vlasko-Vlasov, V. K., Liu, X., Furdyna, J. K., and Wojtowicz, T. J. (2003). *Phys. Rev. Lett.* **90**, 167206.
[74] Thevenard, L., Largeau, L., Mauguin, O., Partriarche, G., Lemaître, A., Vernier, N., and Ferré, J. (2006). *Phys. Rev. B* **73**, 195331.
[75] Sugawara, A., Akashi, T., Brown, P. D., Campion, R. P., Yoshida, T., Gallagher, B. L., and Tonomura, A. (2007). *Phys. Rev. B* **75**, 241306(R).
[76] Dietl, T., König, J., and MacDonald, A. H. (2001). *Phys. Rev. B* **64**, 241201(R).

[77] Sawicki, M., Matsukura, F., Idziaszek, A., Dietl, T., Schott, G. M., Ruester, C., Gould, C., Karczewski, G., Schmidt, G., and Molenkamp, L. W. (2004). *Phys. Rev. B* **70**, 245325.
[78] Sawicki, M., Wang, K. Y., Edmonds, K. W., Campion, R. P., Staddon, C. R., Farley, N. R. S., Foxon, C. T., Papis, E., Kamińska, E., Piotrowska, A., Dietl, T., and Gallagher, B. L. (2005). *Phys. Rev. B* **71**, 121302(R).
[79] Wang, K. Y., Sawicki, S., Edmonds, K. W., Campion, R. P., Maat, S., Foxon, C. T., Gallagher, B. L., and Dietl, T. (2005). *Phys. Rev. Lett.* **95**, 217204.
[80] Liu, X., Sasaki, Y., and Furdyna, J. K. (2003). *Phys. Rev. B* **67**, 205204.
[81] Liu, X., Lim, W. L., Dobrowolska, M., and Furdyna, J. K. (2005). *Phys. Rev. B* **71**, 035307.
[82] Tang, H. X., Kawakami, R. K., Awschalom, D. D., and Roukes, M. K. (2003). *Phys. Rev. Lett.* **90**, 107201.
[83] Hamaya, K., Taniyama, T., Kitamoto, Y., Moriya, R., and Munekata, H. (2003). *J. Appl. Phys.* **94**, 7657.
[84] Hamaya, K., Moriya, R., Oiwa, A., Taniyama, T., Kitamoto, Y., Yamazaki, Y., and Munekata, H. (2004). *Jpn. J. Appl. Phys.* **43**, L306.
[85] Uemura, T., Sone, T., Matsuda, K., and Yamamoto, M. (2005). *Jpn. J. Appl. Phys.* **44**, L1352.
[86] Yamada, T., Chiba, D., Matsukura, F., Yakata, S., and Ohno, H. (2006). *Phys. Status Solidi C* **3**, 4086.
[87] Fedorych, O. M., Hankiewicz, E. M., Wilamowski, Z., and Sadowski, J. (2002). *Phys. Rev. B* **66**, 045201.
[88] Abolfath, M., Jungwirth, T., Brum, J., and MacDonald, A. H. (2001). *Phys. Rev. B* **63**, 054418.
[89] Takamura, K., Matsukura, F., Chiba, D., and Ohno, H. (2002). *Appl. Phys. Lett.* **81**, 2590.
[90] Sawicki, M., Matsukura, F., Dietl, T., Schott, G. M., Ruester, C., Gould, C., Schmidt, G., Molenkamp, L. W., and Karczewski, G. (2004). *J. Supercond.* **16**, 7.
[91] Hayashi, T., Katsumoto, S., Hashimoto, Y., Endo, A., Kawamura, M., Zalalutdinov, M., and Iye, Y. (2000). *Physica B* **284–288**, 1175.
[92] Pappert, K., Hümpfner, S., Wenisch, J., Brunner, K., Gould, C., Schmidt, G., and Molenkamp, L. W. (2007). *Appl. Phys. Lett.* **90**, 062109.
[93] Burch, K. S., Stephens, J., Kawakami, R. K., Awshalom, D. D., and Basov, D. N. (2004). *Phys. Rev. B* **70**, 205208.
[94] Masmanidis, S. C., Tang, H. X., Myers, E. B., Li, M., De Greve, K., Vermeulen, G., Van Roy, W., and Roukes, M. L. (2005). *Phys. Rev. Lett.* **95**, 187206.
[95] Overby, M., Chernyshov, A., Rokhinson, L. P., Liu, X., and Furdyna, J. K. (2008). *Appl. Phys. Lett.* **92**, 192501.
[96] Liu, X., Sasaki, Y., and Furdyna, J. K. (2001). *Appl. Phys. Lett.* **79**, 2414.
[97] Fid, K. F., Stone, M. B., Ku, K. C., Maksimov, O., Schiffer, P., Samarth, N., Shih, T. C., and Palmstrøm, C. J. (2004). *Appl. Phys. Lett.* **85**, 1556.
[98] Lin, H. T., Chen, Y. F., Huang, P. W., Wang, S. H., Huang, J. H., Lai, C. H., Lee, W. N., and Chin, T. S. (2006). *Appl. Phys. Lett.* **89**, 262502.
[99] Wang, K. Y., Sawicki, M., Edmonds, K. W., Campion, R. P., Rushforth, A. W., Freeman, A. A., Foxon, C. T., Gallagher, B. L., and Dietl, T. (2006). *Appl. Phys. Lett.* **88**, 022510.
[100] Hümpfner, S., Pappert, K., Wenisch, J., Brunner, K., Gould, C., Schmidt, G., Molenkamp, L. W., Sawicki, M., and Dietl, T. (2007). *Appl. Phys. Lett.* **90**, 102102.
[101] Chien, C. L., and Westgate, C. R. (1980). "The Hall Effect and Its Application." Plenum Press, New York.
[102] Jungwirth, T., Qian, N., and MacDonald, A. H. (2002). *Phys. Rev. Lett.* **88**, 207208.
[103] Chun, S. H., Kim, Y. S., Choi, H. K., Jeong, I. T., Lee, W. O., Suh, K. S., Oh, Y. S., Kim, K. H., Khim, Z. G., Woo, J. C., and Park, Y. D. (2007). *Phys. Rev. Lett.* **98**, 026601.
[104] Oiwa, A., Endo, A., Katsumoto, S., Iye, Y., Ohno, H., and Munekata, H. (1999). *Phys. Rev. B* **59**, 5826.
[105] Omiya, T., Matsukura, F., Dietl, T., Ohno, Y., Sakon, T., Motokawa, M., and Ohno, H. (2000). *Physica E* **7**, 976.
[106] Sadowski, J., Mathieu, R., Svedlindh, P., Karlsteen, M., Kanski, J., Fu, Y., Domagala, J. T., Szuszkiewicz, W., Hennion, B., Maude, D. K., Airey, R., and Hill, G. (2002). *Thin Solid Films* **412**, 122.

[107] Yu, K. M., Walukiewicz, W., Wojotowicz, T., Lim, W. L., Liu, X., Sasaki, Y., Dobrowolska, M., and Furdyna, J. K. (2002). *Appl. Phys. Lett.* **81**, 844–846.
[108] Koeder, A., Frank, S., Schoch, W., Avrutin, V., Limmer, W., Thonke, K., Sauer, R., Waag, A., Krieger, M., Zuem, K., Ziemann, P., Brotzmann, S., and Bracht, H. (2003). *Appl. Phys. Lett.* **82**, 3278.
[109] Moriya, R., and Munekata, H. (2003). *J. Appl. Phys.* **93**, 4603.
[110] Osinny, V., Jędrzejczak, A., Arciszewska, M., Dobrowolski, W., Story, T., and Sadowski, J. (2001). *Acta Phys. Polon. A* **100**, 327.
[111] Limmer, W., Glunk, M., Schoch, W., Köder, A., Kling, R., Sauer, R., and Waag, A. (2002). *Physica E* **13**, 589.
[112] Seong, M. J., Chun, S. H., Cheong, H. M., Samarth, N., and Mascarenhas, A. (2002). *Phys. Rev. B* **66**, 033202.
[113] Wang, K. Y., Edmonds, K. W., Campion, R. P., Gallagher, B. L., Farley, N. R. S., Sawicki, M., Boguslawski, P., and Dietl, T. (2004). *J. Appl. Phys.* **95**, 6512.
[114] Wojtowicz, T. J., Furdyna, J. K., Liu, X., Yu, K. M., and Walukiewicz, W. (2004). *Physica E* **25**, 171.
[115] Walukiewicz, W. (1988). *Phys. Rev. B* **37**, 4760.
[116] Yu, K. M., Walukiewick, T., Wojtowicz, T. J., Lim, W. L., Liu, X., Bindley, U., Dobrowolska, M., and Furdyna, J. K. (2003). *Phys. Rev. B* **68**, 041308(R).
[117] Mašek, J., Turek, I., Kudrnovský, J., Máca, F., and Drchal, V. (2004). *Acta Phys. Polon. A* **105**, 637.
[118] Jungwirth, J., Wang, K. Y., Mašek, J., Edmonds, K. W., König, J., Sinova, J., Polini, M., Goncharuk, N. A., MacDonald, A. H., Sawicki, M., Rushforth, A. W., Campion, R. P., Zhao, L. X., Foxon, C. T., and Gallagher, B. L. (2005). *Phys. Rev. B* **72**, 165204.
[119] Chiba, D., Takamura, K., Matsukura, F., and Ohno, H. (2003). *Appl. Phys. Lett.* **82**, 3020.
[120] Stone, M. B., Ku, K. C., Potashnik, S. J., Sheu, B. L., Samarth, N., and Schiffer, P. (2003). *Appl. Phys. Lett.* **83**, 4568.
[121] Edmonds, K. W., Bogusławski, P., Wang, K. Y., Campion, R. P., Novikov, S. N., Farley, N. R. S., Gallagher, B. L., Foxon, C. T., Sawicki, M., Dietl, T., Buongiorno Nardelli, M., and Bernholc, J. (2004). *Phys. Rev. Lett.* **92**, 037201.
[122] Malfait, M., Vanacken, J., Moshchalkov, V. V., Van Roy, W., and Borghs, G. (2005). *Appl. Phys. Lett.* **86**, 132501.
[123] Adell, M., Ilver, L., Kanski, J., Stanciu, V., Svedlindh, P., Sadowski, J., Domagala, J. Z., Terki, F., Hernandez, C., and Charar, S. (2005). *Appl. Phys. Lett.* **86**, 112501.
[124] Kirby, B. J., Borchers, J. A., Rhyne, J. J., te Velthunis, S. G. E., Hoffmann, A., O'Donovan, K. V., Wojtowicz, T. J., Liu, X., Lim, W. L., and Furdyna, J. K. (2004). *Phys. Rev. B* **69**, 081307(R).
[125] Gonnenwein, S. T. B., Wassner, T. A., Huebl, H., Brandt, M. S., Philipp, J. B., Opel, M., Gross, R., Koeder, A., Schoch, W., and Waag, A. (2004). *Phys. Rev. Lett.* **91**, 227202.
[126] Thevenard, L., Largeau, L., Mauguin, O., Lemaître, A., Khazen, K., and von Bardeleben, H. J. (2007). *Phys. Rev. B* **75**, 195218.
[127] Barden, J. G., Parker, J. S., Xiong, P., Chun, S. H., and Samarth, N. (2003). *Phys. Rev. Lett.* **91**, 056602.
[128] Panguluri, R. P., Ku, K. C., Wojtowicz, T. J., Liu, X., Furdyna, J. K., Lyanda-Geller, Y. B., Samarth, N., and Nadgorny, B. (2005). *Phys. Rev. B* **72**, 054510.
[129] Chiba, D., Matsukura, F., and Ohno, H. (2004). *Physica E* **21**, 966.
[130] Ogawa, T., Shirai, M., Suzuki, N., and Kitagawa, I. (1999). *J. Magn. Magn. Mater.* **196–197**, 428.
[131] Abe, E., Matsukura, F., Yasuda, H., Ohno, Y., and Ohno, H. (2000). *Physica E* **7**, 981.
[132] Matsukura, F., Abe, E., and Ohno, H. (2000). *J. Appl. Phys.* **87**, 6442.
[133] Lim, W. L., Wojtowicz, T. J., Liu, X., Dobrowolska, M., and Furdyna, J. K. (2004). *Physica E* **20**, 346.
[134] Wojtowicz, T. J., Cywinski, G., Lim, W. L., Liu, X., Dobrowolska, M., Furdyna, J. K., Yu, K. M., Walukiewicz, W., Kim, G. B., Cheon, M., Chen, X., Wang, M., and Luo, H. (2003). *Appl. Phys. Lett.* **82**, 4310.
[135] Yanagi, S., Kuga, K., Slupinski, T., and Munekata, H. (2004). *Physica E* **20**, 333.
[136] Panguluri, R. P., Nadgorny, B., Woitowicz, T., Liu, X., and Furdyna, J. K. (2007). *Appl. Phys. Lett.* **91**, 252502.
[137] Panguluri, R. P., Nadgorny, B., Wojtowicz, T. J., Lim, W. L., Liu, X., and Furdyna, J. K. (2004). *Appl. Phys. Lett.* **84**, 4947.

[138] Matsukura, F., Ohno, H., Shen, A., and Sugawara, Y. (1998). *Phys. Rev. B* **57**, R2037.
[139] Matsukura, F., Sawicki, M., Dietl, T., Chiba, D., and Ohno, H. (2004). *Physica E* **21**, 1032.
[140] Ohno, H., and Matsukura, F. (2001). *Solid State Commun.* **117**, 179.
[141] Jan, J. P. (1957). *Solid State Phys.* **5**, 1.
[142] Tang, H. X., Masmanidis, S., Kawakami, R. K., Awschalom, D. D., and Roukes, M. K. (2004). *Nature* **431**, 52.
[143] Tang, H. X., Kawakami, R. K., Awschalom, D. D., and Roukes, M. K. (2006). *Phys. Rev. B* **74**, 041310(R).
[144] Baxter, D. V., Ruzmetov, D., Schreschiligt, J., Sasaki, Y., Liu, K., Furdyna, J. K., and Mielke, C. H. (2002). *Phys. Rev. B* **65**, 212407.
[145] Jungwirth, T., Abolfath, M., Sinova, J., Kučera, J., and MacDonald, A. D. (2002). *Appl. Phys. Lett.* **81**, 4029.
[146] von Molnár, S., and Kasuya, T. (1968). *Phys. Rev. Lett.* **21**, 1757.
[147] Okabayashi, J., Kimura, A., Rader, O., Mizokawa, T., Fujimori, A., Hayashi, T., and Tanaka, M. (1998). *Phys. Rev. B* **58**, R4211.
[148] Kawabata, A. (1980). *Solid State Commun.* **34**, 431.
[149] He, H. T., Yang, C. L., Ge, W. K., Wang, J. N., Dai, X., and Wang, Y. Q. (2005). *Appl. Phys. Lett.* **87**, 162506.
[150] Honolka, J., Masmanidis, S., Tang, H. X., Awshalom, D. D., and Roules, M. L. (2007). *Phys. Rev. B* **75**, 245310.
[151] Wagner, K., Neumaier, D., Reinwald, M., Wescheider, W., and Weiss, D. (2006). *Phys. Rev. Lett.* **97**, 056803.
[152] Katsumoto, S., Oiwa, A., Iye, Y., Ohno, H., Matsukura, F., Shen, A., and Sugawara, Y. (1998). *Phys. Status Solidi B* **205**, 115.
[153] Pappert, K., Schmidt, M. J., Hümpfner, S., Rüster, C., Schott, G. M., Brunner, K., Gould, C., Schmidt, G., and Molenkamp, L. W. (2006). *Phys. Rev. Lett.* **97**, 186402.
[154] Chiba, D., Yamanouchi, M., Matsukura, F., Dietl, T., and Ohno, H. (2006). *Phys. Rev. Lett.* **96**, 096602.
[155] Tatara, G., and Fukuyama, H. (1997). *Phys. Rev. Lett.* **78**, 3773.
[156] Miyake, K., Shigeto, K., Mibu, K., Shinjo, T., and Ono, T. (2002). *J. Appl. Phys.* **91**, 3468.
[157] Yamanouchi, M., Chiba, D., Matsukura, F., and Ohno, H. (2004). *Nature* **428**, 539.
[158] Partin, D. L., Karnezos, M., deMenezes, L. C., and Berger, L. (1974). *J. Appl. Phys.* **45**, 1852.
[159] Levy, P. M., and Zhang, S. (1997). *Phys. Rev. Lett.* **79**, 5110.
[160] Pu, Y., Johnston-Halperin, E., Awshalom, D. D., and Shi, J. (2006). *Phys. Rev. Lett.* **97**, 036601.
[161] Pu, Y., Chiba, D., Matsukura, F., Ohno, H., and Shi, J. (2008). *Phys. Rev. Lett.* **101**, 117208.
[162] Mott, N. F., and Jones, H. (1958). "The Theory of the Properties of Metals and Alloys." Dover, New York.
[163] Ando, K. (2006). *Science* **312**, 1883.
[164] Szczytko, J., Bardyszewski, W., and Twardowski, A. (2001). *Phys. Rev. B* **64**, 075306.
[165] Casey, H. C. Jr., Sell, D. D., and Wecht, K. W. (1975). *J. Appl. Phys.* **46**, 250.
[166] Kuroiwa, T., Yasuda, T., Matsukura, F., Shen, A., Ohno, Y., Segawa, Y., and Ohno, H. (1998). *Electron. Lett.* **34**, 190.
[167] Ando, K., Hayashi, T., Tanaka, M., and Twardowski, A. (1998). *J. Appl. Phys.* **83**, 6548.
[168] Beshoten, B., Crowell, P. A., Malajovich, I., Awshalom, D. D., Matsukura, F., Shen, A., and Ohno, H. (1999). *Phys. Rev. Lett.* **83**, 3073.
[169] Szczytko, J., Mac, W., Twardowski, A., Matsukura, F., and Ohno, H. (1999). *Phys. Rev. B* **59**, 12935.
[170] Hayashi, T., Tanaka, M., Seto, K., Nishinaga, T., and Ando, K. (1997). *Appl. Phys. Lett.* **71**, 1825.
[171] Kimel, A. V., Astakhov, G. V., Kirilyuk, A., Schott, G. M., Karczewski, G., Ossau, W., Schmidt, G., Molenkamp, L. W., and Raising, Th. (2005). *Phys. Rev. Lett.* **94**, 227203.
[172] Héroux, J. B., Ino, Y., Kuwata-Gonokami, M., Hashimoto, Y., and Katsumoto, S. (2006). *Appl. Phys. Lett.* **88**, 221110.
[173] Burch, K. S., Awshalom, D. D., and Basov, D. S. (2008). *J. Magn. Magn. Mater.* **320**, 3207.
[174] Kacman, P. (2001). *Semicond. Sci. Technol.* **16**, R25.
[175] Okabayashi, J., Mizokawa, T., Sarma, D. D., Fujimori, A., Slupinski, T., Oiwa, A., and Munekata, H. (2002). *Phys. Rev. B* **65**, 161203(R).

[176] Szczytko, J., Mac, W., Stachow, A., Twardowski, A., Becla, P., and Tworzydło, J. (1996). *Solid State Commun.* **99**, 927.
[177] Heimbrodt, W., Hartmann, Th., Klar, P. J., Lampalzer, M., Stolz, W., Volz, K., Schaper, A., Treutmann, W., Krug von Nidda, H. A., Loidl, T. R., and Sapega, V. F. (2001). *Physica E* **10**, 175.
[178] Śliwa, C., and Dietl, T. (2008). *Phys. Rev. B* **78**, 165205.
[179] Myers, R. C., Poggio, M., Stern, N. P., Gossard, A. C., and Awshalom, D. D. (2005). *Phys. Rev. Lett.* **95**, 017204.
[180] Stern, N. P., Myers, R. C., Poggio, M., Gossard, A. C., and Awshalom, D. D. (2007). *Phys. Rev. B* **75**, 045329.
[181] Zener, C. (1950). *Phys. Rev.* **81**, 440.
[182] Schliemann, J., König, J., and MacDonald, A. H. (2001). *Appl. Phys. Lett.* **78**, 1550.
[183] König, J., Schilermann, J., Jungwirth, J., and MacDonald, A. H. (2003). *In* "Electronic Structure and Magnetism of Complex Materials" (D. J. Singh, and D. A. Papaconstantopoulos, eds.), p. 163. Springer-Verlag, Berlin.
[184] Das Sarma, S., Hwang, E. H., and Priour, D. J. Jr. (2004). *Phys. Rev. B* **70**, 161203(R).
[185] Bhatt, R. N., and Berciu, M. (2001). *Phys. Rev. Lett.* **87**, 10723.
[186] Akai, H. (1998). *Phys. Rev. Lett.* **81**, 3002.
[187] Katayama-Yoshida, H., Sato, K., Fukushima, T., Toyoda, M., Kizaki, H., Dinh, A. D., and Dederichs, P. H. (2006). *Phys. Status Solidi A* **204**, 15.
[188] Park, J. H., Kwon, S. K., and Min, B. I. (2000). *Physica B* **281–282**, 703.
[189] Fillipetti, A., Spaldin, N. A., and Sanvito, S. (2005). *Chem. Phys.* **309**, 59.
[190] Paalanen, M. A., and Bhatt, R. N. (1991). *Physica B* **169**, 223.
[191] Nagai, Y., Kunimoto, T., Nagasaka, K., Nojiri, H., Motokawa, M., Matsukura, F., Dietl, T., and Ohno, H. (2001). *Jpn. J. Appl. Phys.* **40**, 6231.
[192] Hirakawa, K., Oiwa, A., and Munekata, H. (2001). *Physica E* **10**, 215.
[193] Burch, K. S., Shrekenhamer, D. B., Singley, E. J., Stephens, J., Sheu, B. L., Kawakami, R. K., Schiffer, P., Samarth, N., Awshalom, D. D., and Basov, D. N. (2006). *Phys. Rev. Lett.* **97**, 087208.
[194] Jungwirth, T., Sinova, J., MacDonald, A. H., Gallagher, B. L., Novák, V., Edmonds, K. W., Rushforth, A. W., Campion, R. P., Foxon, C. T., Olejník, E., Mašek, J., Eric Yang, S. R., Wunderlich, J., Could, C., Molenkamp, L. W., Dietl, T., and Ohno, H. (2007). *Phys. Rev. B* **76**, 125206.
[195] Paalanen, M. A., Graebner, J. E., Bhatt, R. N., and Sachdev, S. (1988). *Phys. Rev. Lett.* **61**, 597.
[196] Ohno, Y., Young, D. K., Beschoten, B., Matsukura, F., Ohno, H., and Awschalom, D. D. (1999). *Nature* **402**, 790.
[197] Kohda, M., Ohno, Y., Takamura, K., Matsukura, F., and Ohno, H. (2001). *Jpn. J. Appl. Phys.* **40**, L1274.
[198] Jonston-Halperin, E., Lofgreen, D., Kawakami, R. K., Young, D. K., Coldren, L., Gossard, A. C., and Awschalom, D. D. (2002). *Phys. Rev. B* **65**, 041306.
[199] Kohda, M., Kita, T., Ohno, Y., Matsukura, F., and Ohno, H. (2006). *Appl. Phys. Lett.* **89**, 012103.
[200] Van Dorpe, P., Liu, Z., Van Roy, W., Motsnyi, V. F., Sawicki, M., Borghs, G., and De Boeck, J. (2004). *Appl. Phys. Lett.* **84**, 3945.
[201] Sankowski, P., Kacman, P., Majewski, J. A., and Dietl, T. (2007). *Phys. Rev. B* **75**, 045306.
[202] Hayashi, T., Shimada, H., Shimizu, M., and Tanaka, M. (1999). *J. Cryst. Growth* **201/202**, 689.
[203] Chiba, D., Akiba, N., Matsukura, F., Ohno, Y., and Ohno, H. (2000). *Appl. Phys. Lett.* **77**, 1873.
[204] Ohno, Y., Arata, I., Matsukura, F., and Ohno, H. (2002). *Physica E* **13**, 521.
[205] Tanaka, M., and Higo, Y. (2001). *Phys. Rev. Lett.* **87**, 026602.
[206] Julliere, M. (1975). *Phys. Lett.* **54**, 225.
[207] Ohno, H., Akiba, N., Matsukura, F., Shen, A., Ohtani, K., and Ohno, Y. (1998). *Appl. Phys. Lett.* **73**, 363.
[208] Mattana, R., George, J. M., Jaffrés, H., Nguyen Van Dau, F., Fert, A., Lépine, B., Guivarc'h, A., and Jézéquel, G. (2003). *Phys. Rev. Lett.* **90**, 166601.
[209] Ohya, S., Hai, P. N., and Tanaka, M. (2005). *Appl. Phys. Lett.* **87**, 012105.
[210] Ohya, S., Hai, P. N., Mizuno, Y., and Tanaka, M. (2006). *Phys. Status Solidi C* **3**, 4184.
[211] Ohya, S., Hai, P. N., Mizuno, Y., and Tanaka, M. (2007). *Phys. Rev. B* **75**, 155328.
[212] Mizuno, Y., Ohya, S., Hai, P. N., and Tanaka, M. (2007). *Appl. Phys. Lett.* **90**, 162505.
[213] Chiba, D., Sato, Y., Kita, T., Matsukura, F., and Ohno, H. (2004). *Phys. Rev. Lett.* **93**, 216602.

[214] Elsen, M., Boulle, O., George, J. M., Jaffrès, H., Mattana, R., Cros, V., Fert, A., Lemaitre, A., Giraud, R., and Faini, G. (2006). *Phys. Rev. B* **73**, 035303.
[215] Chiba, D., Kita, T., Matsukura, F., and Ohno, H. (2006). *J. Appl. Phys.* **99**, 08G514.
[216] Slonczewski, J. C. (1996). *J. Magn. Magn. Mater.* **159**, L1.
[217] Sankey, J. C., Cui, Y. -T., Sun, J. Z., Slonczewski, J. C., Buhrman, R. A., and Ralph, D. C. (2008). *Nature Phys.* **4**, 67.
[218] Chiba, D., Matsukura, F., and Ohno, H. (2006). *J. Phys. D* **39**, R1.
[219] Moriya, R., Hamaya, K., Oiwa, A., and Munekata, H. (2004). *Jpn. J. Appl. Phys.* **43**, L825.
[220] Rüster, C., Borzenko, T., Gould, C., Schmidt, G., Molenkamp, L. W., Liu, X., Wojtowicz, T. J., Furdyna, J. K., Yu, Z. G., and Flatté, M. E. (2003). *Phys. Rev. Lett.* **91**, 216602.
[221] Rüster, C., Gould, C., Jungwirth, J., Sinova, J., Schott, G. M., Giraud, R., Brunner, K., Schmidt, G., and Molenkamp, L. W. (2005). *Phys. Rev. Lett.* **94**, 027203.
[222] Giddings, A. D., Khalid, M. N., Jungwirth, T., Wunderlich, J., Yasin, S., Campion, R. P., Edmonds, K. W., Sinova, J., Ito, K., Wang, K. Y., Williams, D., Gallagher, B. L., and Foxon, C. T. (2005). *Phys. Rev. Lett.* **94**, 127202.
[223] Saito, H., Yuasa, S., and Ando, K. (2005). *Phys. Rev. Lett.* **95**, 086604.
[224] Yamanouchi, M., Chiba, D., Matsukura, F., Dietl, T., and Ohno, H. (2006). *Phys. Rev. Lett.* **96**, 096601.
[225] Tatara, G., and Kohno, H. (2004). *Phys. Rev. Lett.* **92**, 086601.
[226] Barnes, S. E., and Maekawa, S. (2005). *Phys. Rev.* **95**, 107204.
[227] Lemerle, S., Ferŕe, J., Chappert, C., Mathet, V., Giamarchi, T., and Le Doussal, P. (1998). *Phys. Rev. Lett.* **80**, 849.
[228] Yamanouchi, M., Ieda, J., Matsukura, F., Barnes, S. E., Maekawa, S., and Ohno, H. (2007). *Science* **317**, 1726.
[229] Nguyen, A. K., Skadsem, H. J., and Brataas, A. (2007). *Phys. Rev. Lett.* **98**, 146602.
[230] Tatara, G., Vernier, N., and Ferré, J. (2005). *Appl. Phys. Lett.* **88**, 252509.
[231] Duine, R. A., Núñez, A. S., and MacDonald, A. H. (2007). *Phys. Rev. Lett.* **98**, 056605.
[232] Ohno, H., Chiba, D., Matsukura, F., Omiya, T., Abe, E., Dietl, T., Ohno, Y., and Ohtani, K. (2000). *Nature* **408**, 944.
[233] Chiba, D., Yamanouchi, M., Matsukura, F., and Ohno, H. (2003). *Science* **301**, 943.
[234] Chiba, D., Yamanouchi, M., Matsukura, F., Abe, E., Ohno, Y., Ohtani, K., and Ohno, H. (2003). *J. Supercond.* **16**, 179.
[235] Nazmul, A. M., Kobayashi, S., Sugawara, S., and Tanaka, M. (2004). *Jpn. J. Appl. Phys.* **43**, L233.
[236] Chiba, D., Matsukura, F., and Ohno, H. (2006). *Appl. Phys. Lett.* **89**, 16250.
[237] Biercuk, M. J., Monsma, D. J., Marcus, C. M., Becker, J. S., and Gordon, R. G. (2003). *Appl. Phys. Lett.* **83**, 2405.
[238] Olejník, E., Owen, M. H. S., Novák, V., Mašek, J., Irvine, C., Wunderlich, J., and Jungwirth, T. (2008). *Phys. Rev. B* **78**, 054403.
[239] Stolichnov, I., Riester, S. W. E., Trodahl, H. J., Setter, N., Rushforth, A. W., Edomonds, K. W., Campion, R. P., Foxon, C. T., Gallagher, B. L., and Jungwirth, T. (2008). *Nat. Mater.* **7**, 464.
[240] Chiba, D., Sawicki, M., Nishitani, Y., Nakatani, Y., Matsukura, F., and Ohno, H. (2008). *Nature* **455**, 515.
[241] Koshihara, S., Oiwa, A., Hirasawa, M., Katsumoto, S., Iye, Y., Urano, C., Takagi, H., and Munekata, H. (1997). *Phys. Rev. Lett.* **78**, 4617.
[242] Kanamura, M., Zhou, Y. K., Okunuma, S., Asami, K., Nakajima, M., Harima, H., and Asahi, H. (2002). *Jpn. J. Appl. Phys.* **41**, 1019.
[243] Oiwa, A., Słupinski, T., and Munekata, H. (2001). *Appl. Phys. Lett.* **78**, 518.
[244] Liu, X., Lim, W. L., Titova, L. V., Wojtowicz, T. J., Kutrowski, M., Yee, K. J., Dobrowolska, M., Furdyna, J. K., Potashnik, S. J., Stone, M. B., Schiffer, P., Vurgaftman, I., and Meyer, J. R. (2004). *Physica E* **20**, 370.
[245] Oiwa, A., Mitsumori, Y., Moriya, R., Słupinski, T., and Munekata, H. (2002). *Phys. Rev. Lett.* **88**, 137202.
[246] Kondo, T., Nomura, K., Koizumi, G., and Munekata, H. (2006). *Phys. Status Solidi C* **3**, 4263.
[247] Nazmul, A. M., Amemiya, T., Shuto, Y., Sugawara, S., and Tanaka, M. (2005). *Phys. Rev. Lett.* **95**, 017201.

[248] Wang, J., Khodaparast, G. A., Kono, J., Oiwa, A., and Munekata, H. (2004). *J. Mod. Opt.* **51**, 2771.
[249] Wang, J., Sun, C., Kono, J., Oiwa, A., Munekata, H., Cywiński, Ł., and Sham, L. J. (2005). *Phys. Rev. Lett.* **95**, 167401.
[250] Wang, J., Cotoros, C., Dani, K. M., Liu, X., Furdyna, J. K., and Chelma, D. S. (2007). *Phys. Rev. Lett.* **98**, 217401.
[251] Csontos, M., Mihály, G., Jankó, B., Wojtowica, T., Liu, X., and Fyrdyna, J. K. (2005). *Nat. Mater.* **4**, 447.
[252] Boukari, H., Kossacki, P., Bertolini, M., Ferrand, D., Cibert, J., Tatarenko, S., Wasiela, A., Gaj, J. A., and Dietl, T. (2002). *Phys. Rev. Lett.* **88**, 207204.
[253] Park, Y. D., Hanbicki, A. T., Erwin, S. C. T., Hellberg, C. S., Sullivan, J. M., Mattson, J. E., Ambrose, T. F., Wilson, A., Spanos, C., and Jonker, B. T. (2002). *Science* **295**, 651.
[254] Weisheit, M., Fähler, S., Marty, A., Souche, Y., Poinsignon, C., and Givord, D. (2007). *Science* **315**, 349.
[255] Sato, K., and Katayama-Yoshida, H. (2000). *Jpn. J. Appl. Phys.* **39**, L555.
[256] Pearton, S. J., Abernathy, C. R., Overberg, M. E., Thaler, G. T., Norton, D. P., Theodoropoulou, N., Hebard, A. F., Park, Y. D., Ren, F., Kim, J., and Boatner, L. A. (2003). *J. Appl. Phys.* **93**, 1.
[257] Bergvist, L., Eriksson, O., Kudrnovský, J., Drchal, V., Korzhavyi, P., and Turek, I. (2004). *Phys. Rev. Lett.* **93**, 137202.
[258] Sato, K., Scheika, W., Dederichs, P. H., and Katayama-Yoshida, H. (2004). *Phys. Rev. B* **70**, 201202(R).
[259] Saito, H., Zayets, V., Yamagata, S., and Ando, K. (2003). *Phys. Rev. Lett.* **90**, 207202.
[260] Fukumura, T., Yamada, Y., Tamura, K., Nakajima, K., Aoyama, T., Tsukazaki, A., Sumiya, M., Fuke, S., Segawa, Y., Chikyow, T., Hasegawa, T., Koinuma, H., and Kawasaki, M. (2003). *Jpn. J. Appl. Phys.* **42**, L105.
[261] Toyosaki, H., Fukumura, T., Yamada, Y., Nakajima, K., Chikyow, T., Hasegawa, T., Koinuma, H., and Kawasaki, M. (2004). *Nat. Mater.* **3**, 221.
[262] Sato, K., Katayama-Yoshida, H., and Dederichs, P. H. (2005). *Jpn. J. Appl. Phys.* **44**, L948.
[263] Fukushima, T., Sato, K., Katayama-Yoshida, H., and Dederichs, P. H. (2006). *Jpn. J. Appl. Phys.* **45**, L416.
[264] Singh, R. K., Wu, S. Y., Liu, H. X., Gu, L., Simith, D. J., and Newman, N. (2005). *Appl. Phys. Lett.* **86**, 012504.
[265] Jamet, M., Barski, A., Devillers, T., Poydenot, V., Dujardin, R., Bayle-Guillemaud, P., Rothman, J., Beller-Amalric, E., Marty, A., Cibert, J., Mattana, R., and Tatarenko, S. (2006). *Nat. Mater.* **5**, 653.
[266] Kuroda, S., Nishizawa, N., Takita, K., Mitome, M., Bando, Y., Osuch, K., and Dietl, T. (2007). *Nat. Mater.* **6**, 440.
[267] Dietl, T. (2006). *Nat. Mater.* **290**, 1395.
[268] Ye, S., Klar, P. J., Hartmann, Th., Heimbrodt, W., Lampalzer, M., Nau, S., Torunski, T., Stolz, W., Kurz, T., Krug von Nidda, H. A., and Loidl, A. (2003). *Appl. Phys. Lett.* **83**, 3927.
[269] Shinde, S. R., Ogale, S. B., Higgins, J. S., Zheng, H., Millis, A. J., Kulkarni, V. N., Ramesh, R., Greene, R. L., and Vankatesan, T. (2004). *Phys. Rev. Lett.* **92**, 166601.
[270] Dietl, T. (2006). *Physica E* **35**, 293.
[271] Akinaga, H., Manago, T., and Shirai, M. (2000). *Jpn. J. Appl. Phys.* **39**, L1118.
[272] Zhao, J. H., Matsukura, F., Takamura, K., Abe, E., Chiba, D., and Ohno, H. (2001). *Appl. Phys. Lett.* **79**, 2776.
[273] Shirai, M. (2003). *J. Appl. Phys.* **93**, 6844.

AUTHOR INDEX

Note: page numbers followed by *f* indicates figure and *t* indicates table.

C

D

G

L

N

O

S

T

Z

SUBJECT INDEX

Note: page numbers followed by *f* indicates figure and *t* indicates table.

D

S

T